

Pellet-clad Interaction in Water Reactor Fuels

Seminar Proceedings
Aix-en-Provence, France
9-11 March 2004



Nuclear Science

Pellet-clad Interaction in Water Reactor Fuels

**Seminar Proceedings
Aix-en-Provence, France
9-11 March 2004**

Hosted by
CEA Cadarache/DEN/DEC

In co-operation with
EDF, COGEMA, FRAMATOME ANP, IAEA

© OECD 2005
NEA No. 6004

NUCLEAR ENERGY AGENCY
ORGANISATION FOR ECONOMIC CO-OPERATION AND DEVELOPMENT

ORGANISATION FOR ECONOMIC CO-OPERATION AND DEVELOPMENT

The OECD is a unique forum where the governments of 30 democracies work together to address the economic, social and environmental challenges of globalisation. The OECD is also at the forefront of efforts to understand and to help governments respond to new developments and concerns, such as corporate governance, the information economy and the challenges of an ageing population. The Organisation provides a setting where governments can compare policy experiences, seek answers to common problems, identify good practice and work to co-ordinate domestic and international policies.

The OECD member countries are: Australia, Austria, Belgium, Canada, the Czech Republic, Denmark, Finland, France, Germany, Greece, Hungary, Iceland, Ireland, Italy, Japan, Korea, Luxembourg, Mexico, the Netherlands, New Zealand, Norway, Poland, Portugal, the Slovak Republic, Spain, Sweden, Switzerland, Turkey, the United Kingdom and the United States. The Commission of the European Communities takes part in the work of the OECD.

OECD Publishing disseminates widely the results of the Organisation's statistics gathering and research on economic, social and environmental issues, as well as the conventions, guidelines and standards agreed by its members.

* * *

This work is published on the responsibility of the Secretary-General of the OECD. The opinions expressed and arguments employed herein do not necessarily reflect the official views of the Organisation or of the governments of its member countries.

NUCLEAR ENERGY AGENCY

The OECD Nuclear Energy Agency (NEA) was established on 1st February 1958 under the name of the OEEC European Nuclear Energy Agency. It received its present designation on 20th April 1972, when Japan became its first non-European full member. NEA membership today consists of 28 OECD member countries: Australia, Austria, Belgium, Canada, the Czech Republic, Denmark, Finland, France, Germany, Greece, Hungary, Iceland, Ireland, Italy, Japan, Luxembourg, Mexico, the Netherlands, Norway, Portugal, Republic of Korea, the Slovak Republic, Spain, Sweden, Switzerland, Turkey, the United Kingdom and the United States. The Commission of the European Communities also takes part in the work of the Agency.

The mission of the NEA is:

- to assist its member countries in maintaining and further developing, through international co-operation, the scientific, technological and legal bases required for a safe, environmentally friendly and economical use of nuclear energy for peaceful purposes, as well as
- to provide authoritative assessments and to forge common understandings on key issues, as input to government decisions on nuclear energy policy and to broader OECD policy analyses in areas such as energy and sustainable development.

Specific areas of competence of the NEA include safety and regulation of nuclear activities, radioactive waste management, radiological protection, nuclear science, economic and technical analyses of the nuclear fuel cycle, nuclear law and liability, and public information. The NEA Data Bank provides nuclear data and computer program services for participating countries.

In these and related tasks, the NEA works in close collaboration with the International Atomic Energy Agency in Vienna, with which it has a Co-operation Agreement, as well as with other international organisations in the nuclear field.

© OECD 2005

No reproduction, copy, transmission or translation of this publication may be made without written permission. Applications should be sent to OECD Publishing: rights@oecd.org or by fax (+33-1) 45 24 13 91. Permission to photocopy a portion of this work should be addressed to the Centre Français d'exploitation du droit de Copie, 20 rue des Grands Augustins, 75006 Paris, France (contact@cfcopies.com).

FOREWORD

Once the fuel-clad gap has closed in light water reactors – one to three years after commencing irradiation – the compressive stress experienced by the cladding and due to the primary fluid pressure is reversed to a tensile stress induced by continued fuel swelling. Enhanced clad stress is likely to occur in the region of the pellets' ends, especially when the fuel rod is submitted to power ramps, e.g. in relation with incidental transients in the operation of the reactor. In the presence of aggressive fission products released by the pellets, this situation can lead to stress-corrosion-induced failures resulting in primary water contamination. This risk is an important industrial challenge; it must be demonstrated that margins are guaranteed for the different current situations and the various classes of transients encountered in reactor operation. Hence, the justification for the development of so-called PCI-resistant fuel products.

Pellet-clad interaction (PCI) is clearly one of the important topics with considerable industrial issues requiring further investigation to achieve a higher availability and competitiveness of nuclear power, and possibly leading to new fuel products and qualification programmes. The R&D on the very complex and non-linear, thermal, mechanical, chemical phenomena requires the best equipments and relevant experiments are worthwhile pursuing.

A need was identified by experts to address this topic and to carry out further assessments and required investigations. To this purpose, the Commissariat à l'Énergie Atomique (CEA) Direction de l'Énergie Nucléaire (DEN) agreed to organise a seminar on this subject from 9-11 March 2004 at Aix-en-Provence, France, in co-operation with the Nuclear Energy Agency (OECD/NEA) and the International Atomic Energy Agency (IAEA).

This is the third in a series of three seminars that began with a seminar on Thermal Performance in Light Water (High Burn-up) Fuels held in Cadarache, France on 3-6 March 1998, followed by a second on Fission Gas Behaviour in Water Reactor Fuels, also held at Cadarache on 26-29 September 2000.

The aim of this third seminar was to draw a comprehensive picture of our current understanding of pellet-clad interaction and its impact on the fuel rod under the widest possible conditions, and to review recent advances in this area from both the experimental and modelling points of view.

Among the papers proposed, 36 were accepted for presentation plus one invited paper concerning RIA conditions. The seminar was attended by 140 participants from 20 countries representing 46 different organisations, including research laboratories, fuel vendors, NPP operators, nuclear safety institutions and consultancy firms.

The current proceedings provide a summary of the result of the seminar together with the text of the presentations made. The views expressed are the authors' own and do not necessarily correspond to those of the national authorities concerned.

Programme Committee

Philippe Martin (*Chairman, Scientific Secretary*)
Sylvie Lansart, Thierry Forgeron, Clément Lemaignan, Claude Sainte-Catherine
CEA, France

Jean Christophe Couty, Stéphane Béguin, Jean Christophe Couty
EDF, France

Louis-Christian Bernard
FRAMATOME ANP, France

Wolfgang Wiesenack
Halden Reactor Project, Norway

J. Anthony Turnbull
Consultant, UK

Klaus Lassmann
ITU, Germany

Vladimir Onoufrieu
IAEA, Vienna

Mukesh Tayal
AECL, Canada

Katsuichiro Kamimura
NUPEC, Japan

Ian Palmer
BNFL, UK

Gunnar Lysell
Studsvik, Sweden

Ake Nordstroem
PSI, Switzerland

Suresh Yagnik
EPRI, USA

Michel Billaux
Areva, USA

Enrico Sartori
OECD/NEA

TABLE OF CONTENTS

Foreword		3
Executive Summary.....		9
Session Summaries		13
Seminar Programme		25
SESSION I Opening and Industrial Goals		29
<i>Chair: P. Martin</i>		
<i>S.K. Yagnik, D.J. Sunderland, B.C. Cheng</i>		
Effect of PWR Re-start Ramp Rate on Pellet-cladding Interactions		31
<i>M. Billaux, H. Moon</i>		
Pellet-cladding Mechanical Interaction in Boiling Water Reactors.....		43
<i>S. Béguin</i>		
PCI-related Constraints on EDF PWRs and Associated Challenges		53
<i>P. Van Uffelen, K. Lassmann, A. Schubert, J. van de Laar, Cs. Györi, D. Elenkov, B. Hatala</i>		
Review of Operational Requirements with Respect to PCMI in a VVER and the Corresponding Developments in the TRANSURANUS Code		63
<i>C. Vitanza, J.M. Conde Lopez</i>		
PCMI Implications for High Burn-up Light Water Reactor Fuel in Reactivity-initiated Accidents		79
SESSION II Fuel Material Behaviour in PCI Situation (Part 1)		105
<i>Chairs: P. Blanpain, D. Baron</i>		
<i>V.V. Likhanskii, O.V. Khoruzhii, A.A. Sorokin</i>		
Physical Model Development for Prediction of Rim-layer Formation in UO ₂ Fuel		107
<i>S.K. Yagnik, J.A. Turnbull, R.A. Gomme</i>		
Microstructure Investigations of As-irradiated, Annealed and Power Ramped High Burn-up Fuel		123
<i>H-J. Ryu, K-H. Kang, C-J. Park, J-W. Park, K-C. Song, M-S. Yang</i>		
Effect of Thermal and Mechanical Properties of the DUPIC Fuel on the Pellet-cladding Mechanical Interaction		143

<i>L. Caillot, C. Nonon, V. Basini</i> Out-of-pile and In-pile Viscoplastic Behaviour of Mixed-oxide Fuels	153
<i>D. Baron, D. Laux, G. Despaux</i> Mechanical Characterisation of Irradiated Fuel Materials with Local Ultrasonic Methods.....	169
Fuel Material Behaviour in PCI Situation (Part 2)	183
<i>Chairs: M. Billaux, Y. Guérin</i>	
<i>V.I. Arimescu</i> Fuel Swelling Importance in PCI Mechanistic Modelling	185
<i>J-S. Cheon, Y-H. Koo, B-H. Lee, J-Y. Oh, D-S. Sohn</i> Modelling of a Pellet-clad Mechanical Interaction in LWR Fuel by Considering Gaseous Swelling	191
<i>R.J. White</i> The Reduction of Fission Gas Swelling Through Irradiation-induced Re-solution.....	203
<i>P. Van Uffelen, M. Sheindlin, V. Rondinella, C. Ronchi</i> On the Relations Between the Fission Gas Behaviour and the Pellet-cladding Mechanical Interaction in LWR Fuel Rods	213
SESSION III Cladding Behaviour Relevant to PCI.....	229
<i>Chairs: S.K. Yagnik, C. Lemaignan</i>	
<i>A.V. Smirnov, B.A. Kanashov, D.V. Markov, V.A. Ovchinnikov, V.S. Polenok, A.A. Ivashchenko</i> Pellet-cladding Interaction in VVER Fuel Rods.....	231
<i>L. Desgranges, B. Pasquet, X. Pujol, I. Roure, Th. Blay, J. Lamontagne, Th. Martella, B. Lacroix, O. Comiti, L. Caillot</i> Characterisation of Volatile Fission Products, Including Iodine, After a Power Ramp	241
<i>D. Le Boulch, L. Fournier, C. Sainte-Catherine</i> Testing and Modelling Iodine-induced Stress Corrosion Cracking in Stress-relieved Zircaloy-4.....	253
<i>S. Van den Berghe, A. Leenaers, B. Vos, L. Sannen, M. Verwerft</i> Observation of a Pellet-cladding Bonding Layer in High-power Fuel	265
<i>G. Lysell, K. Kitano, D. Schrire, J-E. Lindbäck</i> Cladding Liner Surface Effects and PCI.....	273

SESSION IV	In-pile Rod Behaviour	279
	<i>Chairs: W. Wiesenack, S. Lansiant</i>	
	<i>A.V. Bouroukine, G.D. Lyadov, S.V. Lobin, V.A. Ovchinikov, V.V. Novikov, A.V. Medvedev, B.I. Nesterov</i>	
	Results of WWER High Burn-up Fuel Rod Examinations in the Process of and After Their Testing in the MIR Reactor Under Power Cycling Conditions.....	281
	<i>M. Barker, P. Cook, R. Weston, G. Dassel, C. Ott, R. Stratton, D. Papaioannou, C. Walker</i>	
	Ramp Testing of SBR MOX Fuel.....	291
	<i>C. Nonon, J-C. Menard, S. Lansiant, J. Noirot, S. Martin, G-M. Decroix, O. Rabouille, C. Delafoy, B. Petitprez</i>	
	PCI Behaviour of Chromium Oxide-doped Fuel.....	305
	<i>W. Wiesenack, T. Tverberg</i>	
	PCMI of High Burn-up Fuel as Manifested by Different Types of Instrumentation and Measurements in the Halden Reactor Experimental Programme	321
	<i>C. Mougel, B. Verhaeghe, C. Verdeau, S. Lansiant, S. Béguin, B. Julien</i>	
	Power Ramping in the OSIRIS Reactor: Database Analysis for Standard UO ₂ Fuel with Zy-4 Cladding.....	333
	<i>J.C. Killeen, E. Sartori, J.A. Turnbull</i>	
	Experimental Data on PCI and PCMI Within the IFPE Database.....	347
SESSION V	Modelling of the Mechanical Interaction Between Pellet and Cladding (Part 1)	365
	<i>Chairs: P. Garcia, P. Van Uffelen</i>	
	<i>T. Helfer, P. Garcia, F. Sidoroff, J-M. Ricaud, D. Plancq, C. Struzik, L. Bernard</i>	
	Modelling the Effect of Oxide Fuel Fracturing on the Mechanical Behaviour of Fuel Rods	367
	<i>A.C. Marino</i>	
	Crack and Dishing Evolution Models and PCI-SCC Considerations for Fuel Pellets in a Quasi-bi-dimensional Environment	379
	<i>S. Roussette, J-M. Gatt, J-C. Michel</i>	
	Non-linear Behaviour of Multi-phase MOX Fuels: A Micromechanical Approach.....	399
	<i>R. Montgomery, J. Rashid, R. Dunham, O. Ozer, S.K. Yagnik, R. Yang</i>	
	The Mechanical Response of Cladding with a Hydride Lens Under PCMI Loading Conditions.....	413
	<i>Y-M. Kim, Y-S. Yang, C-B. Lee, D-H. Kim, Y-H. Jung</i>	
	Assessment of Cladding Relaxation and PCMI Models in INFRA.....	425

Modelling of the Mechanical Interaction Between Pellet and Cladding (Part 2)	439
<i>Chairs: J.A. Turnbull, N. Waeckel</i>	
<i>M. Valach, J. Zymák</i> Two-dimensional (2-D) Pellet-cladding Modelling Using FEM at NRI Rez plc	441
<i>V. Guicheret-Retel, F. Trivaudey, M.L. Boubakar, R. Masson, Ph. Thevenin</i> Modelling 3-D Mechanical Phenomena in a 1-D Industrial Finite Element Code: Results and Perspectives	453
<i>C. Garnier, P. Mailhe, P. Vesco, L.C. Bernard, C. Delafoy, P. Garcia</i> The COPERNIC Mechanical Model and its Application to Doped Fuel	465
<i>V. Novikov, A. Medvedev, G. Khvostov, S. Bogatyr, V. Kuznetsov, L. Korystin</i> Modelling of Thermal Mechanical Behaviour of High Burn-up VVER Fuel at Power Transients with Special Emphasis on the Impact of Fission Gas Induced Swelling of Fuel Pellets	477
<i>F. Bentejac, N. Hourdequin</i> TOUTATIS: An Application of the Cast3M Finite Element Code for PCI Three-dimensional Modelling	495
<i>C. Struzik, D. Planq, B. Michel, P. Garcia, C. Nonon</i> Methodology for Multi-dimensional Simulation of Power Ramp Tests.....	507
<i>G. Zhou, J.E. Lindbäck, H.C. Schutte, L.O. Jernkvist, A.R. Massih</i> Modelling of Pellet-clad Interaction During Power Ramps	519
List of Participants.....	531

EXECUTIVE SUMMARY

Introduction

This was the third in a series of three seminars that began with the seminar on “Thermal Performance of High Burn-up LWR Fuel” held at Cadarache, France, on 3-6 of March 1998, followed by that of “Fission Gas Behaviour in Water Reactor Fuels”, which also took place at Cadarache, from 26-29 September 2000.

The aim of this third seminar was to draw a comprehensive picture of our current understanding of pellet-clad interaction and its impact on the fuel rod, under the widest possible conditions.

Pellet-clad interaction

In PWRs and BWRs, once the fuel-clad gap has closed, one to three years after irradiation started (depending on the materials), the compressive stress experienced by the cladding and due to the primary fluid pressure is reversed to a tensile stress induced by continued fuel swelling.

Enhanced clad stress is likely to occur in the region of the pellets’ ends, especially when the fuel rod is submitted to power ramps, in relation for instance with incidental transients in the operation of the reactor.

In the presence of aggressive fission products (e.g. iodine typically) released by the pellets, this situation can lead to stress corrosion induced failures resulting in primary water contamination.

This risk is an important industrial challenge to demonstrate that margins are guaranteed for the different current situations and for classes of transients encountered in reactors operation, and justifies the development of so-called PCI-resistant fuel products.

Fuel and pellet behaviour mechanisms activated in PCI situations

The behaviour of pellets in the interaction depends on many mechanisms potentially activated prior to, or during PCI, namely:

- Densification/solid fission products and gaseous swelling under irradiation.
- Release of fission gases and volatile species.
- Evolution of thermal conductivity, elasticity constants, thermal and irradiation creep, temperature-induced or microstructure-induced phenomena (porosities, re-crystallisation).
- Geometry of the pellets and their modifications by cracking.

As concerns the clad:

- Evolution of elasticity, plasticity, creep parameters (irradiation, temperature-induced).
- Dependence on the microstructure and manufacturing process and its evolution under fluence.
- Oxidation, hydridation.
- Sensitivity to stress corrosion-cracking.

As concerns the interface:

- Formation of contact materials or bonding layers: zirconia/uranate compound including fission products.
- Friction.

PCI experimental assessment

- The mechanisms described above can be quantified to a certain extent by specific experiments on fresh and irradiated fuel, permitting the development of specific models.
- Integral experiments, using for instance re-irradiation of fuel at different burn-up and subjected to power ramps in MTRs, are also being currently performed.
- The PIE of such experimental rods allows for ridging measurements, detailed cladding examination, enhances knowledge of the structure of the pellets and of the bonding layer.

This assessment generally emphasises the following:

- Clad cracking occurs parallel to the rod axis, in the region of the pellets' ends, and seems to be in relation to the "wheat sheaf" shape of the pellets gained under the influence of the radial temperature gradient.
- Higher burn-up seems to provide an alleviation of PCI in relation to the re-crystallisation in the RIM zone.
- MOX fuels seem to behave better than standard UO₂.
- The dishing of the pellets seems to play a role as it allows the fuel to creep axially, thus alleviating the stress induced in the clad at pellet ends.

Manufacturing and design remedies to avoid PCI

The modification of the microstructure of the fuel is one of the possibilities explored for the enhancement of resistance to PCI. Doped pellets with different additives have been developed and tested. Evolution of the cladding material can also contribute to this resistance.

Other possibilities are currently being investigated, through modification of the geometry of the pellets or specific barriers on the inner surface of the clads (“liner” concept for BWRs for example).

PCI and modelling

There are many incentives to progress on PCI modelling, in order to:

- Establish a basis for understanding the phenomena.
- Rank their relative importance.
- Define relevant experiments.
- Justify evolutions of the design.
- Allow a credible prediction of PCI onset and demonstration of a safe operation of the fuel in-core when validated.

Different thermo-mechanical solutions are developed throughout the world for PCI assessment. They are very challenging as they concern very complex mechanisms with non-linearities of different types. They require checking against extended databases in order to support convincing demonstrations.

SESSION SUMMARIES

Session I – Industrial Goals (*Chair: P. Martin*)

An overview of PCI issues was given from the standpoint of history, as well as of reactor types, constraints on plants operation and assessment methods.

PCI failure occurrence was rather high in the 70s. In the 80s, a number of failures were still observed, especially in BWRs, while some restrictions in reactor operation or specific liner design for clads, based on first assessments, were proposed and applied respectively for PWRs and BWRs.

S. Yagnik presented a PCI assessment method based on the FALCON code. Its result is expressed in terms of a time/temperature/stress cumulative damage index, relying on thermal-mechanical analysis on the whole power history of the fuel, and on data of time to failure tests of pressurised clads filled up with iodine and function of stress level, temperature, burn-up and material. Preconditioning guidelines, ramp rate restrictions, etc., can be usefully derived on the basis of such an index.

M. Billaux described the situation and its evolution on BWRs, which may be a bit more sensitive to PCI (power changes associated with blade pulls especially, can result in high linear-heat-generated rate variations – due also to neutronic specificities of BWRs as axial variation of moderation ratio). He commented on the performance of remedies such as clads with a zirconium layer, but concluded that the benefits of improved products and specific restrictions on manoeuvring are in fact in permanent competition with the will to enhance the performances of the fuels. At present the number of failures in BWRs is again increasing, with no fully clear understanding as to why. He mentioned that liner clads are not considered as a definitive solution to PCI. He also emphasised the importance of QA for pellets, as chipped pellets are clearly a factor favouring PCI failures.

S. Béguin commented on how PCI is managed (successfully in the thousand of reactor years accumulated today) in EDF's 58 PWRs to cope with the guarantee asked for by the regulatory authority to preclude PCI in normal and upset (Class 2) transients. The approach relies on a thermal-mechanical criterion, capable of discriminating failure from non-failure on a dedicated ramp programme on the fuel product concerned. The knowledge of the power history (neutronics, thermal-mechanics) of each rod is necessary. A costly, time consuming experimental programme (necessary for each new product), and a huge amount of calculations are requested. At the end, the plant operating diagram is reduced and extended reduced-power operation times must be monitored by operators (dedicated procedures, credit factor), and in some cases be limited, resulting in capacity and load follow-up limitations. These are the reasons why EDF expects quite a lot from new products, sufficiently compliant with regard to PCI hazard to cancel all types of PCI constraint, by the year 2010.

P. Van Uffelen discussed how the PCI (and also LOCA) approach was modified in Eastern countries when independent regulatory authorities were created in the early 90s and introduced new QA and requirements prior to fuel loading in the reactors. The ITU fuel code TRANSURANUS is used as a basis for the assessment of these situations, though it had to be modified to cope with specific designs (hexagonal lattice, annular pellets), materials (Zr1%Nb) and safety criteria of VVERs. Some limits have also been reviewed: allowable strain for instance, for taking into account the speed of the

transient incident. Adaptations and their validation were presented. They are based on Russian work and on experimental programmes such as SOFIT, the IFPE database, and the OECD Halden Reactor Programme, against which the performances of the code were shown. The work (“EXTRA”) is now directed toward accidental and storage conditions.

The invited paper by C. Vitanza was the opportunity to compare PCMI in a RIA situation and in upset situations. On the basis of the Cabri and NSRR programmes, it was shown that RIA-induced PCMI is also governed by fuel expansion due to the power deposit, but generally starts from the outside of the clad. The corrosion (outside oxidation and hydriding of the outer rim of the clad) is very important as it determines how brittle the clad is. Temperature effect on the clad is moderated (maximal inside), as time does not allow for hydride dissolution, but affects nevertheless clad ductility (making quite a difference between NSRR and Cabri fractures). The strain rate (width of the pulse) effect is also moderated (but linked, at last, to temperature). In RIA, PCMI is stronger at high burn-up due to greater fuel swelling.

As a conclusion of the session, there is no doubt that PCI is still a “hot” topic with considerable industrial issues, involving more availability and competitiveness of nuclear power, and maybe new fuel products and qualification programmes. The R&D on the very complex non-linear, thermal, mechanical and chemical phenomena, with the best equipments and relevant experiments seems worthwhile and fully justifies the dedicated sessions to come. To their greater merit, the sessions to come could emphasise some highest-interest tracks on the basis of the current knowledge.

Session II – Fuel Material Behaviour in PCI Situation (Part 1) (Chairs: P. Blanpain, D. Baron)

The first paper, presented by V.V. Likhanskii (SRC.RF.TRINITI), deals with the development of a physical model to evaluate the rim-layer formation in UO₂ fuel based on the redistribution of vacancies close to the dislocations, and the increased mobility of gas atoms, with a relation between the Xe effective diffusion coefficient and the vacancy concentration. The rim bubble growth is made easier by the pinning on dislocation intersections. New irradiation-induced effects of Xe atoms drift in vacancy concentration gradient and Xe redistribution to the vacancy rich regions of the fuel grain are discussed. The assumption proposed is that the main dislocation source is the grain boundary. As a consequence, the dislocation density in the grain volume is inversely proportional to its average radius. In this way, the author explains why large initial grains delay fuel restructuring.

The second paper, presented by Suresh Yagnik (EPRI), is a compilation of all data acquired over the past 10 years on the fuel micro-structural transformation on fuel disc specimens and standard fuel pellets. Conclusions are proposed as concerns the gas localisation and grain boundary interlinkage state, depending upon the local operating conditions and local burn-up reached. The consequences of a RIA transient and fuel dispersal risks are discussed. It is concluded that further works conducted to explore more widely the fuel dispersal phenomenon and quantify the energy released as a function of burn-up, restraint level and heating rates are required.

The third paper, presented by Ho Jin Ryu (KAERI), focuses on the effect of the use of DUPIC fuel, with different thermal and mechanical properties, on the rod PCMI behaviour. The Young’s modulus is assumed not to vary with burn-up, but only with the porosity. DUPIC fuel has a Young’s modulus 5% higher than standard UO₂, and a creep rate about 50 times lower. It is concluded that a decrease in the fuel thermal conductivity results in a large change of the fuel performance of this fuel design. It is also concluded from statistical sensitivity analysis that the fabrication parameter could be optimised to reduce PCMI failure risk in the DUPIC fuel.

The fourth paper, presented by Laurent Caillot (CEA), deals with out-of-pile and in-pile MOX fuel viscoplastic behaviour. The fact that MOX fuel tested under transient conditions behaves particularly well compared to standard UO₂ fuel is discussed. Differences at low burn-up are partly explained by the intrinsic properties of the material, mainly due to the larger primary creep rate and a higher creep rate at low and intermediate stresses. About their amplification at higher burn-up, the microstructural evolution of the Pu clusters and different oxidation of the fuel are likely to be involved. It is concluded that further data are needed to resolve remaining uncertainties as to the different possible explanations.

The last paper, presented by Daniel Baron (EDF), describes a device based on focalised acoustic techniques which has been developed over the past six years, in order to perform local elastic modulus measurements on fuel pellet cross-sections prepared for optical analysis. Firstly, the database shows the predominant effect of the porosity volume fraction and the decrease of the elastic modulus with the accumulation of fission products. A recovery is observed which is likely related to the gaseous fission products' mobility during rim formation or operating at high temperature. This device development is part of a larger project whose goal is to establish overall mechanical properties' evolution in irradiated fuel, both out-of-pile and in-pile. This work has already started with ITU (out-of-pile micro-indentation) and Studsvik (in-pile indentation). Further sponsors would, of course, be a welcome development.

Discussions

The chemical evolution of the fuel material inherent to the local fuel transmutation and local thermal conditions induces an evolution of the fuel materials' local properties, both thermal and mechanical. This is obvious for the fuel regions concerned by the high burn-up structure transformation, but is true for the rest of the material as well. As soon as irradiation starts, a new equilibrium is established in the material defects, particularly in the oxygen sub-lattice. Depending upon the local temperature, the total amount of irradiation defects reaches a balance depending upon the thermal recovery.

It is therefore difficult to trust the validity of data properties acquired on fresh fuel material to accurately compute the in-pile fuel rod thermo-mechanical behaviour and perform the PCMI 3-D calculations. Over the past twenty years a large amount of work has been performed on the fuel thermal properties up to 100 GWd/tM (NFIR, HBRP, HRP experiments). The mechanical properties database is still poor as concerns out-of-pile micro-hardness tests (Jose Spino) and the following of cladding deformation on instrumented rods.

Work on HBS transformation and MOX fuel particularities show that further investigations are needed to understand these changing material properties with regard to the PCMI behaviour.

Recommendations

- 1) More effort is needed to develop clever devices able to provide data on the evolution of the fuel mechanical properties with local burn-up and temperature.
- 2) In order to better understand the reason for MOX fuel's good PCMI behaviour, further work is necessary.
- 3) For the case of rapid transients, further studies should be carried out to more widely explore the fuel dispersal phenomenon and quantify the energy released as a function of burn-up, restraint level and heating rates.

Session II – Fuel Material Behaviour in PCI Situation (Part 2) (Chairs: M. Billaux, Y. Guérin)

Session II.2 addressed the interaction between the stress field and the fission gas behaviour in the fuel pellet.

An increase in the linear heat generation rate may induce important stresses in pellet and cladding. At low temperature the stresses mainly result from fuel thermal expansion. But at high temperature the contribution of fuel gaseous swelling becomes significant. In order to determine the severity of pellet-cladding mechanical interaction (PCMI), all modern fuel performance codes take into account gaseous swelling during power increase.

On the other side the stress field in the fuel pellet plays a significant role in the fission gas behaviour. A high hydrostatic stress resulting from PCMI inhibits gaseous swelling by hot pressing of the inter-granular porosity, and therefore also limits fission gas release.

V.I. Arimescu (AREVA, USA) described a mechanistic gaseous swelling model as well as the multiple interactions between gaseous swelling and the pellet and cladding mechanics. Gaseous swelling is assumed to come from inter-granular bubbles only. The important role of gaseous swelling under ramp conditions is illustrated by the calculation of three Mark-BEB PWR fuel rods irradiated to 62 MWd/kgU in Arkansas Unit 1 and subjected to power ramps to peak power levels of 39.5, 42 and 44 kW/m in the Studsvik reactor. The results show that gaseous swelling accounts for as much as half of the permanent cladding diametral deformation.

J-S. Cheon, *et al.* (KAERI) described a finite-element model based on ABAQUS to describe the mechanical behaviour of the pellet-cladding system. The model is linked with the fuel performance code COSMOS that also includes an integrated fission gas release and gaseous swelling model. The effect of the hydrostatic pressure on gaseous swelling is taken into account, as well as the influence of the friction factor between pellet and cladding. The PCMI model was verified by calculating a PWR MOX rod irradiated to 25 MWd/kgMOX and subjected to five successive power ramps at increasing ramp terminal levels. Each ramp has been followed by a relaxation period of about 24 hours at ramp terminal level (phases 1 to 5). By switching on and off the gaseous swelling model it is demonstrated that the contribution of gaseous swelling on the cladding elongation is small at low power (phase 1), but significant at high power level (phase 5).

For R.J. White (BNFL) the principal driving force for PCI is provided by the two components of gaseous swelling: the intra-granular and inter-granular bubbles. During power transients the finely distributed intra-granular porosity increases with a faster kinetics than the coarse inter-granular porosity. Both processes are constrained by the effect of irradiation induced re-solution. This is illustrated by the comparison between the swelling behaviours of two AGR rods base-irradiated to burn-ups of 12-15 GWd/tU and ramped in the Halden reactor. Both rods were subjected to slow ramps in which the power increased over a period of 45 minutes. One was followed by two fast ramps and then discharged. The other one was maintained at low power for an additional 28 days prior to discharge. Extensive SEM analysis was performed that showed that both intra-granular and inter-granular swelling significantly decrease during the extended period at low power. An irradiation-induced re-solution mechanism is proposed to explain that reduction.

P. Van Uffelen (ITU), *et al.* performed a review of the in-pile and out-of-pile tests reported in the literature describing the effect of the stress distribution in the pellet on fission gas release and gaseous swelling. This was followed by a second literature review assessing the validity of various pellet mechanical models and the use of the hydrostatic stress in the gaseous swelling models. They underline the imperfect modelling of the stress distribution in cracked pellets that would require a 3-D modelling

of the pellet, as well as the limited amount of reliable experimental data. A new experimental device is being developed at ITU that will bring complementary information on the interaction between the fission gas behaviour and the stress distribution in the pellets. One of the proposed experiments consists in analysing the effect of hydrostatic stress via a variable helium pressure, in combination with a variable temperature level in a high burn-up fuel rod segment.

In conclusion, two points seem well established:

- Gaseous swelling has a significant impact on PCI. Fuel failures usually arise only through the additional strains produced by fuel gaseous swelling.
- The stress distribution in the pellet has an important effect on fission gas release and swelling.

There is, however, a need for improvement in the following fields:

- The relative importance of intra-granular swelling is still subject to controversy.
- Reliable experimental data are needed to better characterise fuel gaseous swelling (including irradiation-induced gas atom resolution) under different conditions of temperature, stress and fission rate.
- Despite considerable improvements in pellet mechanical modelling over the last decade, efforts should be pursued. A better characterisation of the local stress (stress tensor against hydrostatic pressure) might be necessary for a comprehensive modelling of the different ways stresses affect the fission gas behaviour. Multi-dimensional mechanical models might help.

It is also recommended to revisit the existing fuel performance databases and re-analyse them with a focus on gaseous swelling.

Gaseous swelling is likely to be a major field of development in the coming years.

Session III – Cladding Behaviour Relevant to PCI (*Chairs: S.K. Yagnik, C. Lemaignan*)

This session contained five excellent papers which addressed experimental observations regarding PCI behaviour.

The first paper concerned PCI behaviour in VVER fuel rods. It presented up to five cycles of PIE data. The key conclusion was that with a large as-fabricated gap, reported cladding strains (maximum ~0.3%) are still well below the allowable limit of 0.4% even at high burn-ups. Further, since VVER fuel behaviour under transient conditions was also the subject of two additional papers in the seminar, collectively these papers will certainly prove useful in modelling and validating predictions of VVER fuel behaviour.

The second paper provided interesting observations concerning volatile fission products after a power ramp, employing SIMS and X-ray mapping techniques. Results showed that Cs and I are not necessarily co-located in the fuel. While some CsI was observed, there was clear evidence of free Cs and I as well. An important question concerned the role of Cd, which could be pursued in the future using these techniques.

The third paper on testing and modelling of I-SCC phenomenon presented useful data on hoop strain versus failure times in an iodine environment on unirradiated and irradiated tubing samples. The two types of samples behaved very differently. It was noted that the texture effects are important, especially for unirradiated samples. Such data, especially on newer cladding materials, are requisite inputs for deterministic modelling of PCI failures. The paper presented a failure model based on the data. But other modelling alternatives, e.g. cumulative damage index, could also benefit from these data.

The fourth paper documented important observation about the pellet-clad bonding layer. Complex triplex layers were found to exist in the fuel, especially – and somewhat randomly – within fuel pellet cracks and at pellet-pellet interfaces. The fuel examined was un-ramped fuel of modest burn-ups. Fuel oxygen potential appears to be an important variable in dictating the nature and composition of bonding layer compounds. The main question remains: How does this bonding layer change the gap conductance and what role does it play in localised stresses on the cladding that may trigger PCI phenomenon?

The final paper studied the micro-hardness measurements of a BWR cladding ID barrier layer. It was noted that fission fragments impinging on the clad ID tend to increase local hardness within about 10 μm , which is the expected range of fission fragments. Micro-hardness measurement techniques could provide insight into how clad properties change with burn-up. When employed on samples from sound and failed BWR rods with improved liners, this technique is likely to provide important data concerning secondary fuel degradation phenomenon in BWRs.

Session IV – In-pile Rod Behaviour (*Chairs: W. Wiesenack, S. Lansjart*)

Six papers were presented in Session IV, devoted to rod in-pile behaviour. They covered different experimental techniques and PIE, different fuel types such as standard and doped UO_2 , VVER fuel and MOX fuel, and a range of burn-ups.

It appears that quite a lot of data are available for understanding PC(M)I.

The IFPE database collects an impressive amount of results from experiments performed over the years for different types of reactors. Modellers were encouraged to make active use of this database and to provide feedback to the NEA. Only then can the continued support of this activity be justified, and the database even extended.

The OECD Halden Reactor Project programme provides many answers to the basic questions concerning contact features:

- When does PCMI appear and how does it evolve with increasing burn-up (indications obtained from in-pile clad length measurements)?
- When does the fuel-cladding gap more or less close and what about the impact of a tight fuel column on axial gas communication?
- How does the fuel-cladding system respond to overpressure, e.g. does the gap open or do fuel fragments relocate in the case of lift-off?

It was shown that the VVER fuel has good power cycling capabilities at the burn-up level tested (50-60 MWd/kg). Progressive relaxation of PCMI strains and a shift of PCMI onset to higher power occurred as the number of cycles increased. Also, two successive ramps to high power demonstrated,

by way of simultaneous measurement of axial and diametral strain, that the fuel has good ramping capabilities. Absolutely no detrimental effect on the cladding integrity was evident as a consequence of these operation modes.

The results of a ramp testing programme were also reported for MOX fuel irradiated in the Beznau reactor to about 30 MWd/kg and then ramped in the Petten MTR. No fuel failure was registered although the failure threshold valid for UO₂ fuel was exceeded. This outcome is further confirmation that MOX fuel is more resistant to failure than UO₂ fuel.

The performance of chromia-doped fuel was evaluated in a ramping programme using the OSIRIS MTR. Although the large grains purposely produced by this kind of doping might imply an inferior PCMI behaviour, the contrary was demonstrated by this experimental programme. No failure was observed, which may be explained by the enhanced visco-plasticity of the fuel as well as the development of a favourable crack pattern with numerous radial cracks on the pellet surface mitigating local stress concentrations in the cladding.

Sixteen ramps have been performed on rods with the same PWR design (standard UO₂ fuel with Zy-4 cladding) in the OSIRIS MTR. If failure occurs due to PC(M)I, it is typically an SCC type of fracture at a location close to a radial fuel crack, in the inter-pellet plane. The results show quite deterministic behaviour of these rods. Linear heat rate may be considered as the best experimental parameter available for ranking the two-cycle rods as regards the extent of the cladding damage.

Concerning the central issue of how to prevent PCMI failure while increasing the economics of nuclear plants, many questions remain open. Standard UO₂ fuel with Zy-4 cladding leads to constraints in plant operation. MOX fuel and Cr-doped fuel appear very promising, but the reason why they work as PCI remedies is not clearly evident. Is it fuel cracking propensity by itself, is it enhanced viscosity reducing the hourglass effect by dish-filling and perhaps favouring peripheral cracking? How does gaseous swelling act, with which kinetics?

These questions might be answered using predictive numerical simulation if it were possible to perfectly model all the fuel properties under irradiation conditions. But in a real world with imperfect knowledge, this is not the case – especially when the effects of high power ratings must be considered. Thus there is a need for new experiments in which the contribution of some phenomena is reduced as much as possible. That is the case for gaseous swelling for the zero-hold-time ramp test which has been proposed on Cr-doped fuel. It would be the case for gaseous swelling plus creep at higher ramp rates.

Relevant comparative analytical data with differences in pellet geometry (e.g. short pellets) could contribute as well to this attempt of varying the relative weight of different phenomena.

Finally, the question of concurrent cladding improvement might be posed. Despite the fact that the liner concept is more or less abandoned for BWRs due to its possible degradation, the question is whether it is unreasonable to expect benefits from a new cladding concept as well.

Session V – Modelling of the Mechanical Interaction Between Pellet and Cladding (Part 1) *(Chairs: P. Garcia, P. Van Uffelen)*

From the review of experimental data obtained in the OSIRIS reactor, it was concluded that the risk of I-SCC is greatest at the pellet interfaces. In line with this, in Session IV.1, authors naturally resort to multi-dimensional modelling in order to describe the specific state of the strain/stress state of the cladding. Furthermore, fuel fracturing appears to have significant consequences on the behaviour

of oxide fuel, in particular on PCMI. This also transpires from the experimental data presented in Session 4 on Cr-doped fuel where the question arose as to whether creep or cracking could account for the improved PCI resistance.

With the introduction of mixed-oxide fuels in LWRs as well as the increase of the fuel assembly discharge burn-up in UO₂ fuel, there is a need to account for the heterogeneous and/or porous microstructure in the thermomechanical analysis of fuel rods. In this respect, one paper describes a novel way of generating visco-plastic fuel behaviour laws for heterogeneous fuels (MOX, IMF, etc.) based on the knowledge of its macroscopic behaviour, its microstructure and on the behaviour of one of the phases.

In design basis accident conditions, the multi-dimensional approach also turned out to be necessary to improve the assessment of the critical conditions for hydrided cladding failure. As a corollary to this analysis, it was pointed out that one should be careful when applying the results from out-of-pile burst tests to in-pile conditions because of the differences between pressure-driven and displacement-driven cladding deformation. Finally, the friction between cladding and fuel was also shown to play a significant role in quantitative analyses in all operating conditions, although very different values are being applied.

Perspectives for model development that emerge from this session include de-cohesive models as an alternative to diffusive crack models to reach a more physical fuel cracking description, and non-uniform transformation field analysis to account for the heterogeneity in some nuclear fuels.

Session V – Modelling of the Mechanical Interaction Between Pellet and Cladding (Part 2) *(Chairs: J.A. Turnbull, N. Waeckel)*

There were seven papers in this session devoted to modelling the mechanical interaction between fuel and cladding. In the period between FUMEX-I and the present meeting, it was good to see the interest and progress made in addressing this topic.

The focus of fuel modelling has progressed from thermal performance and fission gas release (FGR) to pellet-clad mechanical interaction (PCMI). Whereas there has been a common approach to thermal performance and FGR involving 1-D/1.5-D codes, there has been a divergence in approach when moving forward to mechanical interaction involving either 1-D/1.5-D or 3-D codes. Time will tell which is the more successful, however, for applications where many calculations need to be performed “on-line” with reactor operation there is a clear need for the faster-running 1-D/1.5-D codes possibly with input from the slower-running 3-D codes in order to provide “fixes” for simpler models of the PCMI phenomenon.

Many papers concentrated on the behaviour of the pellet, with little attention paid to modern cladding’s improved properties.¹ This is understandable, as the driving force is thermal expansion and the swelling of the pellet. As gaseous swelling is the most onerous contribution to clad strain, it is appropriate to concentrate on this phenomenon. Papers presented in other sessions indicated that there was a large amount of data available on this topic, and modellers were urged to use these data extensively in their development and validation of PCMI models, concentrating in the first instance on

¹ The different types of cladding can be easily differentiated in term of mechanical properties or in-reactor corrosion performance, but in terms of sensitivity to SCC, separate effect tests are not yet capable of discriminating an alloy A from an alloy B. If we assume that the amount of fission products necessary to initiate a SCC crack is always available, one can conclude that it is more relevant to focus on investigating the driving forces (i.e. the pellet induced stresses to the cladding) that can be different from one type of pellet to another.

predictions of clad diameter change and ridge height growth during periods of transient over-power. Additional attention was required in modelling fuel cracking and its consequence, pellet-clad friction coefficient and pellet creep. Regarding the friction coefficient, there was a large variation in the values chosen in the papers presented.

At present the codes are in a development phase with limited testing against experimental data. The ultimate goal of these codes is the prediction of failure probability, which is a future stage in the development of most codes. Again, there were much data openly available from ramp tests in which failure thresholds had been identified for both PWR and BWR systems. It was stressed that for accurate predictions of failure, a large database is required to maximise statistics between failure and non-failure. In addition, it is clear that there is a difference in behaviour between standard UO₂, UO₂ with additives and MOX. It is necessary to explore these differences and understand why the fuels behave differently. In this way, further improvements in PCI-resistant products will be possible. Such a programme including both modelling and experimental approaches is necessary to achieve the goal of a “zero-failure policy”, whereby failure by PCI no longer occurs and is thus no longer a safety issue.

Panel summary (C. Lemaignan)

Towards a PCI-free fuel!

After a very fruitful meeting during which the contributions were numerous and the discussions intense, a few general and/or prospective comments can be proposed. Since all session chairmen have made detailed and accurate reports on the major issues of each session, the purpose of the following comments is mainly to stress interactions between the different aspects presented and to highlight a few points of potential concern or scientific interest.

The three main parameters controlling the failure during a PCI event are the stress distribution, the internal chemistry close to the inner surface of the cladding and the material properties. It should not be forgotten that the fuel rod acts as a system and that these different contributions interact with each other. The meeting has been a very good opportunity to stress this point and the development of thermo-mechanical computer codes, aiming at the integration of the fuel rod system, clearly contributes to such approach. The corresponding modelling procedures are used for a better knowledge of the interacting processes. They are benchmarked with several analytical or global experiments and are developed with an expected capability of forecasting the potential failure of a rod, or the margins for a specific operational condition.

With respect to the mechanical stress state, the interaction between oxide and cladding requires its computation in the two materials with similar accuracy. However, the stress state is not a scalar, but is defined by a tensor. Also, the definition of the stresses can be performed at different scales. For crack initiation, it should be analysed almost at the grain scale, while the analysis of the failure risk of the rods in a core would clearly require a much larger mesh. A critical point is therefore the procedures used for the reduction and condensation of the detailed analysis to the macroscopic scale.

Among the major points raised during the meeting, the large contribution of the gas bubble swelling during a power transient to the stress development in the cladding has been confirmed. The total strain induced by the gas bubble precipitation and fuel swelling has been measured in a very few cases; however, the detailed kinetics of this swelling, for given BU, temperature and hydrostatic stress state histories, is still practically unknown. Due to the visco-elastic behaviour of the oxide and the cladding, the exact knowledge of the kinetics of this swelling will be a critical parameter. In this respect, experiments on fuel rod transients during which the local diameter strain is measured continuously are strongly recommended.

The significant progresses made in thermo-mechanical computations should also not be damped by using a set of physical properties of the materials of low accuracy. The quality of the computations will never deliver results of better value than those limited by the data. This supports the interest for a reassessment of them as described below. This progress also induces a strong requirement for a much finer definition of the boundary conditions (small changes in the geometry of the fuel rod have been shown to severely affect the local stress state...).

The impact of chemistry induced by fission products on the PCI failure is not questionable. It remains, however, that the exact state of the fuel inside the rod is still far from being clearly described. The moderate temperature of the fuel during normal operation is not high enough to obtain phase equilibrium as expected from thermodynamics. However, for high BU fuel, the driving force for such equilibrium is highly increased and observations confirm the existence of phases not observed at lower BU. Due to the observed mitigation of the I-SCC by oxygen, and possibly other species, an improved knowledge of the actual chemistry would allow major progress in understanding PCI mechanisms. With respect to this, the apparent improvement in PCI resistance observed for high BU, Cr-doped or MOX fuel could be due not only to the better visco-plasticity of the fuel, but possibly to an unexpected chemical phenomenon. Detail observations of the phases present in the rod, and specifically in the fuel-cladding gap, would be useful for a better modelling of the chemical environment of the stressed cladding.

As concerns the material properties, most have been considered as “known” for quite some time. However, as the irradiation is known to significantly affect the physical properties of the fuel rod materials, progress is required for their definition in order to maintain at parity computation techniques and physical property data. This will specifically concern thermo-elastic properties (Young’s modulus, thermal expansion coefficient, heat conductivity and the kinetics of their evolutions during thermal recovery) as well as the mechanical properties (yield strength, creep behaviour). In addition, some properties may have a very different meaning if the conditions of use are different from those of data acquisition. This would specifically be the case for the plastic strain behaviour of irradiated Zr alloys. In the case of such a strain softening material, the loading scheme drastically affects the behaviour: pressure tests are load-controlled and will lead to local instability and very limited total strain to failure, while PCI loading is a local strain-controlled loading procedure. The local reduction of strength induced by the strain does not produce local instability.

For the future, the scientific community concerned with the analysis of the behaviour of the fuel should probably follow more closely what is under promising development in the field of material science: computational material science. Due the difficulties and costs in testing materials (including power ramping) and performing very fine examinations on irradiated materials, the rising science of knowledge of the materials as deduced from computations is a major challenge for the forthcoming years. For the fuel rod chemistry and the reaction at the crack tip in the cladding, quantum chemistry and mesoscopic approaches seem to be appropriate tools for inter-atomic interaction description. Regarding the irradiation point defects evolution and their impact on microstructure, molecular dynamics or kinetic Monte Carlo will allow, in the near future, to forecast fission gas bubble nucleation and growth or creep properties of UO_2 or other doped oxides.

These techniques should not ignore the large databases acquired in the early days of the nuclear industry. If detailed experimental conditions are not always reported, a mine of highly valuable scientific results is laying in the drawers of our predecessors. A good use of them would require a continuous feedback on their usability. The power ramp data collected by the NEA is a significant step towards the revitalisation of such old works. Similarly, thermodynamics was in its glory a few decades ago; it now receives much less consideration.

At the end of this meeting one could expect a significant reduction of the PCI constraints imposed on the utilities in the forthcoming years, either by reduction of the susceptibility of the fuel rods to such failure mechanisms, or by reduction of the power manoeuvres responsible for PCI. Could such studies therefore be useless, in the possible context of reduction of PCI frequency? Without being pessimistic, the history of the nuclear industry has shown us that unexpected behaviours are ready to occur when pushing the components to a higher duty, a longer life or reduced operational margins. A scientific knowledge of the fuel behaviour beyond what is strictly required to avoid any PCI failure – and we are unfortunately far from such a scientific knowledge – will not be a waste of time or money, but will allow us to react more efficiently in case of such events occurring.

Overall recommendations and open questions

Fuel material behaviour in PCI situation

- 1) More efforts are needed to develop “clever” devices able to provide data on the evolution of fuel mechanical properties with local burn-up and temperature.
- 2) Reliable experimental data are needed to better characterise fuel gaseous swelling kinetics (including irradiation-induced gas atom re-solution) under different conditions of temperature, stress and fission rate, including the relative importance of intra-granular swelling. Attention should be paid to evaluating the gaseous swelling driving force and its contribution to the local mechanical loading of the clad.
- 3) Despite considerable improvements of the pellet mechanical modelling over the past decade, further improvements are required. A better characterisation of the local stress (stress tensor against hydrostatic pressure) might be necessary for the comprehensive modelling of the different ways stress affects the pellet progressive additional cracking, the visco-plastic flow and the fission gas behaviour. This may necessitate 3-D mechanical modelling.

Cladding behaviour relevant to PCI

- 1) Stress corrosion cracking, especially in an iodine atmosphere, is known to be responsible for PCI failures. Despite many efforts and good analytical work, the need still exists for developing mechanistic models able to reproduce the mechanical tests performed on pressurised tubes as well as to predict the clad crack propagation under true transient conditions. Knowing that the SCC cracks preferentially develop at the pellet-pellet interface and in front of pellet cracks, the need for developing duly validated 3-D models becomes clear.
- 2) In order to better simulate potential clad damage due to power transients, further work is also recommended concerning the migration of potentially aggressive chemical species such as I, Cs, Cd. Since the papers presented focused on the behaviour of I and, to a lesser extent, that of Cs, it is recommended that the experimental efforts be now directed toward understanding the role of Cd.
- 3) It is recommended that micro-hardness measurements be pursued to better quantify the evolution of micro-hardness as a function of burn-up. Such data would be useful not only for the understanding of PCI-SCC, but also other phenomena such as secondary damage in failed fuel rods.

In-pile rod behaviour

- 1) The reasons why MOX fuel and Cr-doped fuel appear to behave better with respect to conventional UO₂ under PCI conditions must be tackled further: Is it fuel cracking propensity by itself, and/or is it enhanced viscosity reducing the hourglass effect by dish-filling and perhaps favouring peripheral cracking? How does gaseous swelling act, with which kinetics? So there is a need for new experiments in which the contribution of the individual phenomena is evidenced. That is the case for gaseous swelling for zero-hold-time ramp tests which have been proposed on Cr-doped fuel. It would be the case for gaseous swelling plus creep at higher ramp rates. In parallel, there is a need for experiments to study the high-temperature phenomena not far from fusion conditions without any cladding damage (columnar grain growth, central void formation, etc.).
- 2) Relevant comparative analytical data with differences in pellet geometry (e.g. short pellets) could contribute as well to this attempt of varying the relative weight of different phenomena.
- 3) The question of the concurrent cladding improvement might be asked. What kind of benefit can be expected from a new cladding concept?

Modelling of the mechanical interaction between pellet and cladding

- 1) The development of de-cohesive models versus diffuse crack models appears promising for the treatment of pellet cracking.
- 2) Mechanical phenomena are assessed differently by 1-D/1.5-D and 3-D models, only the latter having the potential to approach the phenomenon with accuracy. Nevertheless, running times are long and the results are still dependent on materials data and interaction prediction. Thus, it seems that both models should be developed, fast-running 1-D/1.5-D models taking profit of the comprehensive view available from 3-D ones.
- 3) The developments on pellet mechanical models to cope with cracking, and the provision of an accurate description of heterogeneous products, should be used as inputs to PCMI codes and could help to understand the differences exhibited by doped fuels and MOX.
- 4) The ultimate goal of all fuel vendors should be a failure-free operation, with no limits imposed on operation. PCI-resistant products could contribute (see above), but their good performances have to be demonstrated more widely, through modelling and complementary experiments.
- 5) It is recommended to extend the use of the existing fuel performance databases (e.g. IFPE) for model improvement and validation, and in particular to evaluate PCMI effects on gaseous swelling and vice versa. A FUMEX-III exercise devoted to PCMI/PCI effects should be considered.
- 6) Predictive PCI modelling should be presented, not just explanations after the event.

SEMINAR PROGRAMME

Tuesday, 9 March 2004

Registration

SESSION I Opening and Industrial Goals

Chair: P. Martin (CEA/France)

Opening and welcome

S.K. Yagnik (EPRI), D.J. Sunderland, B.C. Cheng (Anatech)
Effect of PWR Re-start Ramp Rate on Pellet-clad Interactions

M. Billaux (AREVA), H. Moon
Pellet-cladding Mechanical Interaction in Boiling Water Reactors

S. Béguin (EDF)
PCI-related Constraints on EDF PWRs and Associated Challenges

*P. Van Uffelen (ITU), K. Lassmann, A. Schubert, J. van de Laar,
Cs. Györi, D. Elenkov, B. Hatala*
Review of Operational Requirements with Respect to PCMI in a VVER and
the Corresponding Developments in the TRANSURANUS Code

Invited paper:
C. Vitanza (OECD), J.M. Conde Lopez
PCMI Implications for High-burn-up Light Water Reactor Fuel
in Reactivity-initiated Accidents

SESSION II Fuel Material Behaviour in PCI Situation (Part 1)

Chairs: P. Blanpain (FRAMATOME ANP/France), D. Baron (EDF/France)

V.V. Likhanskii (SRC RF TRINITI), O.V. Khoruzhii, A.A. Sorokin
Physical Model Development for Prediction of Rim-layer Formation in UO₂ Fuel

S.K. Yagnik (EPRI), J.A. Turnbull, R.A. Gomme
Microstructure Investigations of As-irradiated, Annealed and Power Ramped High
Burn-up Fuel

H-J. Ryu (KAERI), K-H. Kang, C-J. Park, J-W. Park, K-C. Song, M-S. Yang
Effect of Thermal and Mechanical Properties of the DUPIC Fuel on the
Pellet-cladding Mechanical Interaction

L. Caillot (CEA), C. Nonon, V. Basini
Out-of-pile and In-pile Viscoplastic Behaviour of Mixed-oxide Fuel

D. Baron (EDF), D. Laux, G. Despaux
Mechanical Characterisation of Irradiated Fuel Materials with Local Ultrasonic Methods

SESSION II Fuel Material Behaviour in PCI Situation (Part 2)

Chairs: M. Billaux (AREVA/USA), Y. Guérin (CEA/France)

V.I. Arimescu (AREVA)
Fuel Swelling Importance in PCI Mechanistic Modelling

J-S. Cheon (KAERI), Y-H. Koo, B-H. Lee, J-Y. Oh, D-S. Sohn
Modelling of a Pellet-clad Mechanical Interaction in LWR Fuel by Considering Gaseous Swelling

R.J. White (BNFL)
The Reduction of Fission Gas Swelling Through Irradiation-induced Re-resolution

P. Van Uffelen (ITU), M. Sheindlin, V. Rondinella, C. Ronchi
On the Relations Between the Fission Gas Behaviour and the Pellet-cladding Mechanical Interaction in LWR Fuel Rods

Wednesday, 10 March 2004

Registration

SESSION III Cladding Behaviour Relevant to PCI

Chairs: S.K. Yagnik (EPRI/USA), C. Lemaignan (CEA/France)

*A.V. Smirnov, B.A. Kanashov, D.V. Markov, V.A. Ovchinnikov,
V.S. Polenok, A.A. Ivashchenko (SSC RF RIAR)*
Pellet-cladding Interaction in VVER Fuel Rods

*L. Desgranges (CEA), B. Pasquet, X. Pujol, I. Roure, Th. Blay,
J. Lamontagne, Th. Martella, B. Lacroix, O. Comiti, L. Caillot*
Characterisation of Volatile Fission Products, Including Iodine, After a Power Ramp

D. Leboulch, L. Fournier, C. Sainte-Catherine (CEA)
Testing and Modelling Iodine-induced Stress Corrosion Cracking in Stress-relieved Zircaloy-4

S. Van den Berghe (SCK•CEN), A. Leenaers, B. Vos, L. Sannen, M. Verwerft
Observation of a Pellet-cladding Bonding Layer in High-power Fuel

G. Lysell (Studsvik Nuclear AB), K. Kitano, D. Schrire, J-E. Lindbäck
Cladding Liner Surface Effects and PCI

SESSION IV In-pile Rod Behaviour

Chairs: W. Wiesenack (OECD Halden/Norway), S. Lansart (CEA/France)

K. Kamimura (JNESO)

PCMI Behaviour of High Burn-up BWR & PWR Fuels During Power Ramp Test
(Cancelled)

*A.V. Bouroukine, G.D. Lyadov, S.V. Lobin, V.A. Ovchinnikov (FSUE, SCC RF RIAR),
V.V. Novikov, A.V. Medvedev, B.I. Nesterov (FSUE VNIINM)*

Results of WWER High-burn-up Fuel Rods Examinations in the Process of and
After Their Testing in the MIR Reactor Under Power Cycling Conditions

*M. Barker, P. Cook (BNFL), R. Weston, G. Dassel, C. Ott, R. Stratton,
D. Papaioannou, C. Walker*

Ramp Testing of SBR MOX Fuel

*C. Nonon (CEA), J.C. Menard, S. Lansart, J. Noirot, S. Martin,
G-M. Decroix, O. Rabouille, C. Delafoy, B. Petitprez*

PCI Behaviour of Chromium Oxide-doped Fuel

W. Wiesenack (OECD Halden), T. Tverberg

PCMI of High Burn-up Fuel as Manifested by Different Types of Instrumentation
and Measurements in the Halden Reactor Experimental Programme

C. Mougel (CEA), B. Verhaeghe, C. Verdaux, S. Lansart, S. Béguin, B. Julien
Power Ramping in the OSIRIS Reactor: Database Analysis for Standard UO₂ Fuel
with Zy-4 Cladding

J.C. Killeen, E. Sartori, J.A. Turnbull (Consultant)

Experimental Data on PCI and PCMI Within the IFPE Database

SESSION V Modelling of the Mechanical Interaction Between Pellet and Cladding (Part 1)

Chairs: P. Garcia (CEA/France), P. Van Uffelen (ITU Germany)

T. Helfer (CEA), P. Garcia, F. Sidoroff, J-M. Ricaud,

D. Plancq, C. Struzik, C. Bernard

Modelling of the Effect of Oxide Fuel Fracturing on the Mechanical Behaviour
of Fuel Rods

A.C. Marino (CNEA)

Cracks and Dishing Evolution Models and PCI-SCC Considerations for Fuel Pellets in
a Quasi-bi-dimensional Environment

Thursday, 11 March 2004

Registration

SESSION V Modelling of the Mechanical Interaction Between Pellet and Cladding (Part 1, cont.)

Chairs: P. Garcia (CEA/France), P. Van Uffelen (ITU Germany)

S. Roussette (CEA), J-M. Gatt, J-C. Michel

Non-linear Behaviour of Multi-phase MOX Fuels: A Micromechanical Approach

R. Montgomery (Anatech), J. Rashid, R. Dunham, O. Ozer, S.K. Yagnik, R. Yang

The Mechanical Response of Cladding with a Hydride Lens Under PCI Loading
PCMI Conditions

Y-M. Kim (KAERI), Y-S. Yang, C-B.Lee, D-H. Kim, Y-H. Jung

Assessment of Cladding Relaxation and PCMI Models in INFRA

SESSION V Modelling of the Mechanical Interaction Between Pellet and Cladding (Part 2)

Chairs: J.A. Turnbull (Consultant, UK), N. Waeckel (EDF, France)

M. Valach (NRI, REZ), J. Zymák

Two-dimensional (2-D) Pellet-cladding Modelling Using FEM at NRI Rez plc

V. Guicheret-Retel, F. Trivaudet, M.L. Boubakar (MARC),

R. Masson, Ph. Tevenin (EDF)

Modelling 3-D Mechanical Phenomena in a 1-D Industrial Finite Element Code:
Results and Perspectives

C. Garnier (FRAMATOME ANP), P. Mailhe, P. Vesco, L.C. Bernard,

C. Delafoy, P. Garcia

The COPERNIC Mechanical Model and its Application to Doped Fuel

V. Novikov (VNIINM), A. Medvedev, G. Khvostov,

S. Bogatyr, V. Kouznetsov, L. Korystin

Modelling of Thermal Mechanical Behaviour of High Burn-up VVER Fuel at
Power Transients with Special Emphasis on the Impact of Fission Gas Induced
Swelling of Fuel Pellets

F. Bentejac (CEA), N. Hourdequin

TOUTATIS: An Application of the Cast3M Finite Element Code for PCI

Three-dimensional Modelling

C. Struzik (CEA), D. Plançq, B. Michel, P. Garcia, C. Nonon

Methodology for Multi-dimensional Simulation of Power Ramp Tests

G. Zhou (Westinghouse Electric), J.E. Lindbäck,

H.C. Schutte, L.O. Jernkvist, A.R. Massih

Modelling of Pellet-clad Interaction During Power Ramps

PANEL SESSION

End of the seminar

SESSION I

Opening and Industrial Goals

Chair: P. Martin

Introduction by Session Chair

This session undertakes to tell the “story” of PCI, for instance of how it was dealt with in the past by specific manoeuvring criteria, with specific post-refuelling start-up strategies, by the adjustment of linear power and so on, and how there is something of a race between the improvements relative to PCI concerns and the continuous search for higher fuel performances.

Nuclear operators should expose the consequences of remaining constraints and their incentives to alleviate them. PCI shall be examined from the standpoint of different types of water reactors, including CANDU and eastern countries’ VVERs.

This session includes a paper whose subject is a reactivity injection accident; the reason for this is that the organising committee received quite a few proposed papers clearly within the scope of RIA and not on Class 2 transients. It was felt that it was better to have some insight on RIA and subsequently it was decided to invite a paper that should be as neutral as possible so as to bring some elements concerning PCMI into a RIA situation and allow for assessing common (though also specific) issues. RIA will not be examined in further detail during this seminar.

EFFECT OF PWR RE-START RAMP RATE ON PELLETT-CLADDING INTERACTIONS

S.K. Yagnik (EPRI), D.J. Sunderland (ANATECH), and B.C. Cheng (EPRI)

Abstract

To mitigate pellet-cladding interaction (PCI) leading to fuel rod failures, fuel suppliers specify reactor power ramp rate limitations during reactor start-up after an outage. Typical re-start ramp rates are restricted and range between 3-4% per hour of full reactor power above a threshold power level. Relaxation of threshold power and ramp rate restrictions has the potential to improve plant economics.

The paper will compare known re-start power ascension procedures employed in the US, German, French and Korean PWRs after a refuelling outage. A technical basis for optimising power ascension procedures during reactor start-up can be developed using analytical modelling. The main objective of the modelling is to determine the potential for PCI failure for various combinations of threshold power levels and ramp rate levels. A key element of our analysis is to estimate the decrease in margin to cladding failure by ISCC based on a time-temperature-stress failure criterion fashioned after a cumulative cladding damage index. The analysis approach and the cladding damage model will be described and the results from three case studies based on the FALCON fuel rod behaviour code will be reported. We conclude that the PCI behaviour is more affected by ramp rate and threshold power than by the fuel design and that the fuel power history is the most important parameter.

Introduction

Post-refuelling start-up strategies in LWRs depend on several factors, including instrument calibration, coolant chemistry control, and fuel-related ramp rate limitations. Utilities must give careful considerations to optimise the time it takes to return to full power because the area under the curve on the “power vs. time” plot is equivalent to extractable energy, which is directly linked to plant economics.

Power ascensions following refuelling outage may present a greater risk of fuel failures due to the initial lack of fuel conditioning. The fuel is considered “conditioned” once it has operated at a specified power level for a specified time, known as the relaxation time. Typical re-start ramp rates in PWRs are restricted and range between 3-4% per hour of full reactor power above a threshold power level. The intent behind such restrictions is to mitigate potential fuel rod failures due to pellet-cladding interaction (PCI). The implementation of fuel conditioning into re-start operations has resulted in reductions in plant capacity [1]. BWRs have implemented zirconium-lined cladding to substantially mitigate the PCI concerns since the early 1980s. PWRs continue to follow the start-up ramp rate restrictions implemented since the 1970s. Removal or relaxation of any unduly conservative restrictions on the threshold power and ramp rate has the potential to improve plant economics.

Re-start practices

While it is desirable to minimise re-start time (defined as the time needed to reach or exceed 90% of rated thermal power following a refuelling outage), there are certain procedural hold points at intermediate power levels that must be adhered to during a normal re-start. Table 1 summarises a typical scenario in re-starting a PWR.

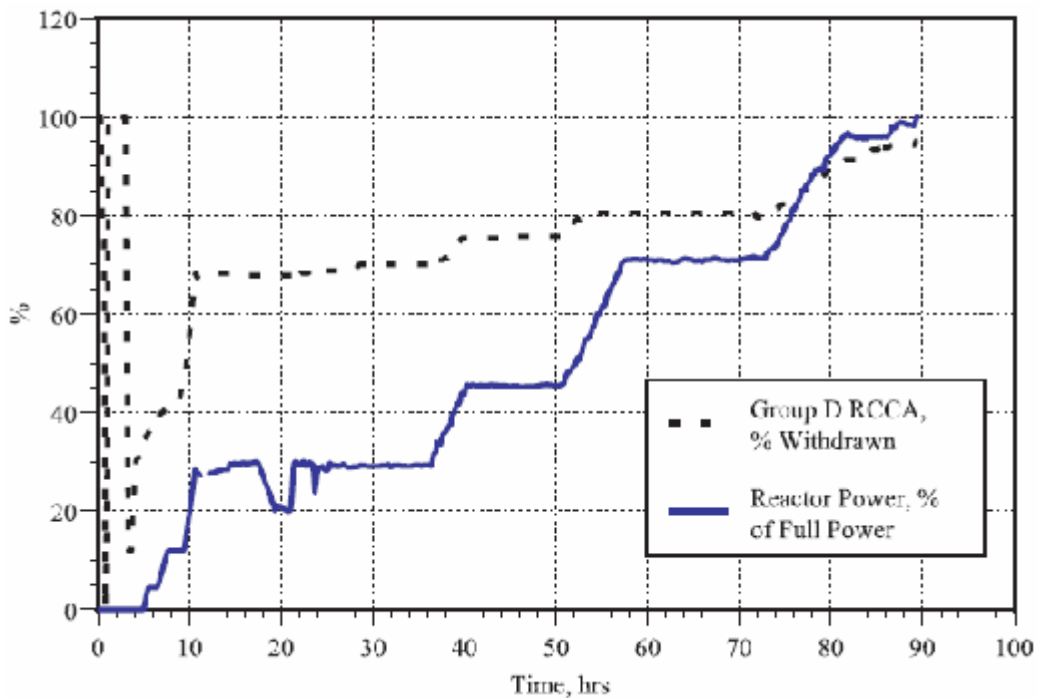
Table 1. Summary of hold points during power ascension after a refuelling outage for a typical Westinghouse NSSS

Power level (%)	Duration* (hrs)	Activity
10-14	1-2	Turbine heat-up and rotation, synchronise generator
28-30	24	Core flux mapping, water chemistry checks
48-50	1-2	Verification of compliance to technical specifications
74-75	18-24	Core flux mapping, water chemistry checks
90	≤ 1	Nuclear instrument calibration
95-96	1	Calorimetric heat balance between primary and secondary sides prior to full power

* The duration of the hold point periods are estimates based on several plants. Actual times vary depending on the individual unit and may be shorter.

As another example, Figure 1 shows the core power level and positions of the Group D control rods [rod control cluster assemblies (RCCAs)] as a function of time during the start-up. In this case, during the period between 0 and 5 hours, zero-power neutronics testing was performed and the Group D control rods were withdrawn and inserted as part of this testing. The power ascension began increasing to approximately 4.5% of full power at which time turbine rolling began. After turbine testing at constant power, the power was increased to approximately 12.7% at which point the turbine/generator was brought on-line. At this power level, the Group D control rods had been withdrawn to 40%. Power was increased to the next hold point of approximately 29% as the control rods were withdrawn to 75%. During the hold, the reactor power was increased very slowly to 30% power, the threshold at which power ramp rate restrictions are imposed. Based on the times and power levels, it is estimated that the

Figure 1. Typical start-up of a US PWR



power ascension rate from 12 to 29% was accomplished at a rate of approximately 16%/hr. The hold at 29-30% power lasted approximately 26 hours, during which time calibration of nuclear instrumentation and secondary side chemistry checks were performed. Subsequently, the full power was attained in three major steps, with intervening hold times, at the rate of ~ 3%/hr.

Current re-start practices in the US, German, French and Korean PWRs have been compared in recent EPRI-led industry studies [2,3]. Typical statistics are compared in Table 2. Compared to the typical US unit represented in Figure 1, the threshold power levels in German units are considerably higher (70%) and thus less restrictive.

PCI phenomenon

PCI-induced fuel failures first surfaced in the early 1970s in several boiling water reactor (BWR) and Canadian (CANDU) power plants. Later, it became recognised as a generic commercial reactor problem. In 1974 an incipient crack was found in an un-failed fuel rod providing unequivocal evidence that the primary mechanism of PCI-induced cladding failures is ISCC [4].

Mechanism

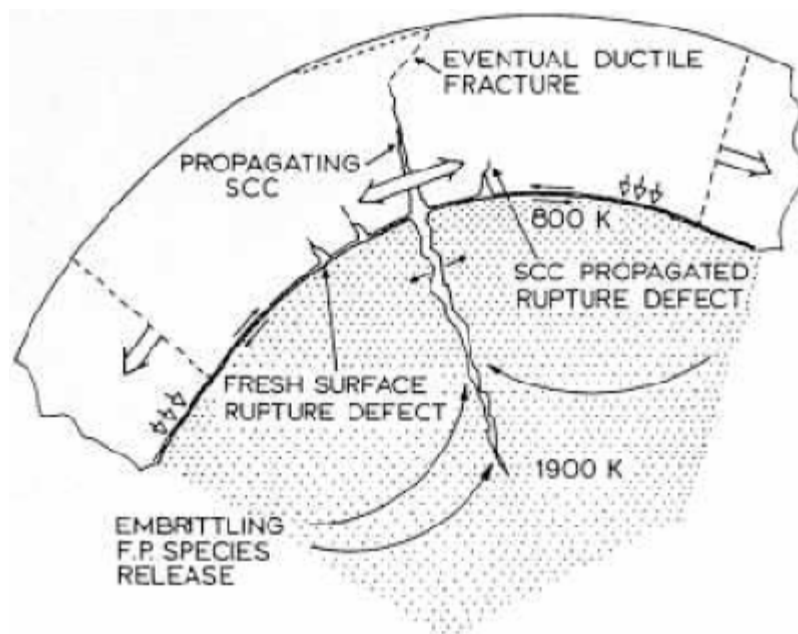
PCI failures are normally induced following substantial power changes. The mechanism involves a synergistic combination of mechanical and chemical interactions between the UO₂ fuel pellets (with iodine and possibly other fission products) and the zircaloy cladding. A technical basis for optimising power ascension procedures during reactor start-up can thus be developed using analytical modelling from fuel performance codes such as FALCON [5,6] with the implementation of an appropriate PCI failure model.

Table 2. Range of re-start parameters in the US, German, French and Korean PWRs

<i>Ramp restriction threshold (power above which re-start limits are imposed)</i>	
Country	Average linear heat rate
US (all)	1.1 to 2.7 kW/ft (36 to 89 W/cm)
France	0.8 to 0.9 kW/ft (26 to 28 W/cm)
Germany	1.6 to 5.8 kW/ft (51 to 189 W/cm)
Korea	2.7 kW/ft (88 W/cm)
<i>Ramp restriction rate</i>	
Country	Average linear heat rate
US (all)	0.16 to 0.17 kW/ft/hr (5.4 to 5.7 W/cm/hr)
France	0.16 to 0.17 kW/ft/hr (5.2 to 5.5 W/cm/hr)
Germany	0.05 to 0.32 kW/ft/hr and larger (1.7 to 10.5 W/cm/hr and larger)
Korea	0.16 kW/ft/hr (5.3 W/cm/hr)
<i>Relaxation time (time at power after which ramp limits are removed)</i>	
Country	Time (hrs)
US (all)	3 to 72
France	72
Germany	0 to 72
Korea	3 to 72

As shown in Figure 2, the physical problem can be described as follows: During service, the fuel pellets sustain a complex behaviour of cracking, relocation and crack healing with burn-up which could result in hard pellet-cladding contacts. Such pellet-cladding contact could impart high local stresses on cladding, even at below-average power levels. (Obviously, local stress state is also a function of power history and burn-up through combined effects of fuel swelling and cladding creep down.)

Figure 2. Schematic zircaloy fuel rod failure mechanism



In addition, certain embrittling fission products (emanating particularly through fuel radial cracks) may chemically attack the clad ID in such regions of high local stresses and pellet-cladding contact. As a result, stress corrosion cracking may initiate on the clad ID. The initial crack may or may not propagate radially outwards. Especially during power changes, however, where additional azimuthal stresses are imparted on the cladding due to pellet-cladding mechanical interactions, the probability for the initial ISCC crack to extend through wall and result in cladding failure increases. This type of failure is highly random, and its prediction is therefore partly a statistical problem. However, a deterministic modelling of this mechanism is useful in evaluating worst-case conditions and in interpreting test results or field occurrences.

Mitigation

PCI-induced fuel failures in commercial LWRs can be mitigated by (1) implementation of fuel preconditioning and ramp rate guidelines, and (2) development of PCI resistant fuel designs. The impact of such restrictions on plant operation is more severe for BWRs because of their higher potential for PCI-induced fuel failure (large diameter rods, large power changes due to control blade movement, higher linear power operation). However, these guidelines have also impacted reactor operations in PWRs by extending reactor re-start times with a corresponding reduction in capacity factor.

Because of the large impact of ramp rate restrictions on BWR operation, fuel designs specifically targeting the mitigation of PCI were developed. These fuel designs were termed barrier fuels because of the presence of a material liner placed between the fuel pellet stack and the cladding [4]. Although other alloys were tested, this liner was typically pure zirconium, metallurgically bonded to the inside of a zircaloy cladding tube. The introduction of barrier fuels into BWRs has greatly reduced the incidence of PCI fuel failures during re-start operations. Barrier-type cladding designs, however, have generally not been used in PWRs due to the expense and the lower incidence of PCI-induced fuel failures. Power conditioning in the form of ramp rate limitations are still the primary method of mitigating PCI-induced fuel failures in PWRs. Another potential mitigation measure could involve fuel pellets with additives, which produce a softer and more compliant pellet structure than the standard UO₂ pellet [7].

Ramp test programmes

Power ramp tests are also conducted on BWR and PWR fuel rods to explore the power ramp fuel failure threshold of commercial fuels after base irradiation. These power ramp tests include numerous tests conducted by fuel vendors [8] and internationally sponsored programmes such as the OVER-RAMP and SUPER-RAMP projects. Such experimental programmes provide useful data on the PCI behaviour of irradiated fuel, which can be used to define safe operating conditions for commercial PWRs. The OVER-RAMP project tested fuels with linear powers in the range of 14-25 kW/m (4.3-7.6 kW/ft) with burn-ups between 12-31 MWd/kgU [9]. The SUPER-RAMP project tested fuels at similar linear powers, but with higher burn-ups ranging between 33-45 MWd/kgU [10].

A comparison of the initial and terminal powers, burn-ups and ramp rates from the OVER-RAMP project and typical preconditioning guidelines (ramp rate restrictions) used in commercial PWRs is shown in Table 3. The OVER-RAMP programme tested fuel rods over similar burn-up ranges but at much higher terminal and threshold powers and ramp experienced in modern PWR operating environments. Results from the OVER-RAMP programme indicate that for the minimum ramp rate (0.9 kW/ft-hr, roughly corresponding to the 10% per hour ramp rate used in PWRs) PCI-induced fuel failures occurred only after terminal powers beyond 13 kW/ft were reached.

Table 3. Comparison of OVER-RAMP programme and PWR power conditions

	OVER-RAMP programme	PWR power conditions
Burn-up	12-31 MWd/kgU	16-51 MWd/kgU
Terminal power	12.2-15.25 kW/ft	6.9-9.95 kW/ft
Threshold power	7-9 kW/ft	1.4-2 kW/ft
Ramp rate	0.9-180 kW/ft-hr	0.3-3 kW/ft-hr (3-30%)

FALCON PCI analysis

PCI model

A key element of FALCON is the ability to estimate cladding failure through ISCC. Clad failure calculations in FALCON are based on a time-temperature-stress failure criterion fashioned after the cumulative damage concept. Such a concept assumes that the material undergoes cumulative damage due to sustained stress – the higher the stress, the shorter the time to failure. This implies that an applied stress of magnitude σ_0 lasting for a fraction of time Δt will cause the fractional damage ΔD as:

$$\Delta D = \Delta t / t_f(\sigma_0) \quad (1)$$

where $t_f(\sigma_0)$ is the time to failure had the stress, σ_0 , been applied for the total time. Eq. (1) depends implicitly on the temperature. Hence for a given constant temperature T_0 , Eq. (1) takes the form:

$$\Delta D(\sigma_0, T_0) = \Delta t / t_f(\sigma_0, T_0) \quad (2)$$

The relationship for the time to failure used in FALCON has been developed from pressurised zircaloy tube tests containing iodine gas [4]. These tests provide the time to failure as a function of stress level, temperature, burn-up and material type. The expression used in FALCON is:

$$t_f = \bar{t} e^{[A_1 \sigma_y + A_2 \sigma_{ref} - A_3 \sigma]}$$

where \bar{t} is a burn-up and temperature-dependent time, σ_y the yield stress, and σ the stress on the cladding. A threshold stress, σ_{ref} , and a minimum burn-up (>5 GWd/tU) are used in the model and both of these values must be exceeded before SCC is initiated. As shown, the threshold stress decreases as function of burn-up and reaches a minimum value near 25 ksi above 20 GWd/tU.

The damage index is calculated in FALCON at each clad element to indicate the potential for cladding failure as a function of time and stress level. The damage index is given by:

$$D = \int_0^{t_n} \frac{dt}{t_f(\sigma, Bu, T)} \quad (3)$$

where D is the amount of damage at t_n , t_f is the failure time at stress σ , temperature T and burn-up Bu .

Damage index values range between zero and 100 in typical PCI analyses. A value of unity represents the best-estimate measure of cladding failure, i.e. 50% probability of failure, provided the uncertainties have been accounted for in the analysis. In the analyses presented in this report, a 0.5 damage index value indicates a high potential for PCI failure. Recommendations for modifying the ramp rate limitations for PWR fuel are based on this limit.

Analysis approach

The general approach used in FALCON analysis had four main steps: (1) identify the range of threshold power levels and ramp rates; (2) identify the fuel rod designs and power histories; (3) perform steady-state analysis for once- and twice-burned fuel (to determine the initial conditions prior the ramp); and (4) perform PCI analysis of the power ramp associated with reactor start-up following a refuelling outage.

The ramp rate limitations vary from plant to plant; they mainly vary in the threshold power level and the ramp rate above the threshold power, as well as the power increase rate to the threshold power level from hot zero power. To evaluate the effects of the threshold power level and the ramp rate on fuel integrity, an analysis matrix consisting of fourteen combinations of parameters was developed for use in the evaluation. The analysis matrix used in the evaluation is shown in Table 4. In an attempt to span a variety of fuel rod designs and plant operating conditions (fuel rod power level), several different plants were chosen for analysis. In this report three types of fuel in three different plants were analysed: 17×17 Vantage-5H fuel in Plant A, 16×16 ABB-CE fuel in Plant B, and 17×17 Vantage-5 fuel in Plant C. The analysis matrix was applied to each fuel type, and in the case of Plants A and B, both once-burned and twice-burned were analysed.

Table 4. Analysis matrix

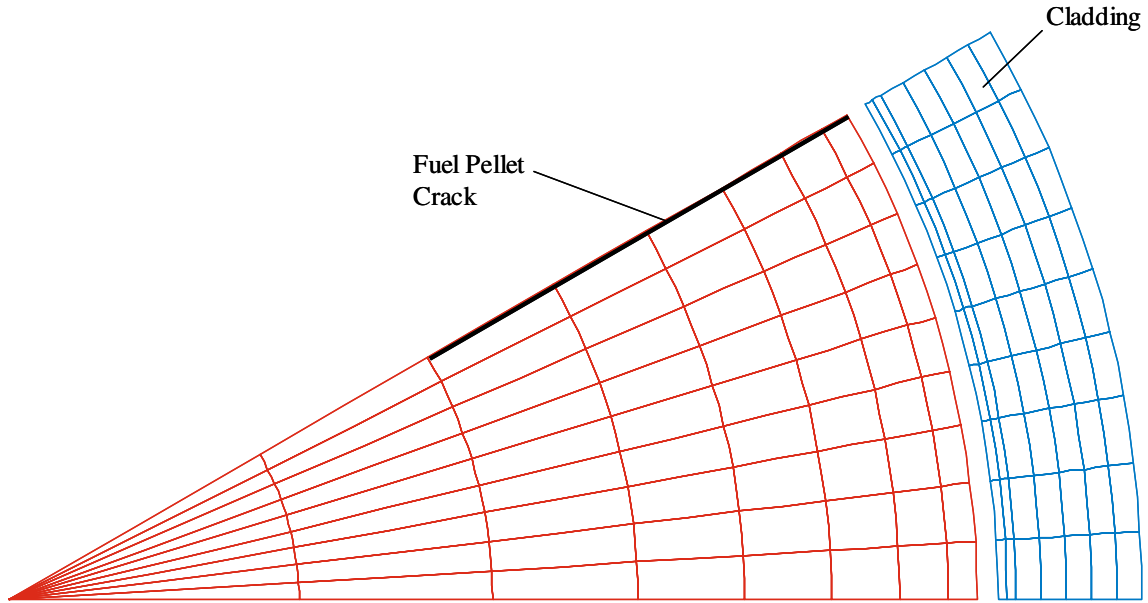
Threshold power (% FP)	Ramp rate after threshold power (% FP/hr)				
	1	3	5	10	30
20		•	•	•	•
40		•	•	•	
60		•	•	•	
90	•	•	•	•	

The combination of a threshold of 20%FP and a ramp rate of 3%FP/hr after the threshold was considered as the base case condition. From the matrix of analysis cases, an optimum threshold power and ramp rate was sought for each fuel design and plant type.

The steady-state analysis to base burn-up before refuelling outage employed one or two cycles of operations prior to re-start power ramp. By selecting both once- and twice-burned fuel, an assessment of the impact of burn-up was performed. This required information describing the fuel rod design (pellet and clad dimensions, etc.) and the maximum fuel rod power history of each cycle of operation. A full-length axi-symmetric analysis was conducted to establish the fuel rod condition at the beginning of the reactor start-up power ramp. The parameters of interest were the peak power and burn-up location on the fuel rod (axial height), the minimum fuel-cladding gap thickness, rod internal pressure, and fast fluence. These conditions were used to define the axial location that may experience the highest potential for PCI failure (largest cladding stresses).

Once the cycle calculation was performed, the PCI analysis was conducted at the axial slice identified in steady analysis that had the highest potential for PCI failure (i.e. highest burn-up and minimum fuel-cladding gap thickness). The PCI analysis was performed in r- θ representation of the fuel and cladding. Figure 3 contains a schematic of the model. The small wedge of the fuel and cladding shown in Figure 3 is used to calculate the cladding stress and damage index response during the power change. The PCI model contains a discrete fuel crack as indicated in the figure. This fuel crack establishes stress and strain localisation in the cladding once fuel-cladding gap closure occurs.

Figure 3. Finite-element PCI analysis in FALCON (r-θ plane)



Typical results and discussion

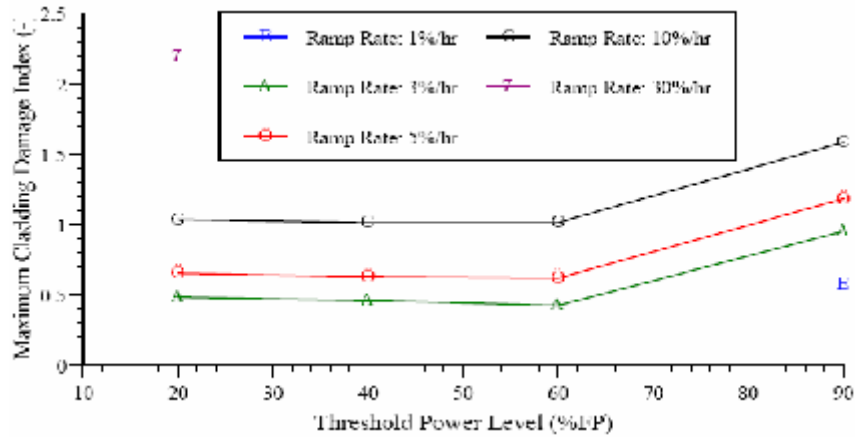
The basic characteristics of the power ramps for the five different cases are provided in Table 5. The cladding stresses are those corresponding to the base ramp case which used at a threshold of 20% and a ramp rate of 3%/hr from the threshold to full power. Each case represents a different set of parameters, including fuel pellet and cladding geometry, making it is difficult to discern trends related to burn-up as the linear powers are different. The CDI is a function of cladding stress, which is directly dependent upon the local LHGR and indirectly dependent on burn-up by virtue of the fuel-cladding gap. At higher burn-ups, the CDI can achieve a given value at a lower LHGR because the fuel-cladding gap has closed due to fuel swelling and cladding creep-down. Thus, when comparing the single Plant C case with the twice-burned case from Plant A with allowance for slight differences in design, the implication is that the linear power to produce a given stress or CDI decreases with burn-up.

Table 5. Results of cladding stress for five power ramp cases

Plant	Fuel type	Burn-up rod/node GWD/MTU	Peak LHGR (kW/ft)	Base conditions		Clad stress (ksi)	CDI
				Threshold power	Ramp rate		
A	17 V5H	26.8/32.0	9.95	20% FP	3%	41.9	0.48
		43.3/51.6	7.98			35.1	0.057
B	16	15.1/16.4	9.17	20% FP	3%	36.1	0.084
		32.3/35.4	6.89			30.7	0.009
C	17V5	36.5/40.3	8.51	20% FP	3%	35.6	0.057

The matrix of thresholds and ramp rates were applied to each of these fuel rod cases, however the once-burned fuel in Plant A produced the maximum cladding stress and CDI for each combination of threshold and ramp rate, and therefore the impact of threshold and ramp rates are discussed with respect to this fuel. Figure 4 shows the CDI as a function of threshold power level for the various ramp

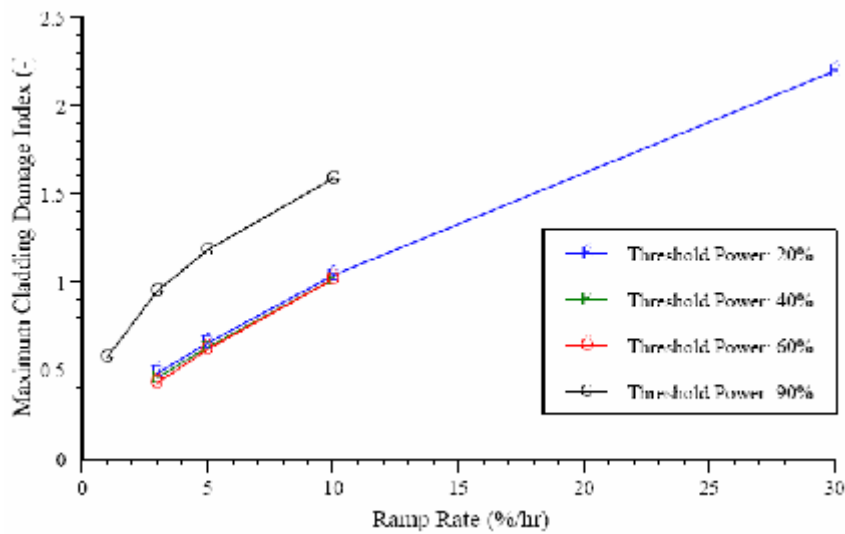
Figure 4. Effect of threshold on cladding damage index for once-burned fuel in Plant A



rates applied above the threshold. The data show that up to a threshold of 60%, the cladding damage index is essentially constant for a given ramp rate, and beyond a threshold of 60%, the damage index increases with increasing threshold. Similar behaviour was observed for the other cases at different burn-ups. The results suggest that PWR fuel could operate with a threshold up to 60% of full power. The exact power level where maximum CDI begins to increase (i.e. the inflection point in Figure 4) is somewhere between 60 and 90% FP, depending on the ramp rate.

The effect of ramp rate on the cladding damage index is shown in Figure 5, in which the CDI data from Figure 4 are now plotted functions of ramp rate for a given threshold. For a particular threshold below 60% of core power, the damage index increases almost linearly as a function of ramp rate. In the case of a threshold at 90% of full power, the subsequent ramp rate would have to be limited to 1%/hr or less. Based on these results, limitations must be placed on ramp rates in order to prevent PCI. These data also suggest that those PWR plants operating with a ramp rate of 3%/hr could operate with ramp rates of approximately 5%/hr without a significant increase reduction in margin to PCI.

Figure 5. Effect of ramp rate on cladding damage index for once-burned fuel in Plant A



Discussions

Our calculations of CDI were under very aggressive conditions. First, they did not account for typical operational hold points such as those described in Table 1 and Figure 1. Second, the effect of coast-down for twice-burned fuel is not included. These tend to precondition the cladding, theoretically making it less prone to PCI. Third, calculations in Figure 4 and 5 represent those with “half-gap”, meaning half the values of fuel-clad gap at maximum LHGR was considered in computing the stress and CDI. This provides for prudent caution in deriving recommendations based on these calculations. On the other hand, it is noted that the PCI model in FALCON is based on out-of-pile iodine test data from the 1980s [1,4].

Overall our results show that margin exists to increase the threshold for imposition of ramp rate restrictions from 20-30% FP into the range of 40-60% FP. Above the threshold, a ramp rate of 5%/hr is likely to be acceptable without reduction of fuel reliability. Plant-specific analysis is recommended, particularly when new cladding alloy is involved.

Acknowledgments

The authors thankfully acknowledge collaborations with colleagues from EDF Septen and Korea Electric Power Company in performing the code calculations.

REFERENCES

- [1] Roberts, *et al.*, “A Stress Corrosion Cracking Model for Pellet-Cladding Interaction Failures in Light-Water Reactor Fuel Rods”, *4th Conference on Zirconium in the Nuclear Industry*, American Society for Testing and Materials (ASTM), ASTM STP 681, pp.285-305 (1979).
- [2] *PWR Restart Ramp Rate Restrictions*, EPRI, Palo Alto, CA, Electricité de France Septen, France, and Korea Electric Power Corporation, Munji-Dong, Yusung-Gu, Taejon, Korea, TR-112140-V1 (1999).
- [3] *Effect of Startup Ramp Rate on Pellet-cladding Interaction of PWR Fuel Rods*, EPRI, Palo Alto, CA, Electricité de France Septen, France, and Korea Electric Power Corporation, Munji-Dong, Yusung-Gu, Taejon, Korea, TR-112140-V2 (1999)
- [4] Armijo, *et al.*, “Development of Zirconium-barrier Fuel Cladding”, *10th International Symposium on Zirconium in the Nuclear Industry*, ASTM STP 1245, pp. 3-18 (1994).
- [5] Yagnik, S.K., “Overview of EPRI Fuel Performance Code FALCON”, *OECD/NEA Proceedings of Meeting on Thermal Performance of High Burn-up LWR Fuel*, Cadarache, 3-6 March 1998.

- [6] Yagnik, S.K., R.L. Yang, Y.R. Rashid, R.O. Montgomery, R. O., “Modeling of Fuel Rod Steady State and Transient Behavior over the Full Range of Burn-up”, *Transactions of the ANS Winter Meeting*, Albuquerque, NM, November 1997.
- [7] *Power Ramp Testing of Additive Fuel Rods in the Halden Reactor*, EPRI, Palo Alto, CA, 1002855 (2003).
- [8] Tsukuda, Y., *et al.*, “Performance of Advanced Fuel Materials for High Burn-up”, *Proceedings of the ENS TopFuel 2003 Conference*, Würzburg, March 2003.
- [9] Djurle, S., “The International OVER-RAMP Project at Studsvik”, *Proceedings of ANS Topical Meeting on Fuel Performance*, Williamsburg, VA, USA, April 1982.
- [10] Djurle, S., “Final Report of SUPER-RAMP Project at Studsvik”, US Department of Energy, DOE/ET/34032-1 (1985).

PELLET-CLADDING MECHANICAL INTERACTION IN BOILING WATER REACTORS

Michel Billaux and Hoju Moon
AREVA, Richland, USA

Abstract

In boiling water reactors (BWRs), the control blade movements are optimised to maximise the energy output from a cycle. The local power transients caused by the blade movements may result in significant pellet-cladding mechanical interaction in the fuel rods close to the control blades. Pellet-cladding mechanical interaction in BWRs is discussed as it relates to the fuel conditioning and manoeuvring criteria. The consequence of fabrication defects, such as pellet chipping, is investigated and presented.

Introduction

In the 1970s the principal cause of fuel rod failures in boiling water reactors (BWRs) was pellet-cladding mechanical interaction (PCI) [1]. About a hundred PCI failures of BWR fuel rods with non-liner cladding were reported in the 1980s [2,3].

PCI fuel failures occurring in BWRs are a manifestation of a stress-corrosion cracking phenomenon. Four factors are simultaneously necessary for failure to occur: sufficient stress at the inner surface of the cladding, sufficient time, a susceptible material and a corrosive environment [4]. The stress in the cladding results from thermal expansion of the pellet during a power increase. Most PCI failures are correlated with control blade manoeuvres. Some failures followed the reloading of fuel assemblies irradiated at the core periphery for one or more cycles to high power central locations [2].

To address these failures, the following remedies for PCI were implemented:

- More restrictive fuel preconditioning and manoeuvring criteria were developed to reduce the risk of PCI failure in fuel rods with non-liner cladding.
- A zirconium liner fuel design concept was introduced by General Electric (GE) in the early 1980s [5,6]. However, with the incorporation of the liner, utilities elected to employ more aggressive operating strategies in order to improve plant capacity factors and economy. The traditional operating restrictions were removed and control blade withdrawals during pattern adjustment were performed at or near full power [8], which accordingly reduced the new margins provided by the liner.
- To reduce the average fuel rod linear heat generation rate (LHGR) and provide greater margins to PCI failure, 9×9 and 10×10 designs were introduced. In most cases, however, the margins are consumed by a more aggressive core management allowing fuel to operate with higher local peaking factors [8].

Post-failure rod degradation also has become a major source of concern for the manufacturers and the operators. Zirconium barrier cladding appears to be more susceptible than standard non-barrier cladding to the formation of long axial splits [7]. After a primary defect has developed, steam penetrates the rod, until the inner and outer pressures are equilibrated. Only then do the fill and fission gases start to escape from the rod. Inside the rod the steam oxidises both the fuel and the cladding. The oxidation process liberates hydrogen in the pellet-cladding gap and other free volumes. The H_2/H_2O ratio consequently increases above and below the primary defect as the distance from the defect increases. When that distance is of the order of 1 m, H_2O starvation occurs and dry hydrogen comes into direct contact with the cladding. The hydrogen diffuses into the cladding and precipitates in the form of hydrides. Cladding hydriding may lead to the formation of blisters, holes, short cracks and eventually a secondary failure. The rod can further degrade with massive cladding hydriding, the formation of circumferential cracks and longer axial splits in the cladding. Fuel may be eroded and released into the coolant. Long axial cracks in non-liner fuel have been observed, but remain uncommon. They are more common in liner fuel because the zirconium liner is much more susceptible to steam corrosion and associated hydrogen pick-up than zircaloy. For those reasons non-liner cladding fuel is still widely used in BWRs in the USA.

In the last few years the number of failures of both liner and non-liner BWR fuel rods has significantly increased. The cause of most failures has not yet been determined. Some of them clearly can be correlated with control blade movements. There are indications that liner-cladding fuel is not immune to PCI failure [8]. In brief, PCI failures in BWRs are still a hot topic.

BWR core management

The control blade patterns for modern BWR fuel cycle designs are based on control blade sequences with long exchange intervals. The control blades are subdivided into four groups: A1, A2, B1 and B2. At any time during normal power operation, control blades belonging to only one of these groups are inserted. Figure 1 shows the map of a 1 150 MW(e) BWR core. It contains 764 fuel assemblies distributed in 185 control cells. Control cells of A1 and A2 groups are explicitly represented in the figure. Each cell consists of a cross-shaped control blade in the centre surrounded by four fuel assemblies. Some fuel bundles at core peripheral locations have no associated control blades and thus are never controlled. A quarter of a cell is represented in Figure 2.

Figure 1. 1 150 MW(e) BWR core. Subdivision of the core in cells of four fuel assemblies.

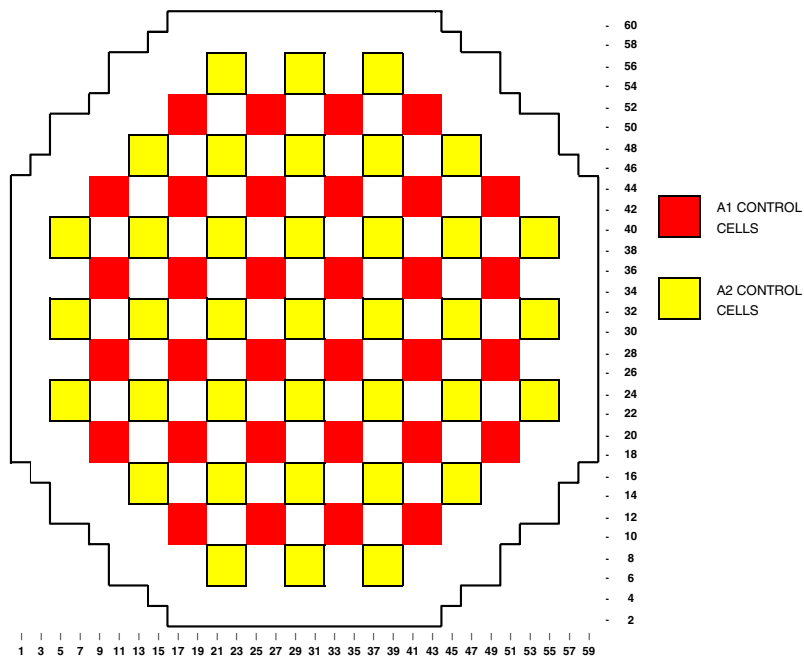
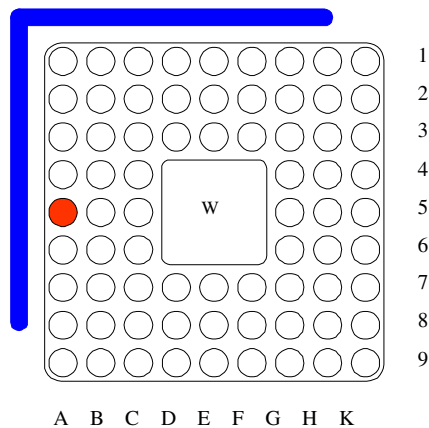


Figure 2. 9 × 9 BWR fuel assembly



Control blades from one group are inserted for a period of time and then swapped with control blades from another group, to maximise the cycle energy while satisfying a number of constraints such as:

- Reactivity constraints.
- Axial power shape constraints.
- LHGR and axial planar LHGR (APLHGR) constraints.
- Cladding dry out constraints.

The optimisation of control blade patterns for a whole cycle involves a large number of variables. The determination of an optimised control blade pattern is a complex process requiring a large amount of computing resource. It can be done manually or with the help of an optimisation tool. Methodologies have been developed that generate blade patterns with a quality equal to or better than an expert manual design within a fraction of the time required for the manual design [9,10]. The solution of the problem depends on a series of basic options such as:

- The fuel loading pattern (strategic loading of fuel bundles in core regions to minimise bundle power peaking while achieving the maximum cycle energy).
- Fuel lattice design (strategic distribution of ^{235}U enrichment among all fuel rods and positioning of gadolinia bearing rods within an axial zone of a fuel bundle).
- The fuel cycle energy or length (12, 18 or 24 months).
- The control blade sequence, e.g. A2→B2→A1→B1 (from one to four groups of control blades may be involved).
- The length of the period of time between control blade sequence exchanges (from one to several thousands of MWd/tU).
- Reduction of core flow during the early part of a fuel cycle to achieve an economic spectral shift operation.

The average axial power shape is controlled to form large bottom peaking in the beginning through the middle of the cycle. This results in heavy duty for the bottom zone of fresh fuel bundles within the LHGR and APLHGR constraints. Near the end of a cycle a middle- to top-peaked axial power shape ensues with low LHGR in the bottom zone. The radial power distribution is made as flat as possible in the interior zone of the core. This results in uniform burn of fuel bundles, which in turn results in an end-of-cycle radial power distribution satisfying the thermal margin constraints with minimal or no control blade intervention [10].

Operational transients in BWRs

For control and calculation purposes the fuel assemblies and the rods are axially subdivided into 24 or 25 (about 152.4 mm long) axial regions also called “nodes”. Nodes can be “controlled” or “uncontrolled”. A node is controlled if it is covered by the adjacent control blade. Owing to the softness of the neutron spectrum, the insertion depth of the control blade has a considerable effect on the axial power distribution in the adjacent fuel rods. The LHGRs in controlled nodes are often lower than

15 kW/m, while they can exceed 40 kW/m in uncontrolled nodes. In the US reactors the control blades are moved by two notches at a time. Each pair of notches corresponds to an axial node. A two-notch control blade movement is quasi instantaneous. For that reason the control blade sequence exchanges are performed at reduced reactor power. Even so the nodal powers of fuel rods are subjected to rapid changes during control blade sequence exchanges and the high-enriched rods close to the control blades (e.g. Rod A5 in Figure 2) may be subjected to significant power ramps.

Figure 3 shows the changes of the axial power distribution in a rod close to a control blade calculated with the MICROBURN-B2 BWR Core Simulator of AREVA [9]. Three incremental control blade pulls of two notches each at 92% core power were followed by return to 100% power. Figure 4 illustrates the evolution of the nodal LHGR. At Node 13 the power increased abruptly from 10.4 to 12.0 kW/m at the first blade pull, then to 26.5 kW/m at the second blade pull 10 minutes later, then to 29.6 kW/m at the third blade pull 13 minutes after the second blade pull, and eventually to 32.3 kW/m after return to full power.

Figure 3. Effect of three successive two-notch control blade pulls followed by return to full power on the axial power distribution

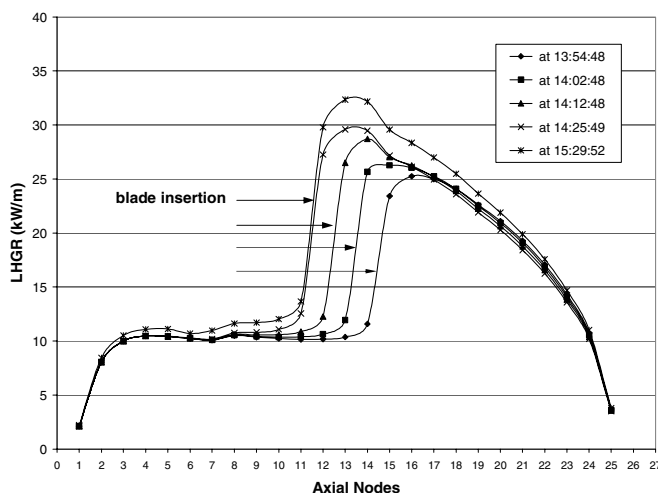


Figure 4. Effect of three successive control blade pulls followed by return to full power on the nodal power

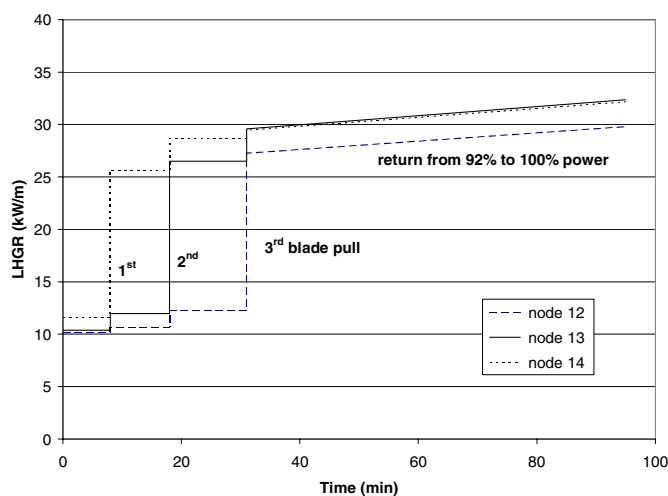
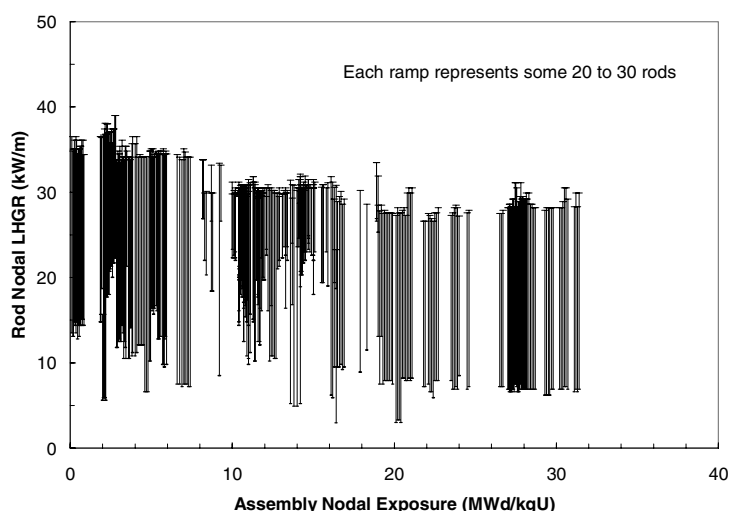


Figure 5 shows a selection of fast power ramps resulting from control blade pulls. They were recorded by the POWERPLEX® Core Monitoring Software Systems (CMSS), developed by AREVA, installed in two BWRs: one loaded with 8×8 fuel, the other one with 9×9 fuel. POWERPLEX CMSS monitors the power at each assembly node. Each vertical line represents the power ramp experienced by the peak power rod in the assembly. In fact, 20 to 30 rods at each node experienced a similar power change to within 1.5 kW/m of the peak power rod. Therefore Figure 5 summarises an experience of some 7 000 to 10 000 power ramps. In some of them the power increased almost instantaneously by more than 30 kW/m. It is remarkable that none of these rods failed.

Figure 5. Power ramps of 8×8 and 9×9 BWR non-linear fuel resulting from control blade withdrawal



Fuel conditioning and manoeuvring criteria have been developed to reduce the risk of PCI failure. These criteria are based on fast ramp experimental databases and fuel thermal-mechanical calculations. The objective is to maintain a margin to PCI failure of at least 6 kW/m at any node and any time to cover statistical uncertainties and small rod defects. But even so a large number of rods are subjected to significant PCI.

Pellet missing surface

The golden age of ramp tests was in the beginning of the 1980s. It was the time of the now-classic Studsvik tests. In 1981 and 1982 eight interesting slow ramp tests on GE fuel were performed at Studsvik: the Super-Ramp BG8 and BG9 tests [11]. The profiles of the BG ramps are presented in Figure 6. These tests were designed to demonstrate that no failure occurs when the ramp rate is slower than typically 0.3 (kW/m)/h. The BG tests were performed at ramp rates in the range 0.20 to 0.34 (kW/m)/h. Five of the eight rods failed: four at 40 kW/m or more, one at only 34 kW/m.

It was quickly recognised that at high power, gaseous swelling of the fuel may prevent stress relaxation and was responsible for the large cladding deformations observed in ramp tests [12]. The BG failures at 40 kW/m or more were consequently attributed to the pellet-cladding mechanical interaction resulting from the combined effect of thermal expansion and gaseous swelling. But thermal expansion and gaseous swelling in rod BG8/1 were too low for the explanation of a PCI failure to be feasible. Careful analysis of the ceramography of the BG8/1 rod showed that the edge of the pellet had been chipped just in front of the crack in the cladding (see Figure 7).

Figure 6. Super-Ramp BWR subprogramme

Reduced ramp rate test results

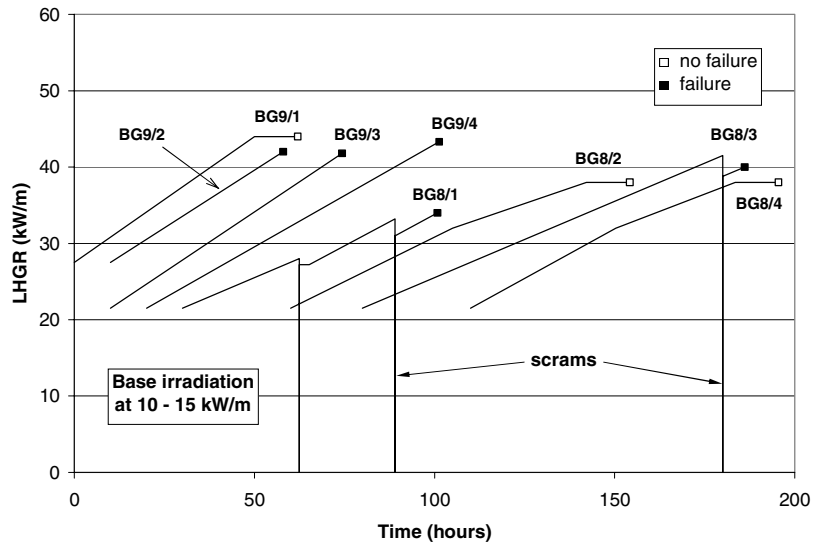
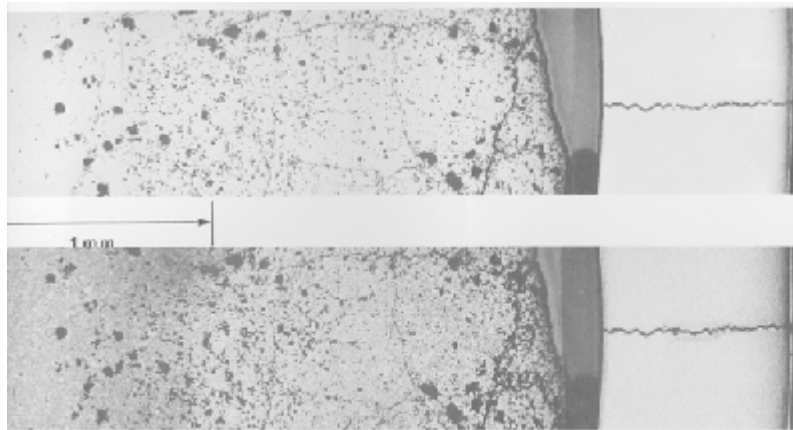


Figure 7. Super-Ramp BG8/1

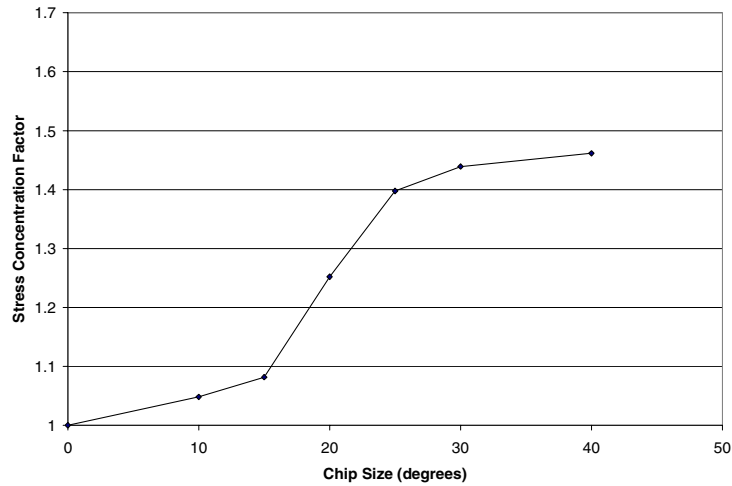
Pellet missing surface



The conjunction of a “pellet missing surface” with a cladding crack has also been observed a number of times in commercial reactors [13,14]. A pellet missing surface breaks the symmetry of the pellet-cladding mechanical system resulting in a stress concentration at the cladding inner surface. Three-dimensional finite element calculations were performed and a stress concentration factor for the tangential stress at the cladding inner surface was calculated as a function of the size of the missing surface. The results obtained at AREVA are presented in Figure 8. The size of the missing surface in front of the BG8/1 failure is 17° , which according to Figure 8 would lead to a stress concentration factor of about 1.15. This means that if the tangential stress failure threshold calculated using a standard methodology is 415 MPa [15], the failure threshold for BG8/1 calculated with the same methodology would only be 360 MPa.

Figure 8. Pellet missing surface

Stress concentration factor for the tangential stress at the cladding inner surface



Conclusions

When fuel is operated at low power for an extended period of time, fuel solid swelling and cladding creep-down both contribute to close the pellet-cladding gap and to establish a moderate contact pressure between pellet and cladding. This strongly reduces the ability of the fuel to sustain power ramps. The fuel is said to be “deconditioned”. This happens in fuel loaded for one cycle or more at the periphery of the core and then moved to a high-power central location. When the control blades are pulled out during the start-up procedure there is a significant potential for severe PCI. The situation is even worse if the deconditioned fuel is loaded into a controlled cell. Severe PCI may then occur during the first control blade sequence exchange of the new cycle. Long periods of time between control blade sequence exchanges increase the probability of severe PCI.

As already mentioned above, advanced 10×10 designs have been developed and introduced to help reduce the average LHGR and provide new margins to PCI failure. However, in most cases the margins are consumed by a more aggressive core management allowing fuel to operate with higher local peaking factors. A secondary effect of the introduction of the 10×10 designs is a larger fraction of fully deconditioned nodes in the core. In such conditions the complex control blade sequence exchanges imposed by the fuel preconditioning and manoeuvring criteria may result in a significant decrease of the plant capacity factor with negative economic consequences. Therefore a balance has to be found between a not-too-aggressive core management and not-too-restrictive preconditioning and manoeuvring criteria. The latter will have to be based on sound physics and an adequate fast ramp experimental database.

REFERENCES

- [1] Armijo, J.S., "Performance of Failed BWR Fuel", *Proceedings of the International Topical Meeting on Light Water Reactor Fuel Performance*, pp. 410-422, West Palm Beach, Florida, 17-21 April 1994.
- [2] Sofer, G.A., L.F.P. van Swam, C.A. Exarhos, "Performance of Exxon Nuclear Company Fuel in Light Water Reactors", *Proceedings of the ANS Topical Meeting on Light Water Reactor Fuel Performance*, pp. 1-53, Orlando, Florida, 21-24 April 1985.
- [3] Potts, G.A., R.A. Proebstle, "Recent GE BWR Fuel Experience", *Proceedings of the International Topical Meeting on Light Water Reactor Fuel Performance*, pp. 87-95, West Palm Beach, Florida, 17-21 April 1994.
- [4] Cox, B., "Pellet-cladding Interaction (PCI) Failures of Zirconium Alloy Fuel Cladding – A Review", *J. Nucl. Mater.*, 172, 249-292 (August 1990).
- [5] Davies, J.H., H.S. Rosenbaum, J.S. Armijo, E. Rosicky, E.L. Esch, S.B. Wisner, "Irradiation Tests on Barrier Fuel in Support of a Large-scale Demonstration", *Proceedings of the ANS Topical Meeting on LWR Extended Burn-up – Fuel Performance and Utilization*, pp. 5-51, Williamsburg, Virginia, 4-8 April 1982.
- [6] Baily, W.E., L.D. Noble, R.G. Serenka, C.S. Kennedy, R.A. Proebstle, "Performance Experience of GE Boiling Water Reactor Fuel", *Proceedings of the ANS Topical Meeting on LWR Fuel Performance*, pp. 12-20, Williamsburg, Virginia, 17-20 April 1988.
- [7] Harbottle, J.E., M.W. Kennard, D.J. Sunderland, A.A. Strasser, "The Behavior of Defective BWR Barrier and Non-barrier Fuel", *Proceedings of the International Topical Meeting on Light Water Reactor Fuel Performance*, pp. 391-397, West Palm Beach, Florida, 17-21 April 1994.
- [8] Sunderland, D.J., M.W. Kennard, J.E. Harbottle, "An Evaluation of the Potential for PCI in BWR Barrier Fuel Failures", *Proceedings of the International Topical Meeting on Light Water Reactor Fuel Performance*, pp. 372-376, Portland, Oregon, 2-6 March 1997.
- [9] Moon, H., "Advanced Core Design Using MICROBURN-B2 BWR Core Simulator," *Proceedings of the ANS Topical Meeting on Advances in Nuclear Fuel Management*, pp. 5-47, Myrtle Beach, SC, March 1997.
- [10] Moon, H., R.G. Grummer, S. Misu, "Implementation of BWR Control Rod Pattern Optimization in MICROBURN-B2", *ANS Topical Meeting on Advances in Nuclear Fuel Management*, Hilton Head Island, South Carolina, 2003.
- [11] Mogard, H. and H. Heckermann, "The International Super-Ramp Project at Studsvik", *Proceedings of the ANS Topical Meeting on Light Water Reactor Fuel Performance*, pp. 6-17, Orlando, Florida, 21-24 April 1985.

- [12] van Vliet, J. and M. Billaux, "Investigation of Fuel Rod Behaviour During Power Ramps with COMETHE", *IAEA Specialists Meeting on Water Reactor Fuel Element Performance Computer Modelling*, Bowness-on-Windermere, UK, 9-13 April 1984 [see also *Res. Mechanica*, 17, 269-291 (1986)].
- [13] Yagnik, S.K., O. Ozer, B.C. Cheng, R.L. Yang, R.O. Montgomery, Y.R. Rashid, J.H. Davies, E.V. Hoshi and R.B. Adamson, "Assessment of BWR Fuel Degradation by Post-irradiation Examinations and Modeling in the DEFECT Code", *Proc. of the International Topical Meeting on Light Water Reactor Fuel Performance*, pp. 329-336, Portland, Oregon, 2-6 March 1997.
- [14] Groeschel, F., G. Bart, R. Montgomery, S.K. Yagnik, "Failure Root Cause of a PCI Suspect Liner Fuel Rod", *IAEA Technical Meeting on Fuel Failure*, Bratislava, Slovakia, 17-21 June 2002.
- [15] Billaux, M.R., S-H. Shann, L.F. Van Swam, F. Sontheimer, H. Landskron, "SIERRA: A Code to Predict the Mechanical Behavior of LWR Fuel Rods", *14th International Conference on Structural Mechanics in Reactor Technology*, Lyon, France, 17-22 August 1997.

PCI-RELATED CONSTRAINTS ON EDF PWRs AND ASSOCIATED CHALLENGES

Stéphane Béguin

Électricité de France

Nuclear Engineering Division, SEPTEN

Abstract

Through the years, EDF PWRs have been progressively subjected to more and more operating constraints related to PCI fuel behaviour. Today in France, safety requirements impose that no fuel failure by PCI should occur in normal operation as well as in incidental situations. Specific methods have therefore been developed to define the protection system set points and operating specifications in order to avoid the risk of PCI failure during Class 2 transients.

EDF experience feedback shows that PCI failure has never occurred in any of its 58 PWRs, which is a source of great satisfaction from a fuel reliability point of view. However, meeting such safety requirements goes together with heavy constraints. In addition to the licensing requirements for new fuel products and the heaviness of PCI Class 2 analysis, the PCI-related operating technical specifications are so constraining that they could even lead to the shutdown of a reactor.

Within a strongly competitive environment, the need to reduce the overall PCI constraints is crucial for EDF since more demanding fuel management strategies are planned. Several options are currently being investigated to take up this challenge, with the final objective of operating PWRs in the 2010s without any PCI-related constraint.

Introduction

Electricity from nuclear power plants in France is generated by 58 standardised PWRs owned by EDF and representing 75-80% of the annual electric production. As a consequence, the entire fleet of plants has to follow the demand of the grid, leading to a significant plant manoeuvrability need: frequency control, daily load follow, extended reduced power operations (ERPO).

The generalisation of load follow operation in the 1980s was subjected to requirements from the French nuclear safety authority. In particular, EDF was asked for guarantees against pellet-cladding interaction (PCI) failure during upset conditions (Class 2 event). Since then in France, safety requirements impose that no fuel failure by PCI should occur during normal operation, as well as during incidental situations.

In this particular context, the purpose of this paper is to present the PCI issues in France from the utility standpoint. First the paper gives an overview of the PCI Class 2 methodology currently in use to meet the safety requirements on EDF PWRs. The constraints due to the prevention from the PCI fuel failure risk are then examined. The paper ends with a discussion of the options currently investigated to take up the challenge of reducing the overall PCI constraints.

PCI Class 2 methodology for EDF PWRs

PCI failures are due to stress corrosion cracking in the cladding material and are associated with high local power variations. The damage in the clad is limited to a crack. The clad maintains its structural integrity and the fuel temperature is not affected by the PCI failure mechanisms, which is not the case for DNB or LOCA situations. In particular, there is no direct contact between fuel pellet and primary coolant. The main consequence of PCI failure is a contamination of the primary coolant by fission gases.

The risk of PCI failure during Class 2 transients was considered while NPPs were already in the operating phase, so it was not conceivable to apply the standard design basis rules. Moreover, it should be mentioned that the PCI failure risk is considered at such a level only on French PWRs. Many power ramp test programmes have been carried out within international frameworks since the 1970s, though it has not been possible to rely on international feedback regarding PWR operations.

Therefore, EDF, in close co-operation with FRAMATOME-ANP, has constructed a specific methodology and specific rules to take into account the PCI Class 2 risk during the operating phase. The solution was to make the best of the existing core protection system and to adjust the protection set points in order to avoid the PCI failure risk during Class 2 events.

The PCI technological limit

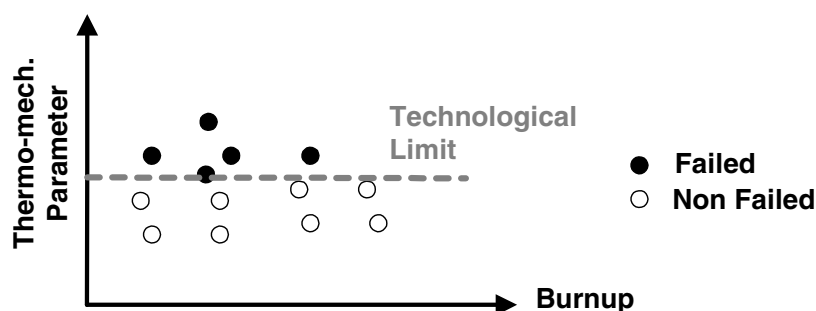
The PCI failure criterion is based on power ramp tests that are performed in experimental reactors such as OSIRIS at CEA and R2 in STUDSVIK. These facilities are equipped with test loops which can combine PWR conditions and power increase rates typical of Class 2 power transients. The tests are performed on PWR pre-irradiated fuel rods. The experimental procedure for power ramp tests aims at simulating PWR-type Class 2 power transients in a test reactor. Thus, the experimental results can be directly transposed to PWR conditions.

The standard method of analysing power ramp tests in a safety study is to define a safe domain in terms of maximum power, power variations and burn-up. This approach is pretty simple to apply, but it presents two disadvantages. First, it requires a significant number of ramp tests to perform. Second, this approach is delicate to extrapolate to loading conditions that are different from the ones in ramp tests, since it may be over-conservative in some cases and insufficiently conservative in others.

Considering the high safety requirements involved, another approach was followed. The choice was made to base the PCI failure criterion on a thermo-mechanical parameter that is calculated by a fuel behaviour code and that can distinctively discriminate between failed and un-failed rods. In the case of Zy-4 fuel rods, this parameter is the cladding internal stress.

Simulating the power ramp database with a fuel behaviour code allows determining the lower admissible stress boundary before rod failure. This boundary is defined as the PCI criterion and is named “PCI technological limit” of the fuel product (see Figure 1). If the cladding experiences a hoop stress greater than the criterion, it will supposedly fail. The PCI technological limit is independent of burn-up.

Figure 1. Definition of the PCI technological limit



It should be noted that fuel performance codes used within this methodology are qualified for incidental transient conditions, especially in terms of fuel thermal aspects at high temperature and clad mechanical behaviour at high stresses (typically more than 300 MPa). Therefore, creep tests and hardening-relaxation tests are performed on as-fabricated and irradiated clad materials. These tests cover a wide range of conditions in terms of clad temperature, maximum hoop stress and strain rate during loading and are used to elaborate clad creep-relaxation models to be implemented in the fuel performance code. Such code qualification requirements, along with well-specified ramp test conditions, allow transposing with confidence the PCI technological limit from the test reactor to the PWR.

Outlines of PCI Class 2 studies

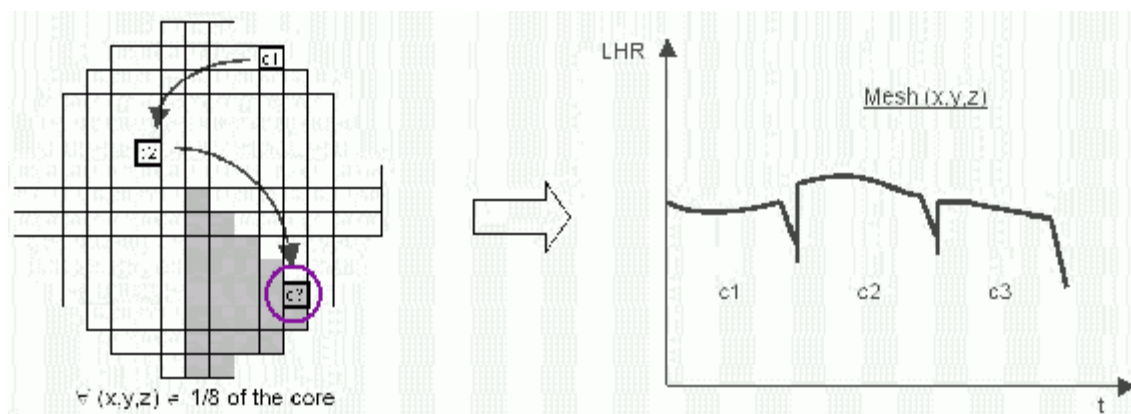
The objective is to define protection set points of the reactor and to elaborate PCI-related operation technical specification (OTS) to avoid any PCI failure during a Class 2 transient. Every type of normal operation has to be studied: base irradiation, load follow, frequency control, ERPO.

The non-failure of PCI must obviously be guaranteed for the entire core. Though the PCI risk has the distinctive feature of being difficult to localise in the core, it is intimately dependent on the initial thermo-mechanical state of fuel rods before transient, which requires a knowledge of the power history of every rod as well as the reactor operation during previous cycles. As a consequence, all the rods of the core have to be computed with neutronic and thermo-mechanical codes, at base irradiation as well as at Class 2 transients.

PCI Class 2 analysis at base irradiation

The local linear heat rate is first calculated for every rod from its introduction in the core until the beginning of an incidental transient. A 3-D neutronic code is used to compute the power distribution $LHR(x,y,z, BU)$ for 1/8 of the core. Calculations are performed for the reference campaign with systematic stretch-out. The thermo-mechanical state of every rod is then calculated using a fuel behaviour code and the core power distribution $LHR_{base}(x,y,z, BU)$ as input data (see Figure 2).

Figure 2. Base irradiation computations



The transients selected for the analysis are conventional Class 2 transients considered as limiting regarding the PCI failure risk, i.e. inducing high local power and fast power variations. They are of three types:

- Excessive increase in secondary system flow.
- Uncontrolled bank withdrawal at power.
- Control rod drop.

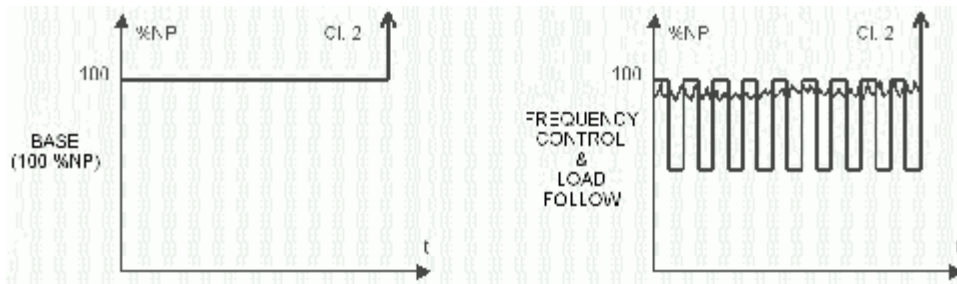
The initial state of the transient is chosen as the most penalising one within the allowed operating range. The transients are computed using a NSSS code which models the local linear heat rate in every mesh of the core during the transient $LHR_{transient}(x,y,z,t)$.

The so-calculated neutronic loadings are used as input data in the fuel behaviour code which calculates the evolution of the discriminating thermo-mechanical parameter for every rod of the core all along the transient. This evolution is then compared with the PCI technological limit which has been determined based on power ramp tests using the same fuel behaviour code. This comparison makes it possible to assess the PCI margins to failure at base operation, for every point of the core and every transient.

PCI Class 2 analysis in load follow and frequency control

Load follow operation as well as frequency control may induce some fuel deconditioning. Thus this type of operation is associated with smaller margins than those computed for base-load operation. Computations are performed using the fuel behaviour code, based on analytical power histories for base, load follow and frequency control operations (see Figure 3). The comparison between these computations leads to the PCI margins for load follow and frequency control operations.

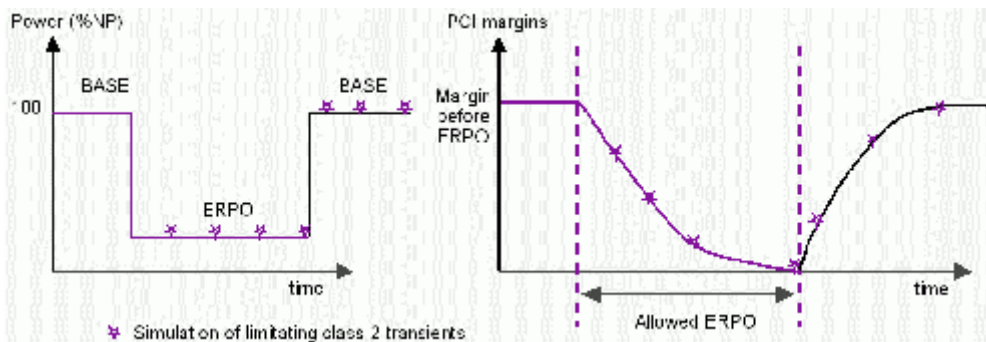
Figure 3. Analytical computations for frequency control and load follow operations



Extended Reduced Power Operation (ERPO) analysis

ERPO is a deconditioning operation regarding PCI fuel behaviour. For given situations, this type of operation must be limited to maintain positive PCI margins. On the other hand, an increase of power after ERPO is a reconditioning operation and thus makes it possible to reconstitute PCI margins. The ERPO analysis consists in simulating the most limiting Class 2 transients at different times during an ERPO and also after the return to nominal reactor power. Calculating the PCI margins' evolution under these conditions allows elaborating deconditioning and reconditioning laws (see Figure 4).

Figure 4. Assessment of PCI margins during and after ERPO



Definition of protection set points and elaboration of Operating Technical Specifications (OTS)

Before achieving the ERPO analysis, the reactor protection set points are defined based on a PCI margin analysis. This analysis depends on the core protection system and thus on the type of plant:

- For 900 MWe PWRs (34 units), the operating point must always remain within the operating diagram described by reactor power and axial offset. The PCI Class 2 study is performed with existing protection set points. The objective is to make sure that PCI margins computed for base operation, load follow and frequency control are kept positive. These positive margins are then allocated to the definition of maximum allowed ERPO lengths.
- The 1 300 MWe and 1 450 MWe PWRs (24 units) are equipped with a digital integrated protection system which continuously compares the hot spot of the core with a modifiable limit. This allows the research of an operating domain compatible with PCI limits. The objective of the studies is therefore to adjust the protection set points. This requires to find a compromise solution between maximum allowed ERPO length and plant manoeuvrability (load follow, frequency control) when adjusting the set points.

Once set points definition and ERPO analysis are completed, the last step of the study consists in elaborating the PCI-related OTS. The deconditioning and reconditioning laws are translated into OTS using a mathematical parameter called the “K credit”. K is given as follows:

$$K = K_0 - \sum_i A_i T_i + \sum_j B_j T_j$$

where K_0 is the initial value of K, A_i is the deconditioning coefficient computed from the deconditioning law, T_i is the ERPO duration, B_j is the reconditioning coefficient computed from the reconditioning law and T_j is the operating duration at full power after an ERPO.

The application of the OTS requires that the plant operators calculate on-line the evolution of K and to ensure that K is always positive, i.e. that ERPO is still allowed regarding the risk of PCI failure.

PCI-related constraints on EDF PWRs

Today, EDF benefits from a significant plant operating experience with its 58 PWR units having accumulated 1 000 reactor-years. Nevertheless not a single PCI fuel failure has ever been detected since the start-up of the first unit in 1977, whatever the type of fuel design and the operation mode (some units always base operating, others submitted to intensive load follow).

From a fuel reliability point of view, this experience feedback is a source of great satisfaction. However, meeting such safety requirements is accompanied with heavy constraints for EDF. These are of three types: constraints regarding fuel licensing requirements, constraints associated with the PCI Class 2 studies and last but not least constraints for plant operation.

Constraints associated with fuel licensing requirements

Performing Class 2 studies for a given fuel product implies that the PCI technological limit of this product has been previously assessed. As a consequence, licensing a new fuel product requires the realisation of a power ramp test programme.

This programme has to be performed on fuel rods pre-irradiated in commercial PWRs and must cover a burn-up range typical of fuel management schemes. Moreover, a significant number of tests is expected to be performed to match the licensing requirements. It is with this aim that rods are extracted from demonstration assemblies during fuel outages. The rods are then shipped to testing facilities for re-fabrication, ramp testing, pre-ramp and post-ramp examinations.

A power ramp test programme including successive irradiations in commercial and experimental reactors runs for five to ten years, thus inducing high time constants. Beyond the financial cost that has to be supported for such a programme, it turns out that the PCI Class 2 qualification is often on the critical path of the whole licensing process. From that standpoint, PCI Class 2 safety requirements slow down the generalisation of new fuel products on EDF PWRs.

Constraints associated with PCI Class 2 studies

The PCI risk has the distinctive feature of being difficult to localise in the core, since it depends both on the initial thermo-mechanical state of the rod and on the local power during the transient.

Besides, rods with a high linear heat rate at base irradiation are not necessarily among those leading to the lowest margins. It is very difficult to highlight neutronic or thermo-mechanical key parameters that would allow simplifying the selection of limiting rods, unless it induces a high degree of conservatism in the studies. Consequently all the rods in the core have to be computed with neutronic and fuel performance codes, at normal operation (base, load follow, ERPO) as well as during Class 2 transients. This represents a huge volume of calculations to perform.

Improvements have certainly been made through the years regarding calculation capacities by means of regular hardware upgrades. But at the same time neutronic and fuel performance codes have benefited from modelling improvements leading to increased calculation times. Therefore PCI Class 2 studies turn out to be very costly: from a financial cost standpoint, then in terms of mobilisation of engineering manpower and finally regarding the time required to perform the entire studies. For example, the current PCI study associated with a future fuel management scheme on the 1 300 MWe plant series is planned over a two-year period and this does not take into account the potential future analyses during the licensing phase with the nuclear safety authority.

Constraints for plant operation

The PCI Class 2-related OTS were first introduced in the entire fleet of PWRs in the early 1990s. Since that time, the conditions of plant operation have been considerably modified in terms of manoeuvrability but also in terms of generation capacity and complexity for operators.

Manoeuvrability restrictions

Taking into account the PCI risk leads to a significant lowering of the protection set points and to a reduction of the plant operating diagram. For current fuel management schemes on EDF PWRs, plant operation limits are mainly due to PCI, which turns out to be more constraining than DNB or LOCA limitations.

This lowering of protection set points goes along with difficulties in following the grid demand, since it may lead to insufficient operating margins for load follow operations. Moreover it requires the operator to be particularly vigilant when returning to nominal power after a low power level.

ERPO limitations

The PCI-related OTS impose limitations in terms of maximum length of ERPO. As a consequence, if the K credit is completely consumed during an ERPO, the only solutions are either to return to full power or to shut down the plant if full power operation is no longer possible for any reason.

Situations of long-lasting ERPO are entirely conceivable due either to unavailability of equipments or due to constraints on the water cooling system mainly caused by severe climatic conditions (loss of performance of cooling towers, restrictions on the discharge temperatures). Besides, ERPO may be the only way of operating a plant until the end of a campaign. Under these conditions, the PCI-induced ERPO limitations constitute a major constraint for EDF in terms of generation capacity.

In the recent past, several units operating in ERPO have been confronted with severe manoeuvrability restrictions in order to avoid an anticipated shutdown. Since then, further studies have led to a partial relaxation of the PCI-induced ERPO limitations.

Power ramp rate restrictions during start-up (normal operation)

It should be mentioned that operation of plants is also affected by PCI-related constraints during the re-start of PWRs following a fuel outage. Start-up conditions have long been subject to strong restrictions on the power ramp rate in order to prevent PCI failures. A legacy of analyses performed in the 1970s has imposed a reactor power ascension rate of 3%/hr between 15 and 100% of core full power after fuel handling.

Further studies performed in the early 2000s have made it possible to relax the imposed power rate to 2%/mn between 15 and 50% of core full power while maintaining PCI safety requirements. The authorisation has been given by the nuclear safety authority and the relaxed OTS are under deployment at the different plant units. The use of less restrictive start-up conditions allows reducing the number of events associated with OTS non-respect because of power fluctuations at low power levels. Moreover it may decrease the time needed to achieve full power operation and therefore improve plant availability at each start-up. But the fact remains that the PCI issue has engendered severe restrictions on normal operation for over 20 years.

A challenge for the next decade: eliminating the overall PCI constraints

Within a strongly competitive environment, the need to reduce the overall PCI constraints is crucial for EDF. On the one hand, the need for plant manoeuvrability does not stop increasing since EDF aims at following the grid demand at its best. On the other hand, there are several plans for new fuel management strategies between 2005 and 2015 in connection with significant discharge burn-up increases up to 70 GWd/t [1]. These future strategies require high levels of performance and reliability from the fuel. In this context, several means of reducing the PCI constraints are currently being investigated so as to meet this challenge.

Beneficiating from the PCI methodology renovation

Advances in terms of fuel behaviour modelling and 3-D neutronic computations materialised in 2000 with the advent of new industrial codes. This came along with the updating of the Zy-4 technological limit based on recent power ramp tests. These developments have necessitated some adjustments in the PCI methodology. Authorisation was given by the nuclear safety authority in 2002 for the so-called “renovated PCI methodology” associated with FRAMATOME-ANP codes.

The use of the renovated methodology should save PCI margins and thus reduce some of the operating constraints. PCI studies related to new fuel management schemes for three of the four plant series and concerning 52 units are currently in progress based on this renovated methodology. These relaxed PCI-related OTS are planned to be progressively deployed as of 2005.

However, it should be noted that operating constraints will only be partly reduced and the need for increasing operating margins will still remain a major issue. Furthermore the volume of calculations to perform – and thus the length of PCI Class 2 studies – has not decreased.

Improving the modelling of phenomena

Another method of investigation lies in the understanding of the phenomena involved in PCI failure. Major improvements have certainly been accomplished in this field within the framework of CEA-EDF-FRAMATOME ANP research programmes. In particular, recent analyses now allow the

ranking of the different phenomena or exhibit numerous experimental evidences regarding the benefits of MOX pellets and high burn-up fuel in terms of resistance to PCI [2]. Moreover, innovative experiments such as ramp tests with zero holding time at power [2] are still in progress and should improve the understanding of phenomena.

With such efforts still under way, developments must now materialise in terms of advanced 3-D modelling [3] as well as in terms of 1-D industrial code [4]. Always bearing in mind the reduction of PCI-related constraints, EDF mid-term objectives for 2005-2007 are based on these improved modellings and aim at:

- Discriminating the behaviour of different pellet materials and thus enhancing the value of fuel products with PCI benefits.
- Rationalising the industrial qualification of future fuel products by optimising the power ramp tests to perform.
- Contributing to the reduction of operating constraints in the context of progressive introduction of PCI remedy fuel in commercial PWRs.

Qualifying a PCI remedy fuel

The most promising means of eliminating the PCI constraints relies naturally on the development and the qualification of a PCI remedy fuel, i.e. without any PCI-related constraint: it is expected from the PCI remedy fuel not only to remove the overall operating constraints but also to reduce the PCI Class 2 studies to the bare minimum.

Fuel vendors have been working for a long time on UO₂ microstructures with enlarged grain size obtained either by specific manufacturing conditions or by incorporation of additives such as Nb₂O₅, Cr₂O₃ or SiO₂. For various reasons, these advanced microstructures have proven to be beneficial regarding PCI behaviour. In this context, irradiations in EDF PWRs of experimental fuel assemblies containing several variants of additives from different vendors are in progress.

High expectations are placed on some of these advanced fuels, in particular the chromia-doped UO₂ pellets, which have already exhibited promising performances [5]. However, experimental programmes have to go further. The emphasis is now on demonstrative power ramp tests: the purpose is to show that the selected additive fuels are an effective remedy against PCI failure, whatever the type of incidental power transient. One should not forget either that the PCI remedy fuel is also expected to exhibit as far as possible an improved behaviour in terms of fission gas release reduction at high burn-up.

Conclusions

The increasing needs in plant manoeuvrability together with high expectations in terms of fuel performance and reliability are no longer compatible with the current PCI-related constraints on EDF PWRs. Several methods are currently being investigated to match the industrial goal of eliminating these constraints. The most promising solutions rely on PCI remedy fuels and should comply with the final objective for EDF of operating PWRs in the 2010s without any PCI-related constraint.

REFERENCES

- [1] Gy, J.F., *et al.*, “High Burn-up Fuel Management Schemes Considered in the French Electric System”, *International Topical Meeting on Light Water Reactor Fuel Performance*, Park City, Utah, April 2000.
- [2] Nonon, C., *et al.*, “Impact of Fuel Microstructure on PCI Behaviour”, *IAEA Technical Committee Meeting on Improved Fuel Pellet Materials and Designs*, Brussels, Belgium, October 2003.
- [3] Struzik, C., *et al.*, “Methodology for Multi-dimensional Simulation of Power Ramp Tests”, *Les Journées de Cadarache 2004, International Seminar on Pellet-clad Interaction in Water Reactor Fuels*, Aix-en-Provence, France, March 2004.
- [4] Masson, R., *et al.*, “Modelling 3-D Mechanical Phenomena in a 1-D Industrial Finite Element Code Results and Perspectives”, *Les Journées de Cadarache 2004, International Seminar on Pellet-clad Interaction in Water Reactor Fuels*, Aix-en-Provence, France, March 2004.
- [5] Nonon, C., *et al.*, “PCI Behaviour of Chromium Oxide Doped Fuel”, *Les Journées de Cadarache 2004, International Seminar on Pellet-clad Interaction in Water Reactor Fuels*, Aix-en-Provence, France, March 2004.

REVIEW OF OPERATIONAL REQUIREMENTS WITH RESPECT TO PCMI IN A VVER AND THE CORRESPONDING DEVELOPMENTS IN THE TRANSURANUS CODE

**P. Van Uffelen, K. Lassmann, A. Schubert,
J. van de Laar, Cs. Györi,¹ D. Elenkov,² B. Hatala³**

European Commission, Joint Research Centre, Institute for Transuranium Elements
P.O. Box 2340, 76125 Karlsruhe, Germany

¹KFKI Atomic Energy Research Institute, P.O. Box 49, H-1525 Budapest 114, Hungary

²Bulgarian Academy of Sciences, Institute for Nuclear Research and Nuclear Energy
Tsarigradsko shousse 72, BG-1784 Sofia, Bulgaria

³VÚJE Trnava, Inc. – Engineering, Design and Research Organisation
Okružná 5, SK-91864 Trnava, Slovak Republic

Abstract

Since the mid-90s, a version of the TRANSURANUS code has been under development for the analysis of the fuel rod performance in Russian-type VVER reactors. This required, among other things, the implementation of specific thermal and mechanical properties for Nb-containing cladding. The first part of the paper summarises the present status of the models for normal operating conditions. Further refinements will include the correlation between the effective creep strain rate and the effective stress.

In the second part of the paper we consider accident conditions for which new correlations have been developed, including plastic deformation, high-temperature oxidation and burst of the cladding. These conditions have been implemented in TRANSURANUS and verified by means of burst tests for as-received, oxidised and irradiated cladding specimens.

Finally, an outlook of the planned activities for code development and validation, including experiments regarding PCMI-related safety criteria for VVER reactors, is presented.

Introduction

Most of the important concepts of the TRANSURANUS code were developed between 1973-1984 at the Technical University Darmstadt [1,2] and in parallel from 1978-1982 at the Karlsruhe Research Centre (URANUS code):

- A clearly defined mechanical-mathematical framework into which physical models can easily be incorporated; “build-in mathematics” supports the modification and extension of the code and guarantees numerical stability.
- A consistent modelling of very different situations, as given for instance in an experiment, under normal, off-normal and accident conditions.
- A high flexibility: different fuel rod designs, time scales of irradiation conditions may range from milliseconds to years, a comprehensive materials database for oxide, mixed-oxide, carbide and nitride fuels, zircaloy and steel claddings and different coolants.
- Incorporation of a Monte Carlo (MC) technique for probabilistic analyses. A simpler probabilistic technique, the Numerical Noise technique, augments the MC technique for specific analyses.

Since 1982 main developments have been carried out at ITU [3,4]. The focus was on fast breeder reactors (FBRs), a development that was abandoned in 1992. Besides oxide, carbide and nitride fuels were also modelled and the TRANSURANUS code was coupled with the European Accident Code (EAC) [5], which aimed at analysing a hypothetical FBR core disruptive accident. Various further improvements were made and the name was changed from URANUS to TRANSURANUS.

In the period 1990-1992, following the political changes in Eastern Europe, the nuclear safety policy in Eastern European countries was reviewed and independent nuclear regulatory authorities were created. One of their main tasks was to establish licensing procedures and quality assurance (QA) systems, as requirements prior to loading nuclear fuel in reactors [6]. In response to this, support from many national and international organisations, especially the NEA of the OECD [7,8], the IAEA and the EU was organised. For example, within the FUMEX (Fuel Modelling at Extended Burn-ups) Co-ordinated Research Programme and two other related IAEA programmes (RER 4/12 and RER 4/19) the TRANSURANUS code was released to eight organisations in six different Eastern European countries. In conjunction with the code release, several training programmes were organised. Two EU PHARE programmes, FERONIA-BG [9] and FERONIA-CZ [10], helped facilitate the transfer of the TRANSURANUS code to two additional organisations in the Czech Republic (NRI Rez) and Bulgaria (INRNE) and to start the development of a specific VVER version of the TRANSURANUS code. Two other projects financed by the EU sustained this effort. The first, called PECO (Pays d'Europe Centrale et Orientale), was a joint project between the INRNE (Bulgaria), KFKI (Hungary), VUJE (Slovak Republic) and ITU, which ended in mid-2002. The second project, EXTRA, was a shared-cost action between KFKI, VUJE and ITU that started in December 2001 and finished by the end of 2003.

The present paper summarises the results of the VVER developments carried out by various partners of the TRANSURANUS user network since the mid 90s. First, we will summarise the main differences in design, safety criteria and operational experience between Western reactors and VVERs. Subsequently, the model developments for normal operating conditions will be reviewed. Developments resulting from the EXTRA project for simulations of accident conditions will then be summarised. In the final section, the different R&D needs will be outlined along with the various ways by which the developers and users of TRANSURANUS plan to tackle them.

Main differences between PWR and VVER fuel performance calculations

The differences of design and the concomitant fuel safety criteria for Western-type PWR and Russian-type VVER reactors call for specific fuel performance code developments. Rather than developing one specific code for each reactor type, the policy of ITU encourages the application of a single fuel performance code in order to promote harmonisation of the nuclear fuel licensing process in all European countries.¹ In 1990 the TRANSURANUS code fulfilled all these requirements for it could already be applied to LMFBRs, PWRs and BWRs during normal, off-normal and accident conditions alike. However, prior to reviewing the specific model developments for the VVER version of the TRANSURANUS code, we will review the main differences in design and safety criteria with respect to PCMI in PWRs and VVERs.

The main dissimilarities between the PWR and VVER fuel rod design [11,12] that have to be accounted for in a fuel performance code are the hexagonal lattice in VVER fuel assemblies, the annular UO₂ and (U,Gd)O₂ pellets, and the zirconium alloy cladding with 1% Nb (E110). The first two features were already implemented in the TRANSURANUS code for FBR applications, while the Nb-containing cladding material required the most important modifications (see below).

The main differences in the criteria that have to be assessed with a fuel performance code in the framework of fuel licensing or design calculations are [11]:

- The PCMI safety criterion is defined to avoid mechanical fracture as a result of stress due to pellet expansion, without the effect of iodine, during a transient. In Western-type reactors it is generally considered that this criterion is met when applying a 1% design limit on the total (elastic and plastic) strain. In VVERs there is a more conservative requirement that the stress remain below the standard yield strength for Class II events² (incidents without cladding failure). As a result, there is negligible plastic deformation and thus no need for a strain criterion. Nevertheless, it was concluded that the PCMI safety criteria should be reviewed in order to take into account the speed of the transient/accident [11].
- The safety criterion for the total oxidation level of the cladding during a LOCA event to prevent fragmentation and maintain a coolable geometry is similar for Western reactors [in general 17% equivalent cladding reacted (ECR)] and VVERs (18% ECR), although they are derived on a different basis. For Western reactors, one should clarify the role of the pre-transient oxidation level in the definition of the limit and complete the set of verification experiments. Nevertheless, for PWR and VVER fuel, typically 1-8% ECR levels and 5-6% ECR levels are observed respectively, so that a sufficient margin exists for actual fuel/core designs.
- The approach for the operational design criterion to prevent fuel failures due to stress corrosion cracking on the inside of the cladding during local power ramping (PCI) is similar between East and West, although the rules and numbers used are fuel-design specific. In general, they result in a restriction of the power increase as a function of time (burn-up).
- Design criteria to prevent cladding damage due to static and cyclic loads are less conservative for Western reactors in comparison with VVERs. For the Western reactors there is a limit on the stress (function of yield and tensile strength), the elastic plus plastic strain (typically 1% at

¹ Nevertheless, the fuel performance code applied by the licensing authorities should remain independent from the code applied by the fuel vendor.

² Reactor operating conditions are divided into 4 classes: Class I for normal operating conditions, Class II for incidents of moderate frequency, Class III for accidents of low frequency and Class IV for serious and hypothetical accidents.

BOL and 2.5% at EOL) and fatigue. VVER fuel rods on the other hand should have a cladding stress less than the standard yield strength, whereas there is only a strain limit for fast transients (max. 0.5% plastic deformation). The creep is also included in the fatigue limit for VVERs, so that the criteria are overall consistent in comparison with those in PWRs.

- For VVERs, the cladding diameter increase due to creep and cyclic accumulation of plastic deformation is limited to 0.4% in order to avoid stress corrosion cracking beyond. Such a design criterion is not defined for Western reactors, although further research was recommended to better understand the different behaviour of zircaloy-4 and Nb-containing Zr-alloys.
- For VVERs the ultimate cladding elongation design criterion is defined for Classes I-IV, whereas for Western reactors, the criterion only applies to Class I and II events. Accordingly, a review of the PWR criterion for rod elongation during Class II and IV events was recommended [11].

These criteria mostly influence the fuel licensing calculations (procedure) rather than the fuel performance code itself, although they highlight the code requirements in terms of application range and precision. The main code modifications required by the different design and safety criteria relate to the cladding oxidation model under LOCA conditions, where one should account for the different kinetics for Zr-Nb alloys when going through the alpha-beta transition (see below).

Despite the design differences and the different safety criteria applied, the same general performance is achieved for PWR and VVER assemblies [12]:

- The bulk of commercial fuel reaches burn-ups of 40-45 GWd/t and limited amounts of fuel are already discharged at 50 GWd/t. Future R&D targets include a burn-up of 60 GWd/t, and the extension of service beyond five years.
- A similar magnitude of fuel failure rates is observed in the range of $(2-5) \times 10^{-6}$ or more. In order to achieve the targets of operational reliability around 10^{-6} per year, further R&D efforts are focusing on grid-to-rod fretting in both types of reactors, while the axial offset anomaly is also an issue in PWRs.

Even though the main R&D objectives for fuel assemblies in VVERs and PWRs are similar, there remains a fundamental difference with respect to the materials research: the main limiting design criteria for VVERs are the mechanical and dimensional stability of fuel elements, as opposed to the cladding corrosion and the associated hydriding issue in PWRs. For these reasons, a material with higher mechanical stability (E635) is being introduced in the structure of new fuel assemblies for VVERs, while several advanced Zr-based cladding materials (e.g. M5, ZIRLO, etc.) have been successfully introduced in PWRs to reduce the external corrosion layer thickness.

A second major difference is the commercial use of MOX fuel in Western-type light water reactors, whereas its use in VVERs is now only considered in the framework of the programme for reactor-based plutonium disposition [13].

In view of the above-mentioned tendencies and related issues, the general requirements for the fuel performance code developments consist of a model for fission gas behaviour in high burn-up fuel, along with the introduction of material properties for new materials (see below). For the generic fuel performance codes, however, it is hard to obtain data for new materials (proprietary data for fuel and cladding). Therefore, networking has proven to be a key element – especially when safety issues are at stake – which is part of the objectives of the TRANSURANUS network.

Present status of TRANSURANUS-VVER for normal operating conditions

Code developments

The following paragraphs provide a brief overview of the VVER-specific model developments incorporated in the TRANSURANUS code so far. In the starting phase, the PINMicro code [14] (dedicated to VVER fuel rod modelling) had been analysed. As far as possible it was used as a basis, as described in Ref. [15].

Pellet properties

The annular cylindrical geometry of the VVER fuel is already treated as standard option in the TRANSURANUS code. The fuel thermal conductivity is modelled by the standard TRANSURANUS correlation for UO₂ fuel that was derived at ITU Karlsruhe from literature as well as in-house experimental data [16].

To describe the fuel densification, a generalised formula containing an exponential dependence on burn-up is used. It is based on experimental results from the OECD Halden reactor project [17]. Fuel swelling is treated by means of a simple rate equation. This approach takes into account the contribution of the swelling to the fuel volume change in the early-life irradiation period. The presently applied swelling rate of 0.9% per 10 MWd/kgHM is being reviewed to account for improvements in the swelling properties of VVER fuel [18].

Cladding properties

Most of the relevant thermal and mechanical properties of the Zr1%Nb cladding were directly derived from the comprehensive report of Volkov, *et al.* [19], which was also the basis for the development of the PINMicro code [14]. More precisely, empirical dependences on the local temperature are implemented for:

- Young's modulus and Poisson's ratio of the cladding (linear dependence).
- Specific heat of the cladding (second-order polynomials).

A compilation of experimental data by Zaimovskij [20] was used as the basis for the development of correlations for:

- The cladding thermal linear expansion coefficient (second-order polynomial).
- The cladding thermal conductivity (third-order polynomial).

In TRANSURANUS an effective creep rate is used for describing the relation between stress and strain. Following the MATPRO-N1 library [19], three optional correlations were implemented. In a first test, these options were compared to the results of additional strain experiments with Zr1%Nb tubes [21,22]. Based on this work, the following expression was chosen for normal operating conditions of VVER fuel:

$$\dot{\epsilon}_{eff} = \left(1.554 \times 10^{-30} \sigma_{eff} + 7.006 \times 10^{-36} \sigma_{eff}^4\right) \Phi + 3.342 \times 10^{-4} \sigma_{eff}^{3.2} e^{\frac{18000}{T}} \quad (1)$$

where $\dot{\epsilon}_{eff}$ is the effective creep rate (1/s), σ_{eff} is the effective stress (Mpa), T is the temperature (K) and Φ is the fast neutron flux with energies $E_n > 1$ MeV (n/m^2s).

The anisotropy coefficients that appear in the flow law (which is not given here) and that define the relation between the effective strain and its radial, tangential and axial components require further consideration. Additional work is also necessary to clarify possible additional time-dependent factors.

In its present version TRANSURANUS uses an empirical dependence of the rod elongation on the burn-up, based on published rod elongation data [23,24]. Further verification of the rod elongation model with experimental data is planned so that the code will enable the corresponding design criterion (see above) to be verified.

Code validation

In the following we summarise the status of the validation of calculated fuel centre temperatures and of fission gas release for normal operating conditions of VVER fuel. Additional validation work regarding dimensional changes and fission gas release, based on experimental data from KOLA3 [25], is still ongoing and is therefore not reported here. Verification of the TRANSURANUS calculations for storage conditions was initiated at AEKI [26] but will be continued in the coming JRC-sponsored enlargement project for Bulgaria.

Central temperatures

In the frame of a comprehensive verification programme, more than 40 000 predictions of fuel centre temperatures by TRANSURANUS had been analysed and compared to experimental results [16]. The data were grouped according to fuel types (standard Western-type UO_2 , UO_2 -VVER and MOX) and irradiation conditions (OECD Halden Reactor Project and the Finnish-Russian SOFIT programme). The vast majority of calculated points deviates less than 10% from the measured data. No overall bias can be seen. The standard deviation for the total amount of data is below 4%.

A number of datasets has been selected to compare the behaviour for both Western-type UO_2 fuel (11 412 data points) and UO_2 -VVER fuel (11 157 data points), irradiated in the same assembly of the OECD Halden reactor. For these two types of fuel, Figure 1 shows the relation between measured and calculated fuel centre temperatures in two different rod geometries (small gap and large gap). Experimental data on VVER fuel had also been obtained from the Finnish-Russian SOFIT programme and compiled in the IFPE database [8]. This data enables an investigation of calculated and measured temperatures under completely independent irradiation conditions. Figure 2 compares the data of the SOFIT programme to those obtained from the OECD Halden reactor project.

The following observations can be made from the data:

- 1) The overall range of deviations between measured and calculated fuel centre temperatures is almost identical for standard Western-type and VVER-type UO_2 fuel. Figure 1 illustrates that the rods of the same gap size have a similar performance, irrespective of the fuel type.
- 2) Very good agreement of the fuel temperature predictions is seen in the small-gap rods [Figure 1(a)]. For the large-gap rods the agreement is still fair [Figure 1(b)] but the results point to a systematic underestimation. In the context of the large fuel-cladding gap (270 μm)

the trend is expected to arise mainly from the application of a constant fuel swelling rate, and because of the relocation effect that affects the eccentricity in large-gap rods.

- 3) The deviation of code predictions from experimental results is consistent for both independent data sources (Figure 2). This is an important step in the verification of the VVER version of TRANSURANUS.

Figure 1. Comparison of calculated versus measured fuel centre temperatures for UO_2 fuel rods irradiated in the OECD Halden reactor

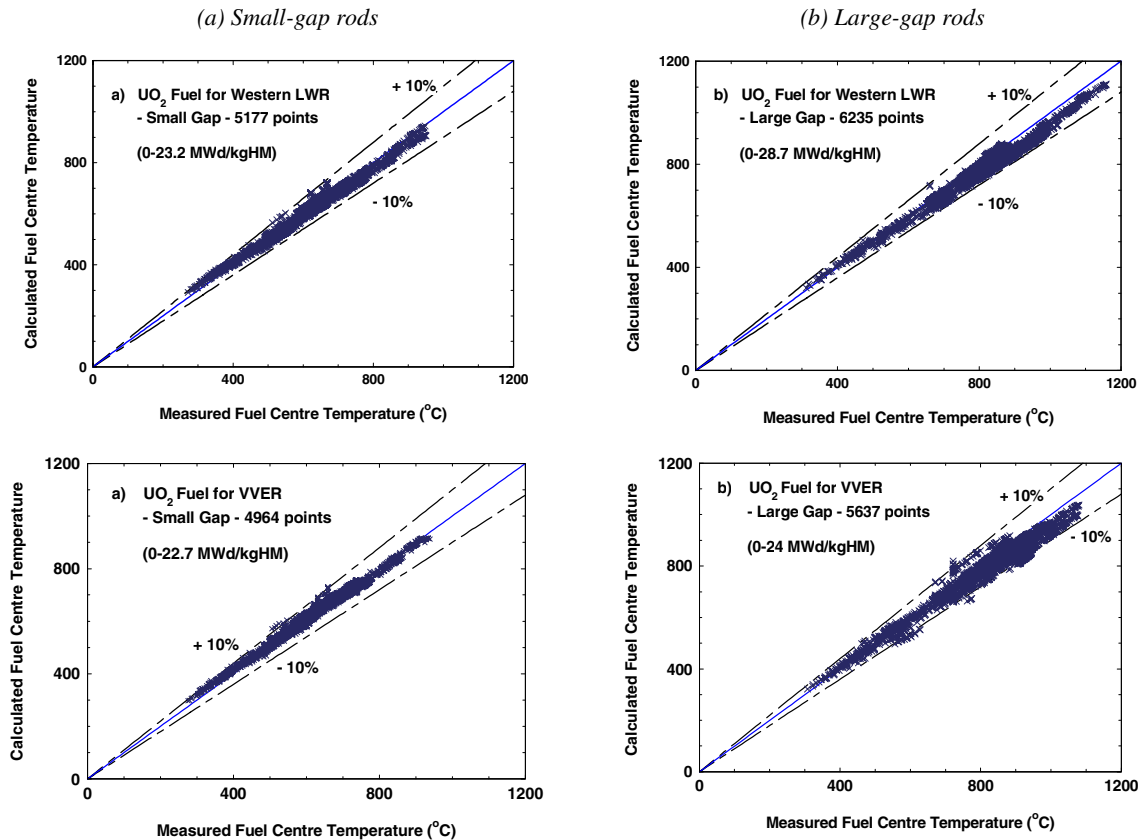
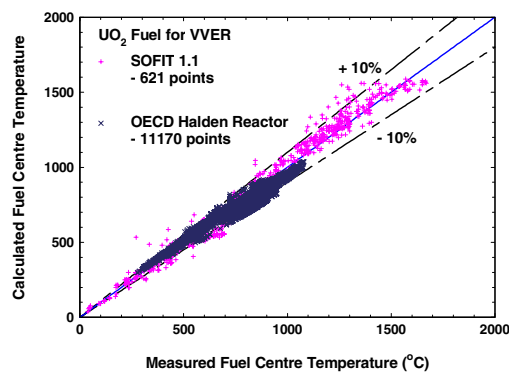


Figure 2. Comparison of calculated versus measured fuel centre temperatures for UO_2 -VVER fuel rods in different irradiation conditions: SOFIT programme, compared to those irradiated at the OECD Halden reactor

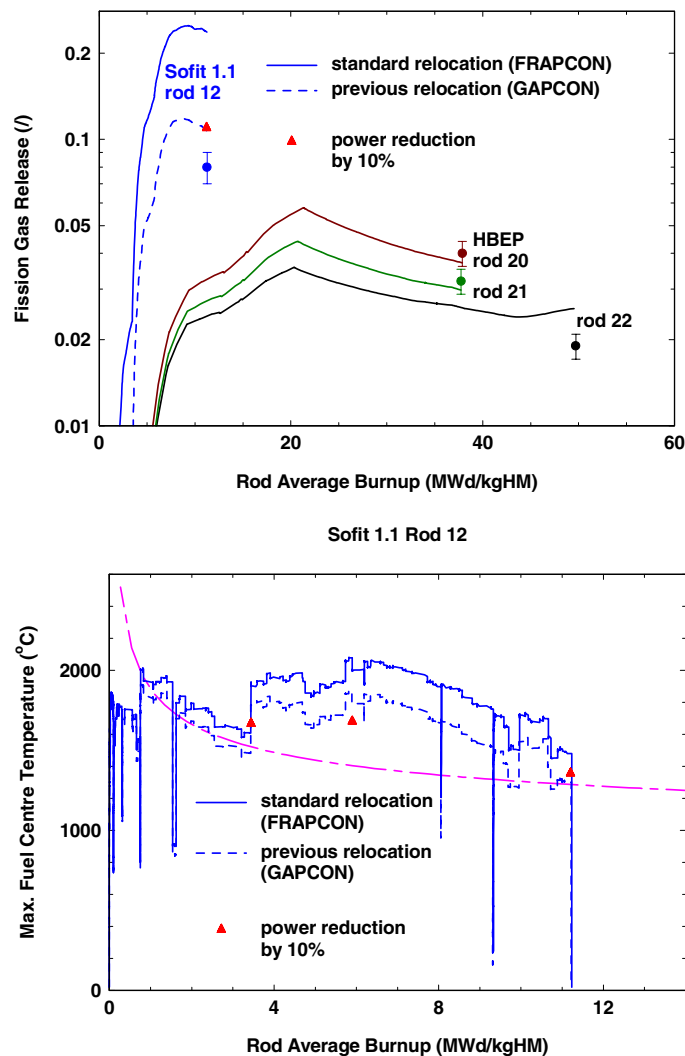


Fission gas release

Systematic analyses of data on fission gas release are much more complicated because most measurements are not performed during the irradiation, but during post-irradiation examinations (PIE). In the SOFIT programme only one VVER fuel rod could be thoroughly analysed for fission gas release. A first comparison with data for Western-type fuel from the IFPE database is described in Ref. [27]. The overall agreement is very encouraging. For three Western-type UO₂ fuel rods selected from the High Burn-up Effects Programme (HBEP) the predicted and calculated fractional fission gas release is shown in Figure 3.

Figure 3. Burn-up dependence of the calculated fission gas release (top) and the calculated fuel centre temperature (bottom) for the UO₂-VVER fuel rod of the SOFIT programme discussed in the text

Note the considerable decrease of both temperature and fission gas release that is caused by a 10% change in linear heat rate. For comparison, the top graph also shows three fission gas release measurements from the High Burn-up Effects Programme (HBEP), together with the values calculated by TRANSURANUS.



However, for the VVER fuel rod investigated in the SOFIT programme the standard options of TRANSURANUS lead to a strong overestimation of the measured fission gas release (Figure 3). The specific rod was operated at very high power (up to 46 kW/m) and had a low initial gas pressure (0.1 MPa He). The analysis confirms the non-linearity of the release response as well as the strong thermal feedback. Applying a non-standard relocation model (GAPCON [28]) results in earlier closure of the gap and considerably lower fuel temperature and fission gas release. It is interesting to note that a simple reduction of the applied linear heat rate by 10% leads to an effect comparable to that of the non-standard relocation. In view of the realistic measurement uncertainties and of the limited number of experimental data it is difficult to draw definite conclusions. A comprehensive verification of the code requires further experimental data for fission gas release of VVER fuel irradiated at low as well as high power, including detailed irradiation histories and pre-characterisation data.

Based on the advent of modern computer technology as well as the more detailed experimental data becoming available, the ITU modelling group has decided to introduce more mechanistic models into the fuel performance code. In a first step, a mechanistic fission gas release and swelling model will be introduced and tested. Although such a model requires more experimental data for the final fitting of the numerous parameters, it should improve our understanding and the description of the detailed phenomena involved in the process.

Present status of TRANSURANUS-VVER for accident conditions

Right from the start of the TRANSURANUS code development, both the numerical techniques and the phenomena were selected so as to enable consistent simulations of normal, off-normal and accident conditions alike in FBRs as well as LWRs. The main specific requirement to also apply the code under accident conditions to VVER fuel was to include specific models for Zr1%Nb cladding in the high temperature range (see above). This constituted the main objective of the EXTRA project that was funded by the 5th Framework Programme of EURATOM [29]. In this project, the best-estimate description of the key phenomena under accidental conditions, as the zirconium-steam reaction, the plastic deformation and the rupture of the Zr1%Nb cladding tube were developed and validated. The empirical correlations were based on a newly compiled database of nearly 400 separate effect tests performed at the AEKI.

Code developments

Cladding oxidation in steam

The zirconium-steam reaction model of the TRANSURANUS code is based on parabolic kinetic correlations for both the oxygen mass gain and the ZrO₂ layer thickness growth and is adequate to simulate the cladding oxidation under temperature transients. The incorporated model calculates the rise of the oxygen concentration in the cladding and the ZrO₂ layer increase by means of the well-known recursive formula:

$$X_i = \sqrt{X_{i-1}^2 + K_i^2 dt_i}$$

where X is the extent of the oxidation, i.e. oxygen mass gain per unit area (Δm) or ZrO₂ thickness (δ_{ZrO_2}), K is the reaction rate constant, dt is the time step length and i is the time step index.

The new best-estimate correlations of the AEKI describing the reaction rate constants for Zr1%Nb alloy in the temperature (T) interval of 800-1 500 K reads as follows:

$$K = \begin{cases} 658 e^{\frac{-10200}{T}}, & \text{if } X = \Delta m \text{ (mg/cm}^2\text{/s}^{0.5}\text{)} \\ 4 e^{\frac{-10200}{T}}, & \text{if } X = \delta_{ZrO_2} \text{ (mm/s}^{0.5}\text{)} \end{cases}$$

In order to define the oxidation kinetics of the cladding an optional VVER-specific model from Solyany [30] is also applicable in the code. This second correlation provides a conservative approach for the oxygen up-take.

Cladding ballooning and rupture

In conformity with the TRANSURANUS mechanical model, the dependence of the effective strain rate on temperature, effective stress and the crystallographic phase of the VVER fuels' cladding is expressed by means of a modified Norton-type equation. However, the evolved creep rate correlation takes into account the actual oxygen concentration in the cladding as well. In this manner, the relevant effect of the oxidation on both the strength and the cladding deformation can also be simulated as follows:

$$\dot{\epsilon}_{eff} = f_{\alpha} k_{\alpha} e^{\frac{-Q_{\alpha} + b(x)}{RT}} \sigma_{eff}^{n_{\alpha}} + (1 - f_{\alpha}) k_{\beta} e^{\frac{-Q_{\beta} + b(x)}{RT}} \sigma_{eff}^{n_{\beta}}$$

where f_{α} is the weight fraction of the α zirconium, $\dot{\epsilon}_{eff}$ is the effective strain rate (1/s), σ_{eff} is the effective stress (MPa), R is the universal gas constant (J/mol/K), T is the temperature (K), k , Q and n are the Norton parameters in the α and β crystallographic phases and $b(x)$ is the oxygen concentration (x) term.

The Norton parameters were fitted to experimental data by a Levenberg-Marquardt method. The oxygen concentration term was evaluated by means of sensitivity analyses.

Table 1. Norton parameters and oxygen concentration term for Zr1%Nb cladding

α -phase (600-800°C)		β -phase (900-1 200°C)	
k_{α}	6.06×10^6	K_{β}	1.44
Q_{α}	3.58×10^5	Q_{β}	1.82×10^6
n_{α}	5.18	N_{β}	5.82
$b(x)$	$-7.06 \times 10^6 x^3 + 5.190 \times 10^4 x^2 - 6.03 \times 10^2 x$ ($x \leq 0.02$) $+1.35 \times 10^3 x^3 - 5.015 \times 10^3 x^2 + 6.94 \times 10^2 x - 8.8$ ($x > 0.02$)		

Beyond a proper strain rate relation, rupture criteria are also necessary to evaluate the number of inhermetic fuel rods and the maximum residual deformation. The failure of the cladding tube can be predicted on the basis of two optional criteria:

- 1) The first (standard) criterion is a typical stress-based evaluation. Cladding failure is indicated when the true tangential stress exceeded the threshold stress defined on the basis of experimental data.
- 2) The second criterion is related to plastic instability conditions. When both the strain and the strain rate exceed certain threshold values (0.02 and 100 1/h, respectively) the cladding is assumed in hermetic. This tentative criterion is suggested to overcome unreliable (very sensitive) predictions of the stress and strain.

Code validation

The validation of the models in the TRANSURANUS code involves various phases. In the first phase, the models are being tested in a separate environment against exact numerical solutions as well as some experimental data from separate effect tests, if available. In a second step, the models incorporated in the code and the updated code predictions are compared with results from other codes and experimental results. The same approach was adopted for the validation of the newly developed models for Zr1%Nb cladding. Nevertheless, in the present paper we limit ourselves to the comparison of the code predictions against experimental data from separate effect tests and integral tests.

Relevant effort has been focused on the verification of the newly developed correlations and the validation of the extended TRANSURANUS code. Comparison of the code results with analytic solutions proved the correctness of the applied algorithms. VVER-specific separate effect tests and integral tests were also simulated in the EXTRA project. The post-test analyses of more than 200 cladding ballooning tests constituted the most important part for the code validation. Isothermal or isobar burst tests performed with as-received, pre-oxidised or irradiated Zr1%Nb tube specimens were simulated. Figure 4 represents the history of a typical burst test analysis when the rod internal pressure was increased linearly under isothermal conditions. The cladding strain, calculated by TRANSURANUS, indicates a highly non-linear process with accelerating creep deformation (ballooning) right before the failure. The calculated burst time and maximum tangential strain can be compared with the experimental data. The comparison of the calculated and measured time of burst for a large number of tests clearly indicated the correctness of the TRANSURANUS simulations (Figure 5). The code reliably predicts the time of failure for the slow as well as for the fast experiments either with as-received, oxidised or irradiated cladding specimens.

Figure 4. Rod internal pressure and tangential strain calculated by the TRANSURANUS code for a cladding burst test

The square point represents the measured residual strain at the time of failure

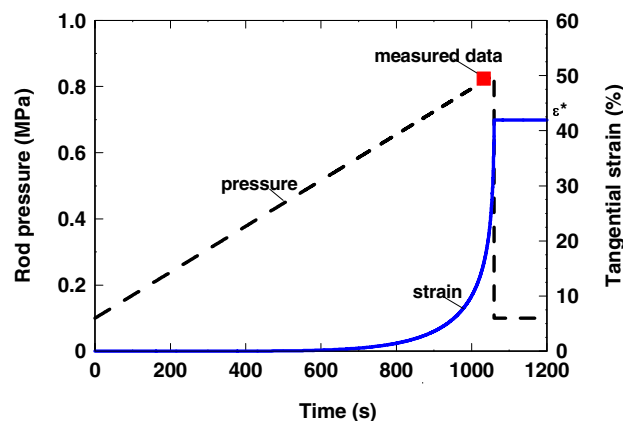
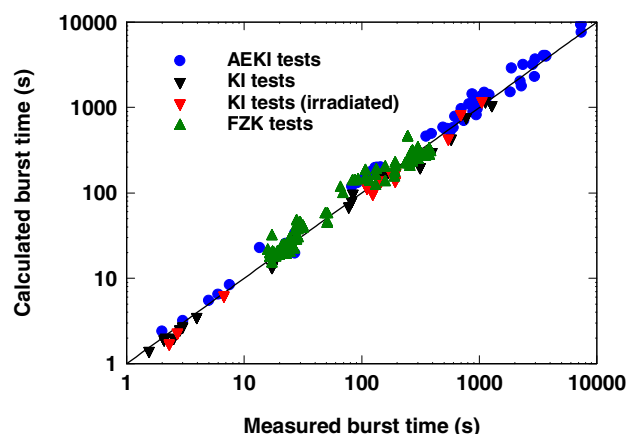


Figure 5. Validation of the extended TRANSURANUS code, comparison of measured and calculated time of failure in 192 cladding burst tests

Experimental data represent the isothermal tests of the AEKI with as-received and pre-oxidised claddings [31], the isothermal tests of the Kurchatov Institute (KI) with as-received and irradiated claddings [32] and the isobar tests of the Forschungszentrum Karlsruhe (FZK) [33] performed in oxidising atmosphere



Conclusions and perspectives for TRANSURANUS-VVER

Since 1990 VVER-specific developments were carried out by various TRANSURANUS users. Support from the European Union was provided through the PHARE projects and the specific enlargement activities of the Joint Research Centre from the European Commission in order to promote the harmonisation of nuclear fuel safety in both Western PWR and Russian-type VVER reactors. The driving forces for developments result from both the differences in design and safety criteria. Our efforts were therefore concentrated on the material properties of Zr1%Nb cladding material for normal operating conditions as well as accident conditions. The validation work has been based on experimental data obtained from the IFPE database as well as from the OECD Halden Reactor Project. The results are very promising, although more data are needed.

Future development work for VVER applications will be primarily directed to the modelling of release and swelling in high burn-up fuel and cladding creep under storage conditions, including the relation between the effective creep strain rate and the effective stress. This work will be supported by the specific enlargement action of the Joint Research Centre.

The validation work will also be extended. AEKI initiated an experimental programme with separate tests to measure the hydrogen absorption and the mechanical properties (yield stress and ultimate tensile strength) of Zr1%Nb as a function of the hydrogen content by means of standardised ring compression and tensile tests. Furthermore, creep tests with both pre-irradiated and as-received cladding segments of Zry-2, Zirlo, M5 and E110 are being carried out in the Halden Boiling Water Reactor. In addition to the separate effect tests, we will analyse the onset of PCMI in a Halden test rig in the framework of the co-ordinated research project FUMEX-II organised by the IAEA. These experiments will help us to further refine the cladding creep models.

As far as the validation work for application of the TRANSURANUS code to design basis accidents is concerned, we are considering participation in two international round robin exercises. The first is part of FUMEX-II, but remains under discussion. The second is organised by the Expert Group on Fuel Safety Margins of the OECD/NEA and would be based on a LOCA test carried out in the OECD Halden Reactor Project.

REFERENCES

- [1] Lassmann, K., "URANUS – A Computer Programme for the Thermal and Mechanical Analysis of the Fuel Rods in a Nuclear Reactor", *Nucl. Eng. Design*, Vol. 45, No.2, 325-342 (Feb. 1978).
- [2] Lassmann, K., *Stand und Problematik der Brennstab-Strukturanalyse*, Kernforschungszentrum Karlsruhe, KfK 2875, Darmstädter Habilitation D 17 (Feb. 1980).
- [3] Lassmann, K., H. Blank, "Modelling of Fuel Rod Behaviour and Recent Advances of the TRANSURANUS Code", *Nucl. Eng. Design*, 106, 291-313 (1988).
- [4] Lassmann, K., "TRANSURANUS: A Fuel Rod Analysis Code Ready for Use", *Journal of Nuclear Materials*, 188, 295-302 (1992).
- [5] Wider, H.U., *et al.*, "The European Accident Code EAC-2: Overview and Status", *International ANS Topical Fast Reactor Safety Meeting*, 12-16 August 1990, Snowbird, UT (USA).
- [6] Chantoin, P., J.A. Turnbull, W. Wiesenack, "How Good is Fuel Modelling at Extended Burn-ups?", *Nuclear Engineering International*, p. 32 (Sept. 1997).
- [7] *Scientific Issues in Fuel Behaviour*, OECD Documents, A report by an NEA Nuclear Science Committee Task Force, Nuclear Energy Agency, AEN-NEA (January 1995).
- [8] Menut, P., E. Sartori, J.A. Turnbull, "The Public Domain Database on Nuclear Performance Experiments (IFPE) for the Purpose of Code Development and Validation", *International Seminar on Fission Gas Behaviour in Water Reactor Fuels*, Cadarache, France, 26-29 September 2000.
- [9] Elenkov, D., K. Lassmann, *FERONIA Final Report*, PHARE/BG/ TSO/VVER/02, June 1998.
- [10] Svoboda, R., *FERONIA Final Report and Project Summary*, PHARE/CZ/TSO/VVER/04, December 1998.
- [11] *Analysis of Differences in Fuel Safety Criteria for VVER and Western PWR Nuclear Power Plants*, IAEA-TECDOC-1381, Vienna, November 2003.
- [12] Weidinger, H.G., "Status and Future Perspectives of PWR and Comparing Views on VVER Fuel Technology", *5th International Conference on VVER Fuel Performance, Modelling and Experimental Support*, Albena (Bulgaria), 29 September-3 October 2003, proceedings in press.
- [13] *Summary Record of the Seventh Meeting of the Expert Group on Reactor-based Plutonium Disposition*, NEA/NSC/DOC(2003)15
- [14] Strijov, P., F. Pazdera, M. Valach, "Code PIN-04M and Verification of its Predictability", *VANT Series Atomnoe Materialovedenie*, 2 (1988).

- [15] Elenkov, D., K. Lassmann, “The Development of the TRANSURANUS-VVER Version”, *Proceedings of the 3rd International Seminar on VVER Fuel Performance, Modelling and Experimental Support*, Pamporovo, Bulgaria, 4-8 October 1999, pp. 245-251.
- [16] Schubert, A., C. Györi, D. Elenkov, K. Lassmann and J. van de Laar, “Analysis of Fuel Centre Temperatures with the TRANSURANUS Code”, *International Conference on Nuclear Fuel ENS TopFuel 2003/ANS LWR Fuel Performance Meeting*, Würzburg (Germany), 16-19 March 2003, shortened version in: *Atw/International Journal for Nuclear Power*, 12/2003, pp. 756-761.
- [17] Devold, H., S. Lemehov, “In-pile Comparative Test of Thermal and Mechanical Behaviour of PWR/VVER Fuel”, *2nd International Meeting on Fuel Performance, Modelling and Experimental Support*, Sandanski, Bulgaria (1997), p. 234.
- [18] Golovanov, V.N., V.I. Kuzmin, S.V. Kuzmin, G.I Mayorshina, *Technical Committee Meeting on Nuclear Fuel Behaviour Modelling at High Burn-up and its Experimental Support*, Windermere, June 2000, IAEA-TECDOC-1233, p. 417.
- [19] Volkov, B.Y., V.F. Viktorov, P.A. Platonov, A. Rjazantzeva, *Library of Subprograms on Physical and Mechanical Properties of the NI-Alloy Fuel Rod Cladding Material*, IAE-4941/11, Moscow (1989) (in Russian).
- [20] Zaimovskij, A.S., *et al.*, “Zirconium Alloys in the Atomic Power Engineering”, Moscow, *Energoizdat* (1994).
- [21] Djourelov, N., “Study of Zr1%Nb Cladding Material Creep Strain Correlations Incorporated in the TRANSURANUS-VVER Code”, *Proceedings of the 4th International Conference on VVER Fuel Performance, Modelling and Experimental Support*, Albena, Bulgaria, 1-5 October 2001, pp. 316-321.
- [22] Kobilianskij, G., A. Novoselov, *Handbook of Reactor Materials – Irradiation Resistance of Zirconium Alloys*, Dimitrovgrad (1996) (in Russian).
- [23] Smirnov, A., V. Smirnov, A. Petuhov, B. Kanashov, V. Kuzmin, A. Novoselov, Y. Bibilashvili, V. Tzibulya, E. Bek, “The Peculiarities of the VVER-440 Fuel Behaviour at Higher Burn-ups”, *Proceedings of the 2nd International Seminar on VVER Fuel Performance, Modelling and Experimental Support*, Sandanski, Bulgaria, 21-25 April 1997, pp. 58-65.
- [24] Markov, D., A. Smirnov, V. Polenok, V. Kuzmin, A. Novoselov, “Validation of VVER-1000 Fuel Rod Efficiency at Operation During Four Fuel Cycles”, *Proceedings of 3rd International Seminar on VVER Fuel Performance, Modelling and Experimental Support*, Pamporovo, Bulgaria, 4-8 October 1999, pp. 147-152.
- [25] Elenkov, D., S. Boneva, N. Djourelov, M. Georgieva, S. Georgiev, “Verification of the TRANSURANUS-VVER Code Version V1M2J00 by SOFIT and KOLA-3 Data Bases”, *Proceedings of the 4th International Conference on VVER Fuel Performance, Modelling and Experimental Support*, Albena (Bulgaria), 1-5 October 2001, pp. 299-315.
- [26] Györi, Cs., Z. Hozer, “TRANSURANUS Simulation of VVER Cladding Creep Under Dry Storage Conditions (IAEA-CN-102 21)”, *Proceedings of IAEA Conference on Storage of Spent Fuel for Power Reactors*, 2-6 June 2003, IAEA Conference and Symposium Papers 20/P, pp. 360-366.

- [27] Schubert, A., K. Lassmann, P. Van Uffelen, J. van de Laar, D. Elenkov, S. Asenov, S. Boneva, N. Djourelou, M. Georgieva, "Analysis of Fuel Centre Temperatures and Fission Gas Release Data from the IFPE Database", *5th International Conference on VVER Fuel Performance, Modelling and Experimental Support*, Albena (Bulgaria), 29 September-3 October 2003, proceedings in press.
- [28] Lanning, D.D., *et al.*, *GAPCON-THERMAL-3 Code Description*, PNL-2434/NRC-1, 3 (1978).
- [29] Györi, Cs., Z. Hózer, K. Lassmann, A. Schubert, J. van de Laar, M. Cvan, B. Hatala, "Extension of the TRANSURANUS Code Applicability with Niobium Containing Cladding Models (EXTRA)", *Proceedings of FISA 2003: Symposium on EU Research in Reactor Safety*, Luxembourg, 10-13 November 2003, pp. 589-594.
- [30] Solyany, V.I., Yu.K. Bibilashvili, V.Yu. Tonkov, "High Temperature Oxidation and Deformation of Zr1%Nb Alloy of VVER Fuels", *Proceedings OECD-NEA-CSNI/IAEA Specialists Meeting on Water Reactor Fuel Safety and Fission Product Release in Off-normal and Accident Conditions*, Risø, Denmark, 16-20 May 1983. p. 163.
- [31] Györi, Cs., Z. Hózer, L. Maróti, L. Matus, "VVER Ballooning Experiments", *EHPG Meeting*, Lillehammer, March 1998, HPR-349/40.
- [32] Yegorova, L., *Data Base on the Behaviour of High Burn-up Fuel Rods with Zr1%Nb Cladding and UO₂ Fuel (VVER Type) Under Reactivity Accident Conditions*, NUREG/IA-0156, NSI RRC 2179, Moscow 1998.
- [33] Erbacher, F.J., *et al.*, *Temperaturtransiente Kriechberstversuche an Zirconium-Niob1-Hüllrohren*, FZKA 5726, Karlsruhe (1997).

PCMI IMPLICATIONS FOR HIGH BURN-UP LIGHT WATER REACTOR FUEL IN REACTIVITY-INITIATED ACCIDENTS

C. Vitanza, J.M. Conde Lopez

Abstract

The state of the cladding is essential for the fuel's ability to withstand RIA transients. In particular, some ductility must be retained in order to accommodate the PCMI caused by the fuel expansion. Other parameters such as RIA pulse width and fuel type may have some effect, but the available information indicates that it would be small as compared with cladding brittleness. The main consideration is cladding oxidation, as this determines how brittle the cladding can become. Cladding oxidation is thus of paramount importance for normal operation as well as for the response to RIA transients. The reason that BWR fuel becomes brittle within a moderate burn-up increment, possibly as consequence of low power operation during the last cycle, deserves attention in future research.

Introduction

The trend to increase the fuel discharge burn-up in commercial reactors has highlighted the fact that the dominant fuel phenomena at high burn-up can be very different from those governing the low burn-up fuel behaviour. Issues like increased fission gas release, fuel thermal conductivity degradation, “rim” formation and precipitation of hydrides within the cladding wall due to increased corrosion can cause changes in fuel performance and under some circumstances impair the cladding integrity. The complexity of these phenomena has also challenged the capability to predict the behaviour of high burn-up fuel, and questions have been raised as to the validity of some of the criteria and parameters used to characterise the safe operation of the fuel under various anticipated accident scenarios.

One of these scenarios is the reactivity-initiated accident (RIA), in which the energy deposited in the fuel rod increases very rapidly – within several milliseconds – causing a fast overheating of the fuel and eventually of the cladding. Experience from pulse test reactors shows that rod failure at high burn-up may occur in the pulse-phase of the transient and that the mechanism responsible for this is the pellet-clad mechanical interaction (PCMI). Due to the fuel and cladding conditions at high burn-up, such failures may occur at appreciably lower energy as compared with fresh or low burn-up fuel.

This paper discusses some basic aspects of PCMI during a RIA transient and addresses the effect of the fuel burn-up on the PCMI occurrence. The discussion is based primarily on the authors’ interpretation of published experimental results from CABRI-REPNa and NSRR tests, which constitute the most valuable database for high burn-up RIA investigations. The main points of this discussion are as follows:

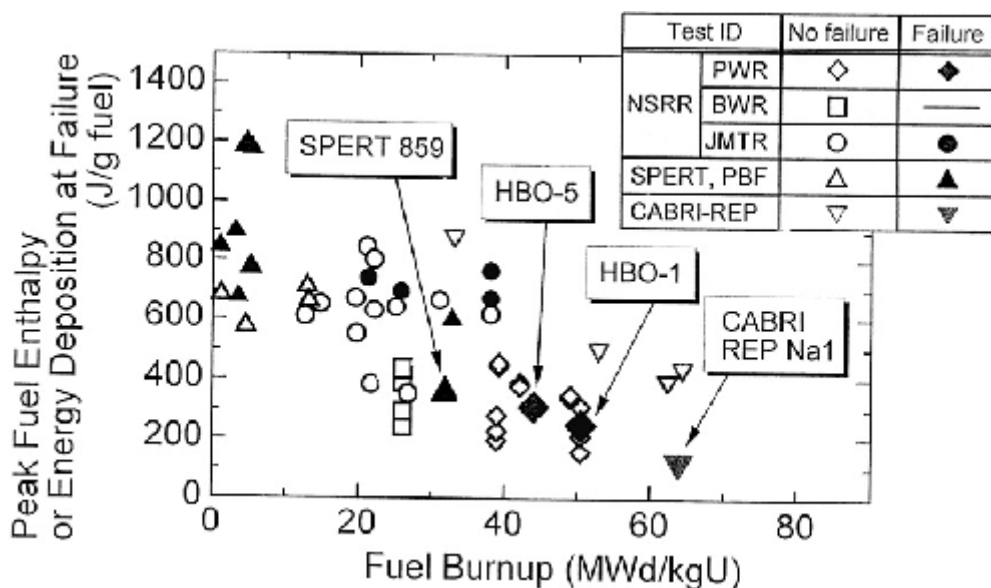
- The onset of PCMI depends on burn-up and, when burn-up is high, on the power level in the last operating period. A simple correlation between the fuel enthalpy at which PCMI starts and the power in the last operating period has been derived. A correlation for calculating cladding strain as function of enthalpy and burn-up has also been derived.
- Spalling of the oxide layer, when it happens, does so in the early phase of the transient, when the enthalpy is low. Thus, it should not induce premature rod dry-out.
- The RIA-induced PCMI can produce incipient cracking starting from the cladding outer surface. Such a cracking pattern is observed in different type of tests, i.e. RIA tests, power ramps and cladding tensile tests of high burn-up specimens.
- The effect of pulse width on PCMI and on failure propensity has been analysed based on experimental data. From the data it does not appear that pulse width has a decisive role on PCMI or failure. Likewise, there seems to be no great difference in behaviour in terms of PCMI between UO_2 and MOX fuels, at least for the range of enthalpy explored in this paper.
- The importance of cladding temperature regarding PCMI behaviour is addressed taking both experimental results and code calculations into account. The cladding temperature is important because of its possible influence on cladding ductility during the transient. However, the analysis performed here shows that a 10-30 ms difference in pulse width should not greatly modify the cladding temperature, and hence the rod failure propensity.
- The correlation for RIA failure threshold developed earlier by Vitanza has been re-visited and slightly adapted for application to transients starting from non-zero power. The effect of decreased ductility for RIA starting from cold zero-power conditions is also discussed.

Overview of PCMI phenomena in a RIA transient

Pellet-cladding mechanical interaction (PCMI) is one of the fuel failure mechanisms associated with reactivity accidents in LWRs. At increasing burn-up, PCMI-induced failures may occur at progressively lower fuel enthalpy as evidenced by the results shown in Figure 1, where the data from various RIA experiments are grouped in the same plot [1]. Although one should be cautious about some of the data, the figure indicates that failures at high burn-up can occur at enthalpy ~3 times lower than for as-fabricated or low burn-up fuel.

Figure 1. Fuel enthalpy for failed and un-failed fuel tested in different programmes

This figure was based on tests available in 1997. Further tests were made after that, but the overall picture has not changed.



The most important reasons for this behaviour are that:

- Fuel swelling and cladding creep-down cause a progressive closure of the pellet-to-cladding gap during base irradiation. In RIA transients, this causes the PCMI to start at lower fuel enthalpy. The fact that high burn-up fuel is normally operated and conditioned at low power can also cause earlier PCMI onset. Further, the large fission product inventory at high burn-up can exacerbate the PCMI as the transient progresses.
- The cladding becomes more brittle with burn-up, partly due to irradiation but more importantly because of cladding corrosion and hydrogen pick-up. The formation of hydride precipitates at the periphery of the cladding (hydride rim) is considered to be the major cause of the low-enthalpy failures registered at high burn-up.

In summary, high burn-up induces an aggravation of the PCMI, while simultaneously embrittlement can reduce the cladding ability to withstand PCMI. This combination of factors can cause RIA failures to occur at relatively low enthalpy.

The experiments carried out in the NSRR and in the CABRI reactor show that cladding brittleness is by far the most important consideration at high burn-up. As seen in Table 1, seven tests with UO_2 fuel were performed in the CABRI REPNa series. There were three failures, all of which occurred at

Table 1. Failure predictions of REPNa tests based on Eq. (9)

Test	$\Delta\tau$	Bu	OX	D	Experiment fuel enthalpy	H_F (Eq. 9)
REP Na-1	9.5	64	80 (spalled)	0	*$H_{Fail} = 30$	63
REP Na-2	9.1	33	4	1	$H_{MAX} = 210$	200
REP Na-3	9.5	53	40	1	$H_{MAX} = 125$	119
REP Na-4	75	62	80	1	$H_{MAX} = 99$	105
REP Na-5	9.5	64	20	1	$H_{MAX} = 115$	107
REP Na-6	35	47	35	1	$H_{MAX} = 148$	142
REP Na-7	40	55	50	1	*$H_{Fail} = 120$	120
REP Na-8	75	60	130 (spalled)	0	*$H_{Fail} \leq 82$	70
REP Na-9	34	28	20	1	$H_{MAX} = 210$	200
REP Na-10	31	62	80 (spalled)	0	*$H_{Fail} = 79$	71

MOX
MOX
MOX

moderate enthalpy, i.e. for $\Delta H < \sim 60$ cal/g. In each of these three failures the cladding had large oxide thickness, i.e. ≥ 80 μm , and had experienced oxide spalling during base irradiation. Oxide spalling is believed to be a factor that can weaken the cladding, because hydrogen can migrate towards the colder spots where spalling has occurred, making the cladding more brittle.

On the other hand, the four UO_2 REPNa rods that did not fail – as well as the two un-failed MOX rods – had only moderate oxidation, i.e. < 80 μm and absence of oxide spalling. Under these conditions, experience shows that the cladding can survive total deformations of about $\sim 2\%$ even at a burn-up of ~ 50 - 60 MWd/kg, as the REPNa-3 and -5 tests indicate.

The PCMI sequence of events in a RIA transient can be summarised as follows:

- The fuel pellet expands rapidly due to thermal expansion during a RIA transient. At high burn-up the pellet-to-cladding gap at normal operating conditions is closed. Consequently, the PCMI will start very early in the transient, as the only space available is the residual gap created by the contraction of the pellet when power was reduced from operating level to zero (for hot-zero-power conditions). As will be shown below, PCMI is expected to begin for an enthalpy increment ΔH_{PCMI} , cal/g, given by the relation: $\Delta H_{PCMI} = 0.14 \times LHR$, where LHR is the fuel heat rating during the last operating cycle in W/cm. This means that for a fuel that operated at 100-150 W/cm, PCMI is expected to start for $\Delta H = \sim 15$ - 20 cal/g.
- After PCMI initiation, highly oxidised cladding may start spalling. While evidence from hot cell examinations¹ suggests that it certainly occurs in the range $0 < \Delta H < \sim 40$ cal/g, oxide spalling is likely to start in the very early phase of PCMI. Because of this, it should not have an important effect on dry-out, which is a relatively high-enthalpy phenomenon. Cracking of the outer hydride rim is also expected to occur early in the transient. This is a critical process in that cracking of the outer hydride rim may constitute the initiation site for cladding through-going cracking. Figure 2 shows examples of incipient cracking in the outer oxide and hydride layer, obtained in out-of-pile tensile testing [2], in NSRR RIA tests [1] and in power ramp tests [21].

¹ This evidence comes for example from REPNa-4 and CIP0-1, where spalling occurred along the entire fuel length, including at fuel end where the pulse ΔH was not greater than ~ 40 cal/g.

- As a consequence of the formation of incipient cracks on the cladding outer surface, a crack may grow within the brittle portion of the cladding outer wall and eventually propagate through the cladding wall as a ductile fracture. An example of failed cladding is shown in Figure 3 [3], which is taken from the NSRR failed rod HB0-5. One can observe that the fracture, which started from the cladding OD, propagated in a brittle fashion up to ~40% of the cladding wall and continued thereafter as ductile fracture.

Figure 2. Three examples of high burn-up cladding that cracked from the outside

Upper left: Spalled ring tested at 250 °C and 0.01 s⁻¹ strain rate at IRSN. The specimen was taken from span 6 of the same fuel rod that was tested in REPNa-1 [2]. Lower left: Cracks in two NSRR test rods [1]. Right: Cracks in PWR fuel rods ramp-tested in Studsvik [21].

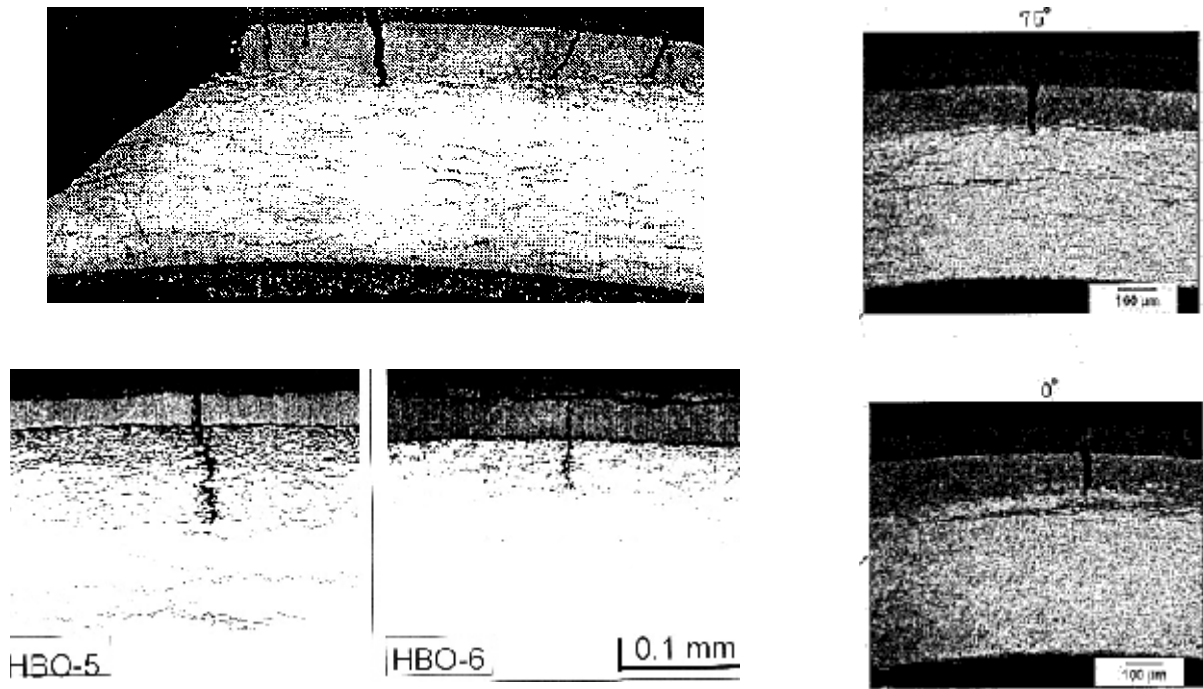
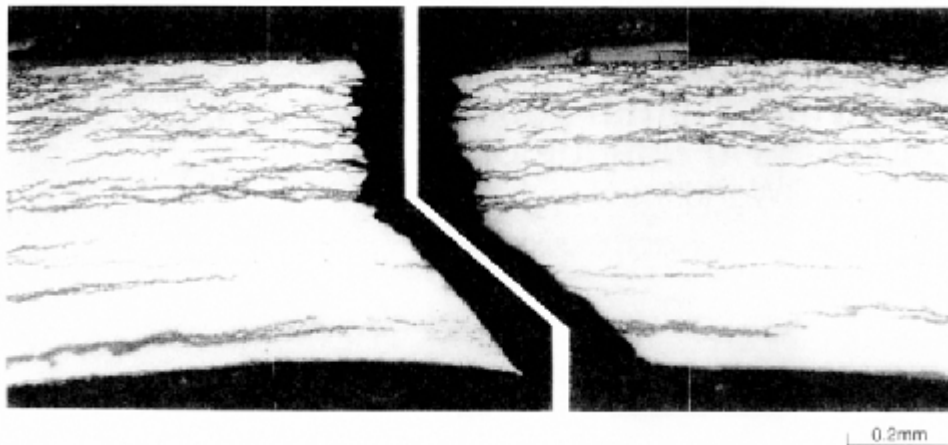


Figure 3. Cladding crack observed in the NSRR PWR fuel test HBO-1

One can observe that the crack started from the cladding outer surface as brittle crack, which extended up to 40% of the wall thickness. The crack propagated further as ductile crack.

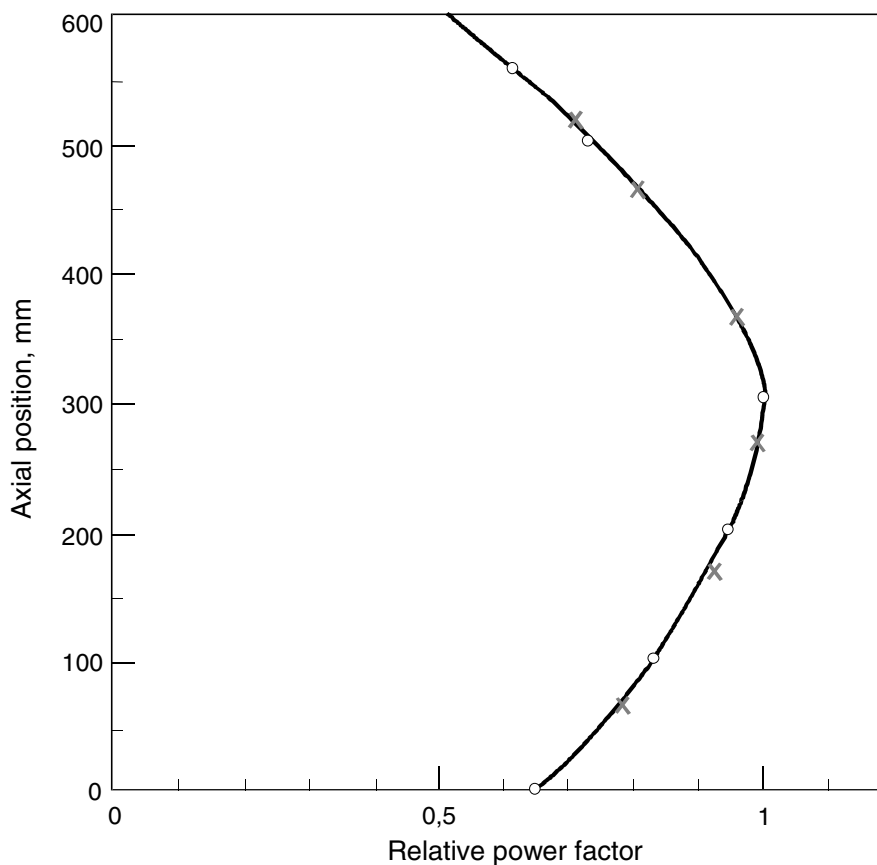


Although in a less clear-cut manner than the REPNa tests, the NSRR tests confirm that cladding brittleness plays an important role in LWR fuel failures. Brittle failures have been observed for instance in the five-cycle BWR fuel rods that were irradiated in the Fukushima-2 reactor [4], in spite of the fact that the oxide layer was small ($\sim 20 \mu\text{m}$) and that the hydrogen content was only $\sim 150 \text{ ppm}$. This point is discussed in more detail later in the paper.

PCMI as function of enthalpy

The CABRI tests are performed with fuel segments that are typically $\sim 500 \text{ mm}$ long. As shown in Figure 4 [5], the CABRI power profile along the fuel exhibits a peak at mid-height and a decrease towards the lower and upper end.

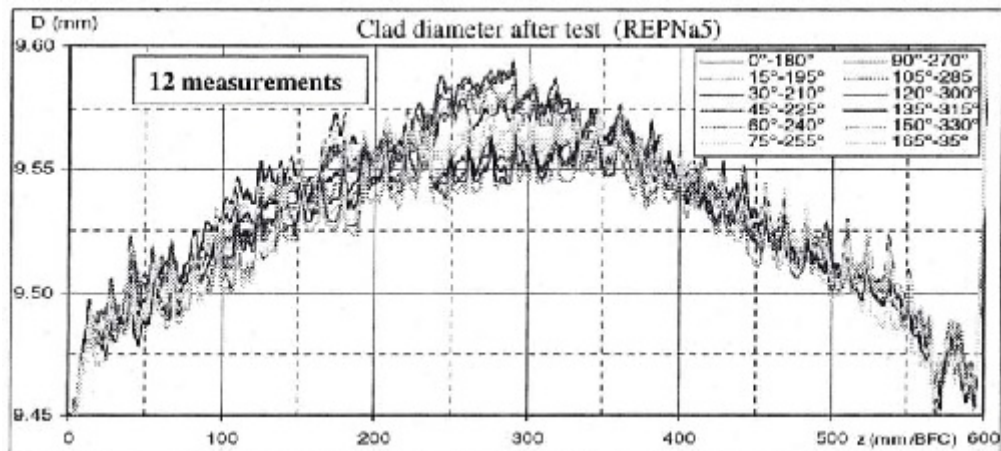
Figure 4. Typical axial power profile in the CABRI tests (REPNA series)



Because the power profile is peaked at mid-height, the post-test profilometry of the CABRI test fuel also exhibits a peak at mid-height, as shown in the example of Figure 5 [6], which gives the cladding diameter vs. height for the REPNa-5 test rod. From this and from the power profile one can determine the residual cladding hoop strain as a function of enthalpy, i.e. the relation $\epsilon_{\text{residual}}$ vs. ΔH determined from the strain and enthalpy profile taken along a test segment.

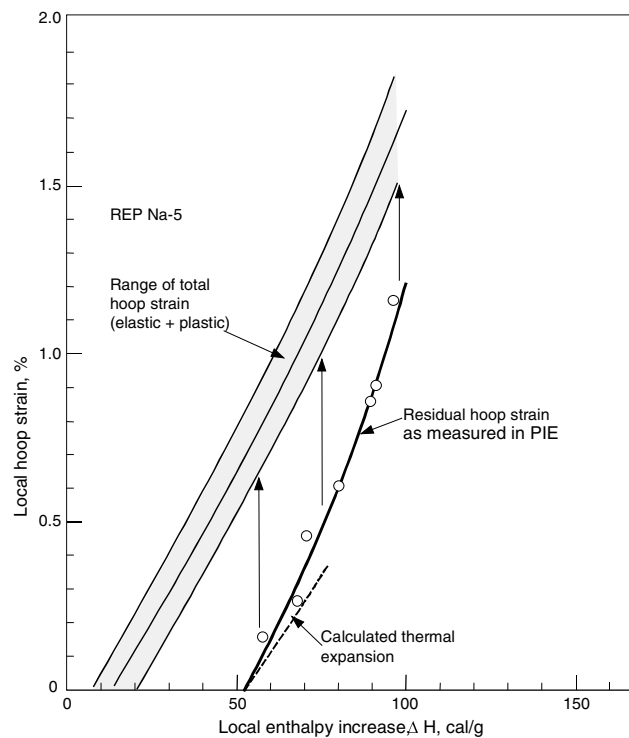
The case of REPNa-5 is particularly suitable for obtaining data on the onset of PCMI, because the segment was relatively long and the fuel cladding strain towards the rod ends was low. Moreover, the oxidation was low and spalling did not occur, making the hoop strain determination more precise.

Figure 5. Cladding diameter profile along the REPNa-5 fuel rod, taken along different “generatrices”. The fuel rod OD prior to the CABRI test was 9.465 ± 0.005 mm.



The $\epsilon_{\text{residual}}$ vs. ΔH for this case is shown in the plot of Figure 6, where the solid line fits the measured strain. One can observe that the slope of the line tends to gradually increase with enthalpy, possibly because fuel gaseous swelling becomes gradually more important and adds on top of the fuel thermal expansion as enthalpy increases. This should not be surprising if one considers that for ΔH approaching 100 cal/g, the average fuel temperature is approximately 1 500°C.

Figure 6. Local hoop strain versus local enthalpy deposition as derived from post-test measurement of residual strain versus height (solid line). The shaded area gives the estimated range of total deformation (elastic + residual). The dashed line gives the calculated strain slope based on fuel thermal expansion.



At low enthalpy (i.e. for ΔH up to ~ 50 cal/g), the strain versus ΔH is comparable with that expected based on thermal expansion, and can be calculated by means of the following expressions:

$$\Delta\varepsilon = \alpha \cdot 100 \Delta\bar{T}_F, \quad \text{i.e. } \Delta\varepsilon = \alpha \frac{4.2 \cdot 100}{cp} \Delta H \Rightarrow \Delta\varepsilon = 0.014 \Delta H \quad (1)$$

In this equation $\Delta\varepsilon$ is the hoop strain change in %, $\Delta\bar{T}_F$ is the fuel mean temperature increment in °C, ΔH is the fuel enthalpy change in cal/g, α is the fuel thermal expansion coefficient ($\alpha = 1.05 \cdot 10^{-5}$) and cp is the fuel specific heat ($cp = 0.31$ J/g °K).

A graphic representation of the above expression, i.e. $\Delta\varepsilon = 0.014 \Delta H$, is given by the dashed line in Figure 6. As the figure shows, the actual deformation rate is $\sim 25\%$ greater than the calculated one, which can be attributed to a burn-up effect. Because of the $\sim 25\%$ greater expansion, the PCMI strain up to moderate enthalpy ($\Delta H \approx 50$ cal/g) can thus be expressed as:

$$\Delta\varepsilon = 0.017 \Delta H \quad (2)$$

As said before, the cladding straining rate $\Delta\varepsilon$ vs. ΔH tends to increase as the transient progresses and becomes more than twice the thermal expansion as ΔH increases from ~ 50 to ~ 100 cal/g.

The data points and the solid line depicted in Figure 6 relate to the residual hoop strain determined in PIE. In order to assess the onset of PCMI, one needs to add the elastic strain to the measured residual deformation. This step would be straightforward if the cladding temperature were known, because the cladding temperature affects the YS of the material and thus the elastic strain. Unfortunately cladding temperature was not measured in the CABRI tests; hence one must rely on calculations.

Calculations performed with the IRSN SCANAIR [7] code indicate that the mid-wall cladding temperature can rise up to $\sim 600^\circ\text{C}$ for $H \approx 100$ cal/g. However, these calculations exhibit a large difference between the cladding inner and outer surface temperature, typically as large as $200\text{-}300^\circ\text{C}$. Thus, the choice of a “mean” cladding temperature that would describe the “average” cladding mechanical properties is not straightforward.

In the present evaluation, a mean cladding temperature in the range $450\text{-}600^\circ\text{C}$ has been considered for the peak power position of REPNa-5 and, consistent with it, a temperature in the range $400\text{-}500^\circ\text{C}$ for the rod-end positions. By using the UTS/YS curves produced for irradiated zircaloy-4 cladding [8] and the elastic modulus versus temperature given in the literature [9], one can estimate the elastic strain to be added on the measured residual strain in order to obtain the total strain. The outcome is the range represented by the shaded area in Figure 6, which indicates that the PCMI for the REPNa-5 fuel rod started already at ΔH between $10\text{-}20$ cal/g. This is because the pellet-to-cladding gap (at power) was closed, and when the RIA test started, the gap available corresponded to the fuel contraction from operational power condition to hot zero-power conditions² – on the assumption that the cladding stress at power is completely relaxed.

The onset of PCMI for hot zero-power RIA can be calculated by balancing the fuel contraction when power was reduced to zero, with the fuel expansion when the RIA started. This balance is expressed by the terms:

² The term gap should not be considered in strict terms at high burn-up, because the fuel and cladding are bonded together. It should be considered as the space available for the fuel to expand without straining the cladding.

$$LHR \left(\frac{1}{6\pi K} + \delta \right) = \Delta H_{PCMI} \cdot \frac{4.2}{cp} \cdot f \quad (3)$$

where LHR is the linear heat rating in the last operating cycle (W/cm), ΔH_{PCMI} is the fuel enthalpy increase from hot zero power to PCMI onset (cal/g), K is the fuel thermal conductivity at high burn-up ($K = 0.026$ W/cm °K in the range 300-600°C at ~60 MWd/kg) [10], δ accounts for the temperature drop in the pellet-to-cladding gap ($\delta = \sim 0.4^\circ\text{C/W/cm}$), cp is the specific heat between 300 and 600°C ($cp = 0.31$ J/g °K) and f is the factor accounting for larger expansion; as discussed earlier is $f = 1.25$.

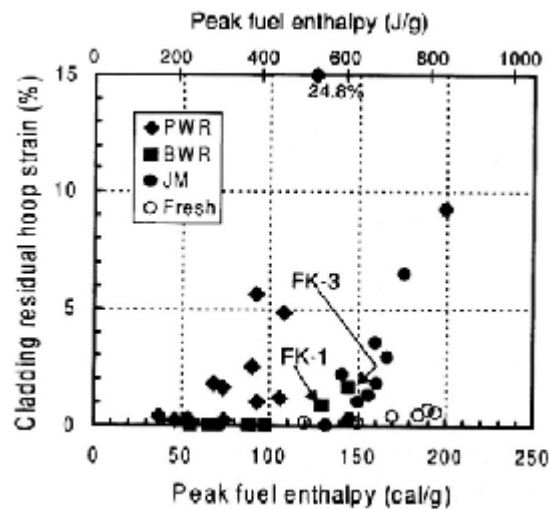
With the values given above, Eq. (3) results in the following expression for ΔH at PCMI onset:

$$\Delta H_{PCMI} = 0.14 \cdot LHR_{\text{last cycle}} \quad (4)$$

This can be used to estimate the enthalpy level below which no PCMI is expected. For the REPNa-5 case, where the heat rating in the last cycle was 130 W/cm, Eq. (4) predicts a $\Delta H_{PCMI} = 18$ cal/g, or, in terms of enthalpy, $H_{PCMI} = 36$ cal/g.³ Similarly, for the debated REPNa-1 test where $LHR_{\text{last cycle}}$ was 170 W/cm, Eq. (4) predicts a PCMI start at $H_{PCMI} = (18 + 0.14 \cdot 170) = 42$ cal/g. Obviously this does not account for possible fuel fragment relocation that might occur during transport, handling and preparation of the fuel specimens before the RIA tests.

The NSRR experimental results substantially confirm the observation made on the REPNa-5 data that at high burn-up the residual strain starts for enthalpy increment of ~50 cal/g. The NSRR tests make use of short fuel segments having a uniform power distribution, thus each test generates only one [$\epsilon_{\text{residual}}$ vs. ΔH] data point. Figure 7 depicts such data for a number of NSRR tests [4]. One can observe that the residual deformation is negligible up to $\Delta H = 50$ -60 cal/g, which is in agreement with what shown in Figure 6. One should note that the large strains seen at higher enthalpy in Figure 7 are likely due to large unrestrained fuel swelling and/or fission gas pressure, which occur when the cladding experiences considerable heat-up and loses strength. This is expected to happen at the NSRR cooling conditions.

Figure 7. Summary of residual hoop strain data obtained in the NSRR tests. The data indicate that plastic strain starts beyond a ΔH of 50 cal/g. This is consistent with that inferred in Figure 6.



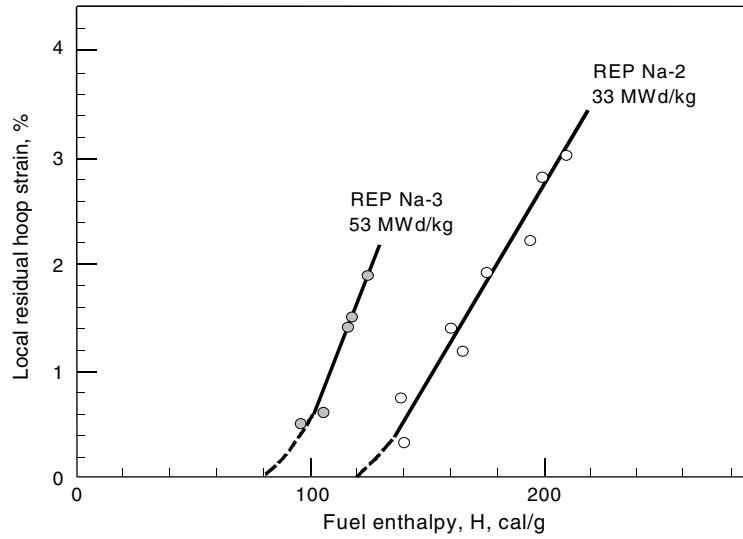
³ The enthalpy at start of the CABRI tests is 18 cal/g, thus $H = 18 + \Delta H$.

Effect of burn-up on PCMI

The REPNa test series with UO₂ fuel include only one case where the burn-up was substantially different from the rest. It is the REPNa-2 test, which had a burn-up of 33 MWd/kg. REPNa-2 can be compared with the REPNa-3 test, which had a burn-up of 53 MWd/kg and is the one that reached the highest fuel enthalpy among the high burn-up CABRI tests.

The comparative PCMI behaviour, plotted in terms of residual hoop strain versus total fuel enthalpy ($H = H_o + \Delta H$) in these two tests, is shown in Figure 8.

Figure 8. Effect of burn-up on PCMI as demonstrated by the comparison of two CABRI tests at 33 and 53 MWd/kg



It is not surprising that the PCMI is stronger for the high burn-up fuel. One can observe that the strain vs. enthalpy line for the 53 MWd/kg fuel is somewhat steeper than for the 33 MWd/kg fuel, which can be attributed to a greater fuel swelling component at high burn-up. More importantly, there is a shift of ~40-50 cal/g between the ϵ versus H curves for the two tests. This difference can be attributed to the fact that the gap in the 53 MWd/kg fuel was closed, whereas the gap in the 33 MWd/kg fuel was still open.

In order to estimate the gap difference, one can use the formula:

$$Gap = \left[D_F \cdot 1000 \cdot \frac{4.2}{cp} \cdot \alpha \cdot f \right] \cdot \Delta H \quad (5)$$

where Gap is the diametral gap (μm), ΔH is the enthalpy difference between the two curves in Figure 8 (40 cal/g), D_F is the fuel pellet diameter (mm), cp is the heat capacity of the fuel ($cp = 0.31 \text{ J/g } ^\circ\text{K}$), α is the fuel coefficient of thermal expansion ($\alpha = 1.0 \cdot 10^{-5}$) and f is a factor accounting for greater thermal expansion in RIA ($f = 1.25$).

It results that:

$$Gap = 1.4 \cdot \Delta H \quad (6)$$

Considering that in the low-strain range of Figure 8 the enthalpy difference between the strain curves of REPNa-2 and -3 is $\Delta H = 40$ cal/g one derives from Eq. (6) that the REPNa-2 fuel had a ~50-60 μm wider diameter gap than REPNa-3.

Based on the discussion so far, one can derive a simplified relation, which can be used to straightforwardly estimate the total strain. This is:

$$\begin{aligned} \varepsilon &= 0.017 \cdot (\Delta H - \Delta H_{PCMI}) && \text{for } \Delta H \text{ and } \Delta H_{PCMI} \leq 50 \text{ cal/g} && (7) \\ \varepsilon &= \varepsilon_{50} + 0.017 \cdot [1 + (Bup/70) \cdot (\Delta H - \bar{h})/100] \cdot (\Delta H - \bar{h}) && \text{for } \Delta H > 50 \text{ cal/g and } \Delta H > \bar{h} \end{aligned}$$

where $\Delta H > \Delta H_{PCMI}$, ε_{50} is strain at 50 cal/g \rightarrow ($\varepsilon_{50} = 0$ if $\Delta H_{PCMI} > 50$ cal/g), ΔH_{PCMI} is MAX $\{[\Delta H_{PCMI} = Gap/1.4]$ and $[\Delta H_{PCMI} = 0.14 \cdot LHR_{last\ cycle}]$ with the pellet-to-cladding gap calculated from cladding creep-down and fuel swelling⁴, \bar{h} is MAX $\{\Delta H_{PCMI}$ and 50 cal/g}, and Bup is burn-up in MWd/kg.

One should note that RIA tests at intermediate burn-up, i.e. between 30 and 50 MWd/kg are rather scarce and that more data are needed in order to cover this burn-up range, which is highly relevant for LWRs.

Effect of pulse width

There have been discussions in the fuel community as to the effect of pulse width on RIA failure. Mechanical tests performed on high burn-up cladding have not evidenced an important effect of strain rate on properties such as UTS or UE [22], thus the deformation rate as such should not be relevant with respect to failure propensity.

One of the points raised is that in larger pulses, i.e. 30-70 ms as compared to 5-10 ms, the cladding temperature can increase substantially during the pulse. Because a higher temperature can render the cladding more ductile, one could envisage that failure propensity would decrease for 30-70 ms pulses as compared to 5-10 ms pulses. However, as discussed in the following, the CABRI results do not show a pulse width effect, either on measured strain or on failure propensity.

As concerns strain, there are only two UO₂ tests in the REPNa series that can be directly compared to assess the effect of pulse width. They are REPNa-5 and REPNa-4, which, as summarised in Table 1, were run with 9.5 and 75 ms width at pulse mid-height respectively. The strain data for these two tests are given in Figure 9. While the small deformation and the oxide spalling that occurred during the REPNa-4 test limit the comparison to the data point at peak power for REPNa-4, one can nevertheless see that the difference between the two tests is not large. Even if the greater oxidation and the cladding temperature difference of REPNa-4 as compared with REPNa-5⁵ is accounted for, the distance between the two would remain limited to ~15 cal/g.

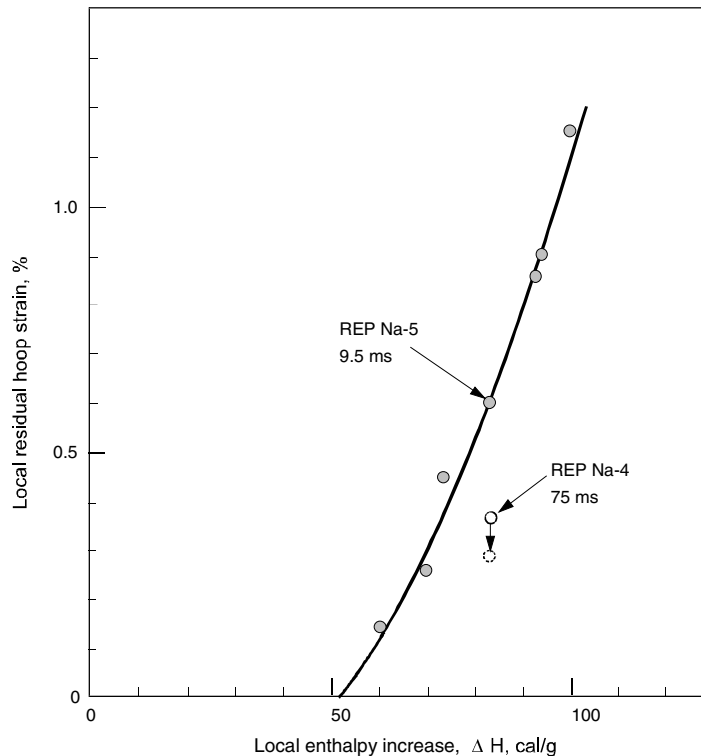
As regarding pulse width effect on failure propensity, the three UO₂-REPNa failures occurred at all three pulse widths that were possible in CABRI, i.e. 9.5, 31 and 75 ms. Although subtle distinctions could be made for each of these three tests, this experimental evidence clearly points out that pulse width should not have a decisive effect on cladding failure.

⁴ For most practical cases one can use the expression $Gap = (0.8 \cdot Gap_o - 0.28 \cdot D_F \cdot Bup)$.

⁵ The oxide thickness was 20 μm for REPNa-5 and 80 μm for REPNa-4.

Figure 9. Effect of pulse width on PCMI, as inferred by comparing a 9.5 with a 75 ms pulse

In order to make the comparison more direct, the effect of wall thinning due to the larger oxidation in REPNa-4 has been evaluated along with the effect of possible cladding temperature difference in the two cases. This would move the data point slightly downwards, as shown in the figure.



As for the NSRR tests, they were all performed with one pulse width, thus an assessment of the effect of pulse width on PCMI cannot be made within the NSRR database. In comparing the NSRR and the CABRI database, one should be aware of the different test conditions, notably coolant temperature, which probably is far more important than pulse width.

The cladding temperature response in a RIA transient will be discussed later.

Comparison between UO_2 and MOX fuel

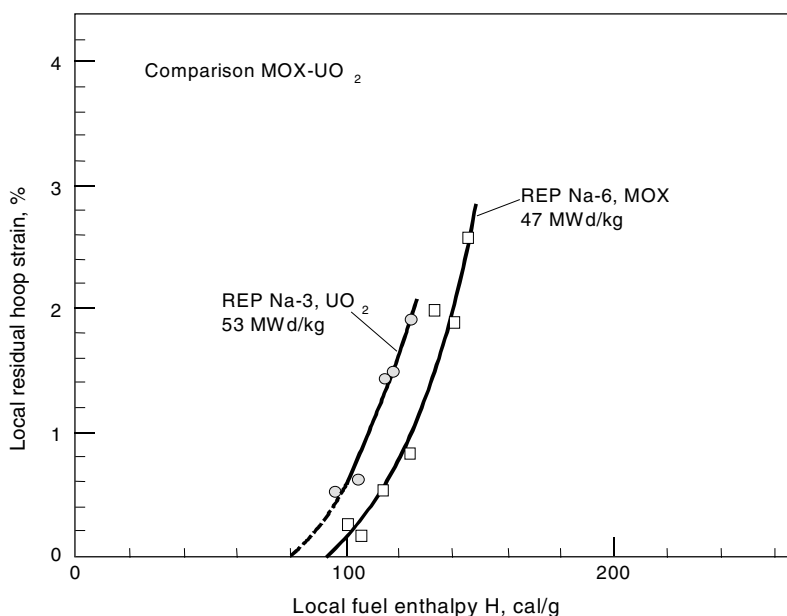
The PCMI of UO_2 and MOX fuel in the high burn-up range can be assessed in a comparative manner by examining the residual strain of the REPNa-3 and the REPNa-6 fuel. The main parameters for these two fuel tests are given in Table 1.

The residual hoop strain versus fuel enthalpy for these two test rods is plotted in Figure 10. The data exhibit a rather similar trend for the two cases, the only difference being a shift of ~ 15 -20 cal/g between the two lines, with the MOX fuel having smaller strain than the UO_2 fuel rod.

There are different factors that can explain this moderate difference. The 10% burn-up difference and the different pulse width, which was 9.5 ms for REPNa-3 and 35 ms for REP Na-6, could add up to explain the 15-20 cal/g difference between the curves shown in Figure 10.

Figure 10. Comparison of the PCMI with MOX-UO₂ and fuel rod as inferred from two REPNa tests

One can observe that MOX and UO₂ fuel behave in a similar manner, with only a 10-15 cal/g enthalpy difference, which can be explained by the slight difference in burn-up and pulse width



In order to assess UO₂ vs. MOX differences, one could also examine the residual strain of test REPNa-2 (UO₂, 33 MWd/kg) and test REPNa-9 (MOX, 28 MWd/kg). However, it is believed that in the latter case the cladding strain was dictated mainly by the high clad temperature and fission gas pressurisation, and not by PCMI.

In conclusion, the experimental evidence discussed here indicates that as long as the RIA fuel enthalpy increment remains within the range $\Delta H < \sim 120$ cal/g, there is no significant PCMI difference between MOX and UO₂ fuel, in terms of measured residual deformation. One cannot exclude, however, the possibility that differences arise for, e.g. higher enthalpy or in relation to post-failure phenomena.

Discussion on cladding temperature in a RIA transient

Cladding temperature during a RIA depends on deposited energy and to some extent on pulse width. As to the latter, it was indicated earlier that there is no direct experimental evidence that wider pulses would result in lower failure propensity. Nevertheless, a discussion on cladding temperature in a RIA transient remains highly relevant for a correct RIA transient analysis. The main points are presented here, and a more extended discussion on cladding transient temperature is given in the Appendix.

- The coolant temperature increase during the pulse is small. This is shown both by NSRR and CABRI tests [14,15]. Even for a 75 ms pulse, the coolant heat-up as measured at the end of the pulse in CABRI remains below 50°C (for final enthalpy of ~ 100 cal/g).
- Cladding temperature is measured only in the NSRR tests. The maximum temperature data shown in Figure 11 [11] demonstrate that the cladding heat-up remains below $< 100^\circ\text{C}$ throughout the transient, including the post-pulse phase, as long as $\Delta H < \sim 60$ cal/g (or $H < \sim 80$ cal/g for a hot zero-power RIA). Since also the post-pulse phase is considered, the

above observation is applicable to any pulse width. This means that in the enthalpy range where PCMI brittle failures occur, i.e. for $H \ll 100$ cal/g, the cladding OD temperature remains relatively low.

- Cladding temperature calculations that were made in the context of this report (Figure 12 [12]) demonstrate that there is a large difference between the heat-up at the inner and at the outer cladding surface. While at the outer (metal) surface the cladding temperature during the pulse (to 70 cal/g) did not rise beyond 400°C, the inner clad temperature reached temperatures in excess of 600°C. Yet, the difference in cladding temperature vs. enthalpy between 10 and 30 ms pulse was moderate, i.e. < 70°C at the OD and < 30°C at mid-wall. Temperature differences of 30-70°C are not expected to cause appreciable differences in mechanical properties, as clearly shown in for instance Ref. [22].
- Experimental work done in JAERI [13] shows that the hydride dissolution process, even at relatively high temperature, takes a much longer time than that available in a RIA transient. This implies that hydride-induced brittleness would not be affected by moderate temperature increments that occur in a time period of the order of milliseconds.

Figure 11. Maximum cladding surface temperature reached during testing in the NRSS

These maximum temperatures were reached well after pulse completion, i.e. in the post-pulse phase. One can note that there is no substantial cladding heat-up for $\Delta H < \sim 60$ cal/g.

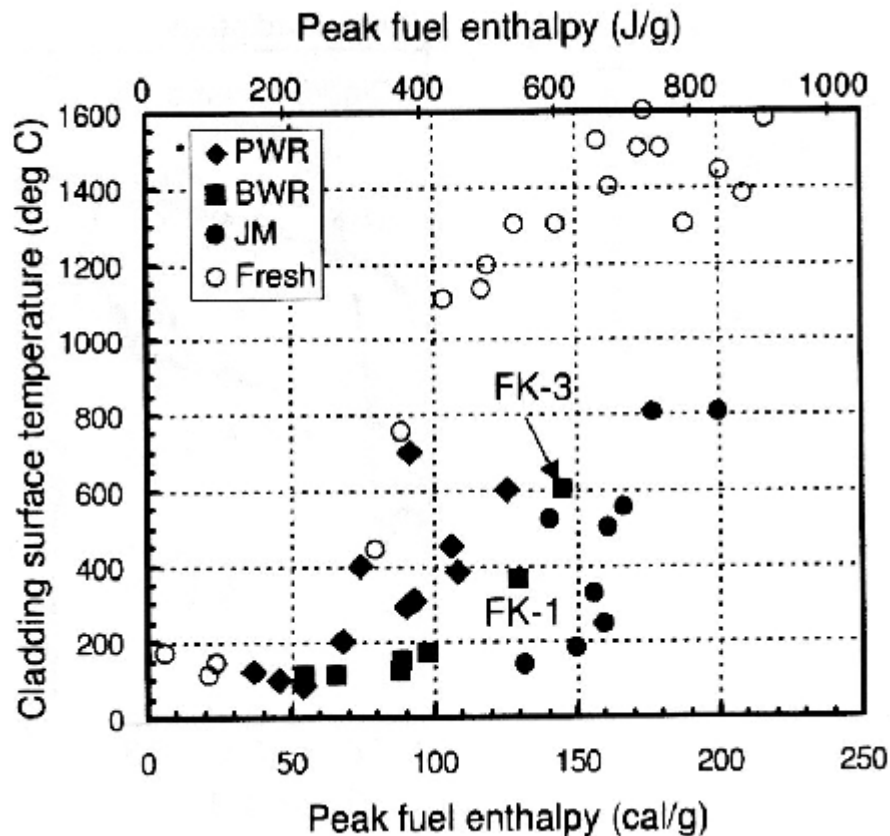
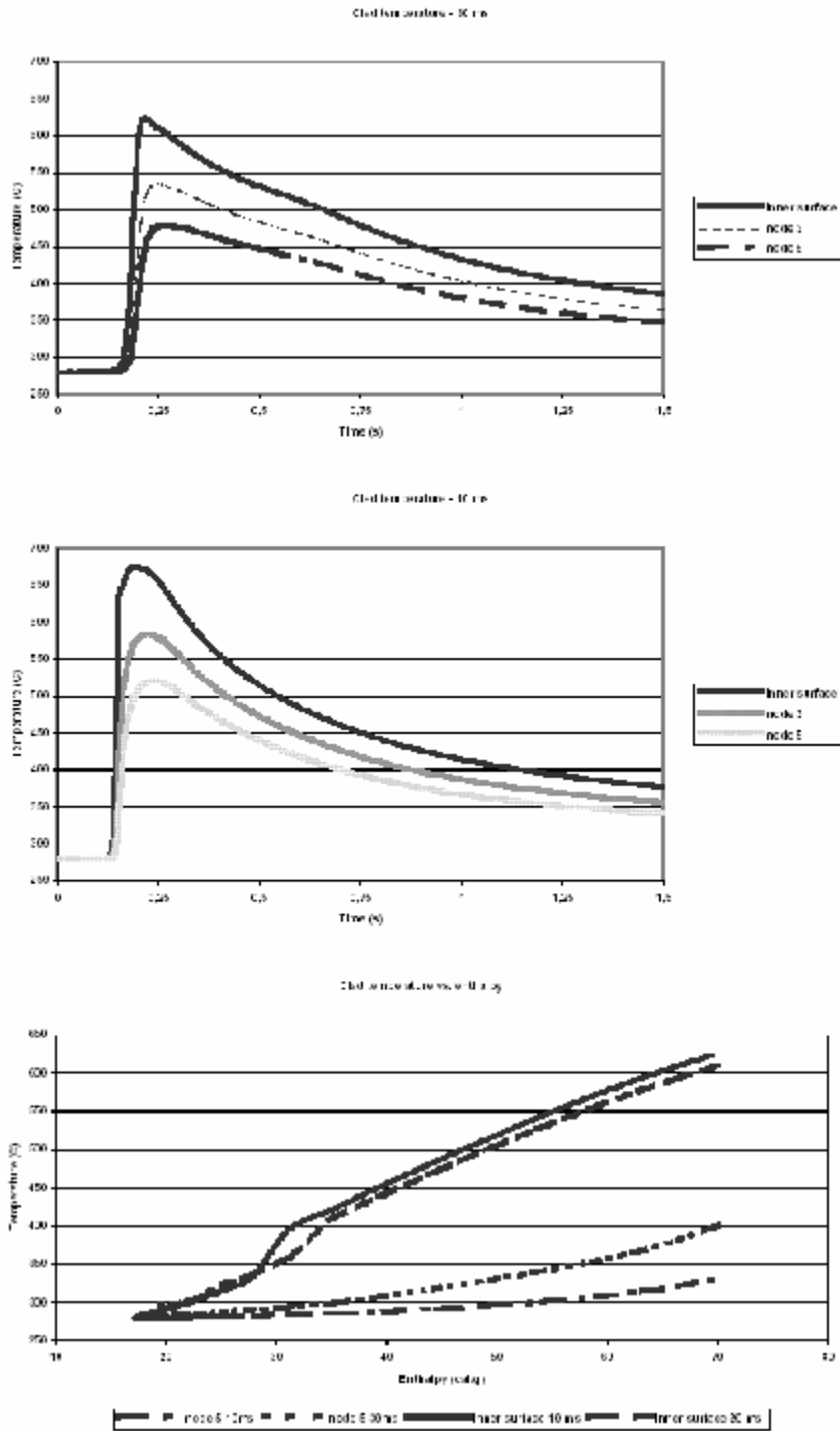


Figure 12. SCANAIR results obtained in calculation run made at CIEMAT (Spain) using the CABRI CIPO-2 fuel as reference

A pulse of 30 ms was used for the upper figure, whereas the lower figure refers to 10 ms pulse. The lowest diagram shows that the calculated cladding temperature for 30 ms was slightly lower at the ID and 50-70°C higher at the (metal) OD in comparison with the 10 ms pulse. The difference in mean cladding temperature between the two cases was ~30°C.



Indirect considerations suggest that the cladding mean heat-up should be moderate for moderate enthalpy. They are based on the following reasoning. The CABRI coolant temperature can exceed 500°C for enthalpy exceeding 200 cal/g (REPNa-2), as the measurements plotted in Figure 13 show. This high coolant temperature is reached after ~300 ms and does not affect the PCMI during the pulse. It would however affect the residual strain measured in post-test examinations, because in a hot cladding the elastic strain would to a significant degree be converted into plastic strain. In fact, as shown in Figure 14 (REPNa-2), there seems to be a systematic difference in residual strain at the top and bottom of the fuel rod. Based on the evaluation of these data made in Section A3 of the Appendix, one infers that the cladding heat-up (in CABRI) should remain moderate, with “mean” temperature not exceeding ~400°C for enthalpy of about 70 cal/g.

Figure 13. Maximum sodium coolant temperature vs. maximum enthalpy in CABRI tests

These temperatures were reached late in the transient, that is 200-300 ms after the pulse

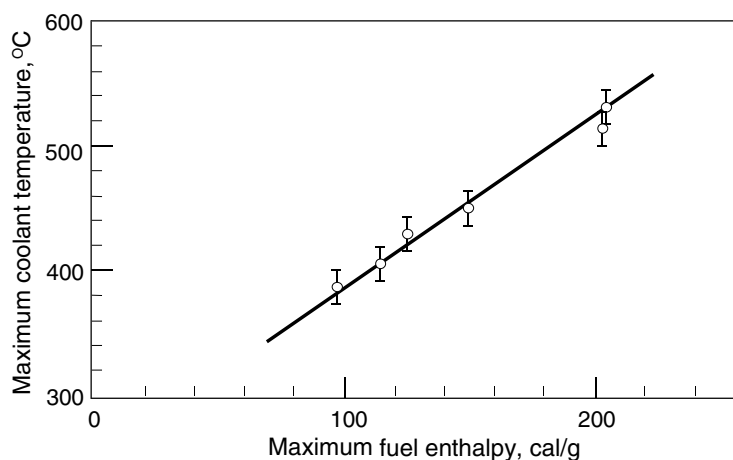
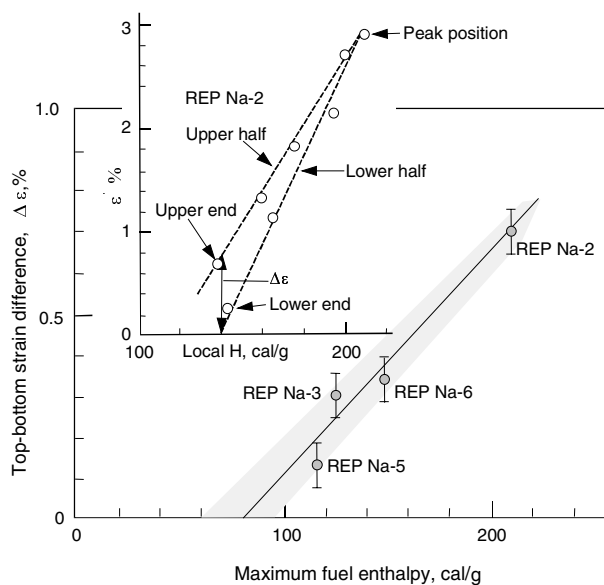


Figure 14. Upper and lower fuel end deformations exhibit a small difference, likely because the sodium temperature at outlet can be significantly greater than at inlet

The case of REPNa-2 is shown in detail in the upper window



There are remaining questions about temperature calculations, which seem to overestimate the cladding heat-up in sodium. Similar questions have been raised earlier [16]. Nevertheless, the calculations made here do not show remarkable differences between a 10 ms and a 30 ms pulse, even though the calculated cladding heat-up at ID was considerable (Figure 12). Based on this and on the points made earlier in this section, one can conclude that the experimental evidence for larger pulses ($H < \sim 100$ cal/g) producing significantly higher cladding temperatures is not very strong.

Cold vs. hot coolant conditions

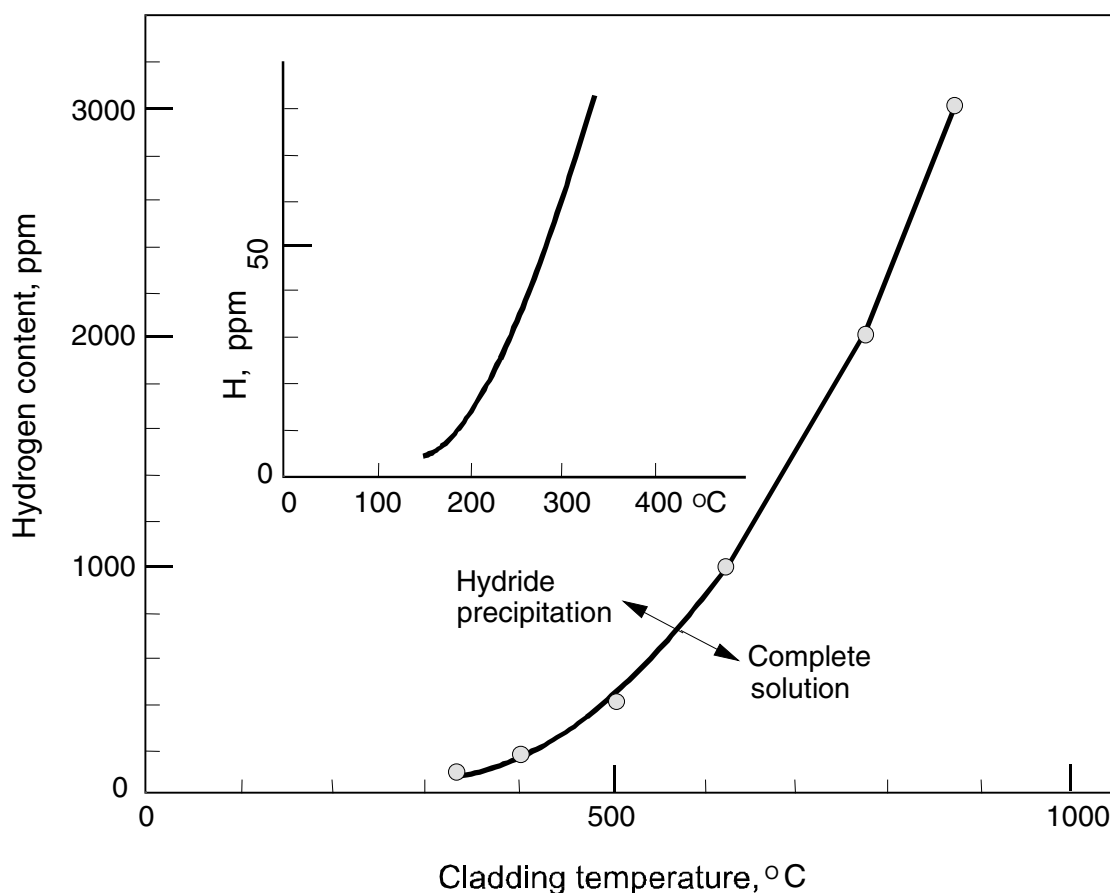
The NSRR tests are run at room temperatures and with stagnant water as coolant, whereas the CABRI tests are run in a sodium loop at coolant inlet temperature equal to 280°C. This coolant temperature difference makes the cladding substantially more brittle in the NSRR case.

According to Ref. [17], the solubility of hydrogen vs. temperature is given by the following correlation:

$$T_{SOL} = 4401 / \ln(1.332 \cdot 10^5 / H_y) \quad (8)$$

where the temperature T_{SOL} is in K and the hydrogen concentration H_y is in ppm. One can observe that the hydrogen solubility drops drastically with temperature and is already well below 10 ppm for $T_{SOL} < 200^\circ\text{C}$.

Figure 15. Hydrogen solubility in zircaloy as function of temperature [17]



This can explain why in the NSRR tests brittle failures were experienced for moderate or low cladding oxidation and hydrogen content. A clear example of NSRR brittle failure has already been described in Figure 3, which refers to a PWR rod having 50 MWd/kg burn-up and less than 50 μm oxide thickness. The cladding also exhibited brittle behaviour in the FK-6, FK-7 and FK-9 tests (see Table 2), which were run with BWR fuel having oxide layer below 20 μm and hydrogen content not exceeding 150 ppm (average across cladding). In these cases the brittle cladding behaviour was enhanced by the presence of radially-oriented hydride clusters [18].

Table 2. Failure predictions of the NSRR PWR/BWR tests based on Eq. (10)

Test	$\Delta\tau$	Bu	OX	Exp. ΔH at failure	ΔH_F [Eq. (10)]	Fuel type
NSRR/PWR						
HBO-1	5	50	48	60	67	PWR
HBO-5	5	44	60*	77	75	PWR
TK-2	5	48	35	60	73	PWR
TK-7	5	50	30	86	73	PWR
NSRR/BWR						
FK-6	5	61	~20	70	59	BWR
FK-7	5	61	~20	62	59	BWR
FK-9	5	61	~20	86	59	BWR

* Maximum value.

One factor that might have made the FK-6, FK-7 and FK-9 cladding more brittle is the very low heat rating (<100 W/cm) of these fuel rods during the last operating cycle. There is a similarity between these RIA tests as described in Ref. [18] and a test that was run under normal operating conditions in the Halden reactor [19]. The latter involved a high burn-up fuel rod, which had also been irradiated in a BWR at very low rating (<100 W/cm) for the last period of time. This test resulted in an unexpected, dramatic failure during a rather moderate power, at a heat rating between 270-300 W/cm. The presence of radial hydrides was also noted in the post-irradiation examination of the Halden test rod [19], similar to the observations made on the BWR fuel that failed in the NSRR tests.

Analogy between RIA and power ramp failures

The mechanisms that cause PCMI brittle failures are basically the same for RIA and power ramp conditions. While the fuel radial temperature profile is different in the two cases, the fuel expansion governs the PCMI in both cases, and in both cases the ability of the cladding to withstand PCMI depends on the cladding residual ductility. The strain rate is very different in the two cases, however, as already mentioned, mechanical tests performed on high burn-up cladding have not evidenced an important effect of strain rate on properties such as UTS. Figure 2 shows that RIA tests and power ramps can produce a similar cladding cracking fashion.

One would thus expect that a relation exists between the power to failure in power ramps and the enthalpy to failure in RIA for cases where brittle fracture is the failure mode, i.e. for failures occurring at enthalpy below ~100 cal/g. This relation is the same as the one derived earlier [for the onset of PCMI in hot-zero-power (HZP) RIA, as related to previous operating power, Eq. (4)], i.e.:

$$\Delta H_{Failure} = 0.14 \cdot LHR_{Failure} \quad \text{Applicable for } \Delta H_{Failure} < 100 \text{ cal/g} \quad (4')$$

The above would predict that if power ramps exhibit failures at, say, 400-450 W/cm, such as in Ref. [21], a hot-zero-power RIA for the same fuel would result in failure for $\Delta H = 55-60$ cal/g, or equivalently $H = 75-80$ cal/g.

Correlation for the RIA failure threshold

A fuel failure correlation has been derived based on an analysis of the CABRI data, in particular taking into account the strain data published in the open literature [20]. For RIA starting at hot coolant conditions such as in CABRI, the correlation is as follows

$$H_F \left[200 \cdot \frac{25 + 10D}{Bu} + 0.3\Delta\tau \right] \left(1 - \frac{0.85OX}{W} \right)^2 \quad (9)$$

where H_F is the fuel enthalpy failure limit, cal/g (if H_F from Eq. (9) is > 200 , set $H_F = 200$ cal/g), Bu is burn-up in MWd/kg, D is a parameter accounting for cladding ductility [$D = 1$ for cladding with residual ductility (at least 1% plastic hoop strain in tests) and $D = 0$ for brittle cladding], $\Delta\tau$ is the pulse width in ms (≤ 75 ms, use 75 ms beyond that), OX is the oxide thickness in μm and W is the as-fabricated wall thickness in μm (576 μm for the REPNa rods).

Details on how D can be expressed as function of cladding oxide thickness and presence of spalling are given in Ref. [20], which also deals with the consideration that in most practical cases one does not know *a priori* if the cladding is spalled or not. (In any case, setting $D = 0$ would provide a conservative failure limit.)

For applications to other cases than the hot zero-power conditions, one should consider the temperature or the power at the start of the transient. For cold, zero-power conditions, such as in the NSRR tests, the failure threshold should be expressed in terms of enthalpy increase above the initial value. This is:

$$\Delta H_F \left[200 \cdot \frac{25}{Bu} + 0.3\Delta\tau \right] \left(1 - \frac{0.85OX}{W} \right)^2 - (18 + 2) \quad (10)$$

which is equivalent to Eq. (9) except that the failure limit is expressed as enthalpy increment ΔH_F instead of total enthalpy H_F .⁶ The ductility parameter D is set $D = 0$ because of the considerations expressed earlier concerning coolant temperature effects.

For RIA starting at non-zero power one can provisionally consider the following expression, based on earlier discussion and on Eq. (5):

$$\Delta H_F \left[200 \cdot \frac{25}{Bu} + 0.3\Delta\tau \right] \left(1 - \frac{0.85OX}{W} \right)^2 - 18 - 0.14LHR_0 \quad (11)$$

⁶ The term 20 cal/g accounts mainly for the enthalpy at start of transient in CABRI, from which the correlation in Eq. (9) was derived. The enthalpy at start of transient in CABRI was in fact 18 cal/g, but there are other minor factors linked to temperature dependence of heat capacity and fuel-cladding thermal expansion. They partly compensate with each other, and when accounted for result in the 20 cal/g term.

The performance of the correlation in Eq. (9) in predicting failures and non-failures in the CABRI REPNa test is illustrated in Table 1. One can observe that all cases are rather well predicted except REPNa-1. When used in the form of Eq. (10) to predict the NSRR tests that resulted in fuel failure, the outcome is illustrated in Table 2. One can observe that there is also a reasonably good predictability for the NSRR failures. Details on these predictions are discussed in Ref. [20].

As a final remark, the correlation described above also acknowledges the important effect of cladding oxidation in that it can influence cladding ductility through hydrogen pick-up [term D in Eq. (9)]. Burn-up also is an important parameter. On the other hand, the present correlation only acknowledges a moderate effect of pulse width ($\Delta\tau$) in accordance with what discussed earlier in this paper.

Concluding remarks

The state of the cladding is essential for the fuel ability to withstand RIA transients. In particular, some ductility must be retained in order to accommodate the PCMI caused by the fuel expansion.

Other parameters such as RIA pulse width and fuel type may have some effect, but the available information indicates that such an effect should be small compared with cladding brittleness.

The main consideration is on cladding oxidation, as this determines how brittle the cladding can become. Cladding oxidation is thus of paramount importance for normal operation as well as for the response to RIA transients.

The reason for BWR fuel to become brittle within a moderate burn-up increment, possibly as consequence of low power operation in the last cycle, deserves attention in future research.

REFERENCES

- [1] Ishijima, K., “NSRR RIA Experiments with High Burn-up PWR Fuels”, *OECD/NEA Meeting on the Behaviour of High Burn-up*, March 1997.
- [2] Limoine, F., M. Balourdet, “RIA-related Analytical Studies and Separate Effect Tests”, *ANS Topical Meeting on LWR Fuel Performance*, Portland, Oregon, USA, March 1997.
- [3] Nakamura, T., *et al.*, “BWR Fuel Behaviour Under RIA Conditions at Burn-up of 41-45 GWd/t”, *Nuclear Technology*, Vol. 129, p. 141, February 2000.
- [4] Fuketa, T., *et al.*, “High Burn-up BWR Fuel Response to Reactivity Transients and a Comparison with PWR Fuel Response”, *28th WRSM*, Bethesda, USA, October 2000.
- [5] Faury, M., Personal communication, 2001.
- [6] Georgetum, V., “Study of the Cladding Ovalisation Observed in the CABRI REPNa Tests”, *4th CABRI Technical Review Meeting*, March 2001.
- [7] Rigat, H., “Influence of Energy Deposition Rate on Transient Rod Behaviour”, *4th CABRI Technical Review Meeting*, p. 8, March 2001.
- [8] Balourdet, M., “Main Outcome of Cladding Mechanical Testing”, *1st CABRI Technical Review Meeting*, Cadarache, France, July 1998.
- [9] *MATPRO*, NUREG/CR-6150, Vol. IV, Section 4.6.
- [10] Vitanza, C., *et al.*, *Summary of Achievements of the OECD Halden Reactor Project in the Period 1994-1996. Conductivity Degradation of UO₂ Fuel*, February 1997.
- [11] Nakamura, T., *et al.*, “BWR Fuel Behaviour Under RIA Conditions at Burn-up of 41-45 GWd/t”, *Nuclear Technology*, Vol. 129, p. 141, February 2000.
- [12] Herranz, L., Personal communication to J.M. Conde, 2003.
- [13] Nagase, F., U. Uetsuka, “Hydride Morphology and Hydrogen Embrittlement of Zircaloy Fuel Cladding Used in the NSRR/HBO Experiments”, *ANS Meeting on LWR Fuel Performance*, Portland, Oregon, USA, March 1997.
- [14] Fuketa, T., Personal communication, 2003.
- [15] Rigat, H., “Status of Interpretation of UO₂ CABRI REPNa Tests”, *3rd CABRI Technical Review Meeting*, June 2000.

- [16] Bessiron, V., *et al.*, “Thermal-hydraulic Studies Under RIA Conditions Based on Patricia Experiments”, *3rd CABRI Technical Review Meeting*, June 2000.
- [17] *MATPRO*, NUREG/CR-6150, Vol. IV, Section 4.2.
- [18] Fuketa, T., *et al.*, “High Burn-up BWR Fuel Response to Reactivity Transients and a Comparison with PWR Fuel Response”, *28th WRSM*, Bethesda, USA, October 2000.
- [19] Jonsson, T., *et al.*, “Post-irradiation Examination of a Failed Rod from IFA-597.2”, *Enlarged Halden Programme Group Meeting*, HRP 351, paper 28, May 1999.
- [20] Vitanza, C., “A RIA Failure Criterion Based on Cladding Strain”, *IAEA Technical Committee Meeting on Fuel Behaviour Under Transient and LOCA Conditions*.
- [21] Kamimura, K., “High Burn-up Fuel Cladding Characteristics as RIA Test Initial Condition”, *OECD/NEA Topical Meeting on RIA Fuel Safety Criteria*, Aix-en-Provence, France, May 2002
NEA/CSNI/R(2003)8, Vol. 2.
- [22] Balourdet, M., “Salient Features from Cladding Mechanical Testing (PROMETRA)”, *2nd CABRI Technical Review Meeting*, Cadarache, France, June 1999.

Appendix

CONSIDERATIONS ON CLADDING TEMPERATURE

A1. Measured and calculated cladding temperatures

Cladding temperature is measured in the NSRR tests, but not in the CABRI tests performed so far on LWR fuel. The experimental evidence from the NSRR test is shown in Figure 11 [12]. As one can observe, there is not substantial cladding overheating as long as the fuel enthalpy increase remains below ~60 cal/g. That is, clad overheating is absent not only during the pulse, but also in the post-pulse phase. Since Figure 11 refers to the entire transient, including the long-term post-pulse phase, this implies that the finding of Figure 11 is applicable for any pulse width, i.e. not only to 5 ms pulses as in NSRR, but also to wider pulses. (This is because if both the pulse and post-pulse phase are considered, a wider pulse will result in a lower fuel surface heat flux.)

On the basis of Figure 11 and on the assumption one can trust the NSRR cladding temperature measurements, one expects no significant temperature increase for $\Delta H < 60$ cal/g. For CABRI tests this means that the clad temperature will remain low as long as $H (= H_0 + \Delta H) < \sim 80$ cal/g. Since the sodium coolant used in the REPNa tests is expected to be a more efficient coolant than the stagnant water used in NSRR, one would actually conclude that the above could apply to even higher enthalpy than 80 cal/g.

If this reasoning is correct, there should not be important temperature effects that would influence the fuel mechanical behaviour or ductility at the OD, where the failures originate, at least for enthalpy in the range $H < 80$ cal/g.⁷

Calculations performed with some of the available codes result in moderate cladding heat-up at the (metal) OD. Figure 12 shows an example of calculations done with one of such codes [12], taking as reference a fuel rod tested in the current OECD-IRSN CABRI programme. The results of Figure 12 refer to 10 ms and 30 ms pulses. All other parameters, including injected energy, were the same in the two runs. The plots in Figure 12 show that the calculated cladding ID temperature rises very promptly, following very closely the enthalpy rise and reaching 600°C for enthalpy approaching 70 cal/g (as shown in the lower plot of Figure 12). The calculated ID temperature versus enthalpy is very similar in the 10 and 30 ms case, the difference being less than 20°C.

The same calculations produced a gradually rising temperature at the metal-oxide interface. Here the difference between the 10 and 30 ms case was 70°C at end-of-pulse ($H = 70$ cal/g, Figure 12). The mid-wall temperature difference was even lower, i.e. 30°C, at mid-wall position.

⁷ This is obviously true assuming one can trust the temperature measurements. Measuring cladding surface temperature by means of thermocouples mounted on the outer surface can be difficult and produce misleading results. However, the authors have no reason to doubt that the temperature measurements made in the NSRR and shown in Figure 11 can be trusted.

It is questionable whether these modest temperature differences can produce large effects on cladding ductility, especially if one considers that they occur in a microscopic period of time, during which the hydrogen effect on brittleness can hardly be changed. This point is discussed in the next section.

A2. Transient temperature effects on cladding ductility

For cladding that is made brittle by hydride formation at the periphery, it can take significant time for temperature to produce beneficial effects on cladding ductility, much longer than the time available in a RIA transient. An experiment carried out at JAERI [13] by annealing pre-hydrated cladding specimens showed that it can take up to 600 s to anneal out an outer hydride rim at 600°C. This indicates that changes in hydride distribution should be quite negligible in the time interval of several milliseconds, especially if only a modest cladding heat-up takes place during the transient. The effect on ductility should thus be very small, especially in terms of the difference between a 10 and 30 ms pulse.

A3. Coolant heat-up

The coolant temperature increases as consequence of the RIA transient. The cladding temperature measurements made in the NSRR tests show that the heat-up during the pulse is negligible, of the order of 20-30°C [14]. Even if one takes into account the time constant of the thermocouples, one would conclude that the cladding temperature heat-up, and hence the coolant temperature heat-up remained within < 50-60°C during the NSRR pulse.

The CABRI coolant temperature measurements also substantially confirm the NSRR finding outlined above for pulses of up to 75 ms. In the REPNa-4 test, in fact, the coolant temperature did not exceed 325°C (from the initial value of 280°C) during the 75 ms pulse [15]. Obviously, it would be even lower than that during a shorter pulse. From this one can conclude that the coolant temperature increment during the pulse is small and thus does not affect the fuel behaviour in the RIA pulse.

After the pulse, however, the coolant temperature may rise considerably. In the case of the REPNa tests, the maximum coolant temperature could rise to ~500°C, depending on the energy injected during the transient. Figure 13 gives the maximum sodium temperature versus test maximum enthalpy in those tests [15]. As seen, for $H = \sim 200$ cal/g the maximum sodium coolant temperature was somewhat higher than 500°C. These peak temperatures were registered ~300 ms after the pulse and thus had no influence on PCMI or on PCMI-induced failures, which at high burn-up occur during the pulse and not in the post-pulse phase. However, the post-pulse temperature rise may affect the post-test strain data because part of the elastic strain is converted into residual (plastic) strain, which is the quantity measured in the post-test examination.

A detailed study conducted here on the REPNa residual strain data has revealed interesting insights and disclosed an implication on cladding temperature, which can be of interest for test interpretation in general. This study is reported on below.

The data in Figures 6, 8 and 10 show a small but systematic difference between the PIE strain at the upper and lower end. That is, the residual strain at the upper end is somewhat larger – for the same enthalpy level – than the residual strain at the lower end. This is shown for instance in Figure 8, where the REPNa-2 data are plotted. One can clearly see that moving from the peak enthalpy (210 cal/g) down towards the upper/lower end after rod (140-150 cal/g) there are data that follow an upper line and other that follow a lower line. This is evidenced in Figure 14, where the same REPNa-2 data

shown in Figure 8 have been fitted with the two dashed lines (one for the data from peak power to upper end, the other for the data from peak power to lower end). The difference in residual strain $\Delta\varepsilon$ at the same enthalpy in upper and lower position was $\sim 0.7\%$ for REPNa-2. The $\Delta\varepsilon$ data derived for the other REPNa tests discussed in this report are shown in Figure 14. As one can observe in Figure 14, there is a trend for the upper-to-lower end strain difference to disappear for tests in which the maximum enthalpy is below ~ 100 cal/g ($\Delta H = \sim 80$ cal/g). This corresponds to a maximum sodium temperature of $\sim 380^\circ\text{C}$, as the data plot of Figure 13 shows.

This means that for maximum enthalpy below ~ 100 cal/g the sodium temperature is $< \sim 380^\circ\text{C}$ compared with an inlet temperature of 280°C . This outlet/inlet temperature difference is not sufficient to induce appreciable differences in residual strain.

There is another, perhaps more important implication of this analysis. Figure 14 shows that the difference between the REPNa-2 outlet and inlet residual strain was as large as 0.7% . This must imply that “almost all” of the elastic component⁸ in the upper end was converted into plastic strain as the coolant and cladding become hot, whereas the elastic component at the lower end was preserved virtually in its entirety as elastic strain. This can only happen if the lower end “mean”⁹ cladding temperature did not exceed $\sim 500^\circ\text{C}$, because beyond that the YS of the cladding and thus the elastic strain would drop considerably.

If one considers that the fuel enthalpy at the lower end of the REPNa-2 rod reached ~ 140 cal/g, and that the conclusion that the “mean” cladding temperature remained below 500°C implies that:

- a) The “mean” temperature for a 70 cal/g pulse would remain below $\sim 400^\circ\text{C}$ throughout the transient. During the pulse the temperature would be appreciably lower than that.
- b) The cladding OD temperature should be even less than the “mean” temperature.

Although this is admittedly an approximate evaluation, it tends to indicate that the cladding temperature during a CABRI RIA pulse might remain relatively low, and possibly lower than predicted by calculations. The corollary of this would be that temperature effects in a pulse should not be very important, which is a confirmation of what already concluded earlier based on a different evaluation.

A4. Conclusion on cladding temperature

The above discussion, based on experimental data and on code calculations, supports the view that there are no significant differences in the cladding temperature evolution versus enthalpy for pulses of different width. The view that broader pulses (from 5 to ~ 70 ms) should be milder because of increased cladding temperature and ductility finds no support on the evaluation made here. The failures registered in NSRR and in CABRI occurred at moderate enthalpy, in a range where one would not expect pulse width to substantially affect the cladding temperature.

⁸ The maximum elastic strain at 280°C is estimated to be $\sim 0.8\%$.

⁹ “Mean” temperature is that which can be used to represent average cladding mechanical properties.

SESSION II

Fuel Material Behaviour in PCI Situation (Part 1)

Chairs: P. Blanpain, D. Baron

PHYSICAL MODEL DEVELOPMENT FOR PREDICTION OF RIM-LAYER FORMATION IN UO₂ FUEL

V.V. Likhanskii, O.V. Khoruzhii, A.A. Sorokin
Troitsk Institute for Innovation and Fusion Research, Russia

Abstract

Results of point defects and gas atom behaviour modelling in UO₂ fuel are presented for the temperature conditions for rim-layer formation. The spatial profiles for vacancy and interstitial atom concentrations in the vicinity of the grain boundaries and near edge dislocations are different. In the initial stage of irradiation, the peak of vacancy concentration is near the grain boundary. During long irradiation the vacancy peak vanishes and a peak of interstitial atoms arises. Vacancy concentration can have a maximum close to the dislocation core. Analysis of gas atom mobility at low temperature irradiation indicates a reducing dependence of Xe effective diffusion coefficient on vacancy concentration. The developed physical models enable the proposal of explanations for experimental facts: grain diameter effect on the threshold for the beginning of fuel restructuring and priority formation of large bubbles on dislocation intersections.

Introduction

For LWR rods, significant changes in fuel structure take place in the peripheral zone of the pellets when the pellet-averaged burn-up exceeds 40 MWd/kgU. The structure modification of the fuel in the rim zone is attended by a considerable increase of local porosity and a subdivision of the original grains into fine subgrains. It is accepted [1-4] that the localisation of structural changes at the pellet periphery is determined by the higher local burn-up, in comparison with the internal part of the pellet, as well as by low temperature. The higher burn-up is caused by additional ^{239}Pu accumulation due to resonant epithermal neutron capture by ^{238}U nuclei. It results in both a higher concentration of fission products and a higher concentration of radiation defects.

The results of numerous measurements [1-16] show that the structural modification of the UO_2 fuel irradiated at nominal conditions up to high burn-up consists of several sequential processes:

- When the local burn-up exceeds a threshold value (~ 70 MWd/kgU) the Xe concentration in the fuel matrix is reduced [4-8].
- Practically at the same burn-up, the increase of local porosity begins [8,14]. Before fuel restructuring, the large bubbles are mainly located on the grain faces and edges; after restructuring, bubbles are also observed in the interior parts of the grains. A short delay of the onset of the porosity growth in comparison with matrix depletion in the Xe stage was observed [13,14].
- At the next stage a large amount of fine grains appear; the crystallographic planes of the fine grains are mutually disoriented by a small angle $\sim 2-7^\circ$ [9,10,16]. The fine grains are formed near boundaries of original grains and at the surfaces of micron-size bubbles.
- An enhancement of UO_2 lattice parameter is observed with increasing fuel burn-up. At a local burn-up of ~ 70 MWd/kgU the increase of the lattice parameter reaches a maximum of $\sim 2 \times 10^{-3}$ [2,15]. When the restructuring begins, the lattice parameter decreases down to some saturation value because of radiation defect recovery during recrystallisation [2,15].
- After accumulation of a significant amount of restructured areas, the original grain boundaries disappear and the rim-zone structure is formed. As the burn-up grows, the restructuring zone propagates into the pellet interior.
- The porosity in the rim zone increases due to growth of bubble size with increasing burn-up [5].
- It is found experimentally that rim-zone formation depends on both irradiation conditions and fuel parameters. Thus, the comparative analysis [2,8,12] of the rim-zone evolution for the standard fuel and the large-grained fuel shows that the matrix depletion in Xe is essentially suppressed for larger grain size; consequently the small-grain structure formation is delayed. The porosity in the rim zone is also a function of mechanical stresses in the fuel. The fuel-cladding interaction may result in significant decrease of porosity (2-3 times compared with the unstressed fuel [8]).

The restructuring process depends not only on fuel burn-up but also on other parameters such as temperature, impurity atom concentration, grain size, fission rate and mechanical stresses. For this reason, the criteria available at present, which are based on threshold burn-up, are approximate and have a wide spread. It is important that the mechanical properties of the fuel change during fine grain structure formation [2,15]. The microstructure changes also result in thermal conductivity changes [1] and affect the temperature in the central part of pellet.

In spite of detailed investigations some issues concerning physical modelling of microstructure changes at low temperature are not yet clarified. First, existing models, which are based on a concept of threshold burn-up, describe the experimental data over a large spread. Second, the models can not explain a short delay of the porosity growth in comparison with Xe matrix depletion. Third, there is no physical explanation for the influence of grain size on the process of Xe release from fuel matrix to bubbles and formation of fine-grain-structure. Fourth, there is a lack of adequate physical modelling of rim-zone porosity including the effect of mechanical stresses caused by pellet-cladding interaction (PCI), gaseous FP release from the rim zone.

Physical modelling is very important for the PCI problem due to the following considerations. Formation of fine grain structure leads to a noticeable change of micro-hardness in the rim zone of the fuel pellet. It has an effect on the regime of PCI. Formation of intragranular and intergranular bubbles in the rim-layer and transition region of the pellet results in gaseous swelling, which is important for the PCI phenomenon. Release of gas and volatile FP (iodine) from the rim layer is related to the problem of stress-corrosion cracking. Thermal conductivity of the fuel depends on the concentration of point defects, the concentration of FP atoms and fuel porosity. All these parameters are sufficiently changed during irradiation. A decrease of thermal conductivity leads to increasing fuel temperatures and it is also important for PCI. The kinetics of point defects originating during the fuel irradiation plays a significant role in the fuel restructuring. This is due to the fact that radiation-induced processes change the FP migration and point defects concentration in the fuel at low temperature. The purpose of the present work is the analysis of the point defect and fission gas behaviour in UO₂ fuel under low temperature irradiation corresponding to the conditions of rim-layer formation.

Point defect distributions near grain boundary

The main source of point defects in UO₂ fuel is caused by lattice atoms' displacement as a result of interaction with fission fragments. It is considered [17] that the mean fragment track length in uranium dioxide is ~ 8 μm and one fragment produces about 5×10^4 vacancies and uranium interstitials. The enhanced point defect concentration, moderated by recombination, leads to secondary defects (dislocations and bubbles) and grain boundaries in the fuel. For analysis of kinetics of vacancy and interstitial atom concentrations C_v , C_i the system of dynamic equations [18,19]:

$$\frac{\partial C_{i,v}}{\partial t} = D_{i,v}^{eff} \Delta C_{i,v} + Q_{i,v} - \beta C_v C_i - \sum Z_{i,v} \quad (1)$$

takes into account defect formation, diffusion, mutual recombination and loss on intragranular sinks (dislocations, bubbles). The following designations are introduced: $D_{i,v}^{eff}$ are effective vacancy and uranium interstitial diffusion coefficients taking into account radiation-induced transfer, $Q_{i,v}$ are point defects sources. The third term in Eq. (1) describes mutual vacancy and uranium interstitial recombination, $\beta \approx KD/\Omega^{2/3}$, $\Omega = 4.1 \times 10^{-23} \text{ cm}^3$ is volume of unit UO₂ cell, coefficient $K = 500$ [19]. Usually for modelling of radiation damages caused by neutrons or gamma radiation the sinks of point defects such as dislocations, bubbles and grain boundaries are of considerable importance. In nuclear fuel the decrease of vacancy concentration in the grain is also correlated with fission product accumulation. There are two mechanisms of annihilation of the vacancies on fission products. The first is due to vacancy annihilation on gas bubbles. The second is due to capture of vacancies by atoms of fission products, including solid fission products. The last process leads to solid swelling ~1% for the burn-up 10 MWd/kgU [2]. In Eq. (1) the vacancy losses to fission product atoms in the fuel lattice are taken into account along with removal to bubbles and dislocations.

Usually stationary profiles of the point defect concentrations near extensive sinks are similar. Neglecting intragranular sinks and assuming that vacancy and interstitial atom sources are the same and the grain boundary is an ideal sink, the ratio between mean concentrations and diffusion coefficient $(C_i/C_v)_b = D_v^{eff}/D_i^{eff}$ is set. Under high temperature, when the effects of radiation-induced transfer are not substantial, the diffusion of interstitial atoms and vacancies is a thermally activated process. In this case the power of intragranular sinks is proportional to the diffusion coefficient for corresponding point defects and the set of non-linear equations in Eq. (1) has steady-state solutions with similar spatial profiles. The constant of proportionality is also equal to the inverse ratio of diffusion coefficients $(C_i/C_v) = D_v/D_i$.

The relations $D_v \approx 10^{-3} \times \exp(-27\ 800/T)$ cm²/s and $D_i \approx 7 \times 10^3 \times \exp(-22\ 000/T)$ cm²/s estimate the thermal component of diffusion coefficients of uranium interstitials and vacancies in uranium dioxide [20]. The radiation-induced component of the diffusion coefficient of uranium atoms is proportional to the fission rate $D_i^{ir} = A\dot{F}$, where $A \sim 1.2 \times 10^{-29}$ cm⁵ [17]. This diffusion coefficient includes uranium atom displacement under interaction with fission fragments and its diffusion as an interstitial atom up to recombination with a vacancy, as well as mixing in the spike. Radiation atomic mixing in the track leads to vacancy diffusion. The radiation component of the vacancy diffusion coefficient is $D_v^{ir} \sim 2\pi\dot{F}r_{tr}^4 l_{tr}$, where r_{tr} and l_{tr} are the radius and the length of the track.

Under temperatures of 300-700°C, the thermal component of the interstitial atom diffusion significantly exceed that of radiation $D_i \gg D_i^{ir}$, but for vacancies the opposite is true, $D_v^{ir} \gg D_v$. Under such conditions, the power of defect sinks, e.g. the grain boundaries, dislocations and bubbles has different dependences on diffusion coefficients. This difference corresponds to the fact that the length of atom jump under thermally activated diffusion is equal to the interatomic distance in the lattice and uranium atom transfer during the passage of a fission fragment is approximately equal to track radius and exceeds the lattice spacing several times. Different dependencies of the vacancy and interstitial atom transport to the grain boundary, dislocation and bubble can cause the essential differences between spatial distributions of the point defect concentrations. For analysis of the influence of different irradiation factors and the fuel parameters (including temperature, burn-up, grain size and fission rate) on point defect distribution in the grain, a computer program was developed. In further calculations the vacancy annihilation on intragranular bubbles and vacancy capture by fission product atom is considered to be proportional to the fuel burn-up.

For validation of the model parameters the calculations were compared with the experimental data found in Refs. [21,22] under small radiation doses, at $T = 150^\circ\text{C}$, when the main processes are accumulation and mutual recombination of the point defects (Figure 1). In [21,22] the change of lattice parameter of dioxide-uranium fuel with radiation dose was measured. It was considered that growth of the lattice parameter corresponds to accumulation of vacancies and leads to an increase of specific volume $3\Delta a/a \approx \Delta V/V \approx C_v$.

The point defect distributions in uranium dioxide grains were calculated for different temperature and fission rates on the assumption of constant conditions and constant power of intragranular sinks. The point defects sink to dislocations and accumulated fission products were taken into account. The calculations showed (Figure 2) that under a given concentration of intragranular sinks, the initial stage was for the vacancy and interstitial atom concentrations in the central grain region to increase up to concentrations at which the point defects recombination process is of considerable importance. Increase of radiation dose leads to increase of vacancy concentration, but to a decrease of interstitial atom concentration down to established values. The vacancies distribution with the grain radius has its maximum near the grain boundary (Figure 3). The maximum vacancy concentration is caused by the

Figure 1. Comparison of calculated dynamics of vacancy concentration (—) with experimental data [21,22] on lattice parameter (\circ, ∇) as a function of irradiation dose

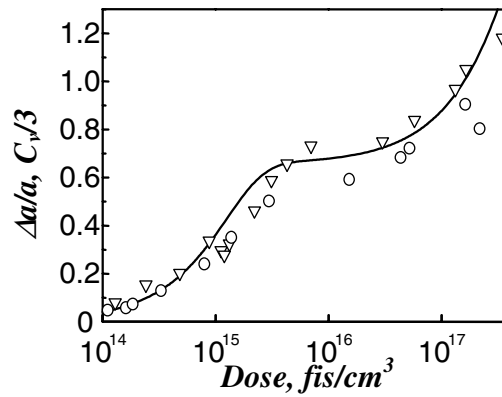


Figure 2. Dependence of vacancy and interstitial atom concentrations in the grain centre on time. Dislocation density is 10^{13} m^{-2} .

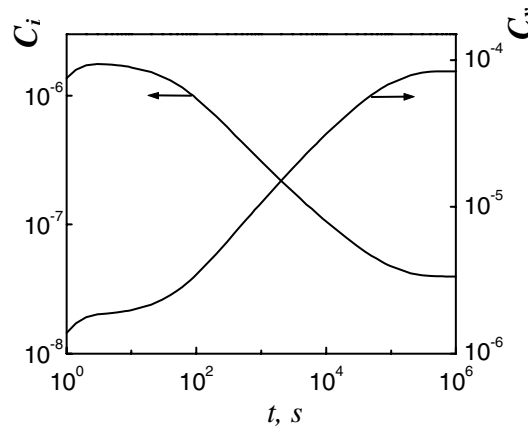
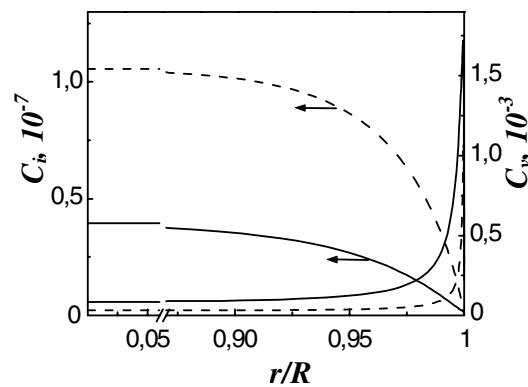


Figure 3. Vacancy and interstitial atom distribution in the grain. Dislocation density is 10^{13} m^{-2} . Irradiation time is 10^4 s (---), 10^7 s (—).



decrease of interstitial atom concentration near the grain boundary as a result of diffusion to sink as well as a decrease in the vacancy recombination rate in that region at almost the same rate of defects accumulation. Since the interstitial atom diffusion coefficient is much more than effective coefficient of vacancy diffusion, interstitial atoms reach the grain boundary quite rapidly. Therefore the burn-up increase leads to increase and obtain the established value of the vacancy concentration. The interstitial atom concentration decreases with time. At $t > 10^6$ s quasi-steady state concentration profiles establish. The calculations were carried out at fission rate $10^{13} \text{ cm}^{-3}\text{s}^{-1}$ and fuel temperature 350°C .

When the dislocation density increases with time, the maximum of interstitial atom concentration arises instead of maximum of vacancy concentration in the vicinity of the grain boundary. The average values of the point defect concentrations are also changed ($N_{\text{dis}} = 10^{15} \text{ m}^{-2}$, see Figures 4,5).

Figure 4. The same as in Figure 2, $N_{\text{dis}} = 10^{15} \text{ m}^{-2}$

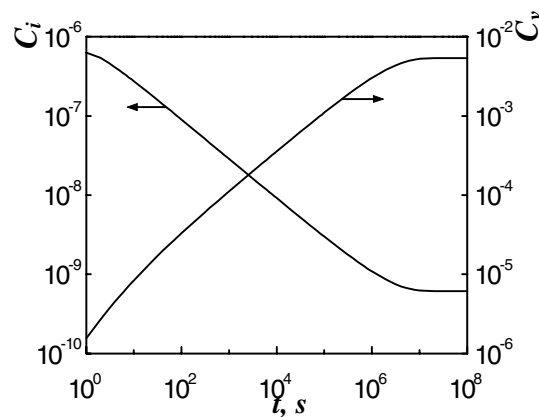
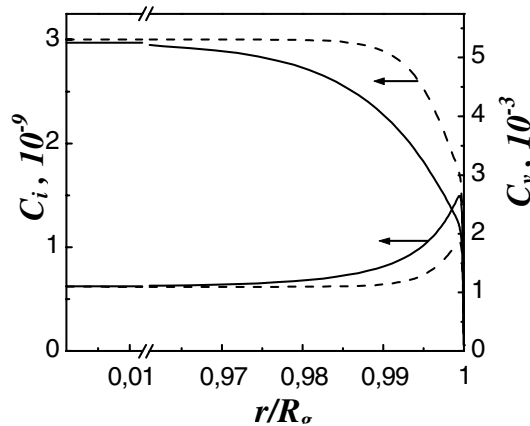


Figure 5. The same as in Figure 2, $N_{\text{dis}} = 10^{15} \text{ m}^{-2}$. Irradiation time is 10^5 s (----), 10^7 s (—).



It is noticeable that at short time ($t < 10^6$ s) the vacancy distribution has a maximum near the grain boundary; a maximum concentration of the interstitial atoms is achieved in the centre of the grain. With increased burn-up ($t > 10^6$ s) the profiles become essentially deformed: near the grain boundary, the maximum interstitial atom concentration is obtained, the maximum vacancy concentration occurs in the centre of the grain (Figure 5). The differences in the spatial vacancy and interstitial atom distributions in the grain of the fuel are caused by the fact that the sink power at the boundary and the sink power inside the grain volume are not proportional and the mutual point defect recombination is of importance. At the beginning of irradiation the interstitial atoms rapidly move to the grain boundary

as a result of high mobility. Therefore the vacancy concentration increases in this region more rapidly than far from the boundaries, and vacancy concentration maximum arises at the distance determined by $L_m \sim [D_i^{eff} D_v^{eff} / (\beta Q)]^{1/4}$. The fact that the ratio between sinks for interstitial atoms and for vacancies is different at the grain boundary and within the grain volume leads after a long time to a vacancy concentration maximum near the grain boundary in the case of $Z_v / (2\pi N_{dis} D_i^{eff}) > \sqrt{Q D_v^{eff} / \beta D_i^{eff}}$ (Figure 3). If this is not the case, the interstitial atom concentration maximum is set near the grain boundary (Figure 5). Z_v is the volume vacancy sinks (on bubbles and fission products). Interstitial atoms in the grain volume annihilate on dislocation.

The differences in distributions of the point defect concentrations shown in Figures 3 and 5 at different dislocation densities could be one of the explanations for grain size influence on the fine grain structure formation.

Point defect distributions near the core of the edge dislocation

Let us consider interstitial atom drift in a non-uniform field of mechanical stress and the possible motion of a dislocation line under the imbalance of uranium interstitial and vacancy flows for the determination of spatial distribution of the point defects near the core of the edge dislocation.

The interstitial atom flow on the dislocation, defined by drift in the stress gradient, is equal to $D_i \nabla C_i \nabla (E_i / kT)$. E_i is the energy of the interstitial atom in the field of mechanical stress produced by dislocation, T is the temperature. As an order of magnitude for the linear edge dislocation $E_i \sim G \Omega_i b / 3\pi r$ [23], where $G \approx 7.5 \times 10^{10} Pa$ is shear modulus [24], Ω_i is dilatation volume ($\Omega_i \approx 4 \times 10^{-23} cm^3$), $b \approx 2.7 \times 10^{-8} cm$ is the size of dislocation core. In this approximation, the flow of interstitial atoms to the length unit of the edge dislocation is $Z_{i,dis} = 2\pi D_i L_i \nabla C_i$, where $L_i \approx G \Omega_i b / 3\pi kT$.

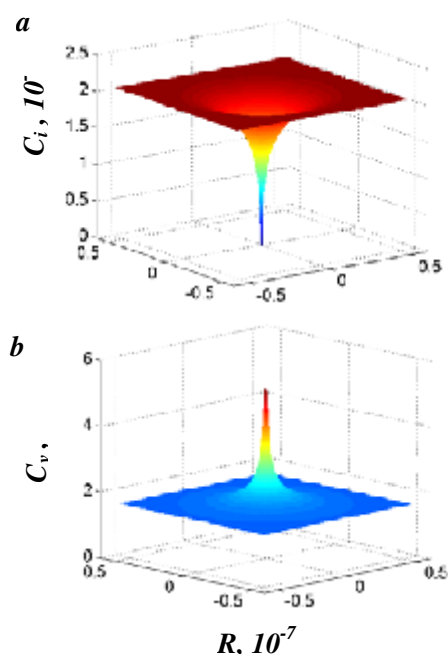
Vacancy drift in the field of mechanical stress can be neglected because of the small thermal component of the diffusion coefficient. The vacancy flow to the dislocation is $Z_{v,dis} = B \times D_v^{ir} C_v b^2 / r_r^2$. Coefficient B is about 1. The decrease of vacancy flow to the dislocation is approximately b^2 / r_r^2 times in comparison with the case when the diffusion jump length is equal to the lattice spacing, relating to the fact that only such part of vacancies, intermixing in the track, arrives at the region, where vacancy annihilation on the dislocation takes place. The velocity of the dislocation line due to the arrival of point defects is determined by the difference between vacancy and uranium interstitial flows $v_{dis} = (2\pi D_i C_i - Z_{v,dis}) / \Omega^{1/3}$.

For the conditions of in-pile irradiation of dioxide uranium fuel the main processes are the generation and mutual recombination of point defects. These two processes practically compensate each other. Near the core of the edge dislocation the uranium interstitial concentration is inhomogeneous. Since the uranium interstitials rapidly move to the dislocation (high thermal diffusion coefficient), and the vacancy concentration decreases due to capture by gas bubbles and fission products, a vacancy distribution with a maximum concentration near the core of the edge dislocation can be obtained. This effect takes place when the transition time of the vacancy redistribution at the length of inhomogeneous interstitial atom distribution is essentially less than the time of displacement of the dislocation line at the same length. Calculations show that at irradiation times more than 10^7 s the vacancy concentration essentially exceeds the interstitial atom concentration and the length, at which interstitial atom concentration changes near dislocation, is defined with the point defect recombination $L = \sqrt{D_i / \beta C_v}$.

Thus the condition for the existence of the vacancy concentration maximum near the core of the edge dislocation is $D_v^{ir}/D_i > \bar{C}_i L/\Omega^{1/3}$ or $D_v^{ir}/D_i > \bar{C}_i/\sqrt{K\bar{C}_v}$. With the increase of burn-up and dislocation density, the uranium interstitial concentration decreases and such a condition may be achieved with excess. For example, at a dislocation density 10^{14} m^{-2} the time of the maximum vacancy concentration occurs at $t > 10^7 \text{ s}$.

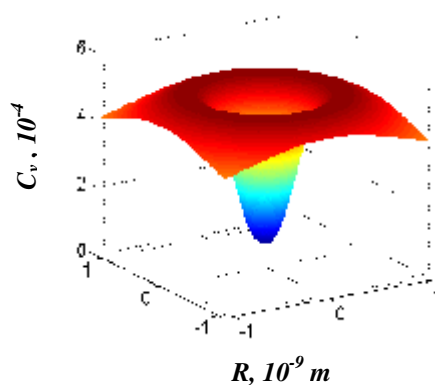
Figure 6 shows an example of a calculation of point defect distribution near the core of the edge dislocation. The concentration of uranium interstitials monotonically drops to the dislocation core, whilst the vacancy concentration reaches a maximum at the dislocation core.

Figure 6. Distribution of interstitial atoms (a) and vacancies (b)



The scale factor at the horizontal scales is 10^{-7} m . A larger scale for vacancy distribution, corresponding to Figure 6, is shown in Figure 7. One point at the horizontal scale in Figure 7 is 10^{-9} m . The spread of minimum close to dislocation core has the size of lattice spacing $\sim 3 \times 10^{-10} \text{ m}$, which is much less than the half width of the distribution peak $\sim 10^{-8} \text{ m}$.

Figure 7. Vacancy distribution near the edge dislocation



The ratio of maximum vacancy concentration to the average concentration increases with the decrease of dislocation density and increase of the density of uranium interstitial sinks. The effect of a non-uniform distribution of the point defects can be considerable, if $4C_i(L/\Omega^{1/3})^2 > D_v^{ir}/D_i$, which takes place for conditions of the fuel irradiation in the periphery pellet region. Thus, condition $(\Omega^{1/3}/L)^2/4 < C_i D_i / D_v^{ir} < \Omega^{1/3}/L$ has to hold true in order that near dislocation vacancy distribution peak occurs and maximum concentration considerably exceeds the average one.

The calculations, taking into account the anisotropy by the angle of point defects mechanical energy in the tension field of edge dislocation, showed that the peaks in point defect distribution and average concentration values have the similar values, but angle deformation of distributions close to dislocation core takes place.

Irradiation influence on FP transfer in UO₂ grain

The main mechanism of FP atom transfer in the fuel is diffusion. In general, the diffusion coefficient includes several components.

$$D = D_T + D_{ir,T} + D_{ir} \quad (2)$$

It is considered that under high temperatures ($T > 1\ 200$ K) FP atoms diffuse by a vacancy mechanism with diffusion coefficient D_T , depending mainly on temperature. Under low temperatures ($T < 1\ 000$ K) it is supposed that the main transfer mechanism is connected with fuel irradiation. D_{ir} is proportional to the fission rate and is called a radiation-induced diffusion component. The $D_{ir,T}$ component depends on fission rate as well as on the temperature. This is caused by the fact that for the vacancy mechanism the diffusion coefficient depends on temperature, because the vacancy concentration is defined by both temperature and fission rate in the fuel. This term plays a significant role in the intermediate temperature range (800-1 200 K).

Radiation transfer includes various physical mechanisms, which lead to randomised atom displacements in the fuel interacting with fission fragments. Such mechanisms are: atomic mixing in the track, interstitial atom “extrusion” from the hot part of the track due to high pressure and atom knock-out by fission fragments. The radiation-induced component for different atoms in a UO₂ fuel lattice can significantly differ. The results of [25] demonstrate that under low-temperature fuel irradiation and the same fission rates the diffusion coefficients can significantly differ depending on the burn-up and the microstructure. These facts indicate that the current values of the point defect concentrations along with noted transfer mechanisms can play a significant part in D_{ir} . Let us consider Xe atom transfer for analysis of the possible influence of the point defect concentrations on the efficient diffusion coefficient under low-temperature irradiation. Xenon atoms will be considered to be able to be knocked into interstitial sites of the fuel lattice along with the mechanism of atomic mixing in the track during the fission fragment passage in the fuel. Interstitial Xe atoms can diffuse with corresponding diffusion coefficient by interstitial sites, which significantly exceeds the diffusion coefficient by vacancy mechanism at low temperatures. The transfer equations for Xe interstitials and for Xe atoms coupled with the three-vacancy complex, uranium vacancy and two oxygen ones, are given by:

$$\begin{aligned} \dot{C}_{Xe,i} &= D_{Xe,int} \Delta C_{Xe,i} - BC_{Xe,i} \bar{C}_v + A \cdot \dot{F} \cdot C_{Xe,v} \\ \dot{C}_{Xe,v} &= D_{Xe,rad} \Delta C_{Xe,i} - BC_{Xe,i} \bar{C}_v - A \cdot \dot{F} \cdot C_{Xe,v} \end{aligned} \quad (3)$$

The xenon atom diffusion, vacancy annihilation at xenon interstitials and xenon atom knock-out from a vacancy-coupled complex into an interstitial site are taken into account. This set of equations for the transfer of xenon atom concentration ($C_{Xe} = C_{Xe,int} + C_{Xe,v}$) results in a diffusion equation with efficient diffusion coefficient:

$$D_{Xe,eff} = \frac{D_{Xe,rad} \cdot \tau_{rad} + D_{Xe,int} \cdot \tau_{an}}{\tau_{rad} + \tau_{an}} \quad (4)$$

$$\tau_{an} = (B \cdot D_{Xe,int} \cdot b \cdot \bar{C}_v)^{-1}$$

$$\tau_{rad} = (A \cdot \dot{F})^{-1}$$

For temperature, corresponding to the cold region of the pellet $D_{Xe,rad} \ll D_{Xe,int}$ and in the case when $\tau_{an} \ll \tau_{rad}$, the efficient diffusion coefficient of the Xe atom increases with the decrease of the vacancy concentration and proportional to the fission rate in the fuel. This is related to the fact that until the vacancy captures the Xe atom, the interstitial Xe rapidly diffuses with an interstitial diffusion coefficient. Once captured, the Xe atom becomes immobile for the time τ_{rad} until the following knock-out during fission fragment pass.

The dependence can be important for the description of fission gas release from high burn-up fuel under low temperature conditions. At average burn-ups more than 40 MWd/kgU the formation of fine-grain structure in the cold region of the pellet, rim-zone formation, occurs. At the same time the ‘‘cleaning’’ of the crystal UO_2 matrix from the point defects takes place and this fact results in an increase of the diffusion coefficient of Xe atoms and to increase its release rate from the fuel, as was shown above. In the present system the effect of radiation-induced drift of the fission gas atoms in the presence of vacancy concentration gradient appear along with the effect of essential dependence of radiation-induced diffusion coefficient of the gas atoms in the fuel on the vacancy concentration. The transfer equation for the gas atom concentration $C_{Xe} = C_{Xe,int} + C_{Xe,v}$ in the fuel is:

$$\frac{\partial C_{Xe}}{\partial t} = \frac{D_{Xe,rad} \cdot \tau_{rad} + D_{Xe,int} \cdot \tau_{an}}{\tau_{rad} + \tau_{an}} \Delta C_{Xe} + (D_{Xe,rad} - D_{Xe,int}) \frac{\tau_{rad} \cdot \tau_{an}}{(\tau_{rad} + \tau_{an})^2} \frac{\nabla \bar{C}_v}{\bar{C}_v} \nabla C_{Xe} \quad (5)$$

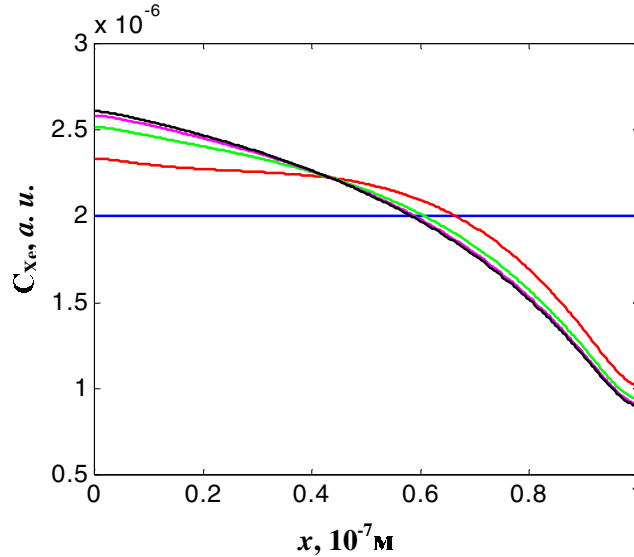
The first term of Eq. (5) describes the Xe atom transfer by the diffusion way with effective diffusion coefficient of Eq. (4). The second term of Eq. (5) describes the effect of fission gas redistribution at the presence of non-uniform vacancy concentration in the crystal lattice. The present effect is in many aspects like the effects of atom drift in crystals in temperature gradients (thermo-diffusion effect), drift in tension gradient, etc. However in this case this drift is not bounded up with the realisation of thermodynamic equilibrium in the system and does not appear in the absence of fissions in the fuel.

As an example, Figure 8 shows the time evolution of the concentration profile of Xe atoms in the fuel. The vacancy concentration at 10^{-7} m is approximately a linear function of the distance $\bar{C}_v = 10^{-4}$ at $x = 0$ and $\bar{C}_v = 10^{-5}$ at $x = 10^{-7}$ m (the concentration is in the units per the volume of the UO_2 lattice). At initial time the Xe atom distribution is homogeneous to the length, but in due course the essential redistribution of xenon atoms take place due to the effect of radiation-induced Xe drift in vacancy gradient. Xenon concentration has a maximum in the region with maximum vacancy concentration.

The effect of radiation-induced drift in vacancy gradient may be significant from the point of view of the formation and development of the intragranular and intergranular bubbles in the UO_2 fuel.

Figure 8. Redistribution of Xe atoms in UO₂ fuel at the presence of vacancy gradient

The blue line shows the initial Xe atom distribution, the red line shows the distribution at time $t = 2 \times 10^6$ sec, green line $t = 4 \times 10^6$ sec, violet line $t = 6 \times 10^6$ sec, black line $t = 8 \times 10^6$ sec



Discussion

Two opposite standpoints currently exist to explain rim-layer development. The first supposes that the grain subdivision arises as a result of radiation damage, with large bubbles and dislocation net formation following the grain subdivision. The second believes that the bubbles and dislocation net are formed before the grain subdivision. Several self-consistent physical models were proposed to predict a beginning of the high burn-up structure formation. Here, attention is only directed toward two models [19,26].

In Ref. [19], the rim structure formation was proposed as a result of an instability in the development in the coupled system of vacancies, interstitial uranium atoms, dislocations and fission gas atoms. Numerical investigation of the equations indicates the possibility of the spatial instability development in this system. But in the paper the diffusion coefficient of the interstitial uranium atoms between spatial segments was increased by a factor of 2 in the process of numerical analysis. We carried out a stability analysis of the equations of [19]. This analysis shows that spatial instability can occur when diffusion coefficients for spatial transfer of the point defects are different from the diffusion coefficients, which are used in other physical processes (defects recombination, annihilation of the point defects on dislocation, etc). The following question emerges: What physical process can change the effective diffusion coefficients? An answer may lie with spatial non-uniform point defect distributions inside the fuel grain.

It was proposed in [26] that the rim structure formation is initiated by the cascade of atomic movements of the fission fragments when the gas atom concentration exceeds some critical value inside the grain. But calculations of the critical gas concentration and its dependence on different parameters (temperature, fission rate, grain diameter) indicated that the model can not explain the grain size influence on threshold burn-up for rim-layer formation. Point defects and gas atoms behaviour in the grain may eliminate this imperfection.

Presented models of the individual physical processes for point defects and gas atoms behaviour under low temperature irradiation conditions are able to describe the order of events during rim-layer formation. Let us consider the consequences of the models as the fuel burn-up increases.

In the initial stage of the fuel irradiation the concentrations of the vacancies and uranium interstitials increase at the same rate up to values, which result in the defects recombination, restricting the further combined growth of the defect concentrations. Thereafter the concentration of uranium interstitials decreases due to losses on intragranular and grain boundary sinks. The fast departure of the uranium interstitials to the sinks is on account of their high diffusion coefficient. Vacancy losses are defined by vacancy annihilation at gas bubbles, on dislocations, on grain boundaries and due to capture of vacancies by atoms of fission products. The diffusion coefficient of interstitial uranium atoms is substantially high in comparison with the vacancy diffusion coefficient. With increasing burn-up the vacancy concentration increases and concentration of uranium interstitials decreases.

In accordance with the dependence of the point defect concentrations on irradiation time, the edge dislocation motion is subject to retardation. When the concentration of interstitials falls to a critical value, a maximum vacancy concentration appears in the vicinity of the edge dislocation core. This non-uniform distribution of vacancy concentration leads to redistribution of fission gas atoms. The concentration of gas atoms increases near the dislocation core inside the grain volume. Thus super-saturated gas atom regions arise.

It is known that intragranular bubbles are formed along the track of fission fragments. Bubbles of small radius are broken when the next fission fragment passes through the bubble. When the bubble has a sufficiently large radius, the fission fragment can not destroy the bubble. In displacement spikes, formed along the track, a cascade of atomic displacement arises. The size of the bubble nucleated from the spike increases with gas atom concentration. When the gas atom concentration in the super-saturated region exceeds a threshold value, the bubbles unbroken by fission fragment will be formed.

The appearance of an unbroken bubble population increases the intragranular porosity and decreases the vacancy concentration. Large stable bubbles can result in pinning of dislocations and the formation of a dislocation net. Decreasing the vacancy concentration initiates the rate of the gas atom diffusion and leads to Xe depression in the fuel matrix. As a result the gas pressure inside large intra- and intergranular bubbles increases. The pressurised bubbles can initiate fine grain formation.

Conclusion

The analysis has shown that point defects distribution close to the grain boundaries and in the vicinity of the edge dislocation core could be essentially non-uniform with different spatial distributions of vacancies and interstitial uranium atoms. An increase in dislocation density can cause the qualitative change of the distributions at high burn-up.

Such behaviour of point defects can be one of the explanations of the grain size influence on the bubble growth kinetics, and, as a consequence, on the process of small grain formation in the periphery region of the fuel pellets. On the assumption that the main dislocation source is grain boundaries, the dislocation density in the grain volume is inversely proportional to its radius. Then the dislocation density in small grains becomes greater than in large ones. Therefore the intragranular gas bubbles have to grow more efficiently in the fuel with small grains and the matrix cleaning from the gaseous fission products occurs earlier, which corresponds to the experiments.

A new model of diffusion transfer for low temperatures takes into account the fission product interaction with the tracks, atom diffusion through interstitial sites in the lattice and the fission product atom capture by the vacancies. The model explains the significant differences in diffusion coefficients for different chemical elements at temperatures below 1 000°C, which are experimentally observed. The atom diffusion coefficient is shown to depend on vacancy concentration at the temperatures of rim-zone formation, and the vacancy concentration increase can cause the decrease of effective diffusion coefficients for gaseous fission products.

Under UO₂ fuel irradiation the effect of radiation-induced drift in the vacancy gradient can take place. The present effect is important for the modelling of the dynamics of the intragranular and intergranular gas bubble growth in the fuel, as well as for the modelling of edge dislocation dynamics.

Acknowledgements

This paper was partially supported by the Russian Foundation for Basic Research, project No. 02-02-16494.

REFERENCES

- [1] Kinoshita, M., E. Kolstad, Hj. Matzke, *et. al*, “High Burn-up Project. (II) Irradiation and Examination to Investigate Rim-structured Fuel”, *Proceedings of the ANS Meeting on Light Water Reactor Fuel Performance*, Park City, Utah, 10-13 April 2000, 590-603 (oral session).
- [2] Baron, D., J. Spino, D. Papaioannou, “Rim Formation and Fission Gas Behaviour: Some Structure Remarks”, *International Seminar on Gas Behaviour in Water Reactor Fuels*, Cadarache, France, 26-29 September 2000.
- [3] Matzke, Hj., M. Kinoshita, “Poligonization and High burn-up Structure in Nuclear Fuels”, *J. Nucl. Mater.*, 247, 108-115 (1997).
- [4] Mogensen, M., J.H. Pearce, C.T. Walker, “Behaviour of Fission Gas in the Rim Region of High Burn-up UO₂ Fuel Pellets with Particular Reference to Results from an XRF Investigation”, *J. Nucl. Mater.*, 264, 99-112 (1999).
- [5] Cunningham, M.E., M.D. Freshley and D.D. Lanning, “Development and Characteristics of the Rim Region in High Burn-up UO₂ Fuel Pellets”, *J. Nucl. Mater.*, 188, 19-27 (1992).
- [6] Une, K., K. Nogita, S. Kashibe, M. Imamura, “Microstructure Change and its Influence on Fission Gas Release in High Burn-up UO₂ Fuel”, *J. Nucl. Mater.*, 188, 65-72 (1992).
- [7] Noirot, J., L. Desgranges, P. Marimbeau, *International Meeting on Light Water Reactor Fuel Performance*, 10-13 April 2000.

- [8] Une, K., K. Nogita, Y. Suzava, *et al.*, “Effect of Grain Size and PCI Restrain on the Rim Structure Formation of UO₂ Fuels”, *Proceedings of the ANS Meeting on Light Water Reactor Fuel Performance*, Park City, Utah, 10-13 April 2000, pp. 615-625 (oral session).
- [9] Kinoshita, M., T. Kameyama, S. Kitajima, Hj. Matzke, “Temperature and Fission Rate Effect on the Rim Structure Formation in a UO₂ Fuel with a Burn-up of 7.9% FIMA”, *J. Nucl. Mater.*, 252, 71-78 (1998).
- [10] Ray, I.L.F., Hj. Matzke, H.A. Thiele, M. Kinoshita, “An Electron Microscopy Study of the RIM Structure of a UO₂ Fuel with a High Burn-up of 7.9% FIMA”, *J. Nucl. Mater.*, 245, 115-123 (1997).
- [11] Nogita, K., K. Une, “Irradiation Induced Recrystallization in High Burn-up UO₂ Fuel”, *J. Nucl. Mater.*, 226, 302-310 (1995).
- [12] Une, K., M. Hirai, K. Nogita, *et al.*, “Rim Structure Formation and High Burn-up Fuel Behavior of Large-grained UO₂ Fuels”, *J. Nucl. Mater.*, 278, 54-63 (2000).
- [13] Schimtz, F., J. Papin, “High Burn-up Effects on Fuel Behaviour Under Accident Conditions: The Tests CABRI REP-Na”, *J. Nucl. Mater.*, 270, 55-64 (1999).
- [14] Spino, J., D. Baron, M. Coquerelle, A.D. Stalios, “High Burn-up Rim Structure: Evidences that Xenon-depletion, Pore Formation and Grain Subdivision Start at Different Local Burn-ups”, *J. Nucl. Mater.*, 256, 189-196 (1998).
- [15] Spino, J., D. Papaioannou, “Lattice Parameter Changes Associated with the Rim-structure Formation in High Burn-up UO₂ Fuels by Micro X-ray Diffraction”, *J. Nucl. Mater.*, 281, 146-162 (2000).
- [16] Thomas, L.E., C.E. Beyer, L.A. Charlot, “Microstructural Analysis of LWR Spent Fuels at High Burn-up”, *J. Nucl. Mater.*, 188, 80-89 (1992).
- [17] Matzke, Hj., T. Wiss, “Radiation Damage in Nuclear Materials”, Review Article in *Annual Report of Institute for Transuranium Elements*, pp. 30-42 (2000).
- [18] Rest, J., G.L. Hofman, “An Alternative Explanation for Evidence that Xenon Depletion, Pore Formation, and Grain Subdivision Begin at Different Local Burn-ups”, *J. Nucl. Mater.*, 277, p. 231 (2000).
- [19] Kinoshita, M., “Towards the Mathematical Model in Rim Structure Formation”, *J. Nucl. Mater.*, 248, pp. 185-190 (1997).
- [20] Griesmeyer, J.M., N.M. Ghoniem, “The Response of Fission Gas Bubbles to the Dynamic Behavior of Point Defects”, *J. Nucl. Mater.*, 80, pp. 88-101 (1979).
- [21] Nakae, N., A. Harada, T. Kirihara, S. Nasu, “Irradiation Induced Lattice Defects in UO₂”, *J. Nucl. Mater.*, 71, pp. 314-319 (1978).
- [22] Nakae, N., T. Kirihara, S. Nasu, “Irradiation Induced Volume Change in UO₂”, *J. Nucl. Mater.*, 74, pp. 1-9 (1978).

- [23] Hirth, J., I. Lothe, "Theory of Dislocations", *M. Atomizdat* (1972) (in Russian).
- [24] Olander, D.R., *Fundamental Aspects of Nuclear Reactor Fuel Elements*, TID-26711-P1, US Technical Information Center, Springfield, VA (1976).
- [25] Turnbull, J.A., C.A. Friskney, *et al.*, "The Diffusion Coefficient of Gaseous and Volatile Species During the Irradiation of Uranium Dioxide", *J. Nucl. Mater.*, 107, pp. 168-184 (1982).
- [26] Lee, C.B., Y.H. Jung, "An Attempt to Explain the High Burn-up Structure Formation Mechanism in UO₂ Fuel", *J. Nucl. Mater.*, 279, pp. 207-215 (2000).

MICROSTRUCTURE INVESTIGATIONS OF AS-IRRADIATED, ANNEALED AND POWER RAMPED HIGH BURN-UP FUEL

S.K. Yagnik,¹ J.A. Turnbull,² R.A. Gomme³

¹EPRI

²Independent Consultant

³AEA-T

Abstract

Quantitative scanning and transmission microscopy studies have been performed on high burn-up fuel specimens retrieved from (a) fuel discs irradiated isothermally in the Halden BWR and (b) commercial BWR and PWR fuel rod segments after base irradiation and power ramping in the R2 test reactor. Comparative microstructure evolution in the as-irradiated condition and subsequent to various out-of-pile annealing [for (a) specimens] and in-pile power ramping [for (b) specimens] will be reported. The study focuses on precipitate, intra and intergranular bubble distributions, and dislocation densities as a function of the fuel temperature history. It is demonstrated that irradiation temperature and estimated maximum temperatures reached at the positional origin of the specimens are important factors in defining their microstructure.

The highest burn-up specimens examined contained a fuel structure usually found in the rim region of LWR fuel pellets discharged at high burn-up. The behaviour of these samples during periods of increased temperature deviated from that of lower burn-up specimens. This response is presented and discussed in the context of its possible impact on LOCA and RIA at high burn-up.

Introduction

A comprehensive programme [1-3] to measure thermal conductivity and associated properties of irradiated urania and gadolinia-doped urania as a function of burn-up and temperature has been completed in order to underpin the empirical correlations used within the nuclear industry in support of high burn-up fuel operations. Some of the programme results relating to the study of thermal conductivity have already been published [4]. The purpose of the present paper is to describe the observations relating to the evolution of microstructure as a function of: burn-up, out-of-pile heat treatment and in-pile power ramps [5]. Since changes in microstructure with irradiation have a direct impact on fuel rod performance, e.g. through fuel swelling and densification, the results are of interest both quantitatively and qualitatively in understanding PCI phenomenon. In addition, the results provide insight into the distribution and kinetics of irradiation damage and the disposition of solid and gaseous fission products within the grains and on grain boundaries under various operating conditions.

The irradiated fuel specimens retrieved for microstructure investigations had two separate origins: (a) fuel discs irradiated isothermally in the Halden BWR and (b) commercial fuel rod segments base irradiated and power ramped. Fuel type (a) was extensively pre-characterised as well as examined by various PIE techniques in as-irradiated condition and subsequent to various out-of-pile anneals. Many of these anneals were integral parts of test matrices for measuring other properties of the programme such as thermal diffusivity (TD) by the laser flash technique or fission gas release (FGR) with the ^{85}Kr method. The temperature-time histories of various disc specimens were thus experimentally known. For type (b) fuel, available detailed power histories of base irradiation and power ramping were used in estimating irradiation temperatures of the specimens retrieved for PIE.

Thus by evaluating the microstructure data in the context of burn-up and the temperature-time history “seen” by the specimen, it has been possible to draw certain related conclusions concerning high burn-up fuel behaviour in general and FGR and PCI in particular.

Experimental

PIE techniques

Several techniques were employed for the examination of the microstructure of the materials studied. In particular, optical microscopy, scanning electron microscopy (SEM) and transmission electron microscopy (TEM) were employed to examine the specimens at different levels of magnification to discern a wide range of bubble and precipitate sizes and concentrations. Optical microscopy was performed on polished and etched surfaces. SEM was performed on fractured surfaces, which revealed both inter- and transgranular fracture whilst TEM was employed to examine carbon replicas and sections thinned to electron transparency. From these it was possible to examine the grain boundary and intragranular bubble populations, respectively.

Fuel discs

The fuel discs were especially fabricated [1] and irradiated to obtain uniform burn-up samples [2]. They were obtained from pellets of UO_2 and $(\text{U,Gd})\text{O}_2$ with 10% gadolinia content and 19.7 wt.% ^{235}U for rapid burn-up accumulation during irradiation. The discs were 9.5 mm in diameter and 1 mm thick. Both materials had a grain size $\sim 25\ \mu\text{m}$ and were $\sim 96.6\%$ theoretical density; consequently there was very little densification in the standard 1 700°C for 24 hr re-sintering test.

During irradiation in HBWR [2], the fissile discs were stacked individually between molybdenum discs in specially designed rodlets. This design ensured a radially uniform temperature across each disc with most of the generated heat transported through the molybdenum discs. The design also ensured a radially uniform power and burn-up distribution. A high burn-up of ~80 MWd/kg was achieved after ~2.5 years irradiation. Lower burn-up material was obtained by unloading rodlets from the assembly at stages throughout the irradiation. Average heat rates for the UO₂ discs ranged from ~120 kW/m (180 W/g) at the start of the irradiation, reducing gradually to ~80 kW/m (120 W/g) at the end due to depletion. The corresponding values for the (U,Gd)O₂ discs were ~30 kW/m at the start rising to ~100 kW/m at the end as the gadolinium burnt out. At these powers, the average irradiation temperature was in the range 500-800°C, with discharge temperatures typically in the range 500-700°C for all discs. At these power levels, the estimated maximum temperature gradient between the centre of a fissile disc and its outer surface was ~25°C in the axial direction and 50°C radially. Table 1 summarises the fuel discs specimens.

Table 1. Sample identification, composition and burn-up of fuel disc specimens

Specimen	Composition	Burn-up MWd/kgU
U0	UO ₂	0
U2	UO ₂	26.8
U4	UO ₂	38.8
U6	UO ₂	63.6
U8	UO ₂	80
G0	(U,Gd)O ₂	0
G4	(U,Gd)O ₂	23
G6	(U,Gd)O ₂	45.9

Commercial fuel

Three samples originated from an ABB rod base irradiated to an average burn-up of 58.5 MWd/kgU in Ringhals between 1980-1992. A part of the rod was re-fabricated for ramp testing in Studsvik R2. This was subjected to a slow rise in power to 33 kW/m and held for 3 hrs before being down-ramped at a rate of 2 kW/m/min. A second rod G11 was supplied by Framema, base irradiated for four cycles in Cruas 3 to a rod average burn-up of 52.4 MWd/kgU. A section G11/5 was re-fabricated and ramped in the Studsvik R2 reactor where it experienced 16 hrs at 16.5 kW/m before being ramped at 9 kW/m/min to 41.3 kW/m, held for 12 hrs then down-ramped at 0.9 kW/m/min.

Smaller sections from ramp tested fuel segments were shipped to a hot cell laboratory at which specimens were cut from cross-sections to provide samples used for TD measurements and microstructure studies. These specimens are listed in Table 2.

Test series

The programme consisted of three separate series of tests. During the TD measurements [4], each fuel disc sample was subjected to stepped temperature ramps between 300 and 1 500°C with laser flash measurements being made during the 10-15 min hold periods at 100°C intervals. A typical test sequence was as follows, all in steps of 100°C: (i) 300 – 700 – 300°C, (ii) 300 – 1 100 – 500°C, (iii) 500 – 1 500 – 300°C, (iv) 300 – 1 600 – 300°C.

Table 2. Commercial fuel samples and their estimated temperatures

Specimen ID	Local power in ramp	Location of specimen across pellet	Estimated irradiation temperatures °C		Maximum in-pile temperature °C during power ramps
			Pellet centre	Specimen position	
ABB/E4	Un-ramped	Mid-radius	575	400	950
ABB23	23 kW/m	3/4 radius	1 130	650	1 130
ABB32	32 kW/m	1/4 radius	1 500	1 450	1 106
G11/5	41.3 kW/m	Near pellet centre	1 900	1 850	1 717

One of the findings of this test series was that TD values at the end of a test were significantly higher than at the start of a test indicative of a progressive recovery of the thermal conductivity with increasing test temperature. This so-call thermal conductivity recovery of as-irradiated fuel specimens during out-of-pile anneals has been reported by the NFIR Program [4] and elsewhere [6,7].

In order to elucidate the mechanism and kinetics of such thermal conductivity recovery, a second series of tests was performed (see Table 3) on disc samples of U4 (the UO₂ was irradiated to 38.8 MWd/kgU) [5].

Table 3. Out-of-pile annealing in the second test series

IT test	Form of test
1	Anneal for 4 hours at 700°C
2	Anneal for 4 hours at 800°C
3	Two anneals for 4 hours at 900°C
4	A multi-stage temperature history with three periods of 1 hour at 600°C
5	As per IT1 with 16 hours at 700°C
6	A four-day test comprising holds of 10, 5, 5 and 10 hours at 800°C
7	Conducted over three days with stepped temperature ramps to 1 200°C held for 5 min, 30 min and finally 4 hours
8	A single rapid temperature rise to 1 200°C followed immediately by a temperature reduction
9	Annealed for 100 hours at 1 200°C

In the third series of tests specimens cut from fuel type (b), i.e. commercially irradiated rods power ramped in the Studsvik R2 reactor, were subjected to thermal diffusivity measurements as well as pre- and post-test PIE.

In the remainder of this paper we report microstructure observations on the as-irradiated specimens and following the annealing performed in the three test series described above.

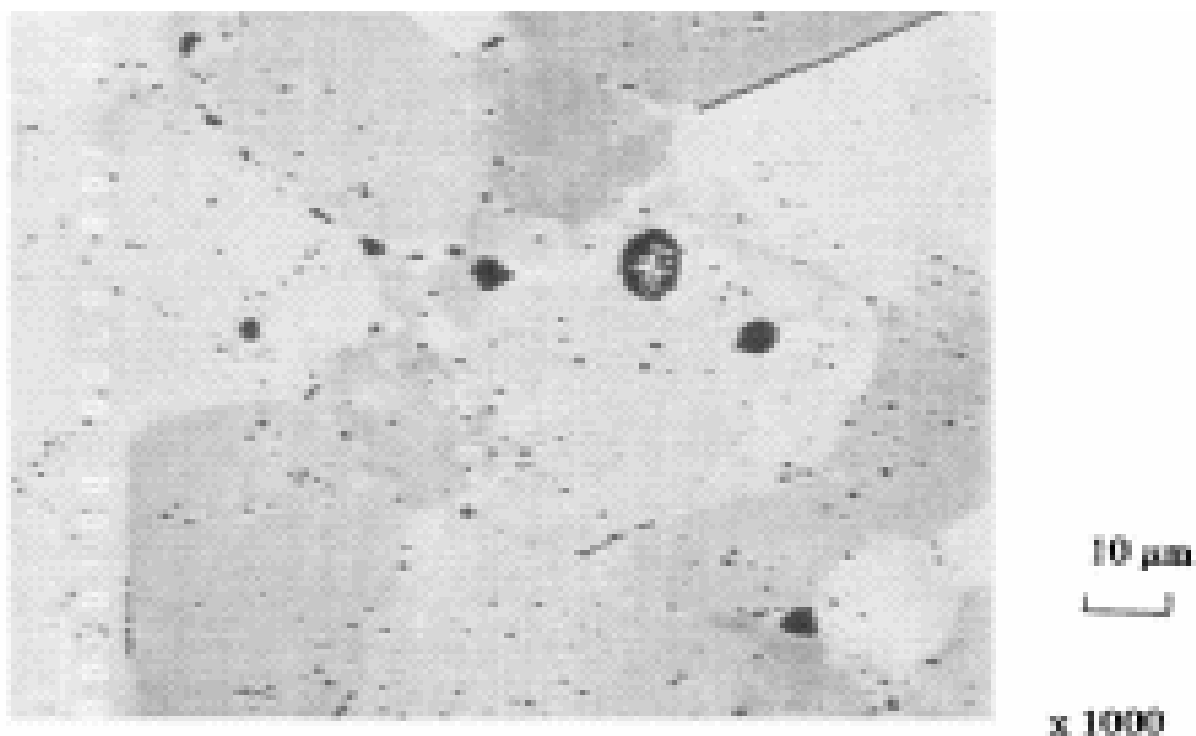
Microstructure of as-irradiated fuel materials

Fuel discs

Examination by optical microscopy revealed little change in microstructure for specimens U2 and U4, although the latter did show the start of some inter-granular porosity at the centre of the disc. U6 exhibited some circumferential cracking characteristic of a brittle material. Intragranular porosity

was observed close to but not on grain boundaries and these extended towards the grain interior at the rim of the disc (Figure 1). After etching small intergranular bubbles were seen near the centre of the disc. There was no discernible grain structure apparent in the high burn-up U8, but there was evidence of a high level of porosity and intergranular cracking.

Figure 1. SEM of U6 at 0.6 mm from disc rim

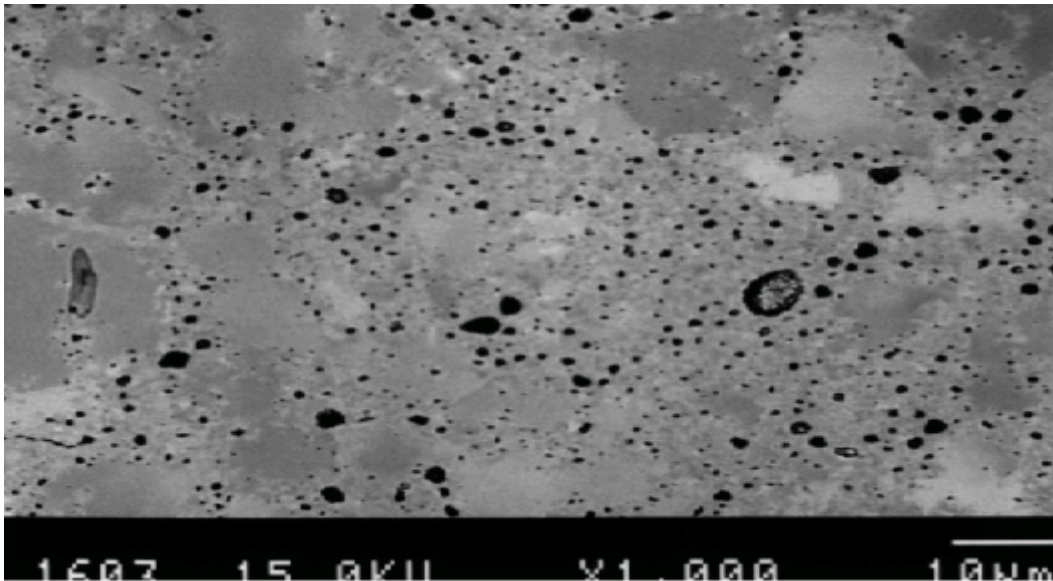


SEM examination of U2 showed the disappearance of sub-micron porosity, but no change in overall pore volume. In U4, there were few pores smaller than 1 μm except at grain boundary triple points, where there was evidence for the start of tunnel formation. Grains were free of intragranular porosity except at the rim where intragranular pores $< 1\mu\text{m}$ were evident. In U6 the intragranular porosity observed by optical microscopy was better resolved as $\sim 1\mu\text{m}$ bubbles concentrated on either side and in the general vicinity of grain boundaries.

TEM was carried out on replicas taken from small radial matchstick samples. There was no evidence of any grain boundary network of porosity in any of the specimens U2-U6. Intragranular bubbles $\sim 7\text{ nm}$ diameter and precipitates $\sim 5\text{ nm}$ diameter were seen in U2; similar observations were made for U4 and U6 but with increased density and size.

In conclusion the observations showed that at these irradiation temperatures, irrespective of burn-up, there was no large accumulation of gas at grain boundaries nor was there significant intergranular porosity. The structure at low burn-up, U2 and U4 was similar to that for un-irradiated material. At higher burn-up, the observations are consistent with the start of a High Burn-up Structure (HBS), possibly near grain boundaries in U6 and with greater coverage of HBS in the 80 MWd/kg specimen U8 (Figure 2).

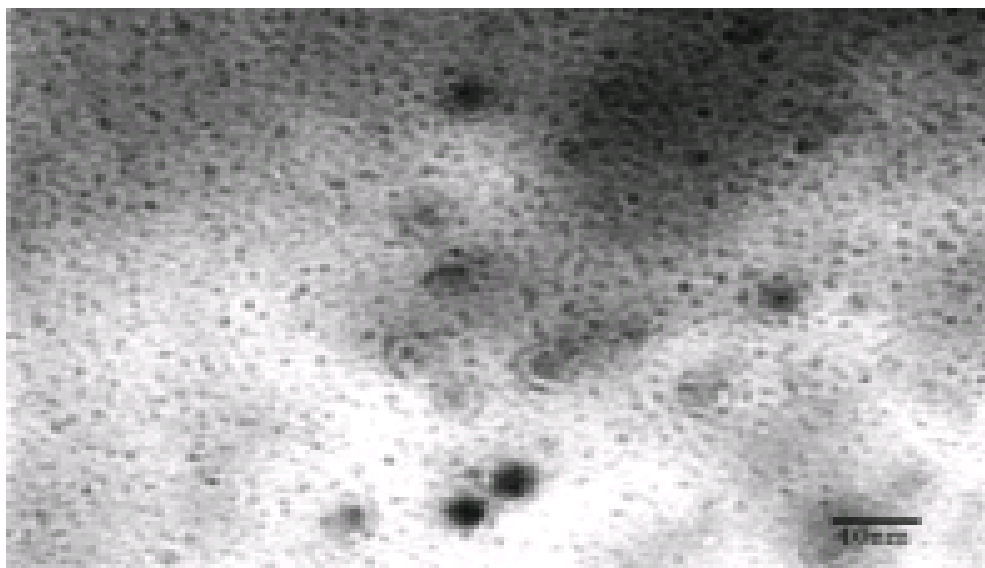
Figure 2. Backscattered SEM image of U8 at 1.44 mm from disc rim



Commercial fuel

ABB/E4 was taken from an un-ramped section of fuel. When examined by SEM the structure was typical for high burn-up and low irradiation temperature. The fractured surface was predominantly transgranular with no evidence for inter- or intragranular porosity. TEM revealed a high concentration of 5 nm solid fission product precipitates and intragranular bubbles with a mean diameter of 1.1 nm and concentration $2.2 \times 10^{24} \text{m}^{-3}$; this corresponded to an intragranular swelling of 0.15% (Figure 3). The dislocation density was $5.9 \times 10^{13} \text{m}^{-2}$. It was noticed that for *all* ramped specimens examined the dislocation density was slightly lower and in the region of $2.4\text{-}2.6 \times 10^{13} \text{m}^{-2}$.

Figure 3. TEM of specimen ABB/E4 showing uniformly nucleated fission gas bubbles of ~ 1 nm diameter. Solid fission product precipitates can be seen under focus.



Effect of temperature history on microstructure

First test series – TD and FGR tests

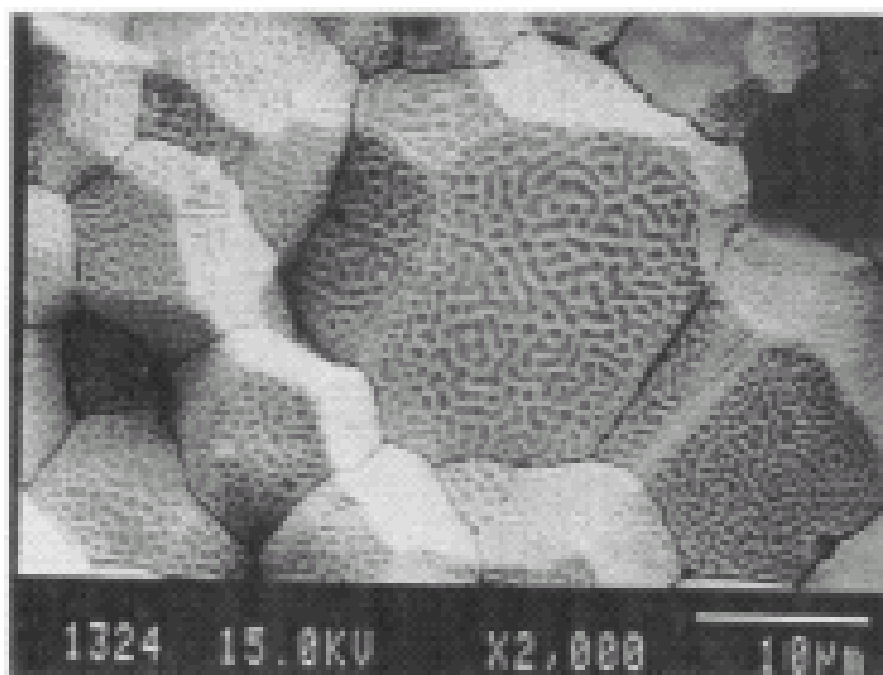
With the exception of U8, all TD specimens experienced a temperature ramp up to a maximum of 1 600°C and all FGR specimens up to a maximum of 1 800°C. While the temperature history during laser flash TD measurements was not prescribed by the test procedure *per se*, it was known precisely for the FGR tests [3]. In both cases, however, the anneal time above 1 500°C can be summarised as in Table 4.

Table 4. Time exposure above 1 500°C for TD and FGR samples

Specimen	Annealing time spent $\geq 1\,500^\circ\text{C}$	
	TD samples (approximate)	FGR samples (exact)
U2	33 min	–
U4	53 min	8 hrs 15 min
U6	80 min	8 hrs 15 min
G4	51 min	–
G6	39 min	8 hrs 15 min

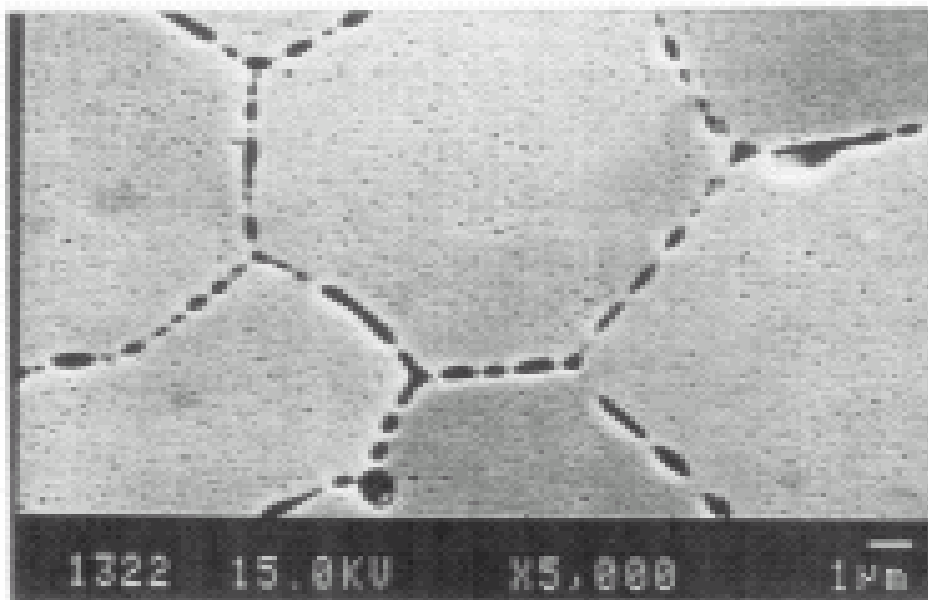
Optical microscopy showed the presence of micro-cracks in all specimens whose severity increased with burn-up. The degree of grain boundary decoration also increased noticeably with burn-up. In U2, the intergranular porosity appeared as isolated bubbles 0.2-0.8 μm in diameter along all grain boundaries. The lack of interconnectivity was confirmed by TEM of replicas taken from areas of intergranular fracture. SEM also resolved intragranular porosity $\sim 0.1\ \mu\text{m}$ diameter whilst TEM resolved an increase in the as-irradiated 7 nm bubbles to 20-30 nm and precipitates from 5-10 nm.

Figure 4. Intergranular porosity in U4 post-TD anneal



The intergranular porosity of U4 was larger $\sim 1 \mu\text{m}$ diameter and more interconnected than for U2 (Figure 4). There was also an extensive concentration of $0.1 \mu\text{m}$ intragranular bubbles (Figure 5), TEM resolved 70 nm intragranular bubbles, which increased in size to 100 nm near the rim of the disc. Compared to U2, the precipitate diameter had also increased to 30 nm .

Figure 5. Grain boundary interlinkage and intragranular porosity in post-TD anneal U4



Centre

U6 was severely cracked after testing with local de-cohesion of grain boundaries. SEM showed that grain boundaries were now well defined with $1\text{-}2 \mu\text{m}$ diameter interconnected bubbles. There was a low concentration of large intragranular bubbles $\sim 2 \mu\text{m}$ in diameter. TEM revealed 60 nm intragranular bubbles and 30 nm precipitates.

The discussion on U8 is presented in a later section.

After the FGR tests, the amount of fission gases remaining in the samples was less than 25%. The U4 sample showed an increase in grain size of a factor of two. The grain boundaries contained a highly developed interconnected porosity of $5\text{-}10 \mu\text{m}$ bubbles; there were acicular $3 \mu\text{m}$ intragranular bubbles as well as a sub-micron population. G6 also had a highly interlinked grain boundary structure, within the grains was a variety of bubbles with the largest ones adjacent to grain boundaries, very like the TD tested material but of larger size (Figure 6).

It was clear that the heat treatment received by each specimen had affected the microstructure to differing degrees. Each specimen went through a thorough image analysis with data being obtained on pore size and density; a summary of the total porosity is given in Table 5.

Figure 6. Interlinked bubbles in G6 at disc rim post-FGR anneal

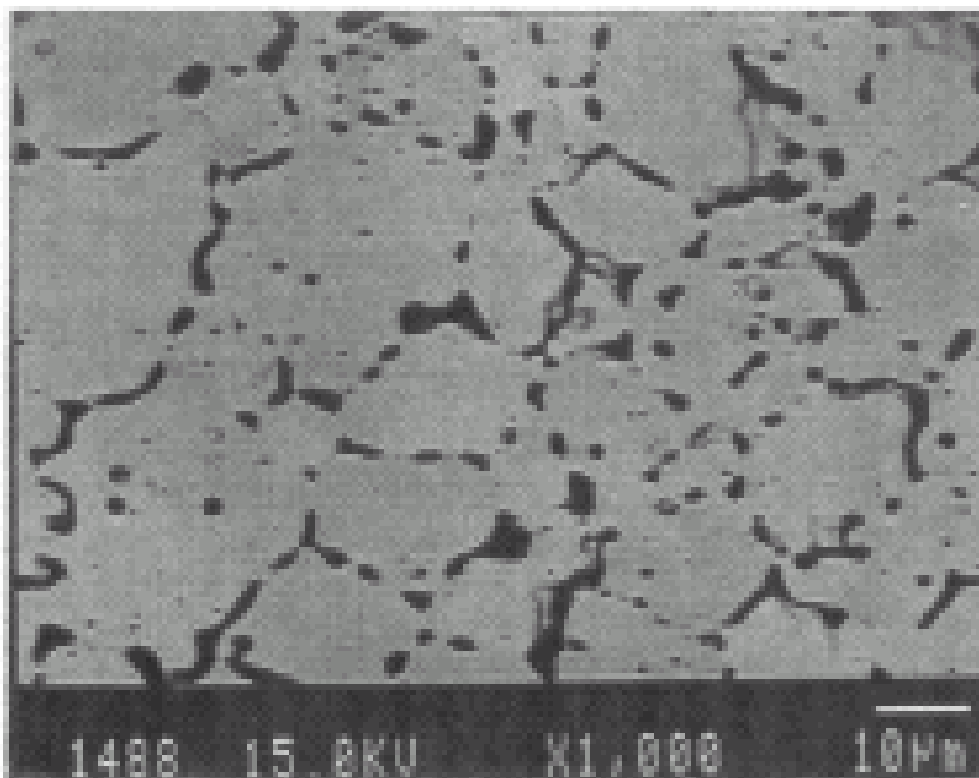


Table 5. Image analysis results

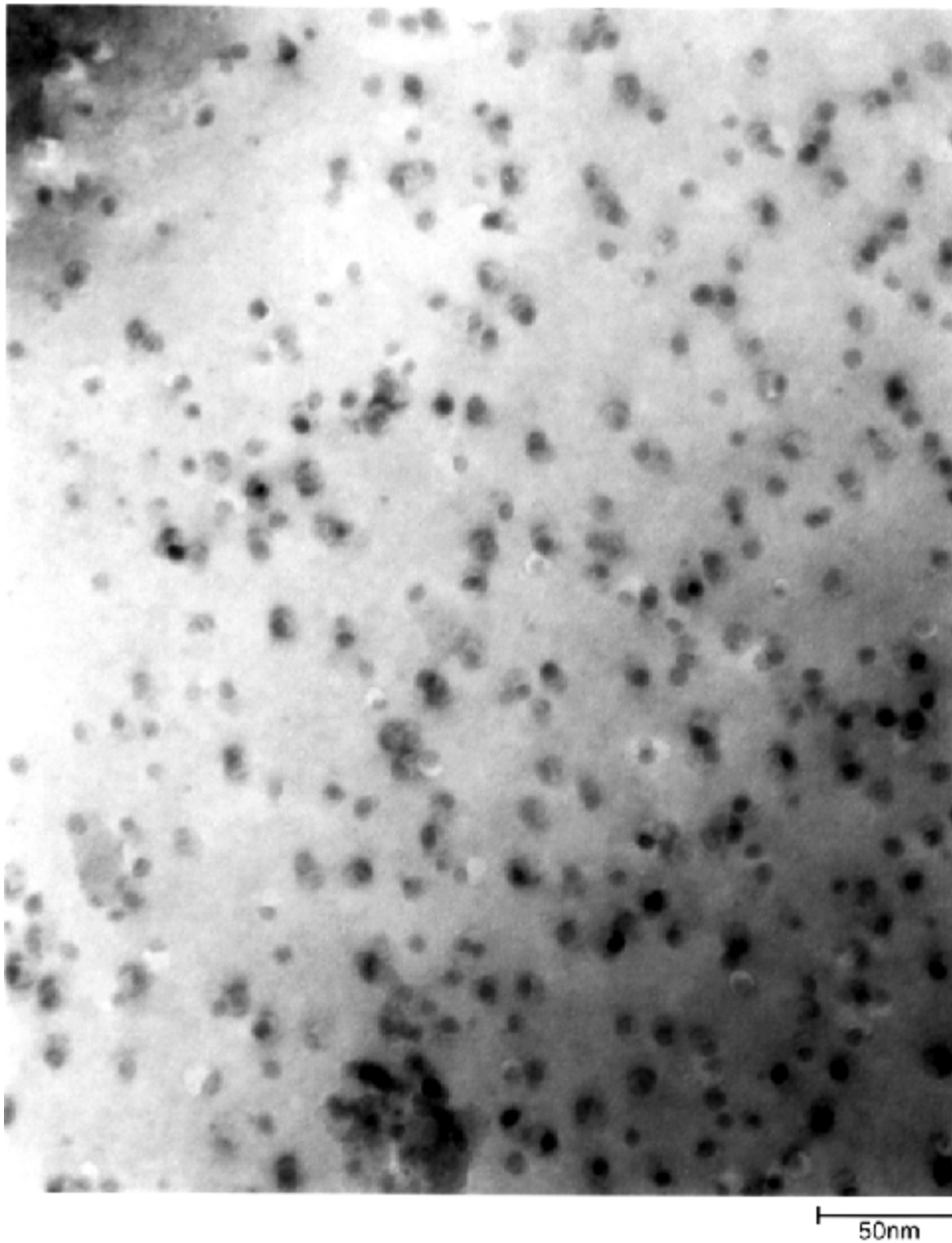
Specimen	As-irradiated %	After TD test %	After FGR test %
U2	2.0-3.0	1.5-5.0	–
U4	3.1	4.1 at rim	8.1
U6	2.5	2.0-2.3	5.7-16
G4	3.0-4.2	3.5-4.0	–
G6	2.8-4.1	4.3-5.5	14.1

Second test series – IT tests

These tests were conducted on U4 specimens at a burn-up of 38.8 Mwd/kgU. The first six tests were at temperatures between 600-900°C. Although significant recovery was measured in the TD, there was no significant change in the microstructure as observed by either SEM or TEM. Intragranular bubbles in the as-irradiated U4, and in specimens annealed to 600, 800 and 900°C were < 1 nm with number densities in the range $2.2-4.5 \times 10^{24} \text{ m}^{-3}$. Dislocation densities were in the range $1-4 \times 10^{13} \text{ m}^{-2}$.

The ramp to 1 200°C produced a slight increase in matrix bubble diameter (maximum 2 nm) and number density, although the latter may have resulted from a better visibility, rather than nucleation effect (Figure 7). The four-hour anneal at 1 200°C increased the bubble diameter further (maximum 5 nm) and reduced the number density, indicating that coarsening was occurring.

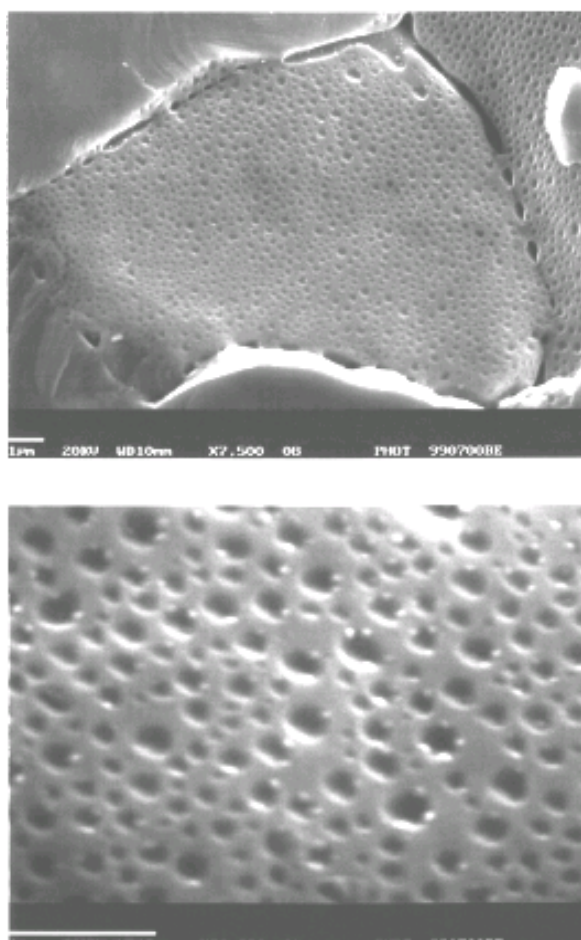
Figure 7. Growth of matrix bubbles after 1 200°C ramp in IT8 specimen



The findings may be compared with those of Baker [8] and those in Ref. [5], which examined LWR fuel irradiated to a burn-up of 38 GWd/tU and subsequently annealed at temperatures between 1 250-1 660°C. In as-irradiated material, matrix bubbles were ~1 nm in diameter, at a number density $>10^{24} \text{ m}^{-3}$. After 24 hours at 1 250°C the mean diameter had increased to 6.5 nm, while the number density was estimated as $\sim 10^{23} \text{ m}^{-3}$ (each bubble also contained a solid fission product precipitate). Anneals at higher temperatures resulted in further coarsening of the population. The 24 hour/1 250°C anneal also produced fine intergranular bubbles, $\sim 0.2 \mu\text{m}$ in size, on all grain boundaries, with small solid fission product precipitates visible in the larger ones; at higher temperatures these bubbles grew and interlinked.

The above observations and the present results indicate that 1 200°C is the lowest annealing temperature at which microstructural changes occur which are observable by electron microscopy. At short anneal times of the IT7 samples (up to four hours), growth of intragranular bubbles was barely measurable using TEM, while SEM failed to reveal conclusive evidence of intergranular bubbles. The sample annealed for 100 hrs at 1 200°C showed considerably more bubble growth to a size of 4.9 nm compared to ~1 nm when ramped to 1 200°C and ~2 nm after four hours at 1 200°C. Grain faces showed a well-developed population of intergranular bubbles ~100 nm in diameter (Figure 8). The aerial coverage varied from 14.8-17.8% with a mean of 15.7%. Solid fission product precipitates were in the range 20-60 nm. Intragranular bubbles of 4.8 nm diameter were present at a density of $0.2 \times 10^{24} \text{ m}^{-3}$ giving rise to a calculated swelling of 1.5%.

Figure 8. Intergranular bubbles in IT9



Third test series – ramped commercial fuel

The IT series of tests suggested that heat treatments below 1 200°C had no observable influence on the microstructure as observed by SEM and TEM. For this reason, it is assumed that the observations reported in this section relate to the end of irradiation conditions and are not influenced by the measurement of TD.

ABB specimens

During preparation, the specimen ABB23 fractured in a predominantly transgranular manner. Limited grain boundary porosity was visible $\sim 0.1 \mu\text{m}$ diameter mostly associated with solid fission products with a small degree of interconnection. At the resolution of the SEM, there was no evidence of intragranular porosity. TEM revealed precipitates and intragranular bubbles larger than for ABB/E4. The precipitates had grown to 5-10 nm whilst the mean bubble diameter increased to 3.2 nm but at a reduced concentration of $0.8 \times 10^{24} \text{ m}^{-3}$; the intragranular swelling contribution was estimated to be 2.4% (Figure 9).

Figure 9. TEM image of fission gas bubbles in sample ABB23

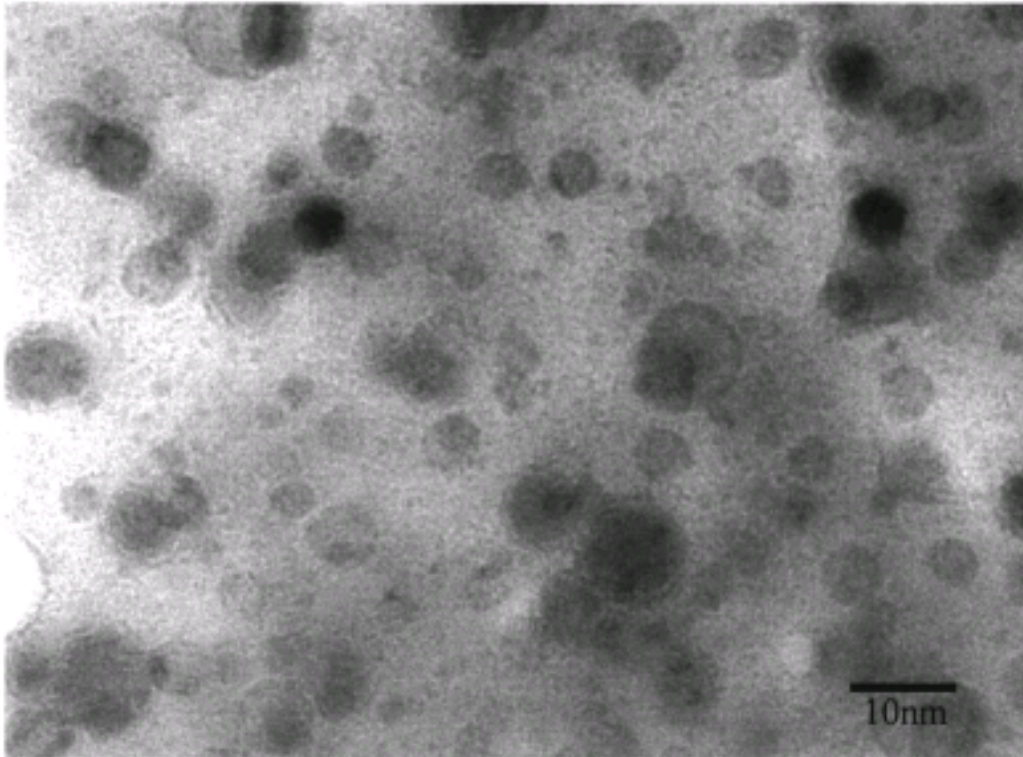


ABB32 had a greater proportion of intergranular fracture which showed substantial areas of interconnected grain boundary porosity with a diameter $\sim 0.25 \mu\text{m}$ (Figure 10). Transgranular faces showed evidence of intragranular porosity 20-50 nm diameter. At the higher magnification of TEM, there was evidence for further growth of precipitates to $> 10 \text{ nm}$ and larger but fewer intragranular bubbles, 4.9 nm in diameter at a concentration of $0.2 \times 10^{24} \text{ m}^{-3}$, contributing to 1.4% swelling, as shown in Figure 11.

The observations of grain boundary interlinkage are in accord with the estimated irradiation temperature and FGR threshold at the burn-up of 58.5 MWd/kgU. From Halden experiments [10] it is suggested that the FGR threshold temperature should be in the region of 800-900°C. The local temperatures of ABB/E4 and ABB23 were estimated to be 400°C and 650°C respectively, whereas for ABB32 the temperature was 1 450°C. This explains the lack of intergranular porosity for ABB/E4, the limited intergranular porosity in ABB23 and the substantial areas in ABB32.

Figure 10. Intragranular bubbles in specimen ABB32

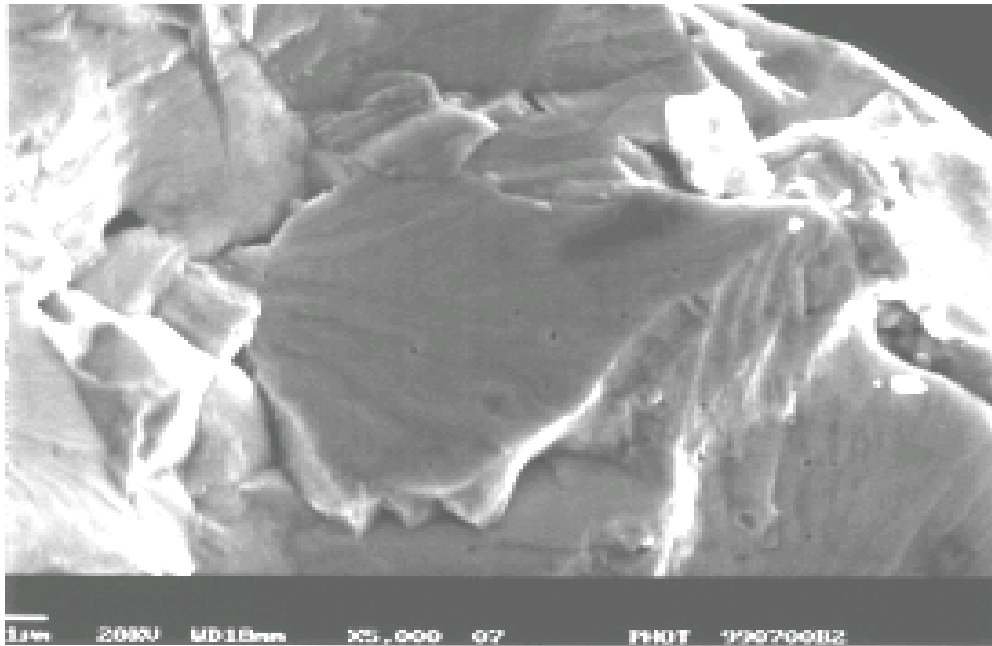
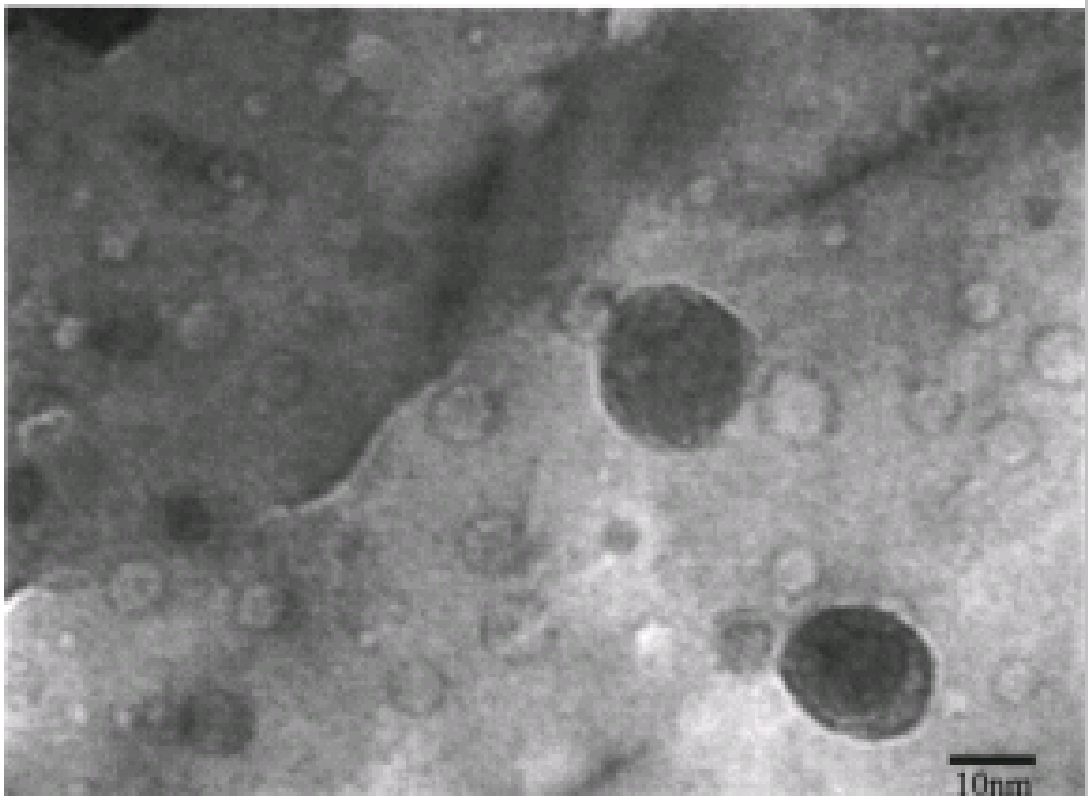
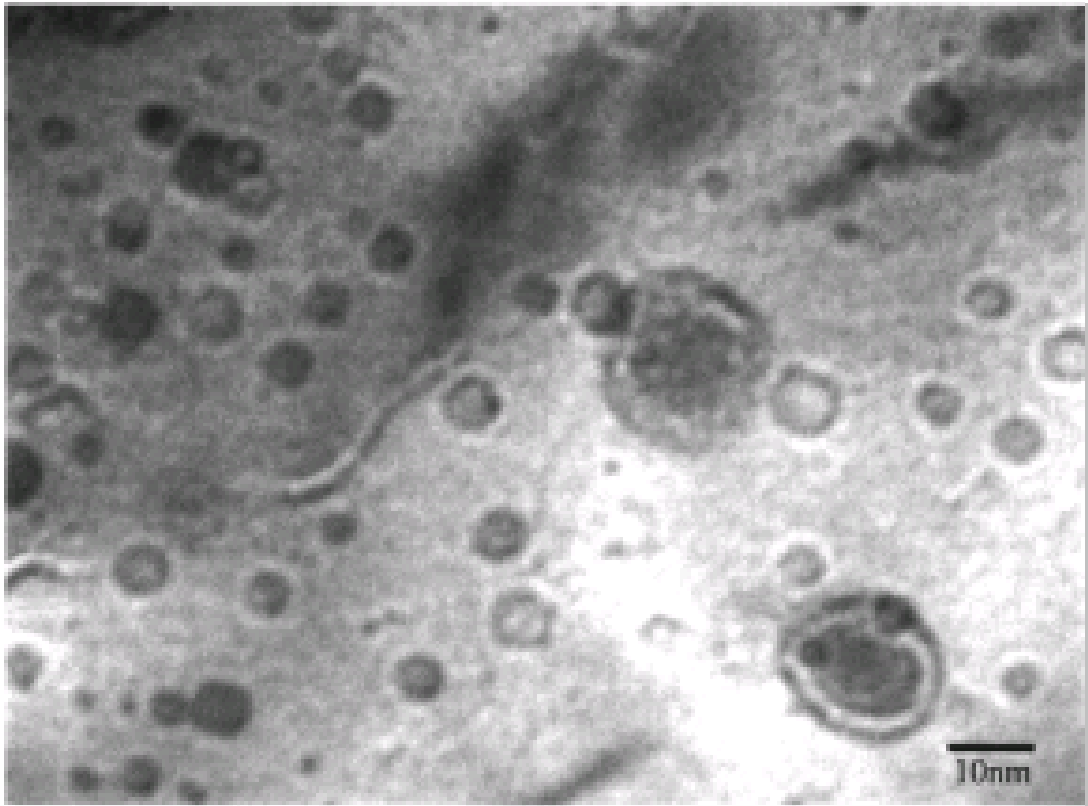


Figure 11. TEM view of bubbles and precipitates in specimen ABB32



Fragema specimens

Specimen preparation of G11/5 produced a mostly transgranular fracture showing a high but variable density of pores $\sim 0.45 \mu\text{m}$ in diameter; they were generally faceted and accounted for a volume swelling of $\sim 3.7\%$. Isolated but large intergranular porosity appeared to be tunnels associated with grain edges (Figure 12). The large intragranular pores made for difficult TEM specimen preparation; the resulting foils had a lace-like structure. In electron transparent areas, between large precipitates, $\sim 1 \text{ nm}$ diameter bubbles were visible, mostly in short lines and at a density of $\sim 2.4 \times 10^{24} \text{ m}^{-3}$ (Figure 13). Intragranular volume swelling was estimated at 3.7% from the large pores and 0.11% from the lines of small bubbles.

Figure 12. Fracture surface of G11/5

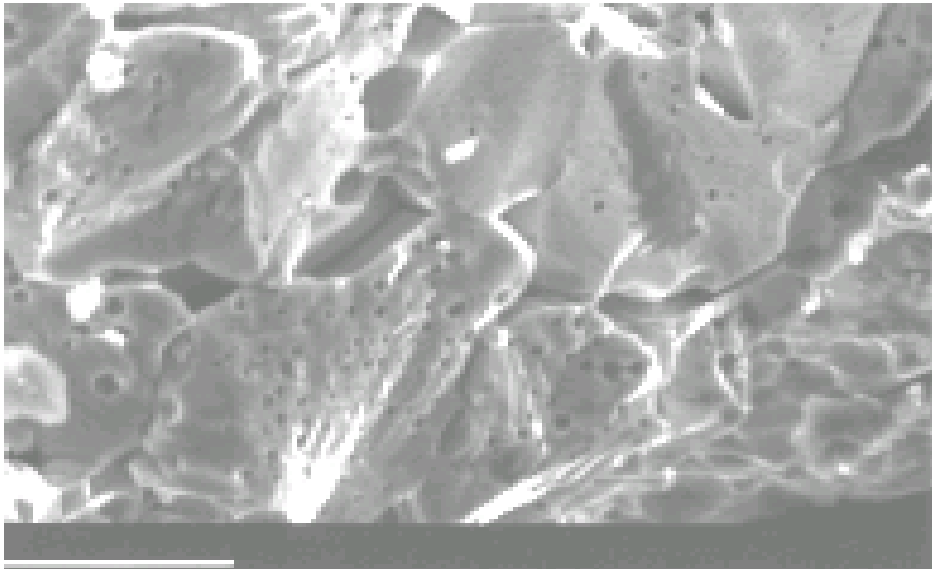
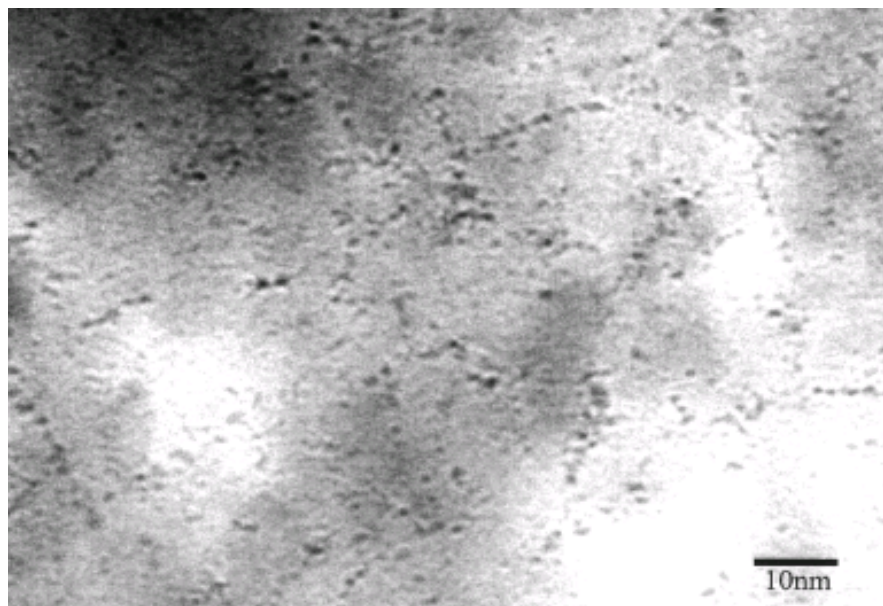


Figure 13. TEM image of bubbles in specimen G11/5 appeared to have nucleated in lines

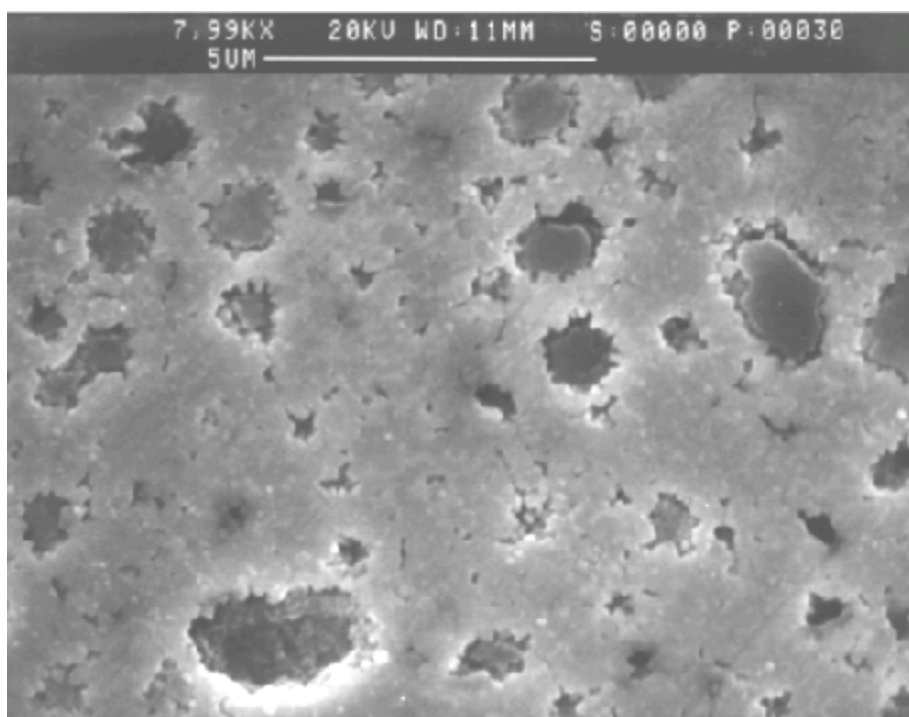


At the local end of ramp temperature of 1 730°C, it is clear that much of the fission gas was released through the highly developed grain boundary tunnel structure, or resident in the large diameter intragranular pores. The small diameter bubbles in lines are identical to those seen at lower burn-up, or low gas concentrations, and result from the formation of bubbles in the wake of fission fragments [9].

Response to increased temperature of material containing HBS

The as-irradiated microstructure of U8 was a development of that observed in U6 and there was evidence of extensive intergranular micro-cracking. Near the centre of the disc, micron-sized porosity existed in a network of high concentration bands in the vicinity of grain boundaries. High magnification examination of the porosity revealed that the pore surfaces had a “lumpy” appearance on a scale of ~0.2 µm. This was consistent with the surface of the pores being formed from re-structured grains of the HBS (Figure 14). Towards the specimen rim, the width of the bands increased until the original grain structure became obscured. An examination of the pore size distribution showed that within the observed size range, 0.1-3.6 µm, the density of pores decreased linearly with increasing size. The variation in porosity as a function of position showed a high value of ~8% within 0.5 mm of the disc rim, falling to 3-4% a distance 1 mm from the rim and ~1.5% at the centre.

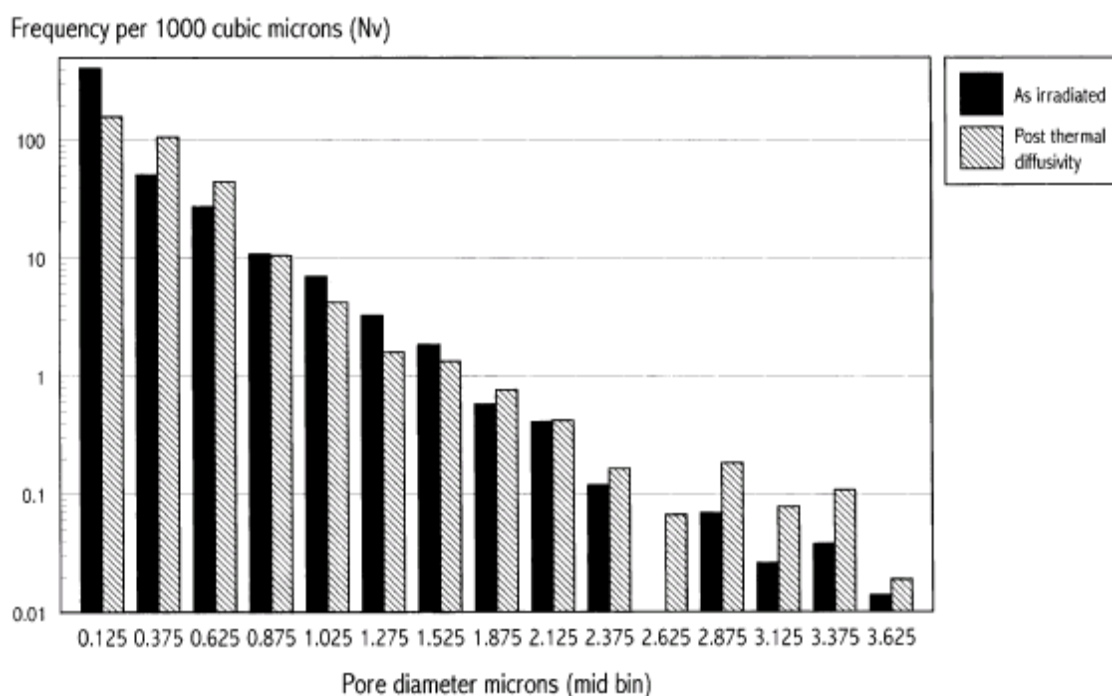
Figure 14. Faceted cavities in U8 fragments heated to 800°C



During TD and specific heat measurements on U8, it was found that the specimens explosively fragmented, sometimes with sufficient impulse as to displace the cover to the crucible in which they were contained. Because of this, special heating tests were conducted specifically to observe the specimen response. On heating specimens to temperatures of 800°C and 1 500°C, i.e. above the irradiation temperature, they fragmented energetically as before. The resulting fragment size was variable within the range of several hundred microns down to several microns and smaller. The average fragment size after the 1 500°C heating was smaller than that at 800°C.

The microstructure of the fragments appeared very little different from the as-irradiated state. However, a detailed image analysis of the pore distribution indicated that the heating induced a decreasing density of the very smallest pores, $\sim 1 \mu\text{m}$, also pores in the range $1\text{-}2 \mu\text{m}$ and an increase in density of $0.3\text{-}0.6 \mu\text{m}$ and pores $>2 \mu\text{m}$ (Figure 15). In the size range up to $3.75 \mu\text{m}$ there was an estimated total increase in swelling from 2.9% to 3.4%.

Figure 15. Pore size distribution in U8 in as-irradiated condition and after TD anneal



The implication of these observations is that heating fuel containing HBS or partially developed HBS above its previous temperature can lead to energetic fragmentation and dispersal. As such, it has the potential to enhance PCMI in a rapid power transient. This is particularly the case for RIAs as in these cases, the rim of the pellet, where such restructuring is likely to exist, experiences a significant increase in temperature. It must be pointed out that in the observations on U8, the material was not under any external stress, unlike the situation in an operating fuel rod, where at high burn-up the cladding is in intimate contact with the fuel. Thus in practice, the outcome is likely to be significantly less onerous. However, experiments have shown that the energy for failure for high burn-up fuel in a simulated RIA is significantly depressed compared to fresh fuel. One contribution to this is known to be the enhanced brittle nature of the cladding due to waterside oxidation and hydrogen uptake. The observations presented here are clearly an additional feature of high burn-up and as a consequence will act together with embrittled cladding to decrease the failure enthalpy. For this reason there is a compelling incentive to explore this fragmentation further and to quantify the energy released as a function of restraint.

Conclusions

This paper has reported results from quantitative studies of microstructural evolution, performed on high burn-up fuel specimens, both isothermally irradiated as discs, and commercially irradiated and subsequently ramped samples. Key observations/conclusions are as follows.

At irradiation temperatures 500-700°C, irrespective of burn-up, there was no large accumulation of gas at grain boundaries nor was there significant intragranular porosity. The structure at low burn-up (< 40 MWd/kg) was similar to that for un-irradiated material. At higher burn-ups, the observations were consistent with the start of a High Burn-up Structure (HBS), occurring near grain boundaries in fuel irradiated to ~60 MWd/kg, but with greater coverage of the HBS in fuel irradiated to 80 MWd/kg.

Results from a series of tests employing isothermal anneals have indicated that 1 200°C is the lowest annealing temperature at which microstructural changes occur which are observable by electron microscopy. At short anneal times (up to 4 hours), growth of intragranular bubbles was barely measurable via TEM, while SEM failed to reveal conclusive evidence of intergranular bubbles. A sample annealed for 100 hours at 1 200°C showed considerably more bubble growth to a size of 4.9 nm compared to ~1 nm when ramped to 1 200°C and ~2 nm after 4 hours at 1 200°C. Grain faces showed a well-developed population of intergranular bubbles ~100 nm in diameter. The aerial coverage varied from 14.8-17.8% with a mean of 15.7%. Solid fission product precipitates were in the range 20-60 nm. Intragranular bubbles of 4.8 nm diameter were present at a density of $0.2 \times 10^{24} \text{ m}^{-3}$ giving rise to a calculated swelling of 1.5%.

Observations of grain boundary interlinkage were in accord with the estimated irradiation temperature and FGR threshold at the burn-up of 58.5 MWd/kgU, which in-pile data from the Halden Joint Program suggest should be in the region of 800-900°C. Observations of intergranular porosity in commercially irradiated samples were in accord with estimated local temperatures. For ABB/E4 (estimated temperature 400°C) no such porosity was observed, whilst there was limited porosity for ABB23 (650°C), but substantial porosity in ABB32 (1450°C).

In unrestrained conditions, fuel containing HBS or partially developed HBS can disperse if heated rapidly above the peak temperature previously attained. As such, it has the potential to enhance PCMI in a rapid power transient. However, the situation in an operating fuel rod, where at high burn-up the cladding is in intimate contact with the fuel, is quite different from our tests. Thus such energetic fuel dispersal as we observed is unlikely in LWR rods. Nevertheless, there is a compelling incentive to explore fuel dispersal phenomenon further to quantify the energy released as a function of burn-up, restraint level and heating rates.

Acknowledgements

The work was performed under the auspices of the EPRI-led NFIR Program. The authors acknowledge NFIR Steering Committee members for many helpful technical discussions throughout the programme and for their permission to publish these results.

REFERENCES

- [1] *High Burn-up UO₂ and (U,Gd)O₂: Specimen Fabrication and Pre-characterization*, EPRI Report, NP-6878-D, Jul. 1990.
- [2] *High Burn-up UO₂ and (U,Gd)O₂: Specimen Irradiation*, EPRI Report, TR-102760, Jul. 1993.
- [3] *High Burn-up UO₂ and (U,Gd)O₂: Thermal Diffusivity Measurements and Post-irradiation Characterizations*, EPRI Report, TR-106501, Dec. 1996.
- [4] Yagnik, S.K., “Thermal Conductivity Recovery Phenomenon in Irradiated UO₂ and (U,Gd)O₂”, *ANS Topical Meeting on LWR Fuel Performance*, Park City, Utah, USA, 10-13 April 2000.
- [5] *Understanding of Thermal Diffusivity Recovery with Thermal Annealing*, EPRI Report TR-111068, Nov. 1999 and its Addendum AD-111068, Apr. 2000.
- [6] Nakamura, J., *et al.*, “Thermal Diffusivity Measurements of High Burn-up UO₂ Pellets”, *ANS Topical Meeting on LWR Fuel Performance*, Park City, Utah, USA, 10-13 April 2000.
- [7] Amaya, M., *et al.*, “Thermal Conductivities of Irradiated UO₂ and (U,Gd)O₂ Pellets”, *J. Nucl. Mater.*, Vol. 300 (1), 57-64 (2002).
- [8] Baker, C., *Properties of UO₂ Irradiated to High Burn-ups (TEM and SEM Study)*, EPRI Report NP-5188-LD, Research Project X101-7 Final Report 1987.
- [9] Turnbull, J.A., “The Distribution of Intragranular Fission Gas Bubbles in UO₂ During Irradiation”, *J. Nucl. Mater.*, Vol. 38, 203-212 (1971).
- [10] Turnbull, T., E. Kolstad, “Investigation on Radioactive and Stable Fission Gas Release Behaviour in the Halden Reactor”, *Proceedings of OECD/NEA International Seminar on Fission Gas Behavior in Water Reactor Fuels*, Cadarache, France, 26-29 September 2000.

EFFECT OF THERMAL AND MECHANICAL PROPERTIES OF THE DUPIC FUEL ON THE PELLET-CLADDING MECHANICAL INTERACTION

**Ho-Jin Ryu, Kweon-Ho Kang, Chang-Je Park,
Joo-Whan Park, Kee-Chan Song, Myung-Seung Yang**
Korea Atomic Energy Research Institute
150 Deokjin-dong, Yuseong-gu, Daejeon 305-353, Korea

Abstract

The material properties of DUPIC fuel, such as thermal conductivity, thermal expansion, creep rate, Young's modulus and hot hardness were measured using simulated DUPIC fuel to evaluate their effects on the irradiation behaviour such as the pellet-cladding mechanical interaction (PCMI). Experimentally characterised properties of the DUPIC fuel were employed in the performance evaluation code and the finite element analysis to estimate the ridge height, plastic strain of the cladding, and the hoop stress of the pellet and the cladding. Some fuel fabrication parameters were suggested for optimisation for a decrease in the PCMI of the DUPIC fuel as a result of a statistical sensitivity analysis.

Introduction

A dry re-fabrication process was developed under the auspices of an international co-operation in order to re-use fissile elements in the spent fuels of pressurised light water reactors (LWR) without the aqueous separation or extraction of sensitive nuclear materials [1]. The benefits of the dry re-fabrication process are the saving of uranium resources and the reduction of accumulated spent fuel while maintaining proliferation resistance during the process [2]. The dry re-fabrication technology is known as DUPIC (*Direct Use of spent PWR fuel In CANDU reactors*).

In the fabrication of the DUPIC fuel, spent fuel pellets separated from the claddings of spent LWR fuel are oxidised from UO_2 to U_3O_8 at 450-500°C in an oxidising atmosphere and reduced into UO_2 at 650-700°C in a reducing atmosphere [3]. Spent fuel pellets are then pulverised during repeated oxidation and reduction, which is called the OREOX (*Oxidation and REDuction of OXide fuel*) process, due to the phase transformation and volume change between cubic UO_2 (10.96 g/cm³) and orthorhombic U_3O_8 (8.3 g/cm³). Using the spent fuel powder prepared from the OREOX process, fresh DUPIC fuels for CANDU reactors are fabricated after compaction and sintering processes in a shielded hot cell. Fission gas species and volatile fission products are removed during the OREOX and sintering processes [4].

The mini-elements of the DUPIC fuel fabricated in a hot cell using a spent fuel discharged from the Gori-1 nuclear power plant in 1986 after an average burn-up of 27 300 MWd/MTU are undergoing a series of irradiation tests in the HANARO research reactor for the performance evaluation of the re-fabricated fuel pellets. Post-irradiation examination of the irradiated fuel showed that the microstructural evolution and fission gas release behaviour of the DUPIC fuel are similar to the UO_2 fuel [4].

The DUPIC fuel has a different chemical composition due to the solid fission products and the resulting material properties vary from those of the fresh UO_2 fuel [5]. The DUPIC fuel also differs from the high burn-up oxide fuel because it does not contain fission gas elements or volatile fission products. Therefore, it is necessary to characterise the material properties such as thermal conductivity, thermal expansion coefficient, creep rate, Young's modulus and hot hardness to evaluate the performance of the DUPIC fuel. In this study, the thermal and mechanical properties of the DUPIC fuel were characterised using simulated DUPIC fuel to analyse the effect of the material properties of the DUPIC fuel on the pellet-cladding mechanical interaction.

Experimental procedures

Because the experiments with spent fuel are very complicated due to a high radioactivity, characterisation of the material properties was performed using simulated fuel consisting of natural UO_2 powder blended with stable chemical additives simulating the composition of the spent fuel. In the OREOX process, the sintered pellets were heated to 450°C in air to oxidise the UO_2 into U_3O_8 and then heated to 650°C in H_2 to be reduced into UO_2 again. After three cycles of oxidation and reduction, attrition milling of the OREOX treated powder was carried out to enhance the sinterability. The milled powder was compacted into cylindrical pellets and sintered at 1 700°C for four hours in a H_2 atmosphere. Thermal conductivity and thermal expansion of the simulated DUPIC fuel was measured by the laser flash method and by a push rod type dilatometer (DIL402C, Netzsch), respectively. Creep rate was measured by a compressive creep test at 1 500, 1 600, 1 700°C in a H_2 atmosphere. Young's modulus of the simulated DUPIC fuel was measured by a resonance ultrasound spectroscopy (RUS) and hot hardness and fracture toughness were measured by a high temperature micro-Vickers hardness tester (QM-2, Nikon). Scanning electron microscopy was employed to observe the microstructure of

the simulated DUPIC fuel after milling, sintering and hot hardness test, respectively. The material models in the performance evaluation code and the finite element analysis were modified according to the measured data of the simulated DUPIC fuel. ELESTRES (ver. M11K) and ANSYS (ver. 7.0) were used for the performance evaluation and the finite element analysis, respectively.

Results and discussion

The OREOX process of the UO_2 -based sintered pellet simulating a spent fuel with a burn-up of 27 300 MWd/tU produced pulverised powder as shown in Figure 1. As the cycle of the OREOX process is repeated, the average particle size decreases and the specific surface area increases because of the cracking by the transformational volume change between UO_2 and U_3O_8 . Figure 1(c) shows the refined powder of the simulated DUPIC fuel after dry milling in an attritor. Sintered density of the simulated DUPIC fuel was increased with the milling time. In this study the theoretical density was calculated as 10.789 g/cm^3 according to the content of the additives and the average relative density of the simulated DUPIC fuel was about 95% after sintering at 1700°C for four hours in a flowing H_2 atmosphere [6,7]. A scanning electron micrograph of the sintered microstructure of the simulated DUPIC fuel is exhibited in Figure 2. Except for some metallic precipitates found in the grain boundary region, the microstructural features are almost similar to the typical UO_2 fuel.

Figure 1. Scanning electron micrographs of (a) 1 cycle OREOX treated powder, (b) 3 cycle OREOX treated powder and (c) attrition milled powder for 15 min after OREOX treatment

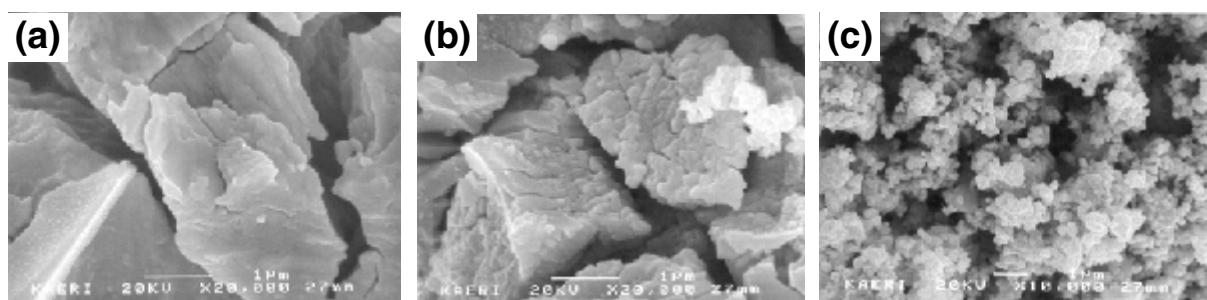
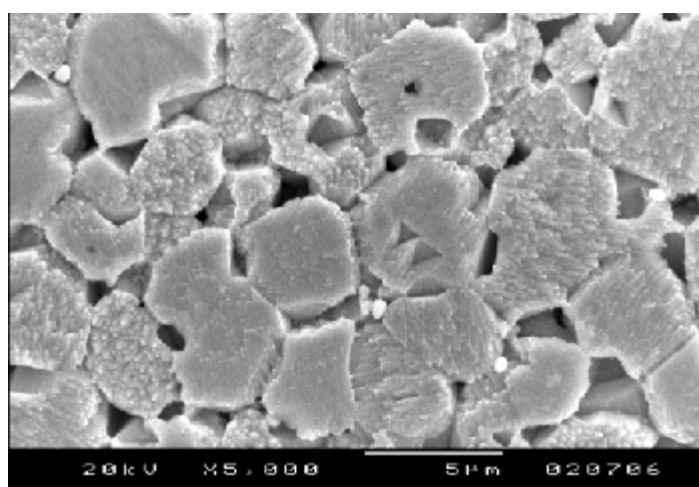


Figure 2. Scanning electron micrograph of the simulated DUPIC fuel after sintering at 1700°C for four hours in a flowing hydrogen atmosphere



The thermal properties and mechanical properties of the simulated DUPIC fuel were measured to modify the material models in the performance evaluation codes such as ELESTRES for the CANDU fuel element. The changed material properties result in important changes in the irradiation behaviour such as centreline temperature, fission gas release (FGR) and pellet-cladding mechanical interaction (PCMI). Figure 3(a) shows that the thermal conductivity of the simulated DUPIC fuel was lower than UO_2 due to the presence of the solid solution elements such as Zr, Nd, Ce, etc. in the fuel [8]. It has been reported that the thermal conductivity decreased as the target burn-up of the simulated fuel increased [6,7]. Thermal conductivity of the DUPIC fuel was fitted with the Harding-Martin equation and modelled as follows [9]:

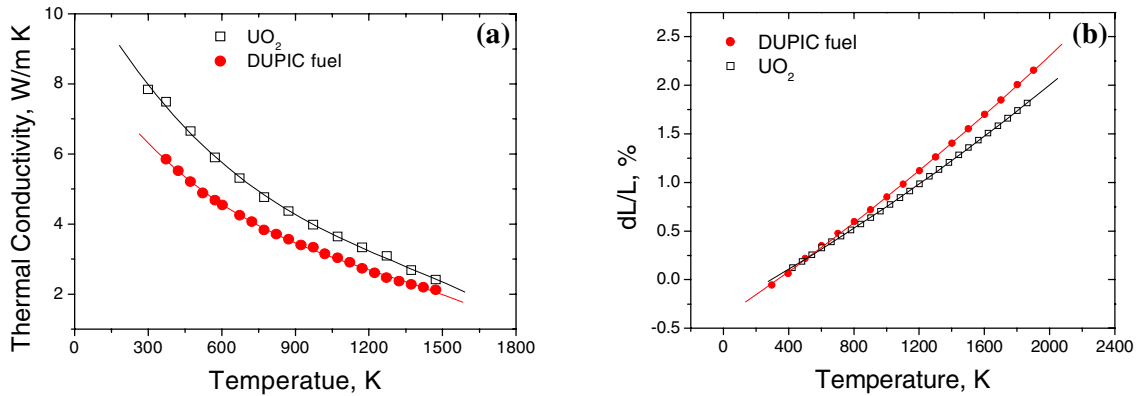
$$k_o = \frac{1}{0.0944 + 2.027 \times 10^{-4} T} + \frac{4.715 \times 10^9}{T^2} \exp\left(\frac{-16361}{T}\right)$$

The coefficient of the thermal expansion of the simulated DUPIC fuel is larger than that of UO_2 as plotted in Figure 3(b) [10]. Thermal expansion of the DUPIC fuel is modelled as follows:

$$dL/L = 11.8 \times 10^{-6} T + 3.97 \times 10^{-10} T^2$$

The decrease in thermal conductivity and the increase in thermal expansion are not desirable changes for the fuel performance.

Figure 3. (a) Thermal conductivity and (b) thermal expansion of UO_2 and the simulated DUPIC fuel with temperature



As for the view of the pellet-cladding mechanical interaction, soft fuel is a desirable concept for preventing the cladding from severe deformation. But Figures 4 and 5 show that the simulated DUPIC fuel is not a softer fuel than UO_2 . Time-dependent plastic deformation and time-independent elastic and plastic deformation are more difficult in the simulated DUPIC fuel. Solid solution hardening and precipitation hardening occur in the simulated DUPIC fuel. From the hot hardness test as shown in Figure 5, the high temperature yield strength of the simulated DUPIC fuel can be calculated by the empirical relationship between the hardness and yield strength. Fracture toughness can also be calculated from a hot hardness test by the indentation crack length method. Figure 6(a) exhibits indentation cracks at the corners of the indent after a hot hardness test. For brittle materials, fracture toughness is formulated as a function of the crack length, Young's modulus and hardness as follows [11]:

$$K_C = 0.028 (H/E)^{-1/2} \cdot Ha^{1/2} (cla)^{-3/2}$$

where H is the hardness, E is the Young's modulus, a is indent diagonal distance, and c is the crack length. The simulated DUPIC fuel has comparable fracture toughness to UO_2 , as shown in Figure 6(b).

Figure 4. (a) Creep rate and (b) Young's modulus of UO_2 and the simulated DUPIC fuel

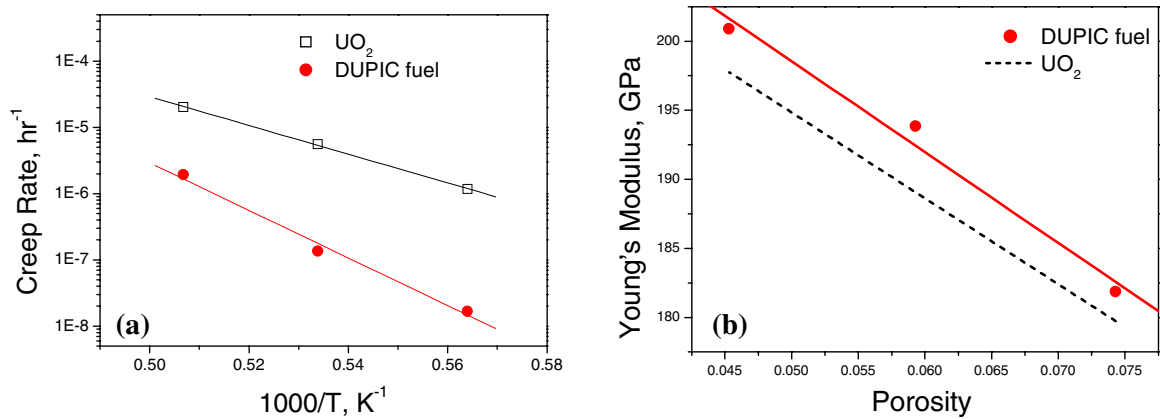


Figure 5. Hot hardness of UO_2 and the simulated DUPIC fuel measured by the high temperature micro-Vickers hardness test

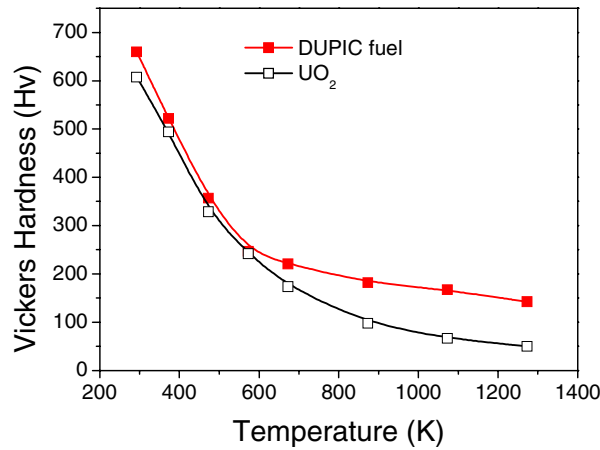
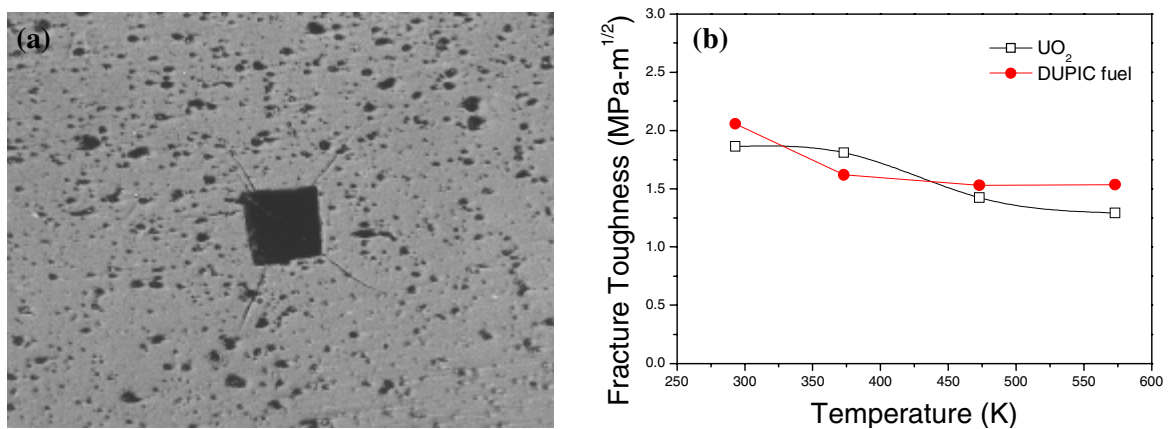
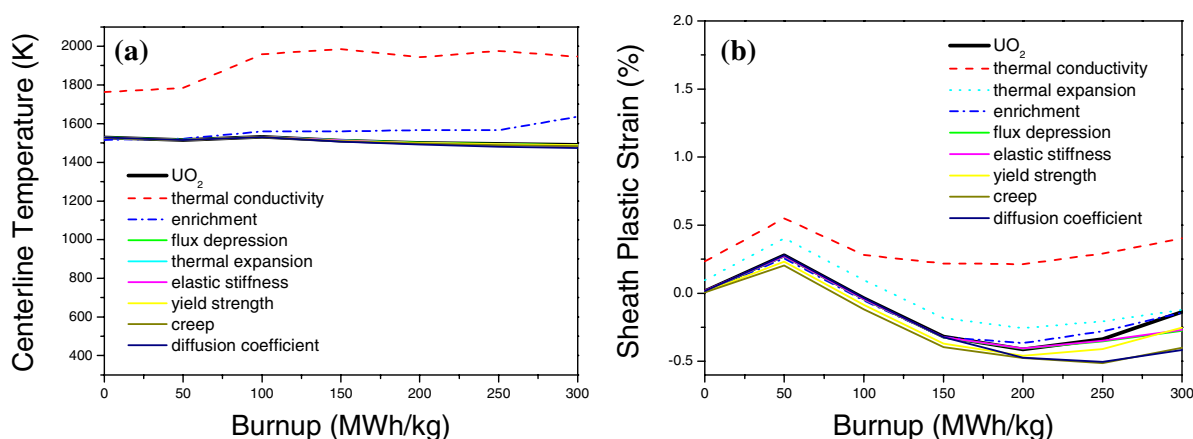


Figure 6. (a) Scanning electron micrograph showing an indentation crack after the hot hardness test of the simulated DUPIC fuel at 100°C and (b) the fracture toughness of UO_2 and the simulated DUPIC fuel obtained by the indentation crack length method



Because the DUPIC fuel is designed to be utilised in existing CANDU reactors, the ELESTRES code has been used for the fuel element performance evaluation of the DUPIC fuel [12,13]. Some important material models adopted in the ELESTRES code were modified one by one to measure their contribution to the fuel performance. Figure 7 shows the calculated results of the centreline temperature and sheath plastic strain by the modified ELESTRES code when one of the material models such as thermal conductivity and thermal expansion are changed for the DUPIC fuel. The change in thermal conductivity resulted in the most remarkable changes of the centreline temperature and sheath plastic strain, while the other factors did not exhibit quite such an influencing deviation. This preliminary sensitivity analysis shows that the pellet-cladding mechanical interaction of the DUPIC fuel was found to be greatly affected by the thermal conductivity of the fuel and the resulting centreline temperature of the fuel. A higher centreline temperature of the DUPIC fuel also increases the internal pressure of the fuel element due to the increased fission gas release. Initial rise of the sheath plastic strain as shown in Figure 7(b) is originated from the thermal expansion of the fuel pellet and the second rise of the sheath plastic strain at an increased burn-up results from the increased internal pressure by the fission gas release.

Figure 7. The effect of the performance variables on (a) the centreline temperature and (b) plastic strain of the sheath of the DUPIC fuel with burn-up at a linear heat rate of 40 kW/m

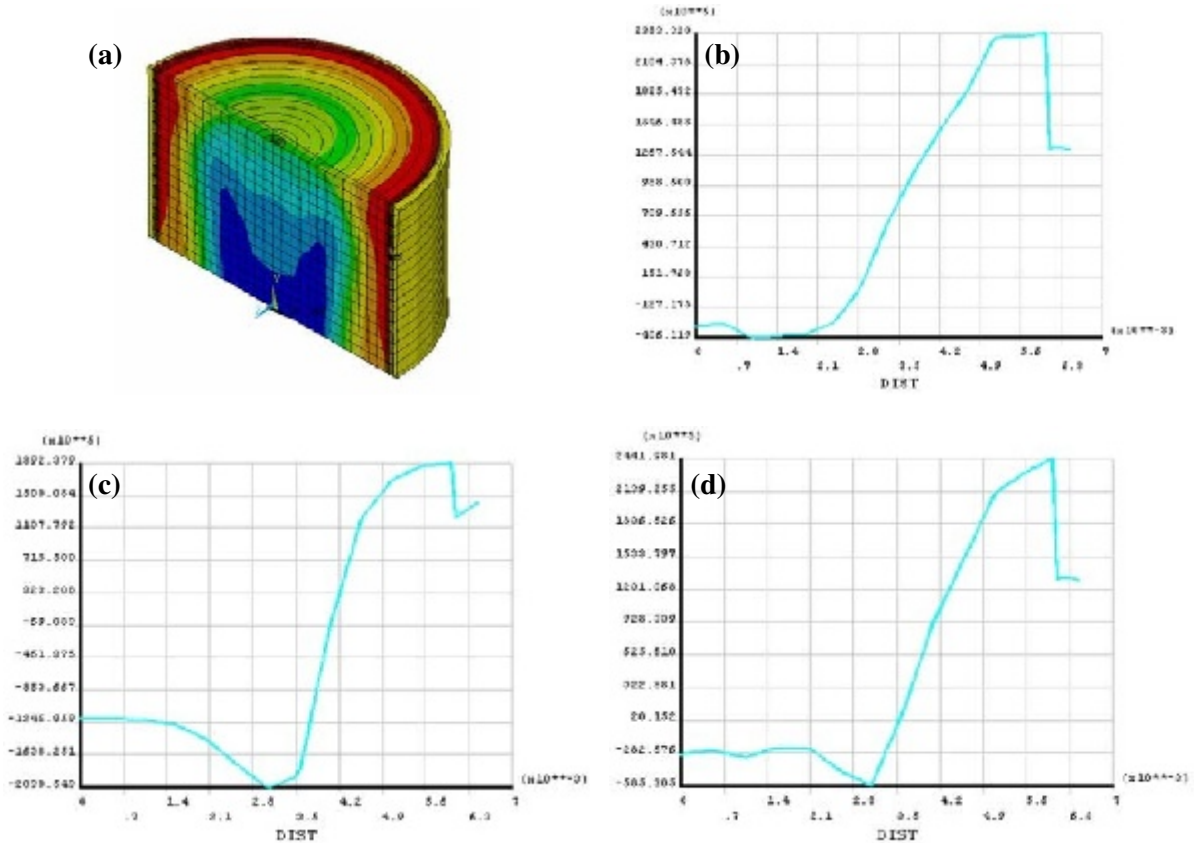


Finite element analysis (FEA) software can be used as another tool for the comprehensive evaluation of the pellet-cladding mechanical interaction of the DUPIC fuel due to the adaptive calculation of the thermal and mechanical behaviour [14,15]. The modification of the existing performance code can be verified by a comparison with the results of the calculation by the FEA software. An FEA study was carried out using ANSYS 7.0 to verify the modified performance evaluation code and to understand the detailed thermal and mechanical behaviour of the DUPIC fuel [16]. Distribution of the hoop stress of the DUPIC fuel at an initial burn-up with a linear heat rate of 40 kW/m is shown in Figure 8. Compressive hoop stress forms in the inner region of the pellet while tensile hoop stress occurs in the outer region of the pellet and the cladding. The maximum tensile hoop stress is found at the corner of pellet end.

Table 1. Fuel design variables and boundary conditions for the finite element analysis

Fuel design variables	Value	Boundary conditions	Value
Pellet radius	6.075 mm	Gap conductance	$75.1 \times 10^3 \text{ W/m}^2\text{K}$
Pellet height	16.0 mm	Film coefficient	$46.1 \times 10^3 \text{ W/m}^2\text{K}$
Cladding thickness	0.39 mm	Coolant temperature	561 K

Figure 8. (a) Hoop stress contour plot of the upper half pellet and radial variation of the hoop stress at (b) UO₂ pellet end, (c) DUPIC fuel mid-pellet and (d) DUPIC fuel pellet end with a linear heat rate of 40 kW/m

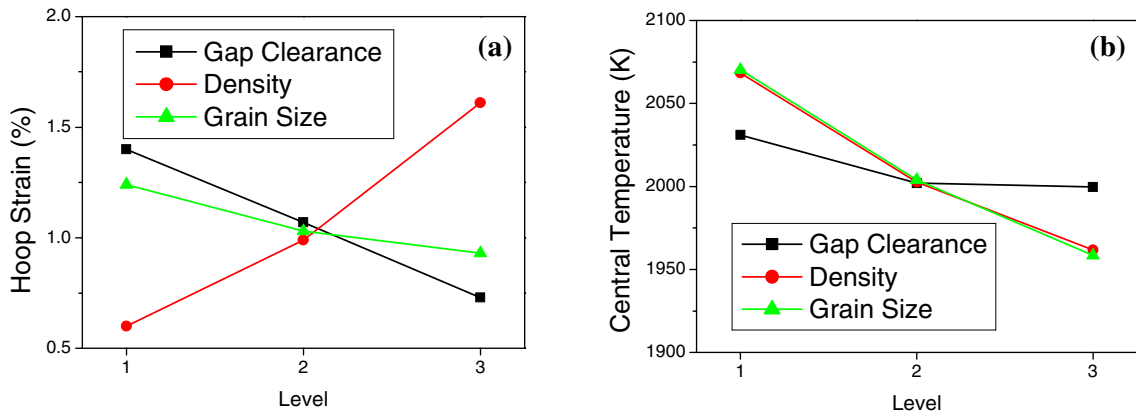


Parametric sensitivity analysis was carried out using modified ELESTRES codes to suggest the optimum fabrication variables within the ranges of the fuel specifications. Statistical sensitivity was analysed by employing the orthogonal array design (OAD) involving three fabrication factors with three levels as shown in Table 2 [17]. Fuel density, gap clearance and grain size were selected as the major fabrication variables influencing the performance of the DUPIC fuel. As shown in Figure 9, the fuel density was the most controlling factor for the increase of the hoop strain due to the strong PCMI. It is recommended to decrease the fuel density and to increase the gap clearance to reduce the PCMI of the DUPIC fuel. Although the decrease in the fuel density may result in a rise of the centreline temperature of the DUPIC fuel, Figure 9(b) shows that the effect of the recommended change of the fabrication parameter within the fuel specification is acceptable compared to the melting point of the DUPIC fuel.

Table 2. Fabrication factors and their levels used in the orthogonal array design

Fabrication factors	Level 1	Level 2	Level 3
Fuel density	10.30 g/cm ³	10.45 g/cm ³	10.60 g/cm ³
Gap clearance	40 μ m	80 μ m	120 μ m
Grain size	5 μ m	15 μ m	25 μ m

Figure 9. Statistical variation of the (a) total strain at pellet end and (b) centreline temperature of the DUPIC fuel with the levels in orthogonal array design



Conclusions

The thermal properties and mechanical properties of DUPIC fuel were measured using simulated DUPIC fuel for the performance evaluation. Among many variations of the material properties, the decrease in the thermal conductivity resulted in the largest change of the fuel performance of the DUPIC fuel. The pellet-cladding mechanical interaction resulting in a large ridge height and plastic strain of the cladding also increased when the material models in the performance evaluation code and finite element analysis were modified for the DUPIC fuel. Statistical sensitivity analysis showed that the fabrication parameters such as fuel density, initial gap and grain size should be optimised to reduce the PCMI of the DUPIC fuel.

Acknowledgements

This study was carried out as a mid- and long-term research project of the National Nuclear R&D Program sponsored by the Ministry of Science and Technology (MOST) of Korea.

REFERENCES

- [1] Lee, J-S., K-C. Song, M-S. Yang, K-S. Chun, B-W. Rhee, J-S. Hong, H-S. Park, C-S. Rim, *Proceedings of the International Conference on Future Nuclear Systems: Emerging Fuel Cycles and Waste Disposal Options (GLOBAL '93)*, Seattle, Washington (1993).
- [2] Ko, W-I., H-D. Kim, M-S. Yang, *Nuclear Technology*, 138, 123 (2002).
- [3] Song, K-W., Y-H. Kim, B-G. Kim, J-W. Lee, H-S. Kim, M-S. Yang, H-S. Park, *J. Kor. Nuc. Soc.*, 28, 366 (1996).

- [4] Ryu, H-J., K-C. Song, G-I. Park, J-W. Lee, M-S. Yang, *International IUPAC Conference on the High Temperature Materials Chemistry XI*, Tokyo, Japan, 19-23 May (2003).
- [5] Kang, K-H., K-K. Bae, H-S. Park, K-C. Song, J-S. Moon, *J. Kor. Powder. Metall. Inst.*, 7, 123 (2000).
- [6] Lucuta, P.G., R.A. Verrall, HJ. Matzke, B.J. Palmer, *J. Nucl. Mater.*, 178, 48 (1991).
- [7] Lucuta, P.G., HJ. Matzke, R.A. Verrall, H.A. Tasman, *J. Nucl. Mater.*, 188, 198 (1992).
- [8] Kang, K-H., K-C. Song, M-S. Yang, *J. Nucl. Sci. Tech., Suppl.* 3, 776 (2002).
- [9] Harding, J.H. and D.G. Martin, *J. Nucl. Mater.*, 166, 223 (1989).
- [10] Kang, K-H., K-C. Song, M-S. Yang, *Inter. J. Thermophys.* 24, 1373 (2003).
- [11] Lawn, B.R., A.G. Evans, D.B. Marshall, *J. Am. Ceram. Soc.*, 63, 574 (1980).
- [12] Suk, H-C., *et al. ELESTRES.M11K Program Users' Manual and Description*, KAERI/TR-320/92 (1992).
- [13] Tayal, M., *ELESTRES Code Description*, Atomic Energy of Canada Ltd. Report, AECL-9331 (1987).
- [14] Massih, A.R., T. Rajala, L.O. Jernkvist, *Nucl. Eng. Des.* 156, 383 (1995).
- [15] Denis, A., A. Soba, *Nucl. Eng. Des.*, 223, 211 (2003).
- [16] *ANSYS User's Guide for Release 7.0*, ANSYS, Inc.
- [17] Taguchi, G., *System of Experimental Designs*, Vol. 1-2, Kraus, New York (1987).

OUT-OF-PILE AND IN-PILE VISCOPLASTIC BEHAVIOUR OF MIXED-OXIDE FUELS

L. Caillot, C. Nonon, V. Basini
CEA Cadarache

Abstract

MOX fuel tested under transient conditions behaves particularly well from the pellet-cladding interaction point of view and can undergo power variations above the current standard UO_2 threshold.

So as to complete understanding of the specific mechanical properties of MOX fuel, experimental programmes have been undertaken within the framework of a co-operation between EDF, FRAMATOME ANP and CEA. Since the MOX benefit is attributed to its higher fuel creep, analytical tests were performed to attempt to characterise the specific in-pile thermo-mechanical behaviour of MOX fuels and to compare it to that of UO_2 .

In-pile diameter measurements with the DECOR device in the SILOE reactor on fuel rodlets were performed under transient conditions. A small increase of creep rates was observed on fresh MOX fuel compared to UO_2 at the same power, mainly due to the effect of the lower conductivity on the fuel temperature. On a two-cycle PWR fuel, in-pile and PIE observations evidenced a significant increase of creep properties compared to those observed at beginning of life. Another evidence of the higher viscoplasticity of MOX fuel is provided through a comparative examination of two-cycle MOX and UO_2 fuel rods after power ramping in the OSIRIS reactor with zero holding time at ramp terminal power level.

The correlation between creep studies by compression experiments at intermediate temperature on as-fabricated MOX MIMAS pellets and irradiation results are discussed, especially as concerns the impact of the differential thermal behaviour of MOX and UO_2 on the thermal creep.

Background

Since the first reload in 1987 in the Saint-Laurent B1 unit, MOX fuel utilisation in EDF PWRs has been widely developed [1]. The “MOX parity” project was launched to achieve parity between MOX and UO₂ fuel performances up to an assembly discharge burn-up of 52.0 MWd/tM. The huge experience feedback, completed by experimental programmes, has been used in order to improve the understanding of MOX fuel behaviour under nominal and transient conditions. Concerning mechanical properties, ramp tests proved that MOX fuel behaves particularly well from the pellet-cladding interaction point of view [2]. Indeed, none of the power ramps carried out on the MIMAS-type MOX fuel rods irradiated for two and three cycles in PWR conditions resulted in cladding failure. All the rods tested survived transients with conditions above the UO₂ threshold (up to 490 W/cm). Similar conclusions are reported in open literature [3].

This better behaviour is always attributed to higher creep properties of MOX fuels compared to UO₂, but only few (or old) data on this topic are available. The objective of this paper is to provide an overview of an analytical programme aiming at understanding the specific behaviour of MOX fuels in PCI conditions and to highlight some new results about the higher MOX pellet creep during power transients. This programme has been undertaken within the framework of a co-operation between EDF, FRAMATOME ANP and CEA. It includes three sections:

- Instrumented irradiations.
- Analytical power ramps.
- Compression tests on non-irradiated pellets.

Instrumented irradiations on MOX fuel rodlets

The two experiments described in this section (DEFORMOX 1 and 2) aimed at characterising the specific in-pile thermo-mechanical behaviour of MOX fuels. To this end, the cladding deformation was measured at different power levels using the DECOR irradiation device in the SILOE experimental reactor.

The DECOR device [4], which is a part of the GRIFFON rig operating in boiling conditions (water pressure is 130 bars), is a device designed to perform a complete diametral profilometry of a short rodlet during the irradiation. The fuel pellet stack is about 20 cm long, and the rod total length is about 30 cm. The technology of the measure is based on strain gauges. A calibration is performed for every measurement thanks to diameter standards screwed at each extremity of the rodlet. The accuracy of measurements with this device is ± 3 microns; nevertheless relative evolutions of the order of the micron are expected to be significant.

The DEFORMOX 1 experiment was performed on fresh MOX and UO₂ fuels, while the DEFORMOX 2 experiment aimed at characterising a two-cycle MOX MIMAS PWR fuel rod.

DEFORMOX 1 experiment

This beginning-of-life (BOL) experiment was undertaken:

- To compare the thermo-mechanical behaviour of different types of MOX fuels (MIMAS ADU and MIMAS AUC) and UO₂.
- To attempt to evaluate the effect of burn-up by comparing DEFORMOX 1 (BOL) and DEFORMOX 2 (after two PWR cycles).

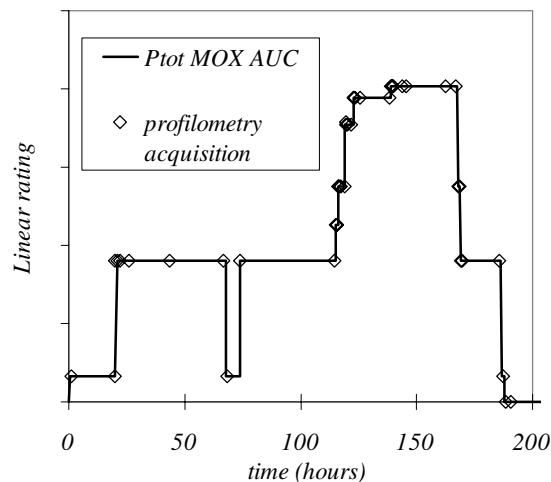
In order to allow a direct comparison of results, the three different types of pellets were irradiated in a single experimental rod. The fuel stack is made of six pellets of each fuel type. Most of the parameters were chosen in order to make the direct comparison as easy as possible. The pellets' characteristics are given in Table 1.

Table 1. Fabrication and irradiation characteristics of the three experimental programmes

	DEFORMOX 1			DEFORMOX 2	ZHT ramp
Geometry	17 × 17				
Clad	Zy4				
Fuel	MOX MIMAS	UO ₂	MOX MIMAS	MOX MIMAS	MOX MIMAS
UO ₂ powder fabrication route	ADU	–	AUC	AUC	ADU
Pu or U content (mass)	PuO ₂ /MOX 6.6%	²³⁵ U/U 7.0%	PuO ₂ /MOX 6.7%	Pu/(U+Pu) 6.6%	Pu/(U+Pu) 6.6%
Density (g.cm ⁻³)	10.50	10.46	10.52	10.47	10.40
Rodlet burn up	0	0	0	28.5 GWd/t. hm	28.1 GWd/t. hm

The power history of the fuel rod is given in Figure 1. The power of MOX and UO₂ fuels are not exactly the same because of isotopic composition differences. The MOX pellets were submitted to increasing power steps ranging from 200 W/cm to 400 W/cm, while the UO₂ pellets were irradiated up to 430 W/cm. The ramp rises were performed at 40 W/cm/min. During each power plateau, several diameter measurements were performed. The date of acquisitions is pointed out with dots in Figure 1.

Figure 1. DEFORMOX 1 power history



During the first long power plateau at 200 W/cm, the evolution of profilometries evidenced the densification of the pellets. Taking into consideration the duration of the following power plateau, this phenomenon can be neglected during the rest of the sequence.

Thanks to the profilometries measured after each power step, it was observed that the deformation tends to be more homogeneous in the case of MOX pellets when the power increases. Primary ridges are smaller than those of UO₂, with a slightly better behaviour of the MOX ADU compared to MOX AUC. At the end of the irradiation, differences between the three fuel batches are highlighted through the out-of-pile cladding diameter measurement (Figure 2).

Signs of creep of the MOX fuel start to be seen at 350 W/cm, as shown in Figure 3, with a slight decrease of the difference between inter-pellet and mid-pellet diameters (a few microns). This evolution, which continues during the next power plateau, is not observed for UO₂.

The deformation of MOX pellets, and in particular of MIMAS ADU pellets, evidences a relative decrease of primary ridges compared to UO₂. This is due to a higher fuel creep accumulated during the time of the different power plateaus, in spite of a lower linear rating for the MOX pellets.

Figure 2. Comparison of out-of-pile cladding diameter measurements before and after the test

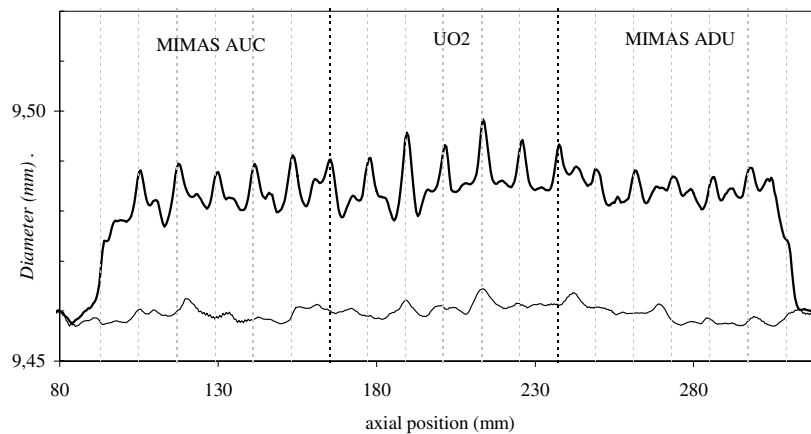
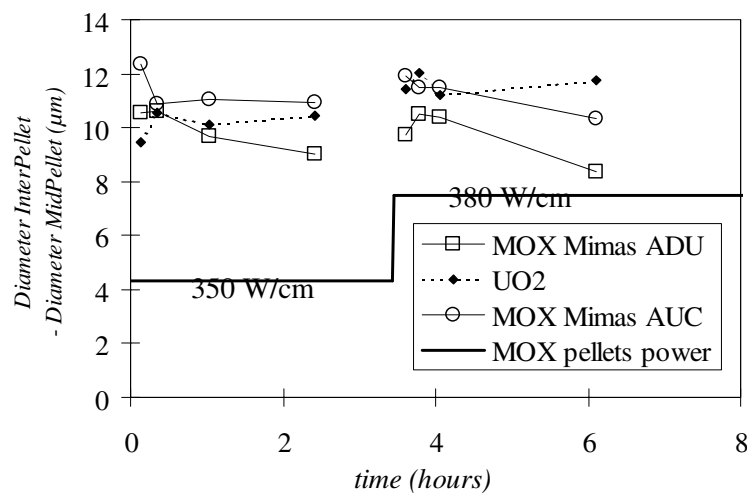


Figure 3. Time and power dependence of difference between inter-pellet and mid-pellet diameters



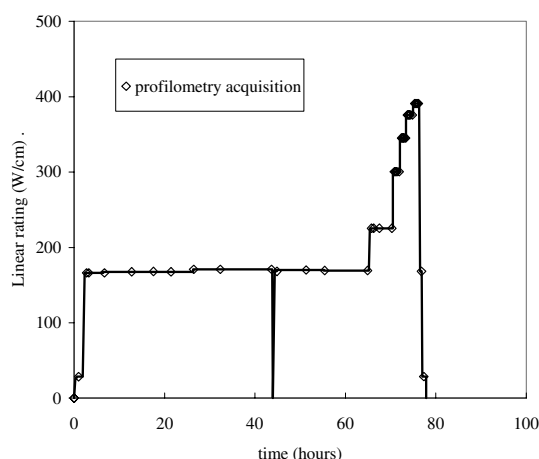
The temperature in the centre of the UO_2 pellets can be estimated to be approximately $1\,400^\circ\text{C}$ during the higher power plateau (435 W/cm). The temperature differences between MOX and UO_2 pellets can be as large as 200°C at the same power. Under the DEFORMOX 1 experiment conditions, however, the power of the MOX pellet is lower due to isotopic composition. Consequently, the MOX pellet temperature is higher by 100°C . Higher fuel creep for MOX fuel can thus be partly explained by the higher level of temperature in the pellet. Nevertheless, it should be noted that no filling of pellet extremity dishings was observed on longitudinal post-irradiation ceramographies.

DEFORMOX 2 experiment

The DEFORMOX 2 experiment was performed under similar conditions as DEFORMOX 1, using the DECOR device in the SILOE reactor just before its definitive shutdown at the end of 1997.

This experiment was performed on a MOX fuel rod irradiated in a French EDF reactor during two cycles and refabricated by the FABRICE process. Fabrication and irradiation characteristics are provided in Table 1. The power history of the DEFORMOX 2 experiment is given in Figure 4.

Figure 4. Power history of the DEFORMOX 2 experiment



This power history is similar to that of the DEFORMOX 1 experiment: after a conditioning plateau at 170 W/cm , the power was increased by steps at 50 W/cm/min , and diameter measurements were performed during each power plateau so as to characterise the evolution of the cladding deformation at constant power. These profilometries exhibit a slight increase of primary ridges height up to 345 W/cm . Thereafter, primary ridges do not increase whereas secondary ridges grow at the mid-pellet planes. Cladding deformation tends to become more homogeneous.

The creep behaviour of MOX pellets was analysed through the evolution of the cladding deformation when held at constant power (Figures 5 and 6).

At 300 and 345 W/cm , the difference between inter-pellets and mid-pellet diameters decreases with time. During the first plateau, the primary ridges' height diminishes and secondary ridges begin to appear, while mean diameter does not evolve. This is a clear evidence of creep-type phenomenon. This means that fuel creep in the MOX case, can be activated as soon as the temperature reaches $1\,300^\circ\text{C}$ (estimated temperature at the centre of the pellet at 300 W/cm). Later, from 345 W/cm , the fuel gaseous swelling contribution begins to be significant, leading to the increase of the mean diameter during the hour of holding time.

Figure 5. Fuel rod profilometry evolution during holding time at 300 and 345 W/cm

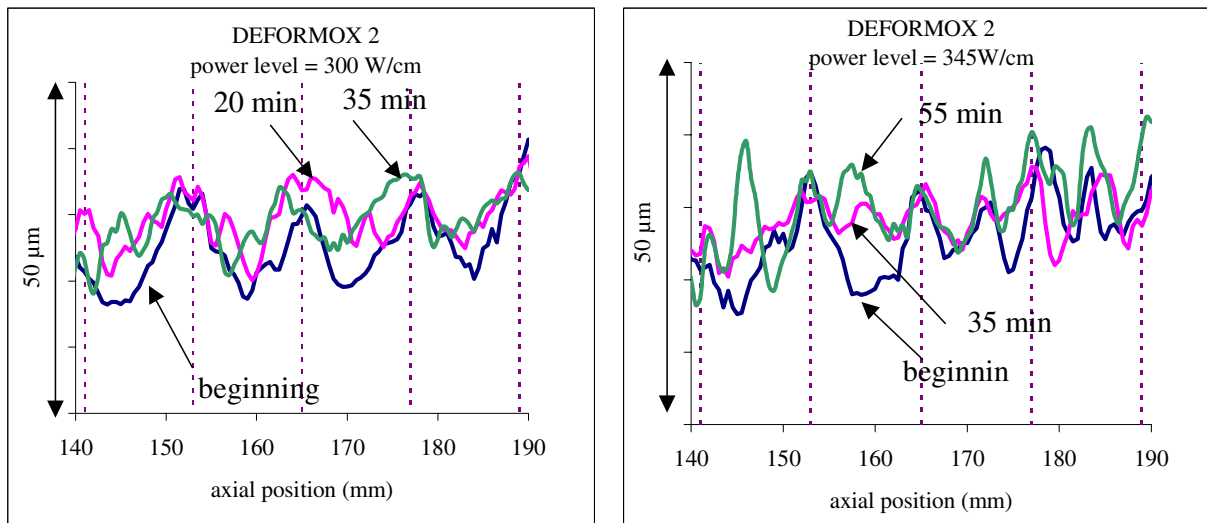


Figure 6. Evolution of difference between diameter at inter-pellet plane and diameter at mid-pellet plane during holding time (mean measurements of four pellets)

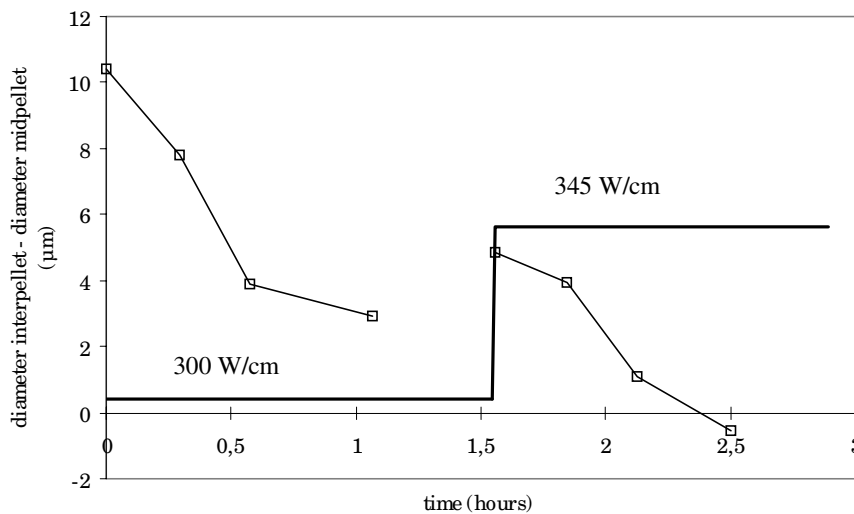


Figure 7 compares permanent cladding deformations induced by DEFORMOX 2 (maximum power = 390 W/cm) and a power ramp on a two-cycle UO_2 at a comparable maximum power level (395 W/cm – 12 hours of holding time).

In spite of the shorter time at full power, the MOX fuel exhibits a higher mean deformation due to swelling, and a complete fading of primary ridges at inter-pellet.

Such observations have been reported in other experiments. For example, Figure 8 compares similar results obtained on a two-cycle MOX ramped in R2 and a two-cycle UO_2 ramped in OSIRIS under very similar conditions (≈ 430 W/cm – 12 hours of holding time). The higher the power, the more the primary ridges are flattened.

Figure 7. Comparison of fuel rod profilometry evolution between DEFORMOX 2 and a two-cycle UO₂ submitted to a similar ramp test power history

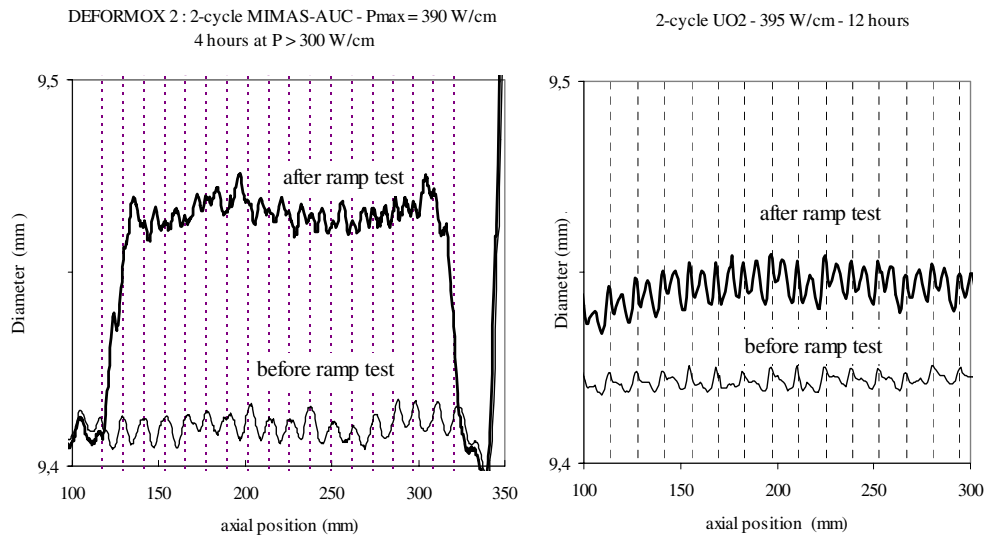
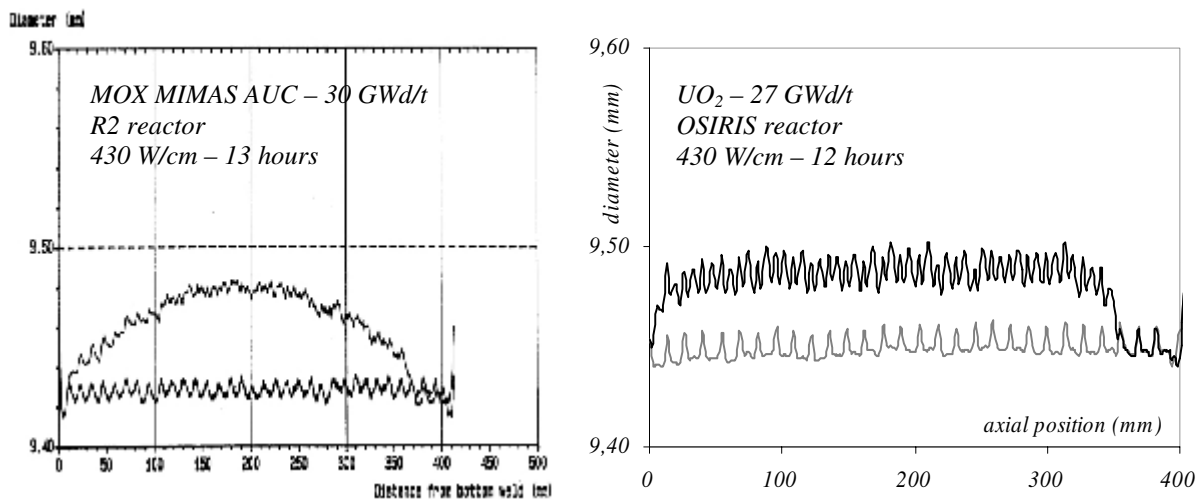


Figure 8. Comparison of fuel rod profilometry evolution (before and after ramp) between MOX and UO₂ submitted to a similar ramp test power history

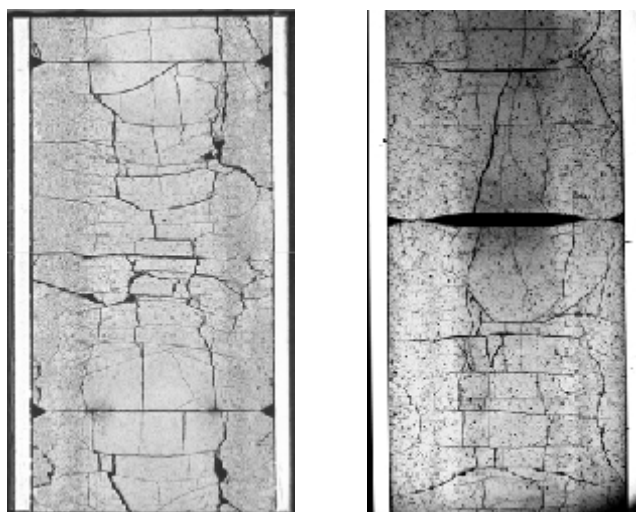


The primary ridges' evolution provides the evidence of the higher creep of MOX pellets. This is confirmed by the analysis of longitudinal ceramographies. Filling of dishings of DEFORMOX 2 pellets is complete, while there is still free volume in the UO₂ case (Figure 9). Both effects – fuel creep and gas swelling – contribute to the larger filling of MOX dishings as compared to UO₂.

Comparative analysis of DEFORMOX 1 and 2

The DEFORMOX 1 and 2 experiments have revealed signs of creep occurring at lower power for MOX fuels as compared to UO₂, leading to a more homogeneous deformation of the cladding, probably due to a combination of intrinsic properties and temperature effects. The latter has been estimated to be around 100°C in the DEFORMOX 1 experiment.

Figure 9. Longitudinal sections from DEFORMOX 2 experiment (left) and from a two-cycle UO₂ (right) submitted to a power ramp test (395 W/cm – 12 hours holding time)



In the DEFORMOX 2 experiment, signs of MOX fuel creep have been highlighted for temperatures as low as 1 300°C, while such features were not as manifest for UO₂ after operation up to 1 600°C (corresponding to a power level of 395 W/cm).

Furthermore, it is obvious that the differences between MOX and UO₂ are smaller at beginning of life than at higher burn-up: after two cycles of PWR irradiation, the primary ridges' evolution is much higher (tens of microns compared to a few microns) and filling of dishings is significant.

Nevertheless, due to the holding time at different powers in this type of experiments, creep phenomena can not be clearly separated from gaseous swelling, which is the reason why zero holding time power ramps were performed.

Zero holding time (ZHT) power ramp

This type of irradiation is performed in the OSIRIS reactor located in CEA Saclay. The analytical ramp tests were performed in the ISABELLE 1 irradiation loop [5]. This loop, used for standard PCI ramps, allows reproducing PWR thermo-hydraulic conditions.

The test scheme applied is a conditioning power plateau followed by a transient at approximately 100 W/cm/min, and zero holding time at the terminal power level. The conditioning is operated at an appropriate power level to re-establish the thermo-mechanical and chemical state of the rod achieved at the end of the base irradiation.

The aim of this type of ramp test is to provide new data for understanding the main mechanisms involved during the transient and to observe the rod thermo-mechanical state at the end of the power increase phase. The absence of holding time allows reducing the risk of screening major PCI features by various time-dependent parasitic effects such as gaseous swelling.

Three experiments were conducted on a two-cycle UO₂, a four-cycle UO₂ and a two-cycle MOX respectively. The final power at the end of each transient has been specified to be the same value, about 450 W/cm, in order to make comparisons among the three rods behaviour easier.

The results of these three zero holding time ramp tests are detailed in [6]. Fabrication and irradiation characteristics of the two-cycle MOX rod are given in Table 1. Conclusions related to post-irradiation examinations and post-calculations for the MOX ramp test, in comparison with those obtained for UO₂ are reported hereafter:

- No cladding failure occurred, as expected.
- The permanent cladding deformation is slight ($< 15 \mu\text{m}$), due to the absence of holding at high power and the absence of fuel swelling (Figure 10).
- The permanent deformation of the MOX rod is 1.5 times higher than that of the UO₂ rod in the central part of the rod where power level is maximum. This is fully explained by the computed difference of thermal loading: thermal conductivity of MOX fuel induces an average temperature increase of 125°C at the centre of the pellet (1 840°C against 1 715°C at the maximum power level).
- No evolution of primary ridges was measured, while an increase is observed for UO₂ under similar conditions (Figure 11).
- The partial filling (25%) of pellet extremity dishings has been quantified through axial ceramographies (Figure 12). This result has been compared to examinations on UO₂ after ZHT ramp. Dishings filling was very slight (only 7%). In addition, closer examinations in the vicinity of the partially filled MOX pellet dishings revealed oriented intergranular fractures, typical of fuel creep mechanism. This feature was not observed in the UO₂ case.
- Differences in crack patterns were highlighted on longitudinal sections: a smaller crack volume in the MOX pellet, compared to two-cycle UO₂ where large fractures can be observed (Figure 12).

MOX fuel exhibits a higher gaseous swelling at equivalent power for burn-up in the range of two-cycle irradiation. Since fission gas swelling and fuel creep both contribute to ridges' evolution and dimples' filling, results of the ZHT ramp test for which fission gas swelling is reduced, provide crucial features as concerns the difference of creep behaviour between MOX and UO₂.

Figure 10. Comparison of cladding deformation after a ZHT ramp test between a two-cycle UO₂ and a two-cycle MOX

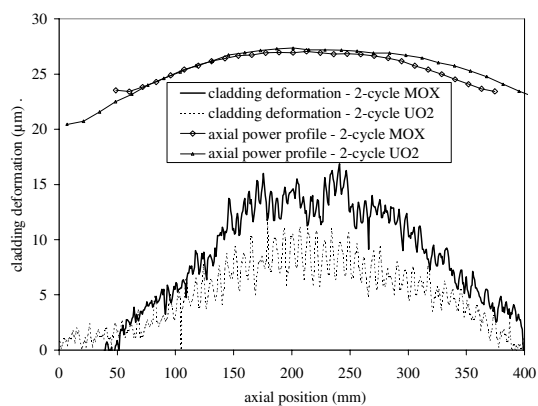


Figure 11. Primary ridges' height evolution versus local power

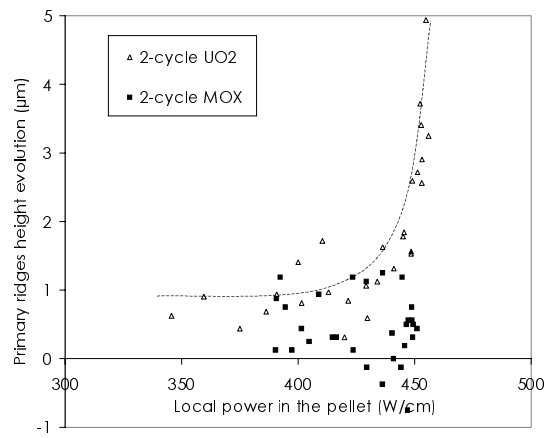
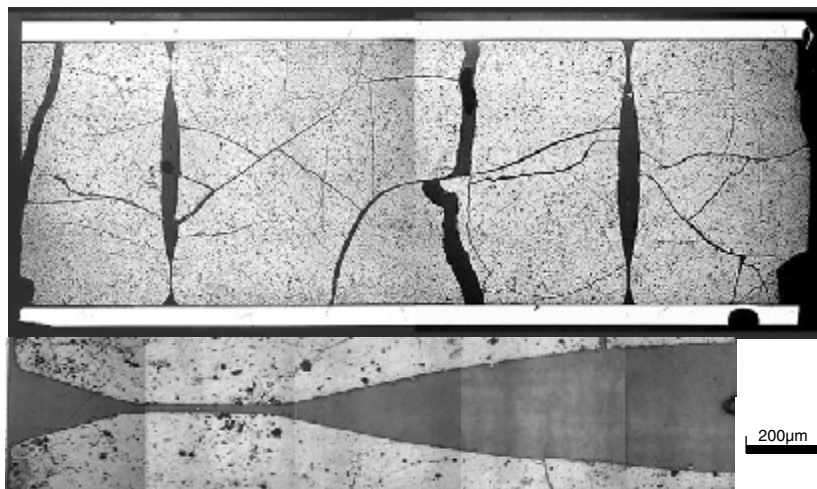
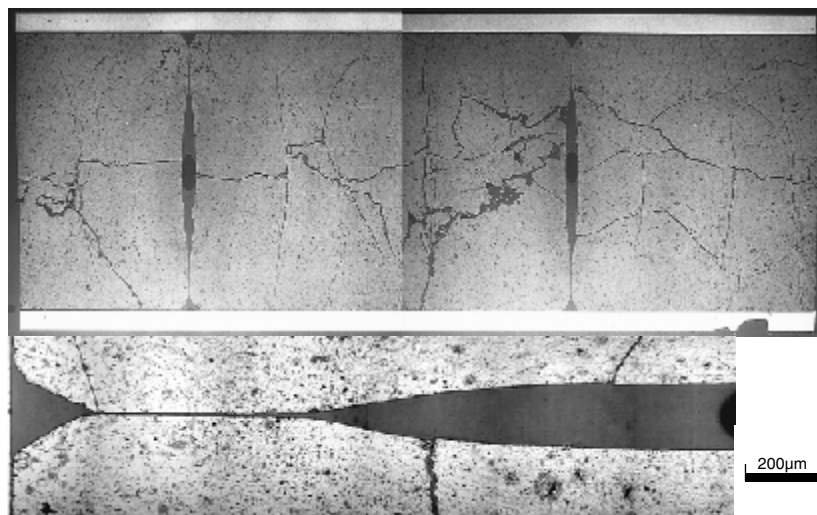


Figure 12. Longitudinal sections from two-cycle UO₂ and two-cycle MOX fuel rodlets after zero holding time ramp test

UO₂ – two cycles



MOX – two cycles



Indeed, post-calculations of the ZHT experiment allowed concluding on the absence of gaseous swelling during the transient. Moreover, they lead to the conclusion that evolution of primary ridges, (as well as dishings filling and crack pattern) can be explained by the higher fuel creep rate for MOX than for UO₂ during the short time scale of the transient (several minutes). In this way, the results complement those obtained in the DEFORMOX 1 and 2 experiments, showing that creep occurs at lower power levels compared to UO₂.

This higher creep rate can be explained by:

- The higher temperature of MOX fuel due to the lower thermal conductivity. In the range of power of PCI ramp, the difference in central temperature between MOX and UO₂ is about 100-150°C (1 840°C against 1 715°C at 450 W/cm in the ZHT experiment). This difference in temperature has of course a direct consequence on the thermal creep.
- A difference in intrinsic creep properties of the materials, as reported in the past on FBR fuels [7,8].

In order to improve our knowledge on these two points, mechanical testings on non-irradiated MOX and UO₂ fuel were performed.

Compression tests on non-irradiated fuels

A series of compression tests were performed on as-fabricated pellets in the LEFCA facility of CEA Cadarache. All compression tests were conducted in a suitable adapted furnace on a screw-type Instron machine mounted in a glove-box because of the radiotoxicity of plutonium. Creep tests were performed from 30-100 MPa and temperature tests varying from 1 300°C to 1 700°C were performed under a vacuum atmosphere so as not to modify the O/M ratio during the test.

Tested pellets were fabricated by the MIMAS process using ADU UO₂ powder. Table 2 presents the specimen characteristics.

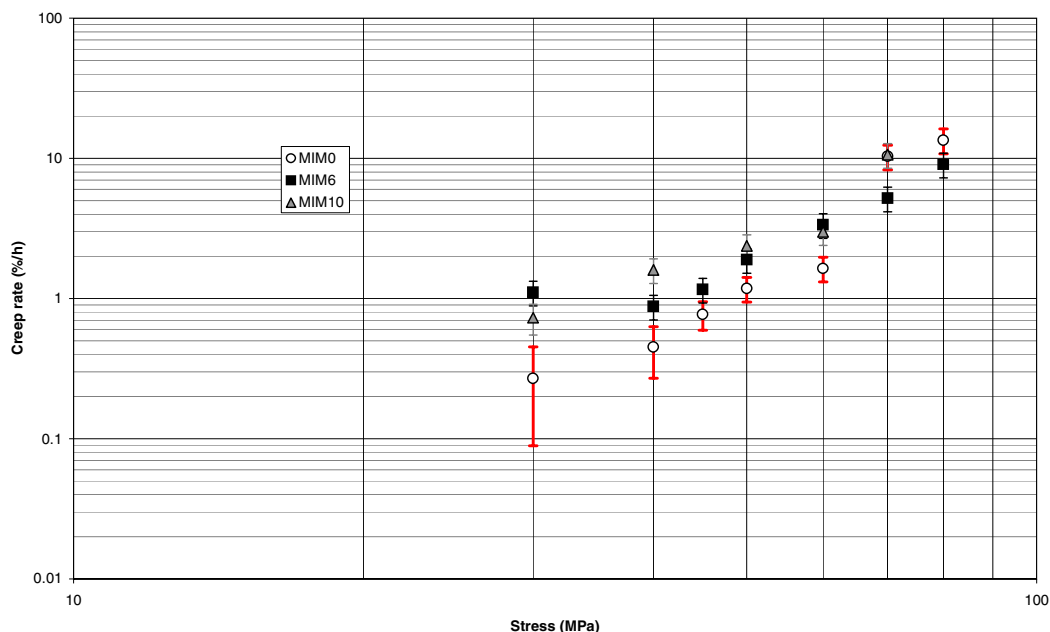
Table 2. Specimen characteristics

Name	Plutonium content (%)	Cluster size (µm)	Porosity (%)	Grain size (µm)		
				(U,Pu)O ₂ zones	UO ₂ zones	Average
MIM0	0	–	5	–	7.3	7.3
MIM6	6	< 150 µm	4.6	9	4.4	5.5
MIM10	10	< 150 µm	4.2	8	< 2	5.5

Figure 13 presents stationary creep rates obtained on different MOX MIMAS-type pellets (laboratory fabrications) at 1 535°C in the range of stresses from 30-80 MPa. Three levels of Pu content were tested: 0, 6 and 10% (“MIMAS 0%” is in fact a UO₂ prepared as MOX pellets by the MIMAS process, through dilution of a master blend made of UO₂ in UO₂, so as to avoid microstructure unlikable effects in the comparison).

The presented results show an increase of the secondary creep rates on MOX fuels compared to UO₂, mainly at low stresses (< 60 MPa); at higher stresses the creep rates of UO₂ and MOX fuels are of the same order of magnitude. The effect of Pu is not significant, whatever the stress.

Figure 13. Compressive test results at 1 535°C



A series of compression tests performed on pellets at different temperatures (range of stresses: 30-100 MPa) allowed to conclude that the activation energy of creep is higher for MOX fuels: the mean values are 501 kJ/mol and 402 kJ/mol for MOX and UO₂, respectively. These values are coherent with literature data [9].

Both results – higher rates at low and intermediate stresses and higher activation energy – are consistent with improved creep behaviour of MOX pellets as compared to UO₂.

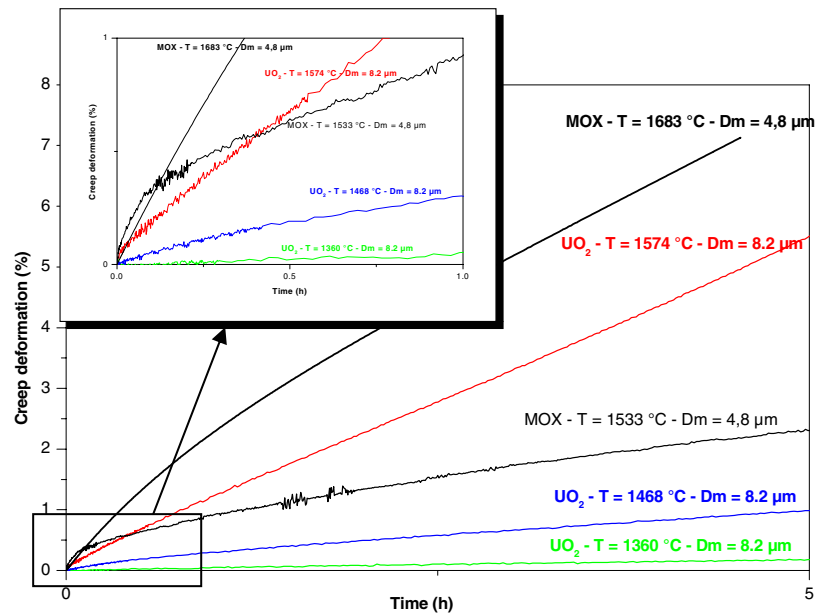
In addition, Figure 14 compares creep test results of MOX and UO₂ (industrial fabrications) under the following conditions:

- Applied stress = 40 MPa.
- UO₂ temperatures are 1 468°C and 1 360°C.
- MOX temperatures are 1 533°C and 1 683°C, i.e. 70°C, 170°C and 300°C more than UO₂.

These temperature levels are near those tested in the DEFORMOX 2 experiment during the 345 and 375 W/cm power plateaus. The differences in temperature between MOX and UO₂ surround those expected in the central volume of the pellets in PCI conditions for power levels in the range of two-cycle UO₂ threshold, as reported in the previous section.

This graph evidences the presence of a longer and higher primary creep in the case of the MOX fuel in spite of lower temperature and grain size. A comparison at similar temperature (1 533°C and 1 574°C for MOX and UO₂, respectively) of creep deformation during the first 30 minutes of tests shows a MOX deformation higher than that of UO₂ (for example, after 3 minutes, MOX deformation is higher by about a factor 2).

Figure 14. Comparison of creep test results on MOX and UO₂



This temperature level corresponds to the range encountered by the MOX pellets in the DEFORMOX 1 experiment, for which enhanced fuel creep was noticed. In addition, this phenomenon can play a role during the power rise under ramp conditions.

Indeed, temperature in the centre of the pellet becomes higher than 1 500°C for power superior to 350 W/cm. The volume of the pellet whose temperature is higher than 1 500°C, represents around 25% of the total volume, at the final power tested during the ZHT ramp test (450 W/cm).

Conclusion

This set of in-pile experiments performed under different conditions, tends to prove that MOX fuel creeps more than UO₂, and that the difference increases between beginning of life and two-cycle irradiation.

The difference at low burn-up is partly explained by the intrinsic properties of the material, even if the observed differences are slight:

- Existence of a larger primary creep stage.
- Higher creep rate at low and intermediate stresses ($\times 3.5$ at 40 MPa).

It is also partly explained by the temperature dependence of the creep phenomenon:

- Due to the lower thermal conductivity of the material, in the typical range of power of PCI conditions, the central volume of MOX pellet temperature is higher by 100°C.
- Due to a higher activation energy for MOX fuels as indicated by compression tests.

As concerns the amplification at higher burn-up of the differences between MOX and UO₂, two possible explanations can be proposed:

- The microstructural evolution of the MOX material with the restructuring of the Pu-rich areas, which leads to the apparition of porous aggregates. One can wonder if these areas act like big pores as assumed by some authors [10].
- The chemical evolution of the MOX material, due to the fact that Pu fissions are more oxidising, with a direct consequence on diffusion driven phenomena such as creep. However, even if the potential of oxygen of (U,Pu)O₂ is higher than those of UO₂, buffering by the fission product Mo and by the Zr clad [11] can impede the overall oxidising environment.

At the present time it is impossible to conclude as to the respective weights of the different mechanisms responsible for the amplification of MOX creep rates by burn-up, due to the lack of experimental data.

As-fabricated features of MOX, such as grain size, porosity or area fraction of the different phases are still studied through out-of-pile mechanical testing on calibrated microstructures. Identification of the parameters governing the fuel creep law is necessary to evaluate the influence of the respective mechanical properties of the matrix and the Pu clusters, and to quantify the effect of cluster shape, size or porosity evolution in each phase [12]. To this end, a very detailed characterisation of the Pu distribution in the matrix is required before as well as after irradiation. The development of specific microanalysis techniques [13] is promising to improve the knowledge of the impact of the fabrication process on the microstructure and thereafter, to understand the link between fresh fuel microstructure and its in-pile behaviour.

Acknowledgements

The authors would like to thank EDF and FRAMATOME ANP for their support of these research and development programmes, and especially S. Beguin, P. Blanpain and B. Julien for their contributions to this work. This paper is published by their kind permission. We also acknowledge all our colleagues involved in the fabrication, irradiation and examinations, who contributed to the success of these experimental programmes.

REFERENCES

- [1] Blanpain, P., *et al.*, “MOX Fuel Performance in the French PWRs: Status and Development”, *ANS International Topical Meeting on LWRs*, Park City (2000).
- [2] Blanpain, P., X. Thibault, J.P. Pages, “Recent Results from In-reactor MOX Fuel – Performance in France and Improvement Program”, *Proceedings of the ANS International Topical Meeting on LWR Fuel Performance*, Portland, Oregon (1997).
- [3] Brown, C., *et al.*, “Overview on MOX Fuel for LWRs: Design, Performances and Testing”, *IAEA Symposium on MOX Fuel Cycle Technologies for Medium and Long Term Deployment*, Vienna, Austria (1999).
- [4] Caillot, L., *et al.*, “Analytical Experiment on PWR Fuel Rods Carried Out in SILOE Reactor at CEA Grenoble”, *IAEA TCM on In-core Instrumentation in Connection with Fuel Behaviour*, Petten, Netherlands, October 1992.
- [5] Alberman, A., *et al.*, “Technique for Power Ramp Tests in the ISABELLE 1 Loop of the OSIRIS Reactor”, *Nuclear Engineering and Design*, 168, 293-303 (1997).
- [6] Nonon, C., *et al.*, “Impact of Fuel Microstructure on PCI Behaviour”, *Proceedings of the IAEA TCM on Improved Fuel Materials and Designs*, Brussels, Belgium (2003).
- [7] Bohaboy, P.E., S.K. Evans, “Compressive Creep Properties of UO₂-PuO₂ Compounds”, *Plutonium and Other Actinides* (1970).
- [8] Routbort, J.L., N.A. Javed, “Compressive Creep of Mixed Oxide Fuel Pellets”, *Journal of Nuclear Materials*, 44, 247-259 (1972).
- [9] Huet, F., “Contribution à l’étude du frittage des oxides mixtes d’Uranium et de Plutonium surtoechnométriques (U_{1-y},Pu_y)O_{2+x}”, Thesis.
- [10] Dienst, W., “Irradiation Induced Creep of Ceramic Nuclear Fuels”, *Journal of Nuclear Materials*, Vol. 65 (1977).
- [11] Matzke, H.J., “Oxygen Potential Measurements in High Burn-up LWR UO₂ Fuel”, *Journal of Nuclear Materials*, 223, 1-5 (1995).
- [12] Roussette, S., *et al.*, “Computational Analysis of Non-linear Structures – Application to MOX Fuel”, *International Seminar on Pellet-clad Interaction in Water Reactor Fuels*, March 2004.
- [13] Oudinet, G., *et al.*, “On the Characterization of Plutonium Distribution in MIMAS MOX by Image Analysis”, *Proceedings of the IAEA TCM on Improved Fuel Materials and Designs*, Brussels, Belgium (2003).

MECHANICAL CHARACTERISATION OF IRRADIATED FUEL MATERIALS WITH LOCAL ULTRASONIC METHODS

D. Baron,¹ D. Laux,² G. Despaux²

¹EDF/DER, Division Recherches et Développement, 77250 Moret/Loing, France

²LAIN, Université Montpellier 2, 34095 Montpellier Cedex 05, France

Abstract

Simulation codes used to predict the nuclear fuel rods' thermo-mechanical behaviour in PWR at base irradiation or under transient operating conditions must be provided with the correct local elastic properties of the fuel. As for the other material properties, the elastic constants are evolving as well with the local burn-up and the physico-chemical material evolution. Therefore, the challenge over the last six years was to find the means to experimentally assess these characteristics on irradiated fuel samples. If classical mechanical testing methods are available for non-irradiated fuel, they become inoperative on irradiated materials because of the pellet cracking and the steep radial temperature gradient and fission density gradient, which lead to a radial gradient in the evolution of the material properties. Since 1996, part of our activity has been focused on the local assessment of mechanical properties with micro-acoustic and micro-indentation methods [1-4]. In this paper, the state of the art of the micro-acoustic methods will be presented.

Introduction

The nuclear fuel evolves in-pile on many scales and its physico-chemical state is modified (fission products in substitution, evolution of oxygen sub-lattice, creation of metallic or ceramic precipitates, lattice defects, porosity, fractures...). If, for non-irradiated pellets, ultrasonic waves are only sensitive to the porosity volume fraction, it is different for irradiated fuel as all the parameters previously enumerated are expected to have an influence of more or less importance. Consequently, the effect of each parameter on ultrasonic waves should be quantified. As such a study would not be realistic, we have simplified the process by dividing the effects into five major groups: porosity, grain size, O/M ratio, dissolved fission products, metallic and ceramic precipitates.

A device easy to operate is now functional in the ITU hot cells; preliminary data has been acquired on irradiated fuel samples at different burn-ups. Recent improvements allow identifying the specific behaviour of the thin rim region in the pellet. Acoustic signatures are performed with ceramographic sampling, and acoustic images can also provide accurate indications of the sub-surface state (cracks and pores).

Assessment of the elastic constants from ultrasonic wave propagation velocities

Elastic moduli (Young's and shear modulus) and Poisson's ratio of an isotropic sample such as a sintered UO₂ body can be calculated from the knowledge of two measured ultrasonic velocities, using the following Eqs. (1) and (2) [5]:

$$E = \rho \cdot V_t^2 \frac{3V_l^2 - 4V_t^2}{V_l^2 - V_t^2}; G = \rho V_t^2 \quad (1)$$

$$\sigma = \frac{E - 2G}{2G} \quad (2)$$

In these expressions ρ (Kg.m⁻³) is the density, E (GPa) the Young modulus, G (GPa) the shear modulus, σ the Poisson's ratio and V_t and V_l the transverse and longitudinal velocities of the ultrasonic waves in the material.

In addition to the longitudinal and transverse bulk waves, the theory of elastic sound propagation in solids shows that surface waves can also propagate under some special conditions. The most well known of these surface waves is the Rayleigh wave. Its velocity (V_r) is related to V_l and V_t with the following Eq. (3) called Viktorov's formula [6]:

$$V_r = \frac{0.715 - 0.995 \left(\frac{V_t}{V_l} \right)^2}{0.75 - \left(\frac{V_t}{V_l} \right)^2} V_t \quad (3)$$

V_l and V_r are determined experimentally and V_t is derived from Eq. (3). The traditional and new acoustic methods employed to measure V_l and V_r are described below. The experimental device now introduced in ITU-Hot Cell in Karlsruhe is also presented.

Ultrasonic techniques

Acoustic microscopy (acoustic signature mode)

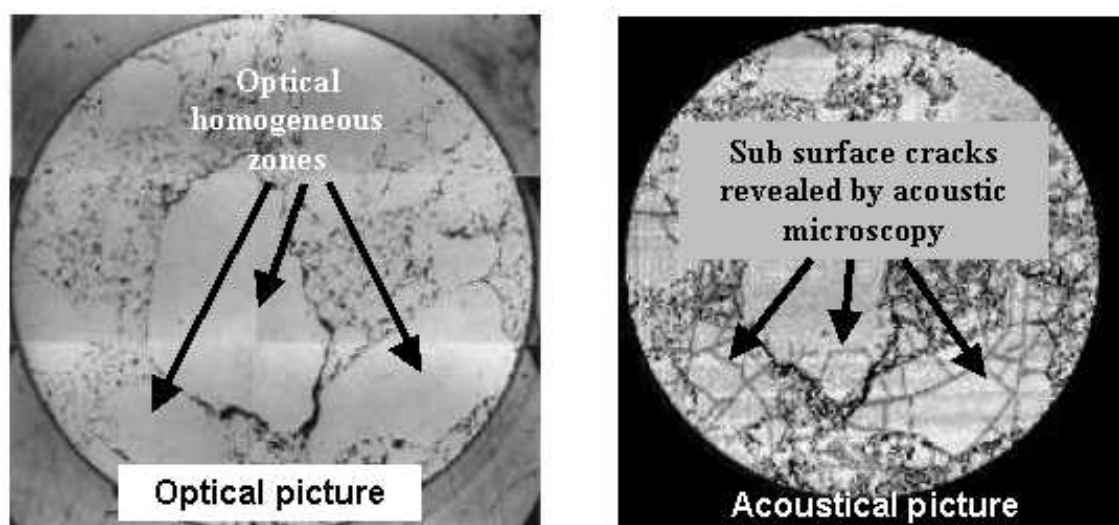
Different information can be obtained by this technique from the mechanical properties of the sample [7]. Acoustical pictures are acquired with an x-y scan performed on the sample with a spherical focused ultrasonic transducer. They give the variations of the coefficient of reflection, which is a function of the density and the ultrasonic waves' velocity. If the sensor is defocused, i.e. focused at given plane below the sample surface, sub-surface structures such as, micro-cracks pores, precipitates, etc. can be visualised. An example of this kind of acoustic image is presented in Figure 1. Although acoustical pictures provide only qualitative information, quantitative results can be obtained with the acoustic signature called $V(z)$. In this operating mode, the spherical ultrasonic transducer is gradually defocused towards the sample surface. Interferences between surface waves and the specular ray create the pseudo-periodic signal $V(z)$. From the theoretical point of view, three pseudo periods exist in the acoustic signature: the first is created by the longitudinal surface wave, the second by the transverse surface wave and the third by the Rayleigh wave. But, in most cases and especially in UO_2 only the periodicity (Δ_z) due to the Rayleigh wave is discernible. Then the Rayleigh wave velocity is calculated with the relation:

$$V_r = \frac{V_{cf}}{\sqrt{1 - \left(1 - \frac{V_{cf}}{2F\Delta_z}\right)^2}} \quad (4)$$

where V_{cf} is the velocity in the coupling fluid present between the sample and the sensor and F (MHz) is the ultrasonic wave frequency. The latter governs the size of the investigated area on the sample; the higher the frequency, the smaller the zone size. In this work two frequencies were used: 15 and 140 MHz. The sizes of the zones analysed are $1 \times 1 \text{ mm}^2$ and $150 \times 150 \mu\text{m}^2$, respectively. For irradiated UO_2 , because of attenuation, 200 MHz seems to be the highest utilisable frequency, leading to minimum probe size of approximately $30 \times 30 \mu\text{m}^2$.

Figure 1. Acoustical visualisation of cracks on a 195 GWd/tM SIMFUEL

Size (1 cm × 1 cm)



Echography in reflexion/transmission mode

Difficulties to measure the longitudinal wave velocity can be overcome with micro-echography. Even if echography is well known in non-destructive testing, it is usually performed on a large zone, in reflection mode. In this configuration, the time interval (Δt) between echoes reflected on the two parallel faces of the sample is measured. Then, if the thickness of the sample (d) is known, the longitudinal velocity can be calculated with the relation:

$$V_1 = \frac{2d}{\Delta t} \quad (5)$$

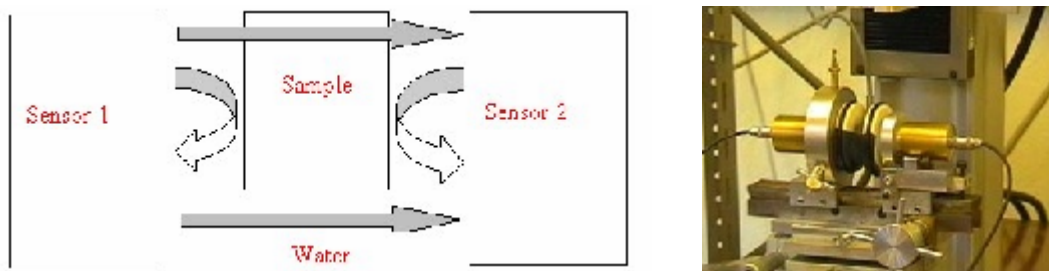
On irradiated UO_2 samples, operating in this mode is difficult because the ultrasonic waves have to propagate a distance “ $2d$ ” through the sample, and due to interaction with porosity and irradiation defects the signal becomes very attenuated. Furthermore, knowing precisely “ d ” is almost impossible in fractured pellets. Nevertheless, using the method of micro-echography in transmission-reflection mode [3], where measurements with two opposed sensors on plane-parallel cut samples are performed, the distance “ d ” can be accurately measured as the ultrasonic waves can only propagate on a length “ d ” across the sample. A scheme of the experimental device used for this purpose is given in Figure 2. Calling 1 the ultrasonic wave that travels through the water, 2 the ultrasonic wave that travels through the sample, and 3 and 4 the signals that are reflected from the sample surface toward the sensors, d and V_1 are calculated as follows, where Δt_{ij} is the time interval between signals i and j :

$$d = \frac{V_{cf} (\Delta t_{13} + \Delta t_{14})}{2} \quad (6)$$

$$V_1 = \frac{d \cdot V_{cf}}{d - \Delta t_{12} \cdot V_{cf}} \quad (7)$$

The operating frequency in this kind of experiment is about 40 MHz and the analysed zone size on the sample is $500 \times 500 \mu m^2$.

Figure 2. Micro-echography in transmission/reflection mode



As using micro-echography is quite difficult in hot cell, we have recently demonstrated [8] that the elastic moduli could be measured with V_R only as follows, with a rather good approximation:

$$E \approx 3\rho V_R^2 \quad (8)$$

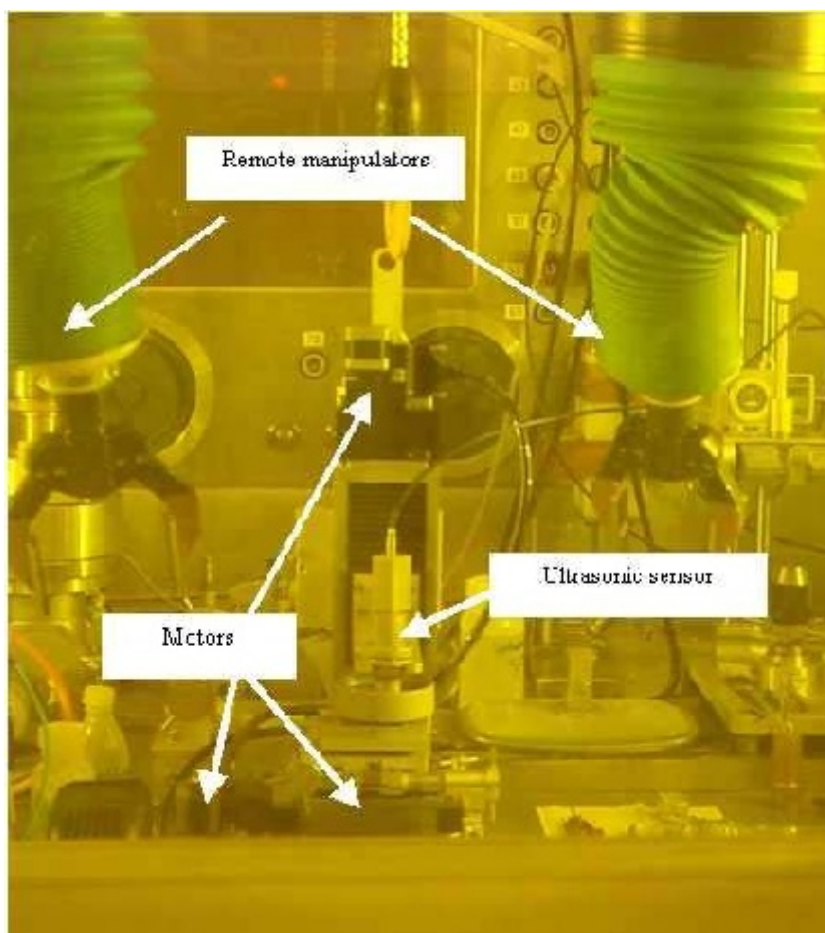
$$G \approx 1.162\rho V_R^2 \quad (9)$$

These relations are very important when the samples are embedded. Indeed, in this case, performing micro-echographic experiments is impossible.

Experimental device introduced in hot cell

The acoustic microscope introduced in an ITU hot cell is able to work both in acoustic microscopy and in micro-echographic mode. All the mechanical parts have been designed to be remote controlled by manipulators. A photograph of the device operating in the acoustic signature mode (acoustic microscope) is presented in Figure 3.

Figure 3. Experimental device introduced in hot cell



UO₂ physico-chemical parameters investigation by acoustic waves

Effect of porosity on the elastic properties of UO₂ in the range 1-20%

The laws already developed by ROQUE for elastic wave propagation (V_1) in UO₂ in the porosity range 1-7% [2-3] have been extended here to cover the range 10-20%. Such an extension was required for the study of highly porous zones in restructured high burn-up fuels, as for instance the so-called "rim". Five batches of samples were especially manufactured with relative porosity volumes of 10.1%, 12.08%, 12.33%, 14.81% and 20.04%. The porosity was determined by immersion density performed by SICN who manufactured the samples, with an accuracy of 0.1%. For each batch, twenty (V_1, V_T) measurements were performed on five different pellets. Moreover, in acoustic signature mode, three ultrasonic frequencies (15, 50, 140 MHz) were used. However, no significant variation was observed on

the Rayleigh wave velocity as a function of frequency. Furthermore, as mentioned in the introduction, no important attenuation occurred, even on highly porous samples. That is the reason why an increase in operating frequency should be possible on irradiated fuel, e.g. 200 MHz in $V(z)$ and 100 MHz in micro-echography mode, in order to assess more local characterisations. According to Mukhopadhyay and Phani [9] the longitudinal wave velocity can be fitted by laws such as $V_l = V_{l0}(1 - ap)^b$ where a , b and V_{l0} have to be tuned on experimental data. Hence, for the evolution of the longitudinal velocity versus porosity, we propose the following laws in Eqs. (9a) and (9b), where p is the porosity volume fraction, which resulted from the fitting of the experimental values plotted in Figure 4(a):

$$V_l = 5465.(1 - 2.05p)^{\frac{2}{3}} \quad (9a)$$

$$\text{or } V_l \approx 5465.(1 - 1.37p - 0.47p^2) \text{ for small values of } p \quad (9b)$$

Figure 4(a). V_l measurements on high porous UO_2

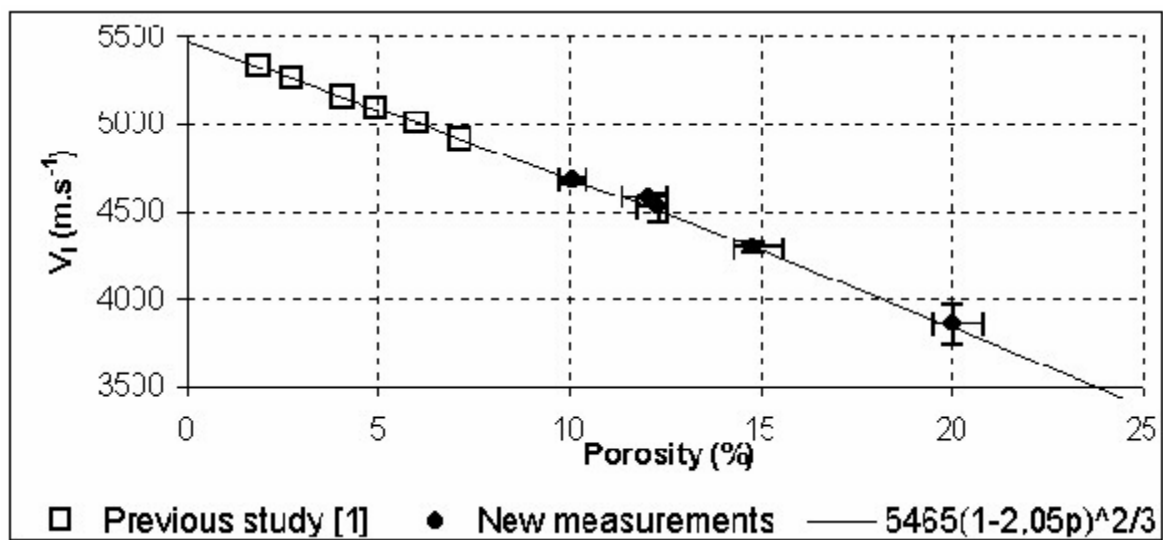
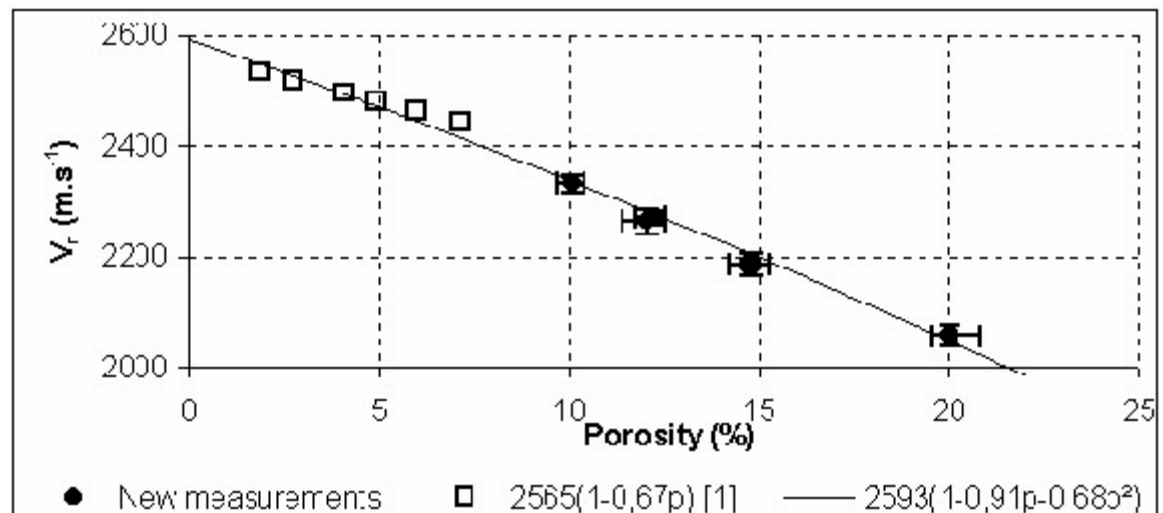


Figure 4(b). V_r measurements on high porous UO_2



Concerning the Rayleigh wave velocity measurements, presented in Figure 4(b), the best fit is given by the polynomial expression:

$$V_r = 2593.(1 - 0.91p - 0.68p^2) \quad (10)$$

Then, according to the evolution of the density given by $\rho = 10960(1-p)$,* E, G and ν can be calculated via Eqs. (1) and (2). Depending on material, many formulas can be proposed to fit the experimental data [10]. On our porous UO_2 , the best polynomial fits are given by the following relations in Eqs. (11), (12) and (13):

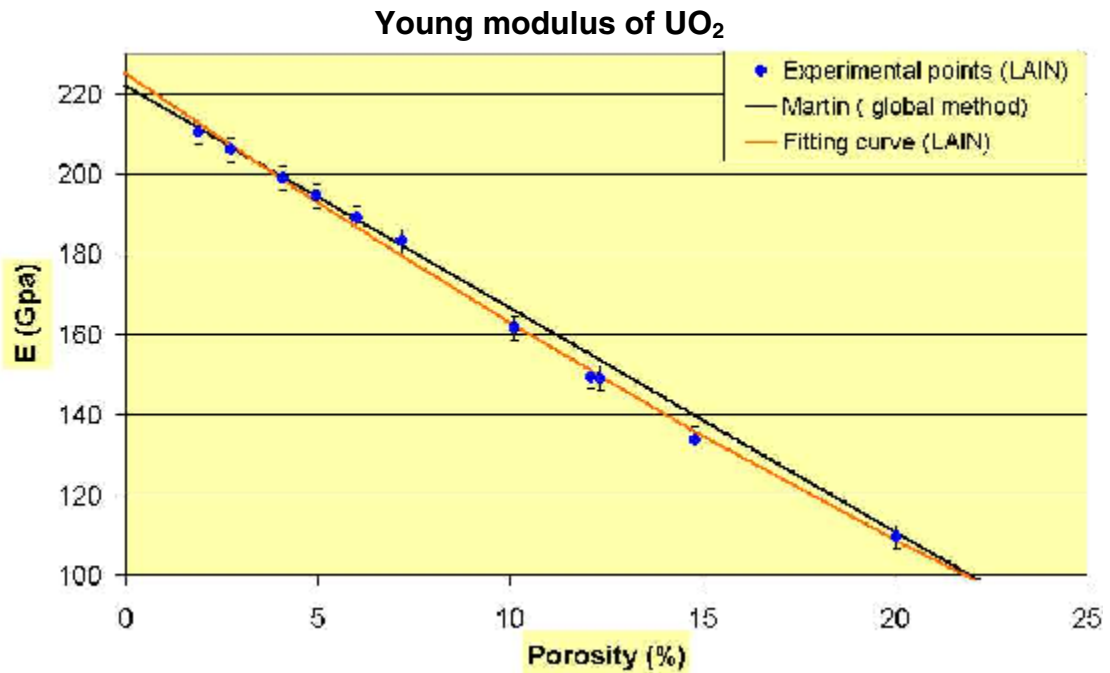
$$E = 225.(1 - 2.94p + 1.79p^2) \quad (11)$$

$$G = 84.9.(1 - 2.76p + 1.62p^2) \quad (12)$$

$$\nu = 0.325.(1 - 0.64p - 2.39p^2) \quad (13)$$

Figure 5 shows the evolution of the elastic modulus with the average porosity volume.

Figure 5. Porosity effect on the fuel elastic modulus at room temperature



However, it should be kept in mind that this kind of relation with porosity is also a function of the pore shape and pressurisation. In the present case, the relation obtained is consistent with a low pressurised lenticular porosity with a b/a ratio around 0.3. For high burn-up fuel, in the rim region one should have to account eventually for more spherically shaped and pressurised pores. In order to account for different kinds of pore shapes, a theoretical approach based on a multi-scaled homogenisation

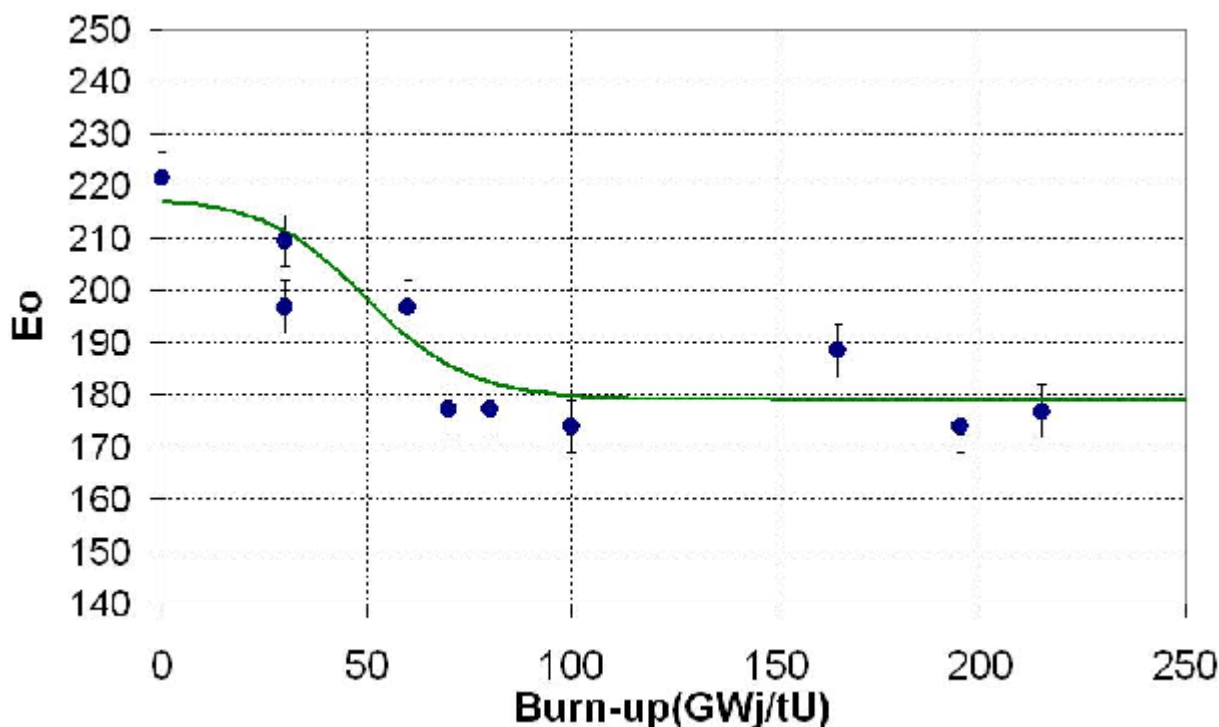
* Remark 1: The samples have been manufactured with depleted UO_2 powders with 0.3% ^{235}U enrichment. The theoretical density is then $10\,960\text{kg/m}^3$. Obviously, this value depends upon the ^{235}U enrichment. Remark 2: For irradiated UO_2 , the theoretical density evolves; the right value must be then used.

methodology can be employed [16]. In the pellet centre, it is again different because most of the porosity is likely to be at grain boundaries, low pressurised and mainly lenticular shaped. Therefore the theoretical approach is necessary in order to adapt these correlations for each local condition.

Effect of fission products (SIMFUEL)

In order to analyse out-of-pile the effect of high burn-up rates on the elastic properties of UO_2 , simulated fuels manufactured at ITU and AECL (SIMFUEL) have been investigated. The simulated fuel samples prepared at ITU were produced by mixing solid “fission product” species with an UO_2 powder followed by pressing and sintering, for contents representative of burn-ups ranging from 30 to 215 GWd/tM. Such samples allow isolating the effect of the fission products in solution from the other burn-up effects (densification, swelling, irradiation damage, evolution of the oxygen potential, etc). The AECL (SIMFUEL) sample corresponded to a burn-up of 3% (~25 GWd/tM). It belonged to a SIMFUEL fabrication series utilised at ITU for physico-chemical measurements, particularly for thermal conductivity determinations (courtesy Hj. Matzke). Its preparation details and characterisation can be found in [11]. The simulated fuel samples were stoichiometric, with a relative porosity volume ranging between 2-4%. The values E_0 (extrapolated to 0% porosity) are reported in Figure 6. This trend indicates a quick variation of E_0 due to the addition of fission products in low content and then a kind of stabilisation for higher content likely due to formation of precipitates which are known to act more on the attenuation of the wave than on the velocity itself. However, discrepancy is observed certainly related to non-homogeneity of the samples used and also a large network of micro-cracks. Nevertheless, thanks to the high spatial resolution of our methods, it has been possible to focus the characterisation on the non-cracked areas (Figure 1). We plan to manufacture improved SIMFUEL samples in the near future in order to obtain more accuracy on this calibration.

Figure 6. Young’s modulus (GPa) reduced to 0% porosity on SIMFUEL provided by TUI



In conclusion, from SIMFUEL acquisitions, it appears that the effects of burn-up on the Young's modulus is concentrated in the small and mean burn-up range, i.e. for values ≤ 50 GWd/tM. In this range, a decrease in E of 20-30 GPa (i.e. 10-15% relative) would be taken into account. Above this burn-up range, the extra decrease appears very small (or even negligible) compared to the effect of a porosity change presented previously in this paper.

Study of irradiated pellets

In order to evaluate the capability of the technique on irradiated materials, the device has been installed by ITU in the hot cells and measurements have been performed on two kinds of samples:

- Two pellet samples extracted from a BR3 standard CEA-FRAMATOME fuel rod, irradiated up to 56.1 GWd/tM rod average burn-up with two average pellet burn-ups, 68 and 30 GWd/tM, respectively. No extensive rim formation has been observed on the highest burn-up pellet.
- Fuel discs pieces kindly provided by the HBRP (High Burn-up Rim Project [17-22]) members with burn-up ranging from 35 to 100 GWd/tM. These fuel wafers experienced different temperatures, representative of different radial locations in a standard pellet. Samples irradiated at the lowest temperature have experienced an extensive fuel transformation with a well established rim structure.

BR3 fuel rod

We present here the measurements performed on the samples extracted from the N118 fuel rod irradiated in the BR3 reactor, similar to a standard PWR design, but one meter long. Initial enrichment was 8.6% ^{235}U and the average radial burn-up of the cross-section used was 68 and 30 GWd/tU. Average initial grain size is 20 μm . The maximum burn-up at the pellet edge was evaluated around 110 GWd/tU. During the first irradiation period the maximum linear rate was nearly 300 W/cm. For the second half of life, the average linear power rate was representative of a standard PWR rod, not higher than 200 W/cm. Even if xenon depletion was observed in the very periphery of the fuel and pores started to build up in the rim region, very little fuel restructuring was observed. This was previously reported by Spino, *et al.* [12] in the JNM. The fuel average density at this burn-up was measured, giving a value of $9.907 \text{ g/cm}^3 \pm 0.2\%$.

- This sample prepared for ceramography observations in the ITU hot cells was studied both by acoustic and optical microscopy. A large 140 MHz picture of the whole pellet is presented in Figure 7. This picture reveals three concentric zones corresponding to three zones where the pores' morphology is different (Figure 7).

Cross-acoustic measurements were performed on fuel pellets, and corresponding elastic moduli deduced from the acoustic wave velocities were recorded. A porosity correction was applied, accounting for the different pore shapes depending upon the origin of the pores (fabrication or pore gas build-up). For the pore shape effect, simplified correlations were obtained from theoretical calculations [16]. Plotting this data reduced to 0% porosity on Figure 8, consistent with the SIMFUEL data previously presented. We evaluated the overall uncertainties, accounting mainly for the uncertainties on local fuel density and porosity. The larger discrepancy is due to the difficulty to assess the local characterisation of the density. However, it will be shown hereafter that there is also a local temperature effect.

Figure 7. Acoustical picture of a N118 BR3 pellet

Porosity evaluation

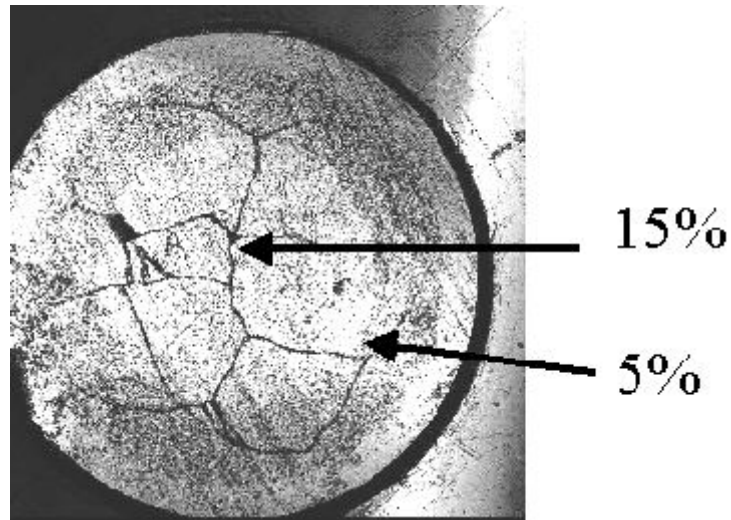
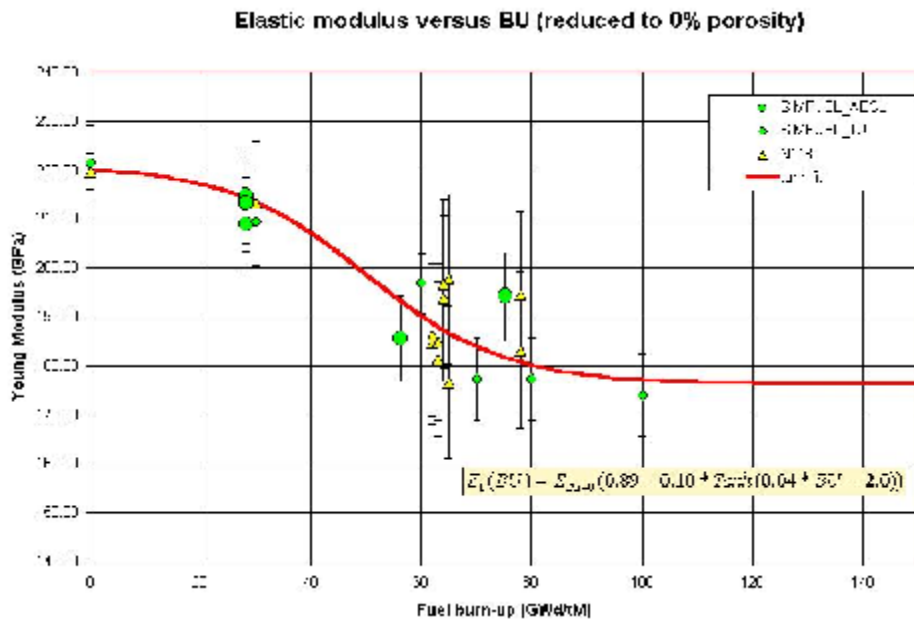


Figure 8. Young's modulus (GPa) extrapolated to 0% porosity measured on SIMFUEL and data from a BR3 N118 fuel rod



HBRP samples

We then performed acoustic measurements on HBRP samples provided by the HBRP members and available in the ITU hot cells. The interest of these samples is that they have been irradiated at relatively constant temperature and with a limited temperature gradient. They are thus more representative of the different radius positions in a standard fuel pellet:

About 450 (rod 1), 750 (rod 2), 950 (rod 3) and 1150 °C (rod 4)

Moreover, the density and porosity characterisations are for these samples very accurate, reducing the overall uncertainties as well. This data set is also consistent with the SIMFUEL data. However, some plots depart from the overall trends. At this stage, it seems that a restoration is obtained for samples having experienced a fuel restructuring, or for samples having experienced the highest temperatures thus allowing the restoration of the irradiation defects. This particular data set is not presented in Figure 8, but will be published at a later date.

The overall trend of the data presented here can be approached by the following formulation:

$$E_1(\text{BU}) = E_{\text{Bu}=0} (0.89 - 0.10 * \text{Tanh}(0.04 * \text{BU} - 2.0)) \quad (14)$$

Conclusions

The acoustic methods developed and presented here already allow a quite accurate assessment of the local elastic properties in an irradiated fuel pellet, as long as the local density is well characterised. The volume of the zone analysed is related to the wave frequency (wave length) used. At present, 140 MHz sensors are used, which gives a wave length around 10 μm .

In order to further improve the methodology, and use it as an alternative device for local porosity measurements, the influence of the main parameters evolving in the fuel matrix during irradiation must be more accurately determined. To this end, a collaboration is underway among ITU, Montpellier University, CEA and EDF/R&D division.

To date, the influence of physical-chemical parameters on the elastic constants of pure UO_2 and simulated fuels has been partly investigated with local acoustic methods. It is planned to enlarge the reference database. The state of the art is as follows:

- The effect of the porosity is well established up to 20% for as-manufactured standard porosity. The slopes obtained are consistent with lenticular shaped pores with a a/b ratio of around 0.3. Theoretical support will allow accounting for an evolution of the pore shape during irradiation. The laws established in Eqs. (11) and (12) with our local ultrasonic method are in good agreement with the evolution of the elastic constants obtained with classic global methods [14]. Furthermore, the values obtained for E and G at 0% porosity are similar to those recommended by Martin [15]: respectively 225 (vs. 223 GPa in [15]) and 84.9 (vs. 84 GPa in [15]).
- The effect of a modification of the oxygen sublattice combined with the effect of additives in solution has also been analysed. The overall burn-up effect can be roughly represented by the following formulation:

$$E_1(\text{BU}) = E_{\text{Bu}=0} (0.89 - 0.10 * \text{Tanh}(0.04 * \text{BU} - 2.0))$$

Nevertheless, recovering effects due to local operating temperature or local fuel restructuring have also been observed. The database has to be enlarged to improve comprehension.

As concerns the overall trend, however, some controversies have appeared, depending on the methodology used. Pujol, *et al.* [23] using synchrotron diffraction under high pressure, has obtained a different conclusion about the burn-up effect, showing an overall increase of the elastic modulus. Analysing more accurately the equivalent samples, it looks like a translation of the data with amplitude increasing with the burn-up. This discrepancy must be clarified. Acoustic is performed with a minimum

perturbation of the material. For the other methodologies, a very high perturbation is induced. For a high physical and chemical material modification, inducing high residual stresses it seems that notions of elasticity and rigidity have to be clarified, mainly when performing under disproportional compressive stresses regarding the standard operating conditions in an industrial fuel (lower than 1 GPa).

Acknowledgements

The authors acknowledge M. Schreiber and M. Rousseau of ITU for their useful help to obtain the apparatus installed and operative in the ITU hot cells and for preparing the samples used in this study. They also acknowledge Dr. J-M. Gatt for the useful discussions about the porosity effect on the fuel mechanical properties, Dr. M. Kinoshita and the HBRP members for providing rare and precious samples for this work.

REFERENCES

- [1] Baron, D., S. Leclercq, J. Spino, S. Taheri, "Development of a Microindentation Technique to Determine the Fuel Mechanical Behaviour at High Burn-up", *IAEA TCM on Advances in Pellet Technology for Improved Performance at High Burn-up*, Tokyo, Japan, 28 Oct.-1 Nov. 1996, paper 6.6.
- [2] Roque, V., B. Cros, D. Baron, P. Dehaut, "Effect of the Porosity in Uranium Dioxide on Microacoustic and Elastic Properties", *J. Nuclear Materials*, 277, 211-216 (2000).
- [3] Cros, B., D. Baron, V. Roque, "Microacoustic Techniques to Assess Local Characteristics of Irradiated Fuel Materials", *6th International Conference on CANDU Fuel*, Niagra Falls, Canada, 26-30 Sept. 1999.
- [4] Laux, D., B. Cros, G. Despaux, D. Baron, "Ultrasonic Study of UO₂: Effect of Porosity and Grain Size on Ultrasonic Attenuations and Velocities", submitted to *J. Nuclear Materials*.
- [5] Kino, G.S., *Acoustic Waves*, Prentice-Hall, Inc., New Jersey (1987).
- [6] Viktorov, I.A., *Rayleigh and Lamb Waves*, Plenum, New York (1967).
- [7] Briggs, A., "Acoustic Microscopy", Clarendon, Oxford (1992).
- [8] Laux, D., G. Despaux, D. Baron, "Application des méthodes micro-acoustiques à la caractérisation des propriétés locales du combustible irradié", *Congrès Matériaux 2002*, Tours, France, poster presented in October 2002.
- [9] Mukhopadhyay, A.K., K.K. Phani, "An Analysis of Microstructural Parameters in the Minimum Contact Area Model for Ultrasonic Velocity-porosity Relations", *J. European Ceramic Society*, 20, 29-38 (2000).

- [10] Boccaccini, A.R., Z. Fan, “A New Approach for the Young’s Modulus-Porosity Correlation of Ceramics Materials”, *Ceramics International*, 23, 239-245 (1997).
- [11] Lucuta, P.G., R.A. Varral, Hj. Matzke, B.J. Balmer, “Microstructural Features of SIMFUEL Simulated High Burn-up UO₂-based Nuclear Fuel”, *J. Nuclear Materials*, 178, 48-60 (1991).
- [12] Spino, J., D. Baron, M. Coqurelle, A.D. Stalios, *J. Nucl. Mater.*, 256, 189 (1998).
- [13] Laux, D., “Caractérisation mécanique de combustibles nucléaires à fort taux de combustion par méthodes micro-acoustiques”, PhD thesis presented in Montpellier, France, 18 October 2002.
- [14] Panakkal, J.P., “Use of the Longitudinal Ultrasonic Velocity as a Predictor of Elastic Moduli and Density of Sintered Uranium Dioxide”, *IEEE Transactions on Ultrasonics, Ferroelectrics and Frequency Control*, Vol. 38, No. 3, May 1991.
- [15] Martin, D.G., *High Temperatures – High Pressures*, Vol. 21, pp. 13-24 (1989).
- [16] Colin, C., “Étude du Fluage du Dioxyde d’Uranium, Caractérisation par des essais de flexion et modélisation mécanique”, PhD thesis, Ecole Nationale Supérieure des Mines de Paris, France, 23 September 2003.
- [17] Kinoshita, M., S. Kitajima, T. Kameyama, T. Matsumura, E. Kolstad, Hj. Matzke, “High Burn-up Rim Project, Progress of Irradiation and Preliminary Analysis”, *ANS Topical Meeting on LWR Fuel Performance*, Portland, Oregon, March 1997.
- [18] Kinoshita, M., T. Matsumura, T. Kameyama, S. Kitajima, E. Kolstad, Hj. Matzke, “High Burn-up Rim Project, Irradiation Program to Study Rim Structure Formation, Outline and Preliminary Analysis”, *EHPG Meeting*, Bolkesjø, 31 Oct.-4 Nov. 1994.
- [19] Kinoshita, M., “High Burn-up Rim Project, (II) Progress of Irradiation and Preliminary Analysis”, *Proceedings of Enlarged HPG Meeting*, Loen, Norway, 19-24 May 1996, HPR-347, OECD Halden Reactor Project.
- [20] Kitajima, S., M. Kinoshita and Hj. Matzke, “High Burn-up Rim Project (III), Examinations to Verify Attainment of the Target Irradiation Conditions”, *EHPG Meeting* (1998).
- [21] Sonoda, T., Hj. Matzke and M. Kinoshita, “Threshold Burn-up of Rim Structure Formation”, *HRP Enlarged Meeting*, Loen, Norway (1999).
- [22] Kinoshita, M., E. Kolstad, Hj. Matzke, “Completed Scope and Needs for Further Study”, *HRP Enlarged Meeting*, Lillehammer, March 2001.
- [23] Pujol, M-C., M. Idiri, L. Havela, S. Heathman, J. Spino, “Bulk and Young’s Modulus of Doped UO₂ by Synchrotron Diffraction Under Pressure and Knoop Indentation”, *JNM*, 324, 189-197 (2004).

SESSION II

Fuel Material Behaviour in PCI Situation (Part 2)

Chairs: M. Billaux, Y. Guérin

FUEL SWELLING IMPORTANCE IN PCI MECHANISTIC MODELLING

Dr. V. Ioan Arimescu
FRAMATOME ANP, Inc
Methods Development Department, Fuel Analysis Methods
Richland, USA

Abstract

Under certain conditions, fuel pellet swelling is the most important factor in determining the intensity of the pellet-to-cladding mechanical interaction (PCMI). This is especially true during power ramps, which lead to a temperature increase to a higher terminal plateau that is maintained for hours. The time-dependent gaseous swelling is proportional to temperature and is also enhanced by the increased gas atom migration to the grain boundary during the power ramp.

On the other hand, gaseous swelling is inhibited by a compressive hydrostatic stress in the pellet. Therefore, PCMI is the net result of combining gaseous swelling and pellet thermal expansion with the opposing feedback from the cladding mechanical reaction.

The coupling of the thermal and mechanical processes, mentioned above, with various feedback loops is best simulated by a mechanistic fuel code. This paper discusses a mechanistic swelling model that is coupled with a fission gas release model as well as a mechanical model of the fuel pellet. The role of fuel swelling is demonstrated for typical power ramps at different burn-ups. Also, fuel swelling plays a significant role in avoiding the thermal instability for larger gap fuel rods, by limiting the potentially exponentially increasing gap due to the positive feedback loop effect of increasing fission gas release and the associated over-pressure inside the cladding.

Introduction

Analysis of fuel behaviour during normal operating conditions in the reactor is only possible through the use of computer models. This is due to the complexity of the fuel rod system, characterised by a non-linear response and the multitude of first-order phenomena taking place simultaneously and interacting with each other through several important feedback loops. It is impossible to decouple the different thermal and mechanical processes to describe the thermal-mechanical behaviour of the fuel rod. Neglecting the positive or negative feedback loops would considerably limit the range of applicability of the overall code. Also, it is highly desirable to develop mechanistic models of various processes so that with adequate calibration/validation the code can be confidently applied both within and outside the calibration domain.

The focus of the present paper is one of the important generic fuel processes, namely gaseous swelling of fuels of any type. As will become clear from the description of the modelling below, fuel gaseous swelling is at the core of the thermal-mechanical feedback loops. It is affected by temperature and grain growth, fission gas atom diffusion inside the grain and by the pellet stress state as dictated by the pellet-to-cladding mechanical interaction (PCMI). In turn, fuel gaseous swelling influences PCMI by causing pellet outward deformation and fuel temperature by changing fuel porosity and the venting of fission gas atoms to the open voidage.

The mechanistic gaseous swelling model described here is part of a best-estimate, mechanistic fuel behaviour code, RODEX4, which was recently developed in-house. RODEX4 includes detailed mechanistic models for both mechanical (developed in SIERRA [1]) and thermal fuel analyses. The fuel pellet mechanical model calculates the stress/strain patterns in the fuel pellet taking into account pellet creep and swelling/densification alongside elastic-thermal deformation in a modified quasi 3-D axisymmetric model. Dish filling and radial cracking are modelled both as instantaneous and permanent deformations. The thermal behaviour is modelled using a thermal conductivity model, which accounts for burn-up degradation and porosity effects as dependent on temperature, based on the most recent data and analyses. The gaseous swelling model is an integral part of the fission gas release model, which was developed and implemented in RODEX4 by the author.

Fuel gaseous swelling model

According to the majority of experimental and theoretical studies, the main contribution to gaseous swelling during irradiation comes from the intergranular bubbles. This is because the grain boundary fission gas bubbles are larger than the submicronic intragranular bubbles.

The grain boundary bubbles are lenticular (i.e. spherical caps, as a result of the difference between free surface and grain boundary surface energies) with an average radius in the grain boundary plane, r_b , and thus their volume can be calculated as:

$$V_{\text{bub}} = C_{\text{lent}} 4\pi r_b^3 / 3 \quad (1)$$

with $C_{\text{lent}} \sim 0.31$, to account for the lenticular shape of the grain boundary bubbles.

The gas pressure inside the bubbles is equilibrated by surface tension, γ , and the hydrostatic stress, σ , in the matrix. However, there are indications that the bubbles are over-pressurised, such that an allowance is made for this, as described in the following relation:

$$p_{\text{gas}} = 2\gamma/r_b + \sigma + p_{\text{ext}} \quad (2)$$

The model simplifies the size distribution of the intergranular bubbles and the initial nucleation process by assuming a given surface density of grain boundary bubbles, N_{gb} . Then the intergranular gaseous swelling, GBSWELL, can be calculated as:

$$GBSWELL = N_{gb} V_{bub} (\text{area}_{GB}/\text{vol}_{GB}) = N_{gb} V_{bub} (3/d_{gr}) \quad (3)$$

where d_{gr} is the grain diameter.

The grain boundary bubbles will grow until an effective coverage, f_{cov} , of the grain boundary surface is achieved. This is assumed to occur in a lattice where each bubble is associated with a square with the side equal to maximum bubble diameter, so that the relation linking the intergranular bubble surface density and bubble maximum radius is:

$$N_{gb} 4r_{bmax}^2 = f_{cov} \quad (4)$$

Then, the calculation of the current grain boundary swelling is dependent on the current grain boundary bubble radius as can be seen from Eq. (1). The grain boundary bubble radius is estimated by calculating the fission gas atom inventory of all grain boundary bubbles and equating it to the given gas atom flux from the grain interior by all transport mechanisms, as calculated in the fission gas release model:

$$\text{Number of fission gas atoms arrived at the grain boundary} = N_{gb} V_{bub} p_{gas}/(kT) \quad (5)$$

After replacing in the above relation V_{bub} from Eq. (1), p_{gas} from Eq. (2), this Eq. (5) becomes a third-order equation in r_b which can be solved analytically. Once r_b is calculated, the grain boundary swelling can be obtained from Eq. (5).

The feedback to the fission gas release model is achieved through the saturation fission gas atom concentration on the grain boundary. This is the value of the grain boundary inventory when r_b reaches the maximum value r_{bmax} :

$$C_{sat} = N_{gb} V_{bubmax} p_{gas}/(kT) \quad (6)$$

This is used in the fission gas release model as a condition for venting to the grain edge tunnels and the ensuing venting to the internal rod volume.

Example of gaseous swelling during power ramps at high burn-up

The MARK-BEB power ramp programme [2] offers a perfect illustration of the importance and effects of gaseous swelling in establishing PCMI during a power ramp. The three rodlets that were subjected to power ramps from a conditioning power level of ~ 27 kW/m to peak power levels of 39.5, 42 and 44 kW/m in the Studsvik reactor had accumulated a burn-up slightly greater than 62 MWd/kgU in four cycles in the Arkansas Unit 1 power reactor.

Because the Studsvik research reactor has a reduced core length, only the lower two-thirds of the rodlets were exposed to a significant power level and within this active length a significant axial power profile created a strong dependency of mechanical and thermal outputs on the axial position. This allows a detailed verification of the temperature effects on various processes as modelled in the code.

The phenomenological aspects related to gaseous swelling were confirmed by the PIE performed on sections cut from the peak power position of the rodlets. It indicated increased total porosity towards the centre and gas bubbles were visible from about 65% of the pellet radius inward. Two of the rods were punctured and the fission gas collected and analysed.

Fission gas release values (Xe values) of 9.3% and 11.2% were measured in two of the ramped rodlets to be compared with the 1.3% measured in a companion rodlet which was not ramped. Thus, the vast majority of the fission gas release occurred during the power ramp and the 12-hour plateau at the terminal power level. The code predictions agree with the measurements, namely, 9% and 11.5% for the ramped rods and 1% for the non-ramped rod, respectively. Therefore the gas atom transport to the grain boundary by diffusion (small component due to grain growth is also captured) is adequately modelled both in terms of kinetics and the level of grain boundary saturation.

There was moderate equiaxed grain growth detected in the central part of the pellet, predicted by the code (approximately by a factor of two in the centre of the peak power section). Thus, these prerequisites for calculating gaseous swelling were well predicted by the code. The gaseous swelling kinetics is the result of gas atom diffusion to the grain boundary. The vacancy and grain boundary gas atom diffusion rates are much higher and are not rate limiting for grain boundary gaseous swelling.

The main effect of gaseous swelling was evidenced as cladding permanent deformation measured along the rodlet by performing a detailed profilometry. Both the axial profile and the magnitude of the cladding permanent strain were very well predicted. This shows that gaseous swelling was properly calculated in the model and also that its interaction with PCMI was adequately represented. To illustrate the importance of gaseous swelling in establishing PCMI and causing important outward cladding strain, Figures 1-3 compares the excellent agreement between calculation and measurement and the considerable lack thereof when simulating the three rodlets with the gaseous swelling model on and turned off, respectively.

Figure 1. Rod R1 deformation differential

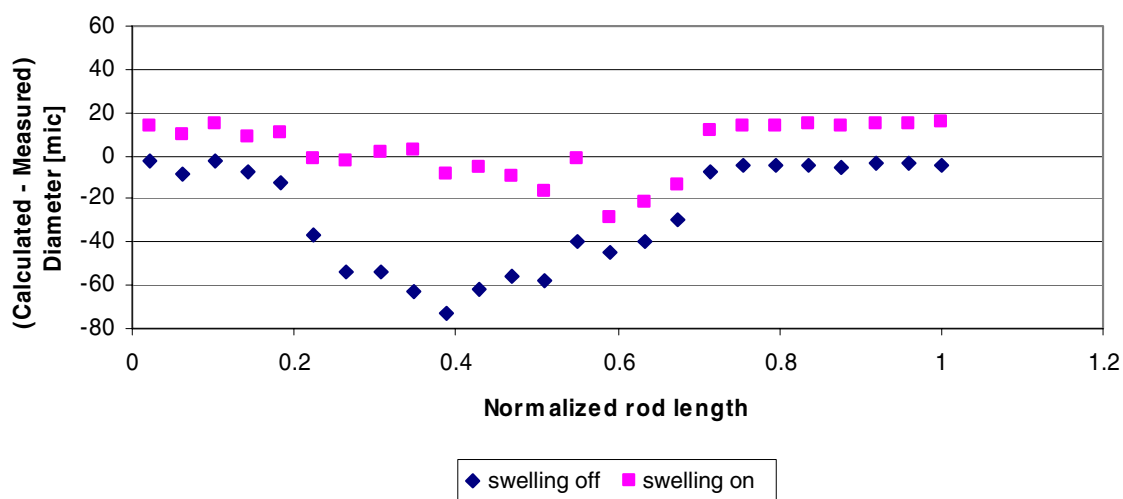


Figure 2. Rod R2 deformation differential

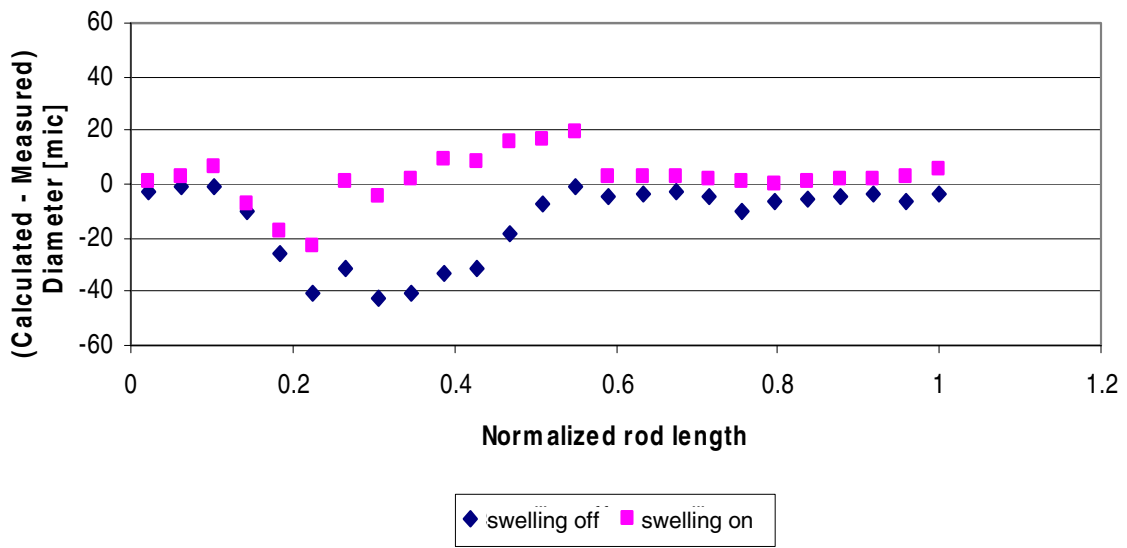
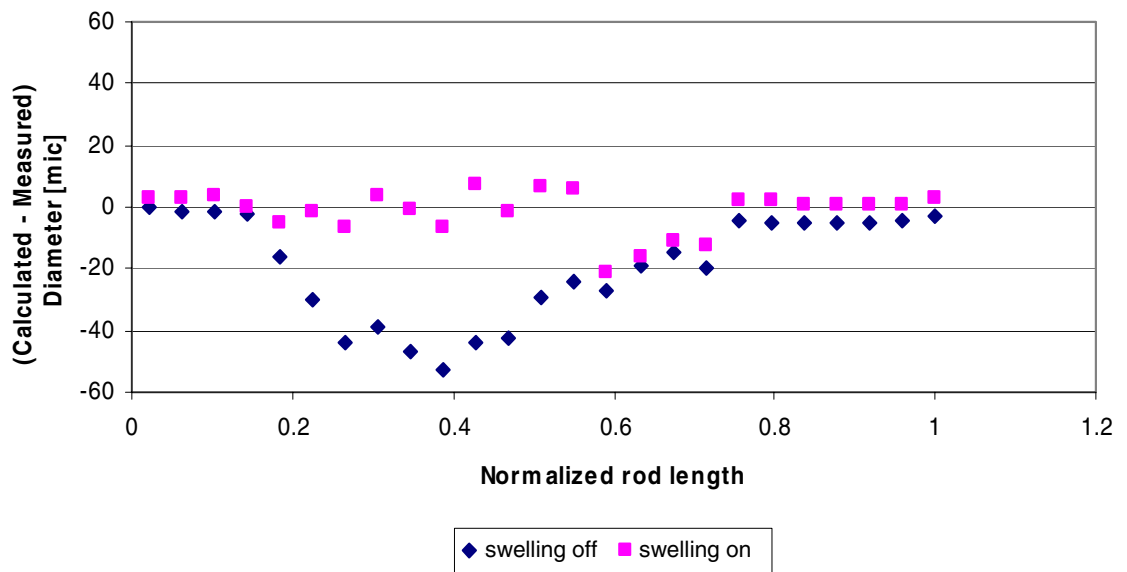


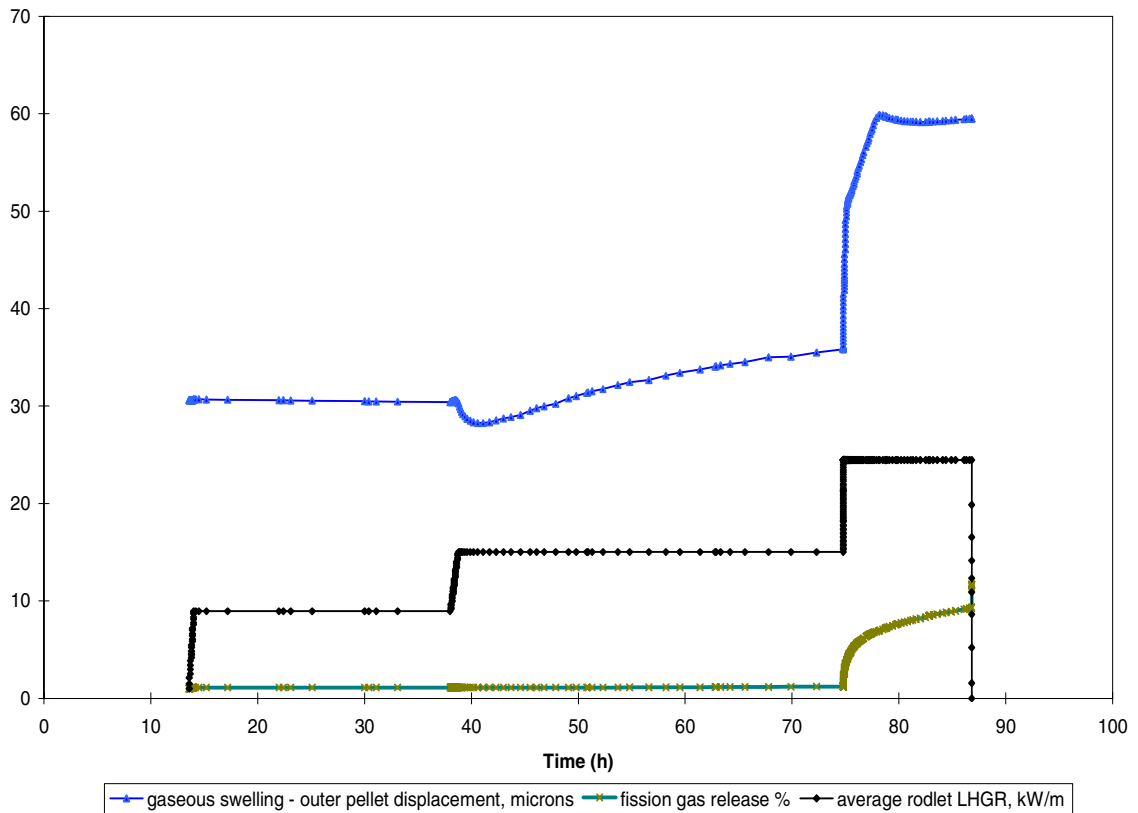
Figure 3. Rod R3 deformation differential



The evolution of gaseous swelling and fission gas release is presented in Figure 4 for the final power ramp portion of the rodlet R3 irradiation. The fast kinetics of gaseous swelling is noted, as the gas bubble growth responds to the temperature increase and increased flux of gas atoms to the grain boundary. Also, the feedback from PCMI is evidenced by the small decrease during the plateau at the terminal power level, as the contact pressure increases and then stabilises to a value consistent with the increased power level.

From the simulations of the three rodlets, it can be concluded that gaseous swelling is responsible for about half of the strain imposed on the cladding by the expanding fuel pellet during the extended power ramp. Therefore, thermal expansion alone cannot explain cladding strain achieved at the ramp terminal level and gaseous swelling is critical in both a correct simulation and estimation of cladding deformation.

Figure 4. Gaseous swelling, FGR and LHGR during R3 power ramp



REFERENCES

- [1] Billaux, M.R., *et al.*, “SIERRA: A Fuel Performance Code to Predict the Mechanical Behaviour of Fuel Rods Up to High Burn-up”, *Proceedings of the International Topical Meeting on Light Water Reactor Fuel Performance*, Portland, Oregon, 2-6 March 1997, pp. 576-585.
- [2] Wesley, D.A., Kazou Mori, Shin Inoue, “MARK_BEB Ramp Testing Program”, *Proceedings of the International Topical Meeting on Light Water Reactor Fuel Performance*, Florida, USA, 17-21 April 1994, pp. 343-351.

MODELLING OF A PELLETT-CLAD MECHANICAL INTERACTION IN LWR FUEL BY CONSIDERING GASEOUS SWELLING

Jin-Sik Cheon, Yang-Hyun Koo, Byung-Ho Lee, Je-Yong Oh, Dong-Seong Sohn
Korea Atomic Energy Research Institute, South Korea

Abstract

This paper describes a finite element model in order to evaluate the fuel rod behaviour due to PCMI during power transients. A connection with KAERI's fuel performance code COSMOS has been pursued for the developed model that is based on a commercial FE code, ABAQUS. Clad deformation is calculated through a coupled temperature-displacement analysis where half of a pellet is modelled axisymmetrically. The effect of the gaseous swelling on clad deformation is investigated. A preliminary parametric study for the PCMI model is performed, and verification of the centreline temperature and clad deformation is conducted using recent in-pile data.

Introduction

As the discharged burn-up of a nuclear fuel increases, several phenomena are of interest. Pellet-clad mechanical interaction (PCMI) is one of the high burn-up related concerns. The possibility of PCMI during power transients increases due to the narrowing gap between the pellet and clad following pellet and clad deformation. PCMI is basically induced by a temperature gradient present in the pellet with a higher thermal expansion and lower thermal conductivity relative to the clad. Axial and radial deformation of the clad could develop. The clad deformation is enhanced by increasing the power of the fuel rod and the hold time at high power. These cladding deformations are brought about by yielding and/or creep of cladding material. The increased clad deformation at high power is further raised as a result of gaseous swelling that is caused by the fission gas atoms accumulated on grain boundaries during base irradiation. A considerable amount of the fission gases would be subsequently released during power reduction after high power hold. The extent of clad deformation is known to be dependent upon residual gap between pellet and clad, differential thermal expansion, pellet crack and bubble swelling [1].

Once PCMI develops and hence external restraint exerts a compressive force on the fuel during power transients, the amount of gas retention on grain boundaries increases while delaying and reducing gas release depending on the magnitude of the restraint. Koo, *et al.* [2] developed a fission gas release model considering the effect of external restraint on the behaviour of gas bubbles in the grain boundaries. The model, however, needs to be improved not only by accounting for the growth of a grain boundary bubble which occurs by the diffusion of vacancies induced by the over-pressure of the bubble [3-5], but also by incorporating the relationship of number density of grain face bubbles with bubble area that is a consequence of bubble coalescence [4-6].

The simulation of PCMI in the presence of gaseous swelling is rather complicated since gas release, bubble growth and PCMI should be modelled in an integrated manner [4,5]. Moreover, a detailed analysis of cladding deformation related to PCMI can be attained by carrying out a finite element (FE) analysis [7,8].

In the present paper, an extension module has been developed by considering the gaseous swelling in order to provide the function of PCMI modelling for the fuel performance code COSMOS [9]. It is based on a commercial FE code, ABAQUS [10]. Detailed modelling works are described. In-pile data is used to compare the calculations with the measurements.

PCMI model description for thermo-mechanical interaction

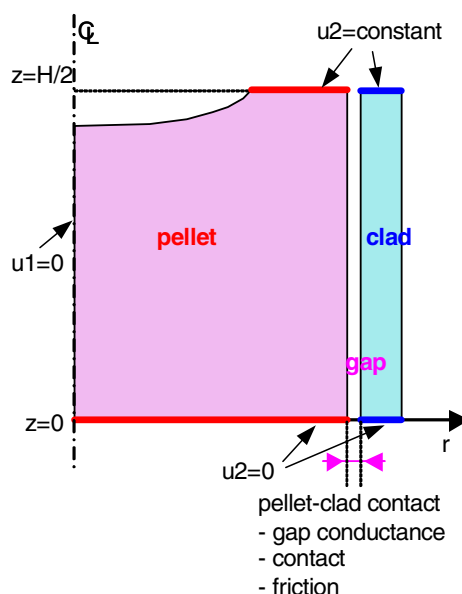
PCMI model description

A fuel performance code is required to analyse the status of a fuel rod before power transient occurs. The gap width between the pellet and clad is most critical among the parameters obtained from the code, and determines whether or not the evaluation of the PCMI is acceptable. The PCMI due to power transients was simulated by the ABAQUS code based on the results of the COSMOS code. User subroutines in FORTRAN for the ABAQUS code were prepared to describe the material, heat transfer, contact and gaseous swelling models. A script program was developed to directly control the PYTHON object corresponding to the ABAQUS keyword and post-processing command. An axisymmetric FE model is applied to the part of the fuel rod as high as a half pellet in the program. Radial power depression in the pellet is considered by dividing the pellet into four equal-sized rings.

A thermal conductivity model of MOX used in this study is similar to the one developed by Wiesenack [11]. The model for the secondary creep rate includes the thermal and irradiation effect. The enhanced irradiation creep rate of MOX is accounted for by the third term of the UO_2 creep equation.

A coupled temperature-displacement analysis is used in this work. Figure 1 displays the boundary conditions for FE analysis. Symmetries at $z = 0$ and $r = 0$ impose the fixed boundary conditions. Axial displacement is coupled on the pellet land and upper clad surface at half the pellet height, H . The boundary condition of the coupled axial displacement on the pellet land is set up since the clad extension is driven by the axial fuel thermal expansion in the pellet land. Hard contact is used for transmission of the contact pressure. The contact problem is solved using a penalty method.

Figure 1. Boundary conditions for PCMI modelling



Parametric study

The validity of the thermo-mechanical modelling of the PCMI program is examined by a parametric study. Clad deformation is calculated as a function of the friction factor, creep rate of the pellet and axial compressive force.

The dimensions of a dished pellet for the parametric study are selected to represent a typical PWR fuel rod: diameter of 8.27 mm, height of 11.9 mm and clad thickness of 0.56 mm. The diametric gap of 20 μm at room temperature is assumed by considering pellet swelling and clad creep-down at a high burn-up. The power history shown in Figure 2 is used with a maximum linear power of 29 kW/m. The burn-up of the pellet is about 25 MWd/kgMOX. Table 1 shows the calculation conditions.

Friction factor between the pellet and clad has been reported in the range of 0.47 to 0.6 [12]. In the fuel rod, however, the pellet might experience a friction force higher than the product of the normal contact force and friction factor due to the interaction between the pellets. An effective friction factor describes the effect of the neighbouring pellets. The parametric study is performed for the effective friction factor of 0.5, 0.75, 1 and ∞ . The effect of the axial compressive force over the pellet land is also examined. It is assumed that the thermal conductivity for UO_2 and MOX is identical for comparing the calculated results at the same temperature distribution.

Figure 3 shows the clad elongation for the 1/2 pellet model when the variation of power is given as in Figure 2. As shown in Figure 3(a), the clad elongation increases further and the PCMI occurs earlier in proportion to the friction factor. The assumption, $\mu_{\text{eff}} = \infty$, seems to be too severe since the clad

Figure 2. Power history for parametric study

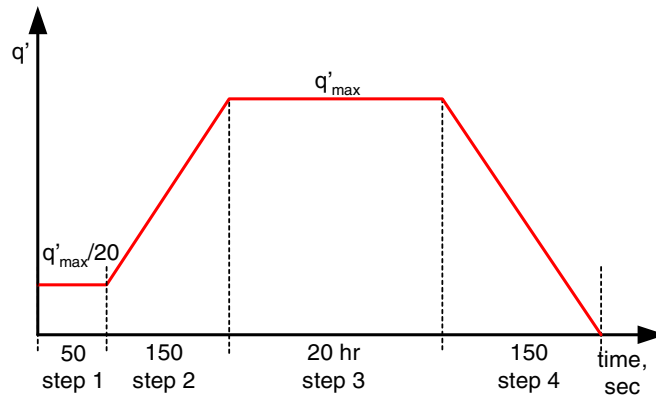
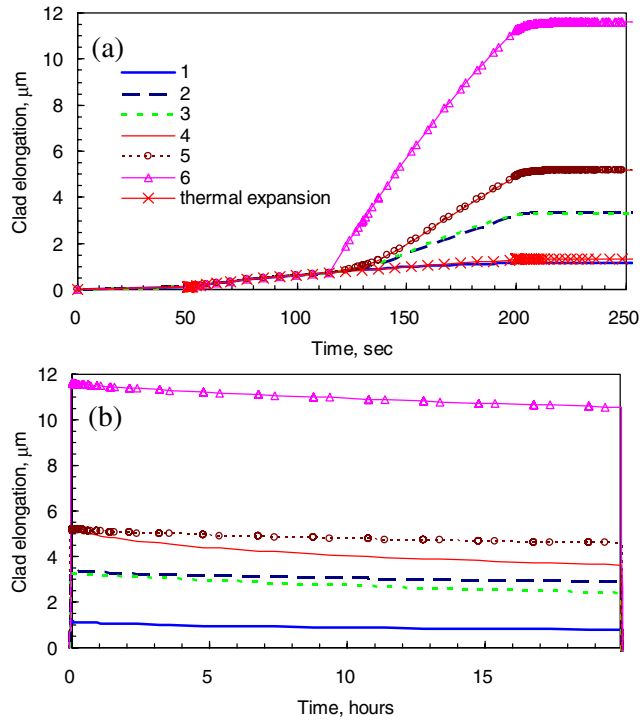


Table 1. Calculation matrix and changes in clad length during power hold

No.	Effective friction factor (μ_{eff})	Axial force per unit area of pellet land	Pellet	Change in clad length, μm
1	0.5	—	UO ₂	0.35
2	0.75	—	UO ₂	0.33
3	0.75	50 MPa	UO ₂	0.82
4	1	—	MOX	1.29
5	1	—	UO ₂	0.34
6	∞	—	UO ₂	0.71

Figure 3. Clad elongation per half pellet obtained by the parametric study. The explanation on the legend is given in the Table 1, (a) during power increase, (b) during power hold.



elongates with the pellet deformation by completely sticking between them even if there is a slight contact. In the case of $\mu_{\text{eff}} = 0.5$, the contact of the pellet with the clad does not sustain but is released at once. This analysis is valid in that the clad elongation is almost equal to the thermal expansion of the clad. It is established that for the case where $\mu_{\text{eff}} = 1$, it exhibits clad elongation closer to the PCMI experimental result.

The tendency of relaxation during a power hold of 20 hours is well represented by the decrease of clad elongation in Figure 3(b). Table 1 summarises the magnitude of clad elongations. The clad elongation for the UO_2 pellet is around $0.34 \mu\text{m}$ if axial compressive force is not applied, and except for $\mu_{\text{eff}} = \infty$ for which even a slight contact might cause severe clad deformation. Axial compressive force causes higher clad relaxation due to the enhanced creep of the pellet. The higher creep rate of MOX than that of UO_2 results in about a four times larger variation of clad deformation relative to the UO_2 . As shown above, the clad elongation could be evaluated during power increase and hold by reflecting the effect of the friction factor, the creep rate of the pellet, etc. on the PCMI.

Fission gas release and gaseous swelling model

It is assumed that all of the fission gas on the grain boundaries is retained in the bubbles. The intergranular bubbles are treated as lenticular bubbles of circular projection with a semi-dihedral angle of 50° . Fission gas atoms in the grain boundaries are balanced by the transport from grain interior, fission-induced resolution from grain boundaries and gas flow to the free volume. The conservation of the gas atoms in the grain boundaries is given by:

$$\frac{\partial m_\alpha}{\partial t} = J_1 - J_2 - J_3 \quad (1)$$

where m_α is the number density of the gas atoms in the grain boundaries (m^{-3}) per unit volume of fuel with a grain size of “a”.

J_1 is the gas flow rate from grain interior to the grain boundary per unit volume of fuel ($\text{m}^{-3}\text{sec}^{-1}$), which is calculated under the assumption of a perfect sink boundary condition by using the Forsberg and Massih algorithm [13]. The coefficients in the approximate kernel are newly determined by Hermansson and Massih [14]. Trapping and resolution due to the intragranular bubbles are considered with an effective diffusion coefficient. The volume diffusion coefficient by Turnbull, *et al.* [15] is used in this calculation.

J_2 is the irradiation-induced resolution flux from grain boundaries. The resolution flux is proportional to the fission density and the instantaneous number of gas atoms in the intergranular bubbles.

J_3 is the gas flow rate through interconnected tunnel network to free volume. The gas flow is modelled by the atomic diffusion mechanisms. On the other hand, the gas release is suppressed with a linear manner in the time-dependence of the release during high-power hold, while taking place mostly at power reduction [16]. The linearity suggests that the on-power gas release is caused by the slow percolation process through the porous fuel. The gas released on the power reduction is understood not only by the decrease in the magnitude of hydrostatic pressure but also by the improvement of in-rod communication. In the case of the diffusion-governed case, the vented fraction, F_{vent} of the grain boundary gas is a ratio of gas released to the sum of gas released and gas retained in the grain boundaries at a point in time [5]. F_{vent} is also expressed by:

$$F_{vent} = 1 - \exp\left[-\left(\frac{F_c}{F_{c0}}\right)^m\right] \quad (2)$$

where F_c is the fractional coverage of grain face by porosity, and F_{c0} and m are fitting constants [4]. The same relationship can be deduced by treating the data published by White [5] with a minor difference in the fitting constants. F_c is the product of number density of intergranular bubble, N_{bl} and average bubble projected area, A_p . In the case of suppressed release case, such a phenomenon was modelled using Poiseuille's law by which the gas flow rate is described by the pressure difference between bubble and free volume, and gas flow conductance through the porous fuel matrix [1,4,17]. Following the same approaches, J_3 is given by:

$$J_3 = \frac{V_{t0} F_{vent}}{\eta} P_{bl} \frac{N_{bl} P_{bl}}{kTa} \quad (3)$$

where the pressure difference is simply represented by bubble pressure, and the flow conductance is given by $V_{t0} F_{vent} / \eta$. The flow conductance consists of gas viscosity, η , venting fraction, F_{vent} , and V_{t0} which corresponds to the volume of hypothetical flow channel when F_{vent} is equal to 1. The rest of the gases which would be released in the absence of PCMI-induced stress are assumed to be vented in proportion to the vented fraction to the free volume at power decrease.

Intergranular bubble growth occurs due to absorption of vacancies generated on the grain boundaries, and the driving force is the balance among hydrostatic pressure, σ , bubble pressure, P_{bl} , and surface tension force, $2\gamma/\rho_{bl}$ where γ is the surface tension of the fuel and ρ_{bl} is the radius of curvature of the bubble [3]. The bubble growth rate is given by:

$$\frac{\partial \rho_{bl}}{\partial t} = \frac{D_g \delta_g \Omega}{4f(\theta)\rho_{bl}^2 kT} \left(\sigma + P_{bl} - \frac{2\gamma}{\rho_{bl}} \right) k_f(F_c) \quad (4)$$

where D_g is the grain boundary diffusion coefficient, δ_g is the grain boundary thickness, Ω is the atomic volume, $f(\theta) = 1 - 3\cos\theta/2 + \cos^3\theta/2$, k is the Boltzmann constant, T is the absolute temperature and $k_f(F_c)$ is given by:

$$k_f(F_c) = \frac{8(1-F_c)}{(F_c-1)(3-F_c)-2\ln F_c} \quad (5)$$

The coefficients of D_g proposed by White [5] are applied in this study.

Bubble coalescence is represented by the model [5] which expresses the correlation between the bubble density and average bubble projected area. N_{bl} is given by:

$$N_{bl} = \frac{N_{bl0}}{1 + 2N_{bl0}(A_p - A_{p0})} \quad (6)$$

where N_{bl0} and A_{p0} are the initial values of N_{bl} and A_p . N_{bl0} and A_{p0} are assumed to be $40 \mu\text{m}^{-2}$ and $0.001 \mu\text{m}^2$, respectively.

The pellet swelling due to the intergranular bubbles is written as:

$$\frac{\Delta V}{V} = \frac{1}{a} 2\pi N_{bl} f(\theta) \rho_{bl}^3 \quad (7)$$

The bubble swelling becomes proportional to ρ_{bl} after the fractional coverage saturated at a value of 0.5.

Verification of the PCMI modelling

Recent MOX experimental data is used to verify the developed PCMI modelling. A fuel rod for modelling verification was manufactured by the MIMAS process and irradiated up to middle burn-up at a PWR nuclear power plant. It was irradiated at an average linear power of 20 kW/m and up to a burn-up of about 25 MWd/kgMOX. The purpose of the irradiation test was to investigate the thermal performance, the fission gas release and PCMI of the MOX fuel rod. The fuel rod contained 32 pellets. Rod power was controlled by regulating the pressure of ^3He in the coil installed in the irradiation rig. Power ramp took place five times during an irradiation of eight days, designated as Phase 1 to 5.

From the parametric study (as displayed in Figure 3), $\mu_{\text{eff}} = 1$ was chosen to take into account pellet-to-pellet interactions. Thermal conductivity of the MOX pellet accounts for the burn-up effect. Based on the irradiation test results, the pellet-to-clad gap width was estimated for the model input. The combination of a reduction of 8% for the MOX thermal conductivity relative to that of UO_2 and a gap width = 20 μm was used for PCMI modelling. Radial power depression in the pellet due to the self-shielding of the thermal neutron is reflected in the modelling.

For the term V_{i0}/η in Eq. (3), it was revealed that the value of around 10^{-33} provided reasonable calculation results through a parametric study. Hydrostatic pressure is a function of stresses that are substantially affected by the decrease in the elastic modulus of the pellet due to crack formation. It is assumed that the hydrostatic pressure to be used in the bubble growth equation is zero if the hydrostatic pressure from the coupled thermo-mechanical analysis is greater than zero (tensile), and is reduced by 50% if it is less than zero (compressive) in the present modelling. For power condensation during a power decrease, linear power is decreased down to zero and again increases up to the power hold level due to imposed boundary condition at $z = 0$ as shown in Figure 4. Linear power at Phase 0 is simply condensed. Total clad elongation of the fuel rod is estimated by the product of the clad elongation of the 1/2 pellet model, a factor of 2 due to symmetry and the number of pellets.

The calculated centreline temperature is compared with the measured one in Figure 4. Figure 4 also shows that the estimated temperature is close to that measured by means of a thermocouple embedded in the annular pellet. For the solid pellet, a comparison is made in Figure 4 in which the estimated centreline temperature reaches more than 1 600°C.

Clad elongation of the fuel rod is shown in Figure 5 for Phases 1 and 5. Five cases are investigated: (1) the gas flow from the grain boundary is suppressed and occurs only through a percolation process ($V_{i0}/\eta = 1 \times 10^{-33}$), (2) gas flow is suppressed ($V_{i0}/\eta = 1 \times 10^{-33}$) during high-power hold and most of the gases vent on power reduction, (3) the same condition as in the second case except for $V_{i0}/\eta = 5 \times 10^{-33}$, (4) gas from grain boundary is released freely, depending on the vented fraction, and (5) without considering the fission gas release and swelling model. The initial elongation of 0.02 mm at hot stand-by is added up to all of the calculated elongations. The onset of significant fission gas release was expected to be around 1 200°C. The centreline temperature is calculated to be 1 280°C and 1 650°C for Phase 1 and Phase 5, respectively. The estimated clad elongation, as a whole, is similar to that of the measured one.

Figure 4. Calculation of the fuel centre temperature during power changes

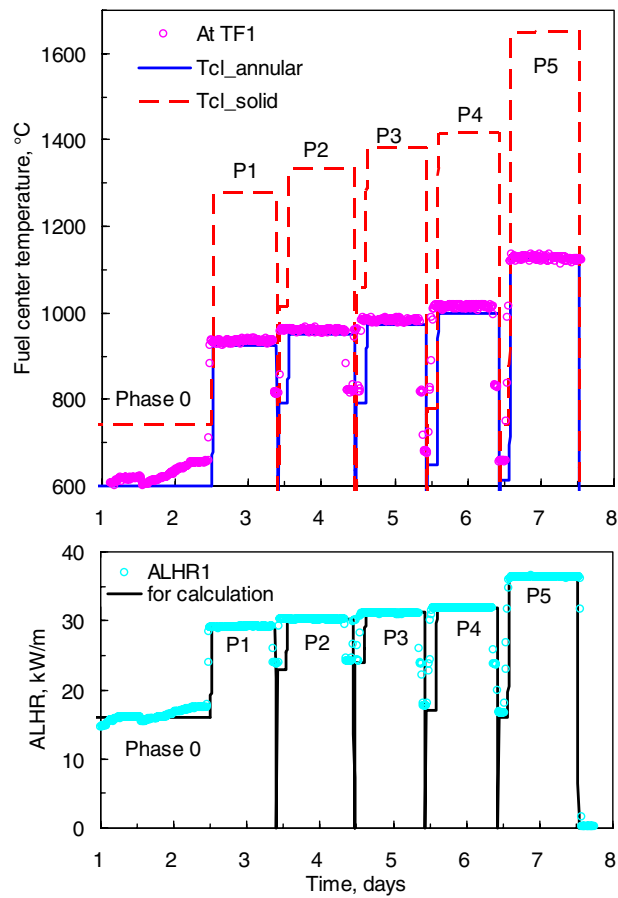


Figure 5. Variation of the clad elongation during power transient

- 1 – Suppressed release ($V_{f0}/\eta = 1 \times 10^{-33}$), 2 – Suppressed release + vent on power reduction $V_{f0}/\eta = 1 \times 10^{-33}$,
 3 – Suppressed release + vent on power reduction $V_{f0}/\eta = 5 \times 10^{-33}$,
 4 – Diffusional release depending on the vented fraction, 5 – Without fission gas release model

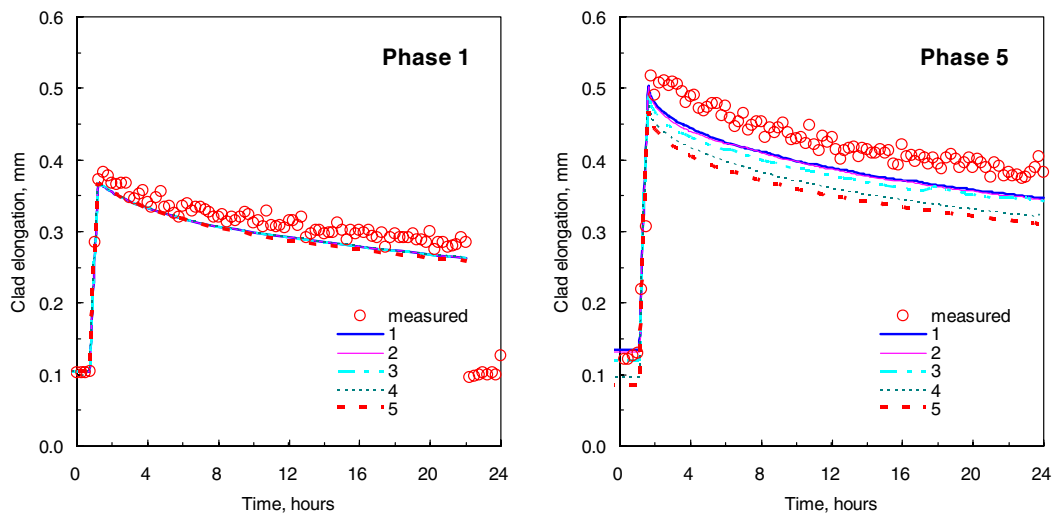
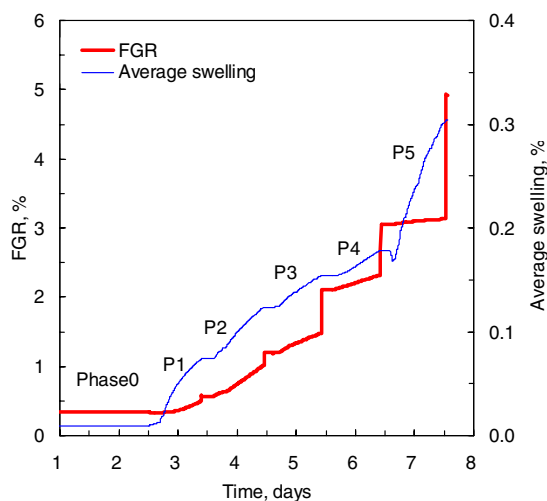


Figure 6 shows the calculated results for fission gas release and average pellet swelling when considering the delay of the gas release ($V_{f0}/\eta = 1 \times 10^{-33}$). The delayed gas release during high-power hold and abrupt increase in the fission gas release at power reduction are well simulated. It is calculated that the fission gas release is below 5% and the average pellet swelling is less than 0.4% for the four investigated cases.

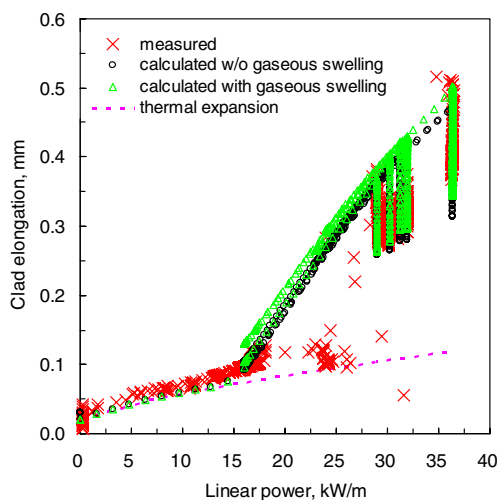
Figure 6. Calculated fission gas release and average pellet swelling in the case of delayed fission gas release ($V_{f0}/\eta = 1 \times 10^{-33}$)



Variation of clad elongation with linear power is shown in Figure 7, in which the effect of gaseous swelling on the clad elongation is compared. The clad elongation predicted for the power levels between high-power holds is excluded in the plot. The initial elongation of 0.02 mm is also taken into account. The general agreement of the calculated clad elongation with the measurement is shown. The slope during the power ramp and the magnitude of relaxation during the power hold are similar for both the measurement and the prediction. It is evident that the present consideration of the gaseous swelling model enables us to predict the clad deformation more precisely.

Figure 7. Clad elongation versus linear power

*The clad elongation under the consideration of gaseous swelling is calculated at $V_{f0}/\eta = 1 \times 10^{-33}$.
The initial elongation, 0.02 mm at hot stand-by, is added up to all of the calculated results.*



Conclusions

PCMI is modelled by a FE method to extend the functions of a fuel performance code, COSMOS. Thermo-mechanical behaviours, contact and interaction of the pellet and clad are represented by the FE model. In particular, the fission gas release and gaseous swelling model is provided for the FE model. Verification of the PCMI model was undertaken using recent MOX experimental data.

The FE model is able to simulate the variation of clad elongation as a function of the factors affecting PCMI. Introducing a simplified model for describing the gas release and swelling makes it possible to more precisely predict the phenomena due to PCMI at higher power. The scope of the modelling includes the observations that the clad deformation increases with suppressing the gas release during high-power hold, and most of the gas release occurs at power reduction. The calculated clad elongation is in reasonable agreement with the measured one.

Acknowledgements

The Ministry of Science and Technology (MOST) of the Republic of Korea has sponsored this work through the Mid- and Long-term Nuclear R&D Project.

REFERENCES

- [1] Kogai, T., Y. Iwano, *J. Nucl. Sci. Technol.*, 27, 1017-1027 (1990).
- [2] Koo, Y-H., B-H. Lee, D-S. Sohn, *J. Nucl. Mater.*, 280, 86-98 (2000).
- [3] Matthews, J.R., M.H. Wood, *J. Nucl. Mater.*, 91, 241-256 (1980).
- [4] Kogai, T., *J. Nucl. Mater.*, 243, 131-140 (1997).
- [5] White, R.J., *J. Nucl. Mater.*, 325, 61-77 (2004).
- [6] Kashibe, S, K. Une, *J. Nucl. Sci. Technol.*, 28, 1090-1099 (1991).
- [7] Bourreau, S., J. Brochard, F. Bentejac, P. Couffin, C. Verdeau, S. Lansiert, N. Cayet, M.C. Grandjean, F. Mermaz and P. Blanpain, "Ramp Testing of PWR Fuel and Multi-dimensional Finite Element Modeling of PCMI", *International Topical Meeting on LWR Fuel Performance*, Utah, USA (2000).
- [8] Nakajima, K., K-S. Sim, *Res Mechanica*, 25, 101-128 (1988).
- [9] Koo, Y-H., B-H. Lee and D-S. Sohn, *Journal of Korean Nuclear Society*, 30, 541-554 (1998).
- [10] *ABAQUS Standard and CAE Version 6.4 Manual* (2004).

- [11] Wiesenack, W., “Assessment of UO₂ Conductivity Degradation Based on In-pile Temperature Data”, *ANS Topical Meeting on Light Water Reactor Fuel Performance*, Portland, USA (1997).
- [12] Nakatsuka, M., *J. Nucl. Mater.*, 96 (1981) 205-207.
- [13] Forsberg, K., A.R. Massih, *J. Nucl. Mater.*, 127, 141-145 (1985).
- [14] Hermansson, P., A.R. Massih, *J. Nucl. Mater.*, 304, 204-211 (2002).
- [15] Turnbull, J.A., C.A. Friskney, J.R. Findlay, F.A. Johnson, A.J. Walter, *J. Nucl. Mater.*, 107, 168-184 (1982).
- [16] Kogai, T., K. Ito, Y. Iwano, *J. Nucl. Mater.*, 158, 64-70 (1988).
- [17] Van Uffelen, P., *Contribution to the Modelling of Fission Gas Release in Light Water Reactor Fuel*, PhD Thesis, Université de Liège, January 2002, BLG-907.

THE REDUCTION OF FISSION GAS SWELLING THROUGH IRRADIATION-INDUCED RE-SOLUTION

Rodney J. White
BNFL, Sellafield, UK

Abstract

The principal driving strain for pellet-clad interaction (PCI) is provided by closed fission gas porosity, that is, porosity bounded by an unbroken fuel interface. Two types of porosity meet this requirement; these are intragranular bubbles and closed grain boundary or intergranular bubbles. Over short periods, during high rating and temperature transients, significant levels of intragranular swelling may occur while for extended transients, grain boundary bubbles begin to develop. For extreme levels of total swelling, fuel failure often occurs; however, in the event that the cladding survives the transient, the swelling levels may subside through irradiation-induced re-solution on return to normal operating conditions thereby mitigating the intensity of future PCI events. This paper compares the swelling behaviour of two ramped rods; in one, the rod was discharged immediately after the transient while in the other, the rod was maintained at low powers for 28 days before discharge.

Introduction

Although differential thermal expansion between fuel pellets and cladding can give rise to pellet-clad interactions (PCI), fuel failures usually arise only through the additional strains produced by fuel swelling. The important components of fuel swelling for PCI are from closed porosity, that is, bubbles with an unbroken boundary, since only these types of bubbles can exert a stress on the cladding. Two types of pore satisfy this requirement, intragranular bubbles and closed grain-face bubbles. Intragranular pores are formed during steady-state operation and are thought to nucleate in the wake of energetic fission fragments [1]. They are also destroyed by the passage of other fission fragments and in this way a dynamic equilibrium population is established with concentrations of around 10^{24} m^{-3} and diameters of the order of nanometres or less. The contribution to swelling under these conditions is negligible.

During transients to higher powers and temperatures, a sub-population of these bubbles – typically $\sim 3 \cdot 10^{20} \text{ m}^{-3}$ – act as fission gas and vacancy sinks and grow by diffusion controlled growth: in some cases the bubble diameters exceed several hundred nanometres, giving rise to swellings of 5-10% [2]. The growth process is constrained by the combined effects of irradiation-induced re-resolution, which reduces bubble sizes and concentrations, and the effects of compressive stresses in the fuel. At some stage the diffusional growth rates will be exceeded by the re-resolution rates, and the swelling will decline. However, by this stage, fission gas atoms will have migrated to the grain boundaries and established a network of small lenticular pores of circular projection. The initial bubble densities are typically in the range of $20\text{-}50 \mu\text{m}^{-2}$ and this value will be maintained until the bubbles cover about 20% of the grain faces after which coalescence will begin to occur [3] and the bubble density decreases. This process gives rise to elongated bubbles and to an increased chance that the bubbles will be vented to the grain edges and will no longer contribute to the PCI process.

The development of intragranular swelling depends critically on the relative rates of diffusional growth and irradiation-induced re-resolution. Although both processes are temperature dependent, the diffusional growth process is likely to be more sensitive to changes in temperature and it is clear that the swelling process could reverse following return to lower temperatures where the re-resolution rate exceeds the growth rate. This is also true for the closed grain-face bubbles from which re-resolution also occurs, so, although large swellings may have been induced by a transient event, the swelling may decrease markedly on return to lower powers. Of course, this is only of any benefit if the rod remains intact following the first PCI event, but accurate assessment of the possible benefits of low temperature re-resolution in mitigation of future PCI events is essential for proper predictive fuel modelling.

Recently, the swelling data obtained from the British Energy ramp experiments conducted on AGR fuel in the Halden Reactor has been compiled [2] and released into the public domain through the NEA Databank. This database contained extensive scanning electron microscopy (SEM) from ramps conducted on AGR fuel of modest burn-ups – typically 9-22 GWd/tU. Of interest with respect to irradiation-induced re-resolution are two slow-ramp tests, one of which was discharged immediately and a second which was maintained at low powers for a further 28 days before discharge.

Test conditions

The rods were base-irradiated to burn-ups of 12-15 GWd/tU under benign conditions and tested in the Halden Reactor using a zircaloy shroud surrounding the cladding in order to simulate CAGR cladding conditions [2]. Both rods were subjected to slow ramps in which the power increased over a period of 45 minutes. In addition, test 4135E was also subjected to two fast ramps in which the power

increased over a period of around 40 seconds. In these ramps the peak power was maintained for 80 seconds. Following the tests, rod 4162E was discharged immediately while 4135E was maintained at low powers for an additional 28 days prior to discharge. The idealised ramp is shown in Figure 1.

Figure 1. Idealised power ramp for the Halden tests. The powers and durations for the various stages are given in Table 1.

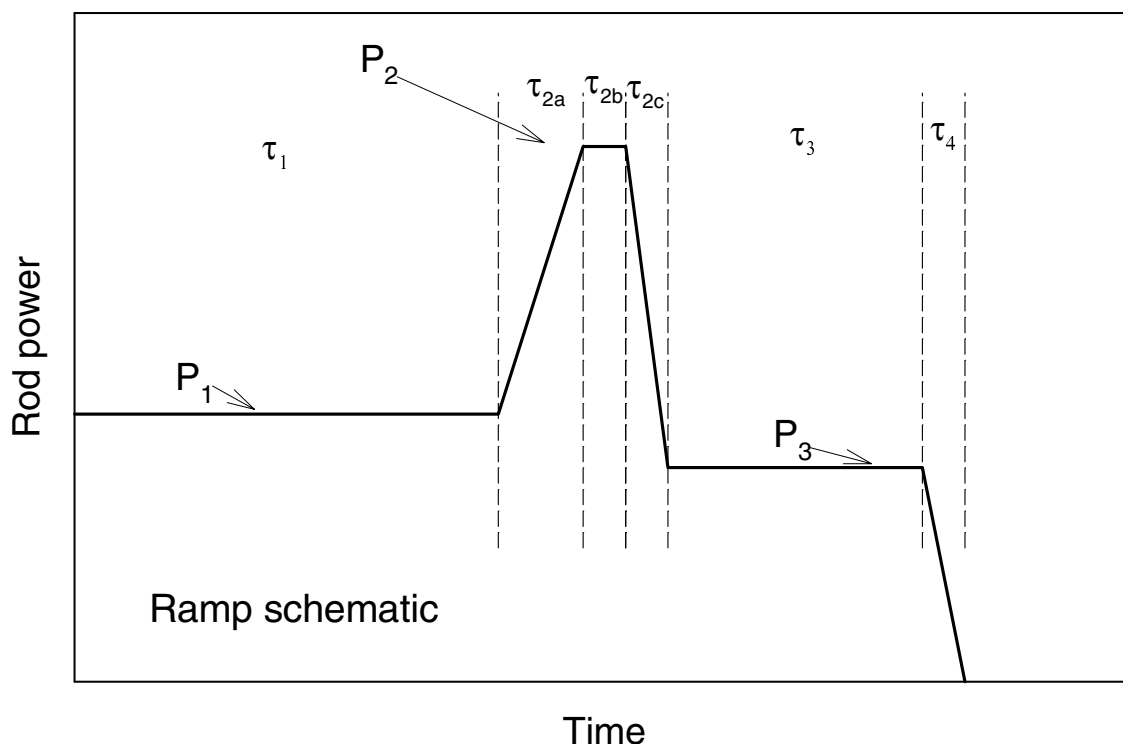


Table 1. Conditions for the ramp tests (with reference to Figure 1)

SEM identifier	Burn-up (GWd/tU)	Ramp no.	Power 1 kW/m	τ_1	τ_{2a}	Power 2 kW/m	τ_{2b}	τ_{2c}	Power 3 kW/m	τ_3	τ_4
4135E	15.0	1	18.5	1 wk	65 m	36.9	0.0	40 s	–		
		2	13.0	8.0 m	40 s	36.9	80 s	40 s	–		
		3	13.0	0.0 m	40 s	36.9	80 s	40 s	16.0	28 d	6 hr
4162E	12.6	1	18.0	3 wk	45 m	40.0	0.0	40 s	18.0	6 m	–

Initial PIE

The fuel was returned to Berkeley Centre in the UK where extensive PIE was performed. This included clad profilometry, puncturing, gas analysis, fuel metallography and scanning electron microscopy (SEM). The immediate-discharge rod (4162E) survived the ramp test and a clad diametral strain of ~0.4% was measured at the peak rated position. In contrast, the extended-dwell rod failed with a peak diametral strain of ~0.8%. Metallographic examination revealed very little evidence of fission gas swelling, an observation subsequently confirmed by SEM.

SEM analysis

The SEM was performed on newly cracked radial sections of the fuel. Images were obtained from five or six locations on a radius working out from the pellet inner-bore. At least six grain-face areas were examined at magnifications ranging from $\times 3k$ to $\times 8k$. Higher magnifications were required for the analysis of intragranular bubbles – typically in the range $\times 20k$ – $\times 40k$ – and three full trans-granular fractures were examined, often requiring around 20 images to cover the whole area. The temperature histories appropriate to the radial locations of each of the SEM specimens were obtained from ENIGMA calculations [2]. These indicated that the peak temperature experienced by the immediate-discharge fuel (4162E) was $1\,798^{\circ}\text{C}$ while the extended-dwell fuel (4135E) reached $1\,782^{\circ}\text{C}$; however, this slightly lower temperature was maintained for 160 seconds.

Typical examples of the grain-face porosity are displayed in Figure 2 and a comparison of the measured swelling parameters for the two tests is given in Table 2.

Figure 2. Grain-face images of fuel ramped in the 4162E and 4135E tests

The 4162E test (left) was discharged immediately after ramping while the fuel in 4135E (right) was held at low powers for an additional 28 days prior to discharge. Note the extensive denudation of the porosity in the extended-dwell test on the right.

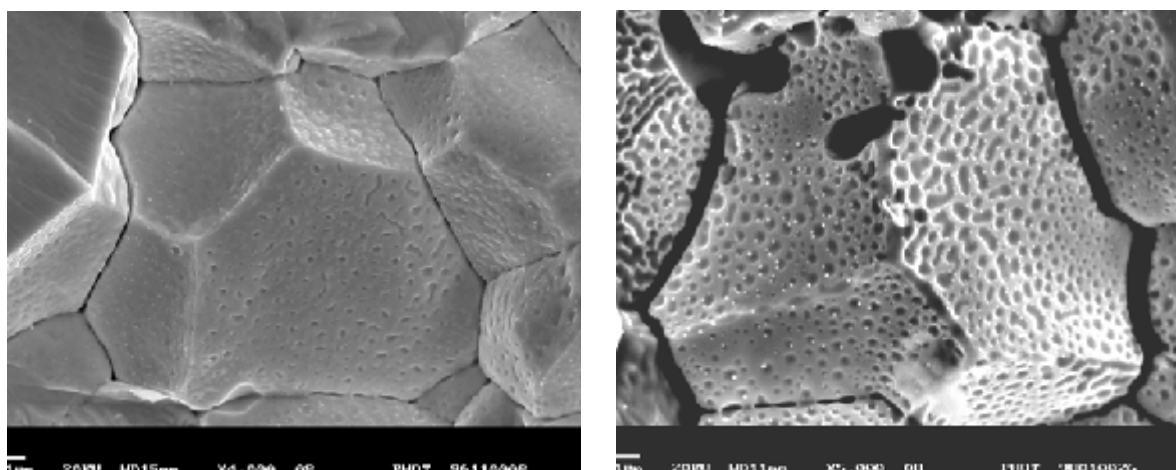


Table 2. Measured grain-face swelling parameters for the two tests

Section	Peak/parked Temperatures ($^{\circ}\text{C}$)	Bubbles/GBs	Nb/Agb (μm^{-2})	Fc (%)	R _P (μm)	L _P (μm)	$\Delta V/V$ (%)
4135e-a	1 782/982	937/7	1.03 ± 0.51	22.8 ± 8.6	0.16 ± 0.03	0.47 ± 0.27	0.42 ± 0.19
4135e-b	1 766/976	1 555/7	1.52 ± 0.25	11.5 ± 2.6	0.12 ± 0.03	0.15 ± 0.08	0.16 ± 0.08
4135e-c	1 725/962	172/1	1.78	8.96	0.09	0.13	0.09
4162e-a	1 798/819	3 046/14	3.15 ± 0.78	37.1 ± 9.0	0.15 ± 0.02	0.15 ± 0.13	0.70 ± 0.26
4162e-b	1 788/817	3 545/12	3.98 ± 1.27	28.1 ± 7.7	0.12 ± 0.02	0.13 ± 0.33	0.46 ± 0.17
4162e-c	1 760/811	3 786/14	4.92 ± 1.50	30.4 ± 7.9	0.13 ± 0.03	0.12 ± 0.38	0.43 ± 0.18
4162e-d	1 698/794	1 654/7	5.38 ± 1.39	27.7 ± 5.6	0.11 ± 0.01	0.06 ± 0.08	0.43 ± 0.22

The third column gives the number of bubbles measured and the number of grain boundaries examined. The remaining columns are the bubble density, the fractional coverage, the bubble projected radius and length, and the volumetric swelling. A brief examination shows that the swellings are generally less in the extended-dwell case than in the immediate-discharge fuel. An analysis of the intragranular bubbles is given in Table 3 and also indicates reduced swelling in the extended-dwell fuel.

Table 3. Measured intragranular swelling parameters for the two tests

Section	Peak/parked Temperatures (°C)	Bubbles/images	C_B (m^{-3})	$\langle R_B \rangle$ (nm)	$\Delta V/V$ (%)
4135e-a	1 782/982	676/20	$4.09 \cdot 10^{19}$	27.5	0.37
4135e-b	1 766/976	414/14	$3.57 \cdot 10^{19}$	25.2	0.25
4135e-c	1 725/962	458/13	$5.39 \cdot 10^{19}$	21.8	0.25
4162e-a	1 798/819	2 279/28	$7.32 \cdot 10^{19}$	35.2	1.34
4162e-b	1 788/817	2 172/25	$1.20 \cdot 10^{20}$	24.0	0.69
4162e-c	1 760/811	1 408/19	$1.66 \cdot 10^{20}$	21.4	0.68
4162e-d	1 698/794	1 121/15	$3.01 \cdot 10^{20}$	17.9	0.72

The measured diametral strain was 0.8% [4] and this is equivalent to an average volumetric swelling across the rod of 2.4%. The initial porosity in the fuel was ~2% but about 1% was removed by in-pile densification [4] so the required level of fission gas swelling to provide the measured diametral strain was about 3.4%. This is a factor of four greater than the peak measured swelling in the extended-dwell rod, so it must be assumed that the swelling was much greater immediately following the ramp but decreased during the dwell.

Evidence for swelling reduction

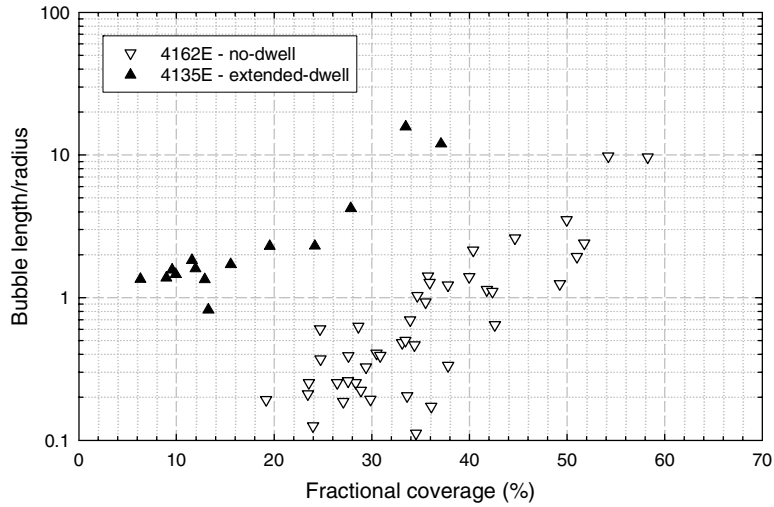
Intergranular swelling

Because of the differences in surface energy of the UO_2/UO_2 interface and the UO_2 /gas interface, the grain-face bubbles nucleate as lenticular pores of circular projection with a semi-dihedral angle of around 50° [5]. These bubbles grow by collecting gas atoms that have migrated to the grain boundaries from within the grains and the presence of gas creates an over-pressure in the cavities such that the pressure is in excess of the bubble capillarity. Equilibrium can be restored if the cavities act as vacancy sinks and this serves to increase the volume and projected area of the cavity.

For a random distribution of bubbles on a planar surface it can be demonstrated that circular bubbles will begin to interact with each other when the fractional coverage exceeds 19.6% [3]. This interaction will result in two bubbles coalescing into a single elongated bubble. This coalescence process introduces an additional state of non-equilibrium in that the surface energy will not be minimised with respect to the volume contained and the bubble will seek to minimise this by changing shape so that it again occupies a circular projection on the grain boundary. Under conditions where bubble growth and coalescence proceed at a faster rate than the shape-change process (morphological relaxation), very long bubbles can be produced but this process should only start when the coverage exceeds the critical value of 19.6%. The variation of the aspect ratio (length/radius) with fractional coverage on the boundary is shown in Figure 3.

The data from the immediate-discharge case (4162E) follows the expected trend with the onset of bubble elongation occurring for fractional coverages of around 19%. Examples of very elongated bubbles with $L_p/R_p \approx 10$ are observed for large fractional coverages. In distinct contrast are the data from the extended dwell case where bubble elongation is observed for fractional coverage as low as 6%. On a statistical basis, this should not occur, so it is possible that the fractional coverages immediately after the ramp were much greater than those measured during PIE.

Figure 3. Variation of the bubble aspect ratio (length/radius) as a function of fractional coverage of the grain boundaries

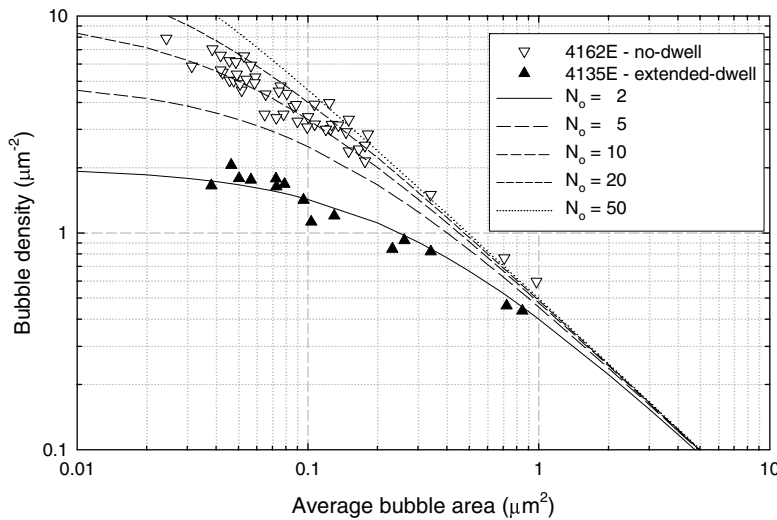


The onset of coalescence leads to a reduction in bubble density and the rate of loss of bubble density, N , as the bubble projected area, A_p , increases is given by:

$$\frac{dN}{dA_p} = -2N^2$$

The variation of the measured bubble densities with bubble-projected area is shown in Figure 4. The lines drawn in Figure 4 are solutions to the coalescence equation with different initial bubble densities. The data from the extended-dwell case appear to be consistent with a lower initial bubble density, but taken in conjunction with Figure 3, the more likely scenario is that bubble volume, and hence, bubble projected area has been lost during the extended-dwell, leading to a leftward shift of the data. It is proposed that the mechanism for this reduction arises from the irradiation-induced re-resolution of fission gas atoms from the grain-face bubble back into the grains.

Figure 4. Variation of the measured bubble density with mean bubble projected area for the two tests



The re-resolution rate of fission gas atoms from grain boundary bubbles was initially calculated by Speight [6] who assigned a probability that a fission gas atom would be knocked back into the grain. Under steady-state conditions a dynamic balance between the re-resolution rate and the diffusion rate back to the boundary would be established thereby modifying the boundary condition for the diffusion process. These arguments have recently been re-examined in the context that the re-resolution process takes place following impact from passing fission fragments. Since the range of a fission fragment is of the same order as the grain size, each fission fragment can interact with only a single bubble. Under these conditions the probability of re-resolution is inversely proportional to the gas atom concentration on the boundary and the Speight formalism becomes invalid. The collision process will actually remove vacancies as well as fission gas atoms from a cavity although the process of removing vacancies is equivalent to knocking matrix atoms back into the cavity. Since energy transfers are involved it makes more sense to consider the re-resolution process as removing a “chip” comprising N_c vacancies and gas atoms in such a way that:

$$\frac{dV}{dt} = -2l_f F F_c N_c \cdot \left(\frac{b + \Omega \varepsilon_{gf}}{1 + \varepsilon_{gf}} \right)$$

In this equation, dV is volume removed from the bubble in time dt . F is the fission rate, F_c is the fractional coverage of the grain boundary. The Van der Waal’s volume of a fission gas atom is b and Ω is the vacancy volume. The number of vacancies per fission gas atom is ε_{gf} .

Calculations using the ENIGMA stand-alone fission gas release model for case 4135E as well as a number of other extended-dwell cases indicate an optimum chip number of 683 ± 325 vacancies and gas atoms ejected per fission fragment collision. Using this value, the results in Figure 5 are obtained. The calculations indicate a leftward shift in both plots consistent with the observations. The full calculations are provided in Table 4.

Figure 5. Calculated bubble parameters assuming irradiation-induced re-resolution of fission gas atoms from grain-face bubbles during the 28 day extended-dwell

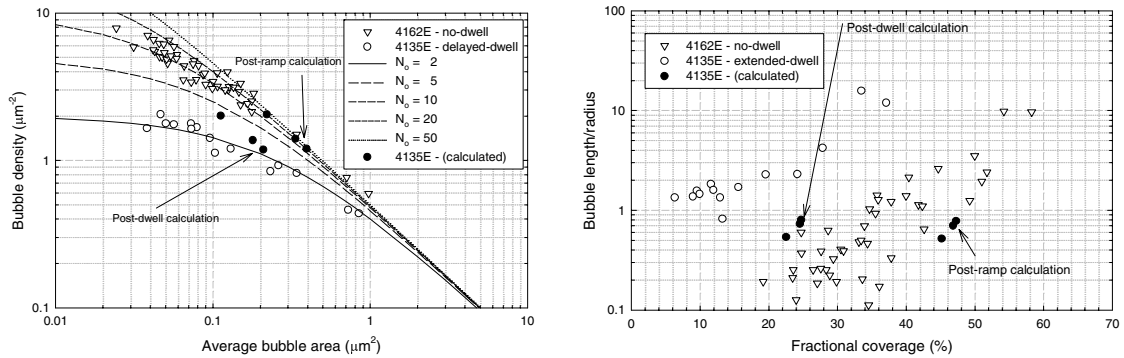


Table 4. Measured and predicted swellings at end of extended-dwell in 4135E

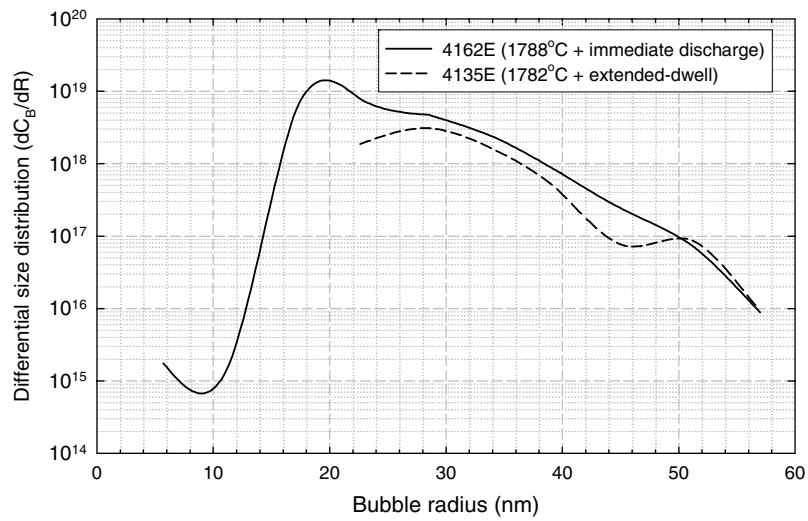
Spec.	P or M	N_b/A_{gb} (μm^{-2})	$\Delta V/V$ (%)	R_p (nm)	L_p (nm)	F_c (%)
4135-a	M	1.03 ± 0.51	0.42 ± 0.19	160 ± 30	470 ± 270	22.8 ± 8.6
	P	1.18	0.50	211	169	24.7
4135-b	M	1.52 ± 0.25	0.16 ± 0.08	120 ± 30	150 ± 80	11.5 ± 2.6
	P	1.37	0.46	198	143	24.6
4135-c	M	1.78	0.09	90	130	9.0
	P	2.01	0.34	163	88	22.5

Intragranular swelling

The volumetric swellings in the extended-dwell test are much lower than in the immediate-discharge case (see Table 2) and this appears to be a result of a reduction in total bubble concentration rather than a reduction in the average radius. Figure 6 shows that the bubbles with radii less than 20 nm have almost disappeared. It is known that irradiation-induced re-resolution is only capable of destroying small bubbles and that volumetric reduction occurs mainly through a whittling-down process whereby bubbles gradually lose volume until small enough to be destroyed. The differential bubble-size distributions for two comparable fuel locations in the two tests are shown in Figure 6.

Figure 6. Differential bubble-size distributions for the two tests at comparable peak temperatures

Note that the total bubble concentration is equal to the area under each curve and that the vertical scale is logarithmic



The re-resolution process from intragranular bubbles is modelled by assuming that a chip of vacancies and gas atoms is removed from bubbles by each fission fragment. Although it is known that large bubbles are not destroyed directly, the damage process is apportioned in such a way as to give both reductions in bubble size and concentrations with the apportioning factor depending on the mean bubble size. The model has previously been optimised over the temperature range from 1 250°C to 1 920°C using data from the BE tests [2]. The present data and two other tests (not reported here) have enabled the optimisation to be extended to temperatures down to 860°C. The intragranular swelling observed at the end of the 28-day dwell is consistent with a chip size of between 40 and 100 vacancies and gas atoms being removed from a bubble by each fission fragment collision, but the chip size increases strongly with temperature. Using the revised chip size, Table 5 gives the predictions of the intragranular swelling.

Table 5. Measured and predicted value of intragranular swelling for the extended-dwell case

Spec.	Predicted/measured	C_B (m ⁻³)	R_B (nm)	$\Delta V/V$ (%)
4135-a	M	$4.09 \cdot 10^{19}$	27.5	0.37
	P	$5.27 \cdot 10^{19}$	21.7	0.23
4135-b	M	$3.57 \cdot 10^{19}$	25.2	0.25
	P	$5.69 \cdot 10^{19}$	22.4	0.27
4135-c	M	$5.39 \cdot 10^{19}$	21.8	0.25
	P	$6.50 \cdot 10^{19}$	23.6	0.36

Predicted total swelling

By tuning the swelling model to provide good estimates of the measured swellings, it is then possible to estimate the swellings immediately following the ramp and before the onset of the extended-dwell. It is this swelling that gives rise to the diametral strain and the values are given in Table 6.

Table 6. Predicted and measured swellings for the extended-dwell case

Spec.	Intragranular swelling $\Delta V/V$ (%)		Grain-face swelling $\Delta V/V$ (%)		Total swelling $\Delta V/V$ (%)	
	Measured post-dwell	Calculated pre-dwell	Measured post-dwell	Calculated pre-dwell	Measured post-dwell	Calculated pre-dwell
4135-a	0.37	5.13	0.42	1.31	0.79	6.44
4135-b	0.25	5.12	0.16	1.21	0.41	6.33
4135-c	0.25	4.72	0.09	0.97	0.34	5.69

Although the post-dwell swellings are quite small, these are consistent with much larger values immediately following the ramps. The total calculated pre-dwell swelling is around 6% for the three sections measured and are consistent with the measured diametral strains indicating the effectiveness of irradiation-induced re-resolution in reducing the overall swelling during low power periods following transients.

Conclusions

Examination of data from the British Energy CAGR ramp tests reveals that rod failure occurred through large diametral strains. In one case, very little evidence of large swellings was observed in the fuel but detailed examination of the SEM data revealed vestigial evidence of swelling. Analysis was performed on the assumption that the swelling decreased during the extended-dwell period following the transient by a process of irradiation-induced re-resolution from intra- and intergranular porosity. Using these assumptions it was possible to estimate that the swelling immediately following the transient was sufficient to provide the observed failure strain.

REFERENCES

- [1] Turnbull, J.A., *J. Nucl. Mater.*, 38, 203 (1971).
- [2] White, R.J., R.C. Corcoran and J.P. Barnes, *A Summary of Swelling Data Obtained from the AGR/Halden Ramp Test Programme*, R&T/NG/EXT/REP/0206/02, December 2002
- [3] White, R.J., *J. Nucl. Mater.*, 325, 61 (2004).

- [4] Clay, B.D. and T.C. Gilmour, *The Post-irradiation Examination of AGR Fuel Ramped in the Halden Test Rig IFA-576.5 – Pin Recovery, Metrology and Ceramography*, TE/EXT/REP/0245/96, IMC Ref. FC/AGR/5003/03, May 1997.
- [5] Reynolds, G.L., W. Beere and P.T. Sawbridge, *J. Nucl. Mater.*, 41, 112 (1971).
- [6] Speight, M.V., *Nucl. Sci. and Eng.*, 37, 180 (1969).

ON THE RELATIONS BETWEEN THE FISSION GAS BEHAVIOUR AND THE PELLET-CLADDING MECHANICAL INTERACTION IN LWR FUEL RODS

P. Van Uffelen, M. Sheindlin, V. Rondinella, C. Ronchi

European Commission, Joint Research Centre, Institute for Transuranium Elements
P.O. Box 2340, 76125 Karlsruhe, Germany

Abstract

In the first part of the paper we review and discuss some of the experimental evidence underlining the effect of the stress distribution on the fission gas release and swelling in oxide fuels. We consider both instrumented tests in a reactor as well as out-of-pile annealing experiments.

The stress distribution in the fuel is generally accounted for in the fission gas release and swelling models via the so-called hydrostatic stress. Various approaches have been applied to determine the hydrostatic stress in fuel performance codes. It is indicated that either the applied approaches cannot satisfactorily reproduce the experimental observations, or that they are based on erroneous assumptions.

The imperfect modelling of the stress distribution in the fuel rod is related to the high complexity of the phenomenon as well as to the limited amount of experimental data. In view of this, the Institute for Transuranium Elements (ITU) is developing a new experimental device: POLARIS (Power Laser Apparatus for Reactor-Irradiated Samples). One of the proposed experiments consists of analysing the effect of hydrostatic stress via a variable He gas pressure, in combination with a variable temperature level in a high burn-up fuel rod segment.

Introduction

In order to ensure the safe and economic operation of the fuel rods, it is necessary to be able to predict their behaviour and life-time. An accurate description of the fuel rod's behaviour, however, involves various disciplines ranging from chemistry, nuclear and solid state physics, metallurgy, ceramics and applied mechanics. The strong interrelationship between these disciplines calls for the development of computer codes describing the general fuel behaviour.

A well known example of the interrelationship is the interplay of the mechanical performance with the fission gas release and swelling phenomena. On one hand, the gaseous fission product swelling promotes gap closure and the subsequent pellet-cladding mechanical interaction, while their release from the pellets increases the internal gas pressure, which in turn drives the cladding creep. On the other hand, almost all gas behaviour models make use of the so-called hydrostatic pressure to describe the state and evolution of gas-filled bubbles, while sudden stress variations may lead to an abrupt fractional release of retained gases, e.g. via cracking.

Despite the common use of the hydrostatic stress in the fission gas behaviour models, there is still debate about the extent to which the stress state affects the fission gas behaviour, about the way in which the hydrostatic should be accounted for in the fission gas behaviour models, as well as about the actual evaluation of the hydrostatic stress itself. The latter is related to the high complexity of the phenomenon as well as to the limited amount of experimental data. In view of this, the present paper intends to shed some light on the debate and to propose a new experimental technique that is under development at ITU.

In the following section of the paper we review and discuss some of the experimental evidence underlining the effect of the stress distribution on the fission gas release and swelling in oxide fuels. We consider both instrumented tests in a reactor as well as out-of-pile annealing experiments. In the third section of the paper, we will summarise and discuss the main theoretical approaches adopted to account for the stress in the fission gas behaviour models, as well as the models used to compute the hydrostatic stresses in the pellets during irradiation. In a subsequent section, the new experimental technique, POLARIS, will be outlined and we will explain how it could contribute to the studies mentioned above. Finally, in the last section we draw the conclusions of our analysis and describe the perspectives of our ongoing research activities in this area.

Experimental evidence

There are data, both from in-pile and out-of-pile experiments, indicating an important effect of the hydrostatic stress on the release of fission gas in nuclear fuel [1-13].

In-pile evidence

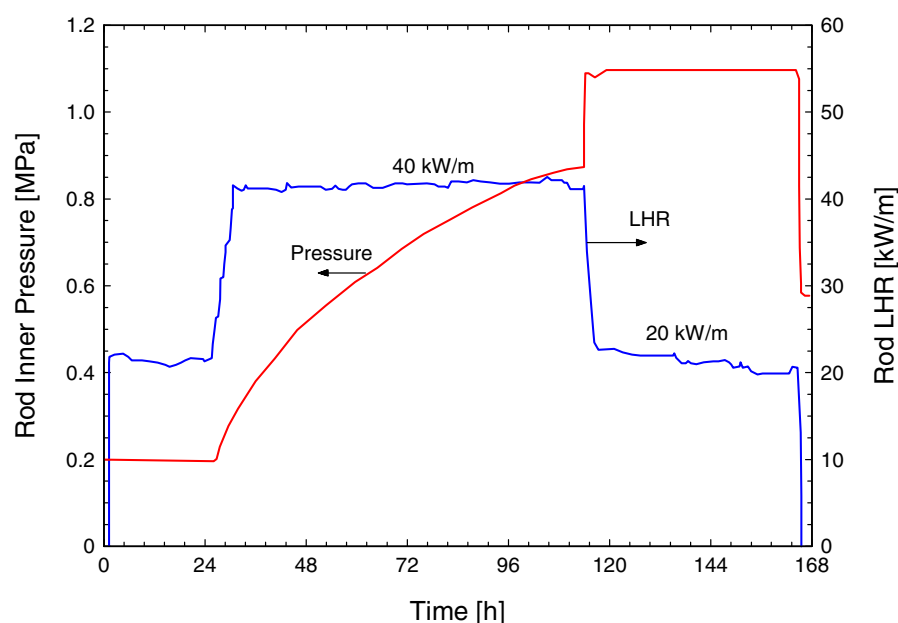
Zimmerman [1] revealed that mechanical restraint (compressive load up to 50 MPa) due to a piston reduced the fission gas swelling in isothermal irradiation tests by a factor 2 in comparison with unrestrained swelling in a temperature range between 1 600 and 1 900 K, and a burn-up range up to 10 at.%.

Later on, Kogai, *et al.* [2] also analysed the effect of pellet-cladding interaction on fission gas release (FGR) in fuel with a burn-up range between 12 and 42 GWd/tM under load following conditions. The distinct FGR behaviour of the fuel rods with different initial gap size and pellet geometry (dished

versus undished) was attributed to the different extent of pellet-cladding mechanical interaction (PCMI) or hydrostatic stress. A model for release through a fine tube has therefore been proposed, in order to account for the different release kinetics with the hydrostatic stress that was estimated to vary between 30 and 150 MPa. Likewise, Mørgensen, *et al.* [3,4] also emphasised the importance of mechanical restraint pressure in fission gas release behaviour during power bump tests. Specifically, they indicated that enhanced release at the end of the test was due to grain boundary opening by micro-cracking.

More recently, Nakamura, *et al.* [5] re-instrumented pre-irradiated medium burn-up fuel with a large initial diametrical gap of 310 μm . They concluded that fission gas release (FGR) increased suddenly when the hydrostatic stress was reduced during a reduction of the linear heat rate between 40 and 20 kW/m. This reduction of hydrostatic stress was attributed to the variation of the thermal stress in the pellet. PCMI was supposed to be absent in view of the large initial gap and the applied burn-up. This assumption was supported by the observation that diffusion-controlled FGR was clearly observed during the high-power operation (Figure 1). Release due to cracking of the fuel during power changes has also been ruled out since the sudden increase of FGR only appeared during a reduction of the power level and not over the course of a power increase.

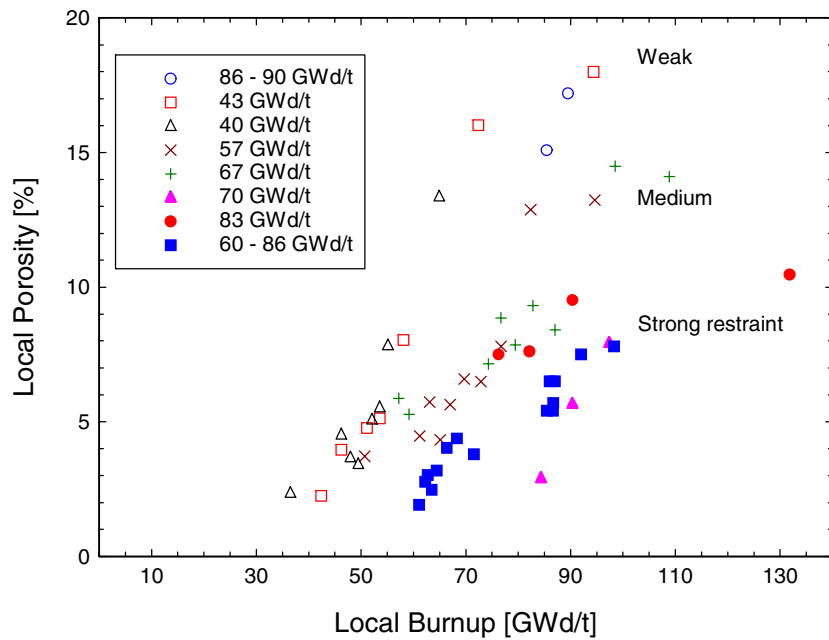
Figure 1. Rod inner pressure change during power variations [5]



K. Une, *et al.* [6] observed the effect of the grain size and the PCMI restraint on the rim structure formation in UO_2 fuel coming from pellets and from isothermally irradiated fuel discs. Significant differences in porosity and size distribution of rim bubbles were detected between a standard grain size pellet of 96 GWd/t with severe PCMI restraint and the fuel discs of 86-90 GWd/t without any restraint pressure, although the extent of the rim structure formation was almost identical for both types of samples (*cf.* Figure 2).

Finally, the observations of Tempest, *et al.* [7] were taken as evidence for the absence of any delaying effect on interlinkage from internally pressurising the rods to 40 bar. Nevertheless, their conclusion is likely due to the range of the hydrostatic pressure applied in their experiments, which is more than one order of magnitude smaller in comparison with the range of the hydrostatic pressure considered in the other experiments.

Figure 2. Relationship between local porosity and local burn-up, showing the effect of restraint on the porosity development in the rim region [6]

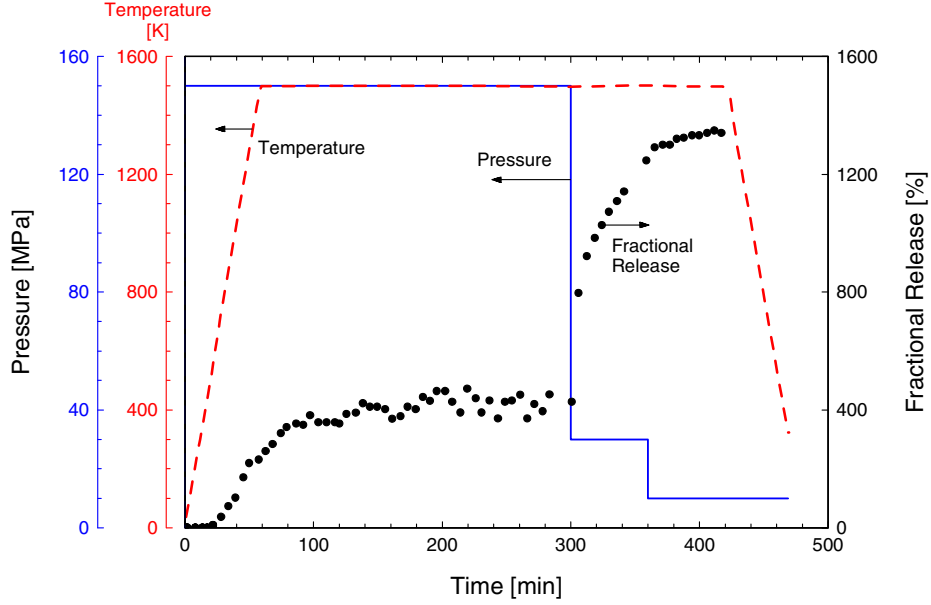


Out-of-pile evidence

P. Bailey, *et al.* [8] investigated gas release from UO₂ and UN out of pressurised closed pores produced by autoclave anneals. The sintered UO₂ was annealed in Ar at 1 000 bar and 1 500°C. The thermal desorption spectrometry revealed that release occurred during both heating and cooling and was attributed to mechanical effects, i.e. fuel fracture connecting grain boundary gas bubbles with the surface.

Kashibe and Une [9,10] extensively assessed the effect of restraint on bubble growth in unirradiated UO₂ fuels by using a high temperature (up to 2 000°C) and a high pressure (up to 200 MPa) furnace. The powder compacts of UO₂ were sintered at 1 800°C in a high pressure Ar/0.2%H₂ mixed gas of 50 or 100 MPa. As a result the bubbles were overpressurised, entailing bubble growth with the pressure difference as driving force. The sintered pellets were then annealed at temperatures ranging from 1 300 to 1 800°C and pressures about 10 to 80 MPa lower than the sintering temperature and pressure. The pressure in the pellets was thus very well controlled and purely hydrostatic. They verified the bubble growth model of Hull and Rimmer [11], which is a simplified version of our model [12] and that of Kogai, *et al.* [13] (*cf.* below). In addition, they have observed fractional release rates of ⁸⁵Kr during annealing tests of UO₂ fuel with a burn-up of 37 GWd/t, which appeared to be completely suppressed by strong external restraint pressures of 100-150 MPa in the temperature range 1 500-1 800°C. The critical pressure for the onset of burst release due to rapid bubble growth and tunnel formation (*cf.* Figure 3) was found to be in the range of 40-60 MPa at 1 500°C [14].

Figure 3. Cumulative fractional release of ^{85}Kr at ramp and isothermal annealing temperature of 1 500°C for rapid descending restraint pressure from 150 to 30 MPa [14]



Theoretical approaches

Implementation of hydrostatic stress in fission gas behaviour models

The hydrostatic stress is defined in a solid as the average normal stress [15,16]:

$$P_h = \frac{\sigma_{rr} + \sigma_{\theta\theta} + \sigma_{zz}}{3} \quad (1)$$

and affects the mechanical equilibrium of gas-filled bubbles in nuclear fuel:

$$P_{bl} + P_h - \frac{2\gamma}{\rho_{bl}} \quad (2)$$

where P_{bl} is the pressure of the gas in the bubble (tensile), P_h is the hydrostatic pressure in the matrix surrounding the bubble (compressive), γ corresponds to the surface tension of the bubble and ρ_{bl} represents its radius of curvature.

In most FGR models [17-27], the hydrostatic stress is only accounted for in the saturation limit of the grain boundary:

$$N_{sat} = \frac{A_f}{T} \left(\frac{2\gamma}{\rho_{bl}} - P_h \right) \quad (3)$$

where N_{sat} is the saturation density of fission gas atoms on the grain boundary and A_f is a function depending on the bubble shape. Consequently, P_h will only affect the onset of release and not the release kinetics once the saturation is reached.

According to Kogai, *et al.* [2] there is also a clear effect of the hydrostatic stress on the release kinetics, as illustrated in Figures 4 and 5. Kogai [13] has therefore accounted for the effect of hydrostatic stress in two complementary ways. First of all, he applies a refinement of the model of Hull and Rimmer [11] for the bubble growth and shrinkage via grain boundary diffusion of vacancies. The driving force for bubble growth/shrinkage consists of the pressure difference between the gas internal pressure, the surface tension and any externally applied (hydrostatic) pressure:

$$\frac{d\rho_{bl}}{dt} = \frac{\Omega\delta_{gb}}{4f(\theta)k} \frac{D_m^v}{T\rho_{bl}^2} \left(P_{bl} + P_h - \frac{2\gamma}{\rho_{bl}} \right) k(\phi) \quad (4)$$

Figure 4. Internal gas pressures, fission gas release fractions and bump power histories of rod M23-1-17R illustrating the influence of PCMI on the kinetics of release [2]

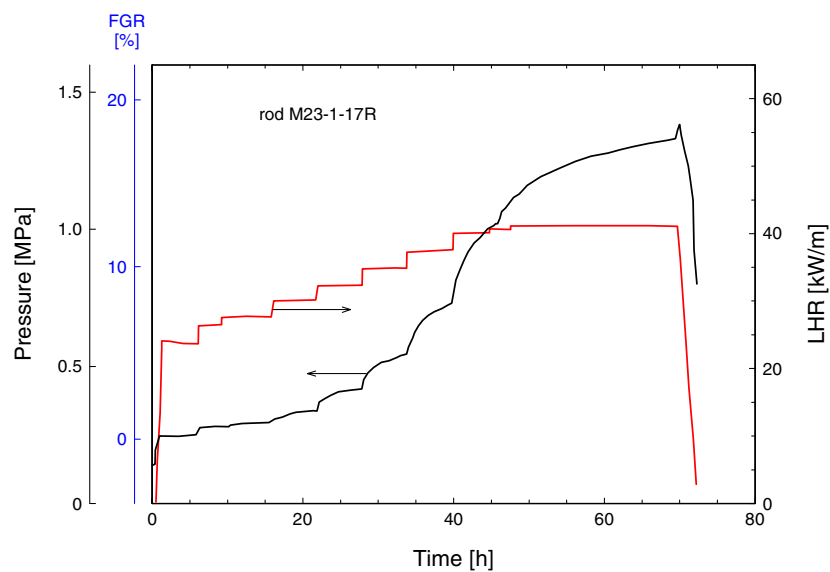
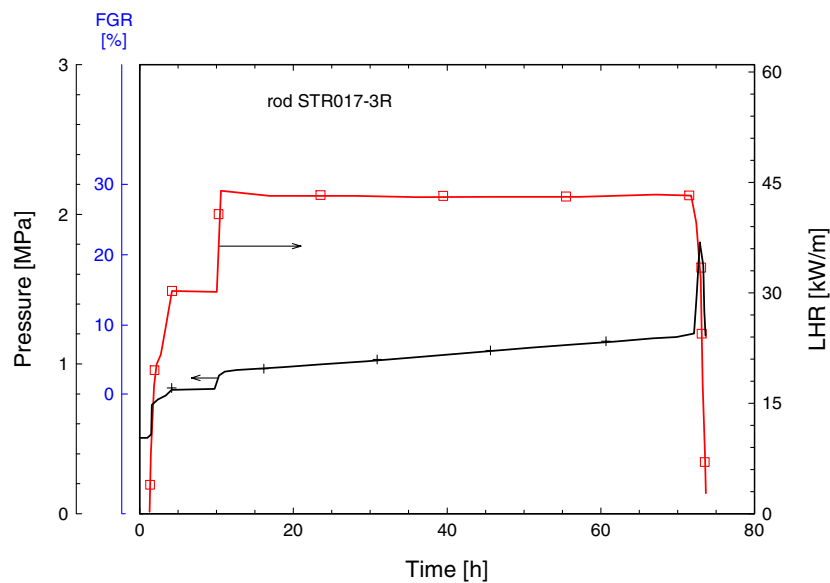


Figure 5. Internal gas pressures, fission gas release fractions and bump power histories of rod STR017-3R illustrating the influence of PCMI on the kinetics of release [2]



Secondly, as the grain boundary bubbles grow, those which are close enough to the grain edges may vent their content to the free volume of the rod. This gaseous flow through the tunnel network is derived from the Poiseuille equation in a thin cylindrical tube, connecting the average bubble with the free volume as illustrated in Figure 6. Kogai [13] supposes that the conductivity of the tube increases by the shortening or thickening of the tube. Therefore, a sigmoidal type of curve was introduced for the volume (corresponding to the tube conductivity):

$$V_t = V_t^0 f(\phi) g(\sigma_e) \quad (5)$$

where:

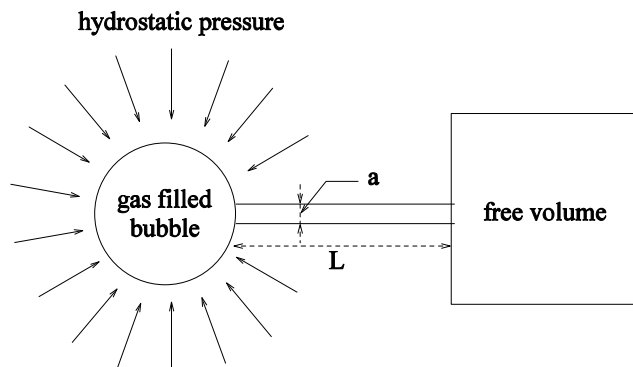
$$g(\sigma_e) = 1 - \exp \left[- \left(\frac{\sigma_e}{\sigma_e^*} \right)^{10} \right] \quad (6)$$

and:

$$\sigma_e = \frac{P_h + \phi P_{bl}}{1 - \phi} \quad (7)$$

According to Eq. (6), both a tensile and a compressive hydrostatic stress will increase the tube conductivity since the even power eliminates the sign of the equivalent stress (σ_e). This is physically unacceptable. In addition, it can be noted that the effect of the hydrostatic stress on the tube conductivity is accounted for twice: once indirectly in the bubble growth law [Eq. (4)] and a second time directly in the sigmoidal curve $g(\sigma_e)$, which is unnecessary. Therefore we propose the following simplification [12]. Like Kogai we account for P_h in the grain boundary bubble growth law, though unlike Kogai we consider the tube conductivity to depend solely on the bubble surface fraction on the grain face: $V_t = V_t^0 f(\phi)$. As a result, both the gaseous swelling and the fission gas release will be affected by the hydrostatic stress level in the fuel through the growth/shrinkage of the bubbles on the grain boundaries, in line with the experimental observations of Kashibe, *et al.* [9].

Figure 6. Schematic representation of the gaseous flow through the interconnected tunnel network along the grain boundaries by a tube connecting the average grain boundary bubble with the free volume in the fuel rod [2]



More recently, White [28] introduced an alternative idea to account for the hydrostatic stress in describing the kinetics of the fission gas behaviour in nuclear fuel. Like Kogai [13], Kashibe, *et al.* [9,10] and Van Uffelen [12] he applies Eq. (4) to describe the bubble growth/shrinkage. Unlike Kogai and

Van Uffelen, however, White included the morphological changes of the grain boundary bubbles after coalescence and introduced an empirical fractional venting depending solely on the bubble length, rather than on the fractional coverage of the grain boundary by the bubbles.

The assessment of the hydrostatic stress in fuel performance codes

A weak point of most fuel performance codes is their mechanical modelling [29]. The mechanics of the cracked pellet and of the anisotropic cladding are generally rather primitive. One of the difficulties stems from the lack of experimental data, e.g. on circumferential stress at the pellet outer surface during reactor operation. Even when there are experimental data for un-irradiated fuel, there is quite some scatter, both in the data themselves as in the ratio of the calculated and measured values (e.g. for the fuel strength and the creep data in MATPRO) [30].

Immediately upon start-up and before swelling or creep has occurred to any appreciable extent, the fuel develops a network of cracks oriented either along radial planes or along horizontal planes perpendicular to the z-axis. These cracks appear because the thermoelastic stress components exceed the fracture strength of the fuel in tension (the tensile rupture stress is of the order of 130-150 MPa) [15,16] when the linear heat rate exceeds 5 kW/m in a fresh solid pellet. The temperature gradient in the pellet induces tensile stresses in the θ - and z-directions in the outer region of the fuel where the fuel is brittle (because $T \leq 1400^\circ\text{C}$). When the fuel cracks, relocation occurs and reduces the initial diametrical gap.

The effect of cracking on the mechanical performance of the fuel cannot exactly be taken into account in the fuel performance codes. To do so would require (1) knowledge of the precise location and size of every crack in the fuel and (2) the solution to the complete three-dimensional stress-strain problem in each of the blocks of intact solid without the aid of the major simplification afforded by the assumption of symmetry around the central axis. Consequently, the phenomenon is modelled by assuming that cracking occurs only on the principal planes, specifically only θ - and z-cracks are considered. The effect of multiple cracking is treated in two different ways: either the elastic constants of an anisotropic homogeneous cylindrical pellet are modified [15,31], or a supplementary strain term is introduced [16,27,32].

In general the hydrostatic stress can have contributions from the inner fill gas pressure, the thermal stress and the stress due to PCMI. For the time being, however, there are different approaches to compute P_h in the computer codes. Except for models that do not mention how P_h is computed [19,25,26,28], we can separate the approaches in three categories. In the first category, P_h is taken to be a uniform and often constant value. More precisely, either they assume a zero hydrostatic stress level [19-21], or they apply a constant value [22,24], which is occasionally inferred from measured cladding strains [13] to account for PCMI. Several codes consider the grain boundary gas saturation condition of Eq. (3) to be constant or only temperature dependent [23,27], corresponding implicitly to assume a constant value for P_h .

The second category of models considers the time-dependent inner gas pressure as well as the contact pressure in the event of PCMI [32-35]. The contribution due to differential thermal expansion is disregarded in the cracked fuel segments. In unrestrained pellets the radial and axial forces are therefore equal, uniform and equal to the time-dependent inner gas pressure, except in some cases where this contribution is neglected, e.g. Ref. [32].

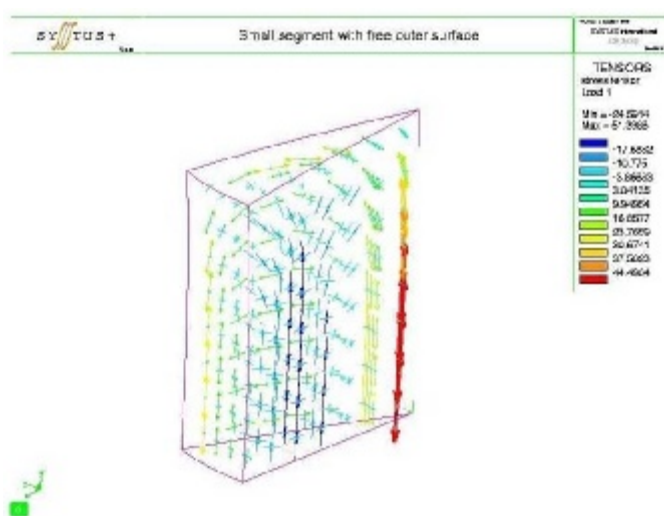
The third group of models accounts for the three contributions to P_h . The above-mentioned approaches seem to be in contradiction with the experimental observations of Nakamura, *et al.* [5] since there appears to be an effect of the hydrostatic stress in the absence of any PCMI. For that reason,

Nakamura and co-workers accounted for the thermoelastic stress along with the contact pressure between pellet and cladding, the inner gas pressure, and alleviation of the thermal stress by creep. However, they did not consider the influence of cracks. They applied Lamé equations that are only valid in a full cylindrical pellet.

Mezzi, *et al.* [36] have shown by means of finite element calculations in two dimensions that thermoelastic stress calculated from a strain analysis with axial symmetry differs radically from that in pie-shaped fuel fragments. We extended the calculations to three dimensions by means of the SYSTUS finite elements code (FEM) [37] in order to re-analyse (qualitatively) the in-pile experiments of Nakamura, *et al.* [5]. The special feature of the experiment is the large initial diametral gap size of 310 μm . Since the burn-up after the base irradiation of the re-instrumented segments was of the order of 25 MWd/kgUO₂, the gap was always open, even during the ramping experiments (40 kW/m). We therefore applied the same approach as that adopted by Garcia, *et al.* [38], except that we also included the axial cracks via the variation of the segment height. The most important lessons drawn from those FEM calculations were:

- The pellet centre is under tension in a wedge-shaped fuel segment, in contradiction with a compressive force in the full cylindrical pellet. This is in line with the conclusions from Mezzi, *et al.* [36] in two dimensions, and confirms that interpreting the experiments of Nakamura, *et al.* [5] by applying the Lamé equations for the thermo-elastic stress in order to assess the hydrostatic stress is misleading.
- The hoop stress in the pellet resulting from the thermo-elastic stress alone is no longer axially symmetric. The tangential stress is zero at the crack surface (provided that adjacent fragments do not interact) but not in the interior of the cracked pieces.
- By comparing the stress tensor resulting from two different temperature (or power) distributions, it is possible to qualitatively explain the burst release during the power reductions in the experiments reported by Nakamura, *et al.* [5] by the reduction of the compressive stress at the mid-radius of the pellet (Figure 7). This is also qualitatively in line with the higher amount of pressure increase seen during a power reduction when the hold-time at high power is extended.

Figure 7. Stress tensor obtained with FEM thermo-elastic calculation in a small fuel segment (height: 6.5 mm, radius: 5.3 mm, angle = 22.5°) and subject to a parabolic temperature gradient ($T_{\text{surface}} = 400^\circ\text{C}$, $T_{\text{centre}} = 1\,000^\circ\text{C}$)



A more recent model of the third category accounts for the thermal stress variations in a pure empirical way [39]. To do so, it was assumed that the entire gas inventory at grain boundaries is released instantaneously when several conditions are fulfilled. In the event of a power increase, burst release is assumed to occur when:

$$\begin{cases} q_e - q_i > 30 \text{ W/cm} \\ q_e > 250 \text{ W/cm} \\ T_e > T_t \end{cases}$$

where q_e and q_i represent the linear heat generation rate of the fuel rod after (e) and before (i) the transient, T_e stands for the fuel temperature after the transient (°C). T_t is the burn-up dependent threshold temperature:

$$T_t = 1500 \left(1 - \frac{bu}{80} \right)$$

where the burn-up is expressed in MWd/kgU. In the event of a power reduction, burst release is assumed to take place when:

$$\begin{cases} q_i - q_e > 30 \text{ W/cm} \\ q_i > 250 \text{ W/cm} \\ T_i > T_t \end{cases}$$

The approach adopted by Koo, *et al.* [39], however, does not provide the hydrostatic stress needed for mechanistic fission gas release models.

From the discussion above, it can be concluded that in addition to a lack of consensus there remains room for improvement in calculating the hydrostatic stress in pellet fragments during irradiation. To this end, it is proposed to extend the series of 3-D FEM calculations to account for the viscoplastic behaviour along with the interaction with the cladding material like S. Bourreau, *et al.* [40]. In addition, more experimental data will be obtained, as explained in the following section.

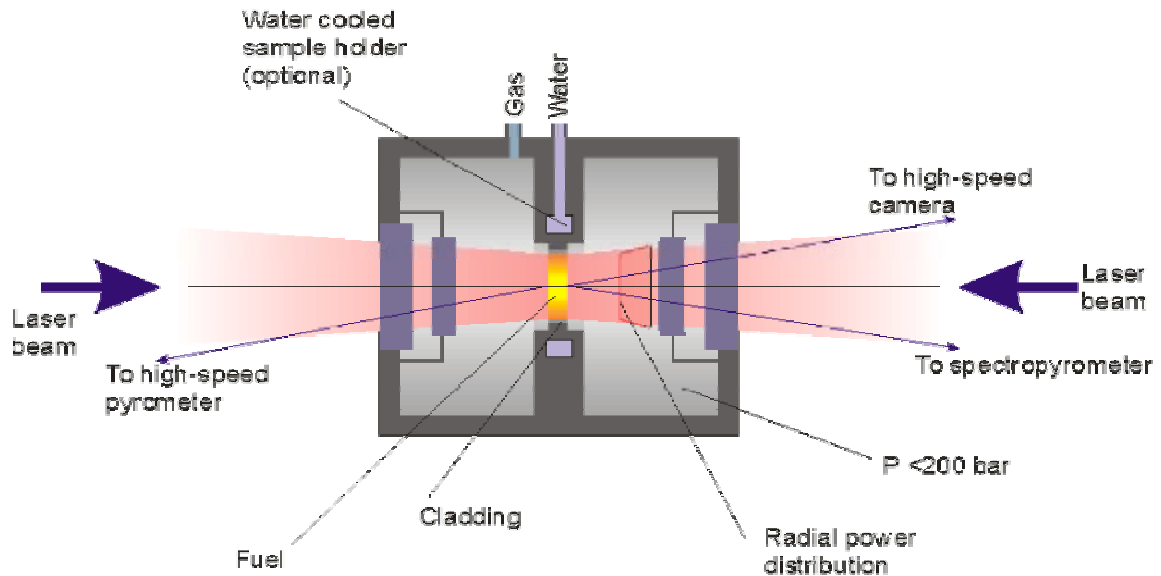
Proposal for a new experimental approach

The imperfect modelling of the stress distribution in the fuel rod is related to the high complexity of the phenomenon (3-D modelling would be required) as well as to the limited amount of experimental data. ITU is developing a new experimental device (POLARIS) by means of which complementary information regarding the interaction of fission gas behaviour and the stress distribution in the pellets will be inferred. A schematic view of the future facility is presented in Figure 8. A detailed description of the design has been provided elsewhere [41].

The tests will be performed in a sealed pressure cell equipped with two oppositely placed windows. The cell is contained in a lead-shielded glove box equipped with telemanipulators. Hydrostatic pressurisation of the cell up to 200 bar (or possibly higher) will be achieved by means of He gas. All the instrumentation for optical diagnostics is situated outside the box. The sample – a slice of the fuel pin including cladding of 1-1.5 mm thickness – is heated on each face by a CW laser beam of equal power that enters the cell through an optical window. The laser focal spots with highly homogeneous radial power profile can be adjusted to cover the whole fuel surface, although they will not impinge on

Figure 8. Schematic experimental set-up for the fuel fragmentation studies in POLARIS

**SIMULATION OF THE IN-PILE THERMAL BEHAVIOUR:
LASER HEATING OF IRRADIATED FUEL**



the cladding. A high-speed CCD camera will allow on-line mapping of the temperature on the whole illuminated surface. The sample will be held in a water-cooled sample holder in order to ensure a radial temperature profile that is representative of in-pile conditions.

In general, the main advantages of the proposed technique can be summarised as follows [41]:

- Very high power densities can be delivered (up to ca. 5 kW/cm^2 over the fuel surface).
- A “furnace” (a laser) is separated from the sample containing the high-pressure vessel.
- Absence of the broadband range self-radiation of the energy source and therefore a possibility of precise optical and temperature measurements.
- Virtually any time-shaped power transients can be applied (1 ms time constant), along with time varying He pressures.

Since the laser power can be programmed arbitrarily as a function of time, three scenarios of the test procedure are envisaged:

- 1) From the baseline temperature slowly raise the fuel temperature until fragmentation occurs.
- 2) From the baseline temperature slowly heat the fuel to just below the fragmentation point and then fire a laser pulse to raise the temperature beyond the fragmentation point.
- 3) From the baseline temperature raise the fuel temperature to just below the fragmentation point by slow heating and then drop the pressure in the cell.

The first two cases will certainly result in fuel fragmentation, whereas the fragmentation is uncertain in the third scenario. The baseline temperature of 300-1 000°C can be ensured by precision power regulation of the laser and its high-power stability.

In addition to the on-line measurement of the temperature distribution in the fuel segment, two other measurements will be of great relevance for assessing the effect of the stress distribution on the fission gas behaviour.

First of all, one will detect the fragmentation point. To do so, the temperature rise of the sample is followed by a fast optical pyrometer (time resolution of ca. 10 μ s). It is anticipated that the temperature corresponding to the fragmentation point of the fuel will be indicated by a knee point and/or a sharp drop in the heating thermogramme. Additional information on the disruption process will be obtained using a high-speed thermo-imaging camera capable of recording 1 000 frames/s. The high-speed camera will also monitor the temperature distribution in the fuel and, in particular, the precise moment of fragmentation as well as the fragmentation pattern.

The second measurement will be dedicated to the integrated fission gas release and is currently being developed. Since the fragmentation tests will be performed in a He atmosphere at 200 bars it is unlikely that the integral release fraction of He can be measured with high accuracy. Nevertheless, heavy gases such as Kr and Xe can be separated in a cold trap and their concentration determined by gamma counting and/or analysed by mass spectrometry. Based on our experience, the “cold-trap solution” with gamma counting seems preferable at present. Even so, the possibility for on-line measurements of the released fractions of fission gases is being investigated.

One of the proposed experiments consists of analysing the effect of hydrostatic stress via a variable He gas pressure, in combination with a variable temperature level in a very high burn-up fuel rod segment subject to a prototypical radial temperature profile (*cf.* above). In addition to the integral measurements mentioned above, complementary post-test examinations by means of SEM and EDX are foreseen. With such an experimental scheme, one will be able to analyse the effect of the variations of the thermal stress distribution along with the hydrostatic stress distribution applied by the filling gas on the fragmentation behaviour as well as the fission gas release in the fuel segments.

The analysis of gas release and swelling by means of a laser-induced fuel fragmentation can thus be considered as a powerful out-of-pile experimental approach complementing the experiments indicated in the previous sections. More precisely, it opens new perspectives in on-line diagnostics that are unavailable in the existing experimental methods.

Summary and conclusions

In the first part of the paper we reviewed and discussed some of the experimental evidence underlining the effect of the stress distribution on the fission gas release and swelling in oxide fuels. Both instrumented tests in a reactor as well as out-of-pile annealing experiments were considered. Despite the considerable number of experiments available, more refined tests are necessary in order to obtain complementary and accurate data regarding the fission gas behaviour as well as the stress distribution in the fuel rods.

The stress distribution in the fuel is generally accounted for in the fission gas release and swelling models via the so-called hydrostatic stress, corresponding to the trace of the stress tensor. The different methods for introducing the effect of P_h on the fission gas behaviour in the models have been discussed.

It is concluded that one should not only account for its effect on the onset of release, but also for its effect on the release and swelling kinetics observed during some in-pile experiments and accounted for in some of the recent models [12,13,28].

The various approaches applied to determine the hydrostatic stress in fuel performance code calculations have been summarised and discussed as well. The simplest approach is to consider a zero hydrostatic stress level based on the low tensile strength of UO_2 . Others have considered a uniform and constant hydrostatic stress level based on either the internal gas pressure and/or the pellet-cladding contact stress. Finally, an attempt has been made to model the time and space variations of the hydrostatic stress based on thermal stress calculations in a cylindrical pellet, or by introducing empirical formulas for fission gas release in order to account for thermal stress variations leading to microcracking during abrupt power changes. From the discussion it clear that the lack of consensus reflects room for improvement. In order to address the problem, it is not only proposed to launch a new set of advanced tests as described above, but also to extend the three-dimensional finite element calculations. This will be necessary in order to enable a proper interpretation of experiments like those of Nakamura, *et al.* [5].

ITU is developing a new experimental device (POLARIS), by means of which complementary information regarding the interaction of fission gas behaviour and the stress distribution in the pellets can be inferred. One of the proposed test scenarios is based on the variation of the hydrostatic stress via a variable He gas pressure, in combination with a variable temperature level in a very high burn-up fuel rod segment. The on-line measurement of both the temperature distribution, the fission gas release along with the fragmentation of the fuel rod segments will be complemented with detailed post-test structure/microstructure examinations. This innovative experimental method complements the series of experiments reviewed in the first part of the paper, and offers a more representative experiment with improved accuracy thanks to its flexible and on-line tuneable control and diagnostics.

Acknowledgements

J. van de Laar is greatly acknowledged for the preparation of the figures. One of the authors (PVU) gratefully acknowledges the fruitful discussions with and the information received from M. Scibetta (SCK•CEN), S. Shihab (BN), J. Nakamura (JAERI), F. Bentejac and S. Sorer (CEA-Saclay). The assistance of M. Scibetta for the SYSTUS calculations are also much appreciated.

REFERENCES

- [1] Zimmerman, H., "Investigations on Swelling and Fission Gas Release in Uranium Dioxide", *J. Nucl. Mat.*, 75, 154-161 (1978).
- [2] Kogai, T., K. Ito, Y. Iwano, "The Effect of Cladding Restraint on Fission Gas Release Behaviour", *J. Nucl. Mat.*, 158, 64-70 (1988).
- [3] Mørgensen, M., C. Bagger, C.T. Walker, "An Experimental Study of the Distribution of Retained Xenon in Transient-tested UO₂ Fuel", *J. Nucl. Mat.* 199, 85-101 (1993).
- [4] Walker, C.T., P. Knappik, M. Mørgensen, "Concerning the Development of Grain Face Bubbles and Fission Gas Release in UO₂ Fuel", *J. Nucl. Mat.*, 160, 10-23 (1988).
- [5] Nakamura, J., M. Suzuki, H. Uetsuka, "Re-irradiation Tests of LWR Spent Fuel at JMTR", presented at the EHPG meeting in Loen, May 1999.
- [6] Une, K., K. Nogita, Y. Suzawa, K. Hayashi, K. Ito, Y. Etoh, "Effects of Grain Size and PCI Restraint on the Rim Structure Formation of UO₂ Fuels", Proc. Int. Top. Meeting LWR Fuel Perf., 10-13 April 200, Park City, Utah, USA.
- [7] Tempest, P., R.J. White, "The Effect of Fill Gas Pressurisation on Fission Gas Release and Thermal Behaviour in IFA-558 and its Prediction by the Fuel Modelling Code ENIGMA", *Proc. Enlarged Halden Program Group Meeting*, OECD Halden Reactor Project, Storefjell, Norway (1993).
- [8] Bailey, P., S.E. Donnelly, D.G. Armour and H. Matzke, "Gas Release from Pressurized Closed Pores in Nuclear Fuels", *J. Nucl. Mat.*, 158, 19-24 (1988).
- [9] Kashibe, S., K. Une, "Effect of External Restraint on Bubble Swelling in UO₂ Fuels", presented at the EHPG meeting in Lillehammer, March 1998.
- [10] Kashibe, S., K. Une, "Densification and Swelling in UO₂ Pellets Under Hydrostatic Pressure Conditions", *J. Nucl. Sc. Techn.*, Vol. 35, No. 11, 796-800 (1998).
- [11] Hull, D., D.E. Rimmer, *Philos. Mag.* 4, p. 673 (1959).
- [12] Van Uffelen, P., *Contribution to the Modelling of Fission Gas Release in Light Water Reactor Fuel*, PhD thesis, Université de Liege, Belgium, January 2002.
- [13] Kogai, T., "Modelling of Fission Gas Release and Gaseous Swelling of Light Water Reactor Fuels", *J. Nucl. Mat.*, 244, 131-140 (1997).
- [14] Kashibe, S., K. Une, "Fission Gas Release from Externally Restrained Uranium Dioxide Fuel", *J. Nucl. Sc. Techn.*, Vol. 37, No. 6, 530-535 (2000).

- [15] Olander, D.R., *Fundamental Aspects of Nuclear Reactor Fuel Elements*, TID-26711-P1, Chap. 21 (1976).
- [16] Bailly, H., D. Ménessier, C. Prunier, *Le combustible nucléaire des réacteurs à eau sous pression et des réacteurs à neutrons rapides*, CEA, Eyrolles (1996).
- [17] White, R., M. Tucker, "A New Fission Gas Release Model", *J. Nucl. Mat.*, 118, 1-38 (1983).
- [18] Denis, A., A. Soba, "Simulation of Pellet-cladding Thermomechanical Interaction and Fission Gas Release", *Nucl. Eng. Des.*, 223, 211-229 (2003).
- [19] Denis, A., R. Piotrkowsky, "Simulation of Isothermal Fission Gas Release", *J. Nucl. Mat.*, 229, 149-154 (1996).
- [20] Maldovan, M., A. Denis, R. Piotrkowski, "Simulation of Isothermal Fission Gas Release. An Analytical Solution", *Nucl. Eng. Des.*, 187, 327-337 (1999).
- [21] Forsberg, K., A.R. Massih, "Diffusion Theory of Fission Gas Migration in Irradiated Nuclear Fuel UO_2 ", *J. Nucl. Mat.*, 135, 140-148 (1985).
- [22] Bernard, L.C., E. Bonnaud, "Finite Volume Method for Fission Gas Release Modeling", *J. Nucl. Mat.*, 244, 75-84 (1997).
- [23] Bernard, L.C., J.L. Jacoud, P. Vesco, "An Efficient Model for the Analysis of Fission Gas Release", *J. Nucl. Mat.*, 302, 125-134 (2002).
- [24] Lösönen, P., "Modelling Intragranular Gas Release in Irradiation of Sintered LWR UO_2 Fuel", *J. Nucl. Mat.*, 304, 29-49 (2002).
- [25] Suzuki, M., H. Uetsuka, H. Saitou, "Analysis of Mechanical Lead on Cladding Induced by Fuel Swelling During Power Ramp in High Burn-up Rod by Fuel Performance Code FEMAXI-6", *Nucl. Eng. Des.*, 229, 1-14 (2004).
- [26] El-Koliel, M.S., A.A. Abou-Zaid, A.A. El-Kafas, "Modeling of WWER-440 Fuel Pin Behavior at Extended Burn-up", *Nucl. Eng. Des.*, 229, 113-119 (2004).
- [27] Lassmann, K., *User Manual for the TRANSURANUS Code* (2003).
- [28] White, R.J., "The Development of Grain-face Porosity in Irradiation Oxide Fuel", *J. Nucl. Mat.*, 325, 61-77 (2004).
- [29] *Fuel Modelling at Extended Burn-up*, IAEA-TECDOC-998 (1998).
- [30] *SCDAP/RELAP5/MOD3.1 Code Manual IV: MATPRO – A Library of Materials Properties for Light Water Reactor Accident Analysis*, NUREG/CR-6150, EGG-2720, Volume IV (1993).
- [31] Lassmann, K., H. Blank, "Modelling of Fuel Rod Behaviour and Recent Advances of the TRANSURANUS Code", *Nucl. Eng. Des.*, 106, 291-313 (1988).
- [32] Shihab, S., "The Elastic Model for Arbitrary Radially Cracked Fuel Implemented in COMETHE-4D", *Proc. TCM on Water Reactor Fuel Element Modelling at High Burn-up and its Experimental Support*, Winderemere, UK, 19-23 September 1994, IAEA-TECDOC-957, pp. 391-401.

- [33] Billaux, M.R., S.H. Shann, L.F. Van Swam, “Transient Fuel Rod Behaviour Prediction with RODEX-3/SIERRA”, *Proc. TCM on Water Reactor Fuel Element Modelling at High Burn-up and its Experimental Support*, Windermere, UK, 19-23 September 1994, IAEA-TECDOC-957, pp. 381-390.
- [34] Berna, G.A., C.E. Beyer, K.L. Davis, D.D. Lanning, *FRAPCON-3: A Computer Code for the Calculation of Steady-state, Thermo-mechanical Behavior of Oxide Fuels for High Burn-up*, NUREG/CR-6534, Vol. 2, PNNL-11513 (1997).
- [35] Garcia, P., C. Struzik, M. Agard, V. Louche, “Mono-dimensional Mechanical Modelling of Fuel Rods Under Normal and Off-normal Operating Conditions”, *Nucl. Eng. Des.*, 216, 183-201 (2002).
- [36] Mezzi, G-P., F. Caligara, H. Blank, “Thermoelastic Stresses in Pellet Fragments and Conditions for Fragments Formation”, *Nucl. Eng. Des.*, 73, 83-93 (1982).
- [37] http://www.esi-group.com/SimulationSoftware/Multi_physics/index_html
- [38] Garcia, P., C. Struzik, N. Veyrier, “Temperature Calculations and the Effect of Modelling the Fuel Mechanical Behaviour”, *Proceedings of Seminar on Thermal Performance of High Burn-up LWR Fuel*, Cadarache, France, March 1998, pp. 165-174.
- [39] Koo, Y.H., B.H. Lee, D.S. Sohn, “Analysis of Fission Gas Release and Gaseous Swelling in UO₂ Fuel Under the Effect of Restraint”, *J. Nucl. Mat.*, 280, 86-98 (2000).
- [40] Bourreau, S., J. Brochard, F. Bentejac, P. Couffin, C. Verdeau, S. Lansiant, “Ramp Testing of PWR Fuel and Multi-dimensional Finite Element Modelling of PCMI”, *Proc. Int. Top. Meeting LWR Fuel Perf.*, 10-13 April 200, Park City, Utah, USA.
- [41] Ronchi, C., V.V. Rondinella, M. Sheindlin, D. Staicu, *POLARIS – Power Laser Apparatus for Reactor-irradiated Samples: Scientific Relevance, Goals, First Envisaged Experiments and Feasibility*, ITU Internal Report, JRC-ITU-TN-2002/16, March 2002.

SESSION III

Cladding Behaviour Relevant to PCI

Chairs: S.K. Yagnik, C. Lemaignan

PELLET-CLADDING INTERACTION IN VVER FUEL RODS

A.V. Smirnov, B.A. Kanashov, D.V. Markov, V.A. Ovchinikov, V.S. Polenok, A.A. Ivashchenko
(SSC RF RIAR)

Abstract

The present paper includes the results of the examination of fuel-clad interaction in fuel rods provided with a cladding that is made of Zr-1%Nb alloy. They rods operated under standard conditions for VVER-440 and VVER-1000 reactors in the burn-up range of 13-64 MWd/kgU. Characteristics and conditions of the contact origin are described in detail. The paper shows the differences in behaviour between VVER-440 and VVER-1000 fuel rods. It is demonstrated that the usage of pellets with facets has a favourable effect on the serviceability of fuel rods in case of fuel-clad interaction. It is also revealed that strains in the VVER fuel rod claddings do not reach their critical values up to a burn-up of 70 MWd/kgU. Based on the results of the reactor tests we defined boundaries of significant mechanical fuel-clad interaction as a function of the linear power of fuel rods and burn-up.

Introduction

The classical design of a VVER fuel rod that was used in the 1970s represented a column of uranium dioxide pellets provided with a central hole and incorporated in Zr-1%Nb cladding. Some of the differences in behaviour between VVER-440 and VVER-1000 fuel rods that are observed have well-known causes. Moreover, there were some fuel rods within the group that differed from the majority as concerns their initial condition characteristics. These variations caused the differences in their post-irradiation condition.

The cladding damage or loss of tightness due to fuel-clad interaction was not revealed during the entire operation period of VVER fuel rods of the above-described design; this was also the case for testing performed under RAMP conditions [1,2]. The present paper summarises the PCI results (pellet-cladding interaction) for VVER fuel rods. An attempt is made to analyse the effect of various factors on the fuel-clad interaction as well as to predict fuel rod behaviour up to burn-ups of 70 MWd/kgU.

Fuel-clad interaction in VVER fuel rods under standard operating conditions

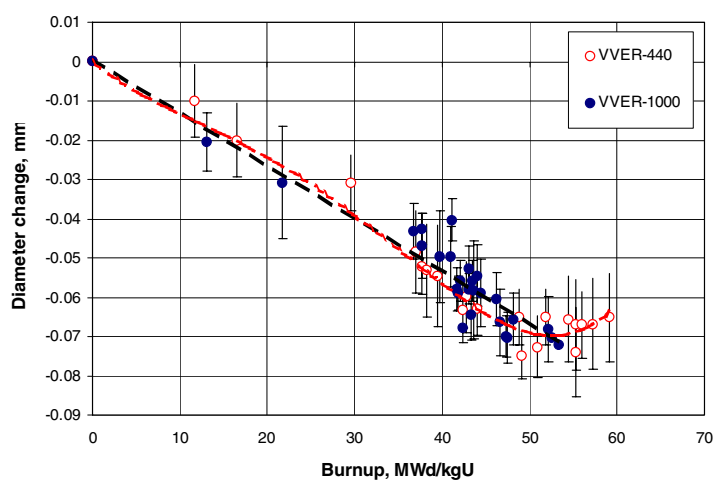
The fuel-clad interaction is preceded by two phenomena: cladding diameter decrease and fuel column swelling.

Decrease of the outer diameter of fuel rods

A decrease of the outer diameter of the cladding depends upon the cladding temperature, pressure drop (circuit coolant-fuel rod) and damage dose before fuel contact with the cladding.

Figure 1 demonstrates the outer diameter decrease in VVER fuel rods as a function of fuel burn-up with regard to cladding affiliation with this or that batch (each point corresponds to one batch of fuel rod claddings). The figure demonstrates that the diameter decrease stops in VVER-440 fuel rods at fuel burn-ups of more than 45-50 MWd/kgU and that the swelling fuel column originates the stage of reverse strain. Such phenomenon is not observed in VVER-1000 fuel rods at the same burn-up levels. Nevertheless, it should be pointed out that the rate of cladding diameter decrease is the same for VVER-440 and VVER-1000 fuel rods.

Figure 1. Change of VVER cladding diameter as a function of fuel burn-up [4]



Fuel column swelling

Volume swelling of the fuel column was studied adequately up to fuel burn-ups of 63 MWd/kgU (VVER-440) and 50 MWd/kgU (VVER-1000) [3]. It is demonstrated that the fuel swelling rate in VVER-440 and VVER-1000 fuel rods differs insignificantly in the first linear approximation and it makes up 0.8-0.9% per 10 MWd/kgU in the range of 30-65 MWd/kgU (Figure 2). Further fuel sintering is equal to 0.2-0.5% in the initial volume at the initial stage of operation (3-5 MWd/kgU) [4].

As shown in Figure 3, the fuel swelling rate is practically the same for VVER-440 and VVER-1000 reactors. However, absolute swelling values are less by a factor of 0.5% for VVER-1000 fuel in comparison with the VVER-440 fuel.

Figure 2. Fuel column swelling of VVER fuel rods during operation [5]

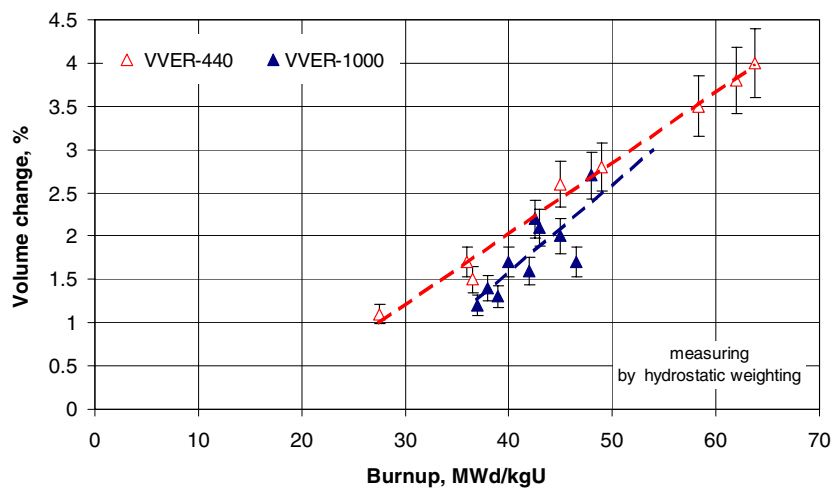
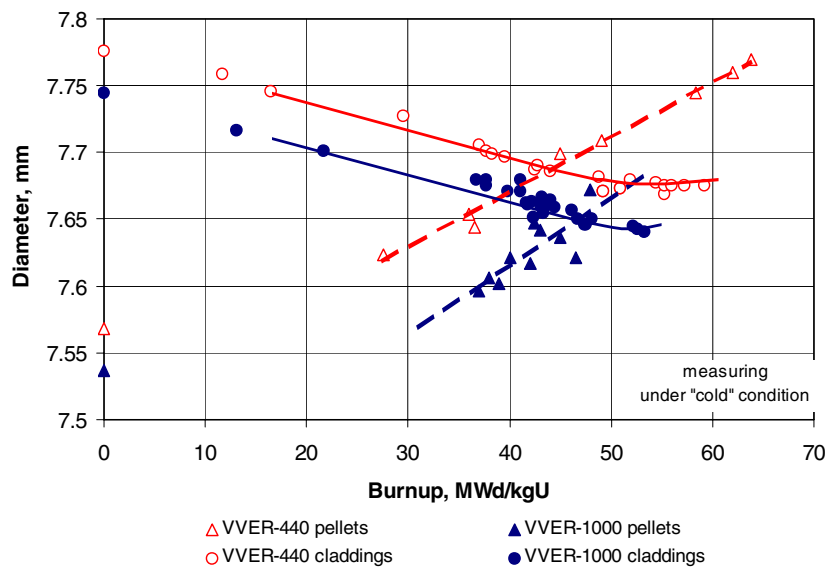


Figure 3. Change of the outer fuel column diameter and inner cladding diameter in VVER fuel rods



Comparison between absolute values of cladding diameter decrease and fuel swelling

The analysis of relative values of cladding diameter decrease and fuel swelling provides an inadequate notion of the real geometrical relationship. That is why an attempt was made to take into consideration the absolute values of the cladding diameter and fuel column in the initial condition as they are delivered from the plant in order to simulate the moment of contact origin. It was found that the cladding diameter and fuel column of VVER-440 and VVER-1000 fuel rods were different according to the analysis of geometric parameters in the initial condition with the use of data [5] as well as data concerning the reference fuel assemblies. In most cases under examination the initial fuel-to-cladding gap was 0.207 mm and 0.230 mm, respectively. In this case the interchange of geometric parameters of VVER fuel rod cladding and fuel column as a function of fuel burn-up will resemble the schema in Figure 3. The figure illustrates the following key features:

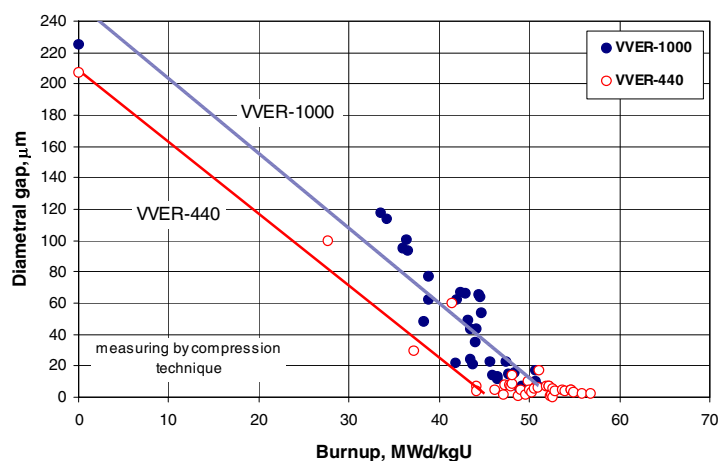
- Intersection of cladding diameter decrease and fuel swelling curves for VVER-440 fuel rods and earlier-noticed stopping of the cladding diameter decrease take place within the burn-up range of 44-48 MWd/kgU.
- Intersection of cladding diameter decrease and fuel swelling curves for VVER-1000 fuel rods is noticed within the range of 48-53 MWd/kgU, which corresponds to the expected moment of contact.

Probably the main reason for the observed differences in behaviour of the two types of fuel rod results from specific operation conditions. Ref. [6] presents data on differences in behaviour between VVER-440 and VVER-1000 fuel during further sintering at the initial stage of operation.

A fuel-to-cladding gap disappearance begins in the middle part of fuel rod that is characterised with the maximum fuel burn-up level and maximum fuel column temperature. From this time on, the “ratcheting” effect affecting the elongation of the fuel rods exhibits itself, mainly in the lower part of the fuel rod. A greater number of fuel column ruptures in this particular region indirectly points to this fact.

As for conclusions that have been drawn based on Figure 3, they are of predictive nature but they are not inconsistent with the experimental data obtained during fuel-to-cladding gap measurement using a compression technique (Figure 4). As indicated in this figure, fuel contact with cladding in VVER-440 fuel rods takes place at a burn-up of 44 MWd/kgU in the cold condition and for VVER-1000 fuel rods it takes place at a burn-up of 48 MWd/kgU.

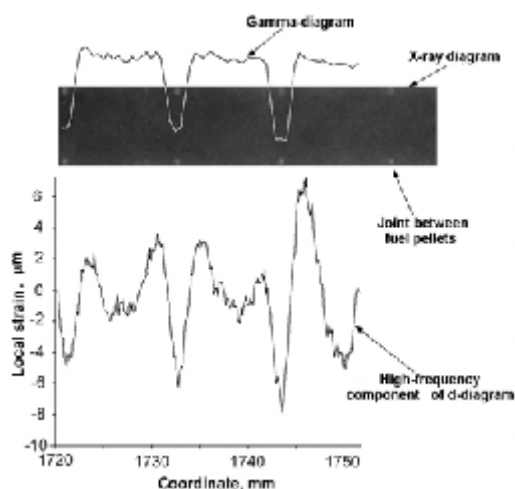
Figure 4. Fuel-to-cladding gap as a function of fuel burn-up in VVER fuel rods [4]



Cladding condition after its contact with fuel

Local changes of the outer cladding diameter, which are known as “ridges” or fuel-clad interaction traces and whose period is equal to the fuel pellet length (11 mm, Figure 5) indicate that there is fuel contact with the cladding. From the contact appearance and on, the height and number of these “ridges” increase with increased burn-up and they can be used as additional evidence of the fact that the cladding is subject to the mechanical effect of the fuel column. Mechanical stresses in the cladding are of opposite sign at the end of service life, i.e. the cladding operates under tension conditions. However a “reverse” diametric cladding strain is no more than 0.03 mm when the fuel burn-up reaches 64 MWd/kgU at the fuel rod cross-section.

Figure 5. Local strain of fuel rod cladding under the effect of fuel pellets



Periodic changes of the outer diameter make it possible to estimate the degree of mechanical fuel-clad interaction.

It is important to classify all fuel rods into two groups: fuel rods with claddings that are free of fuel-clad interaction traces and fuel rods whose claddings carry traces of fuel-clad interaction as local diameter changes. A method of periodogrammes was used in this case. It consists in the fact that the height and a number of ridges on the outer diameter diagram can be characterised by the peak height on its periodogramme (Figure 6). In turn the peak height having a period of ~11 mm can be used as a qualitative characteristic of the degree of fuel-clad interaction.

Figure 6. The outer diameter periodogramme of VVER-440 fuel rod cladding after operation during four fuel cycles

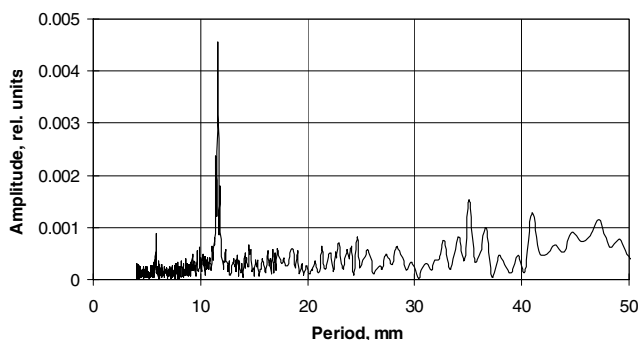
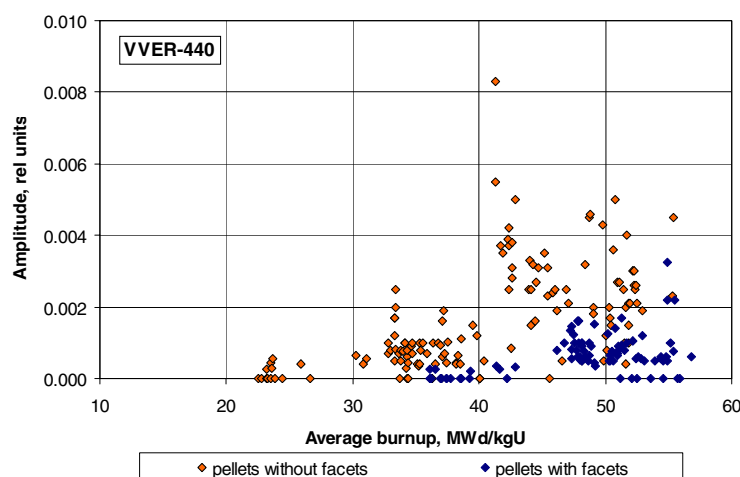


Figure 7 demonstrates the peak height on the periodogramme as a function of fuel burn-up for VVER-440 fuel rods. All examined fuel rods are broken down into two groups on this diagram: fuel rods incorporating pellets without facets and fuel rods incorporating pellets with facets. The figure shows that the presence of facets on the pellet surface is favourable for the mechanical fuel-clad degree of interaction: the peak height of the periodogramme is less in fuel rods incorporating pellets with facets in comparison with fuel rods incorporating pellets. One can also see that the effect is less significant for VVER-1000 than for VVER-440 fuel rods.

Figure 7. Peak height on the outer diameter periodogramme as a function of fuel burn-up in VVER-440 fuel rods



The results of classification allow for the following conclusions:

- Up to one-third of VVER-440 fuel rods incorporating pellets without facets carry traces of fuel contact with cladding at the end of the third fuel cycle (burn-up is ~ 34 MWd/kgU). Fuel contact with cladding is noticed nearly in all fuel rods after four years of operation (burn-up is more than 43 MWd/kgU).
- VVER-440 fuel rods incorporating pellets with facets can be operated during four fuel cycles without any visible traces of thermo-mechanical fuel-clad interaction. Traces of contact (and consequently local strain) appear by the fifth year of operation (fuel burn-up is more than 48 MWd/kgU).

Taking into consideration the traces of interaction with the fuel column, the analysis of the outer diameter diagrams for VVER-1000 fuel rods revealed that similar traces of fuel-clad interaction are practically absent in the fuel burn-up range up to 40 MWd/kgU (Figure 8). It should perhaps be considered that VVER-1000 fuel rod cladding is not subject to tensile stresses during three years of operation at the least. Fuel comes in contact with cladding during the fourth year of operation. There is a minimal gap ($<20 \mu\text{m}$) in about two-thirds of the fuel rods and insignificant traces of fuel-clad interaction are present on the claddings of these fuel rods. No traces of reverse strain caused by fuel column swelling were discovered in the fuel rods after four fuel cycles.

Pellet-cladding interaction affects both the cladding diameter and length as a function of burn-up. Changes of the fuel rod length are shown in Figures 9 and 10. One can see that this dependence is of linear character in VVER-440 fuel rods without PCI and it deviates from the linear in fuel rods with PCI. Perhaps this effect appears in VVER-1000 claddings at burn-ups of more than 55 MWd/kgU.

Figure 8. Peak height on the outer diameter periodogramme as a function of fuel burn-up in VVER-1000 fuel rods

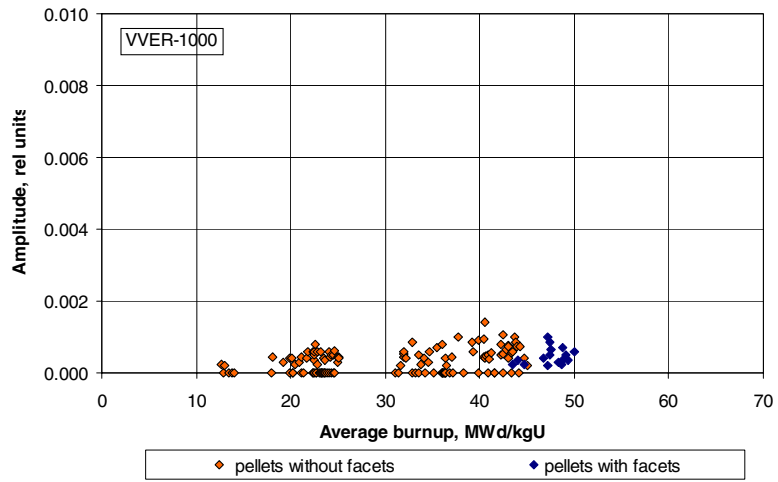


Figure 9. VVER-440 cladding elongation as a function of fuel burn-up [4]

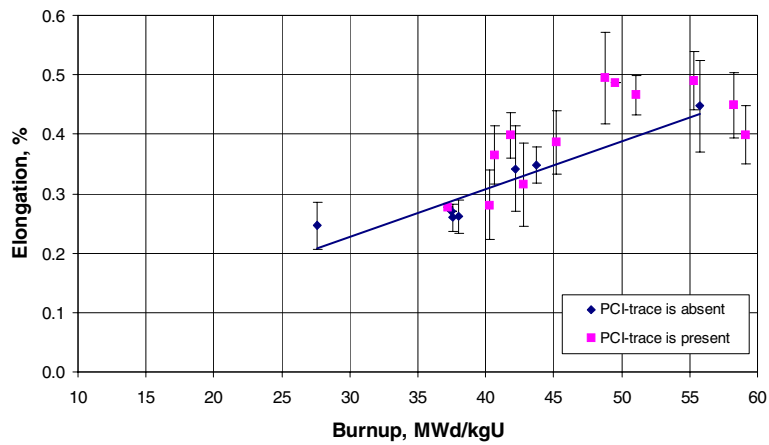
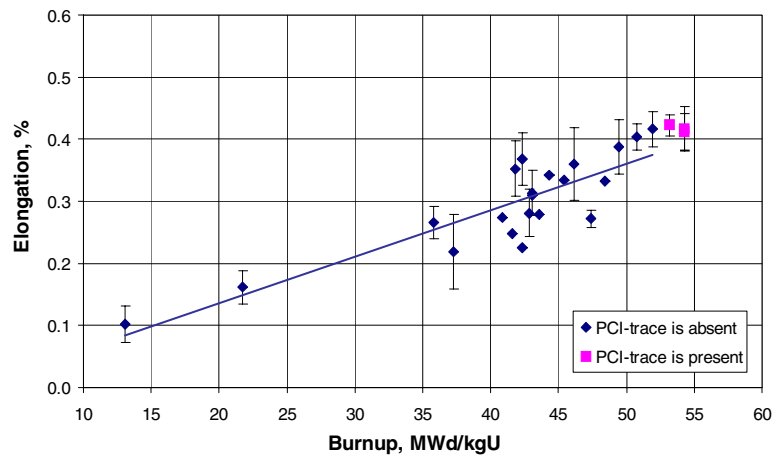


Figure 10. VVER-1000 cladding elongation as a function of fuel burn-up [4]



Mechanisms of fuel rod geometry change

Since fuel comes in contact with cladding, changes in fuel rod geometry take place in accordance with another law. The following mechanisms of shape change are known: radiation-induced growth, radiation-thermal creep and ratcheting.

A rate of radiation-induced growth is characterised by the incubation period [6] and is insignificant up to fluences of $2 \cdot 10^{22}$ 1/cm² (~43-48 MWd/kgU). The radiation-induced growth contribution is less than 0.1% [6] (25-30% from the total cladding elongation, Figures 9 and 10) at such burn-ups. It should be pointed out that there is presently no evidence of a significant ratcheting mechanism contribution as concerns the elongation of the fuel rod cladding.

Thus a shape change of the fuel rods depends upon the radiation-thermal creep and partially the radiation-induced growth before the fuel comes into contact with the cladding (~43-48 MWd/kgU) and thermo-mechanical pellet-cladding interaction occurs after the contact at burn-ups of more than 48 MWd/kgU.

Cladding strain under beyond-permissible loads

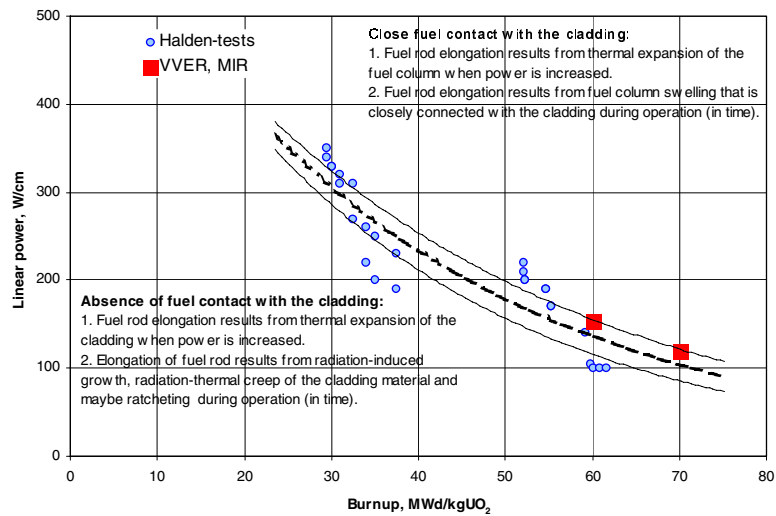
Ref. [7] presented the results of VVER-1000 fuel rod testing. The fuel rods reached average burn-ups of 70 MWd/kgU. The linear power was 490 and 200 W/cm at the initial and final stages of testing, respectively. These testing conditions go significantly beyond the design-basis values and they can be used for conservative estimation of hoop strain. In this case, the reverse diametric strain was 0.03 mm (0.3%).

An insignificant positive diametric strain at the end of the designed service life is the distinguishing feature of standard VVER-440 fuel rods; it practically does not take place in VVER-1000 fuel rods. A high ductility of Zr-1%Nb alloy even when a fluence of $2 \cdot 10^{22}$ n/cm² is reached, results in the fact that this strain is permissible (according to [8] the limiting value is 0.4%).

In-pile tests for determining fuel contact with cladding

A technique used for determining the time of fuel contact with the cladding is based on recording a change in the fuel rod length rate when the power is increased during in-pile tests [9]. A similar test was carried out in the MIR reactor using re-fabricated VVER-440 and VVER-1000 fuel rods, which were equipped with elongation sensors [10]. Fuel rods having fuel burn-ups of 69.1 and 59.5 MWd/kgU, respectively, were subjected to testing. There was a small fuel-to-cladding gap in fuel rods in the cold condition. When there is a tight contact after power increasing, the elongation of fuel rods depends upon the thermal expansion of the fuel column. Fuel contact with the cladding in VVER-440 and VVER-1000 fuel rods was recorded at the linear powers of 120 and 154 W/cm, respectively. Figure 11 demonstrates that these values are comparable with similar values for high burn-up PWR fuel [11]. The figure demonstrates the fact that a contribution of ratcheting in fuel rod elongation diminishes as the fuel burn-up of the fuel rod increases.

Figure 11. Boundaries of fuel-clad interaction in VVER fuel rods as power increases



Conclusion

The experience gained in VVER-440 and VVER-1000 fuel rods after operation for five and four fuel cycles, respectively, under standard conditions proves that fuel-clad interaction has not resulted in fuel rod failure in any of the cases. Post-irradiation examinations and in-pile testing of high burn-up VVER fuel proves that boundaries of fuel damage due to fuel-clad interaction go far beyond the permissible linear power levels. Fuel rods were leak-tight in all the in-pile tests.

REFERENCES

- [1] Chirkov, V., V. Novikov, A. Sharikov, "Operation Experience of VVER-440 FAs and Measures to Increase Fuel Reliability", *IAEA Technical Meeting on Fuel Failure in Water Reactors: Causes And Mitigation*, Bratislava, Slovakia, 17-21 June 2002.
- [2] Kanashov, B., S. Amosov, A. Smirnov, *et al.*, "Changes in Geometry of Claddings and Fuel Columns of Spent VVER-440 and VVER-1000 Fuel Rods Under Steady-state and Transient Operating Conditions", *IAEA Technical Meeting on Fuel Failure in Water Reactors: Causes And Mitigation*, Bratislava, Slovakia, 17-21 June 2002.
- [3] Kuzmin, V.I., V.N. Golovanov, G.I. Mayorshina, *et al.*, "Change of Fuel Condition in VVER Fuel Rods at a Burn-up of 40-60 MWday/kgU", *5th International Conference on Reactor Material Science*, Dimitrovgrad (1997).
- [4] Volkov, B., H. Devold, E. Ryazantzev, V. Yakovlev, *In-pile Data Analysis of the Comparative WWER/PWR Test IFA-503.1: Final Report*, OECD Halden Reactor Project #HWR-590 (1999).

- [5] Shcheglov, A.S., V.N. Proselkov and A.A. Yenin, *Results of Statistical Treatment of Structural and Process Parameters with Regard to VVER-1000 Fuel Rod*, IAE-5334/4, Pre-print, Moscow (1991).
- [6] Kobylansky, G.P., A.Ye. Novoselov, “Radiation Resistance of Zirconium and Zirconium-based Alloys”, Reference Guide on Reactor Material Science, V.A. Tsykanov, Ed., SSC RF RIAR, Dimitrovgrad (1996).
- [7] Bespalov, V., K. Dubrovin, P. Platonov, *et al.*, “Large Cladding Deformation at the Long Term Tests of Fuel Rods in the MR Reactor”, *Proceedings of the 2nd International Conference on WWER Fuel Performance, Modelling and Experimental Support*, Sandanski, Bulgaria, 21-25 April 1997, p. 246.
- [8] Bibilashvili, Yu., “WWER Fuel Rod Acceptance/Design Criteria for Safe and Reliable Operation and Their Justification”, Lecture presented at an IAEA Training Course in Bratislava, Slovak Republic, June 1999.
- [9] Tverberg, T., *PCMI Behaviour of High Burn-up Fuel*, OECD Halden Reactor Project, #HWR-619 (1999).
- [10] Burukin, A.V., .D. Grachev, S.V. Lobin, V.A. Ovchinikov, V.Sh. Sulaberidze and V.A. Tsykanov, “Testing of Instrumented Power Reactor Fuel Rods in the MIR Research Reactor: Status and Development”, *7th International Conference on Reactor Material Science*, Dimitrovgrad, September 2003.

**CHARACTERISATION OF VOLATILE FISSION PRODUCTS,
INCLUDING IODINE, AFTER A POWER RAMP**

**L. Desgranges, B. Pasquet, X. Pujol, I. Roure, Th. Blay,
J. Lamontagne, Th. Martella, B. Lacroix, O. Comiti, L. Caillot**
DEC/SA3C/L2EC
CEA Cadarache, F-13108, Saint Paul-lez-Durance

Abstract

The behaviour of iodine during a power ramp is an important topic in the framework of studies on pellet-to-clad mechanical interaction (PCMI) [1]. Up to now, little experimental data have been available on iodine characterisation in the nuclear ceramic because its concentration is too low to be measured with Electron Probe Micro Analysis (EPMA). However, in our laboratory, a shielded SIMS was recently installed [2], which enables the detection of low abundant species, and a research programme was built up to use these new possibilities in order to better characterise the volatile fission products (FPs) during a power ramp, with a special care given to iodine. This programme was aimed at studying how the volatile FPs can leave the UO₂ ceramic and how they behave once they have left the ceramic. For that purpose a power ramp was designed to have a high thermal level during a short time in order to enhance the release mechanisms and at the same time to limit solid-state diffusion and to avoid failure.

Experimental

Irradiation conditions

The samples were prepared from a re-fabricated rodlet that underwent a power ramp in the OSIRIS reactor. The rodlet was extracted from an UO₂ fuel rod irradiated for three cycles in an EdF power reactor, whose main irradiation conditions are given in Table 1.

Table 1. Irradiation conditions of the UO₂ fuel rod from which the rodlet was extracted

	Burn-up (MWd/tU)	Average power (W/cm)		
		1 st cycle	2 nd cycle	3 rd cycle
Average fuel rod	35 315	160	234	198
Average rodlet	38 801	178	260	214

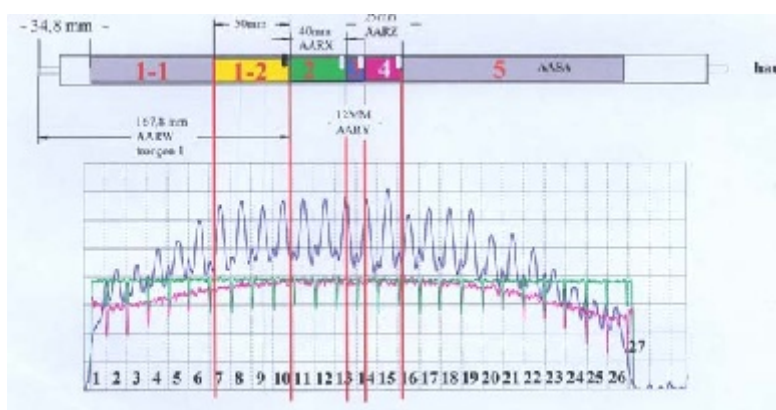
During the power ramp, the rodlet was maintained at a high power during a short time. The main characteristics of this ramp are given in Table 2.

Table 2. Ramp characteristics

Ramp rise rate (W.cm ⁻¹ .min ⁻¹)	Rodlet Pmax (W/cm)	Holding time at maximum power	F(Xe + Kr) (%)
100	520	1 min 30 s	3.8

No failure of the rodlet occurred during the ramp and the holding time. The PCMI led to the formation of primary and secondary ridges characterised by diameter measurements (Figure 1). The accumulation of volatile isotopes (¹³¹I, ¹³²Te, ¹³⁷Cs ...) in front of the pellet chamfers was detected by gamma scanning at the end of the irradiation.

Figure 1. Schematic view of the rodlet with gamma scanning and diameter measurements

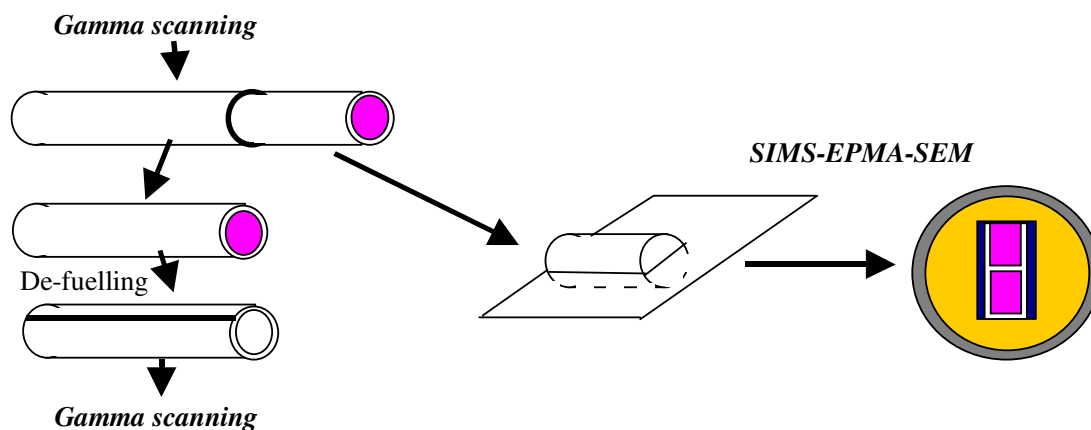


Sample preparation

A 50-mm long slice was cut from the rodlet after the power ramp. This slice is labelled 1-2 in Figure 1. It was shipped from Saclay to the Cadarache centre. It was then measured by gamma scanning in order to check the pellet position. A 15-mm sample was cut at the top of the initial slice. This sample

was then cut along its axis and polished so that the dishing and chamfer could be observed. The remaining of the initial slice had its fuel removed and its cladding was gamma scanned in order to identify some deposits on the inner surface. Figure 2 summarises the preparation of these samples.

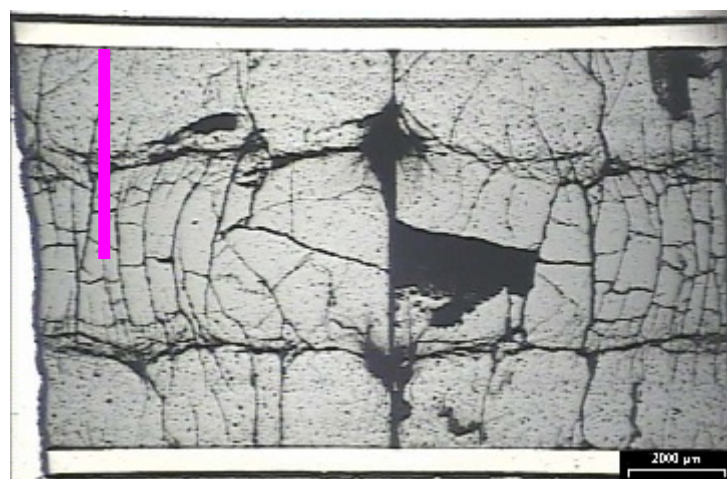
Figure 2. Schematic drawing of the sample preparation



Release of volatile FPs out of the UO₂ ceramic

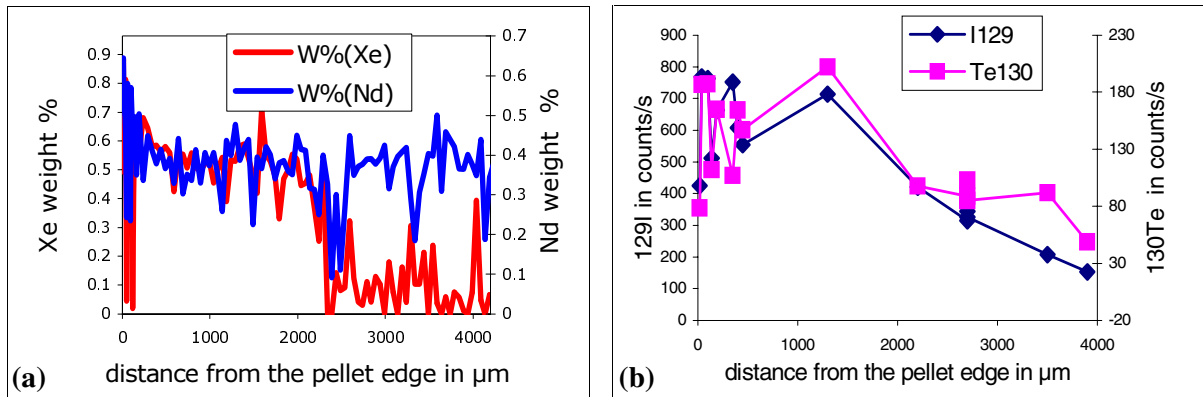
An optical macrography of the polished sample is presented in Figure 3. In the centre of the figure, the previous position of the dishing, which was almost totally filled during the ramp, can be visualised as a black straight line. At the two ends of this line, the chamfers are recognisable as small black triangles. The cracking pattern derives from the thermal gradients, which took place in the pellet during the progress of the ramp. This cracking locally induced some fuel removal during preparation, which appears as black areas on the photo.

Figure 3. Optical macroscopy of the sample



In order to characterise their behaviour as function of the thermal gradient, the concentration of some volatile FPs was measured along a radius of the UO₂ pellet. This radius is located approximately at the pellet mid-height where the gradient was the largest. The xenon profile was measured with EPMA along with the neodymium profile so as to highlight the xenon migration. The caesium

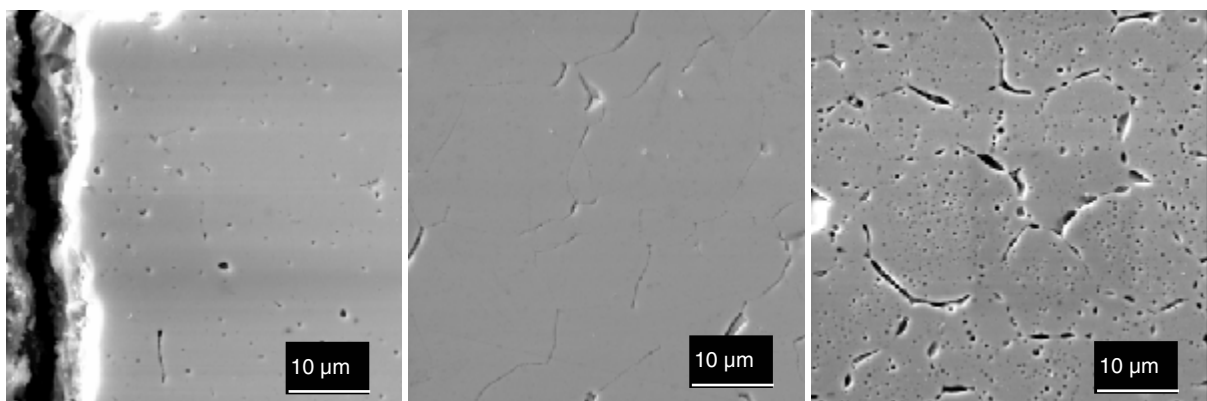
Figure 4. EPMA quantitative concentration profile of xenon and neodymium (a) and SIMS profile of iodine and tellurium measured along the purple radius shown in Figure 3 (b)



measurement was unsuccessful because caesium moved on the sample surface during the preparation and the examination. Iodine and tellurium were measured with SIMS. The SIMS results are given in arbitrary units because no suitable standard was available.

Neodymium is usually considered as a non-volatile FP and its concentration profile is equal to the creation profile. The xenon and neodymium profiles were fitted such that the two curves are superimposed when the xenon concentration is equal to its creation value. The xenon concentration measured by EPMA decreases at mid-radius to nearly zero in the pellet centre. Xenon is known to be badly detected by EPMA when it forms bubbles with a size bigger than a few tenths of micron [3]. The decrease of xenon must then be understood not as a xenon depletion but as a xenon precipitation in bubbles associated with some xenon release. The measured fraction of released gas is indeed only 3.8%, which is not consistent with a total xenon depletion in the pellet centre. This interpretation is consistent with the fuel microstructure observed by SEM in Figure 5. The fuel microstructure is comparable to the fabrication one at the pellet edge. Some small intergranular bubbles are observed at mid-radius. In the pellet centre big intergranular bubbles and intragranular bubbles are evidenced. The formation of bubbles is indeed correlated to the lack of detection of xenon with EPMA.

Figure 5. SEM images of the fuel microstructure at the pellet edge (left), at mid-radius (centre) and in the pellet centre (right)



Xenon precipitation is the consequence of the temperature reached in the pellet during the ramp at the cracking pattern observed in Figure 3. Two different areas can then be defined: a central area where

the temperature is high enough to enable the gas precipitation and potential release during the holding time at maximum power, and a peripheral area where the temperature is lower which prevents the gas from precipitating.

In Figure 4, the iodine and tellurium profiles exhibit a decrease from mid-radius to the centre. This evolution must be understood as a decrease of the quantity of iodine and tellurium contained in the UO_2 ceramic, because the measurement was performed on a dense area after sputtering of a surface layer in order to remove any volatile contribution. This grain depletion of iodine and tellurium in the pellet centre can also be correlated to the high temperature that occurred in the pellet centre during the ramp. In any case, their release mechanism is not necessarily the same that of fission gases. In order to better characterise their release mechanism, SIMS imaging of iodine, tellurium, caesium and uranium was performed at a scale that allows to see if the repartition of these volatile FPs is correlated to the bubbles' repartition. The images were obtained at five different positions: 0, 1 300, 1 700, 2 200 and 3 900 μm from the pellet edge (Figure 6). As was done for the iodine and tellurium profiles given in Figure 4, the images were obtained on a dense area after sputtering of a surface layer in order to remove any volatile contribution.

At the pellet edge, the images are similar for the four isotopes. The contrast here is only due to the different crystalline orientations of the UO_2 grains, which results in different detection yields for all isotopes from one grain to the next [4]. All isotopes are homogeneously distributed in the UO_2 grains, which is consistent with the low temperature in this area during the ramp.

In the pellet centre (3 900 μm from the pellet edge), the images of the volatile FPs are similar but different from that of uranium. The UO_2 grains are observed on the uranium image with some small dots on the grain boundaries, which likely correspond to the bubbles observed in Figure 5. The volatile FPs are all located in small precipitates associated with the bubbles either intra- or intergranular. The temperature in the pellet centre during the ramp is indeed high enough such that all insoluble FPs are released out of the UO_2 crystalline structure.

Between these positions the distribution of the volatile FPs is different and reveals different release mechanisms.

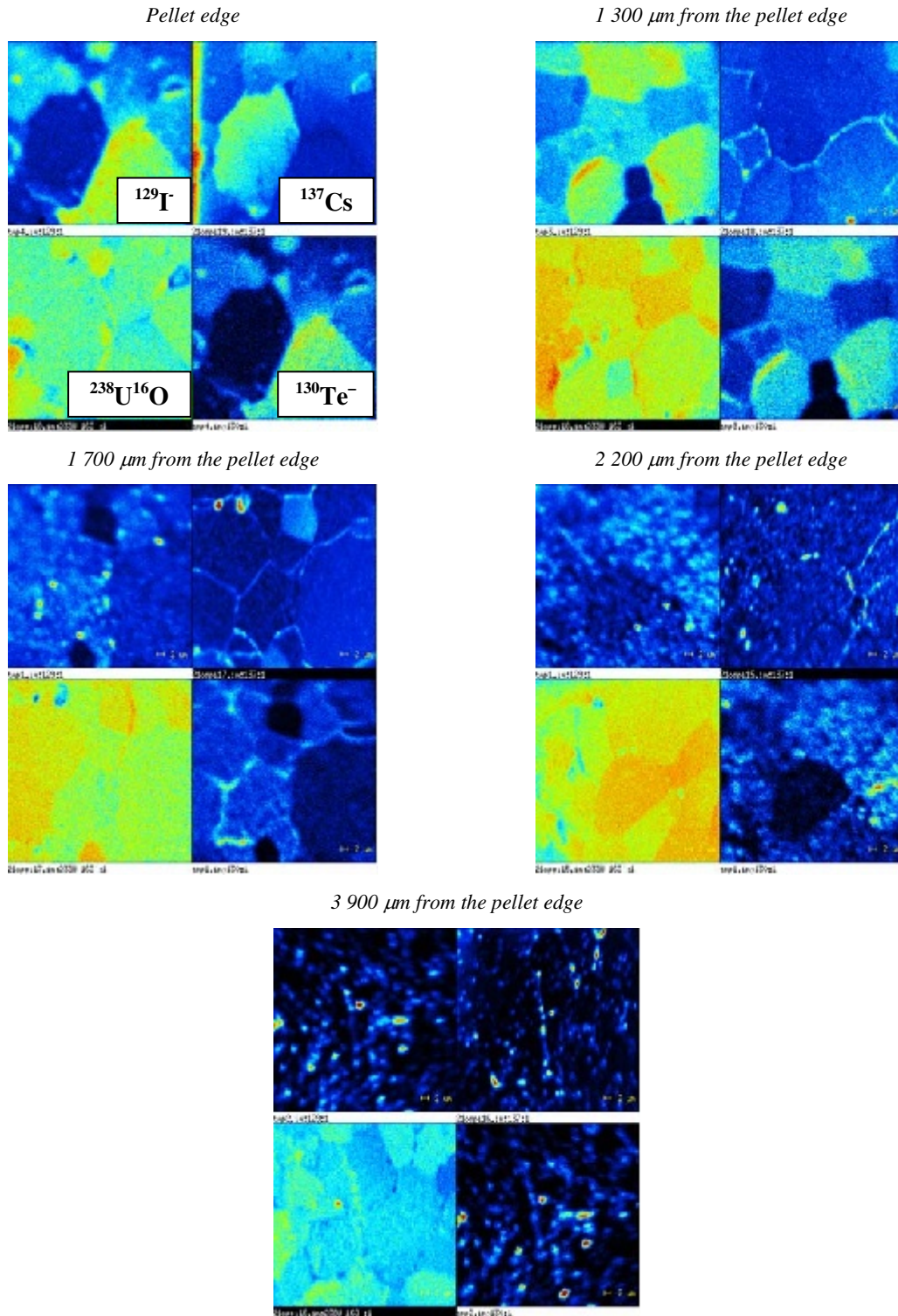
No iodine migration is observed at 1 300 μm from the pellet edge. Iodine starts to form intergranular precipitates at pellet mid-radius. Small intragranular precipitates are formed at 2 200 μm from the pellet edge. In the pellet centre the UO_2 crystalline structure is totally iodine depleted. This iodine behaviour is very similar to the behaviour of the fission gases, and iodine precipitation occurs at the same position as xenon precipitation. Iodine is likely released along with the fission gases.

The behaviour of caesium is clearly different from that of iodine because caesium uniformly covers the grain boundaries at 1 300, 1 700 and 2 200 μm from the pellet edge. Moreover, caesium migration on the grain boundaries is observed at 1 300 μm from the pellet edge where no change of the fuel microstructure is visible, i.e. under conditions where no gas precipitation in the bubbles is activated. Because no porosity is associated to caesium migration on the grain boundaries, caesium is not in a gaseous state during the ramp, but more likely in a caesium-rich solid phase. The release mechanism of caesium could be seen as solid-state diffusion on the grain boundaries up to free surfaces where volatile species could be formed.

The behaviour of tellurium is more complex, with nearly homogenous coverage of the grain boundaries at 1 700 μm from the pellet edge and only precipitates at 2 200 and 3 900 μm from the pellet edge. This behaviour seems intermediate between iodine and caesium and would require a more detailed analysis as a function of the temperature to be totally understood.

Figure 6. SIMS images of $^{129}\text{I}^-$ (left top), $^{137}\text{Cs}^+$ (right top), $^{238}\text{U}^{16}\text{O}^+$ (left bottom) and $^{130}\text{Te}^-$ (right bottom) taken at five positions on the pellet radius, from which the profiles of Figure 4 were also obtained

The images with positive ions (Cs^+ , UO^+) are obtained under the same data acquisition conditions but a different tuning is needed for negative ions (I^- and Te^-) which explains some small mismatches between positive and negative ion images.



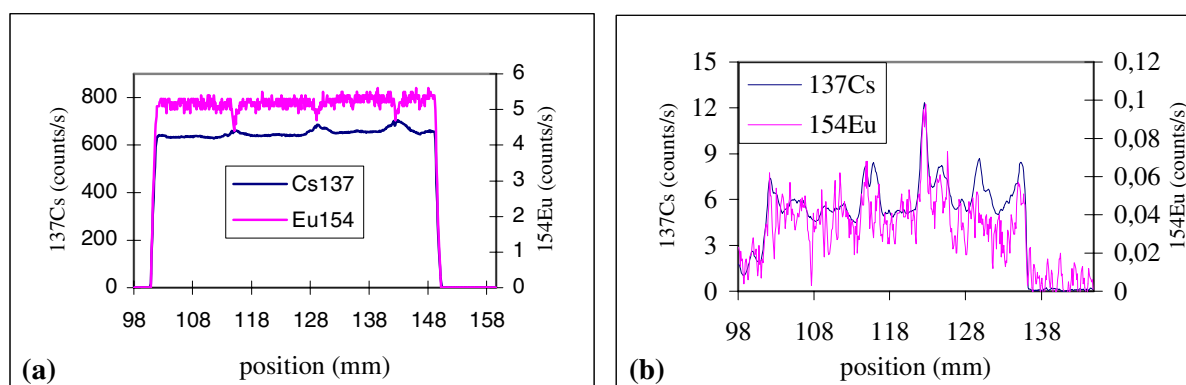
Migration of released FPs

The results presented above clearly demonstrate that the volatile fission products are released out of the UO_2 ceramic with different mechanisms. In this section we aim at studying the migration of the released FPs. This question cannot be easily addressed with the microanalysis methods that were used previously, as the volatile FPs form volatile species which are moved during the sample preparation, especially polishing. Thus iodine, caesium and tellurium have been detected in the pores and the cracks of the fuel but it is not possible to state if the PFs migrated there during the power ramp or during the sample preparation. In order to tackle this difficulty gamma scanning will first be used.

Caesium migration gamma scanning

In-pile gamma scanning evidenced the accumulation of volatile FPs at inter-pellets. This point was confirmed with the gamma scanning performed on the studied slice [Figure 7(a)]. The ^{154}Eu signal has a flat level with a regularly spaced decrease, associated with the pellet dishings and chamfers. At the chamfer position, the ^{137}Cs signal is higher, indicating an axial movement from the inner part of the pellet towards its end. In order to better characterise this mobile caesium, the fuel rod slice had its fuel removed and the remaining cladding was gamma scanned [Figure 7(b)]. The caesium signal is not zero and evidences some caesium accumulation at the chamfer position and at the position of the pellet mid-height. However this caesium accumulation is not due to the existence of volatile caesium species, but to the existence of UO_2 fuel stuck to the cladding as demonstrated by the ^{154}Eu signal, which is proportional to that of caesium within the accuracy of the measurement.

Figure 7. Gamma scanning of the fuel rod slice before (a) and after (b) defuelling

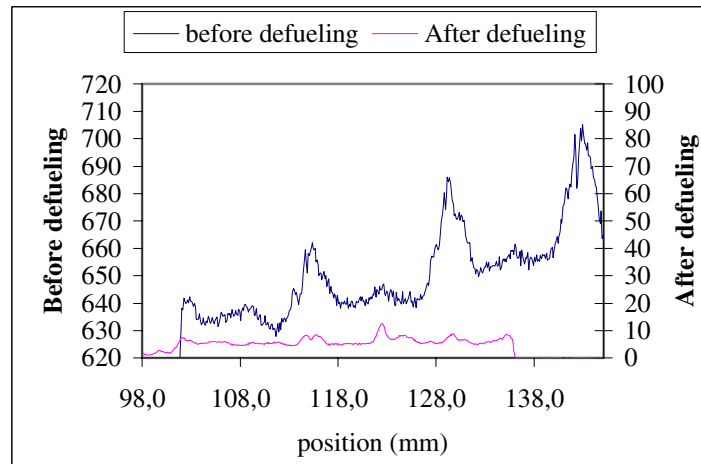


Thus the accumulation of caesium in front of the chamfer position does not correspond to some volatile species stuck to the inner surface of the cladding. This is confirmed when comparing on the same intensity scale the caesium gamma signal before and after defuelling (Figure 8). The caesium gamma signal at inter-pellets before defuelling evidences a caesium accumulation whose absolute intensity is much bigger than the intensity of the remaining gamma signal after defuelling.

Deposit analysis

In order to find out where the caesium which engenders this accumulation at inter-pellets was located, a detailed SEM analysis of the area around the chamfer was performed on the polished sample.

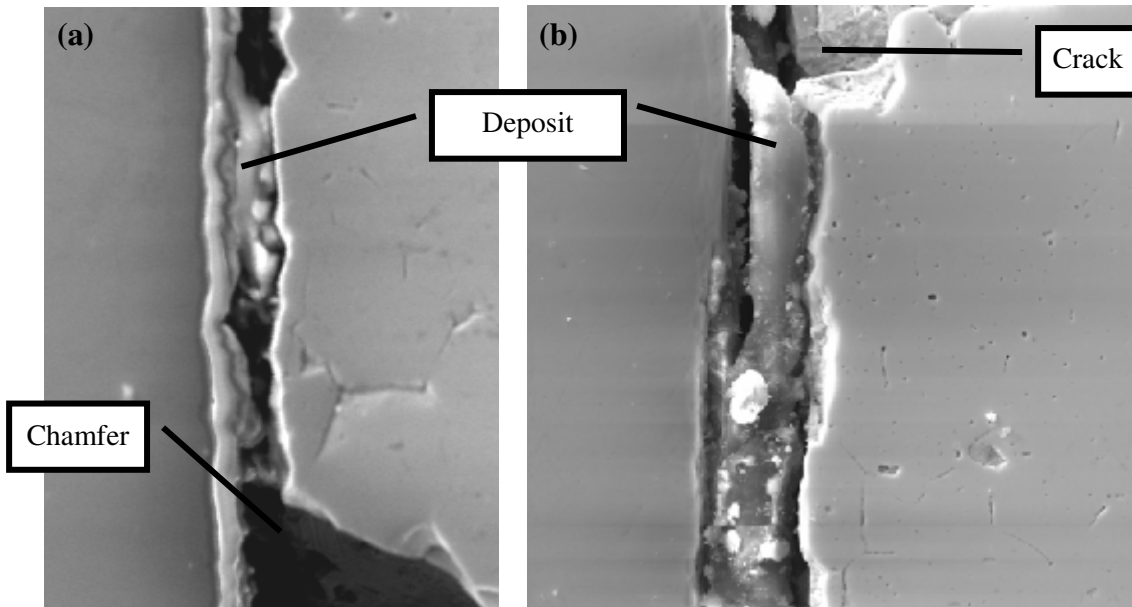
Figure 8. Caesium gamma signal before and after defuelling. The scale of the two curves is adapted to allow a better comparison of the caesium accumulation.



A deposit was evidenced between the fuel ceramic and the cladding [Figure 9(a)]. However the analysis of this deposit was complicated because it turned out to be unstable under the electron beam. That is why EPMA measurement was not possible on this deposit and why only a few SEM images are available. Then the fuel-to-clad gap was also examined and some deposit was also observed near merging cracks in the fuel [Figure 9(b)]. The position of the deposit is not exactly in front of the crack but slightly underneath.

Figure 9. SEM images of deposit near the chamfer (a) and in the fuel-to-clad gap (b)

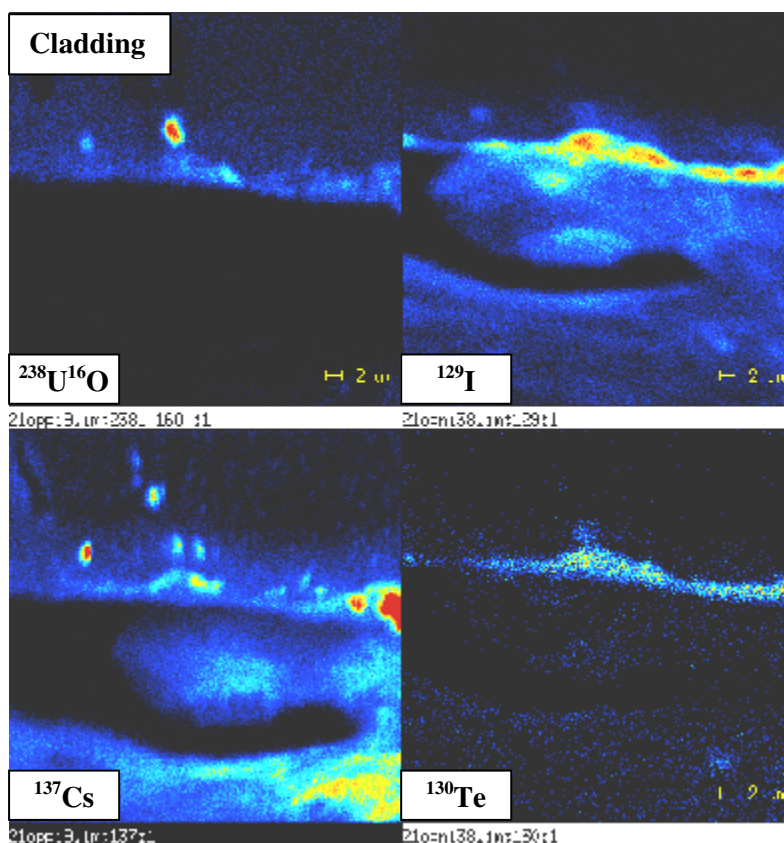
*The cladding is on the left side of the photo and the UO₂ fuel on the right side.
The bright details on photo (b) are due to polishing debris put on the deposit.*



Although this deposit was very sensitive to electron beam, some SIMS imaging has been possible and is presented in Figure 10.

Figure 10. SIMS images of uranium, iodine, caesium and tellurium in the void volume in front of the chamfer

A deposit is visible on the iodine and caesium images. The inner surface of the cladding is visible on the uranium image because of polishing debris that got stuck to it.



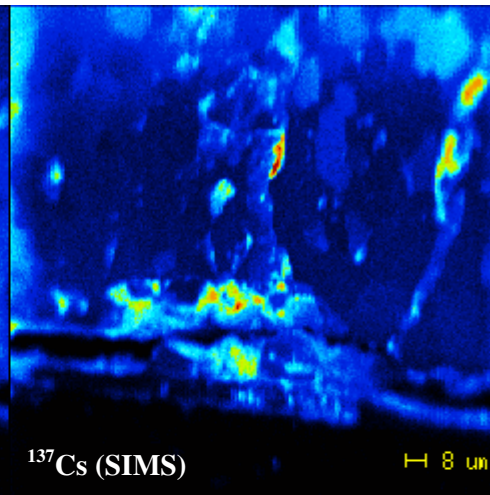
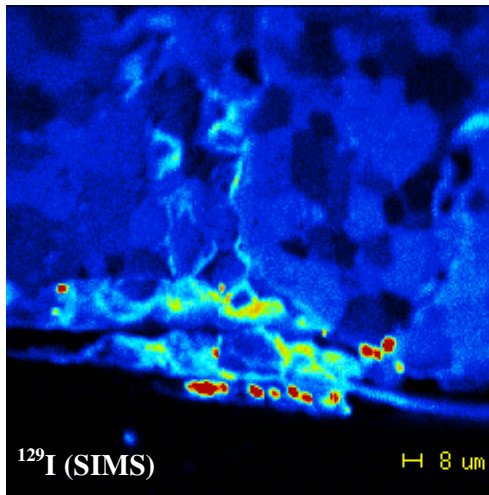
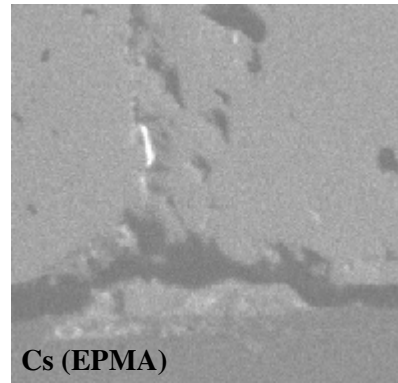
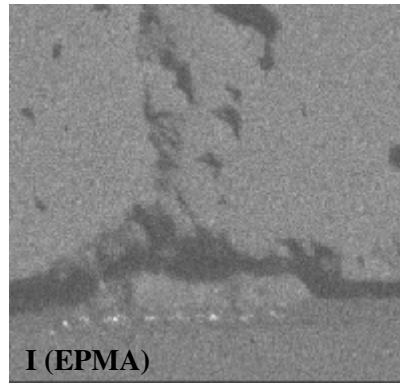
In Figure 10, iodine and caesium are found in a deposit located around the chamfer. However these images cannot be used to determine its chemical composition because the secondary ion yields of caesium and iodine are unknown. Thus even with a bright SIMS image, the concentration of iodine can be low. Moreover, most of iodine is located on the inner surface of the cladding where it forms small precipitates. The tellurium image also evidences an accumulation on the inner surface of the cladding.

The fuel-to-clad gap was then explored to detect other iodine precipitates. Figure 11 presents the EPMA and SIMS images performed on an area where the local iodine concentration was sufficient to detect it with EPMA. A crack in the UO_2 ceramic can be seen on the EPMA images. In front of this crack, some UO_2 grains are adhesive on the oxidation layer of the cladding (UO SIMS image). Iodine precipitates are located at the position of the internal oxidation layer but it is difficult to state if they are in contact with the cladding. The chemical composition of these precipitates is also difficult to determine for two reasons. First, they lie below the polished surface, inducing some shadowing. Second, they can be considered as small dots with a high iodine content embedded in a caesium-containing surrounding so that it cannot be stated if they are CsI precipitates or other iodine-containing precipitates.

Caesium and iodine are thus observed in the fuel-to-clad gap localised in front of the chamfers and in front of the cracks. They consist either of some deposit, not adhesive to the inner part of the cladding, or in small precipitates stuck to the cladding but in too low a quantity to be detected with gamma scanning.

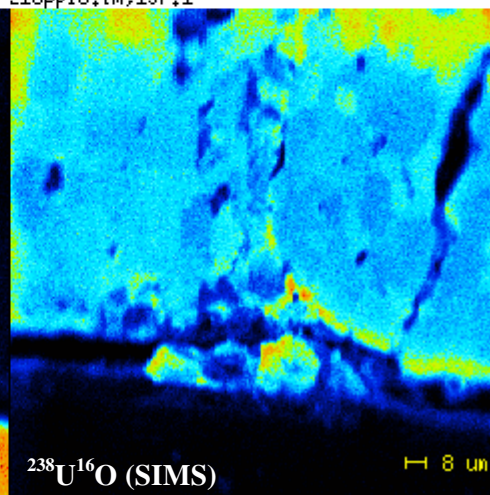
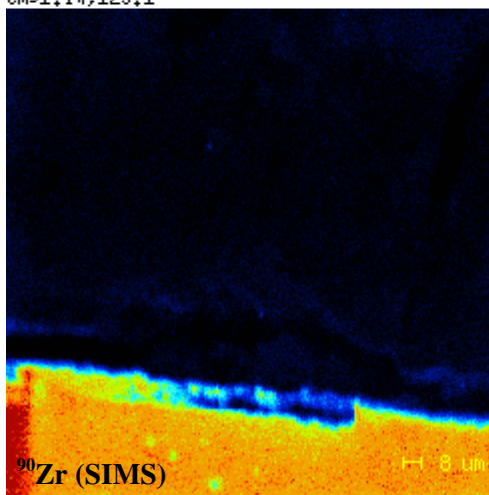
Figure 11. $100 \times 100 \mu\text{m}^2$ SIMS images of $^{129}\text{I}^-$, $^{137}\text{Cs}^+$, $^{90}\text{Zr}^+$ and $^{238}\text{U}^{16}\text{O}^+$ and $66 \times 66 \mu\text{m}^2$ EPMA images of iodine and caesium taken in the same area of the pellet-to-clad gap

For experimental reasons the SIMS and EPMA images are mirror images. The cladding is in the bottom (Zr SIMS image) and the UO_2 ceramic in the top (UO SIMS image). The oxidation layer appears as a lack of zirconium on the Zr SIMS image because it was partially removed and exists only beneath the polishing surface.



tm>1.in;129:1

21oppi8.im;137:1



21oppi3.im;90Zr :1

21oppi8.im;238U 16U :1

Discussion

The original results presented in this paper provide new data on the distribution of volatile fission products after a power ramp. Before discussing them, one must keep in mind that this distribution results not only from the power ramp but also from the three-cycle irradiation, the sample preparation and the contact of the sample with air. Taking all of this into account, the behaviour of iodine and caesium during the ramp can then be discussed.

Iodine

Iodine is likely to behave as a gaseous phase in bubbles in the UO₂ ceramic. As a consequence its release mechanism should be similar to that of fission gases. This is consistent with the results of Peehs [5]. Its chemical form depends on the local thermodynamic conditions, which take place in the bubbles.

The existence of iodine in pores and cracks could be associated with the solidification of the gaseous phase after the power ramp. Like fission gases, iodine would indeed have been released from the inner part of the pellet during the ramp. The released gaseous phase would then have migrated to the colder part of the rodlet through the cracks and could have been solidified there, when the temperature decreased. It is noteworthy that, despite the short holding time at maximum power, some iodine could reach the fuel-to-clad gap in merging fuel cracks or in the chamfer, as shown in Figures 10 and 11.

The quantity of iodine reaching the cladding cannot be estimated with SIMS. In any case, the existence of the bright precipitates observed with SIMS and EPMA proves the existence of an area with a high local iodine concentration in the vicinity of the cladding. Using EPMA data, the quantity of iodine in one precipitate is estimated to be of the order of a tenth of picogramme. Depending on the chemical form of this iodine during the ramp and on the volume it can attain, the estimated quantity of iodine contained in the precipitates of Figure 11 could lead to some stress corrosion [6].

However the origin of these iodine-enriched precipitates is still unclear considering their location in the inner oxidation layer of the cladding as shown in Figure 11. Two hypotheses are possible: either they result from the iodine migration from the pellet centre towards the cladding and subsequent precipitation, or they result from the precipitation of the iodine implanted in the inner oxidation layer during the three-cycle irradiation. Further examination on un-ramped samples is required to answer this question.

Caesium

At intermediate position, from 1 300 to 2 200 μm from the pellet edge in Figure 6, which underwent temperatures ranging from 1 400 to 1 800°C during the holding time at maximum power, caesium is likely to form a caesium-enriched solid phase on the grain boundaries, which could be caesium uranate for example. However this compound is not stable at higher temperatures in the pellet centre because all the caesium is then localised in precipitates. The chemical form of caesium in this precipitate could be CsI, but the quantity of iodine is much less than that of caesium. Other compounds with tellurium or molybdenum, which are also present in the bubbles in the pellet centre, could be possible [7].

The release of caesium depends on its physical state in the fuel and hence on the temperature. At high temperature caesium is likely in a gaseous state because it is located in the bubbles like the other volatile FPs. Its release mechanism could then be similar to that of fission gases but would occur at higher temperature, which is consistent with [5].

The gamma scanning clearly demonstrated that the major part of the caesium, which left the UO₂ crystalline structure, is not adhesive to the inner surface of the cladding. Of course, some small caesium precipitates could exist on the inner cladding but their quantity is not sufficient to allow their detection with gamma scanning.

Conclusion

In this paper, new results using the combination of SEM, EPMA and SIMS analysis, on the characterisation of volatile fission after a power ramp are presented. They provide some new and valuable information. The distribution of iodine, tellurium and caesium in the UO₂ ceramics was characterised. The gaseous behaviour of the released iodine was confirmed. The existence of iodine precipitates on the inner cladding was demonstrated. These results are consistent with the iodine stress corrosion mechanism proposed in the literature.

However, further study is required for a better characterisation of the volatile fission products which left the UO₂ ceramics.

REFERENCES

- [1] Sidky, P.S., *J. Nucl. Mat.*, 256, 1-17 (1998).
- [2] Rasser, B., L. Desgranges, B. Pasquet, *Applied Surface Science*, 203-204, 673-678 (2003).
- [3] Verwerft, M., *J. Nucl. Mat.*, 282, 97-111 (2000).
- [4] Desgranges, L., B.Pasquet, *Nucl. Instr. Method*, B 215, 545-551 (2004).
- [5] Peehs, M., *et al.*, *J. Nucl. Mat.*, 119, 284-290 (1983).
- [6] Yang, T.T., *et al.*, *J.Nucl.Mat.*, 166, 252-264 (1989).
- [7] Kleykamp, H., *J.Nucl.Mat.*, 131, 221-246 (1985).

TESTING AND MODELLING IODINE-INDUCED STRESS CORROSION CRACKING IN STRESS-RELIEVED ZIRCALOY-4

D. Le Boulch, L. Fournier, C. Sainte-Catherine
CEA Saclay, F-91191 Gif-sur-Yvette, France

Abstract

The I-SCC behaviour of SR zircaloy-4 was investigated by means of internal pressurisation tests in both inert and gaseous iodine environments. I-SCC susceptibility was derived from internal pressurisation tests on smooth specimens on both un-irradiated and neutron-irradiated tube claddings. Crack propagation rates were obtained from internal pressurisation tests on pre-cracked un-irradiated tube claddings. Particular attention was paid to the influence of temperature on both I-SCC susceptibility and crack propagation rates. The results of these tests were used for the development of a phenomenological model. This model describes I-SCC in three successive phases, i.e. (i) initiation by rupture of zirconia, (ii) propagation of a subcritical crack under $K_{III-SCC}$, and (iii) propagation of a critical crack once $K_{III-SCC}$ is reached. The originality of this model lies in the integration of the influence of the temperature in the subcritical crack propagation phase.

Introduction

The first fractures induced by pellet-cladding interactions (PCI) were observed during the 1960s in boiling water reactors (BWRs) and CANDU-type reactors. With the development of barrier cladding using an inner layer of pure zirconium in BWR design in the 80s, PCI has since received little attention, except for power transient conditions in pressurised water reactors (PWRs). Indeed, it is well known that cladding failure by iodine-induced stress corrosion cracking (I-SCC) may occur under PCI conditions during power transients in PWRs. Under PCI conditions, I-SCC then results from the synergic effect of (i) the hoop tensile stress and strain imposed on the cladding by fuel thermal expansions during power transients and (ii) corrosion by iodine released from the UO_2 fuel as a fission product.

CEA has been involved for decades in experimental analytical studies in order to understand and avoid I-SCC in PWRs [1-5] as well as in the development of predicting codes [6]. The aim of this paper is to describe both the experimental and modelling approaches used at CEA for the description of I-SCC of stress-relieved (SR) zircaloy-4 tube cladding. The I-SCC model is developed for implantation as a post-processing FORTRAN module in finite-elements (FE) codes for PCI predictions, such as TOUTATIS [7] and METEOR [8], also developed at CEA. FE computations are then used to predict power ramp tests performed in the OSIRIS MTR [9]. This implantation is beyond the scope of this paper and will not be described here.

Experimental procedure and results are first described in this paper. On the basis of the results, the different features of the model are detailed. Future experimental work and refinements of the model are then discussed.

Experimental procedure

The material of this study was SR low-tin zircaloy-4 that is commonly used for fuel claddings in PWRs. The chemical composition of this material is given in Table 1. Both un-irradiated zircaloy-4 cladding and neutron-irradiated zircaloy-4 cladding up to two PWR cycles were investigated.

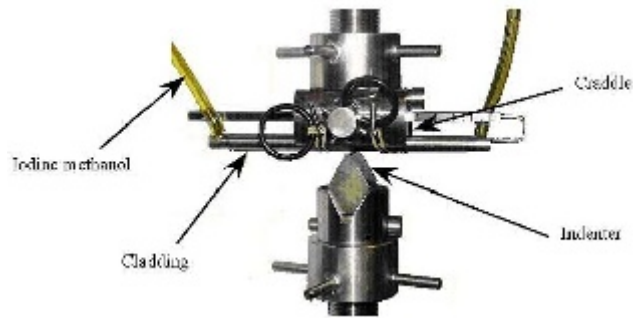
Table 1. Chemical composition of zircaloy-4 (in wt.%)

Zr	Sn	Fe	Cr	O
Bal.	1.3	0.22	0.12	0.130

The experimental I-SCC database was built by means of internal pressurisation tests in both inert and iodine vapour environments on tubular industrial cladding. Approximately 60 mg of iodine was introduced inside each specimen before pressurisation, giving an iodine surface concentration close to 1.5 mg.cm^{-2} . I-SCC susceptibility was investigated by means of internal pressurisation tests on smooth specimens in the temperature range 350°C to 488°C . Internal pressurisation tests on smooth specimens were performed on both un-irradiated and neutron-irradiated cladding, allowing the determination of the influence of neutron irradiation on I-SCC susceptibility.

Internal pressurisation tests were also performed on pre-cracked un-irradiated specimens. Pre-cracking of the inner surface was achieved by corrosion fatigue in an iodine-methanol solution at room temperature. A photograph of the experimental corrosion fatigue pre-cracking set-up is given in Figure 1. The complete procedure for fatigue pre-cracking is given in [10]. Crack growth rate data were derived from internal pressurisation tests conducted on pre-cracked claddings. Fractographic examination was performed on each specimen following an internal pressurisation test in a JEOL 5004 scanning electron microscope.

Figure 1. Corrosion fatigue pre-cracking experimental set-up



Results

I-SCC susceptibility

The evolution of the time to failure as a function of the hoop stress in the temperature range 350°C to 488°C for un-irradiated zircaloy-4 in both inert and iodine environments is given in Figure 2. The increase of temperature leads to a significant decrease in the time to failure for a given hoop stress. This effect of temperature can be correlated with creep damage. At all temperatures, the iodine environment leads to an important decrease in the time to failure for a given hoop stress. As shown in Figure 3, this decrease in the time to failure in an iodine environment is associated with a brittle mode of failure. Interestingly, the I-SCC susceptibility of zircaloy-4 seems to decrease with an increase in temperature, suggesting that creep damage becomes dominant at high temperature.

In Figure 4, the evolution of the time to failure as a function of the hoop stress for un-irradiated and neutron-irradiated (one and two PWR cycles) zircaloy-4 at 350°C is presented. Neutron irradiation is shown to lead to an important increase in the I-SCC susceptibility. As expected, neutron irradiation is also shown to significantly increase the time to failure under an inert atmosphere for a given hoop stress.

Figure 2. Influence of temperature on the evolution of the time to failure as a function of the applied hoop stress during internal pressurisation tests

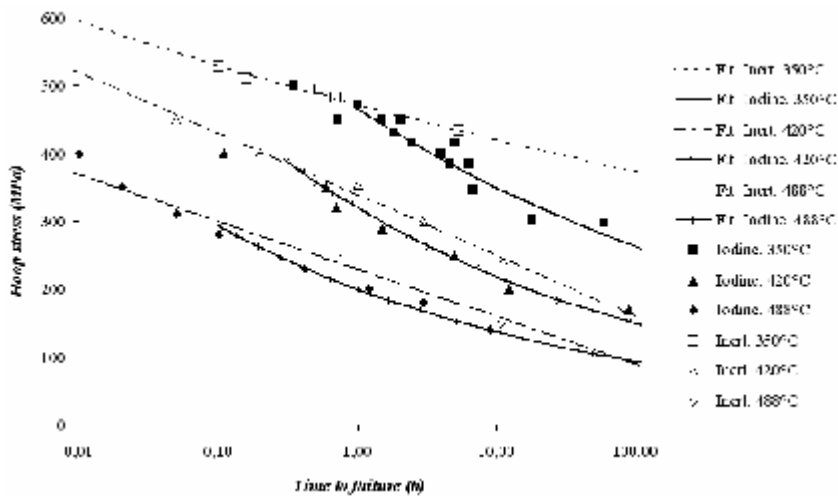


Figure 3. SEM micrographs showing (a) the transition from SCC to transgranular ductile failure and (b) detail of (a) showing TG and IG cracking

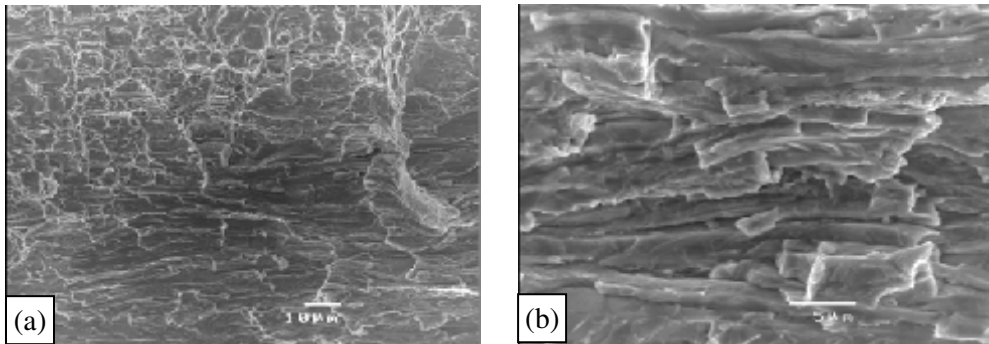
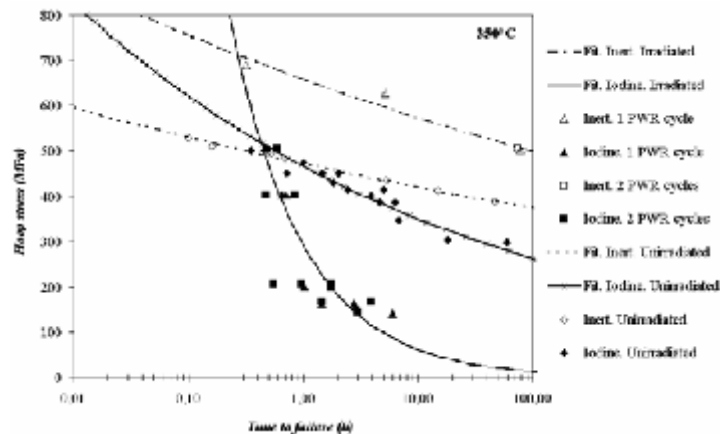


Figure 4. Evolution of the time to failure as a function of the applied hoop stress during internal pressurisation tests on smooth specimens



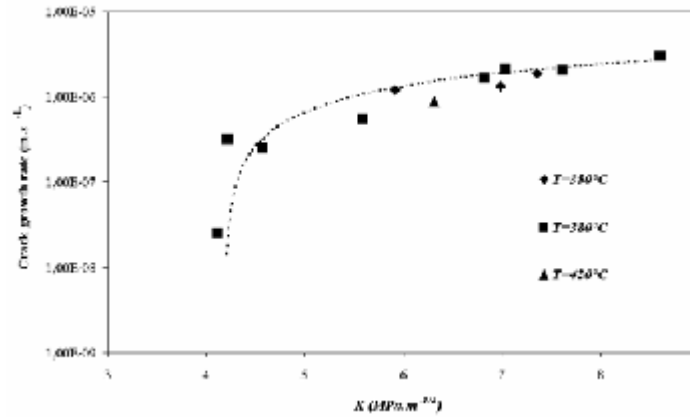
I-SCC growth rate

The evolution of crack growth rate as a function of the initial applied stress intensity factor at 380°C is given in Figure 5. Additional data points at 350°C and 420°C are added to this figure. The results suggest the existence of threshold stress intensity factor value for I-SCC propagation, $K_{III-SCC}$, around 4.2 MPa√m. For K value exceeding 6 MPa√m, crack growth seems to reach a plateau regime where the crack growth is nearly independent of K . The results obtained at different temperatures suggest that the plateau regime is independent of the temperature.

Modelling

The model presented here is based on the initial work of Delette [6]. In this model, the iodine concentration is assumed to be constant at the crack tip and important enough for crack advance by SCC. The main refinement of this model is the description of the effect of temperature on I-SCC. This model describes I-SCC in three successive phases, i.e. (i) initiation by rupture of the zirconia, (ii) propagation of a subcritical crack under $K_{III-SCC}$, and (iii) propagation of a critical crack once $K_{III-SCC}$ is reached. The final ductile failure by extensive shearing (plastic instability) often observed in laboratory studies is neglected in the model.

Figure 5. Evolution of the stress corrosion crack growth rate as a function of the applied stress intensity factor during internal pressurisation tests on pre-cracked specimens



In the following sections, the crack initiation phase, the critical crack propagation phase and the subcritical propagation phase of the model are described successively.

Phase 1: Crack initiation

As already mentioned above, both (i) the rupture of the protective layer of zirconia and (ii) obviously a positive tensile stress are considered to be necessary conditions for crack initiation in the model. The necessary condition on the rupture of the zirconia is conservative since SCC is a local corrosion phenomenon and such event will localise the corrosive effect of iodine.

Assuming that (i) the total tangential strain in the zirconia is equal to the total tangential strain at the inner wall of the cladding, that (ii) zirconia is a fully elastic material, and that (iii) the contributions of axial and radial directions on the tangential elastic behaviour of zirconia can be neglected, one can write:

$$\sigma_z = E_z \cdot \varepsilon_z = E_z \cdot \varepsilon \quad (1)$$

where σ_z is the tangential stress in the zirconia, E_z the Young's Modulus of the zirconia, ε_z the total (elastic) tangential strain in the zirconia and ε the total tangential strain at the inner surface of the cladding. Finally, assuming a fully elastic behaviour in traction for the layer of zirconia, one can derive the following failure criterion:

$$\sigma_z > \sigma_0 \quad (2)$$

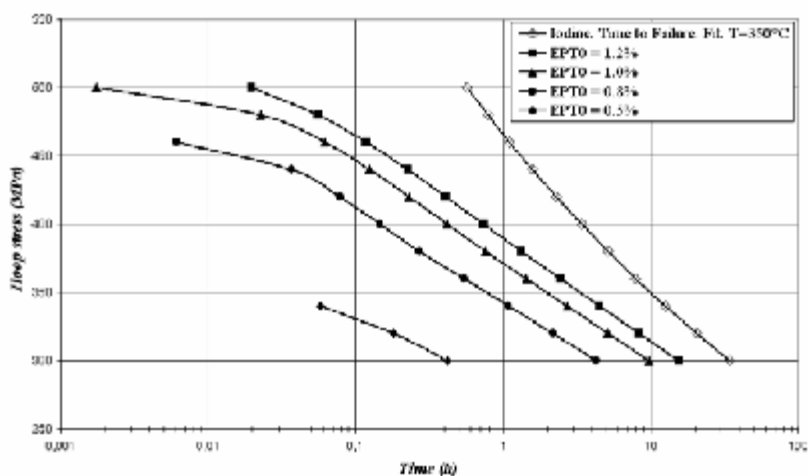
where σ_0 is the failure stress in traction. This criterion is obviously equivalent to the following criterion:

$$\varepsilon > \varepsilon_0 = \frac{\sigma_0}{E_z} \quad (3)$$

This criterion has been applied as post-processing of FE simulations of the internal pressurisation tests presented in the experimental section. The FE simulations were performed with CAST3M (CEA's FE code) in axisymmetric 2-D using the viscoplastic law identified by Soniak, *et al.* [11] for neutron-irradiated and un-irradiated zircaloy-4 at 350°C in the stress range between 300 MPa and

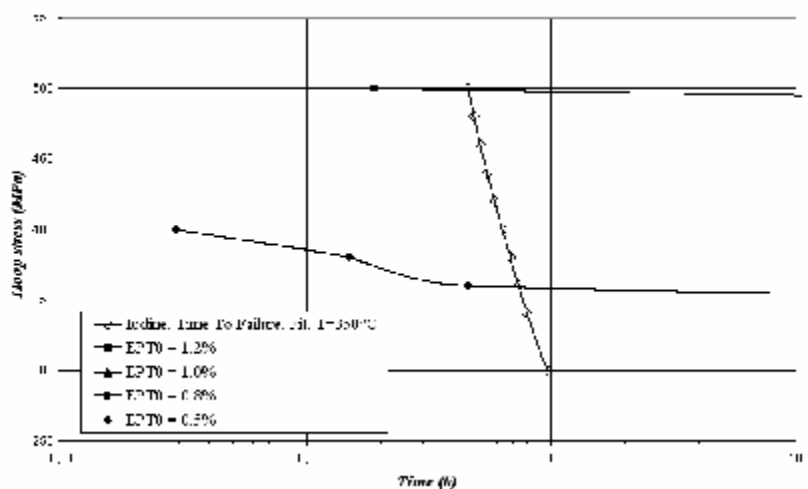
500 MPa, and in a ϵ_0 range between 0.5% and 1.2%. As shown in Figure 6, the results obtained for stress ranging from 300 MPa to 500 MPa on un-irradiated materials show that the criterion defined in Eq. (3) can be used for the rupture of zirconia at 350°C for all ϵ_0 values. In order to be consistent with previous work by Fandeur [5] and assuming $\sigma_0 = 2\,000$ MPa and $E_Z = 200$ GPa, an ϵ_0 value of 1% was used in the model for un-irradiated material.

Figure 6. Comparison between the time required to reach $\epsilon = 1.2\%$, 1% , 0.8% and 0.5% for several applied hoop stresses and the time to failure for un-irradiated Zy-4 during internal pressurisation tests on smooth specimens at 350°C



In contrast, as shown in Figure 7, the results obtained on irradiated materials demonstrate that the criterion defined in Eq. (3) cannot be used. Indeed, the strain to failure observed for irradiated zircaloy-4 at 350°C can be significantly lower than the lowest ϵ_0 value, 0.5%. As a consequence, no criterion on the rupture of zirconia was applied in the model for irradiated zircaloy-4.

Figure 7. Comparison between the time required to reach $\epsilon = 1.2\%$, 1% , 0.8% and 0.5% for several applied hoop stresses and the time to failure for irradiated Zy-4 during internal pressurisation tests on smooth specimens at 350°C



Phase 3: Critical crack propagation

As shown in Figure 5, internal pressurisation tests carried-out on pre-cracked cladding tubes at different temperatures suggest that (i) critical crack propagation is independent of the temperature and that (ii) propagation occurs above a threshold stress intensity factor $K_{III-SCC}$. The critical propagation phase was described by the following relation:

$$\dot{a} = C(1 + D(K - K_{III-SCC})) \quad (4)$$

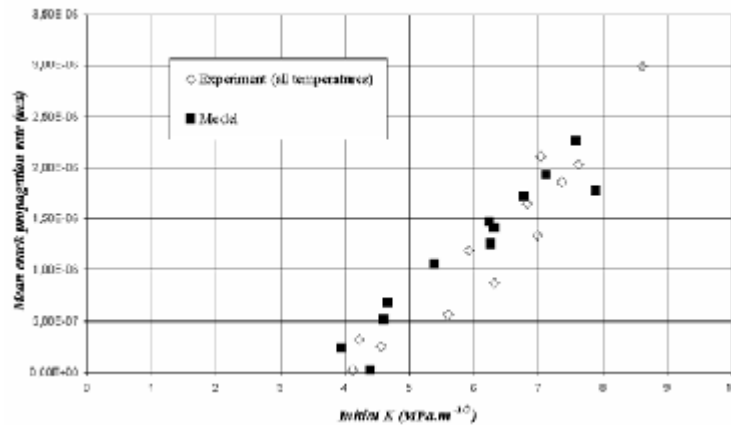
where a is the crack depth, K the stress intensity factor of the crack and C and D are the model's parameters to be identified. This equation is close to the general following formalism widely used in Elastic Fracture Mechanics: $\dot{a} = A \cdot (K - K_{III-SCC})^B$.

The stress intensity factor K is evaluated with the following formula by [12]:

$$K = \alpha(a, 2b) \cdot \sigma \cdot \sqrt{\pi \cdot a} \quad (5)$$

where $2b$ is the crack length, α the crack shape coefficient, and σ the applied hoop stress. In the experimental section, the pre-crack shape coefficient α and the subsequent initial stress intensity factor has been evaluated post-mortem by [13]. For the sake of simplicity, the model was built with a single and constant α value. In order to determine this α value, the initial stress intensity factor determined experimentally for a given pressure was compared with calculated stress intensity factors with α values ranging from 0.9 to 1.2. The results of this comparison are given in Figure 8.

Figure 8. Comparison between the stress intensity factors calculated for different shape factors and stress intensity factors derived from experimental observations

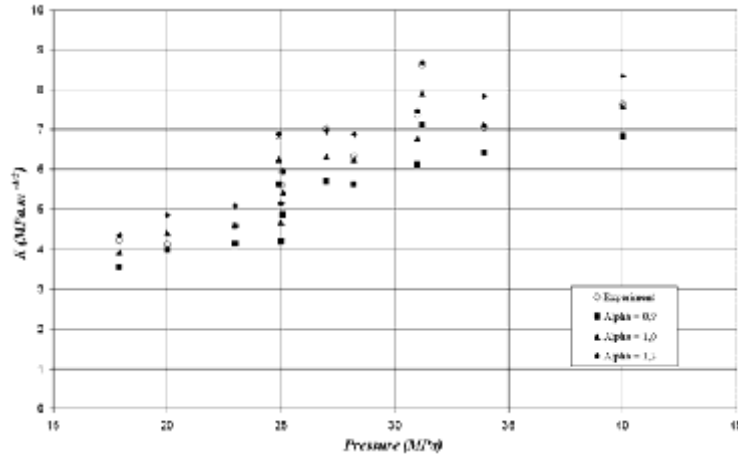


The I-SCC propagation model was then integrated by a Runge-Kutta method to model the results presented in Figure 5. As shown in Figure 9, the following parameters well describe experimental results obtained for un-irradiated zircaloy-4.

$$\alpha = 1, K_{III-SCC} = 4.2 \text{ MPa}\sqrt{\text{m}}, C = 1 \cdot 10^{-10} \text{ m}\cdot\text{s}^{-1}, D = 5500 \text{ (Mpa}\cdot\sqrt{\text{m}})^{-1} \quad (6)$$

Since no results were available for critical crack propagation in irradiated zircaloy-4, identical parameters were used to describe the I-SCC propagation phase of irradiated and un-irradiated materials.

Figure 9. Comparison between calculated propagation rate and experimental data for different initial stress intensity factors



Phase 2: Subcritical crack propagation

In the model, the subcritical crack propagation phase corresponds to the growth of a crack until it reaches a critical depth related to the threshold stress intensity factor for critical propagation. The time corresponding to the subcritical crack propagation phase, t_{sub} , is given by:

$$t_{sub} = t_R - t_Z - t_{propa} \quad (7)$$

where t_R is the experimental time to failure during internal pressurisation test on smooth specimens, t_Z is the time required to rupture the inner layer of zirconia ($t_Z = 0$ on irradiated material) and t_{propa} is the time corresponding to the critical propagation phase.

As mentioned in the previous section, the critical propagation phase does not depend on the temperature. In contrast, the subcritical propagation phase can be described by the following relation:

$$t_{sub} = A e^{\frac{Q}{T}} \cdot \sigma^B \quad (8)$$

Obviously, the I-SCC critical propagation threshold $K_{I/I-SCC}$ defines a critical depth a_{SCC} given by:

$$a_{SCC} = \frac{1}{\pi} \cdot \left(\frac{K_{I/I-SCC}}{\alpha \cdot \sigma} \right)^2 \quad (9)$$

Assuming that during the I-SCC subcritical propagation phase the instantaneous growth rate is equal to the mean growth rate, one can write: $\dot{a} = \frac{a_{SCC}}{t_{sub}}$.

Fitting the results of the internal pressurisation tests presented in the experimental section with Eqs. (7) to (9) leads to the following sets of data for un-irradiated and irradiated zircaloy-4:

$$Q = 20\,240\text{ K}, A = 6.44 \cdot 10^{49}, B = -7 \text{ for un-irradiated zircaloy-4} \quad (10)$$

$$Q = 20\,240\text{ K}, A = 97.562, B = -1.5 \text{ for irradiated zircaloy-4} \quad (11)$$

It should be noted here that (i) these data sets are obtained for stress unit in Pascal and time unit in seconds, and that (ii) the same set of data is considered for irradiated zircaloy-4 at all fluences. The complete I-SCC model integrating Phases 1 to 3 (initiation, subcritical crack propagation and critical crack propagation) has been integrated by a Runge-Kutta method to model internal pressurisation tests performed on smooth specimens and presented in Figures 2 and 4 for un-irradiated and irradiated materials, respectively. Results of this model are presented in Figure 10 for un-irradiated materials and Figure 11 for irradiated material.

Figure 10. Comparison between model prediction and experimental data obtained by internal pressurisation tests on un-irradiated smooth specimens at various temperatures

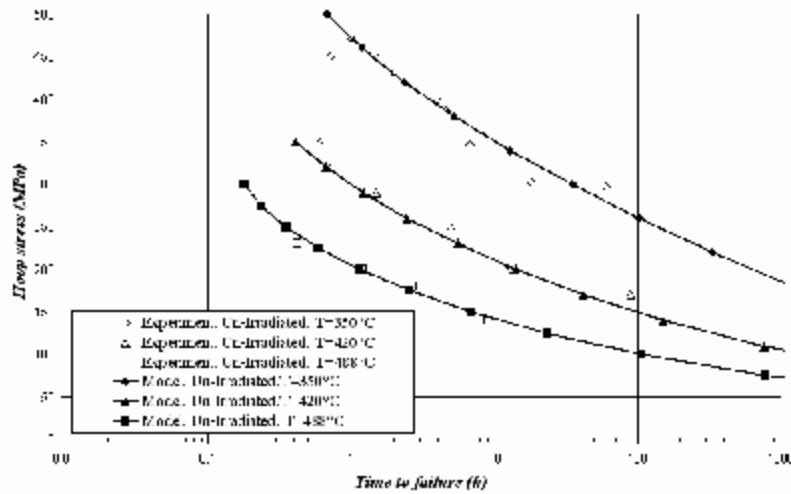
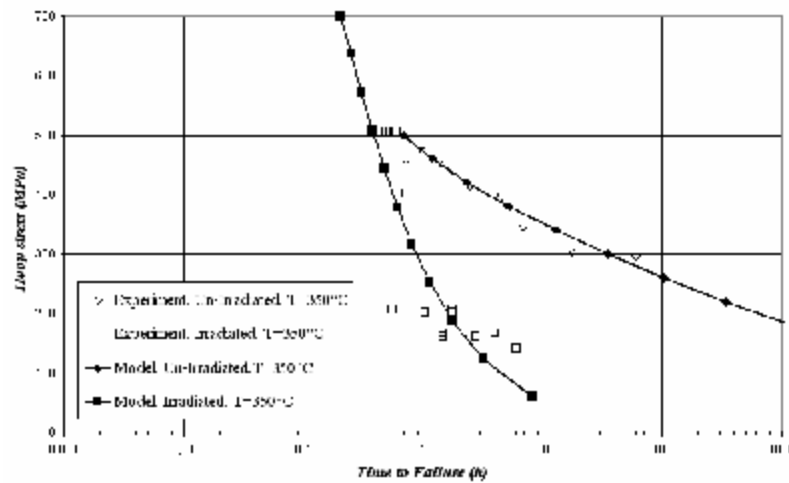


Figure 11. Comparison between model prediction and experimental data obtained by internal pressurisation tests on irradiated smooth specimens at 350°C



Future work

The I-SCC model presented above is based on the results of internal pressurisation tests. During such internal pressurisation tests, the stress on the inner surface of the tube cladding is imposed by the applied pressure while strain may vary. In contrast, during power ramps, swelling of the pellet results in the imposition of a strain to the cladding while stress may change by relaxation. Future work on I-SCC at CEA would be focused (i) on the building of a new database from relaxation tests in order to better simulate the particular loading mode of the cladding during power ramps and (ii) the refinement of the present model to take into account this loading mode.

Conclusions

I-SCC was studied by means of internal pressurisation tests on both smooth and corrosion fatigue pre-cracked tube cladding for irradiated and un-irradiated zircaloy-4. A phenomenological I-SCC model was derived from these results. The originality of this model lies in the integration of the influence of temperature in the subcritical crack propagation.

Acknowledgements

This work was partly supported by EDF and FRAMATOME ANP. The authors gratefully acknowledge this industrial support as well as people that have been involved in CSC-I studies at CEA Grenoble in the past, and obtained some of the experimental results described in this paper.

REFERENCES

- [1] Fregonese, M., G. Delette, G. Ducros, F. Lefebvre, “Amount of Iodine Responsible for I-SCC of Zircaloy-4 in PCI-conditions: Recoil-implanted and Thermally-released Iodine”, *Nuclear Engineering and Design*, 186, pp. 307-322 (1988).
- [2] Fregonese, M., F. Lefebvre, C. Lemaignan, T. Magnin, “Influence of Recoil-implanted and Thermally-released Iodine on I-SCC of Zircaloy-4 in PCI-conditions: Chemical Aspects”, *J. of Nuclear Materials*, 265, pp. 245-254 (1999).
- [3] Jacques, P., F. Lefebvre, C. Lemaignan, “Deformation-corrosion Interactions for Zr Alloys During I-SCC Crack Initiation – Part I : Chemical Contributions”, *J. of Nuclear Materials*, 264, pp. 239-248 (1999).
- [4] Jacques, P., F. Lefebvre, C. Lemaignan, “Deformation-corrosion Interactions for Zr Alloys During I-SCC Crack Initiation – Part II: Localised Stress and Strain Contributions”, *J. of Nuclear Materials*, 264, pp. 249-256 (1999).

- [5] Fandeur, O., *Étude Expérimentale et modélisation mécanique de la corrosion sous contrainte des gaines en Zircaloy-4*, Thèse ECP, Spécialité Mécanique et Matériaux (2001).
- [6] Delette, Gérard, *Intégration au code METEOR 1.1 de la Modélisation de la corrosion sous contrainte des gaines de Zircaloy-4 détendu développé au SECC*, CEA Internal Report, Documentation Technique, DTP/SECC 94106 (1994).
- [7] Brochard, J., F. Bentejac, N. Hourdequin, S. Seror, C. Verdeau, O. Fandeur, S. Lansart, P. Verpeaux, “Modelling of Pellet-cladding Interaction in PWR Fuel”, *SMIRT Conference* (2001).
- [8] Garcia, Ph., C. Struzik, M. Agard, V. Louche, “Mono-dimensional Mechanical Modelling of Fuel Rods Under Normal and Off-normal Operating Conditions”, *Nuclear Engineering and Design*, 216, 183-201 (2002).
- [9] Mougel, C., *et al.* “Power Ramping in the OSIRIS Reactor: Database Analysis for Standard UO₂ Fuel with Zy-4 Cladding”, *AIEA Technical Meeting*, also these proceedings.
- [10] Lemaignan, C., “Controlled Cracking of Tubes”, *International Journal of Pressure Vessels & Piping*, 15, pp. 241-249 (1984).
- [11] Soniak, A., N. L'Hullier, J.P. Mardon, V. Rebeyrolle, P. Bouffioux, C. Bernaudat, “Irradiation Creep Behavior of Zr-base Alloys”, *Zirconium in the Nuclear Industry: Thirteenth International Symposium*, ASTM STP 1423, G.D. Moan and P. Rudling, Eds., ASTM International, West Conshohocken, PA (2002), pp. 837-862.
- [12] Kobayashi, A.S., N. Polvanich, A.F. Emery, W.J. Love, “Inner and Outer Cracks in Internally Pressurized Cylinders. Stress Intensity Factor of Surface Crack in Pressurized Cylinders”, *Journal of Pressure Vessel Technology*, Transaction of the ASME, February (1977).
- [13] Rouillon, *et al.*, *Caractérisation de la phase transgranulaire lors de la fissuration par CSC du Zircaloy-4 détendu en milieu iodé*, CEA Internal Report, DTP/SECC 98/062A (1998).
- [14] Diard, O., *Un exemple de couplage, comportement-endommagement-environnement, dans les polycristaux. Application à l'interaction pastille-gaine*, Thèse ENSMP, Spécialité Sciences et Génie des Matériaux (2001).

OBSERVATION OF A PELLETT-CLADDING BONDING LAYER IN HIGH-POWER FUEL

S. Van den Berghe, A. Leenaers, B. Vos, L. Sannen, M. Verwerft
Belgian Nuclear Research Centre SCK•CEN, Belgium

Abstract

This paper reports on a detailed electron probe micro-analysis investigation of duplex bonding layers observed at the fuel-cladding interface of PWR fuel rods that were subjected to high linear powers (220-320 W/cm). The various phases encountered, from the cladding inward, were identified as Zr, ZrO₂, Zr-Cs-O, U-Cs-O and UO₂. Caesium concentrations as high as 6-7 at.% were observed in the Zr-Cs-O layer and concentrations of about 3 at.% are found in the U-Cs-O layer. High concentrations of Cs were also found on the grain boundaries of the UO₂ fuel, up to several hundred microns into the fuel. The good bonding between cladding and fuel has as a result that the cold gap runs through the fuel, with the bonding layer and a thin fuel layer sticking firmly on the cladding.

In an effort to reproduce the formation of these bonding layers under laboratory conditions, sealed zircaloy tubes, containing caesium molybdate (Cs₂MoO₄), were heated in a tubular furnace to temperatures of 600-800°C. It appears that the oxygen potential plays an important role in the formation of such bonding layers. The formation of Cs-Zr-O interaction layers could be observed at sufficiently low oxygen potentials.

Introduction

Fuel-cladding interaction and the formation of fuel-cladding bonding layers with specific chemical, physical and mechanical properties are of importance regarding the evolution of thermal conductivity as well as in the context of PCMI. It is also important in the framework of long-term storage of spent fuel where the phases formed at the fuel-cladding boundary are considered to be the first to be leached in case of cladding failure.

Inner surface cladding oxidation and subsequent mechanical bonding between the fuel pellet and the cladding are well-known phenomena of high burn-up and high duty fuels but the chemical composition and formation conditions of the complex bonding layers are much less documented. In this study, we report on the detailed observation of caesium-rich phases in pellet-cladding bonding layers of zircaloy-clad high duty LWR fuels. Some straightforward laboratory experiments complement the fuel observations and allow confirming that the formation mechanisms proposed on the basis of thermodynamic considerations apply even though the fuel-clad interface system is never at equilibrium.

Experimental

Fuel samples

The observation of fuel-clad bonding and the formation of multi-layer bonding layers are typical for high-duty fuels. The case study presented here is taken from old fuel samples that were re-investigated in the framework of long-term intermediate storage of nuclear fuel. Samples were taken from UO₂ fuel rods (enrichment of 2.5%) that were irradiated in the Dodewaard boiling water reactor (BWR) between 1971 and 1974. The fuel rods have undergone peak powers between 220 and 320 W/cm and have end-of-life burn-ups of around 23 GWd/t_M. After unloading, the fuel rods were cut and the segments were stored in air in sealed canisters. In 2001, the canisters were unloaded and samples were cut from the segments in the framework of a post-irradiation examination campaign focusing on the long-term interim storage of fuel [1,2]. Because of the irradiation characteristics of these rods, the cladding-fuel interface was also examined closely, resulting in the observations reported below.

Sample preparation and examination

The samples have been embedded in epoxy resin and polished with diamond grinding discs of successively finer grain size, finishing on cloth with diamond paste of 3 μm and 1 μm. Before mounting the sample in the electron microscopes, the samples were coated with carbon to prevent charging.

Optical microscopy was performed on a Reichert Telatom 3 shielded optical microscope equipped with a digital image acquisition system.

Scanning electron microscopy is performed on a shielded Jeol JSM6310 microscope equipped with a secondary electron and backscattered electron detector.

The electron probe micro-analysis (EPMA) is performed on a shielded CAMEBAX-R microbeam, upgraded with digital image and X-ray acquisition programs (SAMx Suite).

Results

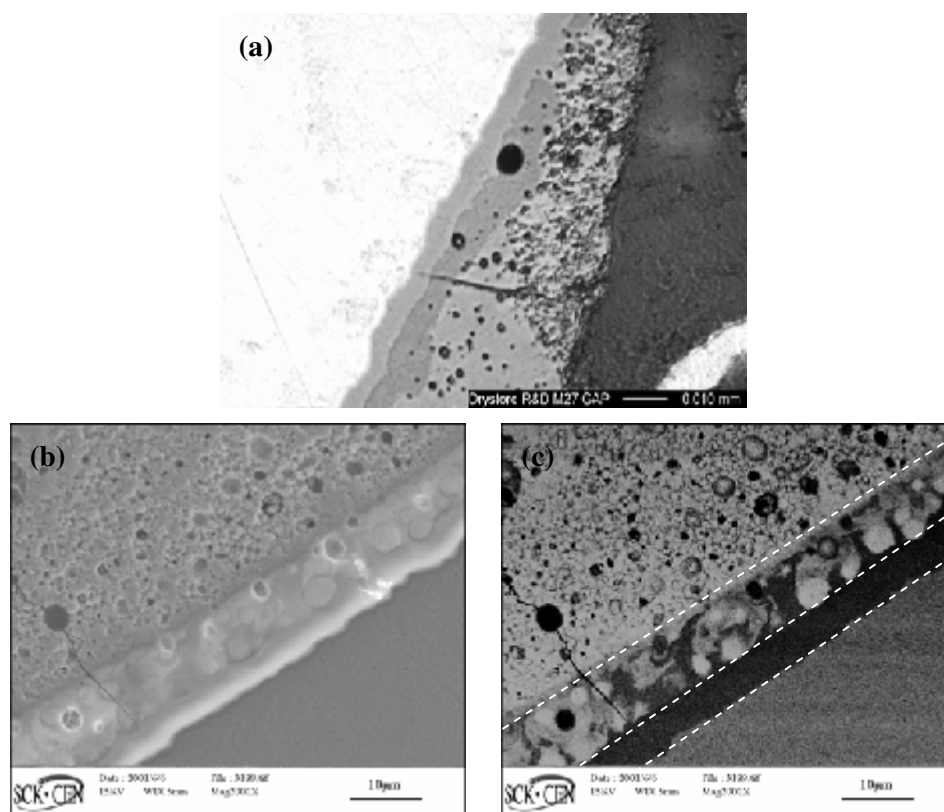
Optical and scanning electron microscopy

The optical micrographs of the sample, taken close to the pellet-cladding interface [Figure 1(a)], show a duplex bonding layer. From the cladding inward, one can first observe the pure zircaloy cladding, then the grey ZrO_2 oxidation layer, followed by the darker grey bonding layer. A piece of fuel material is adhering to this bonding layer, followed by the fuel-cladding gap.

A similar image is generated with scanning electron microscopy [Figures 1(b) and (c)], where the use of backscattered electron imaging provides a clear view of the interaction layer on top of the ZrO_2 [Figure 1(c)]. The backscattered electron image shows that the Cs-Zr-O layer has all the aspects of a liquid or at least viscous mixture of a U-rich phase and a Zr-rich phase.

Figure 1. Optical micrograph (a) and scanning electron images (b and c) of the pellet-cladding interface. (b) Secondary electron image and (c) backscattered electron image.

The backscattered electron image shows composition variation (Z-contrast imaging). Image (c) is taken with backscattered electrons and shows the density distribution. The dotted lines show the boundaries of the different layers.

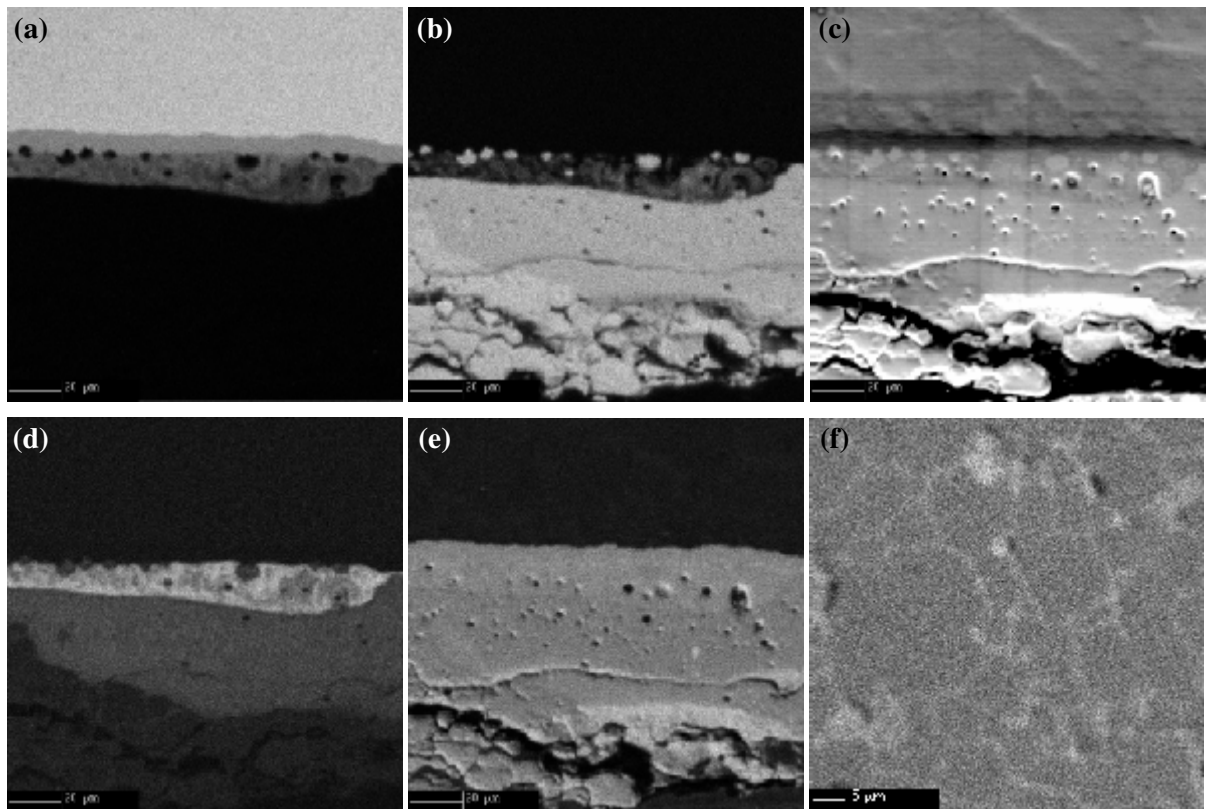


The interaction layer is not visible at all locations on the cladding, but it covers roughly 50% of the fuel-cladding interface. The aspect of the layers is always identical and the bonding between the layer and the fuel is very strong as witnessed by the fact that part of the fuel is always found to adhere to the bonding layer, with the fuel-cladding gap inside the fuel.

Electron probe micro-analysis

The X-ray mappings taken with the microprobe show the repartition of the elements involved in this bonding layer, namely Zr, Cs, U and O. It is evident from the mappings in Figure 2 that the bonding layer consists of three *consecutive* phases. On the cladding, we first find a thin ZrO₂ layer. On this oxide layer, a Cs-Zr-O interaction layer has formed. This layer is not completely homogeneous. Inside it, we observe inclusions of a Cs-enriched U-O phase, similar to the material found in the first zone. Beside the inclusions, the layer also shows some intermixing with the uranium from the fuel. The last layer in the sequence is a Cs-rich uranium oxide layer, which forms the first zone of the fuel adhering to the bonding layer.

Figure 2. X-ray mappings of the pellet-cladding interaction layer, showing the repartition of (a) Zr, (b) U, (d) Cs and (e) O, as well as an SEM image (c). The three consecutive layers ZrO₂, Cs-Zr-O and Cs-U-O are discussed in the text can be clearly discerned. In (f) a detailed view of the Cs-enriched grain boundaries as observed in the fuel is given.



Semi-quantitative line scan data taken across the bonding layer (Figure 3) show the element concentrations in each layer. The line scan is taken across an inclusion of Cs-enriched U-O phase adhering to the cladding. We can distinguish the different phases present: A is the pure zircaloy cladding, B is the ZrO₂ oxidation layer, C is the Cs-U-O interaction phase and D is the Cs-Zr-O phase. It is observed that the Cs concentration does not exceed 10 at.%.

Elevated Cs concentrations on the fuel grain boundaries are observed up to several hundreds of microns into the fuel [Figure 2(f)].

CLADDING LINER SURFACE EFFECTS AND PCI

Gunnar Lysell,¹ Koji Kitano,¹ David Schrire,¹ Jan-Erik Lindbäck²

¹Studsvik Nuclear AB

²Westinghouse Electric Sweden AB

Abstract

A soft, metallurgically bonded inner layer of zirconium with small quantities of alloying elements is used in BWR zircaloy fuel cladding as a remedy against pellet-cladding interaction (PCI) fuel failures.

The inner surface of the liner becomes significantly hardened during irradiation. Local micro-hardness and elemental composition profiles close to the inner surface of the cladding liner have been measured in a fuel rod subjected to power ramp testing. In addition, small incipient cracks in the hardened zone have been detected and characterised after the ramp test. The extent of the hardening, its cause and its impact on the initiation of PCI cracks are discussed in the paper.

Introduction

The PCI stress corrosion cracking of zirconium cladding originate with surface flaws that determine where a crack can initiate. One factor influencing the propensity for crack initiation is the yield strength of the cladding inner layer. If the yield strength is low, both initiation and propagation of SCC cracks are suppressed. This is the background to the success of zirconium liner cladding as a remedy against PCI cracking in BWR fuel. Still, small incipient cracks can be observed in ramp-tested Zr-liner cladding. In metallography, it is seen that these very small incipient cracks occur in a layer of the liner closest to the fuel. Sometimes this layer can be seen in an optical or SEM microscope as it has some property giving a weak contrast to the base material of the liner.

Sample origin

The cladding sample investigated here comes from a Westinghouse Electric Sweden AB 10×10 BWR rod irradiated for three years in the Swedish Barsebäck 2 reactor to a burn-up of 32 MWd/kgU. The pellet enrichment in the rod was 4.2 wt.%, so there was only a minor amount of additional Pu fissions at the pellet periphery due to the rim effect. The cladding with 9.62 mm OD and 8.36 mm ID had a tin alloyed liner about 60 μm thick. In Studsvik the rod was ramp tested, inducing a permanent diametral change of 1.3% at the sample position on the rod. The rod did not fail in the ramp test.

Measurements

The present paper deals with an examination of two properties of the innermost layer of the irradiated liner. First, the micro-hardness was measured as a function of distance from the inner cladding surface. Secondly, electron probe micro-analysis (EPMA) measurements were performed to quantify the content of recoiled fission products in the same region.

Micro-hardness

The micro-hardness measurement device of type MHT-10, mounted on a Leica MEF 4 microscope allows indentation forces down to 1 g. As shown in Figures 1, 2 and 3 a number of indentations were made at different distances from the liner surface facing the fuel. No measurements were made where there was a zirconium oxide layer formed on the liner surface during the irradiation since the oxide renders the distance from the liner surface undefined. Two different forces, 1 g and 50 g, were used for micro-indentation. The 1 g force was used for all the indentations close to the surface, while both 1 g and 50 g indentations were performed in the interior of the liner so as to confirm the accuracy of the 1 g measurements.

When plotted versus distance from the inner surface of the liner the hardness values give the diagram found in Figure 4. The data close to the inner surface show quite a large spread, due both to the difficulty in accurately measuring such small indentations as well as uncertainty in measuring the exact distance from the surface. However, the trend is clear.

The hardness is significantly increased in a layer about 10 μm thick at the liner surface facing the fuel. The depth strongly suggests that fission fragments recoiled from fissions in the fuel pellet periphery is the cause of this hardening. In order to verify this hypothesis, the concentration profile of fission products was measured in the liner using EPMA.

Figure 1. Examples of indentations in the liner as well as a crack in the inner hardened layer

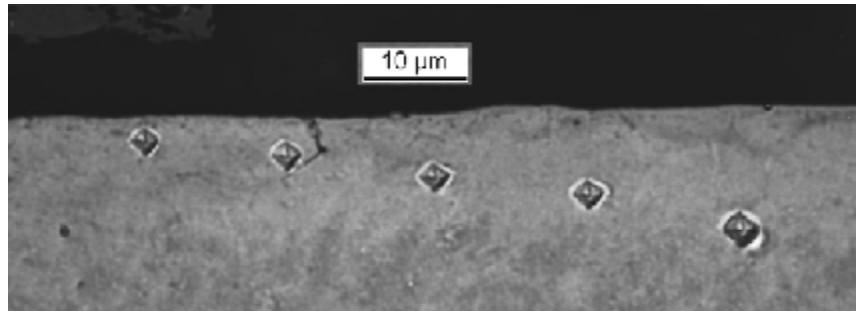


Figure 2. Examples of indentations in the liner as well as cracks in the inner hardened layer

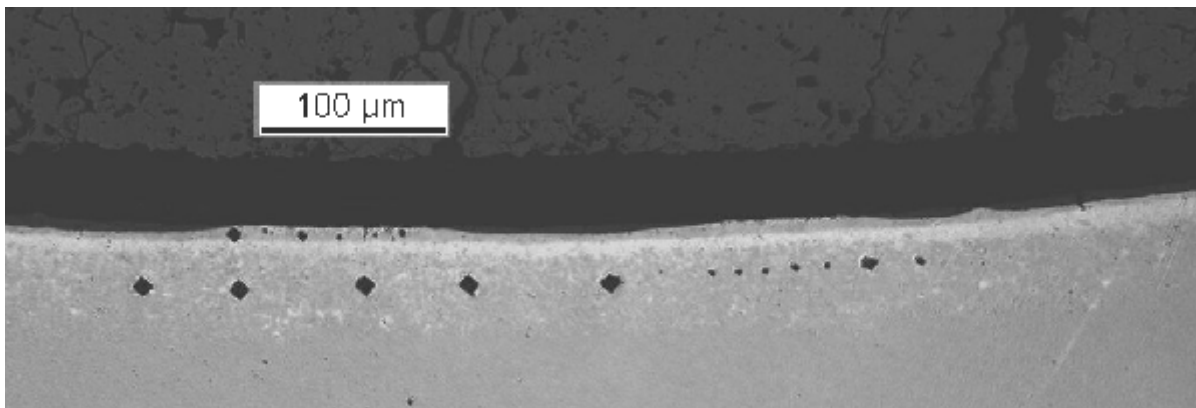


Figure 3. Examples of indentations in the liner and cracks in the inner hardened layer

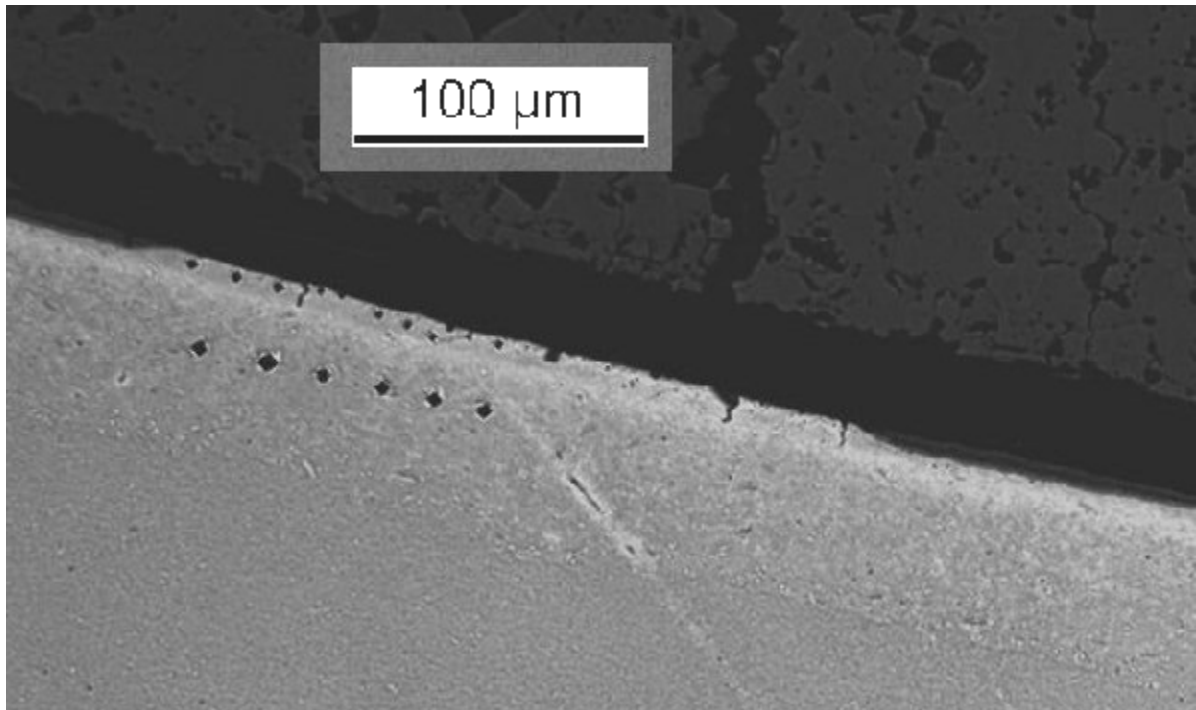
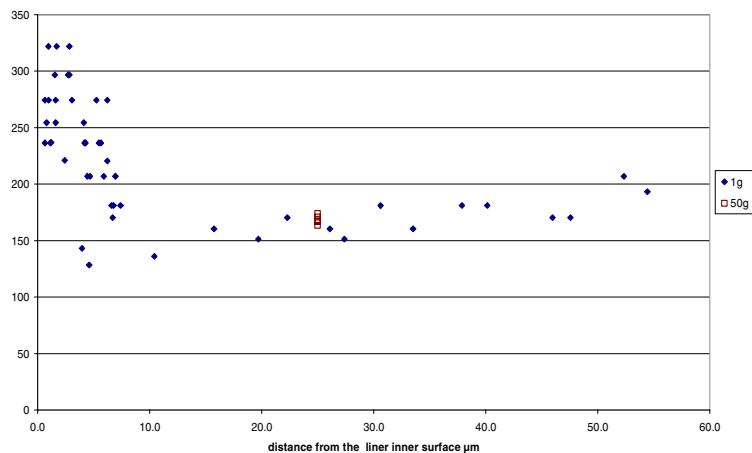


Figure 4. Hardness in the liner showing a hardened layer at the inside

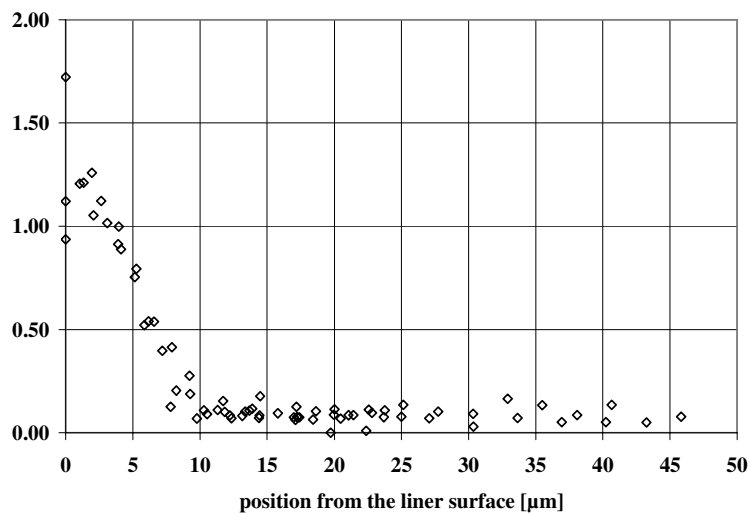


Electron microprobe measurements

The elements analysed by the wavelength dispersive spectrometry (WDS) equipment on the SEM microscope included Zr, Mo, Ru, Xe, Cs, Ce, Nd, O and U. The sum of the analysed fission products, excluding Zr, which is the main constituent of the cladding, is shown in Figure 5 below.

Figure 5. Sum of selected fission products measured by EPMA at the inner surface of the liner

Sum of Ru, Mo, Xe, Cs, Ce and Nd concentration wt%

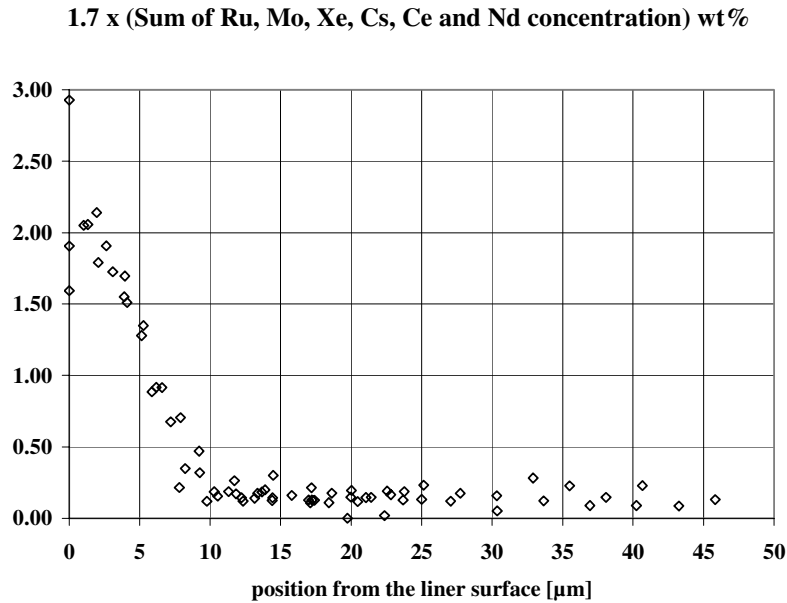


Discussion

To evaluate the total amount of fission products that is expected in the cladding the program ORIGEN was used to calculate the ratio of the sum of all fission products to the sum of Mo, Ru, Xe, Cs, Ce and Nd. This ratio was found to be 1.7.

When plotted versus distance from the inner surface of the liner the total amount of fission products obtained using the 1.7 factor gives the diagram seen in Figure 6.

Figure 6. Total amount of fission products based on measurements of Mo, Ru, Xe, Cs, Ce and Nd



Using the data in Figure 6 the extrapolated concentration of fission products at the inner surface is 2.5 wt.%. This value of 2.5 wt.% of fission products in the cladding closest to the fuel can be compared to the concentration in the fuel. At a burn-up of 32 MWd/kgU corresponding to 3.4% FIMA there should be 3 wt.% of fission products in the UO₂ fuel ($3.4 \times 238/270$). At the surface of the fuel, however, only half of that, 1.5 wt.%, remains in the fuel, while the other half is deposited in the cladding. As the stopping range of fission fragments is about the same, ~10 μm, there should be the same spatial concentration of fission products at the surface of the cladding. As the density of Zr and UO₂ is 6.5 and 10.5 g/cm³ respectively, 1.5 wt.% in the fuel corresponds to $1.5 \times 10.5/6.5 = 2.4$ wt.% in the liner, which is close to the 2.5 wt.% observed at the surface of the liner (see Figure 6).

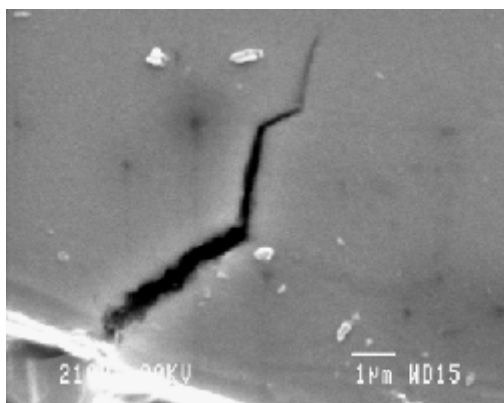
The total amount of fission products deposited in the cladding can also be compared to the total amount produced in the fuel. The fraction in the cladding turns out to be 0.13% of the total fission product inventory in the fuel.

Assuming a 10 μm fission fragment range in the fuel there should theoretically be a linear gradient from full fission product concentration 10 μm from the surface down to half of that at the fuel surface. The theoretical fraction of fission products lost from this zone by recoils is then calculated to be 0.12%, which compares favourably with the measured 0.13% in the cladding.

The hardness increase at the liner surface facing the fuel seems to be a linear function of the deposited fission product concentration. The maximum depth of hardness increase and the presence of fission products is identical, 10 μm, which is a strong indicator that the fission products, and/or the damage they cause in the zirconium lattice, is the reason for the increased hardness. Similar observations have also been reported at higher burn-up [1].

Hardness is directly related to yield strength, which in general increases sensitivity to environmentally assisted cracking like iodine stress corrosion cracking. The small incipient cracks (Figure 3 and Figure 7) have the same depth as the hardened layer, so the unaffected liner material still retains its ability to blunt propagating cracks.

Figure 7. SEM image of incipient crack in the hardened layer of the liner



Although this examination was performed on a BWR liner cladding the same phenomena should also be expected in non-liner cladding, the difference being that incipient cracks formed in the inner layer of cladding facing the fuel in a power ramp are not blunted by the soft liner material but can propagate further through the cladding wall.

Conclusion

Short incipient cracks have been observed near the inner surface of fuel rods with liner cladding subjected to power ramps with significant cladding deformation. The depth of these cracks appears to coincide with the thickness of a 10 µm thick altered layer at the inner surface of the cladding. This inner layer is characterised by a linear increase in hardness towards the surface. This layer is also found to have a linear concentration profile of fission products, from a maximum at the surface and reaching zero 10 µm from the surface. The total amount of fission products in this layer agrees with the fission recoil loss from the fuel pellet.

It is concluded that fission fragment recoils from the fuel causes a hardening of the inside of the cladding, which in turn promotes the formation of incipient cracks when the cladding is subjected to pellet-clad mechanical interaction (PCMI).

REFERENCE

- [1] *Final Report of NUPEC High Burn-up Irradiation Test of BWR Fuel* (2002, in Japanese), description on super micro-hardness measurement is on pages 3.1.9-5 and 3.1.9-23 to 26 of the report.

SESSION IV

In-pile Rod Behaviour

Chairs: W. Wiesenack, S. Lansart

**RESULTS OF WWER HIGH BURN-UP FUEL ROD EXAMINATIONS
IN THE PROCESS OF AND AFTER THEIR TESTING IN THE
MIR REACTOR UNDER POWER CYCLING CONDITIONS**

A.V. Bouroukine, G.D. Lyadov, S.V. Lobin, V.A. Ovchinikov
FSUE, SSC RF RIAR, Russia

V.V. Novikov, A.V. Medvedev, B.I. Nesterov
FSUE VNIINM, Russia

Abstract

This paper describes the measurement results of WWER refabricated fuel rods' cladding deformation under power cycling conditions. Information concerning the results of gas release, fuel temperature measurements and post-irradiation examinations of fuel rods is given here for one of the experiments.

Introduction

The loop channel of the MIR reactor (FSUE, SSC RF RIAR) was used for testing of the WWER refabricated (RFR) and spent full-size fuel rods (FSFR) with a burn-up of 50-60 MWd/kgU under power cycling conditions. The objective of this testing was to obtain experimental data on gas release, cladding deformation and change of fuel rod characteristics. Several experiments were performed. The main feature of one of these experiments with two cycles was that several parameters were measured at the same time using one fuel rod. During the other experiment, repetitive cycling was performed and the fuel rod length and fuel temperature were measured.

Some of the testing results and detailed information concerning the design of the irradiation devices and instrumented fuel rods were provided in the papers [1-3]. The present paper describes the basic results of the post-irradiation examinations of the fuel rod condition in addition to the generalised information about testing.

Testing including complex parameter measuring of the fuel rod of the WWER fuel assembly

This testing was performed in the MIR reactor at the end of 2001. SSC RF RIAR and FSUE VNIINM specialists prepared the testing programme.

Testing conditions and main characteristics of fuel rods

The testing was performed using the loop channels of the MIR reactor. The following coolant parameters were used:

- Pressure – ~15 MPa.
- Inlet temperature – ~250°C.

The increase of the linear power (LP) by ~1.6 times was provided by an appropriate power increase of the nearby operational fuel assemblies of the reactor.

During this testing all parameters of coolant, fuel rods as well as indications of the reactor ionisation chamber and fuel rod integrity control systems were displayed and logged every minute. When the power change occurred quickly (for example, when the control rods were dropped), the frequency of the data logging was 10 Hz.

Six fuel rods (three refabricated and three full-size fuel rods) from the WWER spent fuel assembly were placed into an irradiation device. Figure 1 shows the location of the fuel rods and sensors over the cross-section of the experimental device. Length, diameter and gas pressure were measured using the R75 refabricated fuel rod. For an estimation of the temperature of the R75 fuel rod, the fuel temperature was measured using two similar R74 and R76 fuel rods which were located adjacent to the R75 fuel rod (see Figure 1). The refabricated fuel rods were fabricated from the central part of three full-size fuel rods where the burn-up was the most uniform throughout the fuel rod height. The material of the fuel rod cladding was an Zr+1%Nb alloy, original bore in a pellet is ~1.4 mm. Some characteristics of the fuel rods are given in the Table 1.

Figure 1. Location of the fuel rods and sensors over the cross-section of the experimental device

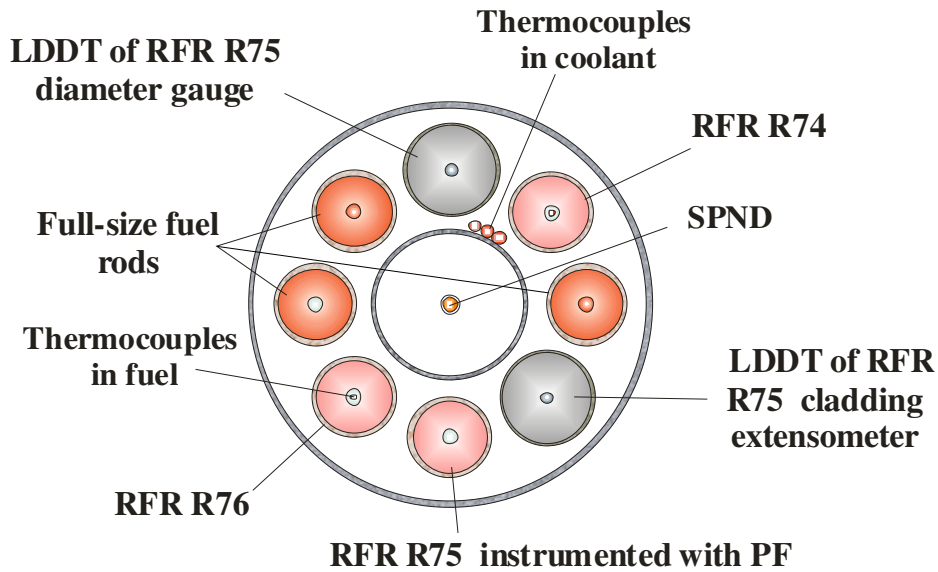


Table 1. Characteristics of the WWER full-size and refabricated fuel rods

Fuel rod type	Fuel rod number	Burn-up, MWd/kgU	Core length, mm	He pressure, MPa	Sensor
RFR	R75	51	~400	0.2	PF, ΔL (CE), ΔD
RFR	R74	"	"	0.6	T2
RFR	R76	"	"	"	T1
FSFR	15	60	~1 300	"	–
FSFR	84	51	"	"	–
FSFR	24	"	"	"	–

Distinctive features of fuel rod parameter change during testing

The parameter change of the fuel rod R75 during testing is shown in Figures 2 and 3.

Figure 2. Change of the maximum linear power (1) of the R75 fuel rod, fuel temperature of the R76 fuel rod (2) and fission gas release (3) in the R75 fuel rod during testing

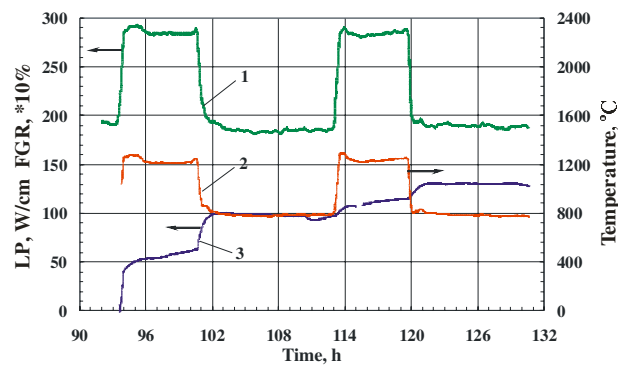
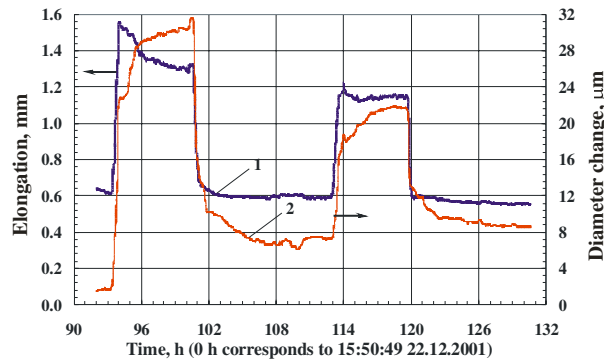


Figure 3. Change of the length (1) and diameter (2) of the R75 fuel rod cladding during testing



Fission gas release from the fuel

Fission gas release under power cycling conditions during testing is shown in Figure 2 and is characterised by the following:

- Fission gas releases into the fuel rod plenum just as power increases and decreases up to the initial level after a certain maintenance at the upper level; fission gas releases mainly during the first cycle.
- At the upper power level after the first and second power increase fission gas release continues, and the rate of fission gas release within ~6 hours of maintenance decreases greatly; at the lower power level fission gas release does not occur.
- The rate difference (at the cycle beginning and during maintenance) proves the existence of two mechanisms of fission gas release (“burst” and “diffused” mechanism).

Changes of length and diameter of fuel rod

The change in length and diameter are shown in Figure 3. Because measuring was performed using one fuel rod, the results can be presented in the form of parametric dependences of some parameters; for example, Figures 4 and 5 show changes of the R75 fuel rod length and diameter as a function of average LP (ALP) throughout the fuel rod height, and Figure 6 shows the relation between the length and diameter changes.

Figure 4. Change of the R75 fuel rod length as a function of average LP

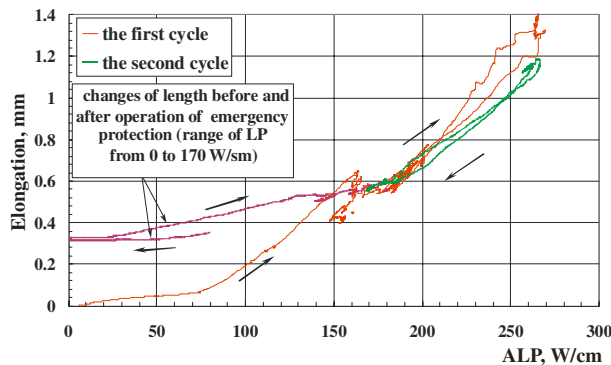


Figure 5. Change of cladding diameter of the R75 fuel rod as a function of average LP

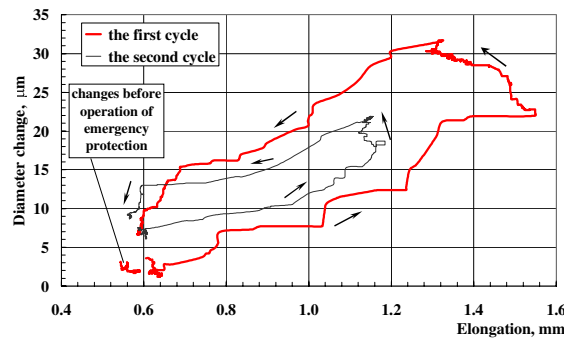
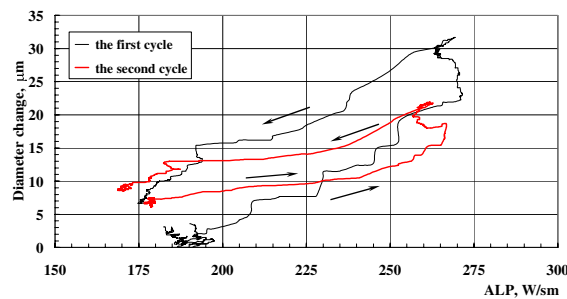


Figure 6. Relation between the length and diameter changes under power cycling conditions



These results evidence the following:

- The tight fuel-cladding connection takes place at a certain linear power level and further power increase results in axial strain of the cladding; further maintenance of the maximum power level results in shortening of the fuel rod length.
- The maximum elongation of the fuel rod takes place under the first power increase.
- The maximum shortening of the fuel rod length after power increase is typical for the first cycle and takes place as a result of creeping and stress relaxation in the cladding material and fuel.
- Practically all residual axial strain of the cladding (it is estimated at approximately 0.08% based on the results of measurements before the reactor comes to power and after reactor shutdown) arises from the first cycle.
- The residual diametrical strain of the cladding makes up approximately 0.1% after the first cycle and preserves after the second cycle. The amplitude of the diameter change reduces significantly in the second cycle and the diameter is changed in the elastic domain.

When the process of FR length change is analysed at the first power increase (see Figure 4) it might be well to point out that the linear power level corresponding to the “tight” fuel connection is around 70-80 W/cm. This LP approximately corresponds with the linear power of fuel rods at the end of the standard fuel assembly operation (~88 W/cm). When the linear power was increased up to the level prior to the first cycle (~180 W/cm) the length of the R75 fuel rod shortened partially during the stable power stage in the linear power range of 150-160 W/cm.

Results of non-destructive examinations

Before and after testing non-destructive examinations of the FRs were performed. The results of measurements of fuel rod length and diameter, determination of gas volume and composition in the free volume of the fuel rod are given in this section. They are compared with the results that were obtained during testing. Gamma scanning was also performed, and the results were taken into account in determination of FR linear power. Typical distributions of fission product activity along the FRs are given in Figures 7 and 8.

Figure 7. Distribution of fission products along the R75 fuel rod after testing

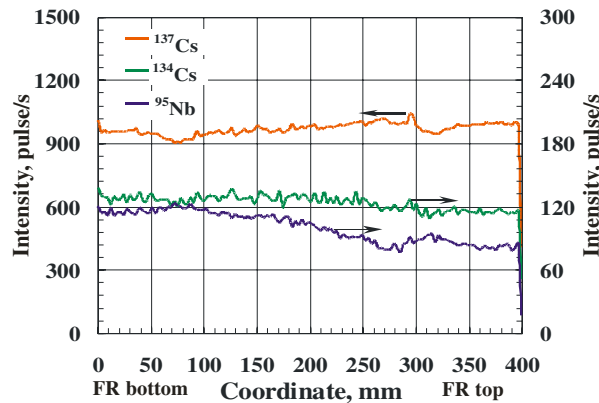
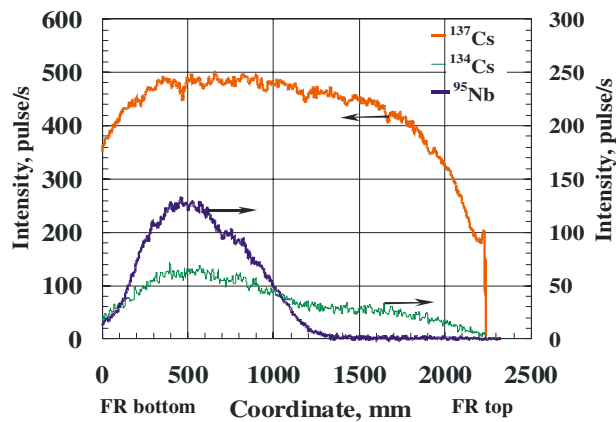


Figure 8. Distribution of fission products along the 84 full-size fuel rods after testing

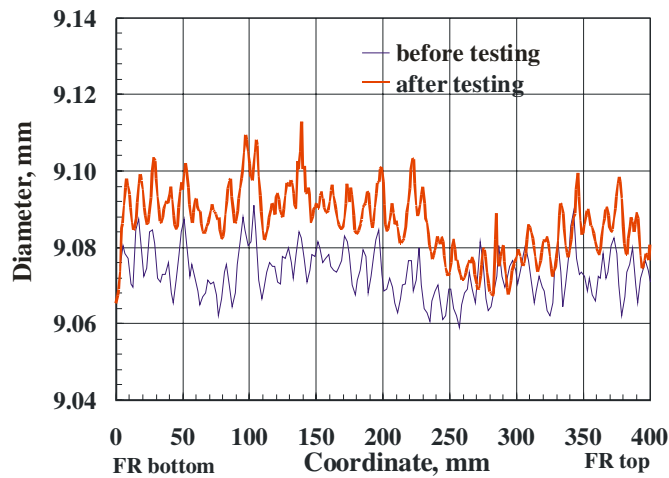


Length increase of the R75 fuel rod made up ~ 0.35 mm (0.09%); this approximately corresponds to the measurement results which were obtained during testing ($\sim 0.08\%$). Figure 9 shows profilogrammes of the R75 fuel rod before and after testing. As shown, at the points where FR diameter changes, the sensor comes in contact with the fuel rod and the increase of diameter is ~ 6 - 10 μm (~ 0.06 - 0.1%). This accords with the results of the residual diametrical strain determination during testing after two cycles (see Figure 3).

The measured volume of the fission gas release from the fuel made up ~ 33.2 cm^3 (under normal conditions); this corresponds to a fission gas release of $\sim 15\%$.

Thus, results of the non-destructive examinations conform to the corresponding data that were obtained during testing.

Figure 9. Diameter of the R75 fuel rod cladding before and after testing



Testing under the repetitive cycling conditions

At the end of 2002, the testing of refabricated WWER fuel rods with a burn-up of 50 MWd/kgU under repetitive power cycling conditions was performed at the MIR reactor. Specialists from SSC RF RIAR and FSUE VNIINM developed the testing programme.

Test conditions and main characteristics of fuel rods

Testing was performed in the water loop channel of the MIR reactor under the following coolant parameters:

- Pressure – ~16 MPa.
- Inlet temperature – ~280°C.

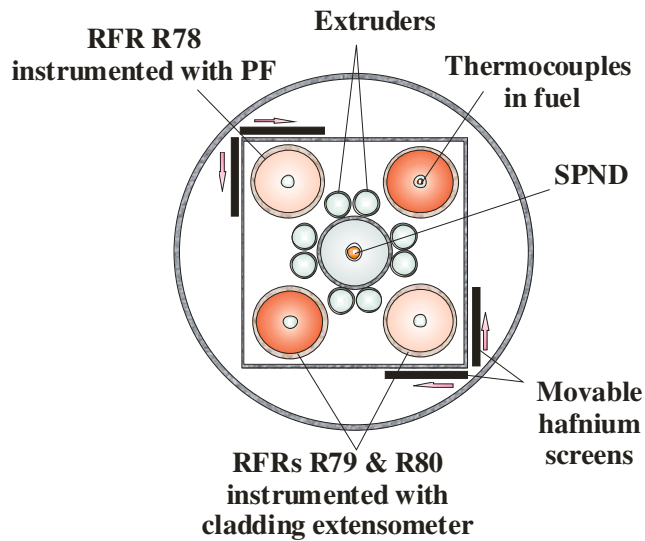
Characteristics of the refabricated WWER fuel rods are given in the Table 2.

Table 2. Characteristics of the refabricated WWER fuel rods

FR number	Burn-up, MWd/kgU	Core length, mm	He pressure, MPa	Sensor
R77	52	400	2.1	T
R78	"	"	1.1	PF
R79	"	"	2.1	ΔL1
R80	"	"	"	ΔL2

The location of fuel rods and sensors throughout over the cross-section of the irradiation device is shown in Figure 10.

Figure 10. Location of fuel rods and sensors over the cross-section of the irradiation device



Change peculiarities of the axial strain of the fuel rod cladding during testing

Cycling was carried out by movement of device screens from two fuel rods to the other two fuel rods (see Figure 10).

Figure 11 shows that the curves of FR power change schematically. Two of four fuel rods were additionally subjected to power ramping after cycling during experiment. All fuel rods preserved their tightness.

Figure 11. Curves of LP change of the WWER FR under cycling conditions

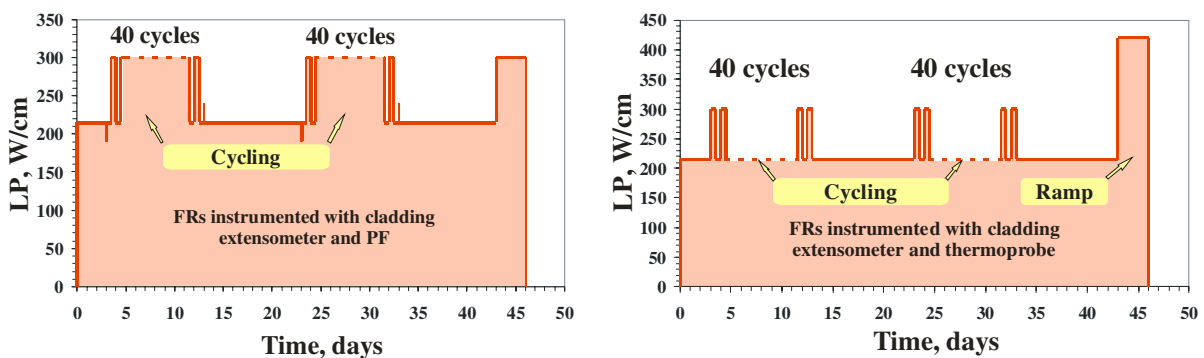
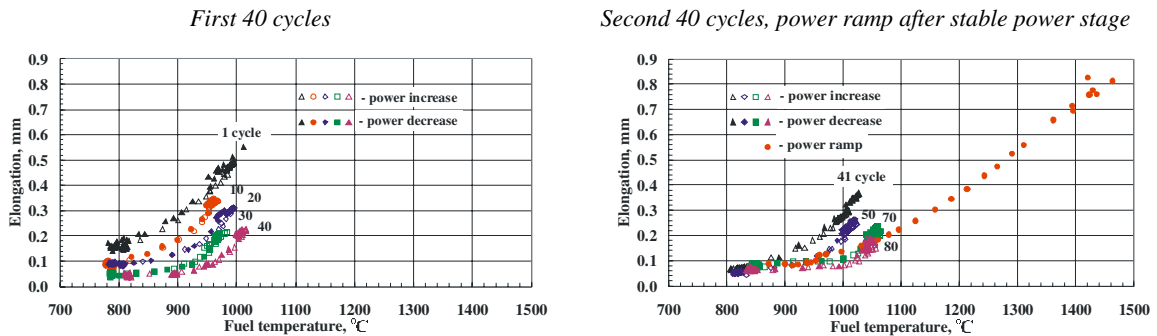


Figure 12 demonstrates changes in the length of fuel rods over the course of power change after different numbers of cycles. As may be seen from the diagram, the amplitude of the axial cladding strain decreases as the cycle number increases. As this takes place, the level of linear power increases and it corresponds to a “tight” fuel-cladding connection.

At present, material science investigations of fuel rods are underway.

Figure 12. Change of fuel rod length during a cycle after different preliminary cycles



Conclusion

In conclusion it can be noted that the results of the performed experiments define the following:

- Change of the axial and radial strain of the WWER fuel rod with a burn-up of approximately 50 MWd/kgU and fission gas release during first power cycles.
- Change of range (amplitude and levels) of cladding axial strain depending on cycle number.
- Linear power change, which corresponds to start of a tight fuel-cladding connection under cycling conditions.

Experimental data can be used for the perfection of calculated codes of strained and stressed state of fuel rods.

REFERENCES

- [1] Bouroukine, A.V., V.A. Ovchinikov, Yu.G. Spiridonov, V.V. Novikov, “Examination of High Burn-up WWER Fuel Rods Under Power Cycling Conditions”, *Meeting of Programme Groups of Halden Project*, Norway, Halden, 8-13 September 2002.
- [2] Bouroukine, A.V., V.D. Grachev, S.V. Lobin, V.A. Ovchinikov, V.Sh. Sulaberidze, V.V. Novikov, A.V. Medvedev, B.I. Nesterov, “Status and Development of Instrumented Fuel Rod Testing Simulating the Power Reactor Operating Conditions in the Research Reactor MIR”, *5th International Conference on WWER Fuel Performance, Modeling and Experimental Support*, Bulgaria, Albena, 29 September-3 October 2003.
- [3] Bouroukine, A.V., K.V. Borisov, G.D. Lyadov, V.A. Ovchinikov, Yu.G. Spiridonov, V.V. Novikov, A.V. Medvedev, B.I. Nesterov, “Results of WWER High Burn-up Fuel Rod Examinations in Process of and After Their Testing in the MIR Reactor Under Power Cycling Conditions”, *7th Russian Conference on Reactor Material Science*, Russia, Dimitrovgrad, 8-12 September 2003.

RAMP TESTING OF SBR MOX FUEL

Matthew Barker, Paul Cook*, Rebecca Weston
BNFL Sellafield, UK

Gerrit Dassel
NRG Petten, Netherlands

Christophe Ott, Richard Stratton
NOK Baden, Switzerland

Dimitrios Papaioannou, Clive Walker
European Commission, JRC, Institute for Transuranium Elements
Postfach 2340, 76125 Karlsruhe, Germany

Abstract

Details of the ramp testing of SBR MOX fuel from assembly M501 are presented. Two full-length rods were irradiated for three cycles in Beznau-1 to an average burn-up of 33 MWd/kgHM. Eight short rodlets, refabricated from the full-length rods, were tested in the Petten HFR where the rodlets survived, without failure, ramp tests to terminal powers of 50 kW/m under PWR conditions. One rodlet experienced a hold time of just 20 min. in order to provide data on fission gas release and swelling under transient conditions. Post-irradiation examination of the rodlets included diameter profilometry, rod puncture and optical ceramography.

Introduction

BNFL commenced fabrication of MOX fuel for commercial power reactors in 1993 using a process known as the Short Binderless Route (SBR). The first four assemblies of SBR MOX fuel were manufactured in a pilot plant, the MOX Demonstration Facility (MDF) with a Westinghouse 14×14 design. These assemblies, designated M501 to M504, were irradiated for three cycles in the Beznau-1 PWR to assembly average burn-ups of 33 MWd/kgHM. In 1998, seven rods were withdrawn from assembly M501 and sent for post-irradiation examination (PIE) at ITU Karlsruhe.

This PIE work has now been widely reported in the open literature [1-7]. Key results are summarised below.

- ECT measurements revealed a peak waterside oxide thickness of 30 μm , ~ 2 500 mm from the rod bottom on high-enrichment rods.
- Profilometry showed clad creepdown along the length of the rods, with strains up to 1%. There was close fuel-clad contact along the majority of the stack. There was no discernible ridge pattern, except for weak primary ridges on the medium-enrichment rods.
- Gamma scanning revealed a net stack elongation of 0.51% as a result of fuel swelling.
- Puncture showed the rod internal pressure to be ~ 33 bar at measurement temperature, with a FGR of 1% or less. The increase in internal pressure relative to the fill gas pressure was primarily due to reduction of the free volume.
- Ceramography revealed the microstructure to be similar to that of as-fabricated pellets. There was an oxide thickness of up to 10 μm on the clad bore. Grain growth of ~ 1 μm was noted in the central pellet regions. Small clusters of pores and fission product precipitates were noted towards the outer surface of the pellets. These features are the visible signature of Pu-rich regions resulting from the fuel fabrication process and are a consequence of high local burn-up.
- EPMA showed that $\sim 1\%$ of the pellet volume was comprised of Pu-rich regions of up to 30 μm diameter, uniformly distributed throughout the matrix. These regions were rich in fission products.
- Density measurements confirmed a net fuel swelling of between 1.5-2% volume.
- Chemical burn-up measurements confirmed the accuracy of the calculated values and power histories.

Following non-destructive examination (NDE) and rod puncture, eight short segments were cut from mid-span positions on two full-length rods and re-fabricated for ramp testing. These rodlets were transported to the High Flux Reactor (HFR) at Petten, where they were ramp-tested under simulated PWR conditions. All eight rodlets survived ramp tests up to a 50-kW/m terminal power level. After ramping the rodlets were subjected to γ -scanning in the NRG hot cells then transported back to ITU for detailed examination.

At ITU all rodlets underwent a further campaign of non-destructive examination and each rodlet was also punctured to determine the fission gas release during the ramp test. Following puncture a number of samples were taken for detailed destructive examination, including ceramography to obtain additional information on MOX fuel behaviour at the high temperatures experienced during reactor transients.

This paper presents a detailed overview of the M501 ramp test programme, presenting the key results from each phase of the project.

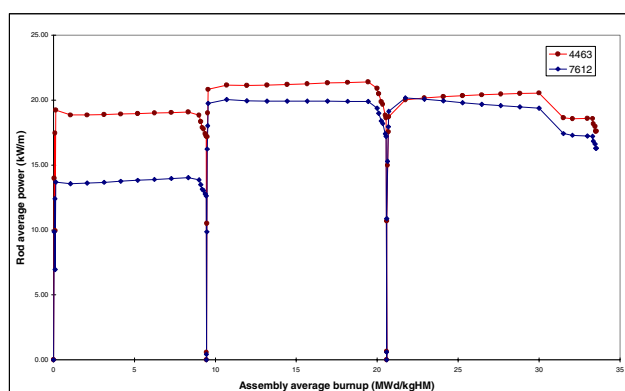
Refabrication

Eight short rodlets were refabricated from two full-length 14×14 fuels rods. Summary data on the parent rods are presented in Table 1. Figure 1 shows the power history of the two rods during base irradiation.

Table 1. Parent rods for ramp test segments

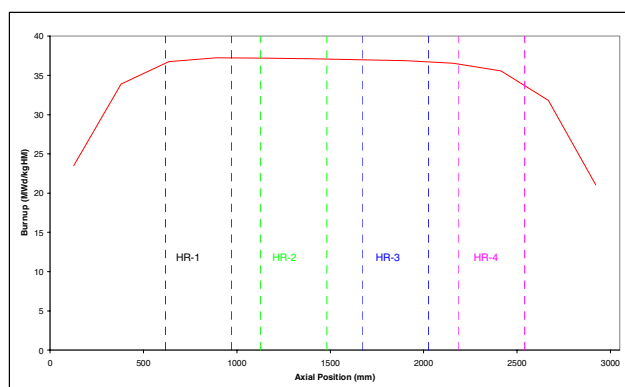
Rod	Pu enrichment (%Pu/U+Pu)	Rod average burn-up (MWd/kgHM)	Fission gas release (%)
9271 4463	5.54	33.7	0.59
9271 7612	3.72	31.2	0.42

Figure 1. Power histories of parent rods during base irradiation



Segments were cut from mid-span positions between grids 2 and 6. Figure 2 shows the axial burn-up profile of rod 9271 4463 and where the rodlets were cut. The segments were labelled HR1 through 4 to denote those taken from the high-enrichment rod 9271 4463. MR series rodlets were taken from rod 9271 7612 at similar positions.

Figure 2. Axial burn-up profile and rodlet location from rod 4463

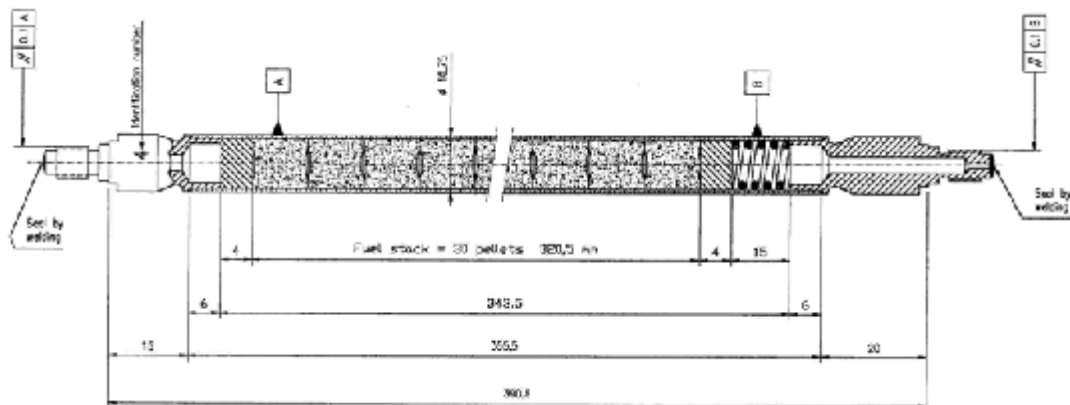


Following segment cutting the refabrication procedure is as follows:

- Micro γ -scanning to determine the position of pellet-pellet interfaces and detailed cutting.
- Removal of 1 to 2 pellets from the lower end.
- Cleaning and preparation of the clad bore at the lower end.
- Insertion of an Al_2O_3 insulator pellet into the lower end.
- Welding an end plug onto the bottom end.
- Removal of 2 to 3 pellets at the top end, to give a 30-pellet fuel stack.
- Cleaning and preparation of the clad bore at the top end.
- Insertion of an Al_2O_3 insulator pellet and the plenum spring.
- Girth welding of the top end plug.
- Pressurisation with helium to ~ 23 bar.
- Seal welding.

Figure 3 shows a drawing of rodlet HR4.

Figure 3. Rodlet HR4



Following refabrication, the integrity of the welds was verified through helium leak testing and radiography. The rodlets then underwent pre-ramp characterisation, including length measurement, γ -scanning (to verify the stack length and condition of the fuel column) and profilometry. The profilometry confirmed the results of the PIE examination both in terms of the degree of creepdown and the lack of primary ridges on the high-enrichment rod.

Prior to ramp testing each rodlet was subjected to a further γ scan to verify that the transport had not damaged the fuel stack and to neutron radiography for comparison with post-ramp images.

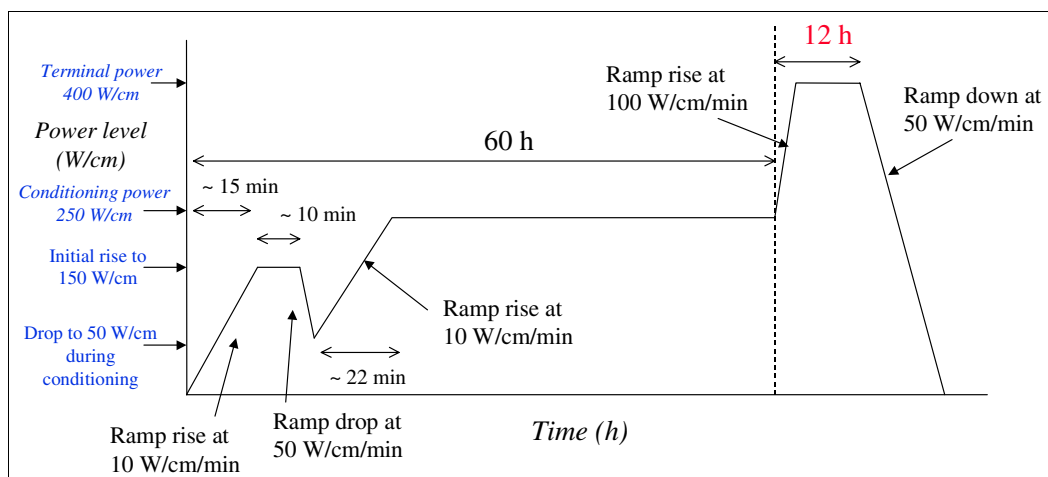
Irradiation

Each rodlet was ramp-tested under simulated PWR conditions of 155 bar coolant pressure. Table 2 summarises the power histories used for the tests. The conditioning power was generally held for approximately 60 h, however, in the case of MR-2 it was slightly longer. All the rodlets were ramped up to terminal power at a rate of 100 W/cm/min. The hold time at final power in seven of the eight tests was 12 h. The eighth test had a hold time of only 20 min., for the specific reason of obtaining data on fission gas release and swelling under transient conditions. Figure 4 shows the typical power profile experienced by each rodlet. The burn-up increment during the ramp test was small, of the order of 0.1 MWd/kgHM.

Table 2. Rodlet power histories

Rodlet	Conditioning power (kW/m)	Terminal power (kW/m)	Hold time at terminal power (h)
HR-1	25	40	12
HR-2	30	39	12
HR-3	20	50	12
HR-4	25	50	12
MR-1	20	40	12
MR-2	25	45	12
MR-3	30	44	12
MR-4	20	45	0.33

Figure 4. Power history used in M501 ramp tests



The eight tests were carried out over a period of a year from May 2001 to June 2002. No failures were detected by coolant activity monitoring while the rodlets were in the Petten reactor. The rodlets underwent gamma scanning and neutron radiography at Petten before being moved to ITU for post-ramp examination. The results of the ramp tests are shown in Figures 5 and 6.

Figures 5 and 6 clearly show that the threshold for PCI failure of SBR MOX fuel is in excess of that for conventional UO₂ fuel [7]. The line indicated in Figures 5 and 6 is the PCI criterion for UO₂ fuel. Similar behaviour has already been reported for other types of MOX fuels [8,9] and in general, test results show MOX fuel is more resistant to this mode of failure.

Figure 5. Ramp test results as a function of terminal power

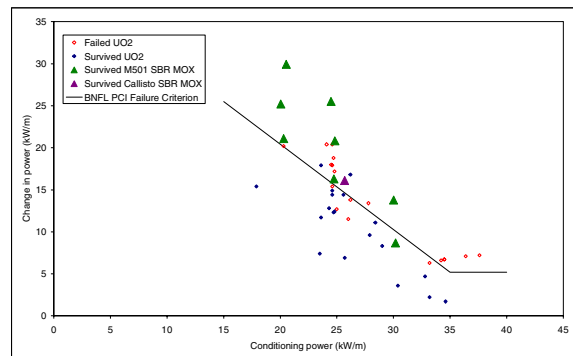
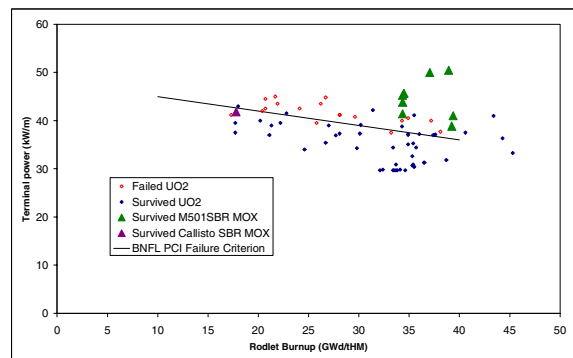


Figure 6. Ramp test results as a function of burn-up



It is well known that the creep rates of MOX pellets are higher than those of UO₂ fuel [10]. It has also been postulated that the clad bore oxide layer, which tends to be slightly thicker in MOX fuel rods (~10 μm in the M501 rods) also helps to protect the cladding from attack by corrosive fission products. Both these factors would tend to reduce the impact of the stress corrosion cracking failure mechanism on MOX fuel rods.

Post-ramp examination

Following ramp testing each rodlet was subject to neutron radiography, gross and isotopic γ -scanning, visual inspection, Eddy Current Testing (ECT) for defects, ECT oxide thickness measurements, profilometry and rod length measurements.

Non-destructive examinations

Visual examination of the rodlets after ramping revealed little of note. ECT defect testing was also undertaken but revealed no indication of rod failure or underlying defects, confirming the initial results of the ramp tests from the on-line coolant activity monitoring.

The pre-ramp γ scans generally revealed a flat power profile during base irradiation. Clear local minima were also visible at pellet-pellet interfaces. Figures 7 and 8 compare the pre- and post-ramp gross γ scans for rodlets HR-1 and HR-4. Note that the pre- and post-ramp scans were performed using different equipment and a precise quantitative comparison is not possible.

Figure 7. Pre- and post-ramp γ scans taken from rodlet HR-1, ramped to 40 kW/m

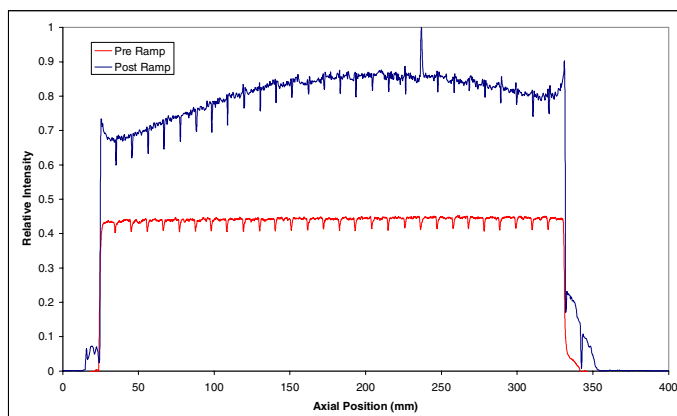
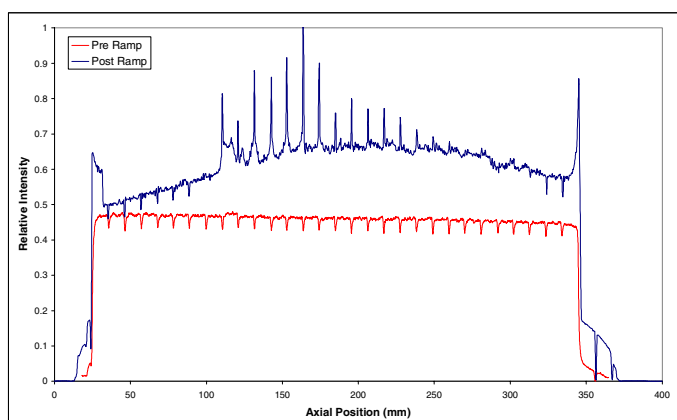


Figure 8. Pre- and post-ramp γ scans taken from rodlet HR-4, ramped to 50 kW/m



Figures 7 and 8 show that the post-ramp γ scans have taken on a parabolic shape due to the axial power profile during the ramp test. Note that only those pellets near to the maxima in the scan actually experience the peak powers stated in Table 2. The figures also show a reduction in definition of the pellet-pellet interfaces, whilst particularly in Figure 8, local maxima are observed at pellet-pellet interfaces and stack extremities due to the redistribution of volatile species such as Cs and I. The migration of the individual species was confirmed by isotopic γ scanning.

Neutron radiography showed changes in the fuel and free volume distribution of the pellets. Figures 9 and 10 show a pellet towards the top of the fuel stack in HR-4 (25-50 kW/m), before and after ramping.

In the pre-ramp segments, which were irradiated under prototypic PWR conditions to a local burn-up of around 35 MWd/kgHM, the pellet dimples are clearly visible. Following ramping to 50 kW/m, there is significant closure of the pellet dimples. This results from pellet creep under the high stress and temperatures induced by the power ramp (predicted peaks of 390 MPa and 2 500°C). These results help to demonstrate that power ramp tests on MOX segments tend to deform the pellets rather than the cladding, leading to an increase in the terminal power threshold before rupture. Also noticeable in Figure 10 is a faint horizontal dark band running through the centre of the pellets in this region that is not apparent prior to ramping.

Figure 9. Section from neutron radiograph taken of HR-4 before ramping

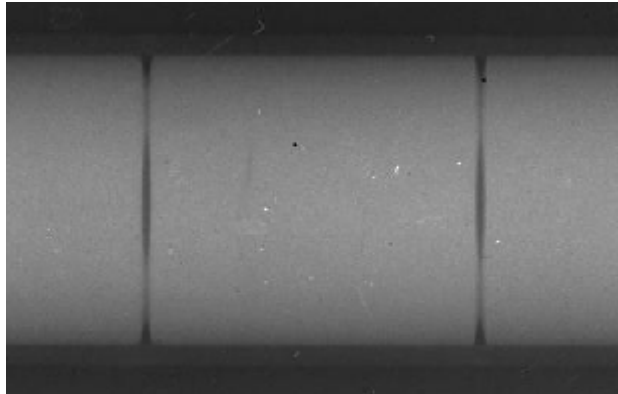
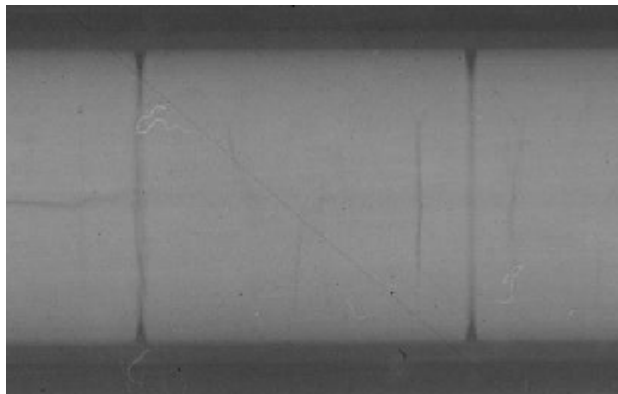


Figure 10. Section from neutron radiograph taken of HR-4 after ramping



ECT oxide thickness measurements showed little change from the pre-ramp values, as expected. However, dramatic changes were encountered during profilometry measurements. Figures 11 and 12 show the results for HR-1 (25-40 kW/m) and HR-4 (25-50 kW/m). HR-1 shows a modest change in the rodlet diameter post-ramping. The change seen in the higher power ramp is more dramatic; a peak strain of close to 2% was experienced.

The increase in fuel rodlet length as a result of ramping ranged from 0.05-0.21%. The stack length also increased as a result of fuel swelling during the ramp test. The measured increases were up to 0.63%, depending on ramp terminal power. However, some caution should be applied to these data as the measured length changes were small and close to the limit of resolution.

Rod puncture

Each rodlet was punctured to determine the internal pressure, free volume and fission gas release after ramp testing. Figures 13 and 14 show the free volume change and fission gas release, respectively. Figure 13 shows that the free volume of all the rodlets increased during the ramp test. The magnitude of the increase is broadly related to the terminal power level, although the precise magnitude of the increase should be treated with caution as no direct measurement of free volume was made during refabrication. The increase in free volume is primarily due to plastic strain of the cladding during the test, followed by opening of the fuel-clad gap on cool-down at the end of the terminal power hold.

Figure 11. Pre- and post-ramp profilometry measurements on rodlet HR-1

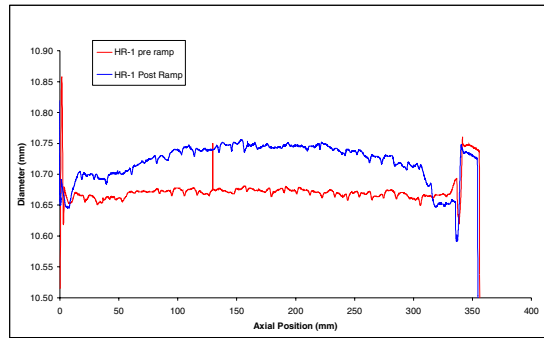


Figure 12. Pre- and post-ramp profilometry measurements on rodlet HR-4

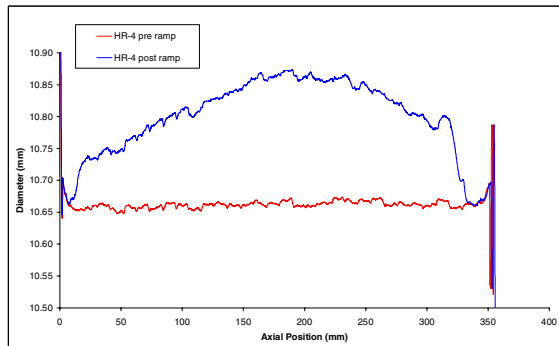


Figure 13. Rodlet free volume increase following ramp testing

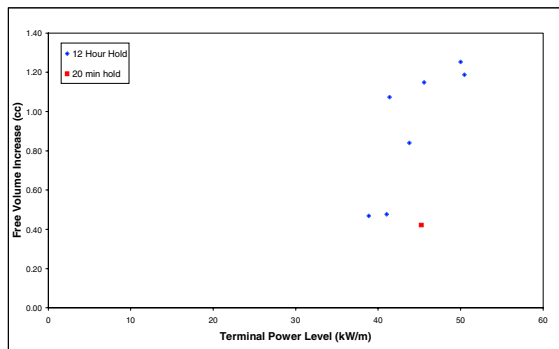
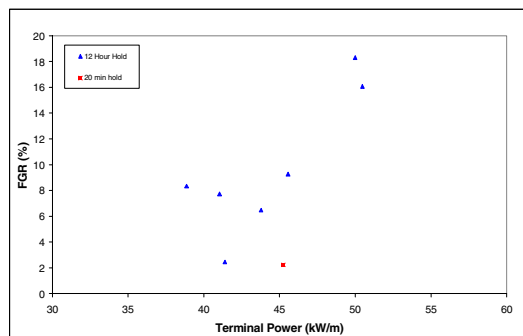


Figure 14. Fission gas release from rodlets during ramp testing



Fission gas release (FGR) varies from 2-19%, once again, broadly correlated with the terminal power level. It is also clear from the puncture measurements that a significant volume, ~5 cc, of helium was released from the rodlets during the ramp test. The average Xe:Kr ratio is ~16, with actual levels of [Xe+Kr] release ranging from 4-36 cc and correlated with terminal power. However, uncertainty in the precise amount of helium added during refabrication (due to the uncertainty in the pre-ramp free volume) limits the accuracy of quantitative calculations.

Destructive examinations

Eight samples were prepared from five of the rodlets. This paper focuses on the three samples listed in Table 3. These samples were subjected to optical ceramography. Additionally, SEM and EPMA are planned, to determine the distribution of Pu and fission products. A particular feature of the examinations is the use of longitudinal samples to obtain visual and chemical information in the pellet-pellet interface regions.

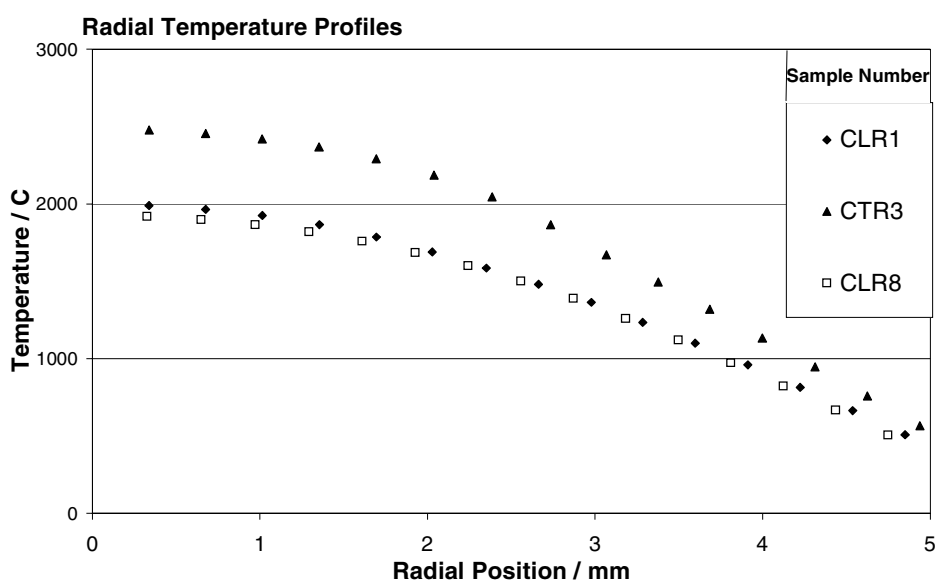
Table 3. Samples for destructive examinations

Sample	Rodlet	Lower cut (mm)	Upper cut (mm)
CLR-1	HR-1	203	220
CTR-3	HR-4	193	203*
CLR-8	MR-4	235	252

* Marks a transverse sample.

A prediction of the radial temperature profile at each of the sample positions was found using the BNFL fuel performance code ENIGMA-B 7.7 [10]. The profiles are shown in Figure 15 and suggest a maximum centre temperature of ~2 500°C. It should be noted that there is little validation for pellet temperatures of this order and the predictions should be treated as indicative.

Figure 15. Predicted radial temperature profiles at sample positions used for destructive examinations



Optical ceramography

Figure 16 shows ceramography results from sample CLR1, which was ramped to 41 kW/m. The images shown are qualitatively similar to all the 12-hour hold samples examined, although the extent of fission gas porosity, for example, depends on the terminal power level.

Figure 16. Optical ceramography of sample CLR1 (rod HR1, terminal power hold of 12 h)

The sample macrograph (a) shows the extent of dimple filling (original magnification $\times 20$). The remaining images are taken at an original magnification of $\times 500$. (b) is from the edge of the fuel structure and includes the fuel-clad gap. (c) is from a region close to the mid-radius, and (d) is from the fuel centre. Pu-rich regions are highlighted.

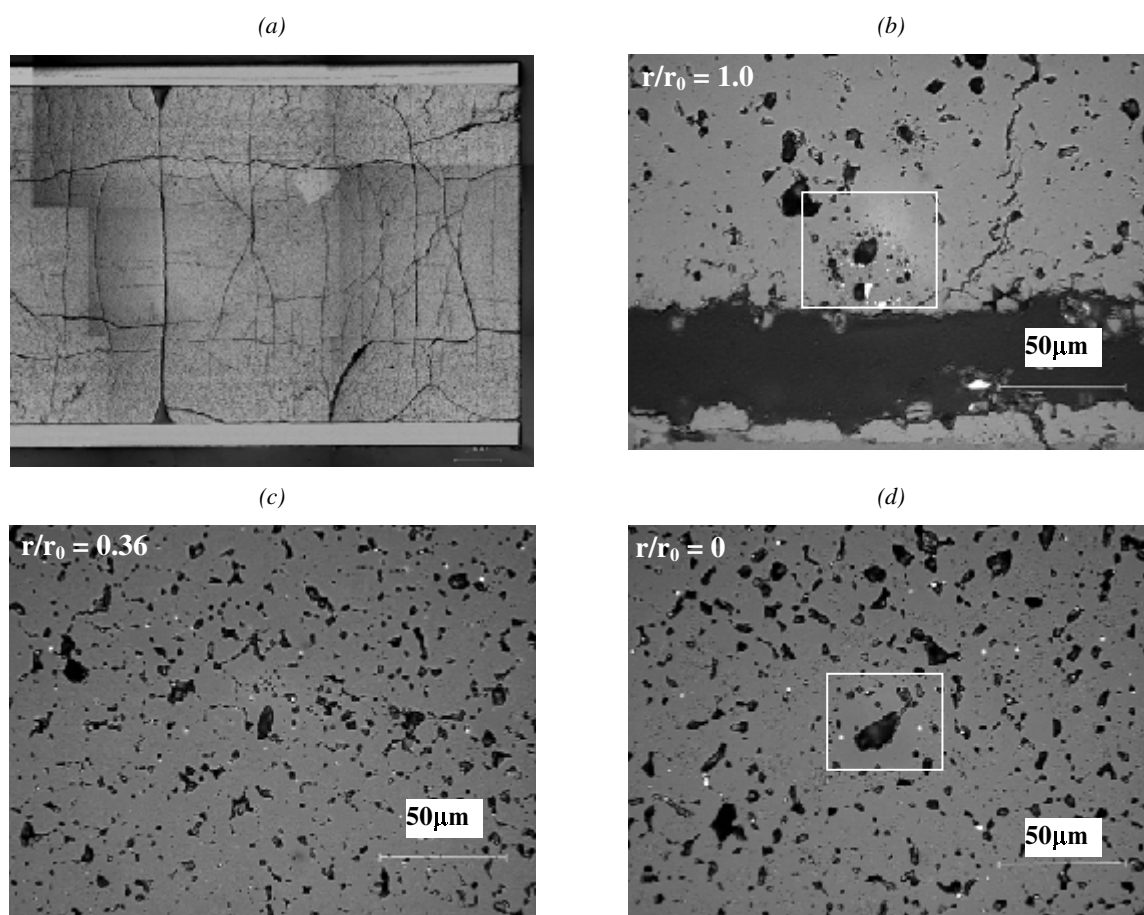


Figure 16(a) is a macrograph of the sample. The pellet dimples are completely filled, as shown in the neutron radiographs, a result of the swelling experienced by the fuel. Cracking of the fuel is both extensive and prominent; this again suggests the high strain and stress that the fuel has been subjected to. Figures 16(b)-(d) are micrographs of the fuel at a magnification of $\times 500$. The outer edge of the fuel pellet ($r/r_0 = 1.0$, where r_0 is the pellet radius) is shown in Figure 16(b). The microstructure at this location is similar to that observed in samples after base irradiation. A continuous oxide layer was present on the clad bore with a similar thickness to that after base irradiation. Some disruption to this layer was noted, particularly at pellet-pellet interfaces. A gap of $\sim 40\ \mu\text{m}$ opened once the pellets were cooled after the ramp test. This confirms the origin of the increase in free volume found during the puncture measurements as due to opening of the fuel-clad gap.

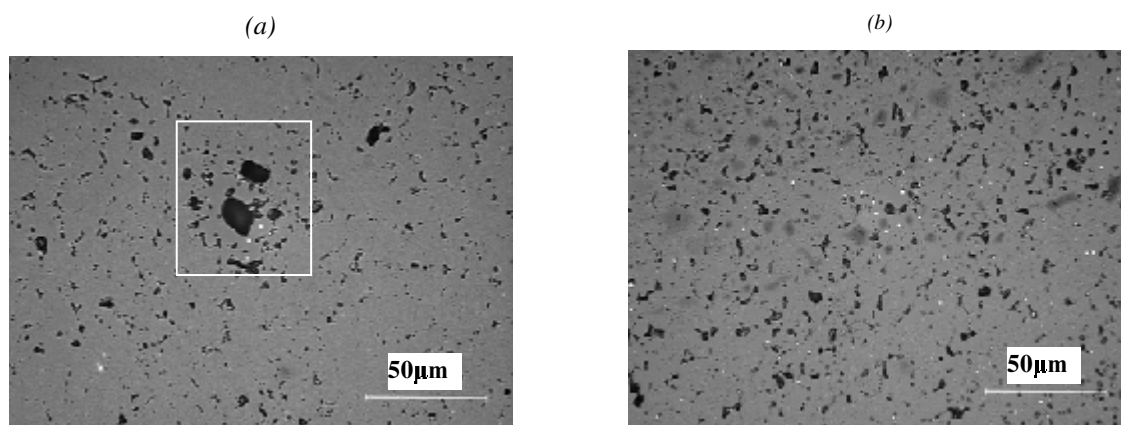
The form of plutonium-rich regions is seen to change along the fuel radius. In Figure 16(b), the Pu spot near the image centre consists of a dense cluster of small gas pores and metallic fission product precipitates, similar to observations after base irradiation. In the more central, hotter regions of the pellet, Figures 16(c) and 16(d), the pores have coalesced to form a large central pore, leaving a pore-free annulus of fuel. Metallic fission product precipitates have grown and coarsened away from the spot. The transition between the two forms of Pu spots occurs in the fuel region that experienced predicted temperatures in the range 1 500-1 800°C during terminal power hold.

In all three micrographs a substantial volume of fission gas bubbles is observed. In the central regions of the fuel, Figure 16(d), bubbles are generally large and located at grain boundary triple points. On moving away from the centre (and hence, down the temperature gradient), the number of smaller, lenticular intergranular bubbles increases.

Figure 17 shows two micrographs from sample CLR8. This sample was taken from rodlet MR4, which was held at terminal power for only 20 min. The most notable feature of these images is the abundance of small gas bubbles as compared to Figure 16. In both Figure 17(a) and 17(b), intergranular bubbles are seen in chains along grain boundaries.

Figure 17. Sample CLR8, ramp power held for 20 min.

(a) shows a well defined Pu-rich region close to the mid radius – spots such as this are evident closer to the fuel centre than in the 12-hour ramp samples



Figures 16 and 17 therefore show a progression in the development of fission gas release and swelling. Figure 16(c) shows evidence of bubble interlinkage. In Figure 16(d), after substantial FGR and linkage has occurred the larger bubbles dominate. The degree of fission gas swelling in the samples is clearly significant and the major contributor to permanent pellet volume change resulting from the ramp tests.

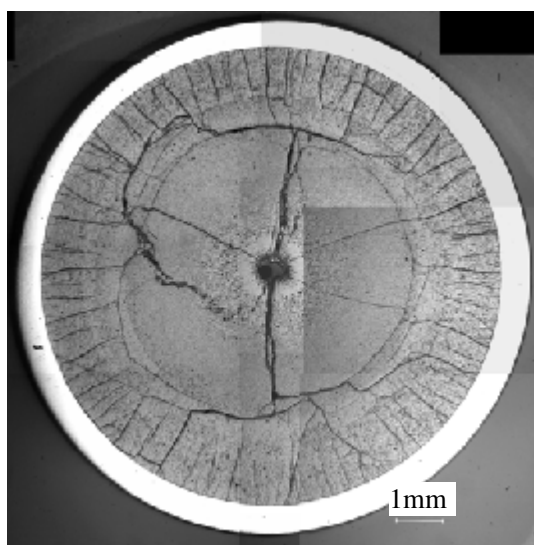
Grain size measurements were also taken from the samples. At the pellet rim, values between 5 and 7 μm were found, typical of the as-fabricated microstructure. Modest grain growth of between 1 and 3 μm was determined at the pellet mid-radius. At the pellet centre, more significant equi-axed grain growth was found, depending on terminal power level. Growth of 20 μm was noted in the rodlets ramped to 50 kW/m. In contrast, sample CLR-8, held at terminal power for 20 min. showed no evidence of significant grain growth at the pellet mid-radius and only a 2 μm increase at the pellet centre.

Sample CTR3 experienced the highest predicted centreline temperatures in this study; a macrograph is shown in Figure 18. The central void and columnar grain formation near the centre [Figure 18(b)]

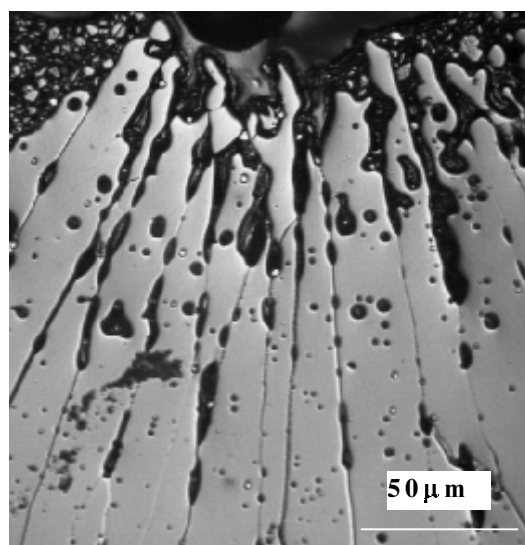
are most reminiscent of irradiated fast reactor fuel [11] and testify to the extreme conditions experienced by the fuel. The formation of the void explains the observed horizontal band shown in Figure 10, and helps to explain the substantial diameter increase of the rod shown in Figure 12.

Figure 18

(a) Macrograph of sample CTR3, with a predicted centre temperature of ~2 500°C



(b) Micrograph of CTR3, close to the central void, showing the formation of columnar grains. Original mag. $\times 500$.



Summary and conclusions

Eight short rodlets were refabricated from two full-length 14×14 fuel rods base-irradiated in Beznau-1 to burn-ups of the order of 33 MWd/kgHM. These rodlets were ramp-tested in the Petten HFR to terminal powers of up to 50 kW/m under PWR conditions without failure.

A comprehensive series of non-destructive examinations showed there to be little visible damage to the rodlets as a result of the tests. However, significant fuel swelling/expansion was apparent, as shown by neutron radiography (dimple filling), γ -scanning (stack length change) and profilometry.

Rod puncture revealed an increase in rodlet free volume resulting from plastic strain of the cladding due to the expansion of the pellets during ramping. FGR of between 2-19% was measured, depending on terminal power and hold time. A release of helium gas was also noted, but is more difficult to quantify.

Eight samples were cut from the rodlets for destructive examinations. Macrographs confirmed the opening of the fuel-clad gap to be responsible for the free volume increase. Optical ceramography also revealed significant changes to the fuel microstructure during the ramp testing, consistent with the predicted pellet temperatures. Widespread fission gas porosity was noted, particularly in rodlets HR-3 and 4, which exhibited the greatest degree of fuel swelling. Some equi-axed grain growth was found in all samples as a result of the power ramp. In addition, in the hottest regions of HR-4 a central fuel void and columnar grain growth were noted.

SEM examinations designed to quantify the degree of fission gas porosity present in the samples remain to be completed. In addition, EPMA will be used to help determine the distribution of plutonium and selected fission products within the fuel rods, noting any differences at pellet-pellet interfaces.

A number of ramp test programmes have now investigated the behaviour of different types of MOX fuel under transient conditions. These tests have shown that the failure threshold for MOX fuel is higher than that of UO₂ fuel of equivalent burn-up. In conclusion, it is suggested that the conventional mechanism of pellet-clad interaction failure is not limiting in MOX fuel. The response of MOX fuel to transients is still of interest, but from the perspectives of fuel swelling and fission gas/helium release, rather than stress corrosion cracking failure of the cladding.

REFERENCES

- [1] Cook, P., I. Palmer, R. Stratton, C.T. Walker, "PIE of BNFL's First Commercially Irradiated SBR MOX Fuel", *IAEA Symposium*, Vienna, Austria (1999), Paper No. IAEA-SM-358-16, p. 42.
- [2] Brown, C., P. Cook, J. Edwards, S. Fisher, G. Gates, I. Palmer, R. White, "Performance of BNFL SBR MOX Fuel for the Next Decade", *TopFuel'99*, Avignon, France, 13-15 Sept. 1999, p. 223.
- [3] Cook, P., R. Stratton, C.T. Walker, "Post Irradiation Examination of BNFL MOX Fuel", *ANS LWR Topical Meeting 2000*, Park City, Utah, USA, 10-13 April 2000, p. 653.
- [4] White, R., S. Fisher, P. Cook, D. Stratton, C.T. Walker, I. Palmer, "Measurement and Analysis of Fission Gas Release from BNFL's SBR MOX Fuel", *J. Nucl. Mater.*, 288, p. 43 (2001).
- [5] Weston, R., I. Palmer, J. Wright, G. Rossiter, R. Corcoran, T. Gilmour, C. Walker and S. Bremier, "Progress on SBR MOX Fuel Development", *TopFuel 2001*, Stockholm, Sweden, 27-30 May 2002, Paper P2-9.
- [6] Fisher, S., R. White, P. Cook, S. Bremier, R. Corcoran, R. Stratton, C. Walker, P. Ivison, I. Palmer, "Microstructure of Irradiated SBR MOX Fuel and its Relationship to Fission Gas Release", *J. Nucl. Mater.*, 306, p. 153 (2002).
- [7] Cook, P., B. Christiansen, G. Dassel, E. Matthews, I. Robinson, R. Stratton, C. Walker, R. Weston, "Performance of BNFL MOX Fuel", *TopFuel 2003*, Wurzburg, March 2003.
- [8] Goll, W., H. Fuchs, R. Manzel, F. Schlemmer, "Irradiation Behaviour of UO₂/PuO₂ Fuel in Light Water Reactors", *Nucl. Technol.*, 102, p. 29 (1993).
- [9] Blanpain, P., L. Brunel, X. Thibault, M. Trotabas, "MOX Fuel Performance in the French PWRs: Status and Developments", *ANS LWR Topical Meeting 2000*, Park City, Utah, USA, 10-13 April 2000, p. 646.
- [10] Palmer, I., G. Rossiter, R. White, "Development and Validation of the ENIGMA Code for MOX Fuel Performance Modelling", *IAEA Symposium*, Vienna, Austria (1999), Paper No. IAEA-SM-358-20, p. 50.F
- [11] Bramman, J., H. Powell, "Redistribution of Fuel and Fission Products in Irradiated Oxide Fuel Pins", *J. Br. Nucl. Energy Soc.*, 14, No. 1, p. 63 (1975).

PCI BEHAVIOUR OF CHROMIUM OXIDE-DOPED FUEL

C. Nonon, J-C. Menard, S. Lansiard, J. Noirot
CEA Cadarache

S. Martin, G-M. Decroix, O. Rabouille
CEA Saclay

C. Delafoy
FRAMATOME ANP

B. Petitprez
EDF/SEPTEN

Abstract

The will of EDF utility to upgrade the economics of its nuclear plants leads both to the extension of the discharge burn-up of fuel rods and to the elimination of PCI constraints. To this purpose, the abilities of large grain size microstructure obtained with chromium oxide doping are investigated within the framework of the CONCERTO programme, which involves the CEA research laboratories, FRAMATOME ANP and EDF. Different types of the fuel microstructures consistent with fission gas retention and plasticity enhancement have been studied in order to optimise the fuel manufacturing process while achieving the characteristics required. Subsequent to mechanical out-of-pile testing, the performances of different doped UO_2 fuels were verified under PWR conditions. Two segments loaded with Cr_2O_3 -doped UO_2 fuel and pre-irradiated in PWR were submitted to high power variation conditions in the experimental reactor OSIRIS. The good PCI behaviour of the rods has been confirmed, since no cladding damage was observed after the ramp tests. A complete analysis of post-ramp examinations was conducted to understand the thermo-mechanical behaviour of this new fuel microstructure. It concludes that the benefits seem to be linked to the fuel viscoplasticity enhancement and to the favourable crack pattern in the pellet, which is expected to decrease the local stress concentration factor in the cladding.

Introduction

Risk of fuel rod failure linked to PCI under normal operating and incident transients has been avoided in French PWRs thanks to proper operating specifications [1]. This solution, very efficient as regards safety aspects, is however restrictive for plant manoeuvrability, by limiting the amplitude of power variations and rate as well as holding time at low power. To improve flexibility and adapt the reactor load to the grid demand, the enhancement of operating margins is needed [2]. In addition, competitiveness can be improved with the extension of fuel assemblies' discharged burn-up, leading to reduced maintenance and fuel cycle costs. To this end, an advanced nuclear fuel is being developed by FRAMATOME ANP, in co-operation with EDF and CEA [3]. Improving fuel performance to reduce fission gas release and increase resistance to PCI is a technical challenge. Both goals can be achieved with large grain microstructures, since grain size enlargement is expected to enhance fuel plasticity as well as fission gas retention capability.

Grain enlargement can be obtained by long annealing at high T° or crystal growth activators. Various techniques are developed by manufacturers using different types of additives: oxides (Al_2O_3 , TiO_2 , Nb_2O_5 [4], Cr_2O_3 , SiO_2, \dots), or more recently, phosphorus [5]. To optimise the technology and converge towards the best choice (grain size, type of dopants and dopants content), it is first necessary to understand the role of dopants on grain size enlargement and on fuel properties. Thereafter, it is necessary to check fuel in-pile behaviour under normal and transient conditions as regards fission gas retention and pellet-cladding interaction with irradiation experiments. The nature of the dopant is the result of manufacturing feasibility and viability analysis. Its influence on a large spectrum of fuel characteristics must be favourable – or at least not detrimental – to achieve all the performances required. Manufacturing and mechanical properties of UO_2 doped with different types of additives have been studied within the framework of the co-operation between CEA, FRAMATOME ANP and EDF, from laboratory scale investigations to the industrial fabrication process [6]. The performances of these different doped fuels under PWR conditions were studied in the CONCERTO programme. Results obtained for chromium oxide are described in this paper. Examination results after ramp testing in the OSIRIS experimental reactor on two-cycle pre-irradiated segmented rods is more specifically discussed.

Out-of-pile mechanical testing

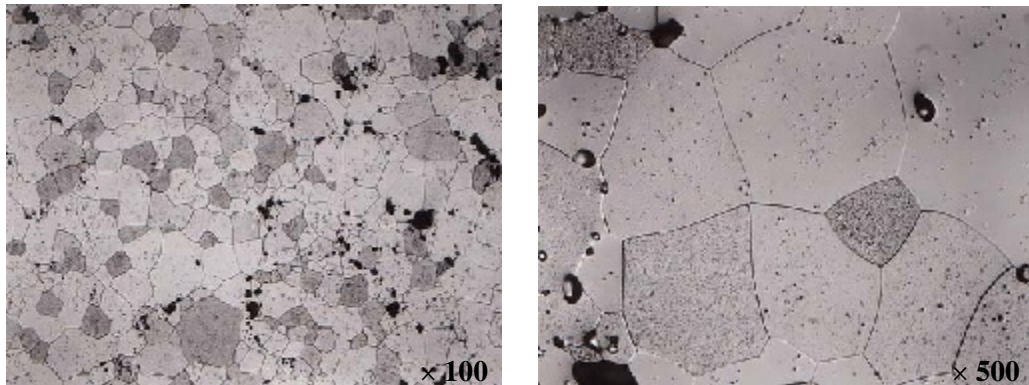
Large grain sized fuels can be produced by through the introduction of less than 1% of chromium oxide (Cr_2O_3) into the UO_2 powder prior to sintering. Chromium appears mainly in solid solution in the UO_2 matrix, which could have a detrimental effect on the viscoplasticity of the fuel. Therefore, to confirm the predominance of the beneficial grain size effect, the Cr_2O_3 -doped UO_2 fuel was studied using out-of-pile compression tests. Large grain size fuel obtained without any doping was also tested.

Pellet manufacturing and characteristics

Various batches of pellets with different characteristics were tested: un-doped UO_2 fuel with standard grain size ($\sim 10 \mu m$), un-doped UO_2 fuel with grain size of 20 and 28 μm obtained by thermal activation during a very long annealing and UO_2 fuel doped with increasing additions of Cr_2O_3 (from 750 to 2 250 ppm) for enlarging the grain size (12 to 61 μm).

All pellets were made from a batch of dry route uranium dioxide powder. The sintering of un-doped UO_2 pellet was carried out under dry hydrogen, while a slightly wet hydrogen atmosphere was used for doped pellets in order to maintain the dopant in the proper valence state and thus to promote the crystalline growth. An example of the microstructure of a doped UO_2 is given in Figure 1.

Figure 1. Microstructure of Cr₂O₃-doped UO₂ fuel



Mechanical testing – experimental procedure

All deformation tests were conducted by compression on a screw-type Instron machine equipped with a furnace, under a controlled atmosphere in order to maintain the stoichiometry of the samples constant during the experiment. The furnace, with tungsten resistance, is operated under vacuum or an inert gas like argon/nitrogen or a reducing hydrogenated/argon atmosphere up to a temperature of the order of 1 700°C. The test specimen is placed between the rams of the machine at room temperature and a load of about 5 MPa is applied. The machine automatically maintains this load during the heating. When the testing temperature is reached and stabilised, the test force is applied. The deformation of samples is obtained by extensometric measurements and the strain value is recorded by a computer.

Mechanical testing – experimental results

Creep tests

Effect of grain size

Laboratory batches of UO₂ pellets with larger grain sizes obtained by long annealing were tested. Curves obtained at a temperature range of 1 400-1 500°C are shown in Figure 2.

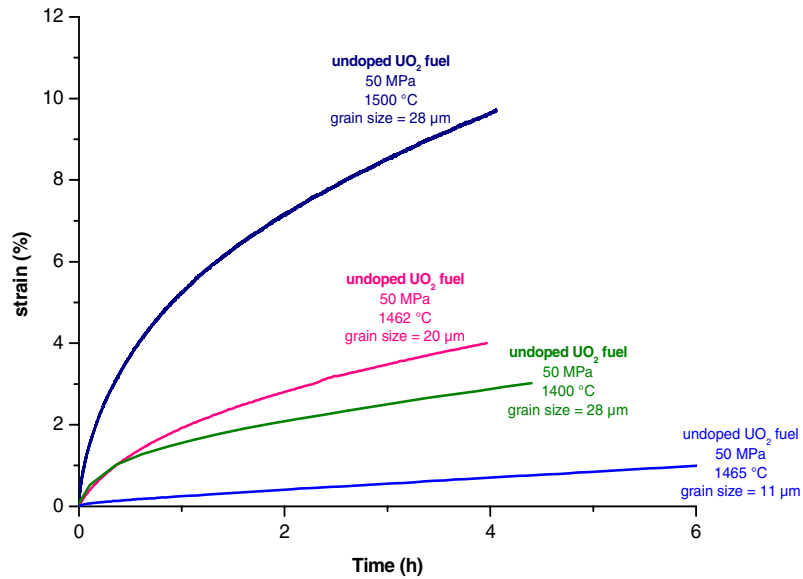
For UO₂ pellets with large grain, the secondary creep regime requires more strain before being clearly established. A primary creep strain of less than 1% is indeed measured for UO₂ with a grain size of 11 μm, instead of almost 10% for UO₂ with a grain size of 28 μm.

Enlarging the grain size of the UO₂ pellet from 11 to 28 μm by thermal activation during a very long annealing improves the secondary creep rate by approximately a factor of 10.

Effect of addition of Cr₂O₃

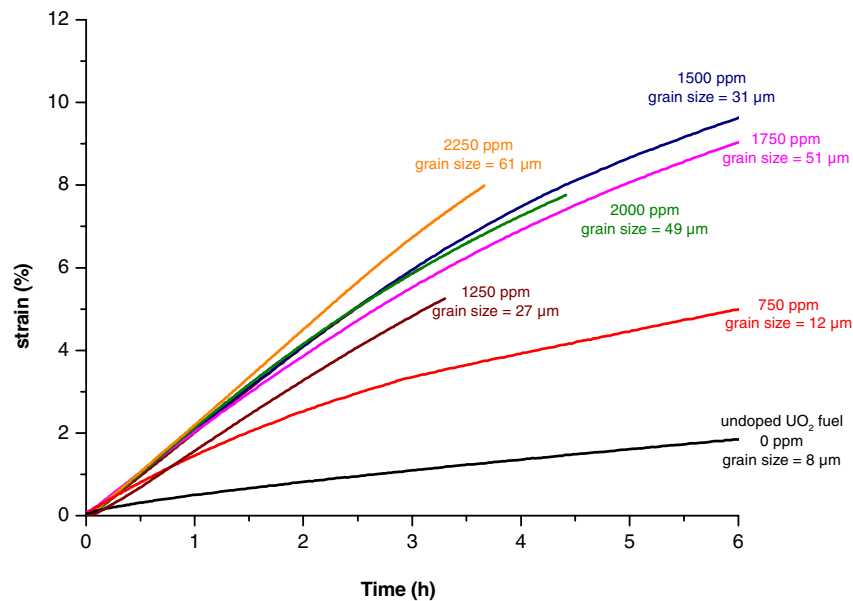
These tests were performed at ~1 470°C and 45 MPa, under a controlled atmosphere of argon with 5% hydrogen to prevent changes in the oxidation and stoichiometry of samples during the experiment. A comparison of the creep rate under compression with the same experimental conditions was made between an un-doped UO₂ and UO₂ samples with varying Cr₂O₃ contents.

Figure 2. Effect of the grain size on fuel creep behaviour at 1 400-1 500°C and 50 MPa. Enlarging of the grain size is obtained by long annealing.



As illustrated in Figure 3, the addition of Cr₂O₃ appreciatively increases the creep rate of the material up to a factor of 10. However, it should be noted that this effect saturates for high additive content, despite the grain size increase.

Figure 3. Effect of Cr₂O₃ addition on fuel creep behaviour at 1 470°C and 45 MPa



Effect of stress on Cr₂O₃-doped UO₂ fuel creep behaviour

Figure 4 displays creep curves of a Cr₂O₃-doped UO₂ fuel with a grain size of 49 μm. Results were obtained at several applied stresses (20-60 MPa), under the same experimental conditions (T = 1 470°C) in order to derive a creep law. The stationary creep rate always increases with the applied stress.

The stationary creep rate of UO_2 doped with Cr_2O_3 can be described with a logarithm plot [7].

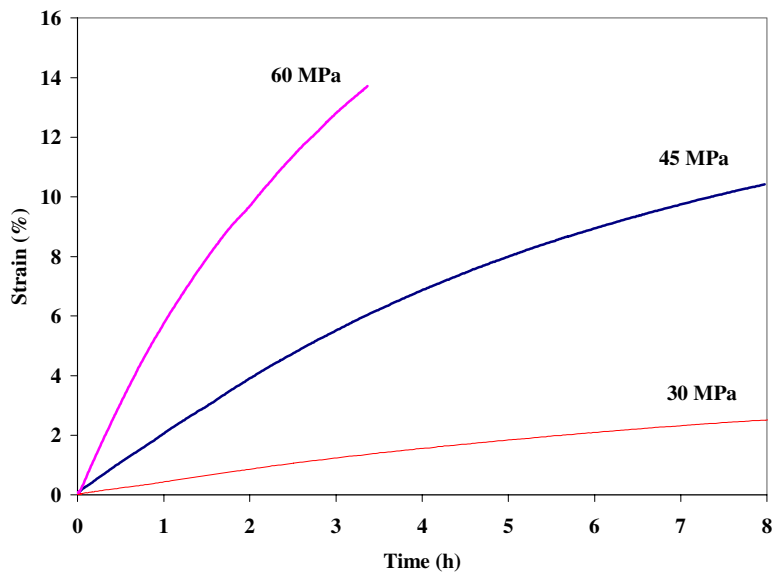
The creep rate can be expressed using a power law: $\dot{\epsilon} = A \cdot \sigma^n \cdot \exp(-Q/R \cdot T)$, where A and n are constants, σ the applied stress and Q the creep activation energy.

Contrary to standard UO_2 with lower grain size where two distinct creep strain regimes delimited by a transition stress value are observed, only a single creep regime is established with a stress exponent value of 4 and an creep activation energy Q close to uranium self-diffusion energy in UO_2 .

The first regime that corresponds to the grain boundary diffusion mechanism does not appear in the explored temperature and stress ranges. We can thus assume that the first deformation regime is shifted towards lower stresses and that the deformation of Cr_2O_3 -doped UO_2 fuel is only controlled by dislocation movements such as sliding and climbing [8].

According to this law, the addition of chromium oxide significantly improves the fuel creep rate in the explored temperature and stress ranges (20-90 MPa; 1 200-1 600°C).

Figure 4. Influence of stress on fuel creep behaviour of UO_2 doped with 0.2 wt.% in Cr_2O_3 at 1 470°C

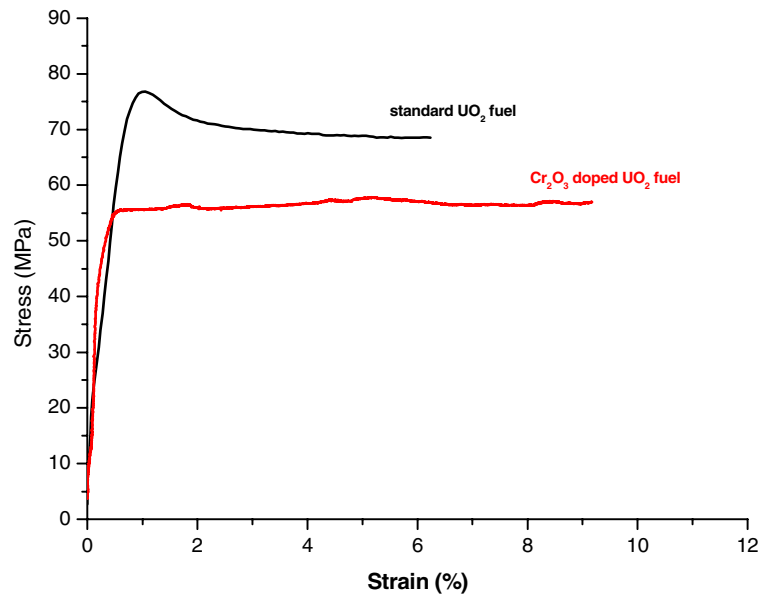


Strain rate controlled tests

These tests were conducted at a crosshead speed of $2.5 \mu\text{m}/\text{min}$, corresponding to a strain rate of $2.5 \times 10^{-3} \text{ %}/\text{s}$. The stress-strain curves show that the addition of Cr_2O_3 lowers the fuel flow stress by about 15 MPa at 1 465°C, as illustrated in Figure 5.

We note the emergence of a stress peak for un-doped standard UO_2 fuel. This peak occurs at a very low strain level, when the density of mobile dislocations is not sufficient to allow deformation according to the imposed constant strain rate. As shown on Figure 5, the addition of chromium oxide eliminates the stress peak and lowers the stress.

Figure 5. Influence of Cr₂O₃ addition on the viscoplastic properties of UO₂ at 1 465°C with a constant applied strain rate of 9%/h



Conclusion on out-of-pile mechanical testing

Enlarging the grain size of UO₂ has a significant effect on fuel creep behaviour. The use of chromium oxide dopant is very efficient, capable of achieving a grain size of up to 70 µm with a reasonable fabrication process duration on an industrial scale. The addition of dopant increases the creep rate of UO₂ but the effect is saturated for content above the solubility limit of Cr₂O₃ in UO₂. Excess doping agent, remaining as inclusions that pin the grain boundaries [9], tend to harden the material. That is the reason why the large grain size microstructure obtained by long annealing revealed a larger primary creep strain under similar testing conditions. Nevertheless, these results suggest that the use of dopant is not detrimental for viscoplasticity at high temperature, as hardening is largely compensated by the increase of grain size.

Base irradiation and intermediate PIE

The CONCERTO programme was launched to verify the behaviour of different doped fuels manufactured by FBFC under PWR conditions. Four types of microstructure were selected, obtained with doping elements Cr₂O₃, Al₂O₃ and SiO₂, used separately or in combination. The doped pellets have average grain sizes of between 44 and 72 µm, depending on the composition considered. Standard UO₂ with a grain size of 9 µm was used as a reference.

For this campaign, four 17 × 17 AFA2G assemblies were loaded with 36 rods in a 900 MWe EDF reactor. The different batches were introduced in either full length or segmented rod types, all equipped with low-tin zircaloy-4 cladding. The segmented rods are composed of seven independent short fuel rodlets screwed end-to-end, three loaded with reference UO₂ pellets and the other four with doped pellets. This design allows direct re-irradiation in the experimental reactor. At the end of this irradiation campaign, the maximum assembly burn-up was close to 60 GWd/t. Among the compositions irradiated, we chose to assess the performance of the UO₂ fuel doped only with chromium oxide, because its

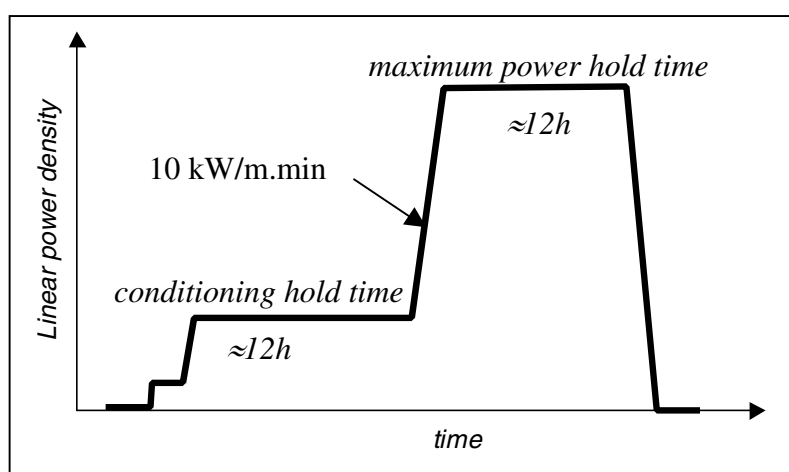
characteristics were judged to fit well with the targets. For that, post-irradiation examinations are planned after each cycle to analyse the overall behaviour up to high burn-up. Also, power ramp testing was performed after two annual cycles that correspond to the PCI worst-case burn-up, thus around 30 GWd/tU.

The segmented rods were subjected to non-destructive examinations in the CEA hot cell laboratories. Diametral measurements performed after two annual irradiation cycles revealed the existence of primary ridges on each segment. It can be concluded that gap was closed between 10 and 30 GWd/t. The average height of the primary ridges on the chromium oxide segment was consistent with values previously observed for UO₂-Zy4 submitted to a similar power history: around 10 µm. The average cladding deformation measured on the doped rods was slightly higher than the reference rods (respectively, 1 and 0.7%). Fuel rod elongation was approximately similar (0.30%) whereas fuel stack elongation is higher for the doped segments. These differences can be attributed to a lower in-pile densification of the doped fuels. This behaviour is in good agreement with the densification measurements made after manufacturing.

Ramp tests

Two segments loaded with chromia-doped pellets and irradiated up to 30 GWd/tU were ramped in 2001 in the ISABELLE 1 loop device of the OSIRIS experimental reactor at CEA Saclay [10]. This device allows simulating PWR thermo-hydraulic and chemical conditions. The movement of the irradiation loop towards the core controls the power level in the rod. The rate of power increase was approximately 10 kW/m/min, to simulate a PWR Class 2 transient. Rod failure is detected during the test thanks to delayed neutron and gamma ray measurements in the coolant and time of failure is determined by the analyse of the elongation sensor signal. The ramp test sequence is shown in Figure 6. Prior to the transient, a conditioning step around 20 kW/m was applied in order to re-establish the thermo-mechanical and chemical state of the rod achieved at the end of the base irradiation.

Figure 6. Sequence of the power ramp tests



The terminal power level of the first ramp test was defined with respect of the current UO₂-Zy-4 PCI threshold [11]. Since no failure was detected during the first test, the terminal power level of the second one was specified to a widely superior value in order to assess the good PCI behaviour of the doped UO₂ rodlet. The power tests' characteristics are gathered in Table 1.

Table 1. Power ramp tests characteristics

	CONCERTO programme			
	Rodlet no. 1	Rodlet no. 2	Rodlet no. 3	Rodlet no. 4
Fuel type	Cr ₂ O ₃ doped UO ₂	Cr ₂ O ₃ doped UO ₂	Standard UO ₂	Standard UO ₂
Peak final power	47.0 kW/m	53.5 kW/m	44.0 kW/m	40.0 kW/m
Final power duration	12 h	12 h	12 h	12 h

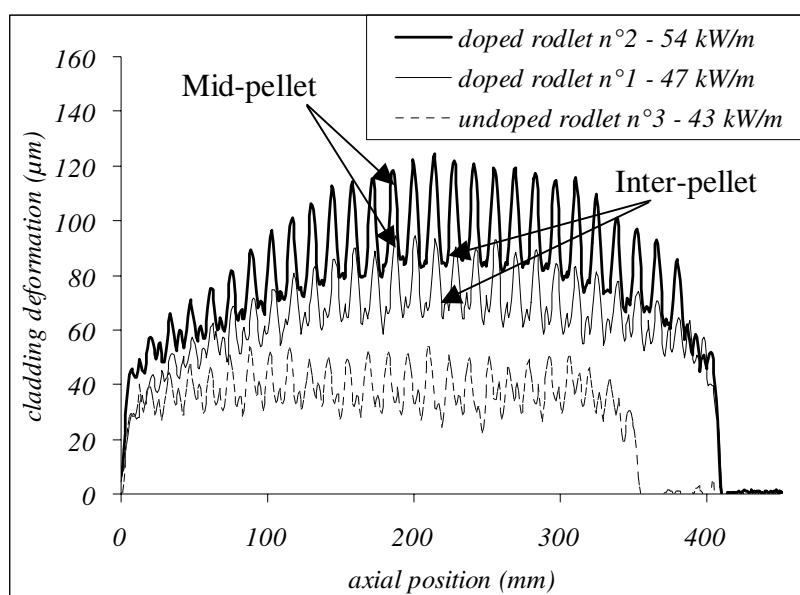
Post-ramp examinations

Non-destructive as well as destructive examinations were performed on the two rodlets following the ramp tests. Profilometry, neutron radiography, eddy current tests and gamma scanning were carried out in the same facilities as before the ramp. Next, rodlets were punctured to evaluate fission gas release fractions and several samples were cut in specific areas for cladding SEM analysis and fuel optical microscopy.

Non-destructive examinations

Figure 7 plots the diametral profiles versus axial position for each doped rod. The results obtained for a previous ramp test performed on a standard two-cycle Zy-4 UO₂ are also reported. It corresponds to the maximum terminal power level tested without entailing failure.

Figure 7. Comparison of doped rods cladding deformation with an un-doped rod ramped at the same holding time and power level near to the two-cycle UO₂ PCI threshold



As usually observed, cladding deformation is function of the local power reached at ramp terminal level, which depends on the axial position [12]. It can be found that deformation underwent by Zy-4 cladding with doped UO₂ is superior to 1% after ramp testing. The permanent cladding strain at mid-pellet is larger than that at inter-pellet. The height of the secondary ridges is a function of local power in the pellet. Growth of these ridges is due to the important gaseous swelling induced by long

holding time at high power. As a consequence, the evolution of the primary ridges is masked by the height of the secondary ridges in most of the part of the column. Analysis of the diameter profiles revealed a permanent cladding strain in the low power zone of rodlet n°1 superior to that of standard UO₂ rodlet n°3 at equivalent local power and burn-up.

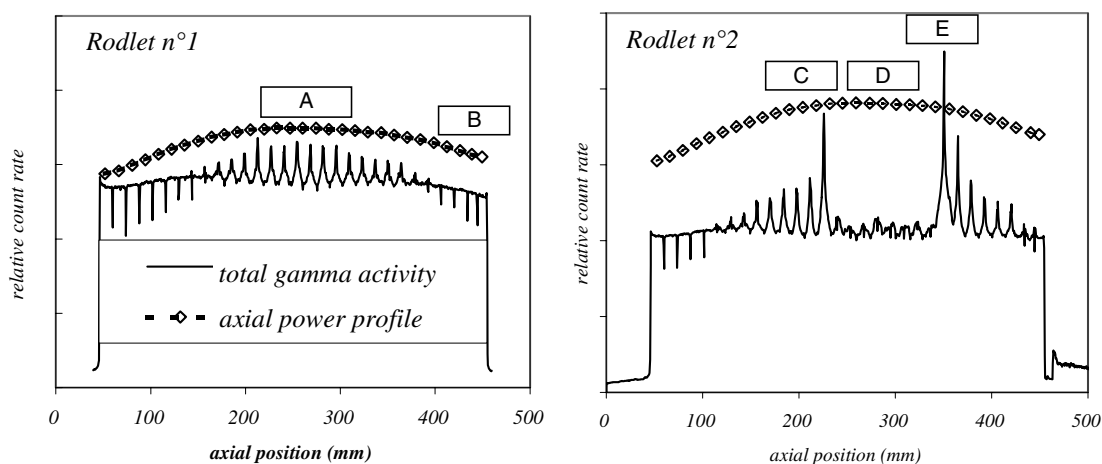
Eddy current tests did not reveal any defect on the cladding after each of the two experiments. The comparison between neutron radiographs of the two segments before and after the ramp tests revealed that the dishes are filled along the main part of the fissile column. A complete gamma scanning examination was performed especially to establish the axial power profile along the rodlets (see Figure 8). Gross gamma scanning indicates peaks at the inter-pellets in the high power regions, due to dishings filling and volatile fission product migration. Caesium and iodine were identified to be responsible for the largest fraction of the total gamma activity.

Destructive examinations

Stress corrosion damage signs have been researched through SEM analysis of the cladding fracture surfaces (sections A and C, Figure 8). Neither rodlet exhibited any iodine-induced stress corrosion cracking in spite of the high fission product concentration and high cladding deformation at the inter-pellets.

Figure 8. Gamma scanning of the doped rodlets after ramp testing

A to E: Samples' section position



The rods were punctured to evaluate fission gas release. Measurements gave values of 8 and 10%, respectively, for the two rodlets. These values seem rather low in comparison with those expected for standard UO₂ at equivalent burn-up, holding time and power.

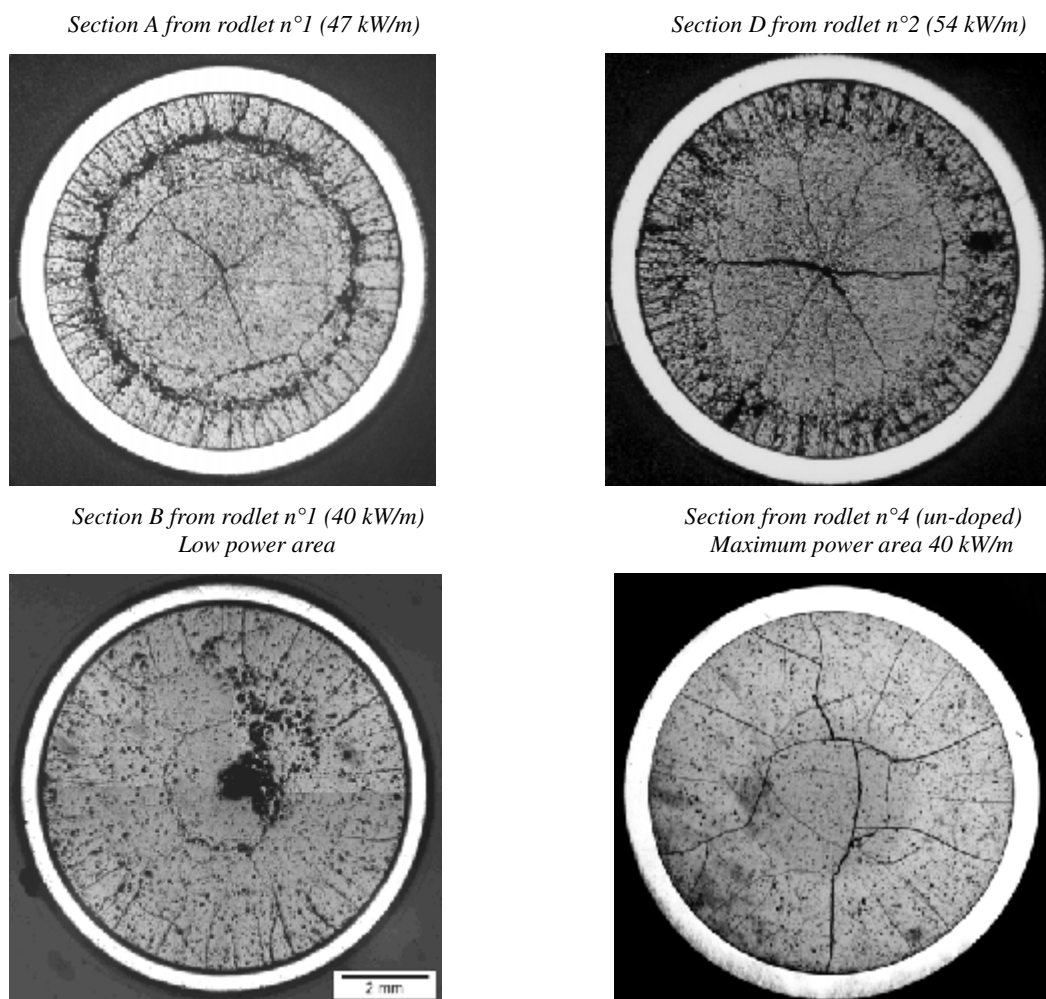
Optical microscopic examinations

Cross-sections at mid-pellet position and longitudinal sections were cut from the two rodlets at different axial positions, corresponding to different local powers in the pellet (Figure 8): the higher rating region of rodlets n°1 and 2 and the top of the fissile column of rodlet n°1 in order to compare examinations to those obtained on un-doped rodlet n°4 in its higher rating region.

Cross-sections are compared in Figure 9. The following features can be observed:

- Cross-sections in the higher rating region of each doped rod are very similar.
- The central part of the pellet is separated from the peripheral part by the circumferential crack, created during cooling. Near the circumferential crack, an important grain boundary cracking is observed, leading to grains pulling-out during sample preparation.
- Peripheral radial cracks created during the ramp tests are intensively numerous whereas original cracks, likely to be created during base-irradiation, are partly healed.
- A new radial crack pattern is created in the central part of each doped pellet in the higher rating region, because of porosity sweeping in the radial direction towards the centre. Columnar grains begin to appear.
- The number of peripheral radial cracks and the radial position of the circumferential crack depend on the power level in the pellet.

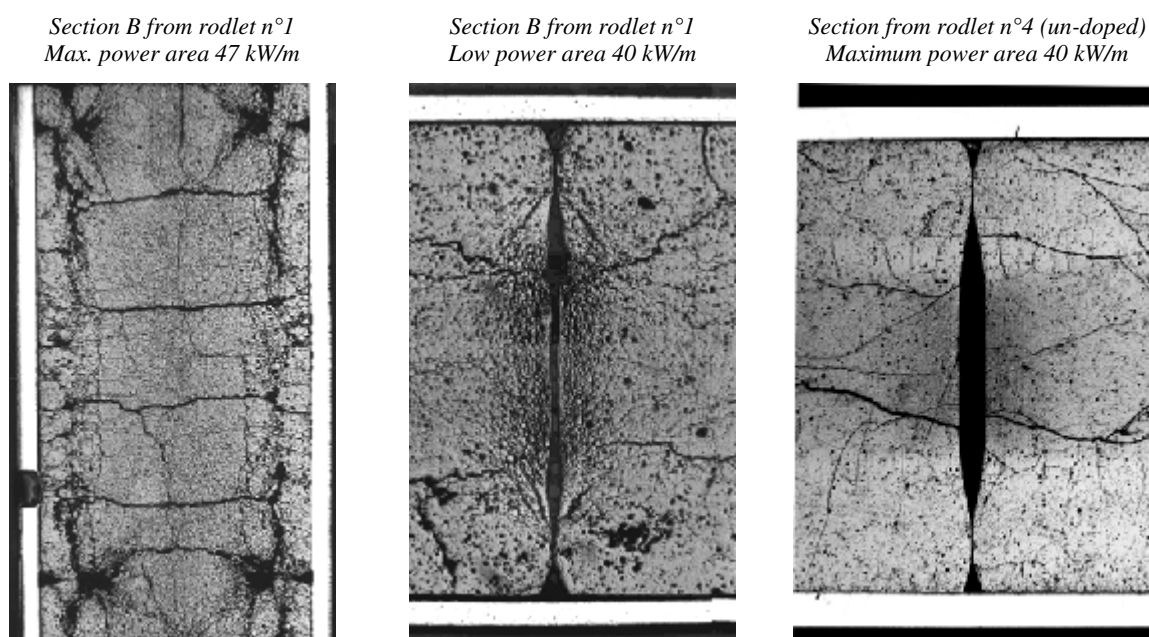
Figure 9. Comparison of cross-sections between doped and un-doped fuel at different local power



At equivalent power and holding time, the cross-section of the doped fuel is very different from that of standard UO_2 fuel. The number of peripheral radial cracks is twice as more important. In the centre of the doped pellet, no radial cracks, expected to be created during base-irradiation, are observed, suggesting crack healing operating from 40 kW/m. In standard UO_2 fuel, crack healing is not clearly observed. Typical features of cracking pattern after two-cycle base-irradiation are indeed still present. In addition, closer examination of the doped pellets revealed a tendency to both intergranular and transgranular crack propagation while fracture is mostly transgranular in the standard UO_2 case.

Longitudinal sections from the higher rating region of each doped rod (sections A and E) revealed a completely filled dishing (Figure 10). The fissile column is almost continuous through the axis of the pellets, as suggested by neutron radiographs. An additional cut in the low power zone of rodlet n°1 (section B) allows comparing the dishings aspect between doped and un-doped fuel. It clearly appears that dishings filling is superior in the doped case (85% as opposed to 33%). Oriented intergranular fractures, typical of fuel creep, are widely developed, whereas no de-cohesion can be observed near the inter-pellet of the un-doped pellet. An absence of radial cracks in the central part of the pellet is observed, as in the cross-section.

Figure 10. Comparison of dishings filling on longitudinal sections between doped and un-doped fuel

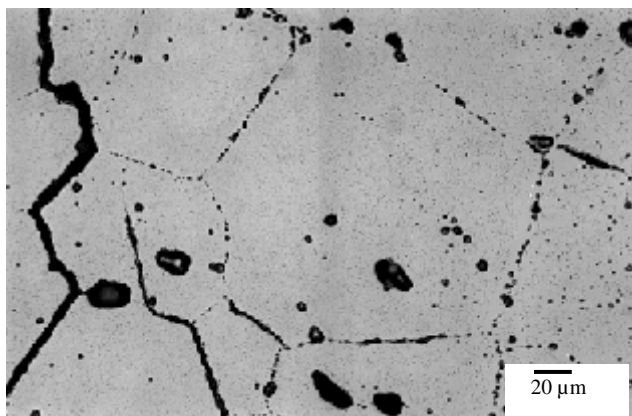


Microstructure analysis confirmed the good fission gas retention capability of the Cr_2O_3 -doped large grain microstructure. In spite of the high power level maintained over several hours, the amount of gas accumulated in the grain boundaries is low. Bubble interlinkage is not as developed as is usually observed for UO_2 after a power ramp test at high power. At the mid-radius position, where the temperature gradient is high, intragranular bubbles are very fine and cover homogeneously the grain surface (Figure 11).

Discussion

The good PCI performance of chromium oxide doped fuel was confirmed since no damage was observed in the cladding, in spite of the large cladding strain and the important concentration of

Figure 11. Microstructure at mid-radius position – rodlet n°1, section A



corrosion fission products after a power ramp testing with final power of 54 kW/m. The gain provided by this advanced fuel is significant compared to current UO₂-Zr₄ PCI threshold: more than 10 kW/m on maximum power.

Signs of fuel creep enhancement are obviously the first element of interest in PIE analysis. However, experimental features were acquired after 12 hours of holding time at very high power level. In consequence, there is a large contribution of fission gas swelling and occurrence of phenomena related to high-temperature operation (temperature superior to 2 000°C): columnar grain in the centre of the pellet, important volatile fission product migration. Difficulties were therefore encountered to highlight fuel creep contribution alone.

Neutron radiographs, gamma scanning and optical microscopy in the high rating regions revealed complete dishings filling along the main part of the fissile columns. This suggests a higher creep rate of doped UO₂ compared to standard UO₂. However, the more interesting results are those obtained in the low power zone of the first doped rodlet. The samples' cut position was precisely specified in order simplify the comparison with an un-doped rod available in the database and submitted to similar ramp test conditions. Differences between doped and un-doped fuel, suggested by examinations in the high-power zones (47 and 54 kW/m), were confirmed in the lower power area (40 kW/m).

Dishings filling is due to the combination of fuel creep and fuel swelling mechanisms. The pellet cracking pattern depends on time-dependent phenomena which affect fuel during holding time, that is to say viscous flow and gaseous swelling [13]. The number of peripheral cracks can be linked to fuel swelling and creep kinetics. Fuel swelling contributes to increased loading of the periphery and may increase the tensile hoop stress in this part of the pellet. The larger the viscous central area of the pellet (influence of temperature distribution or fuel viscoplastic properties), the more fracture energy is dissipated in a reduced volume of the brittle periphery. Radial cracks in the brittle periphery can thus be more numerous and shorter. That is why the number of peripheral radial cracks increases with the power level, as observed in the previous section. The fact that this number is larger in the doped fuel compared to the standard UO₂ fuel submitted to the same power irradiation history is the sign of enhanced fuel creep and gaseous swelling.

In the same manner, crack healing in the centre of the pellet can be explained by fuel creep at high temperature. Fractures are indeed the first available free volume for material flow. This latter assumption will have to be confirmed when further microscopic examinations after base irradiation are available.

Cladding diameter profiles and fuel microscopic examinations seem to conclude on a larger intragranular bubble swelling in the doped, large grain microstructure. This is consistent with rod puncturing results showing the important gas retention capability and the conclusion of the TANOX programme [14]. The large grain size and the intragranular sites are favourable to gas bubble nucleation and pinning. It is clear that fuel creep, fission gas swelling and pellet fracturing are strongly coupled because each of them is a stress-dependent phenomenon which influences stress distribution in the fuel pellet. So in another way, gas swelling in doped fuel could be favoured by fuel creep enhancement, thanks to stress level decrease in the pellet. The relative kinetics of each of these phenomena is important as regards cladding mechanical loading.

Fuel creep reduces deformation at the inter-pellet plane and the stress level in the cladding. Another mechanism has been identified to explain the excellent PCI behaviour of the CONCERTO rods: the intensified cracking at the pellet periphery. Fracture in the cladding is usually observed in front of a main fuel radial crack, created during base irradiation as illustrated in Figure 12. If radial cracks are more numerous, crack mouths opening at pellet-to-cladding interface can be reduced and thus decrease the local stress concentration factor in the cladding. The occurrence of these different interacting phenomena has to be confirmed at the moment when cladding loading is maximum, thus at the beginning of holding time. Experimental results acquired for a power level of 40 kW/m are very promising because they suggest that these mechanisms operate at a relatively low rating and low temperature. Post-calculations of the CONCERTO ramp tests predict a temperature level lower than 1 600°C in the main central part of the pellet at 40 kW/m (Figure 13). Thus, fuel creep and cracking at the periphery are expected to occur during the phase of the transient. These features have already been observed in previous experiments conducted on MOX fuel and high burn-up UO₂ [13]. It can be presumed they will be more accentuated in the doped fuel case. This point will be confirmed soon thanks to the next experiment of the CONCERTO programme: a zero holding time ramp testing.

Conclusion

Significant improvement is brought by the chromia-doped UO₂ fuel under transient conditions with respect to PCI performance and fission gas release. The enhancement of viscoplastic properties provided by the large grain microstructure and suggested by out-of-pile mechanical testing seems to be confirmed with post-ramp examinations. The pellet cracking pattern could also contribute to the PCI performance. To improve the understanding of those mechanisms, it is necessary to complete our

Figure 12. Example of pellet cracking pattern of a failed standard UO₂ rod

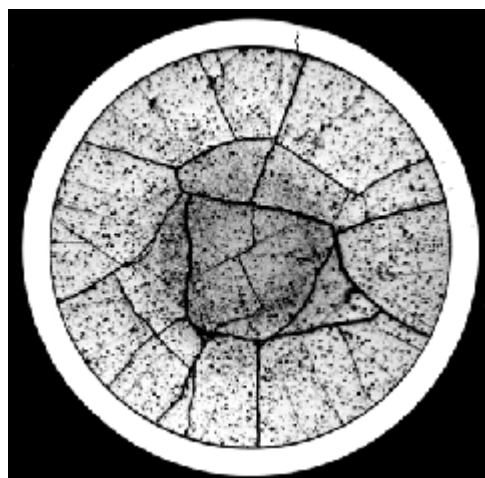
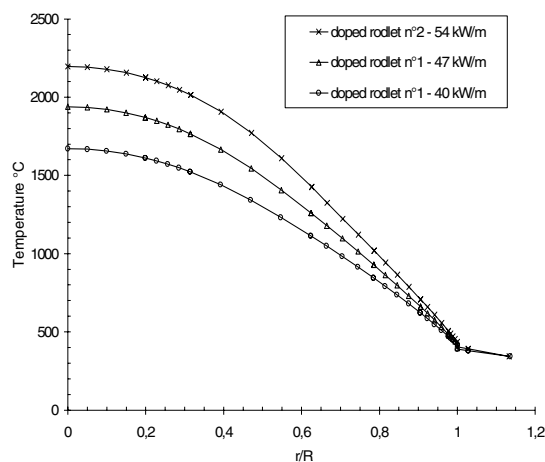


Figure 13. Temperature profile in the pellet at different power levels – post-calculation



knowledge of the interaction between crack formation and the other stress-dependent phenomena. Particularly, the contribution of fission gas swelling, related to the specific behaviour of fission gas products in the doped large grain microstructure will have to be more precisely analysed. With these objectives in mind, an especially dedicated experiment is planned this year. It will provide new results on the specific behaviour of doped UO_2 fuel and on the relative kinetics of fuel creep and pellet fracturing during the single phase of the transient. Furthermore, specific studies on doped fuel fracture processes are also in progress.

To continue with the behaviour analysis of doped fuels under PWR conditions, the fission product retention capability of the large grain size structure of chromia-doped fuel has to be confirmed at high burn-up. The very promising results of the CONCERTO programme have led FRAMATOME ANP, in co-operation with EDF and the CEA, to launch in mid-2001 the irradiation of lead fuel rods with chromia-doped UO_2 pellets loaded in M5™ cladding tubes. This irradiation campaign, performed in a 1 300 MWe EDF reactor, aims to acquire all the data required to demonstrate the ability of this fuel to be a high burn-up PCI remedy in order to satisfy future customer needs for improved fuel management and greater NPP operating flexibility.

REFERENCES

- [1] Permezel, P., P. Pupier, N. Waeckel, “PCMI Limits on French PWR”, *Proceeding of the ANS International Topical Meeting*, Palm Beach (1994).
- [2] Beguin, S., “PCI-related Constraints on EDF PWRs and Associated Challenges”, these proceedings.
- [3] Delafoy, Ch., *et al.*, “Advanced PWR Fuels for High Burn-up Extension and PCI Constraint Elimination”, *Proceedings of the IAEA TCM on Improved Fuel Materials and Designs*, Brussels, Belgium (2003).

- [4] Marsh, G., GA. Wood, CP. Perkins, “Niobia-doped UO₂ Fuel Manufacturing Experience at British Nuclear Fuels LTD”, *Proceedings of the IAEA Technical Committee Meeting*, Tokyo, Japan (1996).
- [5] Sik Kim, K., *et al.*, “Effect of Sintering Gas on the Grain Size of UO₂ Pellets Derived from Different Powder Routes”, *Proceedings of the IAEA TCM on Improved Fuel Materials and Designs*, Brussels, Belgium (2003).
- [6] Dehaut, Ph., *et al.*, “New UO₂ Fuel Studies”, *Proceedings of the IAEA TCM on Advances in Fuel Pellet Technology for Improved Performance at High Burn-up*, Tokyo, Japan (1996).
- [7] Dugay, C., A. Mocellin, Ph. Dehaut, M. Sladkoff, “High Temperature Mechanical Tests Performed on Doped Fuels”, *Proceedings of the IAEA TCM on Advances in Fuel Pellet Technology for Improved Performance at High Burn-up*, Tokyo, Japan (1996).
- [8] Dherbey, F., F. Louchet, A. Mocellin, S. Leclercq, “Elevated Temperature Creep of Polycrystalline uranium Dioxide”, *Acta Materialia*, 50 (2002).
- [9] Bourgeois, L., Ph. Dehaut, C. Lemaignan, A. Hammou, “Factors Governing Microstructure Development of CR₂O₃-doped UO₂ During Sintering”, *Journal of Nuclear Materials*, 297 (2001).
- [10] Alberman, A., *et al.*, “Technique for Power Ramp Tests in the ISABELLE 1 Loop of the OSIRIS Reactor”, *Nuclear Engineering and Design*, 168 (1997).
- [11] Mougel, C., *et al.*, “Power Ramping in the OSIRIS Reactor: Database Analysis for Standard UO₂ Fuel with Zy-4 Cladding”, these proceedings.
- [12] Bourreau, S., *et al.*, “Influence of the Hold Period on the Fuel Rod Behaviour During a Power Ramp”, *Proceedings of the IAEA Technical Committee Meeting*, Nyköping, Sweden (1998).
- [13] Nonon, C., *et al.*, “Impact of Fuel Microstructure on PCI Behaviour”, *Proceedings of the IAEA TCM on Improved Fuel Materials and Designs*, Brussels, Belgium (2003).
- [14] Valin, S., *et al.*, “Synthesis of the Results Obtained on the Advanced UO₂ Microstructures Irradiated in the TANOX Device”, *Proceedings of the IAEA TCM on Improved Fuel Materials and Designs*, Brussels, Belgium (2003).

**PCMI OF HIGH BURN-UP FUEL AS MANIFESTED BY DIFFERENT
TYPES OF INSTRUMENTATION AND MEASUREMENTS IN
THE HALDEN REACTOR EXPERIMENTAL PROGRAMME**

W. Wiesenack, T. Tverberg
Institutt for Energiteknikk
OECD Halden Reactor Project, Norway

Abstract

Fuel performance studies on light water reactor fuels with extended and high burn-up constitute an essential part of the experimental programme of the OECD Halden Reactor Project. A range of irradiation facilities, experimental rigs and in-core instrumentation, supplemented by refabrication and instrumentation capabilities for irradiated fuels, is available to this end. Many phenomena occur in combination with others, and fuel behaviour is therefore viewed from different angles to provide a picture that is as complete as possible.

With respect to PCMI, a number of different types of measurements can provide direct and indirect information. The paper first exemplifies features of PCMI with increasing burn-up as registered by cladding elongation measurements such as:

- Development of initial PCMI, starting with fresh fuel.
- Long-term accommodation of the pellet-clad compound to gradually changing power levels.
- PCMI evolution during power increases for high burn-up fuel with clad bonding.
- Long-term length increase of the cladding due to fuel swelling for bonded fuel.
- Ratcheting and relaxation in conjunction with cyclic power changes.

An experimental series addressing clad lift-off also provides information regarding PCMI. For this particular phenomenon, the interaction of the components' fuel and cladding are of particular importance for modelling and explaining the observations. The available measurements encompass:

- Fuel temperature data as the primary lift-off indicator.
- Gas flow/hydraulic diameter measurements indicating the changing tightness of the fuel column both during power changes and as a consequence of lift-off.
- Cladding elongation noise data indicating the coherence between fuel and cladding.

The picture that one obtains from these data for the lift-off situation is one of a loosening fuel stack that develops internal heat flow resistances while at the same time maintaining sufficiently strong contact with the cladding to transmit fuel swelling and thermal expansion.

Introduction

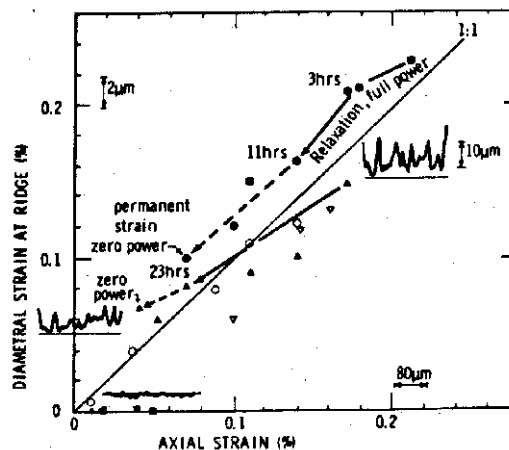
The fuels and materials testing programmes of the OECD Halden Reactor Project are aimed at providing data in support of a mechanistic understanding of phenomena associated with short- and long-term in-pile fuel performance and property changes. To this end, suitable irradiation techniques and instrumentation have been developed and applied for more than forty years. The data obtained can be used for fuel behaviour model development and verification as well as in safety analyses.

The knowledge of pellet-clad interaction as affected by fuel properties, operation conditions and irradiation-induced changes of fuel and cladding is essential for design, failure resistance and alleviation of operational limitations. A number of often interrelated phenomena need to be quantified to obtain adequate predictions, and separate effect studies provide efficient methods for assessing specific effects. Over the years, such studies have addressed the phenomena which are deemed most important for fuel behaviour modelling. Although the experimental focus has shifted in recent years to investigations of high burn-up effects, data based on fresh or low burn-up fuel are valuable as well; they can often be transferred to high burn-up situations or are valid for worst case scenarios which may occur at low or medium rather than high burn-up. Since fuel behaviour modelling and safety analyses have to provide an adequate description for the entire in-core service, it seems important to maintain a complete picture of fuel behaviour from beginning to end-of-life.

In this paper, emphasis is put on PCMI data as obtained from different types of instrumentation. The selected examples from separate and integral effects studies show the relation of the pellet-clad mechanical interaction with fuel swelling, thermal behaviour, aspects of gas communication and mixing.

Pellet-clad mechanical interaction (PCMI) can be measured in-pile in two ways: with a diameter gauge moving along the length of a rod, and with a cladding elongation detector. Since axial elongation can be measured more easily and frequently than diametral deformation, the data should not be neglected. However, the difficulties of modelling axial PCMI for the whole length of a fuel rod are recognised, and only few codes include the effect in a non-simplistic way. Cladding elongation can also provide information on diametral deformation. The close relation between hoop strain and axial strain, both in terms of magnitude and relaxation behaviour, has been shown with Halden Project data comparing elongation and diameter changes obtained in-pile for the same rod [1], see Figure 1.

Figure 1. Similarity between radial and axial load of the cladding due to PCMI



The eventual aim for the fuel modeller would be to provide a unified and seamless description of both the thermal and mechanical fuel behaviour.

Development of onset of interaction between fuel and cladding

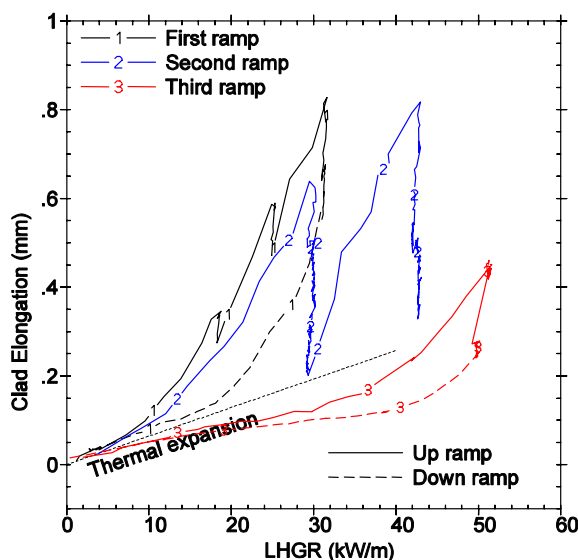
Cladding elongation measurements show that the interaction between fuel and cladding evolves in typical ways through various stages of irradiation. This is depicted with examples in the following sections. A thorough review of Halden data regarding gap closure and pellet-clad interaction is compiled in Ref. [2].

Fresh fuel

It is a common experience that axial interaction during the first rise to power is strong and decreases during the following cycles. This can be attributed to random eccentric stacking of the pellets which are pushed to more central positions in contact with the cladding. The simultaneous radial and axial expansion of the pellets during the power increase generates friction forces which cause the observed cladding elongation.

The data of the selected example are taken from BWR type fuel rods irradiated in the HBWR. The active length was 768 mm, pellet diameter 12.59 mm and diametral gap 170 μm . It should be noted that thermal expansion is not sufficient to close the gap at start-up, thus conventional fuel model based on concentric geometry would not calculate any interaction, obviously at variance with the experimental evidence. The typical development of axial interaction for start-up and two following power changes is shown in Figure 2. Several features are apparent: the relaxation of axial strain during power holds; the immediate continuation of strong PCMI and elongation after the power hold (especially ramp 2); and the shift of interaction onset to higher power (especially ramp 3, but also ramp 2 which is always below curve 1).

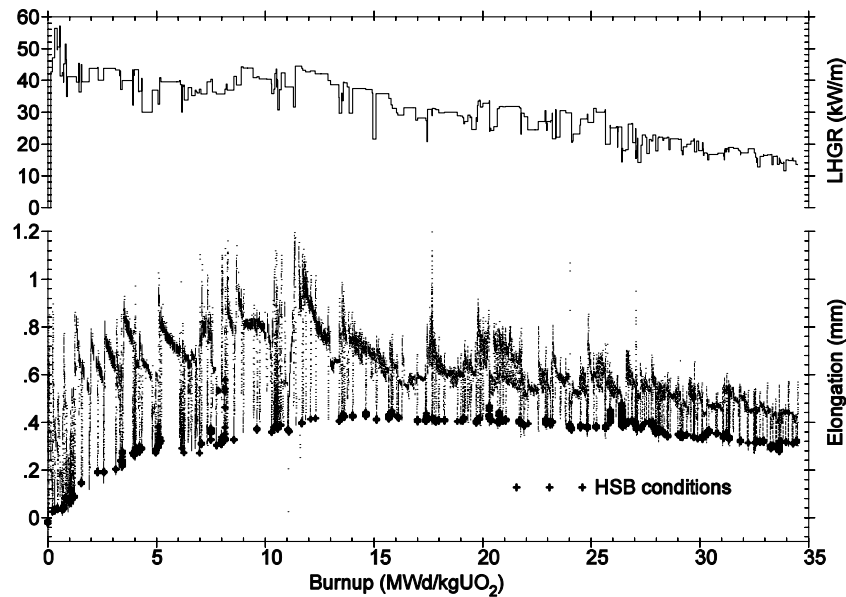
Figure 2. Cladding elongation for three consecutive power ramps, fresh fuel



Low to medium burn-up

As the rod is subjected to further irradiation, PCMI remains (Figure 3). The strong interaction and resulting axial strain is relaxed during periods at constant power. However, a permanent elongation is

Figure 3. Power and cladding elongation history of BWR fuel irradiated in the Halden reactor to medium burn-up



induced in the early part of irradiation (until about 13 MWd/kgUO₂). For a proper assessment of the data shown in Figure 3, it must be noted that cladding elongation is measured relative to the rig structure.

This structure is also made of zircaloy and subjected to about the same irradiation induce growth. The differential, permanent elongation that can be seen at hot stand-by (lower envelope, data points marked with +) is thus mostly due to the accumulation of creep strain increments.

A closer look at individual power ramps reveals that the onset of interaction (defined as point of deviation from free thermal expansion) moves to lower power with increasing burn-up because the pellet-cladding gap closes due to fuel swelling and clad creep-down (Figure 4). This is concurrent with an accommodation of the fuel to the available space, and a balance between fuel swelling and creep caused by contact forces evolves. The cladding elongation data of start-up ramps show a change in curve shape to a more abrupt transition from free thermal expansion to expansion imposed by fuel elongation. However, the interaction remains small as long as power does not exceed previously reached levels. Since there is no gap left between fuel and cladding at power, a transient will lead to cladding load from the beginning.

High burn-up fuel

Two rods previously irradiated in a commercial PWR to a burn-up of 52 MWd/kgUO₂ were re-instrumented with cladding elongation sensors and further irradiated in the HBWR. The operating power during the last cycle in the PWR was about 20 kW/m for both rods.

The elongation behaviour during start-up power ramps is shown in Figure 5. The first ramp just reached the power level to which the fuel had been conditioned during commercial operation. Although the elongation is slightly stronger than estimated for a case of free thermal expansion, an appreciable interaction cannot be discerned. The intermediate ramp to considerably higher power shows definite

Figure 4. Gradually changing onset of PCMI when the fuel accommodates to decreasing power, swelling and clad creep-down

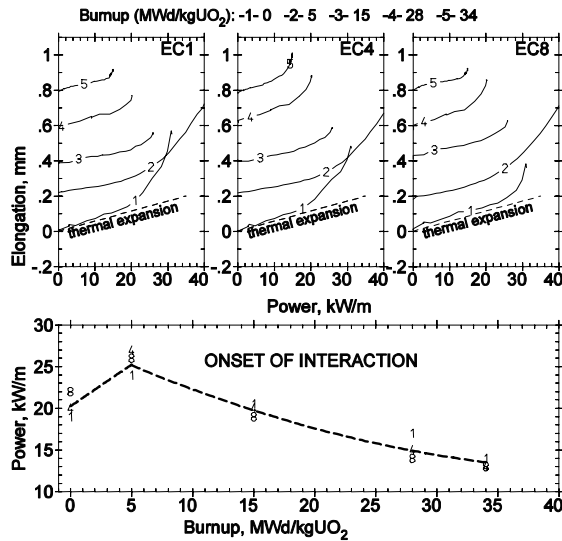
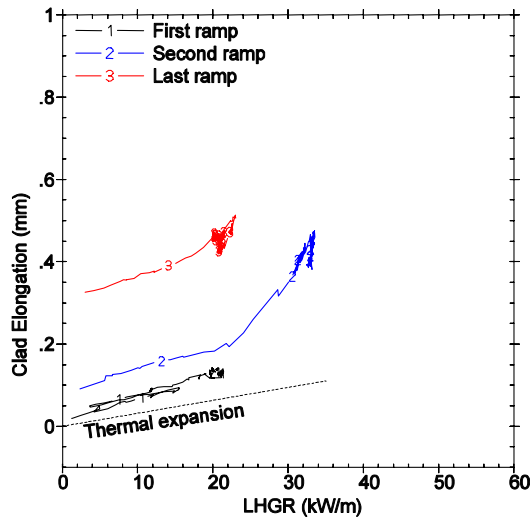


Figure 5. Cladding elongation for three power ramps, high burn-up fuel



PCMI, starting from the conditioning power level of 20 kW/m. The final ramp is similar in that PCMI is visible, however beginning at slightly lower power. Between the intermediate and final ramp, the fuel received a burn-up increment of 2.5 MWd/kg while power was gradually decreasing, thus conditioning the fuel to a lower power level.

The similarity between the PCMI curve shape of fresh fuel after some conditioning (curve 3 of Figure 2) and high burn-up fuel is important to note. At a burn-up of more than 50 MWd/kgUO₂, bonding between fuel and cladding has definitely developed. However, this does not lead to strong PCMI as the term “bonding” might imply. While the slope of the “straight” initial part exceeds thermal expansion, indicating some degree of permanent contact, strong interaction and elongation dominated by fuel expansion only occurs at high power.

Swelling behaviour

Permanent (but not strong) contact between fuel and cladding has consequences for permanent cladding elongation. The following two examples illustrate typical behaviour. Both examples are related to re-instrumented PWR fuel from a commercial power station. The fuel has the following design data: active fuel stack length 433 mm; as-fabricated fuel diameter 9.12 mm; as-fabricated gap 170 μm ; cladding material re-crystallised Zry-4.

Figure 6 shows the cladding elongation of the medium burn-up rod. At the beginning of the re-irradiation, a slight decrease of the cladding elongation is apparent. Thereafter, a permanent elongation with an average rate of 0.15%/10 MWd/kgUO₂ is observed. This is compatible with irradiation-induced growth and less than solid fission product fuel swellings. (The fuels in the two segments differ in grain size, but a definite influence of this parameter on elongation behaviour is not obvious.) It must be concluded that at this burn-up level cladding elongation proceeds independent of fuel swelling.

Figure 6. Cladding elongation of medium burn-up fuel

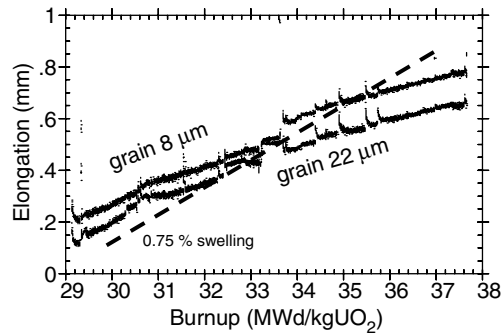
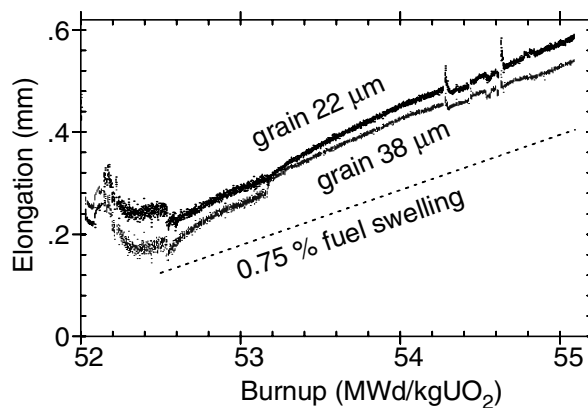


Figure 7 shows the cladding elongation at high burn-up (52-55 MWd/kgUO₂ or 59-62 MWd/kgU). As in the case of lower burn-up, relaxation of the initial PCMI strain can be seen. The process is finished within a burn-up increment of about 0.2 MWd/kg, similar to the lower burn-up case (the difference in scale sensitivity between the two figures should be noted). An appreciable difference can be seen regarding the rate of elongation which reflects a typical rate of fuel swelling. In this high burn-up case, it must be concluded that due to bonding between fuel and cladding the fuel swelling is transmitted to the cladding and imposed as permanent elongation.

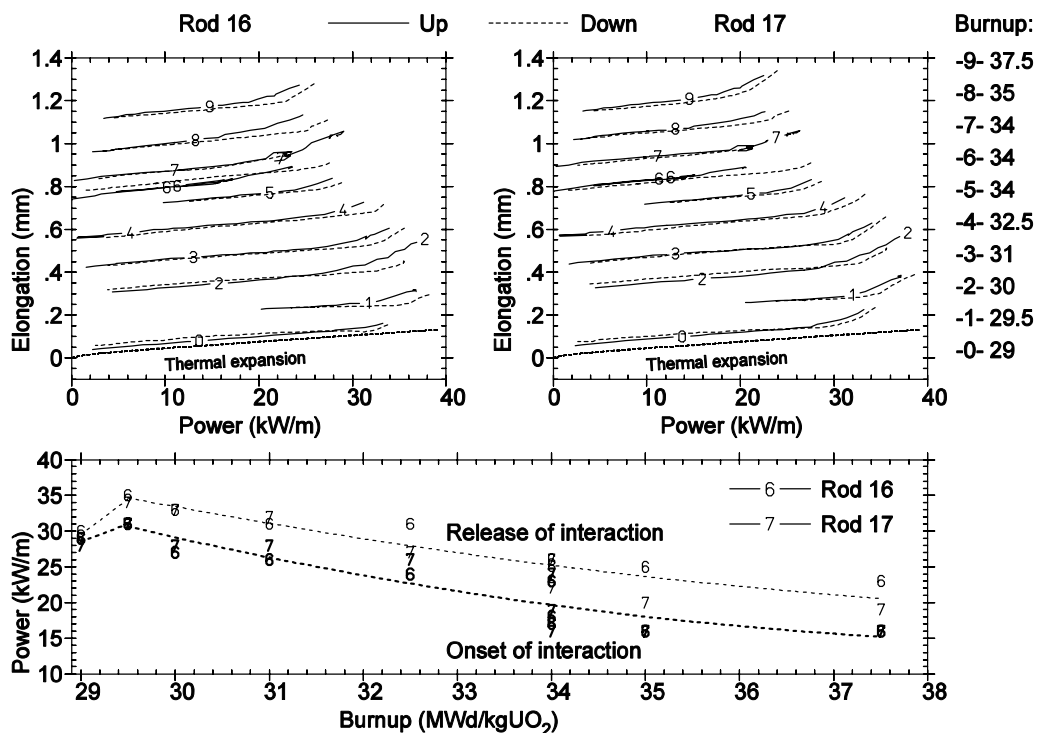
Figure 7. Cladding elongation of high burn-up fuel



Axial ratcheting

Both Figures 6 and 7 show small elongation peaks that decrease to the base rate of elongation after a short time. These peaks are associated with shutdown/start-up sequences. When power is reduced, the release of interaction occurs at a certain power. During the following start-up power ramp, the onset of interaction occurs at a somewhat lower power, leading to an extra amount of elongation. The shutdown/start-up sequences of one of the medium burn-up rods are shown in Figure 8. The points of release and onset of interaction are summarised in the lower part of Figure 8. They show a difference of about 5 kW/m.

Figure 8. Release and onset of PCMI during shutdown/start-up sequences



Both Figure 4 and Figure 8 (upper part) show that stronger PCMI only occurs during the final part of the power ramps if the fuel has accommodated itself to the final power level during the preceding irradiation. That means that power cycles causing axial ratcheting do not necessarily have to go all the way to zero power. Load follow operation maybe sufficient to cause the effect. However, experimental experience from the Halden reactor programme has so far not provided evidence that axial ratcheting would induce strain increment accumulation.

Fuel stack behaviour

The most direct sensor for measuring fuel stack behaviour is the fuel elongation detector. This sensor measures length changes relative to the cladding with the fixed point in the fuel rod end plug. It cannot meaningfully be applied to high burn-up fuel with bonding between fuel and cladding and no relative movement between the two components. But some other types of in-pile measurements also provide a good indication of fuel stack properties.

Hydraulic diameter measurements

Hydraulic diameter measurements relate the flow of gas through the fuel stack to a “wetted perimeter” interpreted as belonging to a gap between pellets and cladding. The technique measures the pressure change in a volume that is emptied through the fuel stack since the flow that can be produced is very small. The basic relation between hydraulic diameter and flow (pressure change) is given by:

$$D_H = const \cdot \sqrt[4]{\frac{\eta \cdot T \cdot \dot{p} \cdot L}{(p_1^2 + p_2^2) \cdot D}}$$

where p is pressure, L is rod length, D is rod diameter and T is average rod temperature.

Figure 9 shows the change of hydraulic diameter (HD) for three fuel rods of identical design (200 μm initial diametral gap), monitored throughout many years of irradiation in the Halden reactor. As the gas can also flow through a multitude of cracks, the HD is a reflection of the free volume in the fuel column, starting with a value given by the original as-fabricated pellet-clad gap. Expected changes can be seen: initial pellet cracking and fragment relocation, solid fission product fuel swelling and the development of a minimal HD as fuel and cladding accommodate to each other.

Figure 9. Change of hydraulic diameter (free fuel column volume) with burn-up

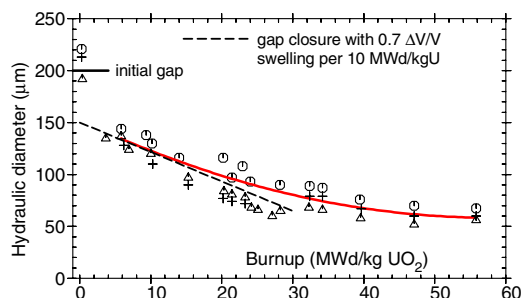
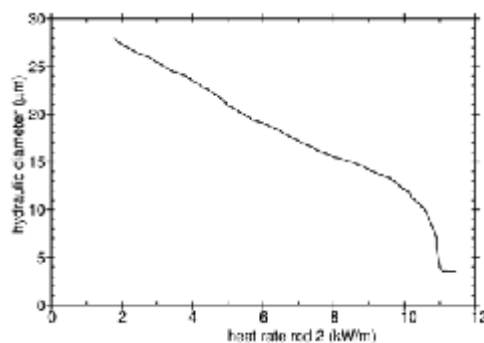


Figure 10 depicts the HD of this fuel at a burn-up of 75 MWd/kg as function of changing power. The HD first decreases linearly with increasing power, reflecting the decrease of internal free fuel stack volume due to thermal expansion. When the accommodation power level is approached, the HD decreases with a much larger rate. This development is parallel to cladding elongation which changes from free thermal expansion to a state of strong contact with the fuel and consequently an increased rate of elongation. Thus these two types of measurement produce consistent pictures of the fuel stack.

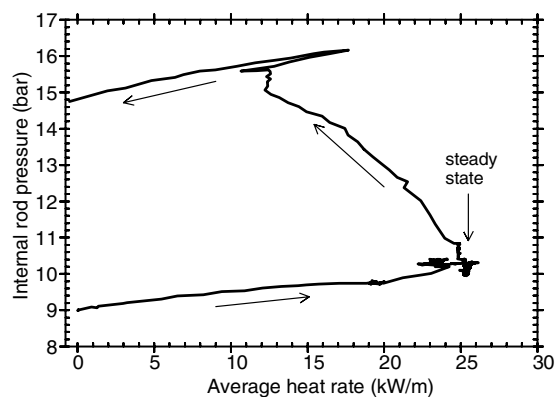
Figure 10. Change of hydraulic diameter or fuel column free volume during a power ramp



Delay of fission gas transport to the rod plenum

The hydraulic diameter measurements require pressure differences of 30-60 bar in order to produce a gas flow of 0.5-1.0 l/min (stp). At power, the fuel column is obviously quite impenetrable. This is also true for released fission gas that remains trapped within the fuel column until a power reduction opens a path to the plenum where the pressure sensor is installed. The observation of “delayed fission gas release” is therefore quite common. An example of this phenomenon can be seen in Figure 11. According to the previous figure, the fuel column becomes penetrable for gas flow after a limited power reduction. Similarly, the release of the inner overpressure to the fuel rod plenum is measurable as soon as some power reduction has occurred.

Figure 11. Delayed fission gas release. Fission gas remains trapped in the fuel column until a power reduction opens a path



Lift-off and noise data

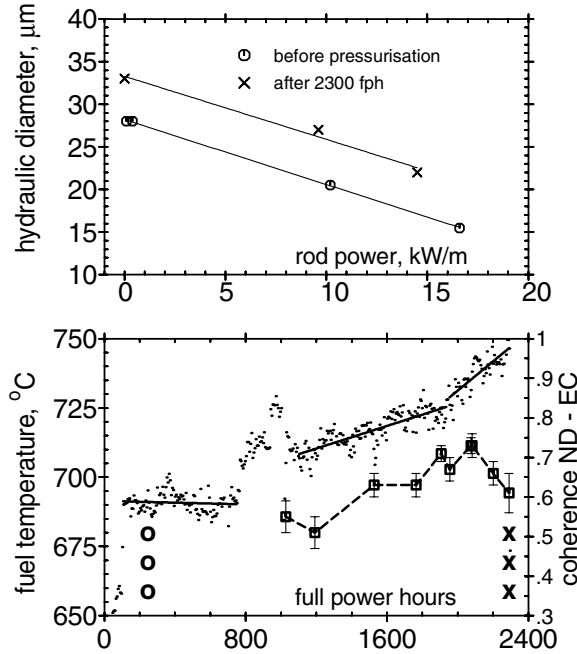
A final example for characteristic behaviour of the fuel stack is taken from the series of Halden reactor experiments that address the tolerable rod pressure limits and clad lift-off issue [3]. Pre-irradiated PWR rods equipped with a fuel centreline thermocouple are subjected to rod overpressure to determine the pressure beyond which fuel temperature will increase as a consequence of clad creep-out. The rod overpressure can be controlled with a high pressure gas supply system connected to the fuel rod with a gas line. In addition to the lift-off feedback on fuel temperature, the experiment allows to assess:

- The temperature response to fill gas change (Ar \leftrightarrow He) during operation.
- Fission gas release by means of gamma spectroscopy.
- The hydraulic diameter.
- PCMI and fuel swelling by means of clad elongation measurements.
- The coherence between fast response neutron detector (power) and clad elongation.

Figure 12 shows the response of the fuel temperature (lower graph) during a measurement period when the overpressure (rod internal pressure minus PWR system pressure, 155 bar) was held at 100, 200 and 300 bar. A definite temperature increase can be observed for the periods with 200 and 300 bar overpressure.

Figure 12. Response to rod overpressure causing clad lift-off

*Upper graph: hydraulic diameter measurements indicate increased fuel column permeability
Lower graph: coherence between clad elongation and power (fuel elongation) is maintained*



Noise analysis has been applied successfully to Halden reactor elongation data to monitor the onset and degree of PCMI [4]. Noise analysis has also been used to study the relation between cladding elongation and power in a state of progressing lift-off. The coherence between fast response neutron detector (power) and clad elongation is indicated in the lower part of Figure 12. It can be seen that the coherence increases slightly during the early phase and drops somewhat during the last phase with the highest overpressure and lift-off rate as indicated by the accompanying temperature measurements. Considering the scatter in the data, at least a constant coherence can be assumed. This is contrary to the prediction of a simple model where fuel and cladding are separated by an annular gap, since any gap opening (lift-off) would imply loss of contact and the breaking down of the coherence between power and elongation. (According to [4], a PCMI-free state is characterised by a coherence value of less than 0.05, and well developed PCMI has a coherence of > 0.2 . During further 2 000 fph with overpressure and continued lift-off, which is not shown here, the coherence shows a decreasing trend ending at about 0.45 which is still considerably above the threshold value of PCMI onset derived in [4].)

Other measurements in this experiment, which are not explicitly shown, resulted in the following:

- The temperature response to fill gas change ($\text{Ar} \leftrightarrow \text{He}$) is small.
- Similar to the high burn-up fuel behaviour shown in Figure 6, the clad elongation reflects fuel swelling. This means that strong contact at the fuel-clad interface exists also during lift-off, supporting the noise analysis results.

From these observations, it may be concluded that the lift-off effect is mitigated by the opening of internal space between fuel fragments rather than the opening of the pellet-clad gap.

Modelling considerations

Fuel behaviour modelling is a compromise. Models assuming axial symmetry are computationally attractive, but actually describe the most unlikely situation from the very beginning. Detailed models using advanced techniques such as FEM have become more affordable from a computational point of view, but remain limited in their predictive power because of non-deterministic, random behaviour such as fuel cracking and details on a micro scale. The observations of fuel behaviour given in this paper are difficult to reconcile with the predictive capabilities of models with concentric arrangements of the fuel within the cladding and a dividing gap. Realising the deficiencies of conventional models with respect to a satisfactory, simultaneous treatment of thermal and mechanical behaviour, Williford, *et al.* proposed as early as 1982 an alternative approach [5] using a “crack compliance model” that links the free space and the stresses in the fuel column:

$$\frac{1}{2} \operatorname{erf}\left(\frac{d}{R\sqrt{2}}\right) = \frac{\sigma}{\sigma + H}$$

where d is crack width, R is surface roughness, σ is stress and H is Meyer hardness.

Their model predicts that there is always some contact between the fuel fragments as well as the fuel and the cladding. The model assumes that there is no relative movement between pellets and cladding. While this assumption is at variance with early-in-life behaviour (relative movement is actually measured by fuel stack elongation detectors), it is a good approach for high burn-up fuel bonded to the cladding. A corresponding model can describe both thermal and mechanical behaviour as for example observed in the lift-off studies at Halden.

Acknowledgements

The results obtained from the experimental work at the Halden Reactor Project are due to the combined efforts of many staff members. For the lift-off test, Stephan Béguin (EDF) did the first pioneering evaluation. His contribution, the contributions of other individuals seconded from organisations participating in the Halden Reactor Project as well as the funding provided by the member countries are gratefully acknowledged.

REFERENCES

- [1] Vilpponen, K.O., “In-pile Measurements of Pellet-cladding Interaction and Relaxation”, *IAEA Specialists Meeting on Fuel Element Performance Computer Modelling*, Blackpool (1980).
- [2] Sim, K-S., J.A. Turnbull, E. Kolstad, *A Review of Halden Data on Gap Closure and Mechanical Behaviour of UO₂ Fuel Rods*, OECD Halden Reactor Project HWR-542, January 1998.
- [3] Beguin, S., *The Lift-off Experiment IFA-610.1 – Initial Results*, OECD Halden Reactor Project HWR-544, January 1998.
- [4] Vallejo, I., J. Blázquez, F. Barrio, “The Use of Noise Analysis for the Detection of the Pellet-cladding Mechanical Interaction”, *Nuclear Engineering and Design*, 180 169-174 (1998).
- [5] Williford, R.E., D.D. Lanning, C.L. Mohr, “A Model for the Effective Thermal and Mechanical Properties of Cracked UO₂ Pellets”, *Nuclear Technology*, Vol. 56, pp. 340-350, February 1982.

POWER RAMPING IN THE OSIRIS REACTOR: DATABASE ANALYSIS FOR STANDARD UO₂ FUEL WITH ZY-4 CLADDING

C. Mougel,¹ B. Verhaeghe,¹ C. Verdeau,¹ S. Lansiaart,² S. Béguin,³ B. Julien⁴

¹Commissariat à l'Énergie Atomique, Saclay, France

²Commissariat à l'Énergie Atomique, Cadarache, France

³EDF/SEPTEN, Villeurbanne, France

⁴FRAMATOME ANP, Lyon, France

Abstract

To prevent PCI failure of fuel rods during incidental transients in nuclear power plants, the French safety approach is based on the interpretation of an experimental database. Thus, in the framework of a co-operative programme with EDF and FRAMATOME ANP, CEA has carried out many power ramps in the OSIRIS experimental reactor and conducted a comprehensive programme of pre- and post-irradiation examinations. This paper discusses the main features of the extensive database now available for FRAMATOME ANP standard rods (UO₂ fuel and Zy-4 cladding). Special emphasis is placed on the consistency of the results and on the characterisation of the damage of the cladding, when it occurs.

Due to the inability to determine local strains at the critical points of the cladding inner surface, maximum power at the ramp terminal level appears to be a good parameter for ranking the different damage states of the differently tested rods. But burn-up is also an important parameter, more particularly at low values, for which the pellet-to-clad gap is far from being closed just before transient and the PCI risk of failure is thus greatly reduced.

Introduction

During Class 2 power transients considered in the context of PWR safety issues, pellet-to-clad interaction (PCI) is enhanced, which can lead to Iodine-assisted Stress Corrosion Cracking (I-SCC) of the cladding [1,2,3]. The first barrier opposed to dissemination of the volatile fission products created within the fuel is thus possibly damaged. In order to prevent cladding failure during any Class 1 or Class 2 operating condition, the French safety approach has been founded on the interpretation of an experimentally adequate database. Experiments consist of power ramp tests, conducted according to a specific protocol, following from the choice of the experimental rod to the specification of the re-irradiation power history.

Part of the data is provided by experiments conducted in the R2 Swedish (Studsvik) test reactor, but another part is based upon CEA experiments performed in the OSIRIS French (Saclay) test reactor. From the analysis of this “unified database” (UDB), FRAMATOME ANP was able to derive a technological limit for its standard rod (i.e. with Zy-4 stress-relieved cladding and UO_2 fuel) and EDF was able to set up efficient operating technical specifications for its nuclear plants, thus avoiding up to the present any PCI-type rod failure.

This paper presents the main features of the CEA results included in the UDB, as well as additional results from specific experiments to improve understanding. All the rods concerned have been first manufactured using FRAMATOME ANP standard materials and have been base irradiated in EDF power plants up to different burn-up levels, corresponding respectively to one, two, three and four annual cycles. All of them have been subjected to a comprehensive programme of pre- and post-ramp examinations. Special emphasis will be given to the complementary aspect of the examinations (non-destructive and destructive) and to the consistency of the results. Due to the importance of the cladding integrity requirement, from the safety point of view, we will then focus on clad deformation and clad damage analysis.

Ramp testing

Experimental rods manufacturing

Short rods are needed for re-irradiation in the OSIRIS test reactor. They are generally re-fabricated in a hot cell from standard mother rods, according to the previously qualified “FABRICE” process [4], except in case of a segmented mother rod. All the mother rods concerned here showed the main characteristics of the FRAMATOME ANP 17×17 design, with Zy-4 stress-relieved cladding (standard or low tin) and UO_2 fuel (without additive). They were base irradiated in an EDF PWR plant during one to four annual cycles, which corresponds to a range of burn-up (BU) from 10 GWd/tU to 55 GWd/tU. After basic characterisation of the mother rods (visual inspection, clad soundness control by eddy current, axial and diametrical clad metrology, outer zirconia thickness measurement, rod X-ray visualisation, pressure measurement and gas analysis), sections are cut right in between the next two grid marks. The adjustment to the specified final length of the experimental rod (about 500 mm) leads to subsidiary cutting. Before setting up the end plugs, fuel is first drilled at each end of the column. On the upper part, the so-formed plenum maintains the marks of the primary ridges of the mother rod, which provides useful references for the determination of the diametrical cladding changes induced by re-irradiation. After introduction of flat plates at each end of the fuel column and of a spring in the new plenum, plugs are welded using the TIG process. The FABRICE rod is then re-pressurised with helium, at the same pressure as the mother rod. For the three rodlets (G2, H2, I2) extracted from a segmented mother rod, the FABRICE process was not used. In those cases, short rods (about 600 mm) were directly available since segmented rods are especially made up of independent short rods screwed end to end.

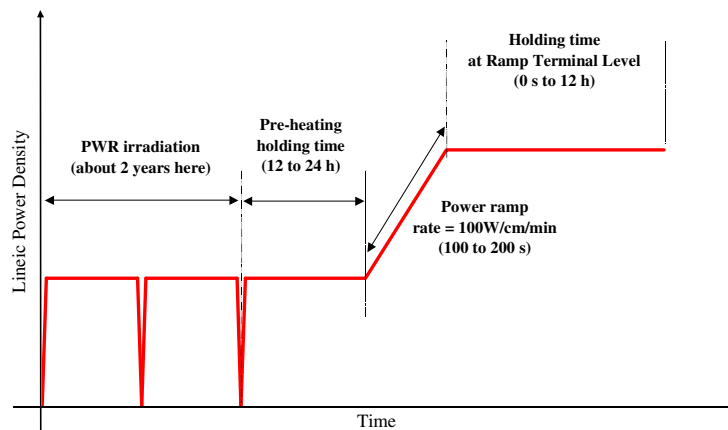
Power ramping

Principle

Ramp tests are performed in the OSIRIS reactor at the CEA centre of Saclay [5]. Rodlets are set in a pressurised loop located in the pool of the reactor and the re-irradiation is performed under PWR coolant conditions (pressure, temperature and chemical conditioning). The required power history is achieved by moving the loop towards the reactor core. The ramp sequence is monitored by neutron flux detectors, calibrated on thermal balance.

The experimental procedure for ramp testing is summarised in Figure 1. The first step is the re-conditioning of a rodlet to the mean power reached during its last PWR cycle, in order to re-establish the thermo-mechanical and chemical state of the rod. The duration of this stage is between 12-24 h. It is defined by the stabilisation of the clad elongation detector signal. The rodlet is then subjected to a power transient at the rate of $100 \text{ W.cm}^{-1}.\text{min}^{-1}$; the power increase usually lasts for approximately 2 minutes. If no failure is detected, the time at final power is generally maintained for 12 h. The power increase is performed by displacing the loop towards the reactor core.

Figure 1. Schematic representation of ramp testings



Primary results

The main characteristics of the ramp tests as well as the results in terms of integrity of the rods and time to failure (in case of failure) are presented in Table 1.

Most experiments were performed on rods with burn-up in the range 20-30 GWd/tU because the thermal mechanical conditioning of the rods was suspected to be the most propitious for PCI failure at that time. The whole database interpretation indeed confirms that the failure threshold, as derived from the two-cycle experiments, is pessimistic for lower and higher burn-up rods.

A further important feature is that time to failure is quite short (a few minutes in all cases) compared to the currently specified holding time at ramp terminal level, 12 hours. This is the reason why holding time was reduced in some cases to a few hours, even to $\frac{1}{4}$ of an hour, without losing the major expected response, that is, cladding integrity or not. Experiments with short holding times provided interesting information concerning the fuel rod evolution at high power. The three experiments with zero holding time aimed at freezing the rod in the worst conditions for the clad mechanical loading and so identifying

Table 1. Ramp testing parameters*The number in the rod name is a reference to the rod number of cycles*

Rodlet	Average burn-up (GWd/tU)	Final power (kW/m)	Time at final power	Failure	Time up to failure
A1	12	50	12 h	N	–
B2	24	47	2 h	Y	4 min
C2	24	53	3 min	Y	1 min
D2	27	46	7 min	Y	4 min
E2	27	44	12 h	N	–
F2	28	42	14 min	Y	5 min
G2	27	40	12 h	N	–
H2	27	41	16 min	N	–
I2-1	26	41	0 s	N	–
I2-2	26	45	0 s	N	–
J3	40	40	2 h	N	–
K3	41	43	12 h	N	–
L3	40	53	6 min	Y	1 min
M3	39	52	2 min	N	–
N4	52	43	4 h	N	–
O4	52	46	0 s	N	–

the inelastic cladding and fuel strains at this step, in order to validate numerical simulations. However, since time to failure is not zero even at relatively high power, these experiments are not relevant for the cladding integrity analysis; they rather provide information concerning the cladding damage possibly due to the sole power increase and thus provide an experimental support to stress corrosion cracking modelling under PCI conditions.

Rod examinations

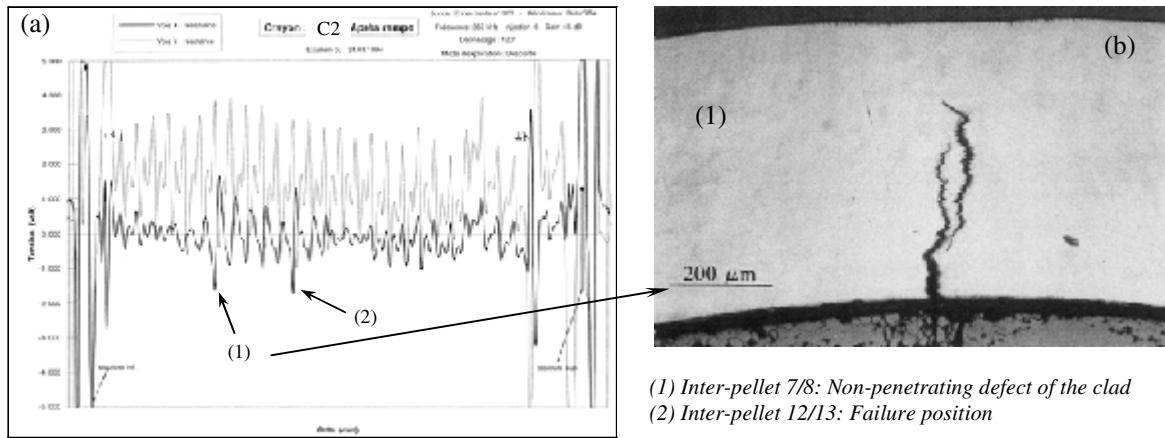
Before and after the ramp tests, a standard set of rod examinations is systematically performed. We will distinguish hereafter between the non-destructive examinations, which are carried out before and after re-irradiation, and the destructive ones, which are only performed after re-irradiation. Examinations before the ramp tests are considered as references and are directly comparable to those made after the irradiation. Results presented below show that each method provides its own data set and that, in case of overlapping between different methods, all the results are quite consistent.

Non-destructive examinations

Apart from the general characterisation of the rod, non-destructive examinations also provide interesting local information.

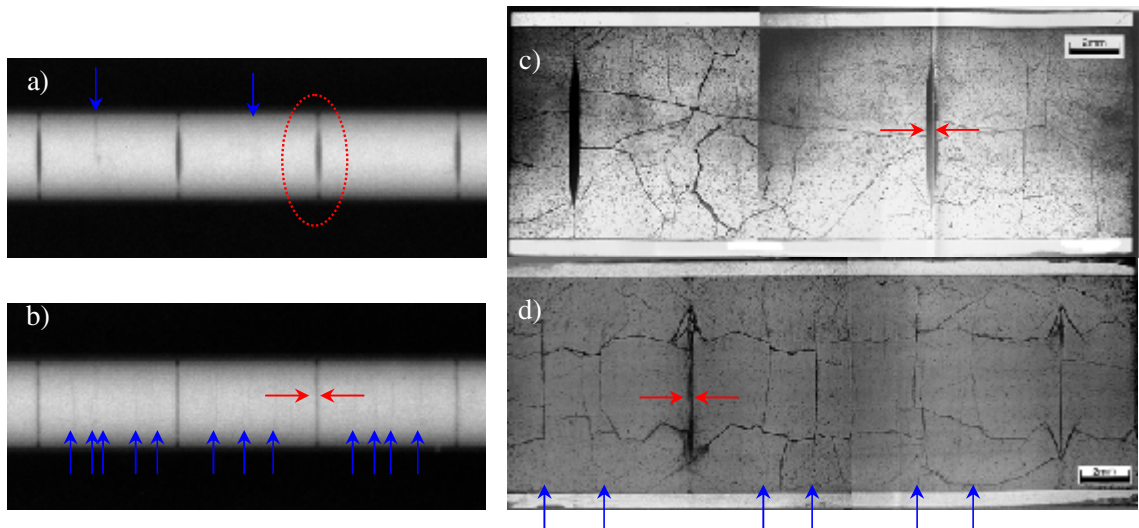
Eddy current measurements are used to control the soundness of the cladding or pointing out the axial position of clad cracks, if any. Figure 2 shows that defects detected by this means (encircling coil in this case) can be precisely observed later on, thanks to the transverse cut for metallography. It is important to note at this step that failures always appear at the inter-pellet plane, where primary ridges also develop, as illustrated by the C2 case. In the next section it will further be seen that cracks penetrating throughout the cladding wall thickness are facing pellet radial cracks.

Figure 2. Clad defects detection by eddy currents (a) and local destructive examination of the cladding (C2 rod) (b)



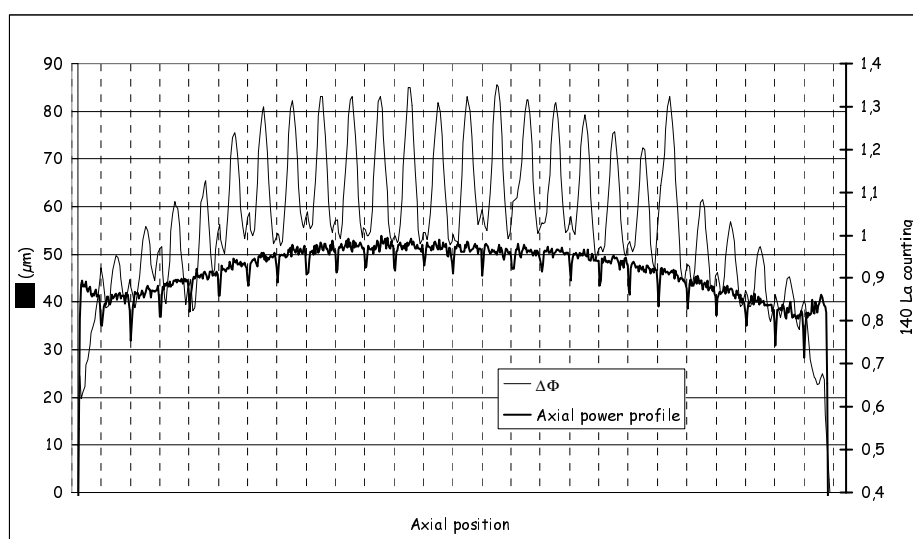
Neutron radiography has some advantages, compared to X radiography, to reveal the exact state of the fuel column and its characteristics. This method is more precise for pellet observation and, in case of clad failure, water in the rod can be easily detected due to the high neutron absorption of hydrogen. Figure 3 shows that neutron radiographic examinations before and after ramp testing allow following the evolution of major pellets cracks and dishes filling. The latter can also be approached by gamma spectrometry but, for precise estimation of the dish surface displacement, ceramography on a longitudinal cut is needed [Figures 3(c) and 3(d)].

Figure 3. Example of rodlet neutron radiography before (a) and after (b) ramp. Evidence of major radial cracks on pellets and of dishes filling. Correlation with destructive examinations: as an example (c) longitudinal cut on O4 rodlet (short holding time), (d) longitudinal cut on N4 rodlet (4 h holding time).



Gamma scanning of short-lived radioactive fissions products is first used at to estimate the axial power profile. The rod diameter profile is measured by profilometry performed at eight different angles before and after ramp testing. Comparison between the power profile and the $\Delta\Phi$ profile (diametral variation after and before the ramp testing, see Figure 4) shows that curves superimpose rather satisfactorily, indicating that cladding plastic deformation is a correlated function of local power.

Figure 4. Comparison between the diametral variation $\Delta\Phi$ and the axial power profile for the L3 rodlet after ramp testing



Destructive examinations

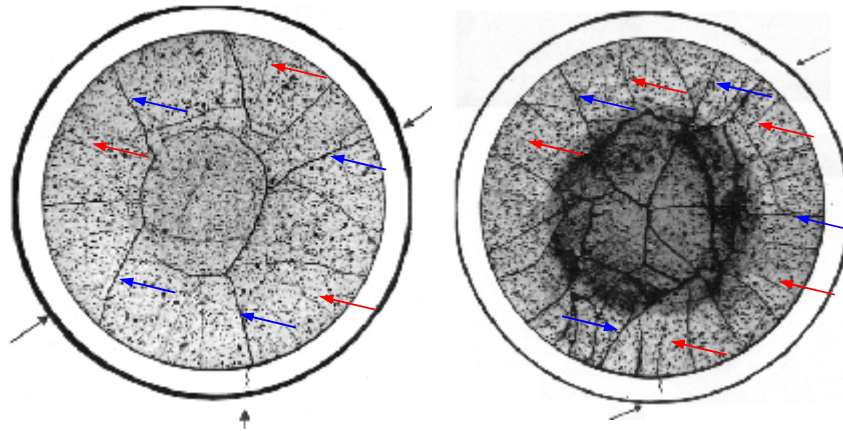
After non-destructive examinations in the hot cell, the rodlet is punctured to measure its internal pressure and to analyse the released gas. It is then cut at specific locations determined from previous examinations in order to perform optical observations of transverse and longitudinal sections as well as SEM examination of the cladding. Optical microscopy is mostly used to characterise fuel microstructure (pore distribution, pellet fragmentation...) [6] and cladding evolution or damage (inner and outer oxide layer thicknesses, hydride distribution, crack shape and azimuthal location...). As mentioned above, in case of a failed rod the observation of the cracks needs to be performed on an optical transverse section very close to the damaged inter-pellet plane. It can thus be observed that cladding cracks are just opposite important fuel radial cracks, as illustrated in Figure 5. The net of larger pellet cracks is a result of pre-irradiation in a PWR plant (blue arrows in Figure 5) while the secondary net of cracks is due to the re-irradiation experiment (red arrows). Figure 5 shows that clad PCI damage may be related to the primary net of pellet cracks as well as to the secondary one. These observations, concerning preferential positions of clad defects, are quite consistent with the evaluation of mechanical loading distribution at the inner surface of the clad [7]. But fuel cracks may also be considered as preferential paths for direct access of aggressive volatile fission products, like iodine, to the clad.

In order to gain a more precise knowledge of the embrittlement scheme of the cladding and compare it to the well known SCC mechanisms [8], SEM analysis has been performed in different cases. This is developed in the next section, in conjunction with clad deformation analysis.

Clad evolution

Since the main goal of the PCI safety approach is to ensure the integrity of rod cladding during severe Class 2 transients, special emphasis is placed here upon the observed evolution of cladding after ramp testing.

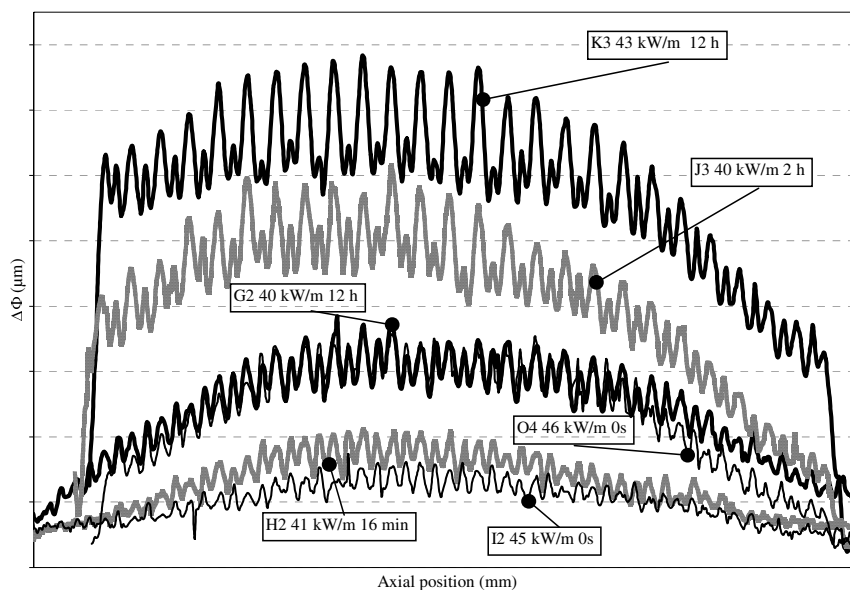
Figure 5. Cross-sections of rods D2 and C2 near the inter-pellet plane. Black arrows indicate the location of clad cracks.



Clad diametrical changes

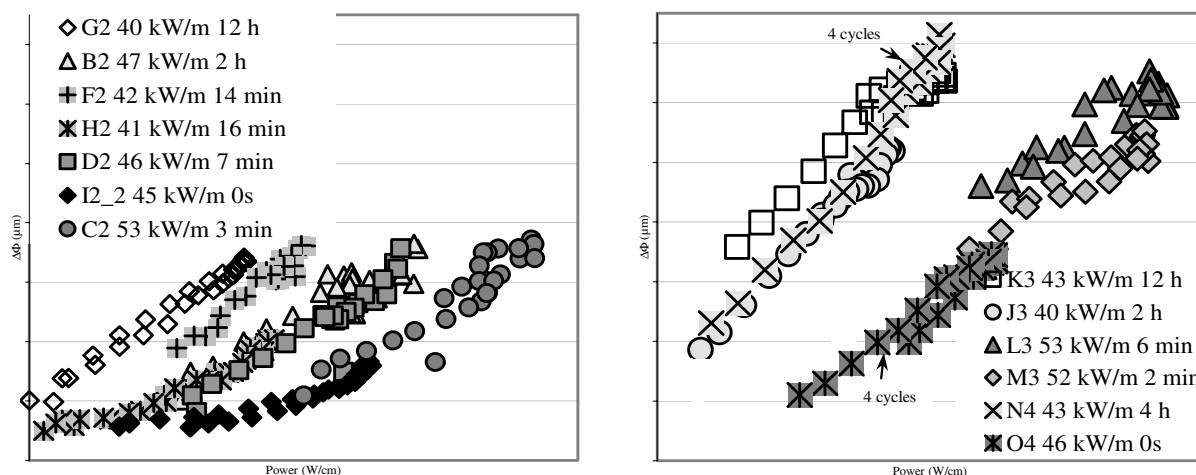
Clad diametrical variations caused by power ramps are shown in Figure 6 for several rods at different burn-ups and holding times. Primary (inter-pellet) ridges as well as small secondary (median pellet) ridges are already present before ramp testing, but their alteration after re-irradiation is more or less spectacular, depending on power level, holding time and burn-up. As illustrated in Figure 6, holding time appears to be an important parameter governing the growth of ridges, for a given burn-up, especially that of the secondary ones which end up developing to the detriment of the primary ridges. The characterisation of the cladding at the mid-pellet plane is probably not of major importance, from the point of view of failure conditions analysis, but it is however interesting to note the general great difference between the diametrical cladding changes observed after a long holding time and the ones existing a few minutes after power increase, which is when failure is likely to occur.

Figure 6. Diameter variations ($\Delta\Phi$) after ramp testing for some rods of the database from two to four cycles. Effect of the holding time, power and burn-up.



Permanent diameter variations at the inter-pellet plane are shown in Figure 7 as a function of local power. This representation facilitates the comparison between rods in spite of their very different experimental conditions.

Figure 7. Plastic diameter variations ($\Delta\Phi$) as the function of power at the inter-pellet plane for several rods from two to four cycles. The scales are the same for both graphs.



Plotted curves evidence the dependence of strain on burn-up and power, apart from the dependence on time. Indeed, for all rods, strain increases almost linearly with local power. Deformation is much more important for high burn-up rods than for low burn-up ones, as one can see for I2 and O4 rods (0 s holding time) or F2 and K3 rods (about 12 h holding time). Burn-up effect is first related to the thermal properties of the rod; that is, to the degradation of the fuel thermal conductivity and to the growth of the external zirconia layer. But high burn-up also results in an important gaseous swelling of fuel, which largely increases the displacement to be undergone by cladding.

Note that the measured deformations only concern the outer diameter of the cladding. Thus, their ranking may not be representative of that of the maximum local mechanical loading at the clad inner surface. Indeed, it is not exceptional that rods with large overall deformations remain sound after ramping [9]. The deformations, however, reveal the importance of the different inelastic phenomena that must be considered for good numerical simulation of PCI risk of failure [10].

Clad damage

The mechanisms of cladding failure by PCI have already been intensively studied. It is commonly accepted that it involves a SCC phenomenon induced by volatile fission products released during power ramp test; the most suspicious being iodine.

When cladding failure occurs during ramp test, optical microscopy examinations on transverse samples or by SEM on devoted samples are systematically carried out. The aims of these observations are to recognise the mechanisms of failure and to compare the different rods which have all undergone different stresses. Figures 8-11 provide typical views of cladding cracks obtained after power ramp tests.

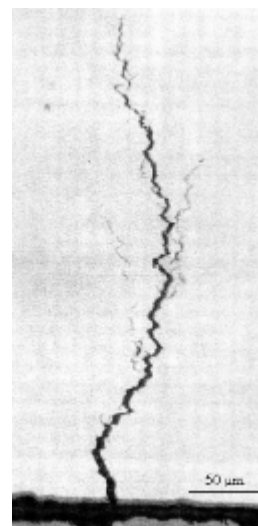
The transverse metallography (Figure 8) shows a branching crack with a 90° orientation to the stress direction. The crack opening is relatively large on the Figure 8(a) due to the final failure by ductile shear, but before total rupture, cracks have very small openings as compared to length in the direction of cladding thickness [Figure 8(b)]. All these characteristics are consistent with I-SCC.

Figure 8

(a) Through wall crack of the D2 rod on cross-section observed in optical microscope. Note the branching crack in the radial direction



(b) Optical micrograph of a partial through wall crack in the B2 rod. The opening of the fissure is very small.



For SEM examinations, cracks are opened to show the fracture surface. An overall view of the fracture is presented in Figure 9. It appears that the crack is very elongated in the axial direction. A more precise observation of the crack shows a typical aspect of SCC failure in all database rods. The crack face bordering the inside clad surface exhibits some intergranular details (Figure 10). At about 20 μm of the inside clad surface and up to $\sim 380 \mu\text{m}$ (which represent 2/3 of the cladding thickness), the fracture surface especially shows transgranular quasi cleavage and fluting (Figure 11) in which some intergranular details are sometimes present. The transition from brittle to ductile behaviour occurs at 2/3 of the clad thickness.

Figure 9. L3 fracture surface in SEM

Total view of the rupture (brighter contrast) with a very elongated form in the axial direction in comparison to the thickness of the clad

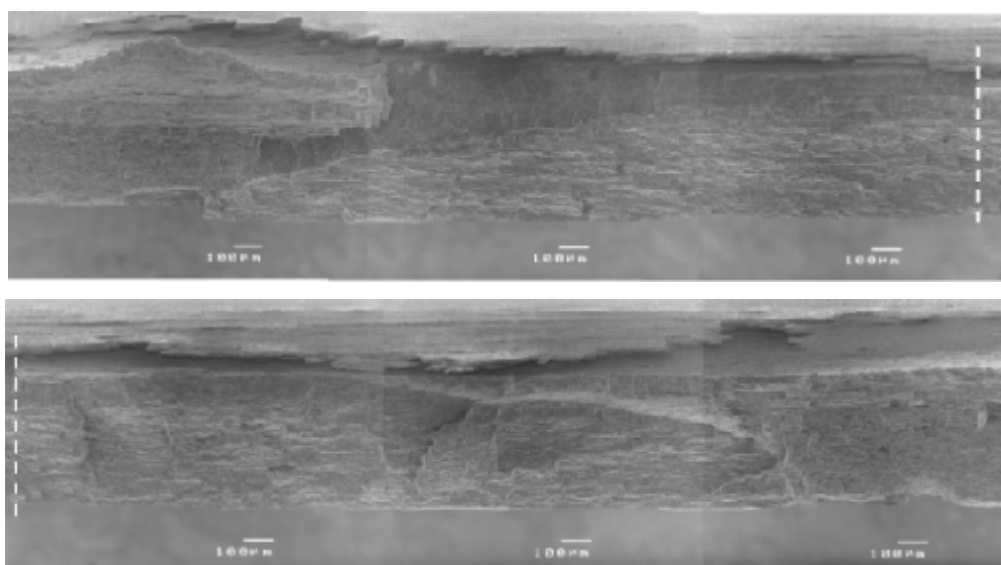


Figure 10. C2 fracture surface in SEM

Intergranular details near the inside clad face (circled in white) and after 15 μm , transgranular rupture with quasi cleavage and fluting (circled in blue)

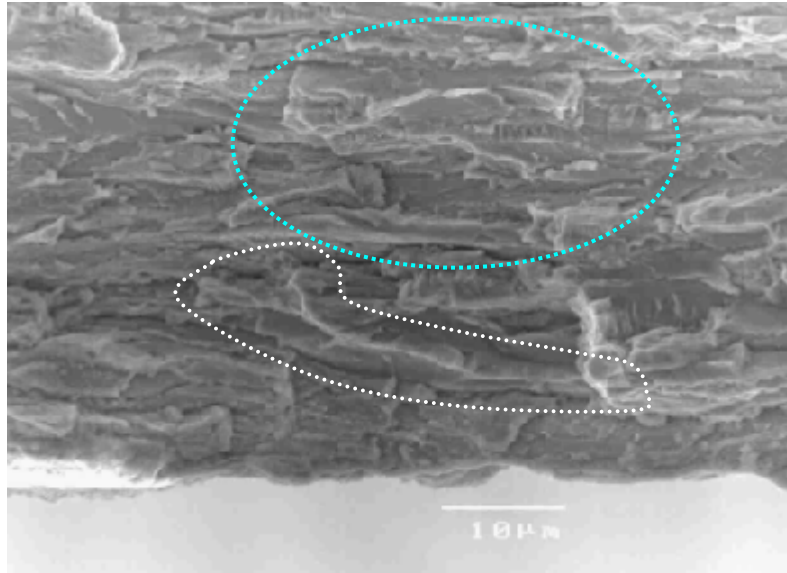
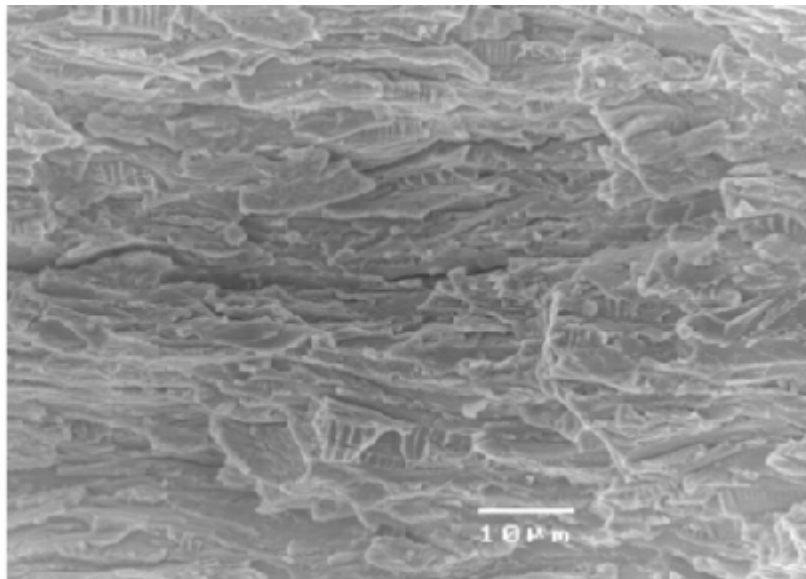


Figure 11. C2 SE micrograph. Transgranular rupture with quasi cleavage and fluting.



It thus appears that the PCI cladding failures all exhibit the same characteristics whatever the ramp conditions: typical SCC appearance, with a relatively large extension of the crack in the axial direction and a brittle to ductile transition arising at about 2/3 of the cladding thickness in the radial direction.

Some SEM examinations of non-cracked rods have also been carried out. A brittle fracture surface is often observed adjacent to the inside clad surface at a depth of a few μm (10-15 μm) even for rods which have been ramped at relatively low power (H2) and for rods maintained a long time at intermediate power (K3 for instance). It is difficult to determine if this embrittlement is due to SCC, because the

structure of the internal clad surface is modified during irradiation by ion implantation among other things, which can affect the appearance of the internal fracture surface after mechanical preparation of SEM samples. The distance of fission product implantation has already been calculated [11] and is estimated to be around 10 μm , i.e. the same order of magnitude as the embrittled surface. These cracks are therefore considered insignificant in terms of SCC embrittlement. Times to failure are provided in Table 2. Rods are ranked by increasing power conditions. For instance L3 has undergone the most severe ramp test conditions in terms of final power and power variation.

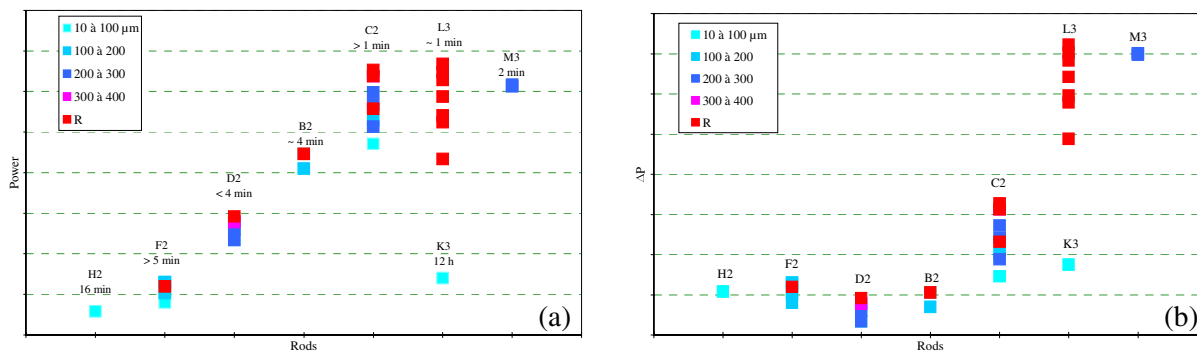
Table 2. Times to failure for ramp testings

	F2	D2	B2	C2	L3
t_R	5 min	4 min	4 min	1 min	1 min

The times to failure are all relatively short (< 6 min). Since the unique SCC mechanism has proven to be at the origin of the rupture, it may be stated that the kinetics of crack propagation are roughly the same as soon as crack initiation is over. Therefore time to failure differences must be essentially the result of differences in crack development kinetics in the initiation step. Crack initiation is closely bound to the mechanical loading of the cladding, generated by the UO_2 pellet fragments' displacement, and it is thus directly related to the power ramp test parameters. As power increases, the probability to initiate a crack increases as well, and for very high final power, the crack may be initiated during the transient, before the power stabilisation, inducing a short time to failure. Previous laboratories studies of I-SCC phenomenon had shown that the transgranular propagation kinetic can be around 150 $\mu\text{m}/\text{min}$ on average [12,13]. For an SCC radial spread of 380 μm , the clad requires more than 2 minutes to fail if cracking starts almost immediately after reaching the high power level, indicating that for all rods (except C2 and L3) crack initiation occurs during the high power level. This is consistent with the observations concerning the I2 rod, which has been ramped up to 45 kW/m with zero holding time. Post-irradiation examinations did not show any significant incipient crack and proved that SCC embrittlement does not occur during the power increase, at least up to this range of power.

The following analysis consists in an attempt to define a purely experimental failure criterion. The depth of clad cracks on different inter-pellet planes was measured on all optical or SE micrographs and ranked as a function of P and ΔP (Figure 12). Only cracks with a radial length higher than 10 μm were considered. It appears that above the power of F2 [Figure 12(a)], the rods exhibit many damaged IPs, particularly C2 and L3, which were tested under very severe conditions. M3 did not fail because it was maintained at high power only for a very short time. The conclusion for the ΔP graph [Figure 12(b)] is not so clear since the H2 rod is not damaged while its ΔP is of the same order as F2, D2 and B2.

Figure 12. Comparison of size of the clad crack with the local power (a) and with the increment of power ΔP (b). On (a) graph-indicated times are rupture times or for lack, holding times.



As local power controls local pellet geometry, with more or less severe cracks providing possible local “punching” of the inner side of the clad, local strain around the end of the power increase is probably a decisive parameter. But the measurements provide only the mean values of the external diameter, moreover at the very end of the test. Only modelling can thus give access to this parameter, at the right time [7]. If such information is lacking, power seems to be a good ranking parameter with a threshold rod: F2.

Note the importance of burn-up on the cladding embrittlement by SCC: for low burn-up no significant crack was observed on A1, whereas this rod underwent a more severe ramp test than B2. High burn-up rods seem to have a better resistance too; see K3 rods with only small cracks (20 μm max.). N4 tested with the same characteristics as K3, and no significant embrittlement was observed. The two-cycle rods are clearly more sensitive to embrittlement through SCC than one-cycle rods. A slight trend toward a better SCC resistance was also observed on high burn-up rods.

Conclusion

This paper aimed to describe cladding embrittlement during ramp tests conducted on Zy-4/ UO_2 standard rods in the OSIRIS reactor at CEA Saclay. Examinations were carried out on rods before and after re-irradiation in order to define clad failure locations and their characteristics. These examinations give access to a large range of complementary experimental results. Analysis of clad deformations shows that results are consistent in terms of burn-up, holding time and power impact. The burn-up effect is clearly evidenced based on the global deformation of the rod. Examinations of clad cracks show that the power ramp test failures all have the same characteristics whatever the ramp conditions: typical SCC fracture appearance, with an extension in the axial direction, and a brittle/ductile transition occurring at about 2/3 of the cladding thickness in the radial direction. A unique mechanism seems to be at the origin of failures. This is confirmed by the consistency of times to failure between the different rods. The analysis of crack lengths shows that two-cycle rods are more sensitive to SCC; the better behaviour of one-, three- and four-cycle rods is confirmed. Analysing the ramp tests in terms of failure criterion indicates that over a given local power, rod IPs can be seriously damaged. Local strain is probably a key parameter, but only modelling can lead to this very local information.

REFERENCES

- [1] Cox, B., J.C. Wood, “Iodine-induced Cracking of Zircaloy Fuel Cladding – A Review”, reprinted from *Corrosion Problems in Energy Conversion and Generation*, AECL Report 4936 (1974).
- [2] Roberts, J.T.A., E. Smith, N. Fuhrman, D. Cubicciotti, “On the Pellet-cladding Interaction Phenomenon”, *Nuclear Technology*, 35 (1977).
- [3] Davies, J.H., H.S. Rosenbaum, T.C. Rowland, J.S. Armijo, “Fuel Pellet-cladding Interaction in Light Water Reactors”, *ASME Annual Conference Proceedings* (1984).
- [4] Joseph, J., J. Royer, M. Grosgeorge, “Transient Behaviour of Fragema Fuel Rods Previously Irradiated Under Commercial Conditions”, *LWR Fuel Performance*, Williamsburg (1988).

- [5] Alberman, A., *et al.*, “Technique for Power Ramp Tests in the ISABELLE 1 Loop of the OSIRIS Reactor”, *Nuclear Engineering and Design*, 168 (1997).
- [6] Nonon, C., *et al.*, “Impact of Fuel Microstructure on PCI Behaviour”, *Proceedings of the IAEA TCM on Improved Fuel Materials and Designs*, Brussels, Belgium (2003).
- [7] Bentejac, F., N. Hourdequin, “Toutatis: An Application of the Cast3M Finite-element Code for Three-dimensional Modelling of PCI in PWR Fuel”, these proceedings.
- [8] Le Boulch, D., *et al.*, “Iodine-induced Stress Corrosion Cracking”, these proceedings.
- [9] Nonon, C., *et al.*, “PCI Behaviour of Chromium Oxide-doped Fuel”, these proceedings.
- [10] Struzik, C., *et al.*, “Methodology for Multi-dimensional Simulation of Power Ramp Tests”, these proceedings.
- [11] Fregonese, M., G. Delette, G. Ducros, F. Lefebvre, “Amount of Iodine Responsible for I-SCC of Zircaloy-4 in PCI Conditions: Recoil Implanted and Thermally Released Iodine”, *Nuclear Engineering and Design*, 186 (1998).
- [12] Lefebvre, F., B. Verhaeghe, L. Rouillon, *Présentation des bases physiques d’un modèle de corrosion sous contrainte par l’iode des alliages de zirconium pour décrire l’endommagement des gainages en situation d’IPG*, internal CEA note (2000).
- [13] Cox, B., “Pellet-clad Interaction (PCI) Failures of Zirconium Alloy Fuel Cladding – A Review”, *Journal of Nuclear Materials*, 172 (1990).

EXPERIMENTAL DATA ON PCI AND PCMI WITHIN THE IFPE DATABASE

J.C. Killeen,¹ E. Sartori,² J.A. Turnbull³

¹IAEA

²NEA

³Consultant

Abstract

Following the conclusions reached at the end of the FUMEX-I code comparison exercise, the International Fuel Performance Experimental Database (IFPE) gave priority to collecting and assembling data sets addressing: thermal performance, fission gas release and pellet-clad mechanical interaction (PCMI). The data available that address the last topic are the subject of the current paper.

The data on mechanical interaction in fuel rods fall into three broad categories:

1. Fuel rod diameter changes caused by periods spent at higher than normal power.
2. The result of power ramp testing to define a failure threshold.
3. Single effects studies to measure changes in gaseous porosity causing fuel swelling during controlled test conditions.

In the first category, the fuel remained un-failed at the end of the test and the resulting permanent clad strain was due to PCMI caused by thermal expansion of the pellet and gaseous fuel swelling. Some excellent data in this category come from the last two Risø Fission Gas Release projects. The second category, namely, failure by pellet-clad interaction (PCI) and stress corrosion cracking (SCC) involves the simultaneous imposition of stress and the availability of corrosive fission products. A comprehensive list of tests carried out in the Swedish Studsvik reactor is included in the database. The third category is a recent acquisition to the database and comprises data on fuel swelling obtained from ramp tests on AGR fuel and carried out in the Halden BWR. This data set contains a wealth of well-qualified data which are invaluable for the development and validation of fuel swelling models.

Introduction

The aim of the International Fuel Performance Experiments Database (IFPE) is to provide a comprehensive and well-qualified database on Zr clad UO_2 fuel for model development and code validation in the public domain. The data encompass both normal and off-normal operation and include prototypic commercial irradiations as well as experiments performed in material testing reactors.

The database is restricted to thermal reactor fuel performance, principally with standard product zircaloy-clad UO_2 fuel, although the addition of advanced products is included where available, e.g. fuel including MOX, gadolinia and niobia, etc., and clad variants. Emphasis has been placed on including well-qualified data that illustrate specific aspects of fuel performance. Following the conclusions reached at the end of the FUMEX-I code comparison exercise, priority was given to collecting and assembling data sets addressing: thermal performance, fission gas release and pellet-clad mechanical interaction (PCMI). Whilst most of the data sets concern irradiation experiments on fuel rods, data on out-of-pile tests investigating fission gas release and fuel swelling are also included. The list of data sets currently available is given in Table 1. No references are given in this paper as all appropriate documentation was scanned and accompanies the data sets on the CDs supplied by the NEA.

The mechanical interaction between fuel pellets and cladding

In the case of water-cooled reactors, the fuel rods are made up of ceramic fissile pellets of UO_2 or $(\text{Pu,U})\text{O}_2$ contained in a zirconium-based alloy tube. At the beginning of the irradiation, there is a distinct circumferential gap between the external face of the fuel pellets and the inner bore of the cladding tube. On raising power, this gap is reduced through thermal expansion of the pellet. This gap becomes less distinct as the ceramic pellets crack under the influence of the radial temperature gradient. The distance between the pellet surface and the cladding inner bore is further reduced as the pellet fragments relocate radially outwards. The free volume is now shared between the residual gap and the space between pellet fragments.

As irradiation proceeds, the cladding diameter reduces by creep driven by the compressive hoop stress induced by the difference between coolant pressure and the internal pressure of the fuel rod. Eventually, the cladding creeps down onto the fuel finally eliminating the fuel-to-clad gap and moving the pellet fragments closer together. As a rough guide, this occurs during the second cycle of irradiation in the burn-up range 10-20 MWd/kg. Prior to gap closure, the cladding is under a compressive hoop stress. Once the gap is closed and the cladding and pellet fragments are in contact, the hoop stress gradually decreases as the pellet fragments resist the reduction in cladding diameter. The hoop stress in the cladding eventually becomes positive when all the internal free space is exhausted and the pellet fragments are in intimate contact.

At any stage during irradiation, an increase in power can cause the pellets to expand through both thermal expansion and fission product swelling to induce a positive hoop stress in the cladding. The immediate reaction of the cladding is to expand outward by elastic deformation and subsequently by plastic strain and creep, thus reducing the interfacial stress. This interaction between the fuel pellet and the cladding is termed pellet-clad mechanical interaction (PCMI). If, however, the clad hoop stress is sufficiently large, and the pellet temperature is high enough to release corrosive fission products, internal cracks may be initiated at the inner bore by stress corrosion cracking (SCC) which grows under the influence of the maintained hoop stress such that the cladding fails. The generic term for this is failure by pellet-clad interaction (PCI).

Operation of commercial reactors with failed cladding is not a viable option as it compromises safety and leads to a highly contaminated primary coolant circuit resulting in difficulties with maintenance and fuel handling on discharge. Reactors are sometimes operated intentionally with a small number of small cladding defects, but wherever possible such failures are avoided by careful choice of materials, manufacturing quality assurance measures and operating constraints. In order to define the limit of safe operation, it is necessary to develop fuel performance codes to calculate PCMI effects and validate the predictions against experimental data on cladding diameter change. To take the predictions further by calculating probability of failure, code predictions must be compared with the results of dedicated ramp tests providing statistics including both failed and un-failed rods.

Such data are available, and it has been the intention of the IFPE Database to include as much useful data as possible for use by code developers. This paper sets out to guide users to the most appropriate data for their requirements. To this end, discussion of the data is provided under the following three headings:

- Fuel rod diameter changes induced by PCMI.
- The definition of the PCI failure threshold.
- Single effects studies to measure fuel swelling during controlled test conditions.

The first two topics have already been discussed. The third has been alluded to when discussing expansion of the fuel pellet. In effect, along with thermal expansion, fuel swelling is one of the driving forces for PCMI. Whereas inexorable swelling caused by the incorporation of fission products in the lattice is a linear function of burn-up, the concern here is the formation and behaviour of gas bubbles when they are created during high-power operation. As will be seen later, the data set included in the database is a highly detailed and valuable study of this phenomenon.

Fuel rod diameter induced PCMI

The major part of this data set is made up of PIE diameter measurement before and after fuel rods have been subjected to a period of high power. There are three main data sets addressing this behaviour. These will be discussed first, followed by a small number of cases concerning the related effect of clad length changes driven by expansion of the fuel column. These are all in-pile measurements which can illustrate some of the dynamic effects of PCMI. Additional data are available from the series of Studsvik ramp tests and these are discussed further on.

The Risø Transient Fission Gas Release Project

In this project, short lengths of irradiated fuel were fitted with in-pile pressure transducers and ramped in the Risø DR3 reactor. The fuel used came from either IFA-161 irradiated in the Halden reactor or from GE segments irradiated in the Millstone BWR. Using this refabrication technique, it was possible to back-fill the test segment with a choice of gas and gas pressure and to measure the time dependence of fission gas release by continuous monitoring of the plenum pressure. The short length of the test segment was an advantage because, depending on where along the original rod the section was taken, burn-up could be a chosen variable, and during the test the fuel experienced a single power. Some segments were tested without refabrication. Here the fuel stack was longer than in the case of the refabricated tests and hence the segments experienced a range of powers during the ramp

depending on axial position in the test reactor. These “unopened” segments were used to confirm that refabrication did not affect the outcome of the tests. Extensive hot cell examination compared the fuel dimensions and microstructure before and after the tests.

Some 17 tests were performed and all but one (which failed) have been included in the database and provide valuable clad diametral deformation (ΔD) and fuel swelling as a function of ramp power and hold time. A summary of the test matrix is given in Table 2 with a brief comment on the degree of PCMI observed. It was noticeable that the Halden irradiated fuel, i.e. the “Risø” tests, showed distinct ridging and ridge height growth, unlike the GE tests, where there was little evidence of this. This contrast in behaviour is illustrated in Figure 1 showing the diameter traces before and after tests Riso-a and GE-a. Figure 2 shows the variation in diameter change observed for GE-i which was tested without refabrication. It is clear that the diameter change is a function of position and hence power during the test.

Figure 1(a). Traces of rod diameter before and after testing for Riso-a, showing distinct ridges and ridge growth

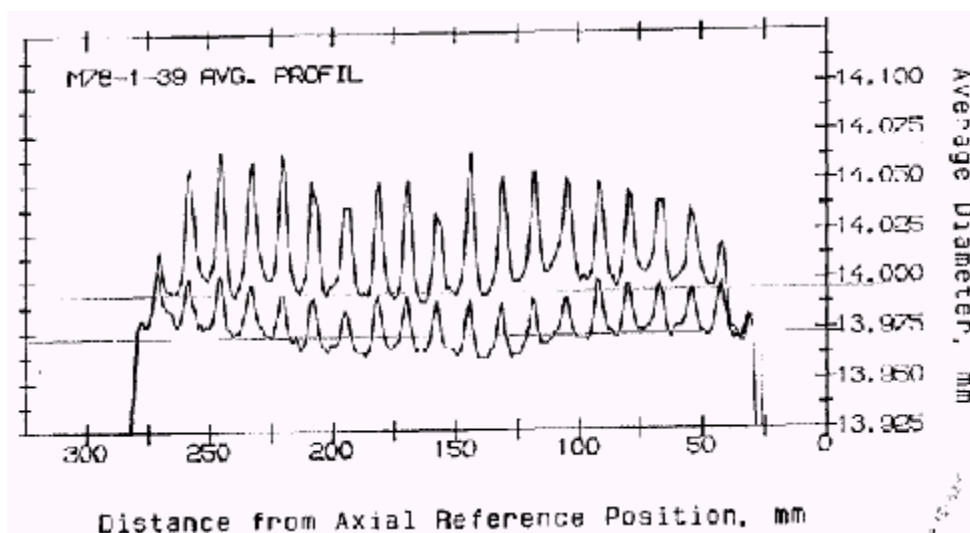


Figure 1(b). Traces of rod diameter before and after testing for GE-a showing indistinct evidence of ridging

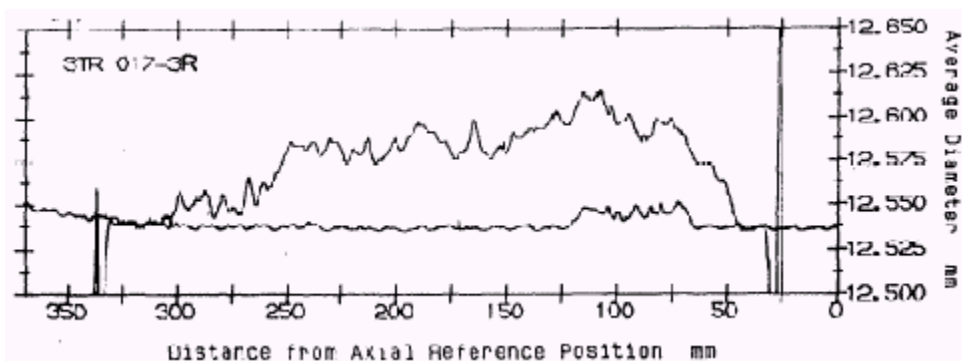
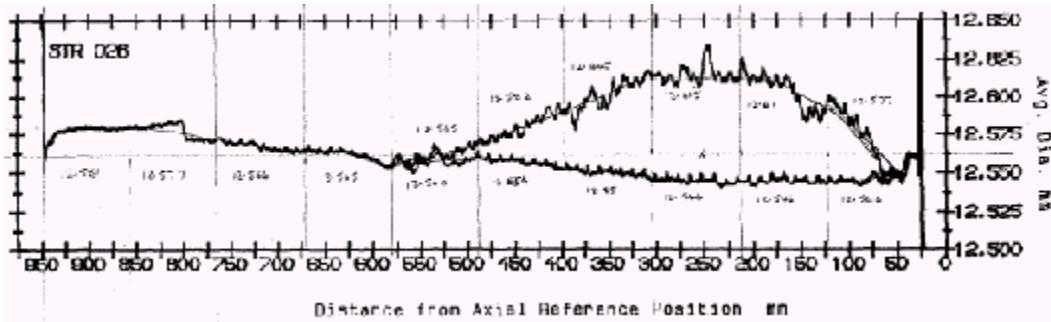


Figure 2. Diameter traces before and after test GE-i showing the dependence of diameter change on position and hence power during the test



The Third Risø Fission Gas Release Project

The third and final Risø project was very similar to the previous one with the exception that many rods were refabricated with pressure transducers and thermocouples, hence the data generated was complemented by knowledge of fuel centreline temperatures during the high-power test. The fuel used in the project was from: IFA-161 irradiated from 13-46 MWd/kgUO₂ in the Halden BWR, GE BWR fuel irradiated from 20-40 MWd/kgUO₂ in Quad Cities 1 and Millstone 1, and ANF PWR fuel irradiated in Biblis A to 38 MWd/kgUO₂. There were seven tests using PWR fuel, three of which were long sections without refabrication. Four tests used GE BWR fuel, one of which was a long section without refabrication and four tests used sections cut from IFA-161 rods. The tests consisted of a period held at a constant high power but, as in the previous project, some tests had short duration over and under power peaks and dips, respectively. These were conducted expressly to investigate axial gas transport to the plenum where the in-pile pressure transducer was situated. An overview of the test matrix is shown in Table 3 whilst an example of diameter traces before and after test AN3 is shown in Figure 3. Note in particular the growth of ridges at the pellet ends and the reduced deformation over the thermocouple. This is on account of the reduced power and lower PCMI induced by the hollow pellets. The large diameter change and its dependence on axial position for test GE7 is shown in Figure 4.

Figure 3. Axial diameter traces before and after test AN3. Note the growth of ridges and reduced deformation over the thermocouple.

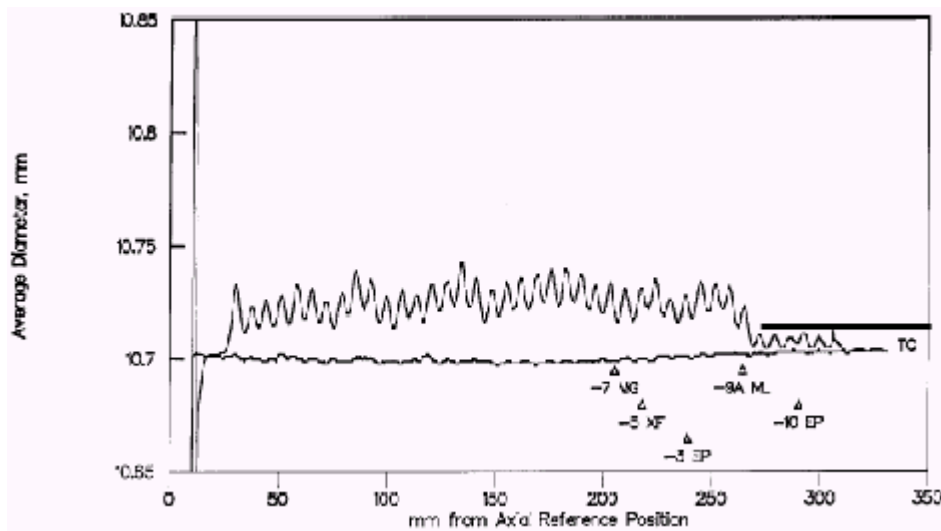
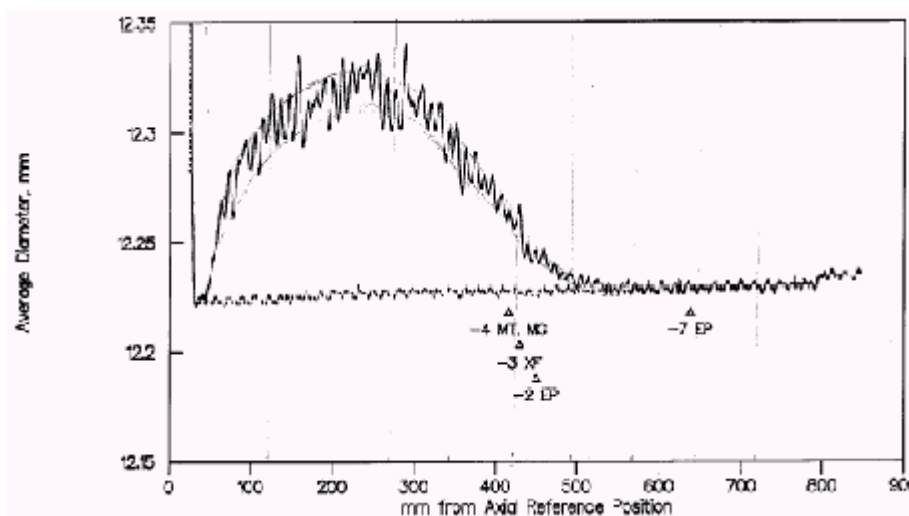


Figure 4. The axial variation in diameter before and after the test GE7. The variation in ΔD is on account of the axial power profile over this long rod.



Both figures show the positions at which sections were cut for PIE by transverse metallography (MT), longitudinal metallography (ML), transverse micro gamma scanning (MG), transverse X-ray fluorescence (XRF) and transverse electron probe micro analysis (EPMA). Thus the diameter changes are accompanied by detailed measurements of grain size, gas bubble and fission product distributions.

CEA/EDF/FRAMATOME PWR rods ramped in OSIRIS

This data set contains details of three standard PWR rods and one segmented rod irradiated in EDF commercial reactors. One rod and one segmented rod were refabricated and ramp tested in the CEA OSIRIS reactor to investigate their PCI resistance. The data set contains details of the pre-characterisation of the fuel pellets, the cladding tube and the assembled fuel rod.

Segment J12-5 was from the fifth span of the segmented rod J12 irradiated for two cycles in Gravelines 5 to 23.8 MWd/kgU. This was refabricated with new end plugs without disturbing either the fuel column or the internal fill gas and ramp tested in OSIRIS. After conditioning at 21 kW/m it was quickly ramped and held at 39.5 kW/m and discharged without failure.

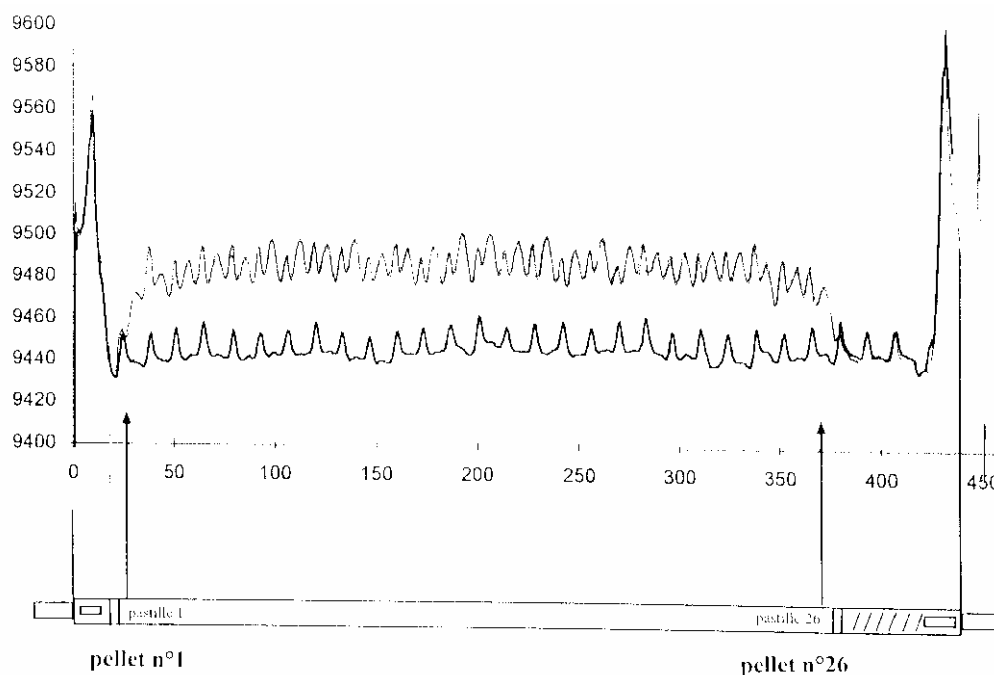
K11 was a full-length rod irradiated to 25.4 MWd/kgU for two cycles in Gravelines 3. A section of this rod was cut from span 5 between grids and ramp tested as K11-5 in OSIRIS. After conditioning at 24 kW/m it was quickly ramped and held at 43.7 kW/m and discharged without failure.

The ramp induced measurable diameter change and ridge height growth in both tests. Figure 5 shows the diameters before and after the ramp for K11-5. Of particular interest in this figure is the growth of secondary ridges located at the mid-length of the pellets. This was also observed in J12-5.

Halden in-pile cladding length changes

Many irradiations carried out in the Halden reactor contain rods fitted with clad elongation detectors. These enable a measure of clad length to be made in-pile providing data as a function of power, time and burn-up. As such, the data are extremely useful for evaluating the interaction between

Figure 5. Diameter traces before and after ramp testing section K11-5 in the CEA OSIRIS reactor

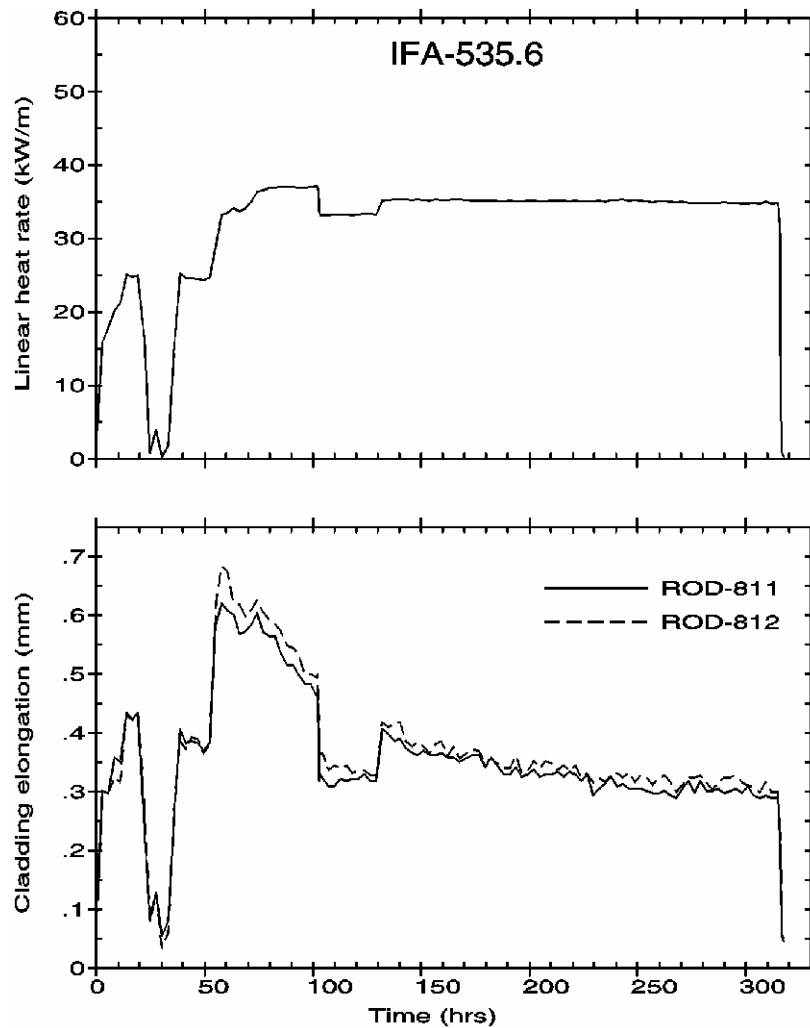


pellet and cladding under various irradiation conditions. The database contains such data for experiments IFA-432 rods 2, 3 and 6, IFA-535.5 and .6 and IFA-597.3 rod 7. IFA-432 contained rods of different grain sizes and was irradiated in the HBWR to provide information on the thermo-mechanical behaviour of fuel rods for code development. PCMI was observed at the start of life for the small gap rod 3, but it was not observed to any degree in the large gap rods 2 and 6 until there was appreciable fission gas release and swelling. IFA-535.5 and .6 were rods irradiated to 44 MWd/kgUO₂ at modest powers in IFA-409 before re-instrumentation and ramping in IFA-535; two rods were fast ramped in loading five and two other rods were subjected to a slow ramp in the sixth loading. The third loading of IFA-597 contained two rods of which rod 7 was fitted with a clad elongation detector. The fuel was cut from rods previously irradiated at low power to a high burn-up of 59 MWd/kgUO₂ in the Ringhals 1 BWR. On re-irradiation in Halden, the rod power was increased to 30 kW/m and decreased slowly to ~22 kW/m at a burn-up of 61 MWd/kgUO₂. In all cases, an increase in power is accompanied by an increase in cladding length which subsequently relaxes. A typical behaviour is illustrated in Figure 6 for the slow-ramped rods in IFA-535.6.

The definition of the PCI failure thresholds

The Studsvik laboratories in Sweden have specialised in performing ramp tests to establish the propensity to failure of different design fuel rods. They have carried out many sponsored programmes of which the database contains the results from the BWR projects INTER-RAMP, SUPER-RAMP, DEMO-RAMP 1 and 2 and TRANS-RAMP 1. Concerning PWR fuel, the database contains results from OVER-RAMP, SUPER-RAMP, TRANS-RAMP 2 and 4; in all, some 54 BWR rods and 80 PWR rods. This section concentrates on the data available to define the failure threshold but, in addition, the PIE carried out in the various programmes also produced good data on diameter change and ridge height growth.

Figure 6. In-pile clad elongation as observed during a slow ramp and hold in the Halden experiment IFA-535.6. Note the relaxation during the period of constant high power.



The Studsvik INTER-RAMP BWR Programme

The objectives of this project were to establish the fail-safe operating limits of 20 standard-type, unpressurised BWR fuel rods on over-power ramping at the burn-up levels of 10 and 20 MWd/kgU. The over-power ramping was to be performed at a fast ramp rate of about 4 kW/m/min with the preceding base irradiation performed to represent the conditions in a typical commercial BWR power reactor. The fuel was manufactured by ASEA-ATOM and irradiated in boiling capsules (BOCA) in the Studsvik R2 reactor. The disposition of the rods in the boiling capsules resulted in “high” and “low” power groups of rods. The study investigated the influence of three main design parameters: clad heat treatment (re-crystallised anneal “RX” vs cold work plus stress relief anneal “SR”), pellet/clad diametral gap size and fuel density. Ramping was to power levels ranging between 41 to 65.4 kW/m resulting in 11 failures. A failure threshold around 42-43 kW/m was found for the low power rods and a threshold of around 47-48 kW/m was found for high power rods. PIE was performed to measure diameter changes and ridge height growth.

The Studsvik SUPER-RAMP BWR Sub-programme

The BWR sub-programme consisted of three groups of rods with variations in design and material parameters. The rods were base-irradiated in BWRs Würgassen or Monticello at average heat ratings in the range 11-23 kW/m to peak burn-ups in the range 28-38 MWd/kgU and were subsequently ramp-tested in the R2 reactor at Studsvik. The major results can be summarised as follows:

- *Standard-type KWU fuel rods, group BK7:*
 - When ramped as a single fast ramp from a conditioning power of 25 kW/m, a failure threshold for PCI/SCC was found at 32.5-36 kW/m and power change of 7.5-11 kW/m. Performing the ramps in two steps with conditioning after the first step for 12-24 hours at 32.5 kW/m increased the threshold to at least 37.5 kW/m with a permissible power change of >12.5 kW/m.
 - Single ramps from 18 kW/m provided a failure threshold of 30-33 kW/m with a power change of 12-15 kW/m.
 - Ramp testing up to 40.5 kW/m produced only small dimensional changes, little FGR and slight fuel structure changes. Thin layers containing uranium and fission products were found on the inside surface of the clad only at pellet-to-pellet interfaces or at the location of pellet cracks.
- *Standard GE fuel rods groups BG8 and BG9.* These rods were tested with various ramp rates and final power levels. It was possible to define the conditions below for which no failures were experienced:
 - Single-step ramping from 21.5 kW/m to 41.5 kW/m for the lowest ramp rates tested, 0.033 W/cm/min.
 - Single-step ramping from 21.5 kW/m to 32 kW/m at a safe ramp rate of 0.044 W/cm/min, and from 32 kW/m to 38 kW/m at 0.033 W/cm/min.
 - Up to 44 kW/m there were considerable dimensional changes, little FGR and moderate fuel structure changes.

The Studsvik DEMO-RAMP 1 BWR Programme

Five rods were manufactured by BNFL and irradiated in Ringhals 1 at powers 16-29 kW/m to burn-ups of 14-17 MWd/kgU. The rods encompassed three PCI remedy candidates:

- Annular short length pellets.
- Nb₂O₅-doped UO₂ of large grain size.
- High helium pressure.

The project demonstrated an improved performance for all potential remedies as no rods failed during R2 ramping to powers in the range 46-61 kW/m.

The Studsvik TRANS-RAMP 1 BWR Programme

Five KWU BWR design test fuel rods were ramp-tested under a very fast power increase after base irradiation in the Würgassen power reactor at heat ratings in the range of 20-30 kW/m to burn-ups in the range of 18-21 MWd/kgU.

After conditioning at 30 kW/m for 24 hours, the rods were ramped at a rate of approximately 1 000 kW/m/min to power levels in the range of 47.5-56 kW/m. Two of the rods were held at the ramp terminal level long enough to give an indication of failure by the rod elongation sensor, after 58 and 74 seconds, respectively, and later a release of fission product activity to the coolant.

Three of the ramp tests were purposely terminated after a very short time (18.5, 35.5 and 55.5 seconds). Incipient cracks with cladding wall penetration up to 20-50% of the wall thickness were found at pellet interfacial positions in the rods tested as interrupted ramp tests. No incipient cracks were observed at axial regions corresponding to local powers below 40 kW/m. It was concluded that incipient cracks are formed in the cladding if the failure threshold power level is exceeded. The development of the cracks is dependent on time and power.

The Studsvik OVER-RAMP PWR Programme

The programme power-ramped 39 individual test fuel rods of two different origins and designs. Twenty-four (24) of the rods were of KWU/CE design and were provided by KWU. They were delivered to the project following base irradiation in Obrigheim to burn-ups in the range 12-31 MWd/kg. Fifteen (15) of the rods were of Westinghouse design and were delivered after irradiation in the BR-3 reactor at Mol, to burn-ups in the range 16-24 MWd/kgU.

The KWU rods were ramped to final power levels in the range 37.8-53.0 kW/m producing failures in seven rods. The Westinghouse rods were ramped to final power levels in the range 37.5-44.5 kW/m producing failures in seven rods. The KWU rods were divided into six sub-sets whilst the Westinghouse rods were in four sub-sets. Taken individually, failures and no failures were obtained in all sub-sets apart from one KWU sub-set where no failures occurred. For all but this sub-set, failure thresholds could be devised, but the small number of rods and hence poor statistics meant that any derived value had a large uncertainty.

The SUPER-RAMP PWR Sub-programme

This consisted of six groups of rods with variations in design and material parameters. The KWU/CE rods were base-irradiated in the Obrigheim power reactor whilst the Westinghouse supplied rods were irradiated in BR-3. KW/CE rods were identified in four sub-groups: PK1, PK2, PK4 and PK6, with burn-up levels 11-12, 21-23, 21-22 and 22-25 MWd/kg, respectively. The Westinghouse rods formed two sub-groups (PW3 and PW5) having achieved 35-38 and 39-41 MWd/kgU, respectively.

The result of the ramp testing can be summarised as follows:

- *Standard-type fuel rods, group PK1 and PK2.* All rods sustained ramping to power levels in the range 41-49 kW/m and power changes 16-24 kW/m without failure, in spite of large deformations, fuel restructuring and fission gas release particularly for the PK2 rods.
- *Standard rods containing gadolinia, group PK4.* The rods all sustained power ramping to levels in the range 39-50.5 kW/m and power changes 14-25 kW/m without failure, in spite of large deformations, fuel restructuring and fission gas release.

- *Test fuel rods containing large grain size fuel, group PK6.* A failure threshold of 44 kW/m and power change of 18.5 kW/m was established for these rods. The fuel restructuring was modest and the fission gas release was low compared to other PK rods. Significant fuel bonding between fuel and cladding was found.
- *Standard rods, group PW3.* A failure threshold of ~37.5 kW/m was found and a power change of 12.5 kW/m.
- *Test fuel rods containing annular pellets, group PW5.* The rods all failed at power levels 38-43 kW/m with a power change of 13-18 kW/m. Hence there was no improvement in failure resistance over standard solid pellet rods.
- *General observations.* The inside clad of all ramped rods in groups PK1, PK2 and PK4 was mostly covered with a thin layer of deposits containing uranium and fission products. On PK6 rods, significant bonding between fuel and clad was found in large patches.

The Studsvik TRANS-RAMP 2 PWR Programme

The project's test programme consisted of ramping six fuel rods manufactured by Westinghouse and irradiated in the Zorita (Jose Cabrera) nuclear power plant in Spain. These rods had been base-irradiated at heat ratings in the range of 20-22 kW/m.

After conditioning at 20 kW/m for six hours the rods were ramped at a rate of about 100 W/cm/min to power levels in the range of 43-60 kW/m. Of the six fuel rods, three failed after 48-80 seconds (from the start of the ramp) while the remaining three were un-failed after 26-60 seconds. These results showed the relationship between rod power at failure and the time.

The rods underwent a thorough examination programme, comprising characterisation prior to the base irradiation, non-destructive examination between the base irradiation and the ramp irradiations, on-line measurements during the ramp irradiation and both non-destructive and destructive examinations after the ramp irradiations. Clad inside inspections give a correlation between the formation of incipient (non-penetrating) cladding cracks and the rod linear power indicating a damage threshold of about 40 kW/m, possibly lower.

The Studsvik TRANS-RAMP 4 PWR Programme

Seven test fuel rods, re-fabricated by the CEA-FABRICE process from full-size PWR fuel rods of standard FRAGEMMA design irradiated to a burn-up of about 28 MWd/kgU in the French reactor plant Gravelines 3, were made available to the project.

Four of the test fuel rods were used for exploratory ramp tests to obtain information on the failure boundary curve and on the ramp test data needed to produce incipient cracks in the cladding of the fuel rods.

The remaining three test fuel rods underwent first a power transient in the R2 loop No. 1, then an irradiation at PWR conditions in a BOCA rig in the R2 to give a burn-up increment of about 4 MWd/kgU, and finally, a second power ramp, to about the same power level as during the first power transient, but with hold to failure.

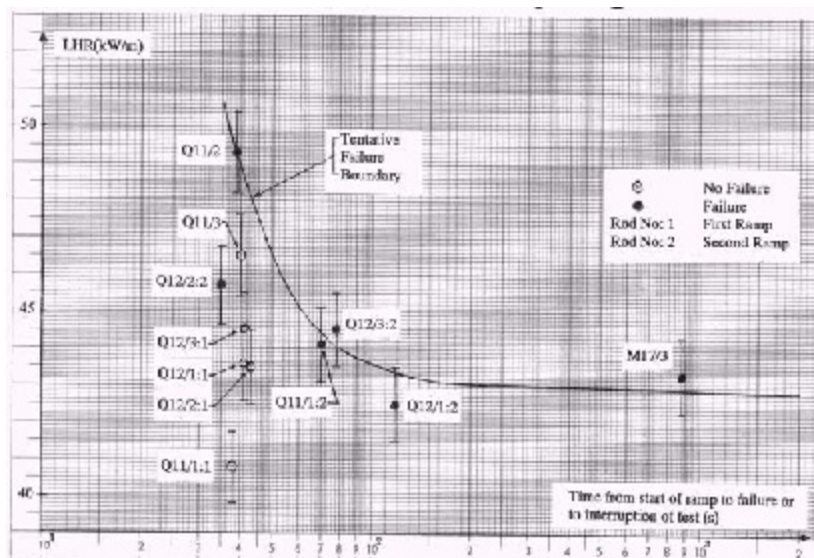
Based on the ramp results and the results of the non-destructive examinations of the three rods performed prior to, between and after the three irradiation phases the following conclusions were drawn:

- The first transient caused the formation of incipient cladding cracks in only one of the rods. This also rod had the largest amount of pellet-to-pellet dish filling.
- The BOCA irradiation caused a propagation of the cracks in the rod containing incipient cracks.
- The second power ramp caused a further propagation of the cracks in the rod containing incipient cracks and caused the rod to fail with a time to failure shorter than would be expected for a rod going through a first transient. This implied that this rod was exposed to cumulative damage which resulted in enhanced failure during the second power ramp.
- For the two other rods it was not possible to draw any firm conclusion about the influence of the first transient on the rod behaviour during the second ramp test due to the lack of an established failure boundary curve for rods ramped only once. Comparing results of previously performed ramp test projects, it seemed probable that the first transient did not influence rod behaviour during the second ramp test.

The test matrix is shown in the table below, whilst the results are synthesised to produce a failure boundary in Figure 8.

Rod	Ramp 1	BOCA irradiation	Ramp 2
M12/3	Yes – failed	–	–
Q11/1	Yes – no failure	–	Yes – failed
Q11/2	Yes – failed	–	–
Q11/3	Yes – no failure	–	–
Q12/1	Yes – no failure	Yes	Yes – failed
Q12/2	Yes – no failure	Yes	Yes – failed
Q12/3	Yes – no failure	Yes	Yes – failed

Figure 8. Failure threshold derived from the results of the TRANS-RAMP 4 PWR programme



Single effects studies on fuel swelling

This data set comprises measurements of inter- and intra-granular porosity and associated swelling from an extensive study of UO₂ fuel power ramped in the Halden reactor. The ramp tests were performed to study the mechanisms of PCI in advanced gas-cooled reactor (AGR) fuel, with the initial clad deformation measurements supplemented by the use of transmission electron microscopy (TEM) and scanning electron microscopy (SEM). Although the cladding in this case was stainless steel, the data on fuel swelling are generic and equally applicable to LWR fuel modelling.

Fuel specimens from 11 ramped rods and two control/reference rods were examined using TEM and SEM. For each specimen, swelling measurements were made at four or five radial locations in the fuel. At least six full grain boundaries were used for the inter-granular study at each location and three complete trans-granular fractures employed for the intra-granular bubbles. In the latter case, the trans-granular regions were examined under very high magnifications to reveal pores as small as 20-25 nm diameter. The SEM study comprises nearly three thousand micrographs.

The microscope study was augmented by use of the ENIGMA fuel modelling code to obtain estimates of the local temperatures and conditions from which the SEM/TEM samples were obtained.

In addition, un-ramped samples of the same fuel were annealed to temperatures of 1 600-1 900°C in a combination of different temperature ramp rates, maximum temperature attained and hold times. Measurements of fission gas release were made during the anneal with porosity distribution and swelling measurements made after the anneal.

The data contained in this data set are extensive and provide invaluable information to fuel modellers on the mechanisms involved in gas porosity formation, both intra- and inter-granular. The use of different ramp rates and the “park” period after ramping allows important conclusions to be drawn regarding bubble nucleation, the effects of vacancy starvation and the influence of irradiation induced re-resolution. As such, the measurements provide the necessary data on which to develop and validate a model describing the dynamics of fuel swelling during the course of an over-power transient. For further details of this data set, reference should be made to the appropriate paper presented at this workshop.

Concluding remarks

Access to the database is through the NEA, who provides the data and documentation on CDs. While every care has been taken in preparing complete error-free data sets, there is sometimes a need to issue revisions. It is important therefore that all users be registered with the NEA so any revisions are sent to them as a matter of course. There is no charge made for this service, but recipients are urged to carefully review data sets that are used and to provide feedback on their experience in using the data. Improvements to the database rely on this interaction offered by users.

The creation of the database has met with universal approval and consequently there has been no difficulty experienced in obtaining data for inclusion. However, new data are always welcome. To gain access to the IFPE Database or to offer new data, contact should be made through:

Dr. Enrico SARTORI	Tel: +33 1 45 24 10 72
OECD/NEA Data Bank	Fax: +33 1 45 24 11 10
Le Seine-Saint Germain	Eml: sartori@nea.fr
12 boulevard des Iles	
F-92130 ISSY-LES-MOULINEAUX	
FRANCE	

More information can be found at the following sites:

<http://www.nea.fr/html/science/projects.html#fuel>

<http://www.nea.fr/html/dbprog/>

Table 1. IFPE database, list of cases as of December 2003

Halden irradiated IFA-432	5 rods
Halden irradiated IFA-429	7 rods
Halden irradiated IFA-562.1	12 rods
Halden irradiated IFA-533.2	1 rod
Halden irradiated IFA-535.5 & .6	4 rods
The Third Risø Fission Gas Release Project	16 rods
The Risø Transient Fission Gas Release Project	15 rods
The SOFIT WWER Fuel Irradiation Programme	12 rods
The High Burn-up Effects Programme	81 rods
WWER rods from Kola-3	32 rods
Rods from the TRIBULATION programme	19 rods
Studsvik INTER-RAMP BWR Project	20 rods
Studsvik OVER-RAMP PWR Project	39 rods
Studsvik SUPER-RAMP PWR Sub-programme	28 rods
Studsvik SUPER-RAMP BWR Sub-programme	16 rods
Studsvik DEMO-RAMP I – BWR	5 rods
Studsvik DEMO-RAMP II – BWR	8 rods
Studsvik TRANS-RAMP 1 – BWR	5 rods
Studsvik TRANS-RAMP 11 – PWR	6 rods
Studsvik TRANS-RAMP IV – PWR	7 rods
CEA/EDF/FRAMATOME Contact 1 & 2	3 rods
AEAT-IMC NFB 8 and 34	22 samples
CEA/EDF/FRAMATOME PWR and OSIRIS ramped fuel rods	4 rods
CENG defect fuel experiments	8 rods
CANDU elements irradiated in NRU	36 rods
Siemens PWR rods irradiated in GINNA	17 rodlets
CEA failed PWR rods irradiated in SILOE: EDITH-MOX 01	1 rod
CNEA six power ramp irradiations with (PHWR) MOX fuels	5 rods
BN GAIN (U,Gd)O ₂ fuel	4 rods
INR Pitesti – RO-89 and RO-51 CANDU fuel type	2 rods
HRP IFA-597.3 rods 7, 8 and 9 (cladding degradation, FCT, FGR at Bu » 60 MWd/kgUO ₂)	3 rods
HRP IFA-534.14 rods 18 and 19 (EOL FGR and pressure, grains size of 22 and 8.5 micrometers and Bu » 52 MWd/kgUO ₂)	2 rods
DOE sponsored BR3 High Burn-up Fuel Rod Hot Cell Programme	5 rods
IAEA/OECD/IFE FUMEX – 1	6 rods
IMC (UK) Swelling data from CAGR UO ₂ fuel ramped in the Halden HBWR	13 rods
NRU MT4 & MT6A LOCA simulation tests	33 rods
Total	502 cases

Table 2. Data from the Risø Transient Fission Gas Release Project

Test	Burn-up MWd/kgUO ₂	Maximum power kW/m	Fill gas bar	FGR %	Comment re: test	Comment re: PCMI
Riso-a	37.27	39.8	1 Xe	(14)	Short section	Clad failure Noticeable ΔD with large ridge height growth
Riso-b	34.87	40.0	1 Xe	15.3	Short section	Small ΔD but large ridge height growth
Riso-e	36.95	41.6	5 He	24.9	Short section Long hold time	Noticeable ΔD with large ridge height growth
Riso-h	26.81	40.4	1 Xe	16.7	Short section	Small ΔD but large ridge height growth
Riso-i	42.31	40.1	1 Xe	13.3	Short section	Large ΔD and large ridge height growth
Riso-k	26.79	40.7	1 Xe	24.6	Short section Large gap	Little ΔD , some ridge growth
Riso-l	26.63	39.8	5 He	15.7	Short section Large gap	Little ΔD , some ridge growth
GE-a	28.54	42.4	5 He	18.8	Short section	Large ΔD indistinct ridge growth
GE-b	29.38	38.7	1 Xe	19.7	Short section	Variable small ΔD
GE-g	26.02	42.3	16 He	18.2	Short section	Large ΔD , indistinct ridge growth
GE-h	26.02	42.7	17 He	5.1	Long section Long hold	Good variation of ΔD as a function of power
GE-i	26.02	43.6	17 He	7.3	Long section Long hold	Good variation of ΔD as a function of power
GE-l	26.02	42.0	5 He	19.3	Power dips	Significant ΔD
GE-k	19.31	42.5	5 He	30.0	Power peaks	Small ΔD
GE-m	14.27	41.7	5 He	11.1	Power dips	No measurable ΔD
GE-n					Not included because of failure during test	
GE-o	26.86	44.5	5 He	33.8	Short section	Large constant ΔD

Table 3. Data from the Third Risø Fission Gas Release Project

Test	Burn-up MWd/kgUO ₂	Maximum power kW/m	Fill gas bar	Instrumentation	Purpose of test	Comment re: PCMI
AN1	36.3	39.8	15 He	PF	Effect of refabrication	Significant ΔD and ridge growth
AN2	35.5	39.0	25 He	U	Effect of power history and refabrication	Large ΔD , good variation of ΔD as a function of power
AN3	36.3	40.7	10 He	PF, TF	Effect of fill gas, see AN4	Significant ΔD and ridge growth; noticeable reduction in ΔD over T/C
AN4	36.3	40.7	1 Xe	PF, TF	Effect of fill gas, see AN3	Significant ΔD and ridge growth; noticeable reduction in ΔD over T/C
AN8	35.5	29.8	25 He	U	Effect of power	Very large ΔD , good variation of ΔD as a function of power
AN10	36.3	34.4	5 He	PF, TF	Effect of power	Small ΔD and ridge growth; noticeable reduction in ΔD over T/C
AN11	36.3	16.9	25 He	U	Low power FGR	No measurements made
GE2	36.9	40.5	5 He	PF, TF	Effect of burn-up and power history	
GE4	20.5	43.3	5 He	PF, TF	Effect of low burn-up and grain size	No change in diameter nor ridging
GE6	37.2	37.9	5 He	PF, TF	Power history	Small ΔD and ridge growth
GE7	35.6	35.5	3 He	U	Power history and fuel type	Very large ΔD and ridge height growth, good variation of ΔD as a function of power
II1	38.4	40.3	1 Xe	TF	Link to 2 nd project	Symmetric variation of ΔD and ridge height growth axially along test section
II2	22.4	42.8	5 He	PF, TF	Link to 2 nd project	Modest ΔD along length with very large ΔD at location of failure
II3	12.8	44.7	5 He	PF, TF	Effect of burn-up	Negligible change in ΔD
II5	42.4	40.1	5 He	PF, TF		Symmetric variation of ΔD and ridge height growth axially along test section

Note: PF refers to in-pile pressure transducer, TF refers to the presence of a fuel centreline thermocouple (T/C). U is a test performed on a rod without refabrication.

SESSION V

Modelling of the Mechanical Interaction Between Pellet and Cladding (Part 1)

Chairs: P. Garcia, P. Van Uffelen

MODELLING THE EFFECT OF OXIDE FUEL FRACTURING ON THE MECHANICAL BEHAVIOUR OF FUEL RODS

T. Helfer, P. Garcia, J-M. Ricaud, D. Plancq, C. Struzik
Cadarache DEC/SESC/LLCC, France

F. Sidoroff
UMR CNRS 5513, France

L. Bernard
FRAMATOME ANP, ANP Nuclear Fuel, Lyon, France

Abstract

Computing stress and strain fields in fuel pellets is essential to modelling the in-pile behaviour of PWR fuel rods, especially under pellet-cladding interaction conditions. Fuel cracking occurs immediately after reactor start-up and is effective in relaxing stresses in the pellet. It is therefore important that the brittle behaviour of oxide fuels be modelled.

A first attempt to take into account fuel cracking involved describing radial and axial fuel cracks in the pellet through a phenomenological modification of Hooke's law. A description of the model is given along with its two-dimensional extension applied to axisymmetrical fuel pellet simulations. The first results pertaining to this model are discussed. Another approach to modelling the damage to pellets induced by cracking involves the use of so-called cohesive models. These models describe the *progressive* loss of cohesion of the material in the damaged area ahead of the crack tip. A short review of these models is presented.

Introduction

Computing a realistic stress and strain field in a fuel pellet is an essential ingredient to any mechanistic approach to fuel behaviour modelling. Given the brittle nature of UO_2 and its low tensile strength [1], fuel cracking occurs under all operating conditions. It determines to a first order the extent to which thermal stresses are relieved in the pellet. Many behavioural models such as pellet creep, fission gas swelling or indeed fuel densification are notoriously stress-dependent. Therefore, the intricate coupling between these phenomena and the state of stress in the fuel can only be described if fuel cracking is taken into account.

Cracking also gives rise to major geometrical changes in the fuel pellet and is thought to be one of the main causes of fuel relocation and fragment repositioning.

The aim of this paper is to illustrate the consequences of fuel cracking on fuel rod behaviour and to review the models which can be used in order to describe this phenomenon.

The first part of this paper is devoted to some of the major consequences of fuel cracking which are examined by comparing selected experimental data to model calculations or discussing calculation results. In the second part of the paper, the MEFISTO model is described in its one- and two-dimensional forms. Application of MEFISTO-type models is a convenient means, albeit phenomenological, of describing stress relief in fractured fuel pellets. Damage models of this kind, however useful, do not provide a physical description of crack growth or propagation. Furthermore, they are unable to account for possible interactions between two contiguous crack surfaces. The last part of the paper is therefore devoted to describing the advantages to be gained from applying cohesive zone models in a three-dimensional fuel behaviour application. Such models have been developed and implemented in the ZEBULON finite element (FE) package developed at the Ecole des Mines de Paris and Onera [2]. Because ultimately the aim is to compare the response of specific fracture models and study multi-dimensional effects, it is important that all calculations be performed with the same finite element package. Throughout the paper all model calculations therefore use the ZEBULON FE package.

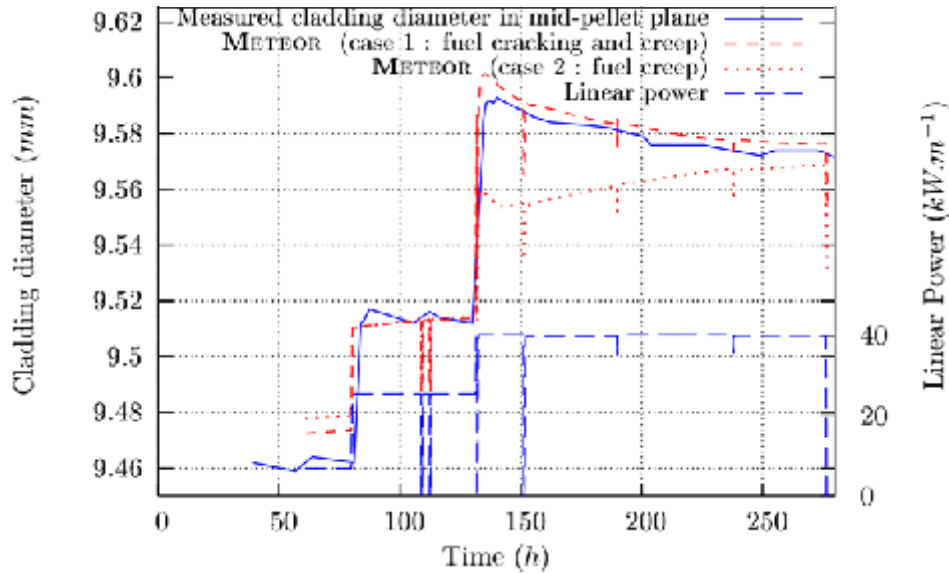
Some consequences of fuel cracking on fuel behaviour

Coupling fuel behaviour models to stress calculations

A comprehensive description of pellet-cladding interaction is made all the more difficult because of the many coupled phenomena involved, which in some cases are strongly stress-dependent. A realistic stress distribution in the pellet is therefore required for a comprehensive and descriptive modelling of those phenomena.

This is the case for fission gas swelling and fuel creep. A mechanistic, stress-dependent, fuel swelling model was applied to the study of the GONCOR experiment. It was carried out in the DECOR rig of the SILOE test reactor at Grenoble [3,4], which provided in-pile cladding diameter measurements. The experiment was initially designed to quantify the effect of high burn-up fission gas induced fuel swelling and fission gas release. To illustrate the importance of stress relaxation due to fuel pellet cracking, two calculations are compared to the experimental results and are shown in Figure 1. This figure indicates measured and calculated cladding diameters as a function of time along with the corresponding linear power changes. In case 1, fuel cracking and creep are modelled by application of the MEFISTO model in its one-dimensional form. In case 2, fuel pellet cracking is not considered. The sharp rise in cladding diameter as the linear power reaches 400 W.cm^{-1} is due to a combination of fission gas swelling and thermal expansion. This increase is adequately calculated in case 1 because fuel

Figure 1. Measured vs. calculated cladding diameters



creep and cracking both contribute to the relaxation of thermal stresses. The model also adequately describes the cladding diameter decrease due to the onset of fission gas release as the experiment proceeds. In case 2 on the other hand, bubble swelling is negligible because the hydrostatic stresses in the fuel which are used as input for the fuel swelling model are overestimated. For the same reason, the fuel creep model applied in conjunction with the plane strain hypothesis leads to a calculated cladding diameter increase at odds with the experimental evidence.

Structural effects

Effect of cracking on stress and strain concentrations in cladding

Pellet fracturing is also liable to have more direct thermo-mechanical consequences, which in certain cases can be quantified using multi-dimensional models. A two-dimensional schematic representation of a pellet-cladding interaction event is shown in Figure 2. Assuming that there is little or no relative movement between the pellet and the cladding, it is then reasonable to assume that stress and strain concentrations will occur in the cladding at pellet fragment interfaces. It is also reasonable to surmise that the number of existing pellet fragments or micro-cracking within each fragment will affect the extent to which load concentrations develop in the cladding.

Effect of cracking on pellet hourglassing

We demonstrate in this section that pellet hourglassing, which is a consequence of the radial temperature gradients in the pellets, is greatly enhanced as a result of the presence of cracks (see Figure 3 for a schematic view). To this end, thermo-elastic test cases relative to one-, two- and three-dimensional models were run and the corresponding displacement fields compared for standard pellet geometries.

The two-dimensional model is one in which the pellet is not fragmented and a symmetry of revolution around the O_z axis is assumed. The three-dimensional model is similar to that described in Ref. [5], i.e. the fuel pellet modelled is assumed to be cracked from the outset, thus forming eight

Figure 2. Stress concentration in the cladding in relation to pellet fragmentation and cracking

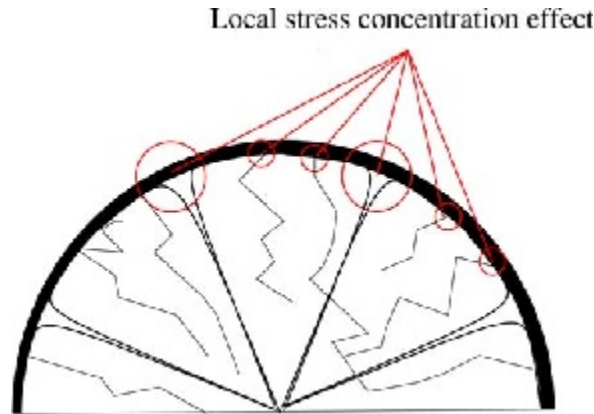
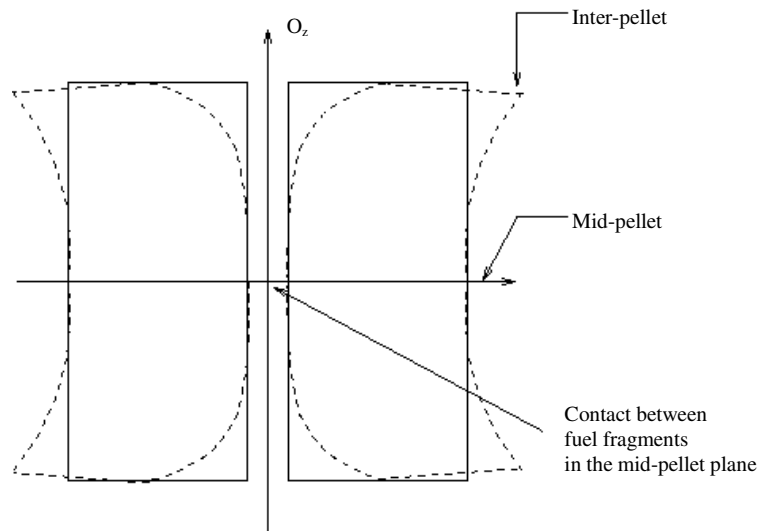


Figure 3. Hourglass distortion

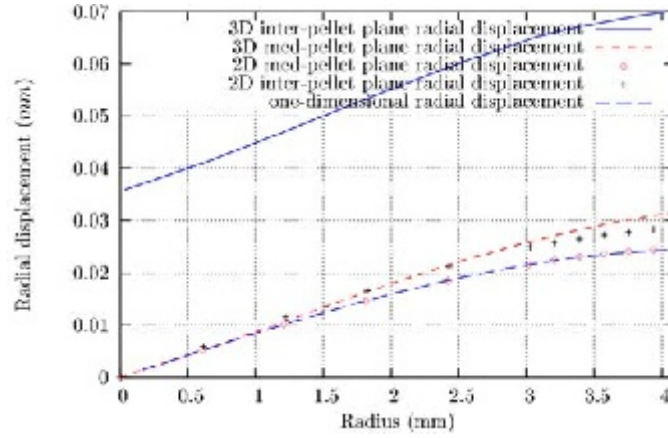


identical fragments. All pellet fragments are identical and have two planes of symmetry, therefore only a quarter of a fragment need be modelled. Unilateral contact conditions are assumed at fragment-fragment interfaces. The mid-pellet plane is assumed to be a plane of symmetry and to remain so in the course of the irradiation which implies that the axial displacements in that plane are uniform.

Figure 4 shows the radial displacements for all three test cases as a function of the pellet radius. Radial displacements in the mid inter-pellet planes are also given for the two and three-dimensional models. The figure illustrates several important results:

1. The radial displacements relative to the one-, two- and three-dimensional calculation results are identical in the mid-pellet plane.
2. The hourglassing effect in the case of an un-cracked pellet is negligible ($\approx 4 \mu\text{m}$).
3. The three-dimensional calculation reveals extensive hourglassing due to pellet fragmentation. The model predicts that in the inter-pellet plane, pellet fragmentation effectively doubles radial displacement in comparison with a one- or two-dimensional calculation.

Figure 4. Structural effects on pellet radial displacements



Point 3 is of considerable importance because it can be compared against outer cladding diameter measurements which reveal that cladding ridging is observed after only a two-cycle irradiation period [6]. This result is entirely consistent with a 39 μm hourglass effect (and conversely inconsistent with that of 4 μm). It is also consistent with fuel relocation models used in one-dimensional fuel behaviour applications [7].

The MEFISTO pellet fragmentation model

In the previous section we emphasised the importance of modelling pellet fragmentation in fuel behaviour applications. In this section a simple way of doing so, applicable to one- and two-dimensional analyses is described.

One-dimensional approach

A one-dimensional approach provides a useful framework for describing the consequences of thermal stress relief. The METEOR fuel performance application, which describes a fuel rod as stacked independent fuel “slices” [8], uses the MEFISTO mechanical model, which accounts for creep and cracking of the oxide fuel pellets and creep and plastic flow of the zircaloy sheath. A complete physical and numerical description of the model and its assessment can be found in [8].

Radial and axial cracks, which appear when the hoop and axial stresses exceed the fuel fracture stress, are modelled through a modification of Hooke’s law. The material is described as losing its stiffness in the direction perpendicular to the crack plane and its elastic properties are reduced accordingly. The initially isotropic elasticity tensor thus becomes an-isotropic and the stress-elastic strain relationship is written as follows:

$$\underline{\underline{\sigma}} = \underline{\underline{\mathbf{D}}}_{\alpha} \underline{\underline{\epsilon}}^{el} + \underline{\underline{\sigma}}_{\alpha}^{B.C.} \quad (1)$$

where α refers to the local crack configuration, $\underline{\underline{\mathbf{D}}}_{\alpha}$ is the matrix expression of the elasticity tensor in the (r,θ,z) cylindrical base and $\underline{\underline{\sigma}}_{\alpha}^{B.C.}$ is an additional term introduced as a boundary condition and which ensures that the stress in the direction normal to a crack is set to the internal pressure of the fuel rod. The value of each term can be found in Table 1.

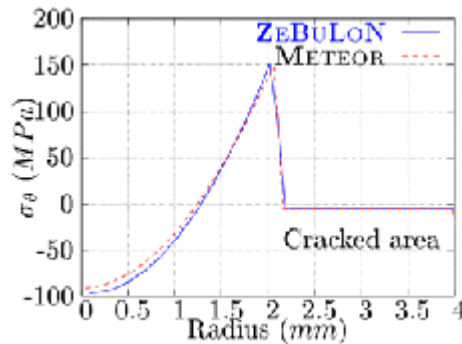
Table 1. Elasticity tensor in every cracked configuration

State	$\underline{\underline{D}}_{\alpha}$	$\underline{\underline{\sigma}}_{\alpha}^{B.C.}$
Un-cracked	$\frac{E}{(1+\nu)(1-2\nu)} \begin{pmatrix} 1-\nu & \nu & \nu \\ \nu & 1-\nu & \nu \\ \nu & \nu & 1-\nu \end{pmatrix}$	0
Cracked radially	$\frac{E}{(1+\nu)(1-\nu)} \begin{pmatrix} 1 & 0 & \nu \\ 0 & 0 & 0 \\ \nu & 0 & 1 \end{pmatrix}$	$-\frac{\nu}{1-\nu} P_i \begin{pmatrix} 1 \\ 1-\nu \\ \nu \\ 1 \end{pmatrix}$
Cracked axially	$\frac{E}{(1+\nu)(1-\nu)} \begin{pmatrix} 1 & \nu & 0 \\ \nu & 1 & 0 \\ 0 & 0 & 0 \end{pmatrix}$	$-\frac{\nu}{1-\nu} P_i \begin{pmatrix} 1 \\ 1 \\ 1-\nu \\ \nu \end{pmatrix}$
Cracked both radially and axially	$E \begin{pmatrix} 1 & 0 & 0 \\ 0 & 0 & 0 \\ 0 & 0 & 0 \end{pmatrix}$	$-P_i \begin{pmatrix} 2\nu \\ 1 \\ 1 \end{pmatrix}$

The MEFISTO model was initially developed for the METEOR fuel performance application. It has since been implemented using the ZEBULON FE package with the aim of applying it to a 2-D or possibly 3-D analysis. This implementation also provides a convenient and efficient means of comparing one-, two- or three-dimensional analyses.

Figure 5 shows the calculated hoop stress distribution in the pellet for a simple thermo-elastic calculation at linear power of 200 W.cm^{-1} . It validates the ZEBULON developments and indicates that a fuel crack extends over approximately half the pellet radius.

Figure 5. Hoop stress distribution in the pellet for a simple thermo-elastic calculation using the MEFISTO stress relief model ($\approx 20 \text{ W.mm}^{-1}$)



Development of a 2-D axisymmetric model

A two-dimensional axisymmetric version of the MEFISTO model would make it possible to describe hourglass effects or dish-filling observed as a result of a combination of fuel creep and fission gas swelling. The difficulty however lies in that in such a version of the model shear stresses appear in the r-z plane, which results in the co-ordinate system defined by the principal axes of stress and the space co-ordinate system being different. Simple crack initiation and propagation criteria cannot be as straightforwardly applied as in a one-dimensional approach.

The idea therefore is to apply the crack initiation criteria in the principal axes of stress co-ordinate system $(\tilde{r}, \theta, \tilde{z})$ in which the elasticity tensor is still given by expressions contained in Eq. (2). Let $\underline{\underline{\tilde{D}}}$ be the expression of the elasticity tensor in this co-ordinate system and alpha the rotation angle between the (r,z) and (\tilde{r}, \tilde{z}) planes. Stresses and strains in both bases are related as follows:

$$\begin{pmatrix} \tilde{\sigma}_r \\ \tilde{\sigma}_\theta \\ \tilde{\sigma}_z \end{pmatrix} = \begin{pmatrix} \cos^2\alpha & 0 & \sin^2\alpha & \sin^2\alpha \\ 0 & 1 & 0 & 0 \\ \sin^2\alpha & 0 & \cos^2\alpha & -\sin^2\alpha \end{pmatrix} \begin{pmatrix} \sigma_r \\ \sigma_\theta \\ \sigma_z \\ \sigma_{rz} \end{pmatrix} \quad (2)$$

which can be symbolically written:

$$\begin{cases} \underline{\underline{\tilde{\sigma}}} = \underline{\underline{\mathbf{R}}}\underline{\underline{\sigma}} \\ \underline{\underline{\tilde{\epsilon}}} = \underline{\underline{\mathbf{R}}}\underline{\underline{\epsilon}} \end{cases} \quad (3)$$

In the $(\tilde{r}, \theta, \tilde{z})$ co-ordinate system the stress-elastic strain relationship follows Eq. (1). Applying Eqs. (2) and (3) to it yields:

$$\underline{\underline{\sigma}} = \underline{\underline{\mathbf{R}}}^t \underline{\underline{\mathbf{D}}}\underline{\underline{\mathbf{R}}}\underline{\underline{\epsilon}} - \underline{\underline{\mathbf{R}}}^t \underline{\underline{\tilde{\sigma}}}_\alpha^{B.C.} \quad (4)$$

with:

$$\underline{\underline{\mathbf{D}}} = \underline{\underline{\mathbf{R}}}^t \underline{\underline{\tilde{\mathbf{D}}}}\underline{\underline{\mathbf{R}}} \quad (5)$$

It therefore appears that a two-dimensional version of the MEFISTO model can easily be implemented in a general purpose finite element package if the stress-strain relationship is modifiable by the user. This is the case of the ZEBULON package, and Figure 6 indicates the hoop and axial stress distributions calculated using this model. Note that the axial crack is localised just below the mid-pellet plane, which is consistent with three-dimensional calculations (see Figure7).

Cohesive zone models

Toward more physical fuel cracking description

Although damage models such as MEFISTO are useful in describing stress relief, they do take into account many of the complex aspects of fuel cracking such as:

1. Crack nucleation and mixed modes crack propagation in a visco-elastic multi-cracked media.
2. Crack closure occurring when linear power decreases.
3. Crack healing or high-temperature material re-sintering, which has been experimentally observed in the central region of fuel pellets in highly rated rods.
4. Unilateral contact or friction between two crack surfaces.

A class of models known as ‘‘cohesive zone models’’ [9] provides a means of accounting for this complex behaviour. A short review of these models is given below.

Figure 6. First results of the extension of MEFISTO to 2-D axisymmetric analysis

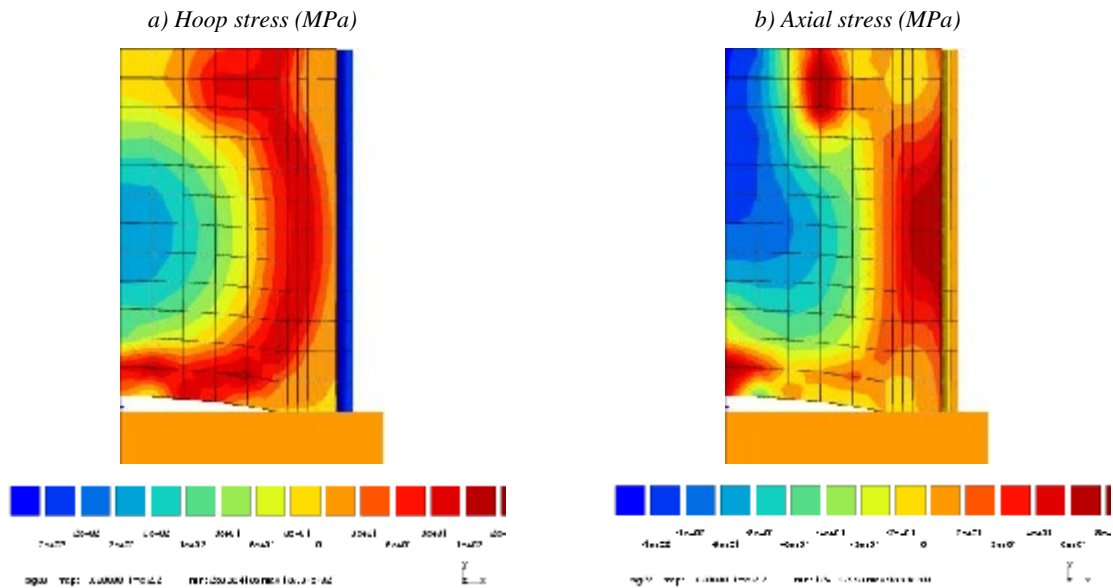
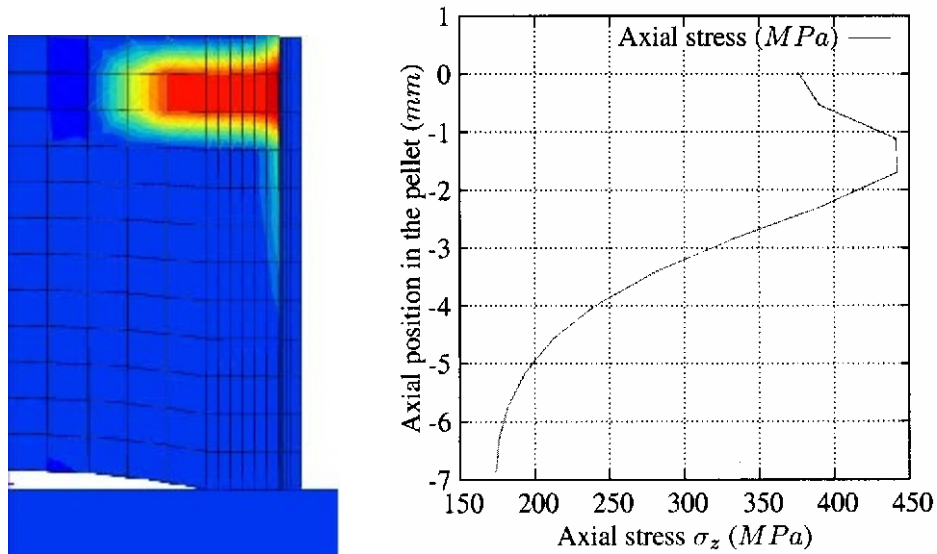


Figure 7. Damage localisation in the (\tilde{r}, \tilde{z}) plane and consistency with three-dimensional thermo-elastic axial stress calculation on the outer pellet face



Cohesive zone models, general formulation

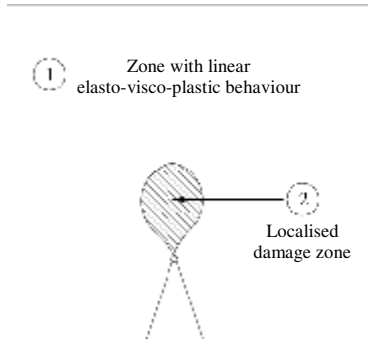
A cohesive zone models consists of a relationship between the tractions \vec{T} and the displacements jump $[\vec{u}]$ across the modelled interface [see Figure 8 (b)]:

$$\vec{T} = F([\vec{u}], \Xi)$$

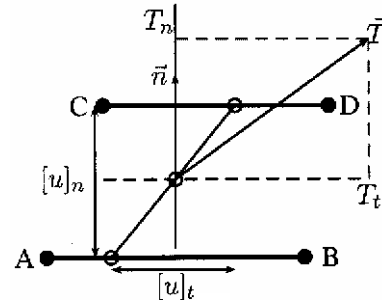
where Ξ is a set of internal variables. Positive $[u]_n$ corresponds to increasing interface separation.

Figure 8

(a) Representation of the process zone



(b) Definition of tractions and displacements jump across a cohesive zone



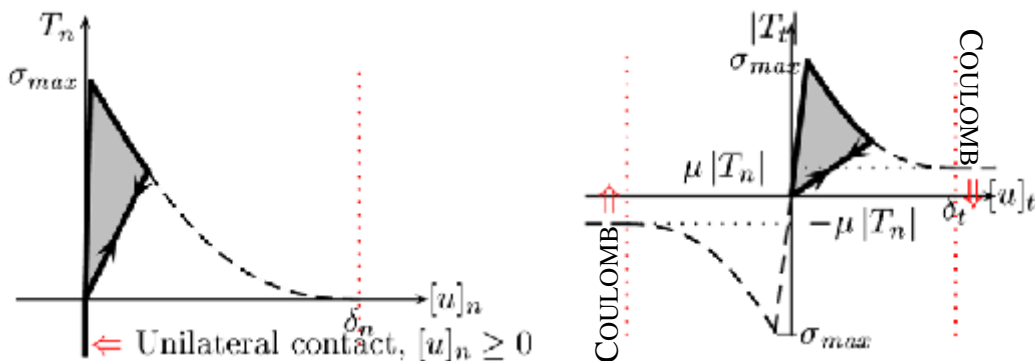
The behaviour of the interface corresponds to the specific non-linear behaviour of the material in the damaged zone ahead of the crack tip [see Figure 8(a)], where the material loses its cohesion, i.e. where crack develops.

Once the crack is formed (i.e. the zone has lost all mechanical cohesion), unilateral contact or sliding behaviour through the use of COULOMB-type dry friction laws between the crack surfaces can be modelled.

Figure 9 illustrates the behaviour of a cohesive zone model. Damage develops once an initiation criterion is reached, such as reaching a critical stress. Progressive de-cohesion occurs under increasing loading. Damage in normal and tangential loading can be coupled. Total de-cohesion under normal loading is characterised by a critical displacement jump δ_n .

Figure 9 illustrates how unloading a reloading can be treated with a particular attention being paid to unilateral contact for $[u]_n = 0$. The tangential behaviour exhibits a progressive evolution from cohesion to friction.

Figure 9. An example of the cohesive zone model under normal loading, unloading and reloading. The dashed part of the curve represents the response to an increasing loading. The grey area corresponds to the energy dissipated during the de-cohesion process [see Eq. (6)].



Energy dissipated during the fracture process

An interesting result is that for a crack propagating in mode I, the energy dissipated during the de-cohesion process can be computed simply by integrating the expression of T_n with respect to u_n :

$$G_{lc} = \int_0^{\delta_n} T_n([u]_n) d[u]_n \quad (6)$$

where δ_n is the distance corresponding to total de-cohesion for an increasing load (valid if no rate effects are taken into account) and $[u]_n$ the displacement jump in the direction normal to the cohesive zone. This energy can be identified to the fracture energy. This illustrates the link between cohesive zone models and linear elastic fracture mechanics which can be useful to determine model parameters experimentally.

The type of behaviour law described above can be implemented in the ZEBULON finite element package through the use of specific interface or boundary elements. Crack paths are then obviously limited to the interfaces between two volume elements.

Conclusion

This paper has shown through selected examples that pellet cracking was essential to modelling the in-pile behaviour of fuel rods, be it from the point of view of the direct effects it has on the mechanical behaviour of the structure or because of the need to use a reasonably well evaluated level of stress as input data for stress-dependent fuel behaviour models. Some results obtained through the implementation of simple damage models currently being developed are shown. These models are extremely useful from an engineering point of view and are relatively easy to use, but they fail to account for some of the more complex aspects of pellet cracking. Although more validation work is required, especially for the two-dimensional approach presented in this paper, research is now focusing on the application to pellet behaviour of “cohesive zone models”. They should eventually provide a mechanistic and physically based description of pellet cracking applicable to all operating conditions.

Notations

The CAUCHY stress tensor is denoted $\underline{\sigma}$ and its components in the (r,θ,z) co-ordinate system are

$$\begin{pmatrix} \sigma_r & \sigma_{r\theta} & \sigma_{rz} \\ \sigma_{r\theta} & \sigma_\theta & \sigma_{\theta z} \\ \sigma_{rz} & \sigma_{\theta z} & \sigma_z \end{pmatrix}. \text{ Supposing small deformations, the total strain tensor is denoted } \underline{\underline{\epsilon}}^{tot}. \underline{\underline{\epsilon}}^{tot} \text{ is related to}$$

the displacement field by the standard formulae $\frac{1}{2} \left(\vec{\nabla} \vec{u} + (\vec{\nabla} \vec{u})^t \right)$ and its components $\begin{pmatrix} \epsilon_r^{tot} & \epsilon_{r\theta}^{tot} & \epsilon_{rz}^{tot} \\ \epsilon_{r\theta}^{tot} & \epsilon_\theta^{tot} & \epsilon_{\theta z}^{tot} \\ \epsilon_{rz}^{tot} & \epsilon_{\theta z}^{tot} & \epsilon_z^{tot} \end{pmatrix}$.

However, for symmetry reasons, some shear components of the strain and stress tensors are zero and those tensors can be written in a vector column for convenience. Fourth-order tensors are then represented by a matrix. For example, in a mono-dimensional analysis, shear components are all zero

and the total strain may be written: $\begin{pmatrix} \epsilon_r^{tot} \\ \epsilon_\theta^{tot} \\ \epsilon_z^{tot} \end{pmatrix}$. The superscript t denotes the transpose operation. (r,θ,z)

denotes the cylindrical basis and $(\tilde{r}, \tilde{\theta}, \tilde{z})$ denotes the principal stress basis.

REFERENCES

- [1] Guerrin, Y., “Le comportement mécanique du combustible nucléaire sous irradiation”, *Ann. Chim. Fr.*, 10:405–414 (1985).
- [2] Buret, H. and G. Cailletaud, “Numerical Techniques for Cyclic Plasticity at Variable Temperature”, *Engng. Comput.*, 3:143–153 (1986).
- [3] Garcia, P. and M. Moyne, “Modelling the Steady State and Transient Mechanical Behaviour of Fuel Rods”, *Proceedings of the 14th SMIRT Conference*, Lyon, France, 17-22 August 1997, number Division C, pp. 263-270.
- [4] Garcia, P., C. Struzik, M. Agard and M. Moyne, “The Effect of Fission Gas Swelling on Cladding Strain During Power Ramp Tests”, *Fuel Chemistry and Pellet-clad Interaction to High Burn-up Fuel*, IAEA, Nyköping, Sweden, 7-10 September 1998.
- [5] Brochard, Bentejac and Hourdequin, “Non-linear Finite Element Studies of the Pellet-cladding Mechanical Interaction in a PWR Fuel”, *Proceedings of the 14th SMIRT Conference*, Lyon, France, 17-22 August 1997.
- [6] Garcia, P., J. Bourgoignon, A. Billerey and C. Struzik, “Modélisation du phénomène de délocalisation et de remise en place des fragments de combustible : analyse de calculs tridimensionnels”, Note technique 99-2021, CEA/DEN/DEC/SESC/LLCC, Septembre 1999.
- [7] Garcia, P., C. Struzik, and Veyrier, “Temperature Calculations and the Effect of Modelling the Fuel Mechanical Behaviour”, *Proceedings of Thermal Performance of High Burn-up LWR Fuel*, Cadarache, France, 3-6 March 1998.
- [8] Garcia, P., C. Struzik, M. Agard and V. Louche, “Mono-dimensional Mechanical Modelling of Fuel Rods Under Normal and Off-normal Operating Conditions”, *Nuc. Eng. and Design*, Vol. 206, 183-201 (2002).
- [9] Monerie, Yann, *Fissuration des matériaux composites : rôle de l'interface fibre/matrice*, PhD thesis, Université Aix-Marseille II (2000).

CRACK AND DISHING EVOLUTION MODELS AND PCI-SCC CONSIDERATIONS FOR FUEL PELLETS IN A QUASI-BI-DIMENSIONAL ENVIRONMENT

Armando C. Marino

Comisión Nacional de Energía Atómica & Instituto Balseiro, Argentina

Abstract

Axial symmetry and generalised plain stress-strain state assumptions lead to quasi-bi-dimensional codes for nuclear fuel rod simulation under irradiation. A model for crack evolution including the opening, closing and sealing of fuel cracks is included in the structure of the BACO code with densification, restructuring, burning and the usual aspect of fuel behaviour plus a model of dishing-shape evolution developed as an extension of crack modelling. The hoop stress predicted by BACO at the inner surface of the cladding correlates well with the fuel failure probability over a wide range of applications. Atucha NPP and CANDU fuel data are used for the identification of PCI events during irradiation along with the illustration of our crack and dishing modelling. A simple criterion of fuel failure under a quasi-bi-dimensional environment, taking into account probabilistic and parametric analysis, is emphasised in this paper.

Introduction

Obtaining the support of safety and economic criteria for nuclear power generation requires an in-depth knowledge of fuel behaviour under many different situations. The economics of the power generation might be greatly improved by means of relatively minor changes regarding the design, fuel processing and operating conditions, which would in turn require careful verification of the fuel design, considering parts performance as well as their in-service thermo-mechanical coupling. In a nuclear reactor, fuel rod materials support relatively large temperatures and suffer the effects of an aggressive chemical and radiation environment. Therefore, mechanical solicitation might sometimes be near the limits of materials endurance even under normal operating conditions. Computer codes are required to obtain results that are quantitatively and even qualitatively valid. Numerical predictions depend heavily on realistic modelling. The classical tool used to study these changes is reliable numerical simulation.

The simulation of behaviour of nuclear fuel rods under irradiation is based on a few strong assumptions. These assumptions lead to programming numerical codes which engender the loss of a complete three-dimensional coverage. In fact, a complete two-dimensional scenario will be followed by the usual quasi-bi-dimensional approach. This is due to the hypothesis of axial symmetry and generalised plain stress-strain state.

Nevertheless, we can recover an approach to the three-dimensional point of view by using an adequate modelling as relocation of pellet fragments and gap heat conductance, as well as via some angular average method, etc.

A realistic fuel rod simulation must include several means of releasing stresses. Mainly creep, plasticity and cracks are responsible of the relaxation of thermo-elastic stresses or the stress originated by swelling, coolant pressure or inner gas pressure. The fuel design includes an engineering solution for the relaxation of stress as for the pellets with “dishing” or “shoulders”.

The challenge for the design or the prediction of the behaviour of nuclear fuel rods is present as the burn-up extension in the Atucha-I NPP with the transition from the original natural UO₂ core to a slightly-enriched uranium (SEU) fuel core.

BACO (*BArra COmbustible*, Spanish expression meaning “fuel rod”) is the code developed at the Argentine Atomic Energy Commission (*Comisión Nacional de Energía Atómica*, CNEA) for the simulation of the behaviour of a cylindrical fuel rod under operation conditions describing the coupling between stress-strain evolution, thermal field and irradiation-induced effects. BACO includes the “extreme case”, parametric (or sensitivity), probabilistic (or statistical) and performance (or full core) analysis. Our modelling approach is based on using effective models, which are however sustained on physically sound ideas and critical evaluation of their consistency.

The BACO code

Presentation of the BACO code

The BACO code structure and models have already been described by Marino, *et al.* [1], including steady-state and transient thermal analysis. Presently, the number of instructions is about eleven thousand FORTRAN 90 sentences. Data post-processing improves the code’s performance and the analysis of results.

When modelling the UO₂ pellet, elastic deformation, thermal expansion, creep, swelling, densification, restructuring, cracks and fission gas release are included. For the Zry cladding, the code models elastic deformation, thermal expansion, anisotropic plastic deformation, and creep and growth under irradiation. The modular structure of the code easily allows the adding of different material properties. It can be used for any geometrical dimensions of cylindrical fuel rods with UO₂ pellets (either compact or hollow, with or without dishing) and Zry cladding.

Fuel rod power history and either cladding or coolant outside temperatures must be provided to the program. Rod performance is numerically simulated using finite time steps (finite differential scheme). The code automatically selects time steps according to physical criteria. Temperature profile within pellet and cladding, main stresses at pellet and cladding, radial and axial crack pattern in the pellet, main strains and hot geometry of pellet and cladding, change in porosity, grain size and restructuring of the pellet, fission gas release to the free volume in the rod, trapped gas distribution in the fuel and in the UO₂ grain boundary, internal gas pressure and current composition of the internal gas, and dishing shape evolution are calculated. The output of the code contains the distribution along the rod axis of these variables.

Cylindrical symmetry is assumed for the fuel rod; our model is bi-dimensional and angular co-ordinates are not considered. However, angular-dependent phenomena, as well as radial cracking, are simulated via an angular averaging method. For the numerical modelling the hypotheses of axial symmetry and modified plane strains (constant axial strain) are adopted. The fuel rod is divided in axial sections in order to simulate its axial power profile dependence. The details of the mechanical and thermal treatment and the pellet, cladding and constitutive equations are available from Ref. [1].

Numerical treatment

A summary of the assumptions taking into account the numerical treatment includes:

- Cylindrical symmetry.
- Pellet and clad are divided into circular concentric rings.
- For the numerical modelling the hypothesis of axial symmetry and modified plane strain (constant axial strain) are adopted. The three-dimensional stress-strain problem is reduced to a quasi-two-dimensional problem.
- Behaviour equations integrated with a finite difference scheme.
- Fuel pin irradiation life is divided into subsequent finite time steps for the temporal integration.

Mechanical treatment

It is assumed that during the time interval $(t_0, t_0 + \delta t)$, the strain-stress increments can be expressed as the superposition of the strain-stress increments due to the different existing deformation mechanisms.

By defining the strain-stress state at time t_0 , at the corresponding time $t_0 + \delta t$ (with δt very small), it is possible calculate as follows:

$$\varepsilon = \varepsilon_0 + \delta\varepsilon$$

where ε_0 is a stress-strain magnitude at t_0 and $\delta\varepsilon$ is the corresponding time step variation.

The equations to be integrated are, essentially, the compatibility equation of each ring, the equilibrium equation, and Hook's generalised equations, subject to the appropriate boundary conditions. That means a system of seven coupled differential equations. The finite difference approximation leads to a non-linear system of algebraic equations, which is linearised through a Taylor expansion. The previously described system for a given time increment can be solved for the main stresses by direct matrix inversion.

Thermal treatment

The temperature distribution in the pellet or cladding for the strain state results from solving Fourier's equation for steady-state heat transmission. The boundary condition is a fixed temperature at the cladding external surface and the amount of heat generated is known.

Modelling cracks in a quasi-bi-dimensional environment

The pellet is allowed to crack radially and axially; circumferential cracks are not included in the mechanical modelling but may be considered in the temperature calculation using relocation of pellet fragments and gap heat conductance. The criterion adopted for crack opening is that the pellet cracks when the tensile stress (radial or axial) is greater than the fracture strength σ_{fr} of the material [2]. As the description of the pellet has an axial symmetry and no dependence on the axial co-ordinate (at each axial section), cracks are smeared in the pellet. This means that both axial and radial cracks are represented as a continuous distribution of infinitesimal cracks in the cracked ring. If ring $i/i + 1$ in the pellet is radially cracked (there is an open crack in the tangential direction), the tangential stress σ_{θ}^{i+1} is given by the boundary condition:

$$\sigma_{\theta}^{i+1} = -p_g$$

where p_g is the internal gas pressure. Taking into account the boundary condition:

$$\sigma_r(r_{ext}) = -p_g$$

where r_{ext} is the pellet radius [1].

This boundary condition is strictly valid at the surface of a radial crack, but the assumption of crack width smearing along the whole ring, as a continuous distribution of infinitesimal cracks, allows for its approximate validity.

Similarly, if ring $i/i + 1$ is axially cracked, the axial stress is defined by the boundary condition:

$$\sigma_z^{i+1} = -p_g$$

When the pellet is cracked in the radial direction, the displacement is:

$$v = r(\varepsilon_\theta + \eta_\theta)$$

and the increment in radial displacement:

$$\delta v = r(\delta\varepsilon_\theta + \delta\eta_\theta)$$

where η_θ is the radial crack opening per unit length normal to its surface (that is, per unit length of the circumference of radius r). The average radial crack opening \tilde{v} , at a radius r is:

$$\tilde{v} = -2\pi r \eta_\theta$$

Since $\delta\varepsilon_r = \frac{\partial\delta v}{\partial r}$, compatibility equation $\frac{\partial(\delta\varepsilon_\theta)}{\partial r} - \frac{\delta\varepsilon_r}{r} = 0$, becomes:

$$\frac{\partial}{\partial r} [\delta\varepsilon_\theta + \delta\eta_\theta] + \frac{\delta\varepsilon_\theta + \delta\eta_\theta - \delta\varepsilon_r}{r} = 0$$

For axial cracks, the generalised plane strain condition, $\delta\varepsilon_z = \Delta E_z$, transforms into:

$$\delta\varepsilon_z + \delta\eta_z = \Delta E_z$$

where ΔE_z is the axial strain.

The cracking modelling is a compromise between the need to maintain axial symmetry and no axial dependence on one side, and the fact that cracks are finite and localised in a real pellet. However, we think that our model takes into account the most important effects of pellet cracking:

- The stress relaxation in the pellet (when the tensile stress reaches a value σ_{fr} , it is relaxed by the opening of a crack).
- The relaxation of tensile stress in the cladding caused by pellet expansion when there is pellet-cladding mechanical interaction (PCI) (i.e. part of the pellet expansion, instead of stressing the cladding, is accommodated by crack closure).

The code distinguishes a sealed crack from a merely closed one. When a crack closes, if the local temperature is high enough, the crack surfaces will disappear due to the combined action of temperature and compressive stresses. In that case, continuity of matter is restored and memory of the previous existence of a crack is lost. On the other hand, if the local temperature is low, the crack surfaces still exist and compressive stresses may be the only ones supported in that region, i.e. any tensile stress will re-open the crack.

The BACO model of the dishing

Pellet dishing has, among others, the effect of reducing the pellet stack axial deformation and of relaxing stresses at the cladding during pellet-cladding interaction. The latter effect is, in fact, due to UO₂ creep into the dishing. Both effects are highly temperature dependent, and therefore will not be properly represented by any dishing model based on generalised plain strain hypothesis, where all radial dependent (and therefore, temperature dependent) axial strains are averaged over the cross-section.

In BACO, the dishing depth at each pellet radius is uniformly distributed along the pellet height. This means that, instead of having dishing at the two (or one) pellet flat ends, there is a continuous distribution of infinitesimal dishing in the entire pellet, in the same way as axial cracks are distributed.

Dishing is modelled as an as-fabricated axial crack; this means that dishing closure will be radially (therefore temperature) dependent. One difference between dishing and axial cracks is that when dishing closes, it always “seals”, and on the other hand, dishing will never re-open in BACO modelling.

It must be kept in mind that this dishing model over-predicts the effect of dishing in reducing axial strains and in relaxing cladding tensile hoop strains during pellet-cladding mechanical interaction.

For this reason, in BACO the possibility of not using the dishing model is left as a user’s option. In this case, the dishing is only taken into account for calculating the rod free volume for internal gas storage; dishing changes are calculated under the generalised plain strain hypothesis by keeping the pellet land width unaltered. The code will predict a higher pellet stack elongation and, if pellet-cladding contact occurs, higher contact pressures and hoop stresses in the cladding. These will be over-predictions of the fuel behaviour.

In conclusion, if users need to make an assessment of cladding integrity based on tensile hoop stress (that is, based on a stress corrosion cracking criteria), it is recommended to run the standard version of BACO, and to repeat the calculation eliminating the dishing model.

Modelling the pellet shape evolution

A cylindrical UO_2 pellet during irradiation becomes as an “hourglass” shape (or “bamboo” effect) due to its temperature profile. The axial strains and stresses at the centre zone of the pellet-to-pellet contact are the highest. Pellet geometry was studied in order to determine effects on sheath strain under normal and ramp conditions [3]. The classical engineering solution is the design of a “dishing” at the pellet flat end in order to reduce these axial pellet-to-pellet stresses along the entire pellet stack and its effects over the cladding (“ridges”). It is interesting to define a model in order to follow the filling of the dishing during irradiation and to improve the design of a dishing with the minimum requirement of volume (and maximise the UO_2 contain), among other things.

A 3-D approximation of the pellet shape modelling

A three-dimensional calculation of stress-strain for a cracked Atucha NPP pellet was performed for Buscaglia, *et al.* [4] using finite elements with *ad hoc* computational tools [5]. Only elasticity was included so as to determine the right influence of the cracks for the release of stress in the pellet. The temperature profile of the pellet was calculated with the BACO code. It was clearly shown that the presence of one crack in a cylindrical pellet releases stresses in a wide UO_2 material region around the cracks. Figure 1 shows the influence of the crack size in the stresses of the pellets during irradiation. The influence of the cracks is clearly seen in the stress release in the zone around the crack and the concentration of stresses at the starting point of the crack (with the temperature profile of Figure 2).

The dishing is not included in order to emphasise the hourglass shape of the pellet during irradiation (see Figure 3). The calculation with no more than elasticity produces the highest stresses in the pellet, and then we find the most extreme deformation of the pellet. The pellet-to-pellet interaction will induce the highest axial stress and pellet-to-cladding radial and tangential stress at the ridge position. This 3-D

Figure 1. Top views of the distributions of von Mises' equivalent stresses

Darker zones correspond to higher stresses

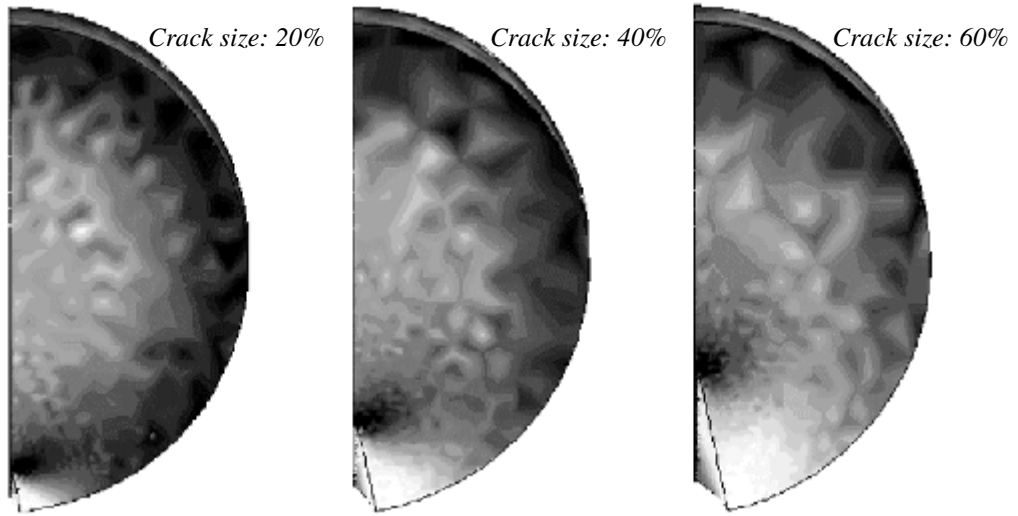


Figure 2. Temperature profile of the pellet under irradiation at the Atucha-I NPP (linear heat generation rate ~500 W/cm)

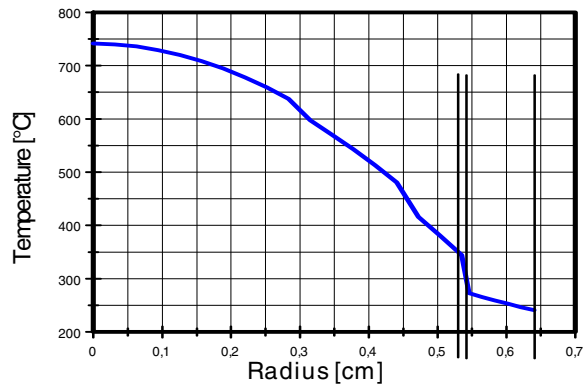
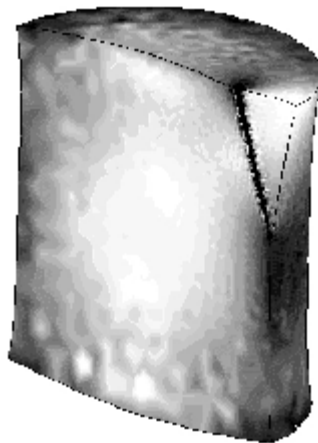


Figure 3. Side view of the distribution of von Mises' equivalent stresses for a pellet with crack size 40%. Strain scale is emphasised in order to magnify the hourglass shape (or bamboo effect).



calculation, assisted by the quasi-bi-dimensional approach of the BACO code, enabled us to design the most conservative dishing depth of the pellet enough to dismiss the pellet-to-pellet interaction at the strongest irradiation conditions keeping UO₂ material.

Reshuffling analysis and SCC criteria at the Argentinean NPPs

Argentina has two nuclear power stations in operation: Atucha-I (a pressure vessel PHWR) and Embalse (CANDU 600 type). The basic fuel design is different in the two cases. The Atucha-I fuel assembly consists of a supporting rod and 36 pre-pressurised, self-standing 600-cm long fuel rods (the active length is 530 cm), similar to the PWR rod except for its unusual length. The CANDU fuel bundle has 37 non-pressurised, collapsible, 50-cm long fuel rods. In both cases, a stress-relieved Zry-4 cladding and UO₂ pellets are used. As natural uranium heavy water reactors, Atucha-I and Embalse NPPs require continuous refuelling and on-power fuel shuffling in radial direction.

Fuel integrity during power ramping depends on many factors: burn-up, ramp height, initial linear heat generation rate (LHGR) and previous time at that power level, ramp rate, etc. Despite the low burn-up at which heavy water reactor (HWR) fuel operates, stress corrosion cracking (SCC) has been identified as a failure mechanism. This requires a concentration of corrosive fission products in the fuels, a strain rate above some initial value and tensile stress on the cladding during certain time. The threshold values for all these variables are inter-dependent.

Stress corrosion cracking of the cladding is a complex function of power history, fission gas release and stress at the cladding. Spino [6] did a careful study of Zry cladding fracture in corrosive media. There, he claims that the threshold value for stress-relieved Zry are much smaller than the plasticity limit [7,8]. The critical iodine concentration for SCC depends on the system [9,10]. However, it appears to be very small in value and it seems to be attained at relatively small burn-up [6,10]. With respect to the stress threshold for SCC, we take this as the critical parameter and adopt a fixed threshold hoop stress ($\sigma_{SCC} = 170$ MPa [6]) as a lower limit for initiation and safe operation at burn-up values over the 1 500 MWd/tU.

Atucha-I NPP fuel rod behaviour

Figure 4 shows an example of a strong power history for Atucha-I. The calculations made with the BACO code include the standard parameters of the reactor and the original design of the fuel element. The power history was provided by the PUMA code (neutronic calculation) [10].

Figure 4. Typical strong power history for the CN Atucha-I

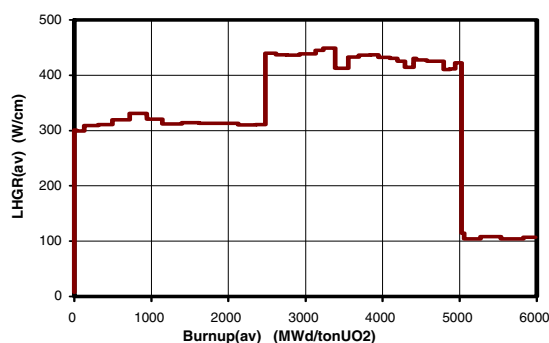
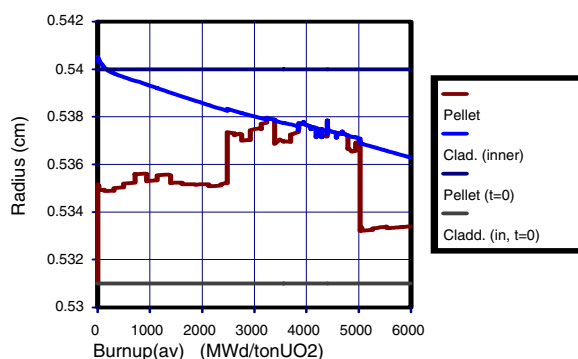


Figure 5 includes the evolution of pellet and cladding inner radius at the same axial section. As a reference were included the same radii at beginning of life. There is a situation of pellet-cladding contact during the irradiation of the second stage. The cladding radius decrement is due to creep-down. After PCI there is a slow reduction of pellet temperature due to the enhancement of the conductance and the pellet diameter is following the cladding evolution.

Figure 5. Pellet and cladding radii evolution due to the power history of Figure 4



Figures 6 and 7 belong to the extreme cases analysis of the Atucha-I fuel. Figure 6 shows the cladding tangential stress at its inner surface (hoop stress). Here, there are compression stresses during the irradiation. At the same plot we include the same curve assuming the hypothesis of minimum gap compatible with the as-fabricated tolerances (maximum values for pellet diameter and density, minimum values for cladding inner and outer radius among others). Here, there is stress reversal at the cladding and we reach a stress of $\sigma = 180$ MPa. That value is slightly up to the threshold to induce failures due to SCC.

Figure 6. Hoop stress at the cladding in the middle of the rod. Standard (thick line) and minimum gap situation (thin line).

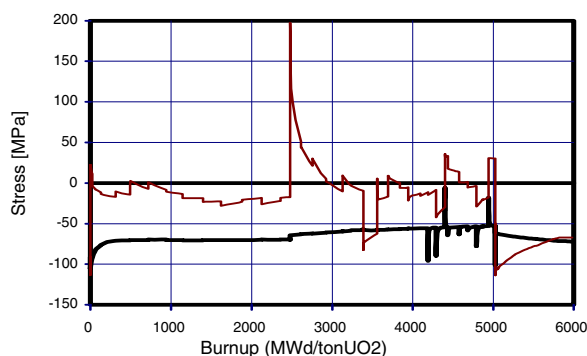


Figure 7 shows the temperature at the pellet centre as a function of burn-up at the central axial section of the fuel rod. In the same plot we include the same curve with the assumption of maximum gap compatible with the as-fabricated tolerances (maximum values for pellet diameter and density, maximum values for cladding inner and outer radius among others).

Figure 8 includes the penetration of radial cracks (produced by tangential stresses in the pellet) from the surface to the pellet centre (cracks out) and the cracks opening from the centre to the pellet surface (cracks in). Figure 9 shows the grain size change during irradiation at the UO_2 pellets of the same axial section of the previous plots. The increment of the dishing depth after 4 000 MWd/tUO_2 is

Figure 7. Pellet centre temperature during the irradiation in the middle of the rod. Standard (thick line) and maximum gap situation (thin line).

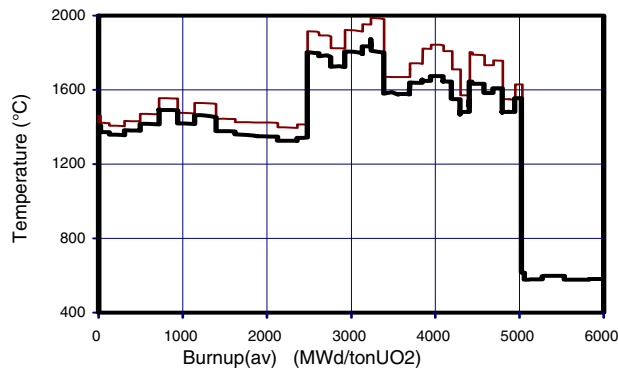


Figure 8. Radial cracks evolution of the UO₂ pellets of the Atucha-I NPP

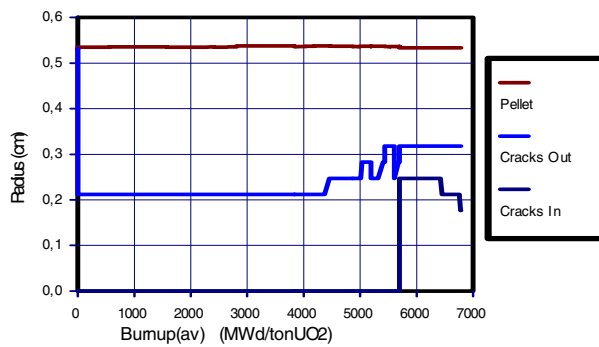
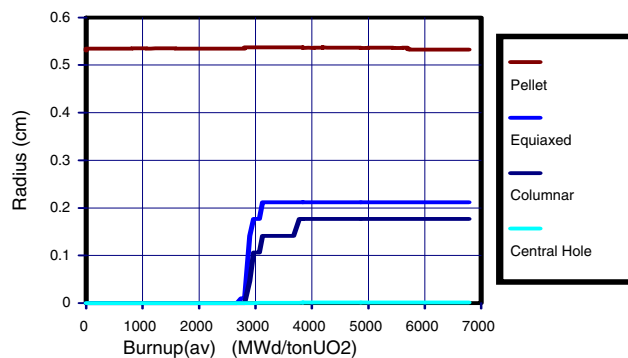


Figure 9. Grain size evolution of the UO₂ pellets of the Atucha-I NPP



due to the pellet restructuring (when the centre temperatures are greater than 1700°C). Figure 10 shows the dishing evolution during irradiation. The increment in the dishing depth at the end of the irradiation is related to the axial crack opening (see Figure 8) and restructuring (see Figure 9) in the centre of the pellet.

A parametric analysis is represented in Figures 11 and 12. The relative influence of the dishing parameters at the maximum power during the first reshuffling in Atucha-I are analysed (See Figure 4). The weight of the different rod parameters is being determined in order to identify its proper influence on fuel behaviour [13].

Figure 10. Dishing shape evolution

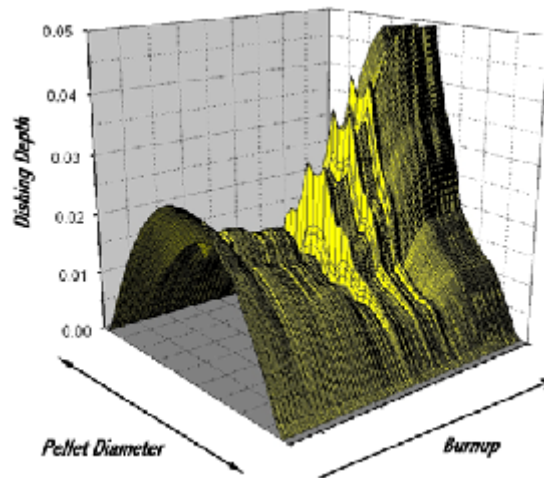


Figure 11. Hoop stress parametric analysis

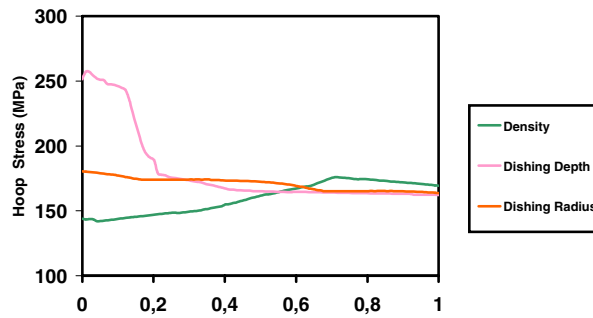
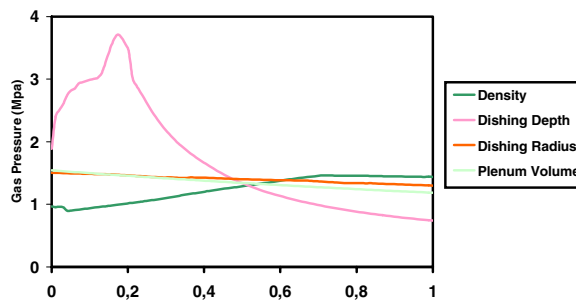


Figure 12. Gas pressure parametric analysis



Figures just include the most significant parameters at the present calculation: dishing depth, dishing radius, UO_2 density and/or plenum volume. For illustrative purposes we vary the parameters between minimum and maximum reasonable values. The figures sketch the BACO results for the hoop stress (see Figure 11) and gas pressure (see Figure 12). We find that the dishing depth is the most relevant fuel parameter in order to reduce the hoop stress at the cladding (see Figure 11). Figure 12 shows the high influence of dishing depth for the gas pressure taking into account its contribution to the free volume, nevertheless the volume plenum is associated to the pellet stack and fuel length with a narrow band of variation.

Atucha-I NPP fuel reshuffling analysis

We studied the power ramps due to fuel reshuffling from a low power channel to a higher power one in an Atucha-I fuel [18]. We assume that operation might be performed within a wide range of burn-up levels at the first position, which is not the case for the fuel paths used at the station, where the position shift is performed approximately at mid-life ($\sim 3\ 700$ MWd/tU). The main parameters of the power history to study the reshuffling operation are dq , the power increase between two reactor channel positions, q_0 and B_0 , respectively the local power and the final burn-up at the axial position of the fuel rod where the maximum power is attained before the ramp. Realistic axial power gradients were also included in the calculation. Fuel integrity under stress corrosion cracking (SCC) was studied [12,18].

We calculated the power increase necessary for dq to reach, at the cladding, the above limiting value of σ_{SCC} during the ramp. We found that the designer's recommendation for reshuffling ramps is conservative for reasonably low burn-ups, as those attained at present by the fuel in the reactor.

As the Atucha cladding is self-standing at reactor pressure, the rod initiates its stay in the reactor with an open fuel-cladding gap. Depending on power and burn-up at the first position, this gap might close during the rod stay at that position or during the reshuffling, reaching a positive hoop stress due to PCI. Therefore, in the case of the initial position corresponding to a low power q_0 channel, or relatively low burn-up for the fuel, a larger power in the second fuel position must be reached before the hoop stress is at the threshold value. The power increase needed is smaller for a larger q_0 . In the case of a relatively large power q_0 at the initial position, the gap might have closed before the power ramp. Therefore, tensile stresses due to PCI have already relaxed at that first fuel position due to UO_2 and Zry creep and the stress tends to a saturation value before reshuffling. This, in turn, implies that the increment in power, dq , needed for reaching the fixed SCC hoop stress threshold has a tendency to be constant.

We conclude that the designer's recommendation for reshuffling is conservative at the burn-up level used at the station for that operation. In the case of developing a high burn-up fuel, that needs to be reshuffled after a larger burn-up than those in the present design; better models of SCC could be needed in our code for testing its performance in a realistic way.

A probabilistic analysis of fuel fabrication tolerance

The sensitivity of cladding hoop stress predictions to fabrication tolerance in fuel geometry is studied in this section [12,1]. To this purpose a probabilistic analysis was performed with the Atucha-I fuel [12,13]. Several hundred BACO input data were randomly selected within assumed fabrication tolerance for pellet diameter and height, inner and outer diameter of the cladding and pellet density assuming a uniform distribution of values between limits. The results shown here have only a qualitative purpose, and are not representative of the variations in the fuel rod fabrication, where the dimensional variations are kept to a very narrow band within tolerance.

The power input data was adopted with $B_0 = 4\ 500$ MWd/tU, $q_0 = 400$ W/cm and a dq ramp of 200 W/cm. The probability that, by varying homogeneously the fuel dimensional parameters within the assumed fabrication tolerances, the cladding tensile stress of 170 MPa could be reached during the power ramp is calculated. The parameter variation leads to several thousand runs, where the code calculates the change in power dq_{scC} within the ramp, which is needed for attaining the hoop stress value σ_{SCC} . For 20% of the cases, the threshold value is effectively reached during the ramp. Table 1 shows the relative contribution to that percentage at different ranges of dq_{scC} within the ramp. It can be seen that, even for dq_{scC} between 100 and 150 W/cm, the probability approaches 5%.

Table 1. Probability of stress threshold $\sigma_{SCC} = 170$ MPa to be reached during a power ramp $dq = 200$ W/cm

Probability values against the range in power difference value, dq_{SCC} , for which the stress threshold is predicted to be reached. Preconditioning power is 400 W/cm. B_0 : Burn-up at reshuffling.

dq_{SCC} (W/cm)		$B_0 = 4\ 500$ MWd/tU	$B_0 = 7\ 500$ MWd/tU
150	< dq < 200 W/cm	15%	24%
100	< dq < 150 W/cm	5%	21%
	dq < 100 W/cm	–	48%

We repeat the above calculation for the same variations in fuel parameters but assuming a higher burn-up (7 500 MWd/tU) at the first position of the fuel. In this case (see Table 2), the prefixed SCC threshold value is attained in 93% of the cases, during the 200 W/cm ramp. It was found that in most cases (48%), this happens right at the start of the ramp (at $dq_{SCC} < 100$ W/cm). Further calculations demonstrate that a larger q_0 value increases the probability of reaching SCC threshold more than a dq ramp larger value. This trend also occurs when the burn-up B_0 at reshuffling is increased [12].

CANDU fuel performance analysis

When pellet and cladding are in contact the best heat transfer from pellet to coolant is obtained, but this is not the best general condition when taking into account the stresses between pellet and cladding. When stress reversal occurs at the cladding surface, the worst condition develops because the cladding is not under compression stresses. Nevertheless, the CANDU fuel rod design incorporates a collapsible cladding in order to improve the heat transfer.

In CANDU reactors, fuel reshuffling is undertaken during reactor operation. During reshuffling, the fuel undergoes a power ramp due to the power distribution along the fuel channel. For this reason, it is interesting to study the behaviour of a CANDU fuel under fast (10-20 minutes) power ramps. The linear heat generation rate (LHGR) before the ramp, the burn-up at which the ramps occurs, and the ramp height, cover a wide range. AECL has published boundaries for safe operation, based on actual experience of power ramping due to fuel reshuffling in nuclear power stations. Usually [15,16], the maximum power increase and maximum power such that fuel operation is below those values present no failures, and are given as a function of burn-up.

The experimental bounds for power increase and maximum power corresponding to the Pickering Stations are plotted by Penn, *et al.* [14]. Power histories simulating reshuffling were simulated with the BACO code. In the code, the criterion for safe operation was based on the maximum hoop stress at the cladding inner surface; this is related to susceptibility to stress corrosion cracking. BACO results are in good agreement with AECL data; even the mispredictions can be explained on a physical basis [18]. A CANDU fuel rod simulation including statistical analysis was included in the Ref. [19].

SEU in Atucha-I NPP

Atucha-I is a PHWR originally fuelled with natural uranium. The programme to introduce SEU (0.85% ^{235}U) fuel in Atucha-I started in 1993, and the first SEU fuels were loaded in 1995. Mean fuel discharge burn-up increased from 5 900 MWd/tU to more than 11 000 MWd/tU. The impact of the fuel on the cost of operation had an important reduction. SEU fuel design analysis was related with the internal pressure, strains in fuel cladding and PCI-SCC sensitivity in power ramps at high burn-up [17].

Behaviour of the SEU Atucha-I fuel rod

We analyse one of the SEU fuels irradiated at the Atucha-I NPP under the most extreme conditions in burn-up, power ramp at reshuffling, and maximum power. The first position of that fuel in the Atucha core was around a power level of 350 W/cm. The reshuffling was done at 4 500 MWd/tU. The second and final position was at the central zone of the core with a linear heat generation rate of 470 W/cm. The average burn-up at end of life was 12 500 MWd/tU and the fuel was discharged at the end of 2003 without any failures. Figure 13 shows the hoop stress at axial section under the most demanding fuel conditions. The maximum temperature calculated was less than 1 600°C and the hoop stresses calculation shows compression during the entire period of irradiation. Figure 14 shows the evolution of the pellet and inner cladding radius during irradiation. There was contact between pellet and cladding after 7 000 MWd/tU₂ with a reduction of 100°C in pellet centre temperature and an increment on the rate of the hoop stress. BACO calculations show no columnar grains during irradiation and a zone at the pellet centre with equiaxed grains after reshuffling. Axial deformations were less than 0.2% and radial strains were less than 0.3%. Fission gas release was less than 1%. Calculations also show that fuel rod internal pressure is below coolant pressure, so no cladding lift-off is expected.

Figure 13. Most demanding hoop stress of a SEU fuel at the Atucha-I NPP with the highest demands

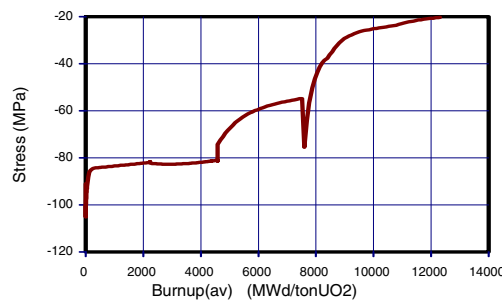


Figure 14. Pellet and cladding inner radius evolution (as-fabricated pellet and cladding radius included as a reference)

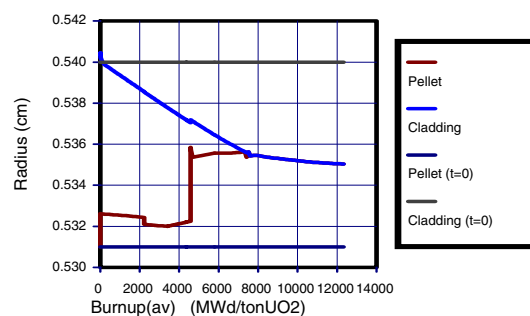


Figure 15 shows the evolution of the dishing during irradiation using our cracks and dishing modelling. The decrement in dishing volume starts at reshuffling; the increment in pellet temperature produces a stress profile with axial expansion at the pellet centre. The stress release is due to creep. The axial cracking is done at the periphery of the pellet. Figure 16 shows the calculated pattern of cracks; in this case, cracks were opened from the surface to the middle of the pellet. Calculations show the absence of opened cracks in the pellet centre and no centre hole.

Figure 15. Dishing depth evolution

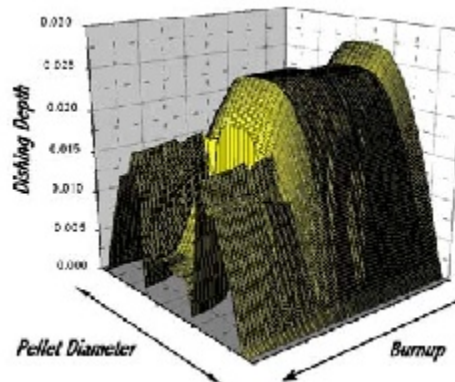
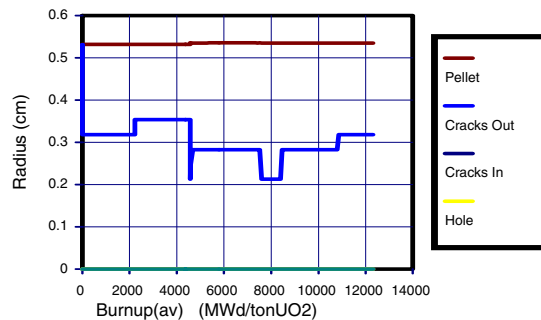


Figure 16. Crack evolution in a SEU pellet

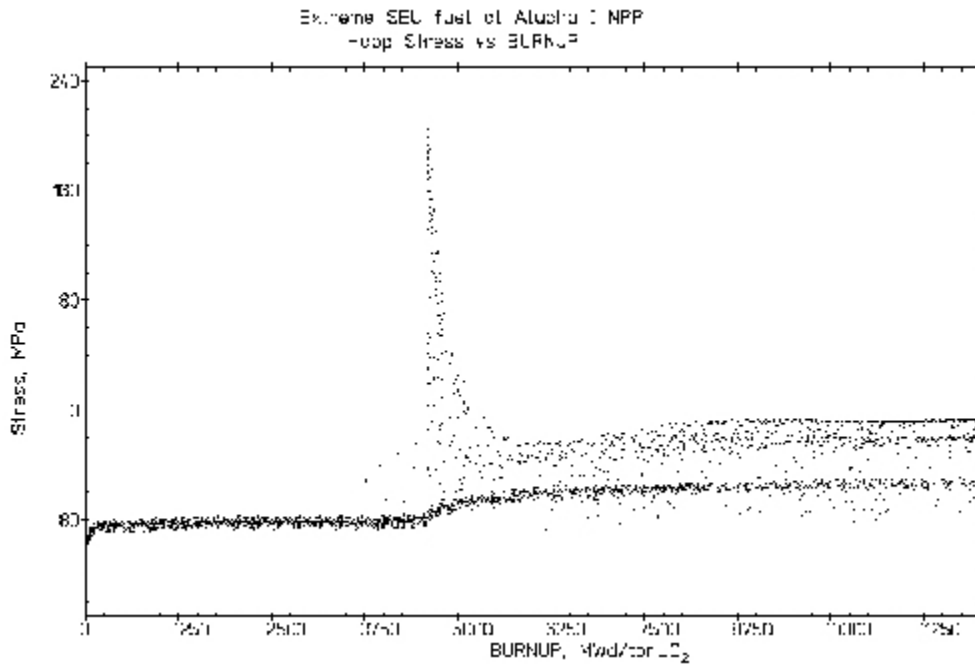


The above calculations are supported by the absence of failure in the SEU fuel element. Nevertheless, the strong demanding conditions during irradiation could produce local failures due to the as-fabricated tolerances. The normal calculations are performed using standard values. The BACO code allows a sensibility analysis taking into account the standard values of the fuel parameters with their as-fabricated tolerances and their statistical distributions.

The probabilistic analysis for the pellet centre temperature presents a temperature band after reshuffling less than 200°C of uncertainty around the standard calculation. This band does not mean a big change in pellet grain morphology and the pattern of cracks. The sensitivity analysis for the gas pressure in the fuel rod shows a progressive increment of the dispersion following the irradiation. This is due to the fact that the gas pressure calculation is the result of the most severe coupling of stress-strain and the temperature calculation, among other effects. Nevertheless, the maximum pressure is less than the coolant pressure. Standard calculations after reshuffling results converge to the maximum values of the sensitivity analysis results.

Figure 17 shows the probabilistic analysis for hoop stress (tangential stress at the inner surface of the cladding). There are similar values before the reshuffling. During reshuffling, a strong dispersion of results and the stress relaxation, especially due to creep after these events, is evidenced. Several points with a stress value greater than 170 MPa are also found. Events of these types at these values suggest a probability to induce a fuel failure due to SCC. Standard calculations produce results sufficient to maintain the integrity of the fuel; nevertheless, after reshuffling the sensitivity analysis results in a probability to produce a failure due to SCC. The random values of pellet and cladding radius between as-fabricated tolerances (among other fuel parameters) produce a great dispersion of the stresses after reshuffling due to the different time at which PCI occurs.

Figure 17. Cladding hoop stress results from the BACO code probabilistic analysis



PIE at the NPP Atucha-I with SEU fuels

The presented fuel was one of the top burn-ups reached at the Atucha-I NPP. The local burn-up at the middle-bottom position of the core was 16 000 MWd/tU. The visual inspection shows the excellent state of the fuel element. The fuel rods presents an oxide layer thickness of about 3-5 microns. (The high burn-up of PWR fuels could produce an oxide layer at the cladding between 30-40 microns.) Ridges at the fuel rods were not clear at all, but were visible (see Figures 18 and 19). The PHWR Atucha-I NPP has a control of the water chemistry sufficient to assert that there is no crud deposition. The water is a reducing agent in the primary circuit of coolant.

Figure 18. SEU Atucha-I fuel rods with small ridges at the cladding surface

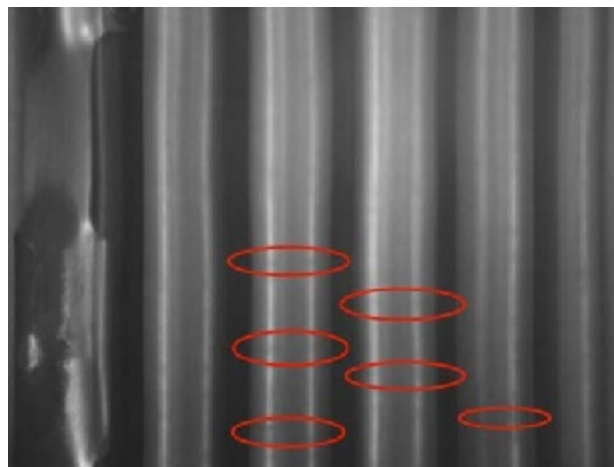
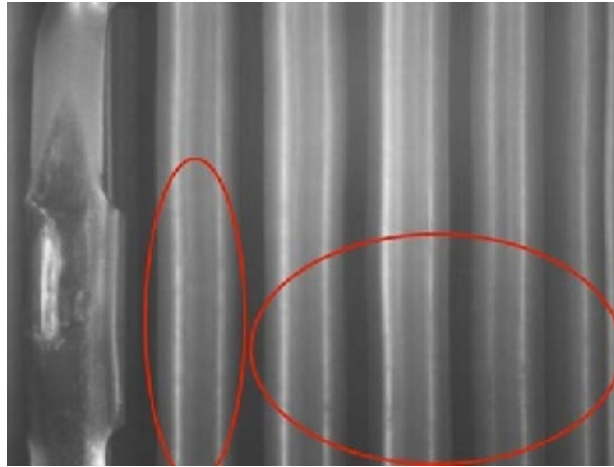


Figure 19. Another view of SEU Atucha-I fuel rods with small ridges at the cladding surface

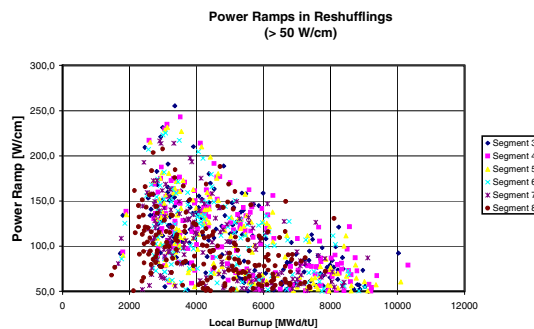


Performance of the first SEU core at Atucha-I NPP

The sensitivity and parametric analysis could be sufficient for the efficient design of fuel rods, taking into account the safety and economic limits from a realistic point of view. The extension of the previous design is the analysis of the performance of irradiated fuel elements when an improvement of the original design is required as the burn-up increment of the SEU fuel at the Atucha-I NPP. The behaviour of the SEU first loading at Atucha-I is analysed in this section.

Figure 20 shows the power ramps at the first reshuffling of the fuels when Atucha-I becomes a homogeneous SEU core. The fuel length is divided into ten axial sections.

Figure 20. Power ramp of the first SEU core at the Atucha-I NPP



BACO allows the calculation of a complete set of irradiations of the same fuel design as the calculation of the complete core of the Atucha-I NPP. Figure 21 presents the maximum hoop stress reached for each fuel rod during each individual irradiation. All the fuels are under the σ_{SCC} value listed in previous sections ($\sigma_{SCC} = 170$ MPa). Just one fuel present stress reversal. The rest of the fuels are under compression during the irradiation. The maximum pellet temperatures for all the fuels present a maximum temperature $\sim 1900^{\circ}\text{C}$. We could expect columnar grains at the pellet centre of the fuel and, for a few pellets, a small hole. All the values of the calculated fission gas release at reshuffling are under 0.9%. The maximum calculated gas pressure in the rod maintains values below the coolant pressure. We find an increment of pressure with burn-up.

Figure 21. Maximum hoop stress calculated for each fuel of the first SEU core of Atucha-I

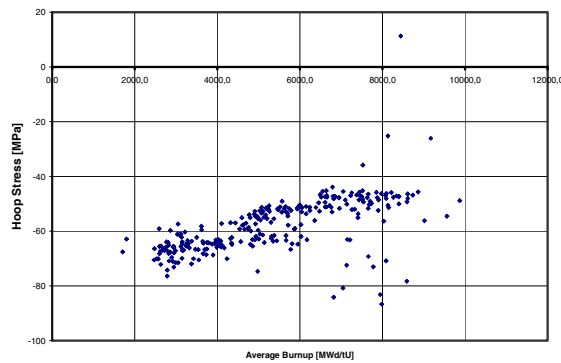
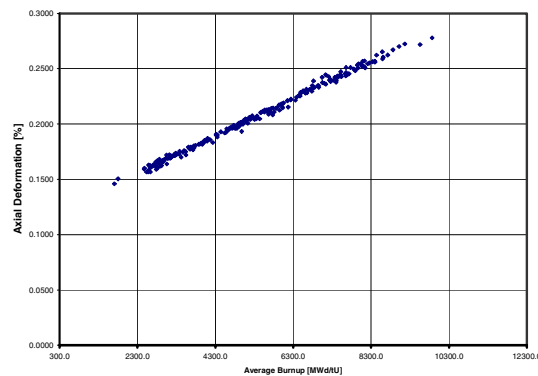


Figure 22 shows the maximum calculated values of axial and radial deformations. These values were calculated at fuel reshufflings. The deformations increase with the burn-up. The radial deformation is done due to creep down of the cladding (see Figure 14).

Figure 22. Axial deformations



The BACO code calculations of hoop stress, pellet centre temperature, axial deformations and gas pressure were made using conservative values [17]. The results are in good agreement with the successful irradiation without any fuel failures of the first SEU core irradiation.

Conclusions

The modular structure of the BACO code and its detailed coupling of thermo-mechanical and irradiation-induced phenomena make it a powerful tool for the prediction of the influence of material properties on the fuel rod performance and integrity. The hoop stress predicted by BACO, for a fixed ramp velocity, at the inner surface of the cladding correlates well with the fuel failure probability over a wide range of pre-conditioned powers and power increments during the ramp.

On-power fuel reshuffling was done at Atucha-I NPP with the original, natural UO₂ core and the new SEU core. For the sake of the exercise, we adopt a hoop stress value at the cladding of 170 MPa as a realistic limiting threshold stress that allows SCC to initiate (though, actually, it only results in a progressive deterioration once the proper atmosphere has been attained inside the rod). A simple rule for fuel failure was included in the calculation of CANDU fuel performance. That PCI-SCC criterion was enough for the understanding of the fuelgrammes of Ref. [15].

The coupling between 3-D application and quasi-bi-dimensional codes can lead to an enhanced understanding of the fuel rod behaviour, as was shown in the analysis of the stress in a cracked 3-D pellet. Otherwise, the models for the cracks and dishing influence in the fuel rod behaviour were presented in a pure quasi-bi-dimensional environment, particularly the stress release, gas pressure in the rod as well the economy of UO₂.

The transition of the core of the Atucha-I NPP from natural UO₂ to SEU was presented from the point of view of the fuel rod behaviour in order to illustrate the BACO code capabilities. Extreme case analysis, parametric (or sensibility), probabilistic (or statistic) analysis plus the analysis of the fuel performance (full core analysis) are the tools developed in the structure of BACO in order to improve the understanding of the burn-up extension in Atucha-I. The PCI-SCC criterion, among others, was sufficient for the complete core transition to SEU fuels without any significant failure.

Acknowledgements

The author acknowledges S. Harriague, E. Pérez and H. Troiani for their help in critically reading the manuscript and providing several suggestions. The contributions of G. Buscaglia for the 3-D plots and solver kit, L. Alvarez for the irradiation database, and G. Ruggirello for the PIE, are also gratefully acknowledged.

REFERENCES

- [1] Marino, A.C., *et al.*, “BACO (Barra Combustible) Code Version 2.20: A Thermo-mechanical Description of a Nuclear Fuel Rod”, *J. Nuc. Mat.*, Vol. 229, pp. 155-168, April 1996.
- [2] Matthews, J.R., *Mechanical Properties and Diffusion Data for Carbide and Oxide Fuels. Ceramic Data Contribution*, Atomic Energy Research Establishment, Harwell, UKAEA, AERE-M 2643 (1974).
- [3] Hastings, I.J., *et al.*, “CANDU Fuel Performance: Influence of Fabrication Variables”, *IAEA-CNEA International Seminar on Heavy Water Reactor Fuel Technology*, S.C. de Bariloche (1983), AECL MISC 250 (1983).
- [4] Buscaglia, G., *et al.*, “Mesh Optimization: Some Results in 3-D Elasticity”, *Proc. ESAIM*, Vol. 2, 1-16 (1997).
- [5] Dari, E., Ph. D. thesis, Instituto Balseiro, Argentina (1994).
- [6] Spino, J., *Fragilización de la vaina de Zircaloy-4 en elementos combustibles PWR por acción de los productos de fisión volátiles. Fenómeno de corrosión bajo tensiones activado por yodo. Influencia interna de la química interna del combustible.*, Ph. D. thesis, Instituto Balseiro, Argentina, February 1988.

- [7] Une, K., "Threshold Values Characterizing Iodine-induced SCC of Zircalloys", *Proc. Specialists Meeting on Pellet-cladding Interaction in Water Reactors*, IAEA-IWGFPT/o, Risø, Denmark, September 1980.
- [8] Une, K., "Deformation and Fracture Behavior of Zircaloy-2 Deformed at Constant Strain Rate in Iodine Environment (I)", *Journal Science & Technology*, 16, 577 (1979).
- [9] Peehs, M., "Out of Pile Testing of Iodine Stress Corrosion Cracking in Zircaloy Tubing in Relation to Pellet-cladding Interaction Phenomenon", *Proc. 4th Conf. on Zirconium in Nuclear Industry*, ASTM-STP 681, pp. 244-260 (1979).
- [10] Shan, S., *et al.*, "Iodine Stress-corrosion Cracking of Zircaloy", *Trans. Am. Nuc. Soc.*, 32, p. 268 (1979).
- [11] Grant, C., *PUMA – Sistema para la simulación del Funcionamiento de Reactores Nucleares; Fundamentos Teóricos y su Utilización*, CNEA internal report, CNEA-Re-163, June 1980.
- [12] Marino, A.C., *et al.*, "Sensitivity Analysis Applied to Nuclear Fuel Performance Related to Fabrication Parameters and Experiments", *Proc. 14th International Conference on Structural Mechanics in Reactor Technology (SMiRT 14)*, Paper C01/7, Lyon, France, 17-22 August 1997.
- [13] Marino, A.C., "Probabilistic Safety Criteria on High Burn-up HWR Fuels", *IAEA's Technical Committee Meeting on Technical and Economic Limits to Fuel Burn-up Extension*, Bariloche, Argentina, 15-19 November 1999.
- [14] Penn, W., *et al.*, "CANDU Fuel – Power Ramp Performance Criteria", *Nuclear Technology*, 34, 34 (1977).
- [15] Truant, P.T., "CANDU Fuel Performance: Power Reactor Experience", *IAEA/CNEA International Seminar on Heavy Water Fuel Technology*, S.C. de Bariloche (1983), AECL MISC 250 (1983).
- [16] Hastings, I.J., *et al.*, "CANDU Fuel Performance: Influence of Fabrication Variables", *IAEA-CNEA International Seminar on Heavy Water Reactor Fuel Technology*, S.C. de Bariloche (1983), AECL MISC 250 (1983).
- [17] Alvarez, L., "SEU Fuel in Atucha 1 NPP, A Valuable Experience for a CANDU-6 Core Enrichment", *6th International Conference on CANDU Fuel*, Niagara Falls, Ontario, Canada, 26-30 September 1999.
- [18] Marino, A.C., *et al.*, "Power Ramp and Reshuffling Analysis for Nuclear Fuels using the BACO Code", *14th International Conference on Structural Mechanics in Reactor Technology, (SMiRT 14)*, Lyon, France, 17-22 August 1997.
- [19] Marino, A.C., "Computer Simulation of the Behaviour and Performance of a CANDU Fuel Rod", *5th International Conference on CANDU Fuel*, Toronto, Ontario, Canada, 21-24 Sept. 1997.

NON-LINEAR BEHAVIOUR OF MULTI-PHASE MOX FUELS: A MICROMECHANICAL APPROACH

Sophie Roussette, Jean-Marie Gatt

Commissariat à l'Énergie Atomique, DEC/SESC, Cadarache, France

Jean-Claude Michel

CNRS, Laboratoire de Mécanique et d'Acoustique, Marseille, France

Abstract

The modelling of mechanical pellet-clad interaction requires knowledge of the thermo-mechanical behaviour of nuclear fuels. Some nuclear fuels such as MOX are composed of several phases. The mechanical properties of these phases, which are elastoviscoplastic in-pile, are changing in-pile. The objective is to formulate a mechanical behaviour law taking all the physical phenomena into account in the different phases, which can easily be introduced into a fuel rod modelling code. Consequently, Non-uniform Transformation Field Analysis (NTFA) is used on the one hand, to correctly capture the heterogeneity of the anelastic strain in the different phases and, on the other hand, to provide a simple overall constitutive law for computational codes. This method is a good way to describe the behaviour of MOX fuel. Transformation Field Analysis (TFA), which corresponds to piecewise uniform transformation fields, is used to perform a sensitivity study.

Introduction

PCI modelling requires knowledge of the thermo-mechanical behaviour of nuclear fuels. This paper focuses on MOX fuels. MOX fuels have a heterogeneous microstructure with several porous phases. MOX material is considered as a uranium-bearing matrix and plutonium-bearing agglomerates. Each phase has elastoviscoplastic behaviour in-pile and its microstructure changes in-pile; this includes an evolution of the porosity and the grain size, the appearance of fission products in solution, gas bubbles and various precipitates.

The aim is to formulate an overall elastoviscoplastic behaviour depending explicitly on the elastoviscoplastic behaviour of each phase, and which can easily be introduced into a fuel rod modelling code. It is known that the effective behaviour of materials made of different elastoviscoplastic phases is itself elastoviscoplastic; however it is composed of an infinity of internal variables which are the fields of local internal variables. In order to obtain effective models which are useable, simplifying assumptions are considered.

Transformation Field Analysis (TFA), proposed by Dvorak [1], assumes that the local fields of internal variables are piecewise uniform. The TFA is simple to implement. It only requires elastic calculations on the Representative Volume Element, using analytical models. However this approach, applied to two-phase models, does not correctly ensure the relation between effective behaviour and the behaviour of each phase. But in the case of MOX fuel, the behaviour law of the uranium-bearing phase [2] is well known and the parameters of the law for aggregates are identified from experimental data which provide information on the macroscopic level. Therefore, the local parameters of the plutonium-bearing phase are obtained from the experimental overall behaviour law and by fixing the uranium-bearing phase law.

In order to improve the predictions of the TFA, Michel and Suquet [3] recently proposed to take the heterogeneity of the local fields of internal variables into account by considering non-uniform transformation fields. This method is called Non-uniform Transformation Field Analysis (NTFA).

The paper is organised as follows. In the first part, microstructures of MOX fuels are presented. The NTFA and TFA methods are described in the second part. In the third part, results obtained with the NTFA method for a two-phase material are presented showing the interest in using this method for MOX fuels. In the last part, the TFA method is applied to MOX fuels. The modified UO_2 behaviour law developed by Monerie and Gatt [2] is used for the matrix and a law in the same form as the UO_2 behaviour law is used for the aggregates. The experimental data are used to determine missing mechanical parameters. A sensitivity study is then proposed to evaluate the effect of the porosity and of the volume fraction of the plutonium-bearing phase.

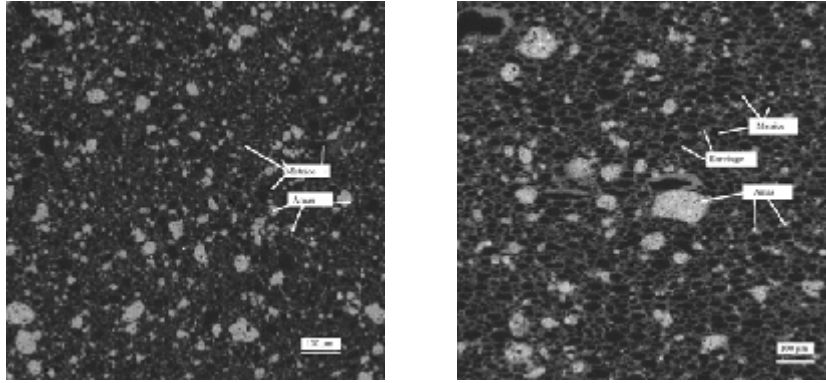
Microstructures of MOX fuels

Industrial MOX fuels (MOX MIMAS) are multi-phase materials. In the case of MOX MIMAS AUC, two phases can be observed:

- Agglomerates full of plutonium: plutonium-bearing phase (clusters).
- A matrix poor in plutonium: uranium-bearing phase (matrix).

For MOX MIMAS TU2, another phase is observed: a network more or less interconnected where the plutonium content is contained between the content of the uranium-bearing phase and the plutonium-bearing phase. Moreover, each phase is porous.

Figure 1. MOX MIMAS AUC and MOX MIMAS TU2



Non-uniform Transformation Field Analysis

Constitutive relations for the constituents

At each material point x the state variables are the strain tensor ε and internal variables which describe irreversible phenomena. Here we will only consider the dissipative mechanism which comes through an anelastic strain ε^{an} . The behaviour of each constituent is defined by two thermodynamic potentials, the free energy ω which defines (through the state law) the stress σ , and the force potential ψ which gives (through the complementary law) the equation of evolution for the anelastic strain:

$$\omega(\varepsilon, \varepsilon^{an}) = \frac{1}{2} (\varepsilon - \varepsilon^{an}) : L : (\varepsilon - \varepsilon^{an}) \quad (1)$$

$$\sigma = \frac{\partial \omega}{\partial \varepsilon}(\varepsilon, \varepsilon^{an}) = L : (\varepsilon - \varepsilon^{an}) \quad (2)$$

$$\dot{\varepsilon}^{an} = \frac{\partial \psi}{\partial \sigma}(\sigma) \quad (3)$$

For simplicity, attention is restricted to isotropic constituents. The elastic tensor L is therefore characterised by a bulk modulus k and a shear modulus G , whereas the force potential ψ depends on the stress σ only through its second invariant σ_{eq} . Under this last assumption, the evolution Eq. (3) reduces to:

$$\dot{\varepsilon}^{an} = \frac{3}{2} \frac{\partial \psi}{\partial \sigma_{eq}}(\sigma_{eq}) \frac{\sigma_{dev}}{\sigma_{eq}} \quad (4)$$

where σ_{dev} denotes the deviating part of σ and $\sigma_{eq} = \left(\frac{3}{2} \sigma_{dev} : \sigma_{dev} \right)^{1/2}$. When there is no evolution of the system, the stress and strain fields in the representative volume element (RVE) solve the following linear elastic problem, with appropriate boundary conditions:

$$\sigma(x) = L(x) : (\varepsilon(x) - \varepsilon^{an}(x)), \text{div}(\sigma(x)) = 0, \langle \varepsilon \rangle = E \quad (5)$$

E and $\varepsilon^{an}(x)$ being known, the strain field $\varepsilon(x)$ solution of Eq. (5) can be written as:

$$\varepsilon(x) = A(x) : E + \frac{1}{|V|} \int_V D(x, x') : \varepsilon^{an}(x') dx' = A(x) : E + D * \varepsilon^{an}(x) \quad (6)$$

where $A(x)$ is the elastic strain-localisation tensor and $D(x, x')$ the non-local operator which gives the strain at the point x created by a transformation strain $\varepsilon^{an}(x')$ at point x' .

Non-uniform transformation fields

In order to reduce the number of internal variables and to improve the TFA, Michel and Suquet [3] proposed to take the non-uniformity of the local fields of internal variables into account by considering non-uniform transformation fields. More precisely, the field of anelastic strain is decomposed on a set of fields, called plastic modes, μ^k :

$$\varepsilon^{an}(x) = \sum_{k=1}^M \varepsilon_k^{an} \mu^k(x) \quad (7)$$

Unlike the classical TFA, the modes μ^k are non-uniform, tensorial and can depend on the position x . Their total number, M , can be different from the number of phases. Further assumptions are made to simplify the theory. (i) *The support of each mode is entirely contained in a single material phase.* It follows from this assumption that, for a given mode k , one can define its characteristic function χ^k , its free energy ω^k , its elastic moduli L^k , its force potential ψ^k as those of the phase which supports this mode. (ii) *For incompressible viscoplasticity, the modes are traceless tensor fields.* (iii) *The modes are orthogonal.* This condition is obviously met when the modes have their support in different phases but has to be imposed to the modes which have their support in the same phase. Finally, in order to have the ε_k^{an} homogeneous to an anelastic strain, (iv) *The modes are normalised:*

$$\langle \mu_{eq}^k \rangle = 1, \text{ where } \mu_{eq}^k = \left(\frac{2}{3} \mu^k : \mu^k \right)^{1/2}$$

Reduced variables and influence factors

Under the approximation in Eq. (7), Eq. (6) becomes:

$$\varepsilon(x) = A(x) : E + \sum_{l=1}^M (D * \mu^l)(x) \varepsilon_l^{an} \quad (8)$$

Multiplying Eq. (8) by μ^k and averaging on the RVE, one obtains:

$$e_k = a_k : E + \sum_{l=1}^M D_{kl} \varepsilon_l^{an} \quad (9)$$

where the reduced strain e_k , the reduced localisation tensor a_k and the influence factors D_{kl} are defined as:

$$e_k = \langle \varepsilon : \mu^k \rangle, a_k = \langle \mu^k : A \rangle, D_{kl} = \langle \mu^k : (D * \mu^l) \rangle \quad (10)$$

By analogy with the equation defining the reduced strain e_k in Eq. (10), one can define the reduced anelastic strain e_k^{an} and the reduced stress τ_k :

$$e_k^{an} = \langle \varepsilon^{an} : \mu^k \rangle, \tau_k = \langle \sigma : \mu^k \rangle \quad (11)$$

Note that the set $\{\varepsilon_k^{an}\}_{k=1,\dots,M}$ can be replaced by the set $\{e_k^{an}\}_{k=1,\dots,M}$, since:

$$e_k^{an} = \langle \mu^k : \mu^k \rangle \varepsilon_k^{an} \quad (12)$$

Constitutive relations for the reduced variables

Since the elastic tensors of the phases are assumed isotropic and the modes incompressible, the reduced stress τ_k is given by:

$$\tau_k = 2G^k (e_k - e_k^{an}) \quad (13)$$

In order to derive an evolution equation for e_k^{an} , Eq. (4) is multiplied by μ_k and averaged over the RVE:

$$\dot{e}_k^{an} = \langle \varepsilon^{an} : \mu^k \rangle = \frac{3}{2} \left\langle \frac{\partial \Psi}{\partial \sigma_{eq}} (\sigma_{eq}) \frac{\sigma : \mu^k}{\sigma_{eq}} \right\rangle \quad (14)$$

The next step is to simplify Eq. (14) to obtain a relation between the different \dot{e}_k^{an} and the τ_k . This is done in Michel and Suquet [3] by replacing in the right-term of Eq. (14) σ_{eq} by $a_r = \left(\sum_{k=1}^{M(r)} \tau_k^2 \right)^{1/2}$, where $M(r)$ denotes the number of modes with support in a given phase r :

$$\dot{e}_k^{an} = \frac{3}{2} \frac{\partial \Psi^k}{\partial \sigma_{eq}} (a_r) \frac{\tau_k}{a_r}, a_r = \left(\sum_{k=1}^{M(r)} \tau_k^2 \right)^{1/2} \quad (15)$$

The system of Eqs. (9), (12), (13), (15) constitutes the effective constitutive relations of the composite. This system is solved along a prescribed path, either in the space of macroscopic stresses or in the space of macroscopic strains, which gives the internal variables ε_k^{an} . Finally, the macroscopic stress is obtained by averaging the stress field which results from Eqs. (2), (7) and (8):

$$\Sigma = \tilde{L} : E + \sum \left(\langle L : D * \mu^k \rangle - \langle L : \mu^k \rangle \right) \varepsilon_k^{an} \quad (16)$$

The tensors $\langle L : D * \mu^k \rangle$ and $\langle L : \mu^k \rangle$ are computed once for all.

Choice of the plastic modes

The choice of the plastic modes is a key point in the accuracy of the method. In this study the plastic modes are determined by using the following procedure. Let $\theta^k(x)$, $k = 1, \dots, M_T(r)$ be the normalised anelastic strain fields in a given phase r , determined for different macroscopic strain states by numerically solving the unit-cell problem along certain loading paths. The Karhunen-Loeve transformation is used to build a new set of modes $\mu^k(x)$, $k = 1, \dots, M_T(r)$:

$$\mu^k(x) = \sum_{l=1}^{M_T(r)} v_l^k \theta^l(x) \quad (17)$$

where v^k , for $k = 1, \dots, M_T(r)$, denote the eigenvectors of the correlation matrix g :

$$\sum_{j=1}^{M_T(r)} g_{ij} v_j^k = \lambda_k v_i^k, \quad g_{ij} = \langle \theta^i(x) : \theta^j(x) \rangle \quad i, j = 1 \dots M_T(r) \quad (18)$$

and λ^k the eigenvalues of matrix g . It is easy to verify that the new modes μ_k are orthogonal. First, $\langle \mu^k : \theta^l \rangle = \lambda^k v_l^k$. Then:

$$\langle \mu^k : \mu^l \rangle = \begin{cases} \lambda^k & \text{if } k = l \\ 0 & \text{if } k \neq l \end{cases} \quad (19)$$

Assuming $\lambda^1 \geq \lambda^2 \geq \lambda^3 \geq \dots \geq \lambda^{M_T(r)}$, another interest of the Karhunen-Loeve transformation lies in the fact that only the $M(r)$ [$M(r) \leq M_T(r)$] first modes of greater eigenvalues can be considered. In all the examples presented, the $M(r)$ principal modes are retained such that the following criterion is satisfied:

$$\frac{\sum_{k=1}^{M(r)} \lambda^k}{\sum_{k=1}^{M_T(r)} \lambda^k} > 0.9999 \quad (20)$$

Transformation Field Analysis

In the case of the TFA, the anelastic strain is assumed to be piecewise uniform within each individual phase or subdomain:

$$\varepsilon^{an} = \sum \varepsilon_r^{an} \chi^r(x) \quad (21)$$

The modes χ^r are the characteristic function of the phase r . They are scalar, whereas the modes for the NTFA are tensorial. Implementing Eq. (21) into Eq. (6), the average strain in the phase r is given by:

$$\varepsilon_r = A_r : E + \sum_{s=1}^N D_{rs} : \varepsilon_s^{an} \quad r = 1, \dots, N \quad (22)$$

where A_r the average strain-localisation tensors and D_{rs} the influence factors depend on the linear elastic properties of the individual phases.

$$\sigma_r = L^r : (\epsilon_r - \epsilon_r^{an}) = L^r : A_r : E + L^r \left(\sum_{s=1}^N D_{rs} : \epsilon_s^{an} - \epsilon_r^{an} \right) \quad (23)$$

so the macroscopic stress is given by:

$$\Sigma = \tilde{L} : E + \sum_{r=1}^N c^r L^r \left(\sum_{s=1}^N (D_{rs} - \delta_{rs}) : \epsilon_s^{an} \right) \quad \text{with} \quad \tilde{L} = \left(\sum_{r=1}^N c^r L^r : A_r \right) \quad (24)$$

The evolution of anelastic strain ϵ_r^{an} follows exactly the constitutive relations in phase r , the stress being estimated as the average stress in phase r :

$$\dot{\epsilon}_r^{an} = \frac{\partial \Psi^r}{\partial \sigma} (\sigma_r) \quad (25)$$

Application of the NTFA to a two-phase material

Configurations, material data

A two-phase composite with a viscoplastic fibre and matrix is considered. The viscoplastic potential for both phases is of the form:

$$\psi(\sigma) = \frac{\sigma_0 \dot{\epsilon}_0}{n+1} \left(\frac{\sigma_{eq}}{\sigma_0} \right)^{n+1} \quad (26)$$

A hexagonal cell is considered where the fibre volume fraction is 25%. Its microstructure is not representative of a nuclear fuel, but this case makes it possible, with mechanical parameters close to MOX data, to underscore the advantages of the NTFA for MOX fuels.

The fibre data are the same for all the calculations:

Young's modulus (GPa)	Poisson ratio	n	$\dot{\epsilon}_0$	σ_0 (MPa)
100	0.3	1	10^{-5}	250

The matrix data are the following:

Young's modulus (GPa)	Poisson ratio	n	$\dot{\epsilon}_0$
180	0.3	1 or 8	10^{-5}

$n = 1$	1	2	3	4	5	6
σ_0 (MPa)	50	100	500	1 000	5 000	10 000

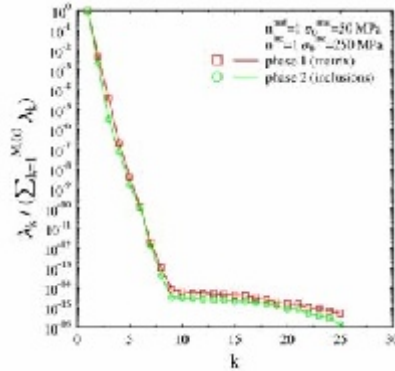
$n = 8$	1	2	3	4	5	6	7
σ_0 (MPa)	13.712	18.286	24.384	32.517	43.362	57.825	77.111

For loading, the direction of the overall stress is imposed (here, a uniaxial tension is imposed) and the magnitude of the overall strain in this direction is controlled.

Viscoplastic modes

The viscoplastic modes are chosen to be actual viscoplastic strain fields under uniaxial tension (the component Σ_{11} is non-zero, the other components are nil). We decided to take 25 modes between 0-5% of macroscopic strain for each phase. Thanks to the Karhunen-Loeve decomposition, we can obtain the principal modes. Figure 2 shows the eigenvalues of each phase. The matrix yield stress is 50 MPa, the fibre yield stress is 250 MPa.

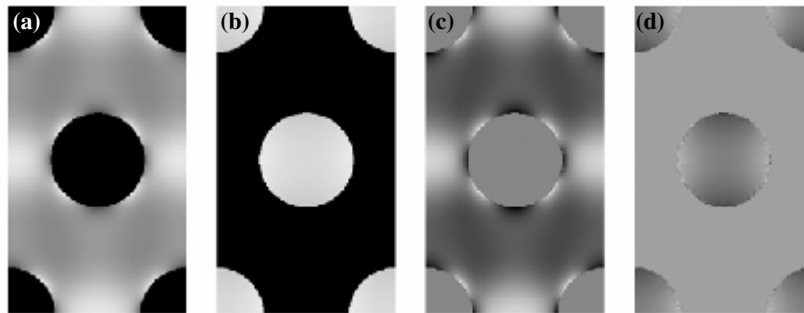
Figure 2. Eigenvalues of the matrix g [defined by Eq. (18)]



It can be seen in Figure 2 that the eigenvalues decrease very rapidly. Generally, the criterion in Eq. (20) is satisfied with only two modes for each phase, sometimes with three in the matrix according to the material data. Figure 3 shows the component μ_{11} of each mode in the matrix and in the aggregates in the case where the matrix yield stress is 50 MPa and the fibre yield stress is 250 MPa.

Figure 3. The component μ_{11} of the four modes used to the NTFA

(a) and (b) represent the mode of the highest energy (e.g. the greatest eigenvalue) respectively in the matrix and in the inclusions, (c) and (d) represent the mode for the following eigenvalue in the matrix and the inclusions

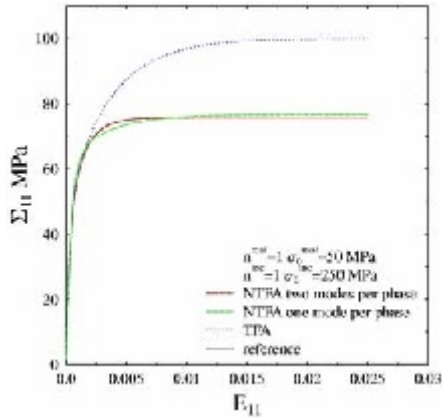


Results

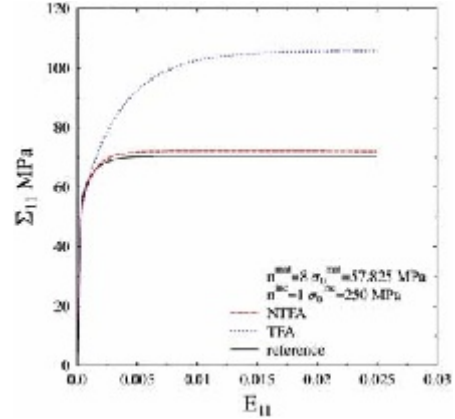
Figure 4 compares the results obtained with the TFA, the NTFA versus the “exact” results (reference) performed by a computational method based on fast Fourier transforms (see Refs. [4,5] for more details about this computational method). The overall stress in the imposed direction as a function of the overall strain in the same direction has been plotted.

Figure 4

(a) Predictions of TFA, NTFA with one or two modes in each phase and exact result in the case where exponent $n = 1$ in the matrix and in the inclusions



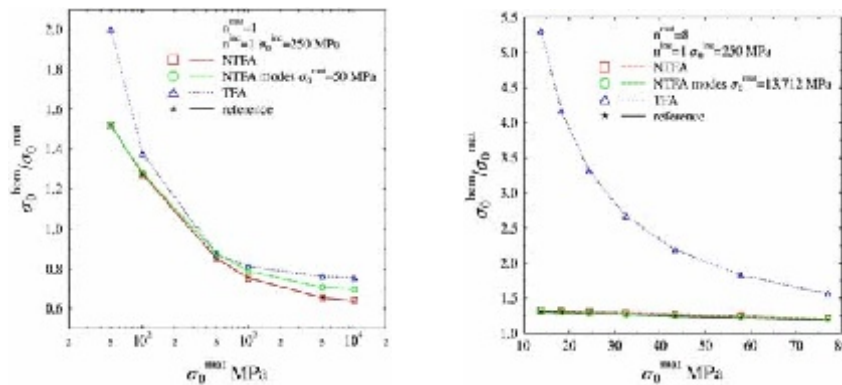
(b) Predictions of TFA, NTFA with two modes in each phase and exact result in the case where exponent $n = 8$ in the matrix and $n = 1$ in the inclusions



In all cases, it can be observed that the TFA provides too-stiff predictions. It can also be seen in Figure 4(a) that the NTFA with only one mode per phase is not in good agreement with the reference, in particular at the level of the bend. On the contrary, with two modes per phase, the NTFA is in excellent agreement with the reference whatever the strain considered.

Next, the effective yield stress obtained with the TFA and the NTFA were compared in all the cases previously presented. Moreover, the yield stress was calculated in all the cases with parameters of the NTFA calculated for another case: for $n = 1$ in the matrix, the matrix yield stress had been taken at 50 MPa, for the case $n = 8$ in the matrix, the matrix yield stress had been taken at 13.712 MPa. The aim of these calculations is to verify the effect of mechanical parameters on the NTFA method; as the parameters for nuclear fuels evolve during irradiation, it is important that the results not be strongly dependant on them.

Figure 5. The effective yield stress versus the matrix yield stress according to the used method, the inclusions yield stress being 250 MPa



It can be seen that the effective yield stress calculated with the TFA is always overestimated, in particular for the cases where $n = 8$; the error can reach more than 300%. Otherwise, the NTFA gives excellent results (the error is not greater than 0.02% in the case $n = 1$ and 2.4% in the case $n = 8$).

When modes calculated with a different matrix yield stress are used, a good agreement with the reference is obtained, in particular in the case $n = 8$, where the error does not exceed 1.7%. This is a very good point for MOX fuels.

Application of the TFA for MOX fuels

For the TFA approach, two phases are considered [the uranium-bearing phase (c^u) and the plutonium-bearing phase (c^p)]. The phases are porous (f^u and f^p are the porosity of each phase) and their behaviours are assumed to verify the following viscoplastic potential [2]:

$$\Psi^r = (1 - \theta^r) \Psi_1^r + \theta^r \Psi_2^r \quad (27)$$

$$\theta^r = \frac{1}{2} \left(1 + \tanh \left(\frac{T - \omega^r \sigma_{eq_r}^q}{h^r} \right) \right) \quad (28)$$

$$\Psi_i^r = \frac{K_i^r}{n_i^r + 1} (d^r)^{m_i^r} e^{-\frac{Q_i^r}{RT}} \left(A_i^r (f^r) \left(\frac{3}{2} tr \sigma_r \right)^2 + B_i^r (f^r) (\sigma_{eq_r})^2 \right)^{\frac{n_i^r + 1}{2}} \quad (29)$$

where d^r is the grain size of phase r , Ψ_i^r the force potential linked with two creeping mechanisms at the microscale (the scattering-creep acts for low temperatures and small stresses, the dislocation-creep acts for high temperatures and high stresses) and θ^r is the coupling function between the two creeping mechanisms.

The elliptical form of this potential allows us to take the creep into account under hydrostatic loading. The evolution of the porosity of each phase verifies the following mass balance equation:

$$\dot{f}^r = (1 - f^r) \frac{\partial \Psi^r}{\partial \sigma_r} \quad (30)$$

In order to evaluate localisation tensors and influence factors, we use the Mori-Tanaka estimate [6].

Introducing the classical isotropy orthogonal base with the 3×3 following matrix [7]: $J = 1/3 i \otimes i$ (where \otimes denotes the classical tensor product, and $i_{ij} = \delta_{ij}$) and $K = I - J$, all isotropy elasticity tensors can be written as:

$$L = 3kJ + 2GK = \{3k, 2G\} \quad (31)$$

where k and G are respectively the bulk modulus and shear modulus. So we have for each phase:

$$L^r = \{3k^r, 2G^r\} \quad (32)$$

With these notations, we can write the effective elastic tensor:

$$\tilde{L} = \{3k^{MT}, 2G^{MT}\} \quad (33)$$

with:

$$\begin{cases} k^{MT} = k^u + c^p \frac{k^p - k^u}{1 + c^u \frac{k^p - k^u}{k^* + k^u}} \\ G^{MT} = G^u + c^p \frac{G^p - G^u}{1 + c^u \frac{G^p - G^u}{G^* + G^u}} \end{cases} \quad (34)$$

the parameters k^* and G^* being defined by:

$$k^* = \frac{4}{3}G^u \text{ and } G^* = \frac{G^u}{6} \frac{9k^u + 8G^u}{k^u + 2G^u} \quad (35)$$

To evaluate localisation tensors A_r , the following equations are used:

$$\begin{cases} \sum_{r=1}^2 A_r = I \\ \sum_{i=1}^2 L^r A_r = \tilde{L} \end{cases} \Leftrightarrow \begin{cases} \text{if } L^u \neq L^p \text{ we have: } \begin{cases} A_u = \frac{1}{c^u} (L^u - L^p)^{-1} : (\tilde{L} - L^p) \\ A_p = \frac{1}{c^p} (L^p - L^u)^{-1} : (\tilde{L} - L^u) \end{cases} \\ \text{else: } A_u = A_p = I \end{cases} \quad (36)$$

To evaluate influence factors, the following equations are used:

$$\begin{cases} \sum_{r=1}^2 c^r D_{ri} = 0 \\ \sum_{r=1}^2 c^r L^r D_{ri} = c^i (I - A_i) L_i \end{cases} \Leftrightarrow \begin{cases} \text{if } L^u \neq L^p \text{ we have: } \begin{cases} D_{pp} = (L^u - L^p)^{-1} : (I - A_p) : L^u \\ D_{uu} = (L^p - L^u)^{-1} : (I - A_u) : L^p \\ D_{up} = -\frac{c^p}{c^u} D_{pp} \\ D_{pu} = -\frac{c^u}{c^p} D_{uu} \end{cases} \\ \text{else: } D_{uu} = D_{pp} = D_{pu} = D_{up} = 0 \end{cases} \quad (37)$$

The constant parameters of potential Ψ^u were identified by considering UO_2 behaviour and results of tests on MIMAS0 (0% of Pu) [8]. In Figure 6, we compare UO_2 (GM) and MIMAS0 (GM*) behaviour laws with experimental data. It is observed that GM behaviour law underestimates the creeping at low stresses and overestimates the creeping at high stresses. GM* law improves the GM model as is shown in Figure 6.

For the potential Ψ^p , MIMAS6 (6% of Pu) and MIMAS10 (10% of Pu) were used [8]. The agreement between experimental data and numerical simulations is plotted in Figure 7.

Figure 6. Comparison between simulate creep rate and experimental data

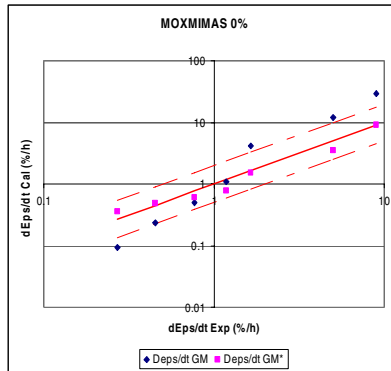
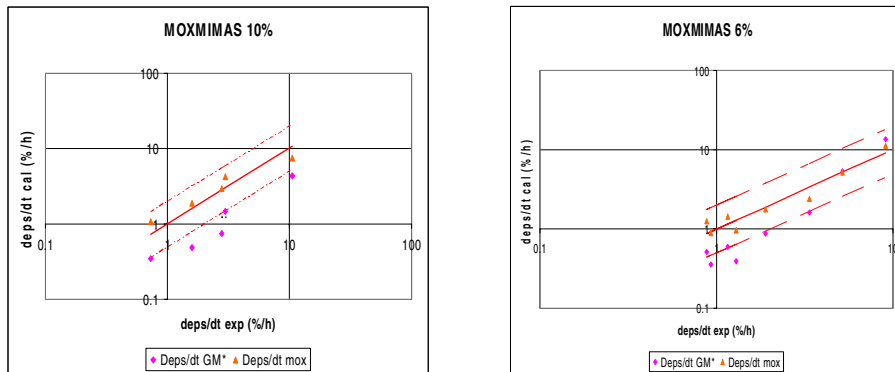


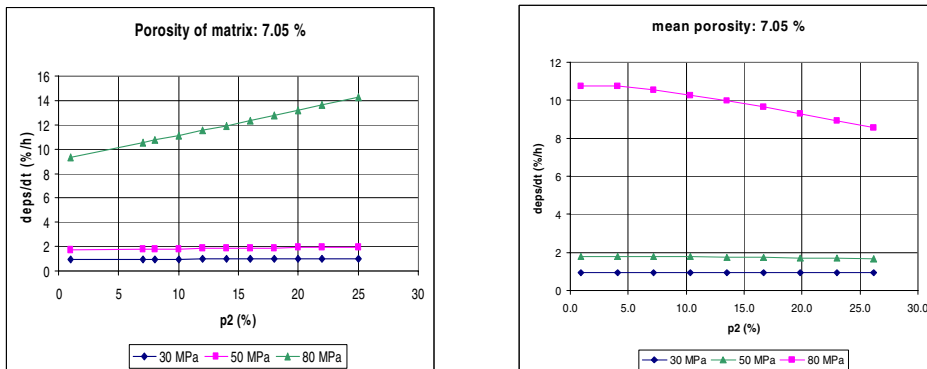
Figure 7. Comparison between simulated creep rate and experimental data



Porosity effect

Figure 8 shows, with different imposed stresses, the creep rate evolution versus the cluster porosity. For the first curves, the global porosity constant (7.05%) is considered. For the second, the matrix porosity constant (7.05%) is considered, and the porosity of clusters made to evolve. The results show a weak porosity effect to the creep rate. This effect is greater at high stresses.

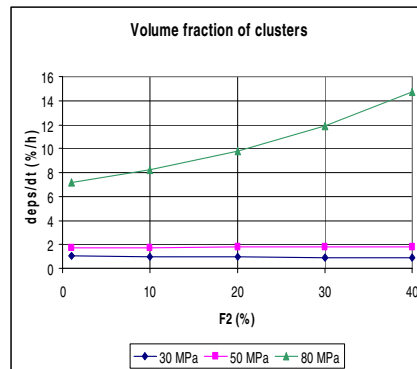
Figure 8. Effect of the porosity, creep rate versus clusters porosity



Volume fraction of clusters

Figure 9 shows the evolution of the creep rate versus the volume fraction of clusters for different imposed stresses. We can observe a weak effect of this parameter at small stresses, however this effect is bigger at high stresses.

Figure 9. Effect of the volume fraction of clusters on creep rate



Conclusions

The NTFA, used with a good choice of modes, provides excellent results and this study has shown that the method would be a good way to describe the behaviour of MOX fuels.

The TFA made possible a sensitivity study. For the porosity in clusters and the volume fraction of the plutonium-bearing phase, the higher the stress, the more these parameters influence the creep rate.

REFERENCES

- [1] Dvorak, G.J., "Transformation Field Analysis of Inelastic Composite Materials", *Proc. R. Soc. London, A* 437, 311-327 (1992). Also: Dvorak, G.J., Y. Benveniste, "On Transformation Strains and Uniform Fields in Multiphase Elastic Media", *Proc. R. Soc. London, A* 437, 291-310 (1992).
- [2] Monerie, Y., J.M. Gatt, "Overall Viscoplastic Behaviour of Non-irradiated Porous Nuclear Ceramics", *Mech. Mat.*, to be submitted (2004).
- [3] Michel, J.C., P. Suquet, "Non-uniform Transformation Field Analysis", *Int. J. Solids Struct.*, 40, 6937-6955 (2003).
- [4] Moulinec, H., P. Suquet, "A Numerical Method for Computing the Overall Response of Non-linear Composites with Complex Microstructures", *Comp. Methods Appl. Mech. Eng.*, 157, 69-94 (1998).

- [5] Michel, J.C., H. Moulinec, P. Suquet, “Effective Properties of Composite Materials with Periodic Microstructure: A Computational Approach”, *Comp. Methods Appl. Mech. Eng.*, 172, 109-143 (1999).
- [6] Mori, T., K. Tanaka, “Average Stress in Matrix and Average Elastic Energy of Materials with Misfitting Inclusions”, *Acta. Metall. Mater.*, 21, 597-629 (1973).
- [7] Suquet, P., M. Bornert, “Homogénéisation en mécanique des matériaux”, M. Bornert, T. Bretheau, P. Gilormini, Ed., *Hermès Science*, Vol. 2, 171 (2001).
- [8] Basini, V., C. Nonon, L. Caillot, “Out-of-pile and In-pile Viscoplastic Behaviour of Mixed Oxide Fuel”, PCI Seminar, Aix-en-Provence, France (2004).

THE MECHANICAL RESPONSE OF CLADDING WITH A HYDRIDE LENS UNDER PCMI LOADING CONDITIONS

Robert Montgomery, Joe Rashid, Robert Dunham
ANATECH Corp., USA

Odelli Ozer, Suresh Yagnik, Rosa Yang
EPRI, USA

Abstract

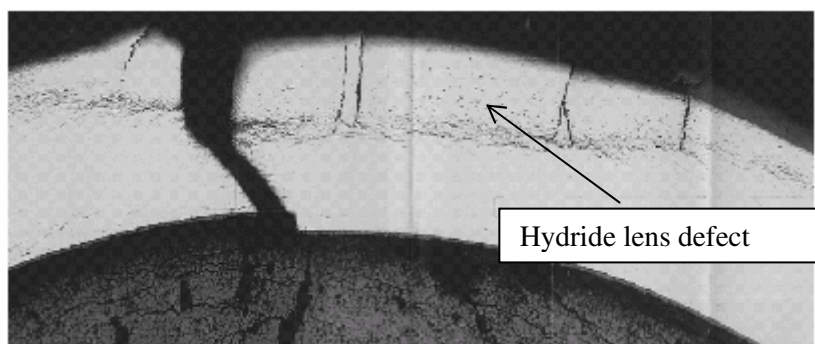
To identify the differences in cladding response between out-of-pile mechanical property tests and in-reactor PCMI of high burn-up fuel, finite element calculations have been conducted to evaluate the stress and strain distributions throughout the cladding in the vicinity of a hydride lens under both PCMI and pressure loading conditions. These calculations were performed using the ABAQUS general-purpose structural analysis code coupled with a specialised zircaloy-zirconium hydride composite mechanical constitutive model. In addition, local effects PCMI calculations were performed using the FALCON finite element fuel behaviour code. The results of the finite element calculations are compared to burst tests performed using irradiated cladding material containing hydride lens defects. Comparison of pressure/low friction loading and PCMI conditions indicate that the friction arising from fuel-clad bonding plays an important role in the development of cladding stress and strain distributions in the presence of cladding defects such as a hydride lens. Because of interfacial pellet-cladding friction, cladding failure models based directly on pressure or low friction mechanical property tests produce a lower-bound failure boundary when applied to the interpretation of cladding failure during PCMI loading of high burn-up fuel.

Introduction

Understanding the primary cause of cladding failure during power transients such as a reactivity initiated accident (RIA) requires a cladding integrity model that considers the cladding conditions and the type of loading applied to the cladding during the event. Typically, out-of-pile mechanical property tests are used to characterise the cladding failure process as a function of several key variables. These variables include: 1) material conditions defined by temperature, fast fluence, and hydrogen content and distribution, 2) geometry effects arising from transverse or longitudinal loading, and 3) loading state such as uniaxial or biaxial tension. Many experimental programmes have been conducted to evaluate the mechanical properties of irradiated zirconium alloy cladding. Several of these programmes are described in Refs. [1-4]. The primary objectives of these experimental programmes are to determine the important mechanical properties used to define the material elastic-plastic constitutive law, namely, yield stress, ultimate tensile strength, uniform elongation and total elongation. Testing methods used to obtain these properties include uniaxial, axial and ring tension tests on tube material, uniaxial tests using plate material and biaxial burst tests [1-5]. These test types are not specifically designed to measure the failure processes of zirconium alloy cladding tubes and as a consequence, using the results from such tests to define the conditions for cladding failure may represent an extrapolation, depending on the differences between the method of loading within the tests and the loading conditions within the fuel rod. Therefore, consideration must be given to the type of mechanical properties tests used to develop a cladding integrity model to determine how representative the test conditions are for the intended fuel rod transient response under evaluation.

Part-wall cladding defects can be formed during the manufacturing process or during normal operation. These defects can lead to through-wall cladding failure by mechanical fracture when sufficient PCMI loading occurs under normal or accident conditions. One type of cladding defect that can form during normal operation under extreme external oxidation conditions is a hydride lens defect [2,6]. Mechanical property tests on cladding material containing hydride lens defects have found a significant decrease in material strength and ductility [2,3] for the pressure or zero-friction loading conditions used in these tests. Also, through-wall cladding failure can occur in heavily hydrided material under PCMI loading conditions, depending on the size of the hydride lens defect. An example of a hydride lens defect resulting in cladding failure has been reported by Papin, *et al.* [7]. This hydride lens defect and through-wall crack is shown in Figure 1 and was observed in post-test examinations of the CABRI REP Na-8 rodlet.

Figure 1. Hydride lens defect and through-wall crack in the underlying zircaloy-4 ligament observed in post-test metallographic examination of the CABRI RE P Na-8 rodlet [7]



It is difficult to apply the failure characteristics exhibited in out-of-pile mechanical property tests to in-reactor fuel rod behaviour to interpret the process of cladding failure shown in Figure 1 because of the differences between PCMI loading conditions experienced in a fuel rod and the available loading

conditions used in mechanical property tests. The results of mechanical property tests generally represent average (circumferential or gauge) properties whereas the failure process is governed by the local conditions at the weak spot or defect. The possibility exists that the local conditions leading to failure evolve differently for PCMI loading than those observed in out-of-pile mechanical property tests. Therefore, an important step in developing an understanding in the process of cladding failure is to identify the differences in cladding mechanical response under the loading conditions used in mechanical property tests and under PCMI loading within a fuel rod.

The objective of this paper is to present a preliminary evaluation of the influence of an incipient cladding defect associated with the formation of a hydride lens on the cladding failure response under: 1) pressure or low friction loading conditions typical of mechanical property tests and 2) PCMI loading conditions representative of high burn-up fuel with the presence of high interfacial pellet-cladding friction. Detailed finite element calculations were performed to determine the influence of an incipient cladding defect on the local stress and strain distributions produced with and without the presence of pellet-cladding friction. By comparing the evolution of the stress and strain localisation in the vicinity of an incipient cladding defect for the different loading conditions, it is possible to identify the impact of the defect on the overall cladding tube response leading up to failure.

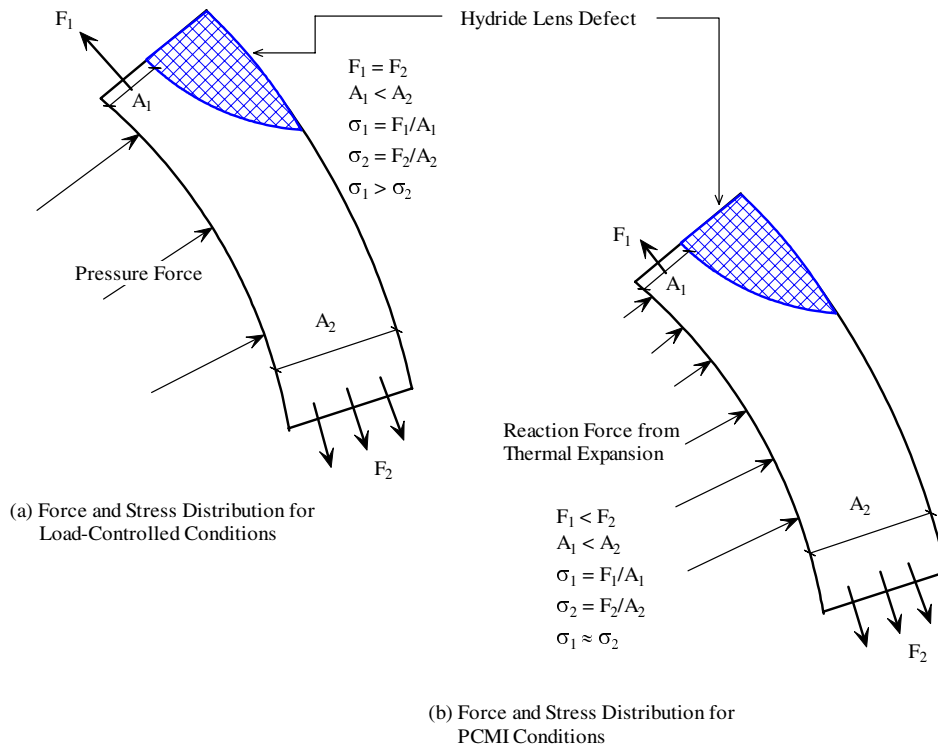
Load-controlled versus PCMI loading conditions

The following addresses, conceptually, the differences in the cladding mechanical response between pressure or zero friction displacement loading (load-controlled) conditions and pellet-cladding mechanical interaction (PCMI) loading conditions. Pressure or zero/low friction displacement loading conditions are generally used in tube burst tests or uniaxial tension tests to measure cladding mechanical properties, whereas PCMI loading conditions are the primary loading process in irradiated fuel under normal and off-normal operating conditions.

Figure 2 shows a schematic comparing both the load-controlled and PCMI loading conditions in the presence of a cladding defect. Pressure or zero friction displacement loading applied to cladding tubes where deformations have little or no influence on the applied force represent load-controlled conditions. Under load-controlled conditions an increase in strain results in an instantaneous increase in stress due to changes in cross-sectional area, and, since the force is maintained (follows the cladding displacement) further strain develops. Once plasticity occurs load-controlled conditions typically result in material instability and failure since the material cannot resist additional stress. Furthermore, the presence of a defect that introduces variations in the cross-sectional area normal to the force causes local stress concentrations as shown in Figure 2. In the case of cladding with a hydride lens, the inability of the hydride lens to sustain a load due to cracking or plastic flow of the hydrides localises the force into the remaining zircaloy ligament. Under load-controlled conditions, the force across the r-z plane of the cladding is the same at all azimuthal locations. This means that the smaller effective cross-sectional area in the vicinity of the hydrides lens produces higher local stresses. This stress concentration results in focusing of the strain, or strain localisation, into the thinner region once plasticity occurs at the defect location.

For PCMI conditions, a mandrel or pellet displaces the cladding inner surface (Figure 2). This displacement is nearly uniform around the circumference under typical PCMI conditions representative of RIA-induced pellet thermal expansion with friction between the pellet and cladding. Under PCMI conditions, the cladding is loaded by displacement-control, i.e. the cladding deformations are limited by the amount of pellet or mandrel expansion. The presence of pellet-cladding friction is an important element of the PCMI loading process. The existence of friction between the pellet and cladding distributes the PCMI force throughout the cladding inner circumference and causes more of the cladding

Figure 2. Schematic of force and stress distribution for (a) load-controlled and (b) PCMI loading conditions



material to participate in the deformation process. As a consequence, PCMI conditions representative of RIA-induced thermal expansion of the pellet minimise the stress and strain concentrations in the presence of cladding defects such as a hydride lens. Furthermore, the cladding cannot strain beyond the amount of displacement resulting from the PCMI imposed forces, unlike the load-controlled condition, which can strain indefinitely because the force is maintained throughout the cladding displacement process.

For un-irradiated tubes or irradiated tubes without large defects, the mechanical response of the cladding under the two different loading conditions differs only beyond the uniform elongation strain range. However, the differences in mechanical response between load-controlled and PCMI loading become more significant with the presence of cladding defects, such as hydride lenses. It is important to understand these differences in order to correctly use and apply the results of mechanical property tests such as tube burst tests or uniaxial ring tension tests in the interpretation of in-pile experiments such as the CABRI REP Na-8 tests that are dominated by PCMI [7].

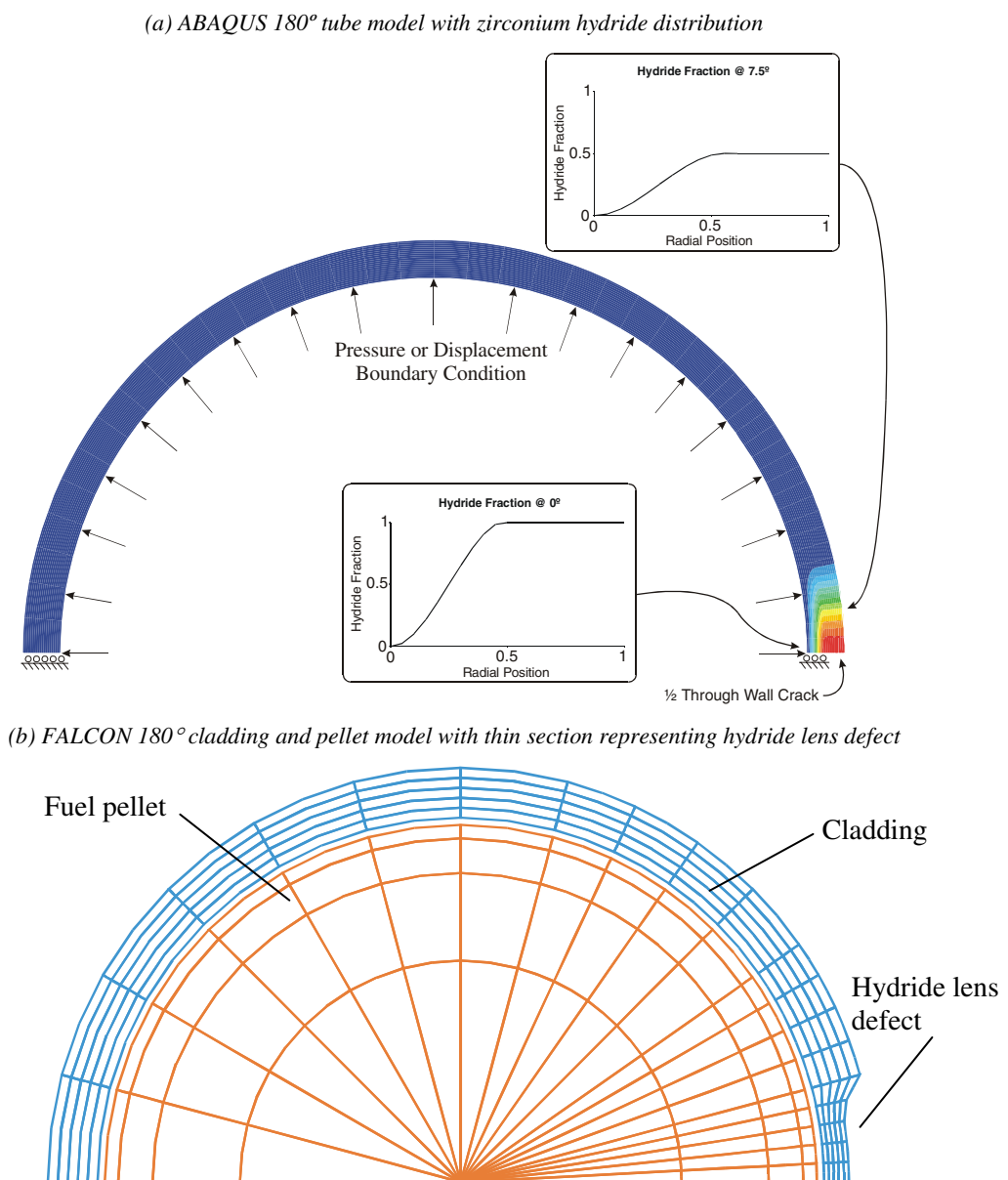
Analysis approach

To evaluate the stress and strain response under both load-controlled and PCMI loading conditions, a detailed finite element (FE) analysis of a cladding region containing a hydride lens was performed using two different methods. First, a cladding tube analysis was performed using the ABAQUS general purpose structural analysis code coupled with a specialised zircaloy-zirconium hydride (ZrH_2) composite mechanical constitutive model [8,9]. The cladding-tube-only analysis considered both a pressure loading condition at the cladding inner surface and an imposed inner cladding surface displacement loading condition. To capture the effects of pellet-cladding mechanical interaction, a second series of finite

element analyses were performed using the FALCON fuel rod behaviour code [10]. Since FALCON is a fuel rod behaviour code, the analysis contained the effects of pellet-cladding mechanical interaction, including the effects of pellet-cladding friction. In addition to pressure loading, pellet thermal expansion from a linear power ramp was used to load the cladding in the FALCON model.

Figures 3(a) and 3(b) contain illustrations of the finite element models used in the ABAQUS and FALCON calculations, respectively. The models shown in Figure 2 contain a 180° cladding tube and fuel pellet (for FALCON only) representation with two symmetry boundary condition locations; 0° corresponding to the deepest location of the hydride lens and 180° corresponding to the far-field location. A generalised plane-strain boundary condition is applied in the axial direction for both the ABAQUS and FALCON finite element models.

Figure 3. Finite element models used in the ABAQUS and FALCON calculations



Both the ABAQUS and FALCON finite element models included the presence of a cladding defect in the form of a hydride lens. The representation of the hydride lens was different between the two analytical approaches. In the ABAQUS analysis, the hydride lens was modelled using a two-phase constitutive elastic-plastic mixture model developed specifically for cladding material containing a distribution of circumferential hydride platelets and solid hydride lenses [9]. Imposing a non-uniform hydride distribution resulted in the two-phase mixture model having a local weak spot representing the hydride lens location. As shown in Figure 3(a), the hydride lens in the ABAQUS model extended more than 50% of the cladding wall and over a distance of $\sim 30^\circ$ around the circumference. As post-test observations generally find that the hydride lens forms a crack at the deepest location, the ABAQUS analysis was performed with a part-wall crack in the hydride at the 0° symmetry boundary location.

The FALCON finite element model shown in Figure 3(b) contains an explicit representation of the remaining zircaloy-4 ligament beneath a hydride lens in the cladding. Such a treatment of the hydride lens was necessary because the two-phase mixture model is not present in FALCON at this time. The approach used in FALCON assumes that the hydride lens cracks at low stress and strain conditions and the main structural component that resists deformations is the remaining zircaloy-4 ligament.

Utilising the models shown in Figure 3, two sets of clad loading conditions were analysed: 1) a pressure boundary condition at the cladding inner surface and 2) a pellet-cladding mechanical interaction (PCMI) boundary condition at the cladding inner surface. The pressure boundary condition at the cladding inner surface represents a load-controlled condition consistent with a tube burst test. The pressure boundary condition case was analysed with both ABAQUS and FALCON. The PCMI boundary condition was modelled using two different methods. Since a fuel pellet model is not readily available in ABAQUS, a radial displacement history was applied to the cladding inner surface nodes of the ABAQUS model to represent the outward expansion of the pellet. In addition, the hoop (or azimuthal) displacement of the cladding inner surface was restrained, compatible with a bonding condition between the pellet and cladding. The displacement boundary condition at the cladding inner surface simulates the PCMI expected during a power rise of a reactivity initiated accident (RIA). Second, the FALCON model includes a fuel pellet and PCMI was represented through fuel pellet thermal expansion. To evaluate the role of friction on the cladding stress and strain distributions, different levels of pellet-cladding interfacial friction were used in the FALCON analysis.

Analysis results

The following presents the analysis results for the cladding stress and strain behaviour obtained from the ABAQUS and FALCON finite element calculations for both the load-controlled and PCMI loading conditions. The load-controlled loading conditions included a linear pressure ramp to 30 MPa in the ABAQUS analysis and both a linear pressure ramp to 60 MPa and a zero-friction PCMI load in the FALCON analysis. The difference in the pressure levels reached in the ABAQUS and FALCON calculations is a result of the hydride lens defect size used in the two models. The PCMI loading conditions used in the ABAQUS consisted of a displacement boundary condition at the cladding inner surface. The radial displacement at the cladding inner surface was linearly increased to a value corresponding to $\sim 2\%$ hoop strain at locations far from the hydride defect. In the FALCON model, a linear power ramp over 5 minutes was used to produce PCMI loading. The pellet-cladding interfacial friction coefficient was varied between zero and 1.0 in the FALCON calculations to evaluate the role of friction on the cladding stress and strain distributions.

To evaluate the effects of a hydride lens defect, the cladding hoop strain in the vicinity of the hydride lens (0°) and at far-field locations (180°) are provided in Figures 4 and 5 from the FALCON and ABAQUS models, respectively. Contained in these figures is a plot of the cladding hoop strain at

Figure 4. The FALCON calculated hoop strain at the defect location as a function of the hoop strain 180° from the defect for both load-controlled and PCMI loading conditions. Different levels of pellet-cladding interfacial friction are shown for comparison.

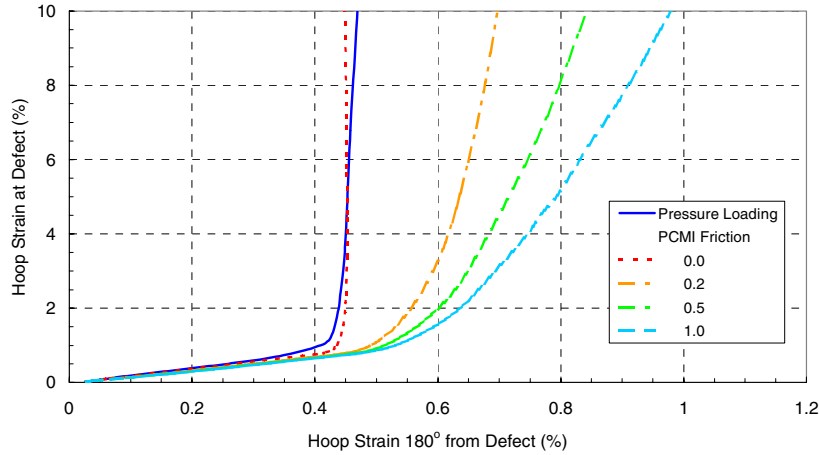
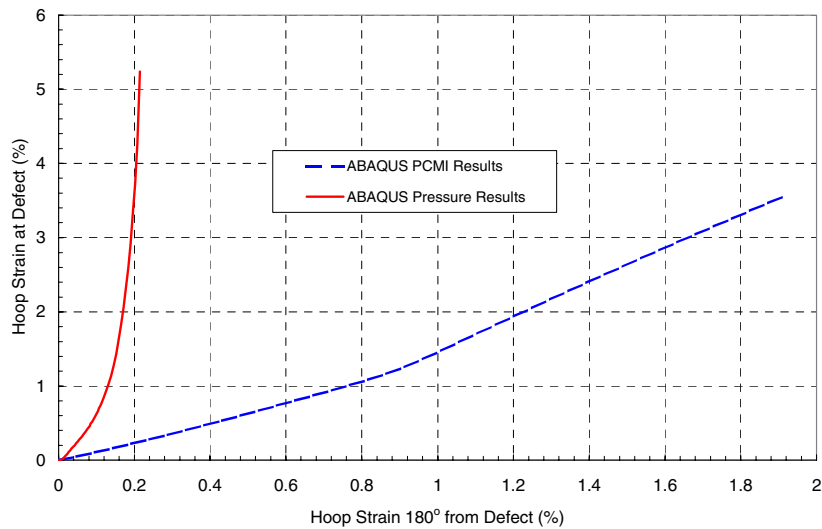


Figure 5. The ABAQUS calculated hoop strain at the defect location as a function of the hoop strain 180° from the defect for both load-controlled and PCMI loading conditions



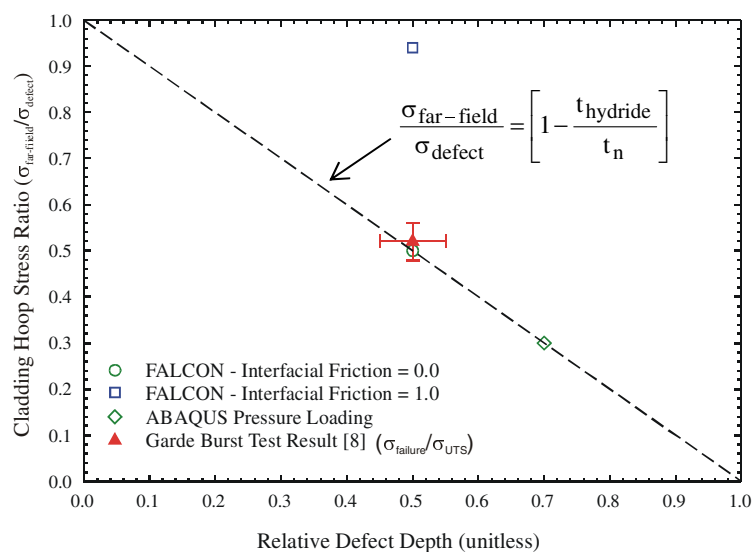
the defect location as a function of the cladding hoop strain at the 180° location during the loading process. In all the figures, the cladding hoop strain at both the defect location and the 180° location are plotted at the radial position corresponding to the mid-wall of the cladding ligament in the defect. The results from both the load-controlled and PCMI loading conditions are shown in the figures.

Both the FALCON and ABAQUS calculated cladding hoop strain for the load-controlled loading conditions, either pressure or zero friction, demonstrate strain localisation once plasticity is reached in the cladding ligament near the hydride lens defect. The strain localisation in the thin ligament section results in plastic instability and ultimately failure at far-field strain levels well within the elastic regime. These results are consistent with tube burst test results on irradiated cladding material containing a hydride lens reported by Garde [2]. In this burst test, the failure stress calculated from the burst pressure using a thin wall tube approximate (Pr/t) was ~50% of the ultimate tensile strength for tubing without a defect, indicating failure in the elastic regime.

Under PCMI loading conditions, the presence of friction between the pellet and cladding causes more of the cladding circumference to participate in the deformation process. As a result, the cladding hoop strain at the far-field location continues to increase even though the ligament at the defect location has yielded and is undergoing plastic deformation. The results shown in Figure 4 and 5 indicate that the amount of strain localisation under PCMI loading conditions is a function of the pellet-cladding interfacial friction. The amount of strain localisation decreases as the interfacial friction is increased in the FALCON analysis. At pellet-cladding interfacial friction coefficients representative of high burn-up fuel conditions ($f > 0.5$), strain localisation is minimised and plastic instability is suppressed until higher far-field strains have developed. The least amount of strain localisation occurs under the pellet-clad bonding conditions as represented in the ABAQUS model. The displacement boundary conditions used in the ABAQUS model restricts the deformations at the cladding inner surface to the radial direction only and prohibits any azimuthal deformations to occur at the cladding inner surface, thus minimising the strain concentration within the ligament at the hydride lens defect. Further analysis work is needed to confirm that the pellet-clad bonding conditions simulated in the ABAQUS analysis are representative of actual PCMI behaviour.

The maximum stress calculated 180° from the defect location (far-field) divided by the maximum stress in the defect location is plotted as a function of the relative hydride lens depth in Figure 6 for the FALCON and ABAQUS results. The relative hydride lens defect depth is given by the ratio of the hydride lens (or defect) depth divided by the nominal cladding wall thickness. As expected, the analysis results show that the stress in the thin ligament section in the defect is linearly proportional to the thickness reduction at the defect under pressure or zero interfacial friction loading conditions. The load-controlled FALCON and ABAQUS calculations agree well with the results of burst tests conducted on cladding with a hydride lens defect present in the sample. Included in Figure 6 is the result from a burst test reported by Garde on cladding suspected of containing a hydride lens defect [2]. The result of this burst test is shown in Figure 6 where the maximum circumferentially-average hoop stress ($\sigma_{failure} = P_{failure} * r_n / t_n$) calculated from the pressure at failure ($P_{failure}$), the nominal tubing radius (r_n) and the oxide-corrected thickness (t_n) is divided by the ultimate tensile strength from tests on cladding tubes without hydride lens defects. Also shown are the uncertainties in the hydride lens depth and variation in ultimate tensile strength.

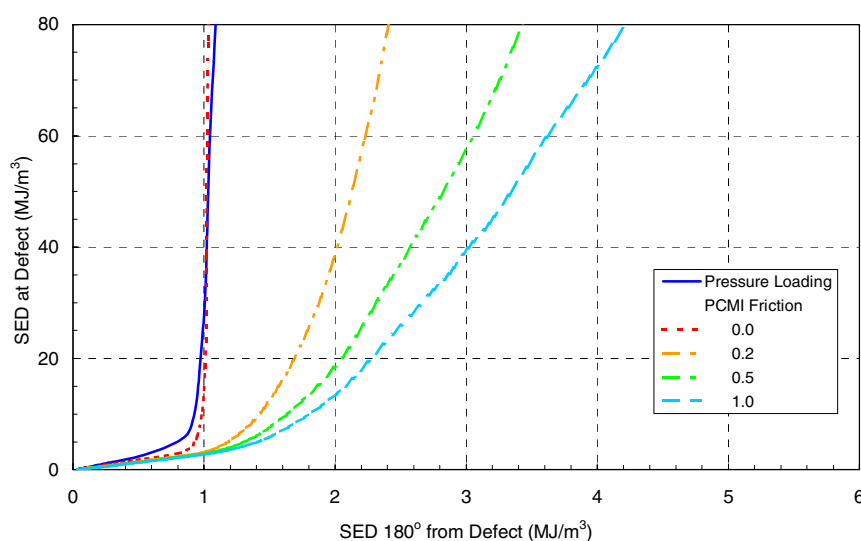
Figure 6. Cladding hoop stress ratio as a function of relative defect depth for the FALCON and ABAQUS calculations. A linear dependence based on a wall thickness reduction formulation is shown for comparison.



Also shown in Figure 6 is the stress ratio from the FALCON analysis including the effects of high interfacial friction ($f = 1.0$). The FALCON calculated stress ratio resides well above the load-controlled loading conditions and a linear function based on a simple wall thickness reduction. This result demonstrates that the presence of friction increases the stress level at regions far from the hydride lens defect location, thus minimising the stress and strain localisation process. As a result, the mechanical work required to produce plastic deformation and strain localisation is higher for PCMI loading with friction than for load-controlled loading conditions.

In order to evaluate the increase in the mechanical work required to cause strain localisation, the strain energy density (SED) calculated in the ligament region is plotted as a function of the SED at the 180° location in Figure 7. The SED this location is a good approximation of the circumferentially averaged SED calculated from mechanical property tests or typical axi-symmetric r-z fuel rod analysis codes. As shown in Figure 7, strain localisation in the defect region results in very low SED values in regions away from the defect for pressure or zero friction load-controlled loading conditions. However, for PCMI loading with interfacial friction, the deformations developed throughout the remainder of the cladding cause the SED in these regions to increase. Depending on the failure characteristics of the ligament, the circumferentially averaged SED could be 3-4 times higher under PCMI loading compared for load-controlled conditions.

Figure 7. FALCON calculated cladding SED at the defect location as a function of the SED at the 180° location. FALCON results are shown of both load-controlled (pressure and zero friction) loading and PCMI loading with different levels of interfacial friction.



Discussion

Some important differences have been observed in the deformation analysis of the load-controlled and PCMI loading conditions for cladding with a hydride lens defect. Load-controlled conditions cause stress and strain localisation in the region of wall thinning associated with a local defect such as a hydride lens. As a result, pressure loading or zero friction loading conditions only mobilise the thin ligament of material beneath a hydride lens. Most of the cladding remains in the elastic regime at stress levels approximately equal to the thin-wall tube (Pr/t) stress. These deformation analysis results are consistent with observations from tube burst tests on cladding with hydride lens defects. On the other hand, PCMI loading conditions with pellet-cladding interfacial friction activates more of the

cladding tube material during the deformation process. As a result, it is necessary to deform more of the cladding tube to achieve deformation in the ligament adjacent to a hydride lens. Although strain concentration occurs in the thin wall section adjacent to the hydride lens, the relative difference between the defect region and the remainder of the cladding is considerably lower.

The finite element analyses performed using more realistic PCMI loading conditions for irradiated fuel demonstrate that burst tests in the presence of cladding defects overemphasises the impact of these defects on the mechanical response of the cladding under PCMI conditions. The friction conditions between the pellet and cladding isolates the local defect and allows more of the cladding material to participate in the deformation process. As a result, the strain localisation process is minimised for PCMI conditions.

It can be assumed that the local stress and strain in the ligament region near the hydride lens defect governs the ultimate failure of the cladding at that location, irrespective of the loading conditions. The deformation analyses described above show that to reach the same local stress and strain conditions within the thinned wall region of the hydride defect, the far-field stress and strain levels could be 2-3 times higher under PCMI loading than for load-controlled loading where most of the cladding wall is only at a fraction of the yield stress. This means that for PCMI conditions, the pellet expansion work needed to strain the cladding to failure is much higher than the pressure work needed to reach failure in burst tests.

Because load-controlled mechanical property tests such as burst tests or ring tension tests overemphasise the stress and strain concentrations caused by wall-thinning near a hydride lens defect, the circumferentially averaged stress, strain and strain energy density determined from these tests will be considerably lower at failure than for conditions of PCMI with a strong friction component. Based on observations from mechanical property tests on heavily hydrided irradiated cladding, several failure models have been developed using strain localisation mechanisms [11-12]. Failure models based on strain localisation such as those by Koss, *et al.* [11] and Jernkvist [12] will over-predict the failure potential for cladding with defects experiencing PCMI loading conditions, especially those typical of an RIA event in high burn-up fuel. These strain localisation models ignore the role of PCMI on the stress distribution throughout the cladding tube. Furthermore, direct application of results from mechanical property tests to interpret cladding failure in RIA experiments as reported by Papin, *et al.* [7] will also over-predict the failure potential for irradiated fuel rods.

Cladding failure models based directly on the results of load-controlled mechanical property tests on heavily hydrided cladding samples containing hydride lenses will be biased downward because of the differences in the stress and strain states between load-controlled and PCMI loading conditions. Such models represent a conservative lower-bound failure boundary when applied to the interpretation of cladding failure under PCMI loading of high burn-up fuel rods. Recently, PCMI loading conditions with friction have been simulated in out-of-pile mechanical property tests using the expansion due to contraction (EDC) testing method [13]. The results of EDC tests performed on cladding material containing hydride defects could provide data suitable to develop cladding failure models applicable to PCMI conditions.

Conclusions

A preliminary evaluation has been performed to identify the influence of an incipient cladding defect associated with the formation of a hydride lens on the cladding failure response under both: 1) pressure or low friction loading conditions typical of mechanical property tests and 2) PCMI loading conditions representative of high burn-up fuel with the presence of high interfacial pellet-cladding

friction. To identify the differences in cladding response between out-of-pile mechanical property tests and in-reactor PCMI of high burn-up fuel, finite element calculations were used to evaluate the stress and strain distributions throughout the cladding in the vicinity of a hydride lens under both PCMI and load-controlled loading conditions. These calculations were performed using the ABAQUS general purpose structural analysis code coupled with a specialised zircaloy-zirconium hydride composite mechanical constitutive model. To support the ABAQUS analysis, local effects PCMI calculations were performed using the FALCON finite element fuel behaviour code. The PCMI calculations performed with FALCON included the effects of pellet-cladding interfacial friction.

Both the FALCON and ABAQUS calculated cladding hoop strain for the load-controlled loading conditions, either pressure or zero friction, demonstrate strain localisation once plasticity is reached in the cladding ligament near the hydride lens defect. This result is consistent with tube burst tests performed on cladding material with hydride lens defects. In contrast, the analysis results for PCMI loading demonstrate that the presence of interfacial friction between the pellet and cladding causes more of the cladding circumference to participate in the deformation process. As a result, the pellet expansion work needed to strain the cladding to failure is much higher than the pressure work needed to reach failure in burst tests. The results of the finite element calculations indicate that the friction arising from fuel-clad bonding plays an important role on the development of cladding stress and strain distributions in the presence of cladding defects such as a hydride lens. Both the ABAQUS and FALCON analysis results demonstrate that the stress and strain concentrations caused by wall-thinning near a hydride lens are larger under burst test conditions as compared to PCMI conditions. As a result, cladding failure models based directly on the results of tube burst tests or low friction ring tensile mechanical property tests on heavily hydrided cladding samples containing hydride lenses will be biased downward because of the differences in the stress and strain states between load-controlled and PCMI loading conditions.

REFERENCES

- [1] Garde, A.M., "Effects of Irradiation and Hydriding on the Mechanical Properties of Zircaloy-4 at High Fluence", *Zirconium in the Nuclear Industry: 8th International Symposium*, ASTM STP 1023, pp. 548-569 (1989).
- [2] Garde, A.M., G.P. Smith, R.C. Pirek, "Effects of Hydride Precipitate Localization and Neutron Fluence on the Ductility of Irradiated Zircaloy-4", *Zirconium in the Nuclear Industry: 11th International Symposium*, ASTM STP 1295, pp 407-430 (1989).
- [3] Balourdet, M., C. Bernaudat, V. Basini, N. Hourdequin, "The PROMETRA Programme: Assessment of Mechanical Properties of Zircaloy-4 Cladding During an RIA", *Proceedings of the Structural Mechanics in Reactor Technology (SMiRT) 15*, Vol. II, pp. 485-492 (1999).
- [4] Wisner, S.B., R.B. Adamson, "Combined Effects of Radiation Damage and Hydrides on the Ductility of Zircaloy-2", *Nuclear Engineering and Design*, 185, pp. 33-49 (1998).
- [5] Pierron, O., *et al.*, "The Influence of Hydride Distribution on the Failure of Zircaloy", *Proceedings of the USNRC Nuclear Safety Research Conference*, October 2002.

- [6] Guedeney, P., M. Troabas, M. Boschiero, C. Forat, P. Blanpain, “FRAGEMA Fuel Rod Behavior Characterization at High Burn-up”, *Proceedings of the International Topical Meeting on LWR Fuel Performance*, Avignon, France, 21-24 April 1991.
- [7] Papin, J., B. Cazalis, J.M. Frizonnet, E. Federici, F. Lemoine, “Synthesis of CABRI-RIA Tests Interpretation”, *Proceedings of EUROSAFE Forum 2003 Conference*, 25-26 November 2003.
- [8] *ABAQUS User's and Theory Manuals, Version 5.8*, Hibbitt, Karlsson, Sorensen, Inc., (1998).
- [9] Machiels, A, *Dry Storage of High Burn-up Spent Fuel – Responses to Nuclear Regulatory Commission Requests for Additional Information and Clarification: Appendix E – Development of a Two-phase Elastic Plastic Mixture Model for Zircaloy Cladding with Distributed Hydrides and Hydride Lenses*, EPRI 1009276, November 2003.
- [10] Montgomery, R.O., *et al.*, *FALCON – Fuel Analysis and Licensing Code, Volume 2: User's Manual*, ANA-97-0230, ANATECH Corp., San Diego, California, December 1997.
- [11] Link, T.M., A.T. Motta, D.A. Koss, “On the Issue of Zircaloy Ductility During a Reactivity Initiated Accident”, *Proceedings of the US NRC 24th Water Reactor Safety Information Meeting (WRSIM)*, 21-23 October 1996, NUREG/CP-0157, pp. 141-149.
- [12] Jernkvist, L.O., “Prediction of Failure of Highly Irradiated Zircaloy Clad Tubes Under Reactivity Initiated Accidents”, *Proceedings of the Structural Mechanics in Reactor Technology (SMiRT) 17* (2003).
- [13] Grigoriev, V., R. Jakobsson, D. Schrire, “Experimental Evaluation of Critical Strain Energy Density for Irradiated Cladding Under Simulated RIA Conditions”, *Proceedings of the ENS Topfuel 2001 Conference*, Stockholm, Sweden (2001).

ASSESSMENT OF CLADDING RELAXATION AND PCMI MODELS IN INFRA

Young-Min Kim, Yong-Sik Yang, Chan-Bock Lee, Dae-Ho Kim, Youn-Ho Jung
Korea Atomic Energy Research Institute, Korea

Abstract

A contact model analysing the PCMI of a LWR fuel rod with the Lagrange multiplier technique was developed, and a model for strain relaxation of cladding was suggested. These models were inserted into a high burn-up fuel performance analysis code. Displacement, strains, stresses, and contact pressure of the pellet and the cladding were calculated at powers between 13 and 60 kW/m and at the frictional coefficients between 0 and 1 using the finite element program and ABAQUS. Results of both the programs showed a very good agreement. Cladding elongation for two ramps of in-pile test data was calculated using the irradiation creep toward the pellet. The result from the calculation described the cladding relaxation well. The frictional coefficients are 0.8 at the ramp during the early stage and 0.2 at the ramp during the late stage of the test.

Introduction

Mechanical behaviour of the fuel rod is the stress and strain distribution in the pellet and the cladding, pellet-cladding mechanical interaction (PCMI), and pellet cracking by thermal stress due to a temperature gradient. Since PCMI greatly affects the failure behaviour, including the crack, of a high burn-up fuel rod, it is important to set up a correct and effective PCMI analysis method. In-pile tests show that the strain relaxation of the cladding during a high power holds, and that the weakening of the PCMI causes the cladding relaxation [1]. The detailed mechanism should be known.

The numerical methods used to traditionally evaluate the PCMI are the penalty method [2,3] and the Lagrange multiplier technique [4,5]. The penalty method is easy to implement into the finite element equation. It maintains the symmetry of the stiffness matrix in the finite element equation. However, the results become erroneous if the value of the penalty constant is not given exactly. In the Lagrange multiplier technique, some constraints are added to the finite element equation. The stiffness matrix is no longer symmetric, and the calculation then becomes very slow. However, the Lagrange multiplier technique produces a correct solution.

In this study, a contact analysis method for estimating the PCMI was set up using the Lagrange multiplier technique, and the irradiation creep of the pellet was selected in order to describe the cladding relaxation. These models were inserted into a finite element modelling (FEM) program for calculating the stress and strain distribution of a structure, and then the integrated FEM module was connected to a high burn-up UO_2 fuel rod performance analysis code. The cladding elongation results from the FEM module and the re-irradiation tests of the fuel rod were compared after the validation of the FEM module.

Modelling of PCMI and cladding relaxation

Finite element modelling module in INFRA

A PCMI analysis program written in FORTRAN was integrated into a previously developed FEM program for structural analysis; the combined program was inserted into the INFRA (*INtegrated Fuel Rod Analysis*) code. INFRA is a high burn-up UO_2 fuel rod performance analysis code developed at the Korea Atomic Energy Research Institute [6]. Figure 1 shows the FEM module in INFRA. The module calculates the mechanical behaviours of a half pellet and the adjacent cladding with a load incremental method using the basic data from the INFRA, and it does not change any functions of the other routines in INFRA. The basic data being transferred from the INFRA to the FEM module are the geometric dimension, the temperature distribution of the pellet and cladding, as well as the mechanical loads, and some physical quantities such as the density, fast neutron flux, fast neutron fluence, etc. Mechanical analysis results from the FEM module are the displacement, stress and strain, as well as the strain energy density of the pellet and the cladding, and the contact state and pressure between the pellet and the cladding.

Finite element modelling of the pellet and cladding

A two-dimensional axisymmetric finite element model, shown in Figure 2, was set up for the pellet and the cladding. A quarter of a pellet was divided into five radial and three axial elements. The adjacent cladding was divided into three axial elements. An eight-node serendipity finite element was employed. The pellet was assumed to move freely in the axial direction. By using the symmetry conditions, it is assumed that the radial centre of the pellet and the axial centre of the pellet and the cladding are not displaced.

Figure 1. FEM module in INFRA

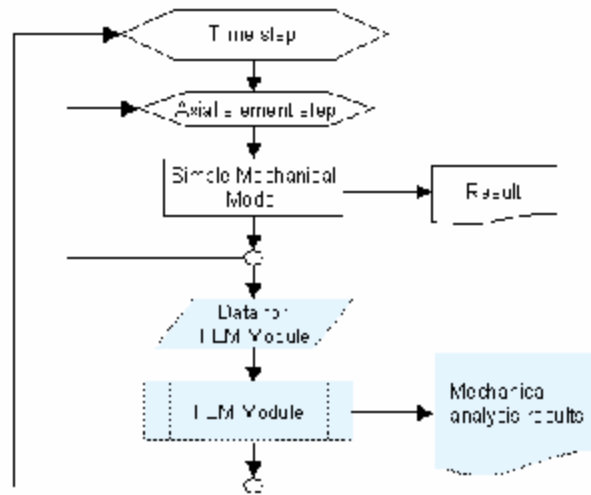
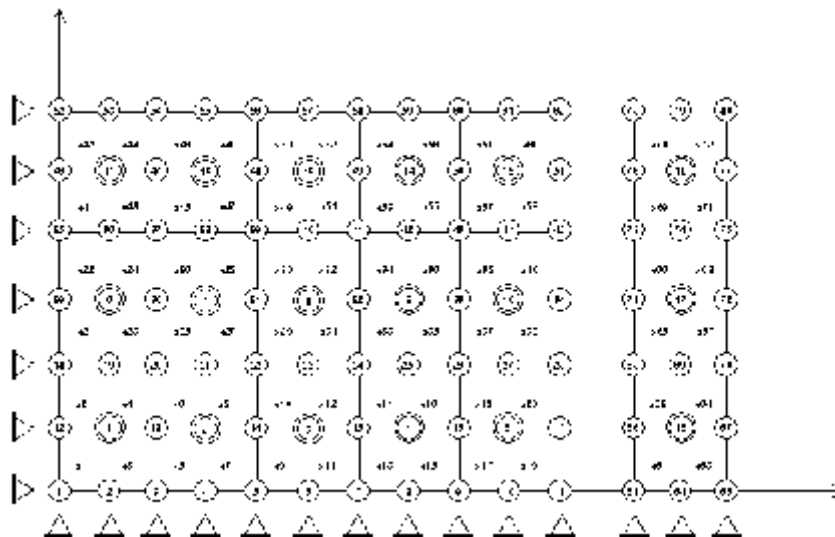


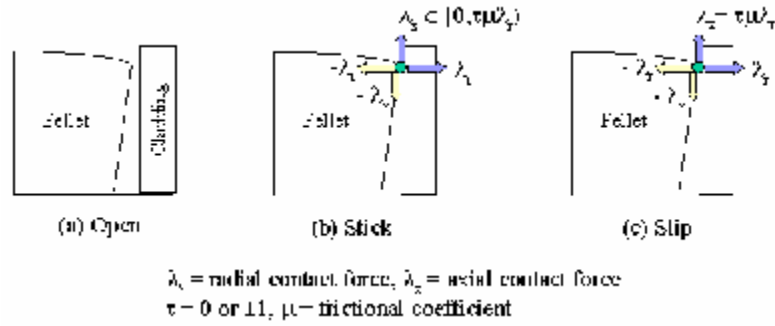
Figure 2. Geometric finite element modelling for the pellet and cladding



Contact analysis model

Contact states and the interfacial pressure at the surface of the pellet and the cladding in the gap should be calculated in order to correctly describe the deformation and failure behaviour of the fuel rod. Figure 3 represents three modes of contact behaviour: open, stick and slip states. In the open state, a pellet approaches the cladding mainly due to thermal expansion and swelling, but the pellet and the cladding are not yet contacted. In the first stage of the stick state, soft contact between the pellet and the cladding occurs. Contact forces of the same magnitude act on the interface of the pellet and the cladding in the opposite direction. Strong contact between the pellet and the cladding occurs with a further expansion of the pellet. The pellet and the cladding slip with each other if the contact force becomes equal to the frictional force on the contact surface.

Figure 3. Contact modes between the pellet and cladding



There are no constraints in the open state of Figure 3(a). The total potential energy for the open system is:

$$\Pi_{OP} = \frac{1}{2} \int_{\Omega} \{\varepsilon\}^T \{\sigma\} d\Omega - \{x\}^T \{r\} \quad (1)$$

where Π_{OP} is the total potential energy for the open surface, $\{\varepsilon\}$ is the total strain vector, $\{\sigma\}$ is the stress vector, $\{x\}$ is the displacement vector, $\{r\}$ is the load vector, Ω is the volume considered and superscript T means the transposed vector or matrix.

In the stick node, the gap thickness is zero and the axial displacement of the pellet node is equal to that of the cladding node. Thus the constraints for the stick node are written by:

$$g_r = g_r^0 - u_p + u_c = 0 \quad (2)$$

$$g_z = -w_p + w_c = 0 \quad (3)$$

where g_r is the radial gap thickness, g_r^0 is the initial radial gap thickness, g_z is the difference of the axial displacement between the pellet and the cladding, u_p is the radial displacement of the pellet node, u_c is the radial displacement of the cladding node, w_p is the axial displacement of the pellet node and w_c is the axial displacement of the cladding node. Constraints for the stick node are applied to the total potential energy as follows:

$$\Pi_{ST} = \frac{1}{2} \int_{\Omega} \{\varepsilon\}^T \{\sigma\} d\Omega - \{x\}^T \{r\} + \{g\}^T \{\lambda\} \quad (4)$$

where Π_{ST} is the total potential energy for stick surface, and $\{g\}^T = \{g_r \ g_z\}$, $\{\lambda\} = \{\lambda_r \ \lambda_z\}^T$ is the vector of the Lagrange multipliers. The Lagrange multipliers, λ_r and λ_z , mean the physically radial and axial contact forces on the pellet surface, respectively. Their values are always less than or equal to zero. Thus the value of $\{g\}^T \{\lambda\}$ is always zero.

In the slip state, the axial displacement of the pellet node is not equal to that of the cladding node any more. The constraint for the slip node is only Eq. (2). The axial force becomes equal to the frictional force. By applying the Coulomb's friction law to the slip surface, the frictional force can be defined as follows [7]:

$$\lambda_z = \tau\mu\lambda_r \quad (5)$$

where μ is the frictional coefficient and τ is the dimensionless variable which represents the direction of the frictional force, defined by:

$$\tau = \begin{cases} +1 & \text{for } w_p - w_c > 0 \\ 0 & \text{for } w_p - w_c = 0 \\ -1 & \text{for } w_p - w_c < 0 \end{cases} \quad (6)$$

The total potential energy for the system including the slip state is:

$$\Pi_{SL} = \frac{1}{2} \int_{\Omega} \{\varepsilon\}^T \{\sigma\} d\Omega - \{x\}^T (\{r\} + \tau\mu\lambda_r \{e\}) + g_r \lambda_r \quad (7)$$

where Π_{SL} is the total potential energy for the slip system and the vector $\{e\}^T$ is equal to $\{0 \dots 0 -1 0 0 \dots 0 1 0 0 \dots 0\}$. In vector $\{e\}$, the elements -1 and 1 appear at the location of the pellet and the cladding node in the finite element equation, respectively. Frictional forces at the pellet and cladding nodes are explicitly added to the loads in the total potential energy.

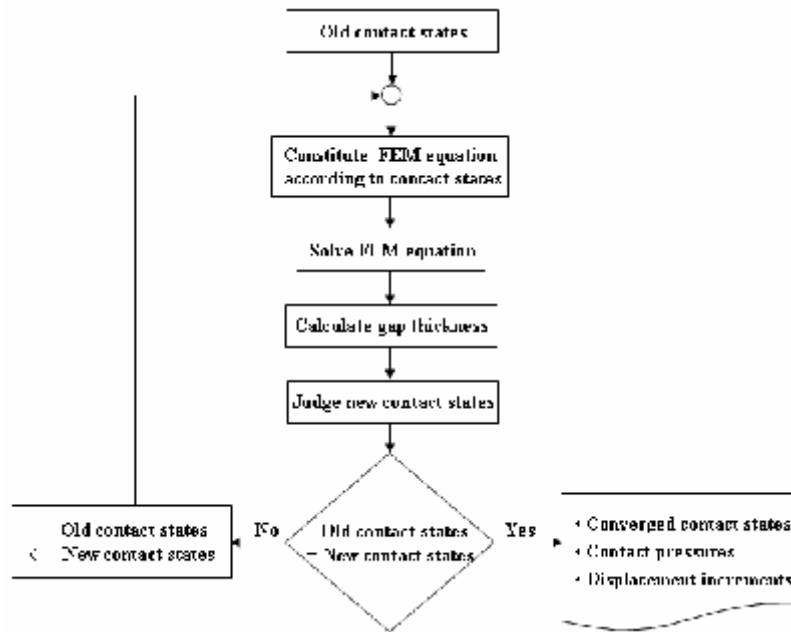
The finite element equation can be obtained by applying the minimum potential energy principle to the contact system like Figure 3 [8,9]. Table 1 shows the finite element equations, gap thickness, and contact forces according to the contact states. Figure 4 is the contact analysis flow for all the nodal pairs in the gap. The deformation and contact states are computed by adding constraints according to the old contact states to the finite element equation. New contact states are determined using contact criteria consisting of the variables newly calculated. The calculated contact forces are converted into contact traction or pressure by equating the work done by the nodal contact forces to the work by the equivalent traction [10].

Table 1. Finite element equations according to the contact states

Contact status	Finite element equation	Gap thickness	Contact force increment
open	${}^e [K] \{x\} = \{r\}$	> 0	$\lambda_{r,k} = 0$ $\lambda_{z,k} = 0$
stick	$\begin{bmatrix} [K] & {}^e \{e_{r,k}\} & {}^e \{e_{z,k}\} \\ \{e_{r,k}\}^T & 0 & 0 \\ \{e_{z,k}\}^T & 0 & 0 \end{bmatrix} \begin{Bmatrix} \{x\} \\ \lambda_{r,k} \\ \lambda_{z,k} \end{Bmatrix} = \begin{Bmatrix} \{r\} \\ -g_{r,k}^0 \\ g_{z,k}^0 \end{Bmatrix}$	0	$\lambda_{r,k} \leq 0$ $\lambda_{z,k} < 0$
slip	$\begin{bmatrix} [K] & {}^e \{e_{r,k}\} \\ \{e_{r,k}\}^T & 0 \end{bmatrix} \begin{Bmatrix} \{x\} \\ \lambda_{r,k} \end{Bmatrix} = \begin{Bmatrix} \{r\} \\ -g_{r,k}^0 \end{Bmatrix}$	0	$\lambda_{r,k} \leq 0$ $\lambda_{z,k} = \tau \cdot \mu \cdot \lambda_{r,k}$

${}^e [K]$ = stiffness matrix, ${}^e k$ = contact nodal pair number, ${}^e \{e_{z,k}\} = [0 \dots 0 \ 1 \ 0 \ 0 \dots 0 \ 0 \ 1 \ 0 \ 0 \dots 0]^T$,
 ${}^e \{e_{r,k}\} = [0 \dots 0 \ 0 \ -1 \ 0 \dots 0 \ 0 \ 1 \ 0 \dots 0]^T$, ${}^e \{e_{\tau,k}\} = [0 \dots 0 \ -1 \ -\mu \ 0 \dots 0 \ 1 \ \mu \ 0 \dots 0]^T$, ${}^e i = 0$ or ± 1

Figure 4. Contact analysis flow for all the nodal pairs in the gap



Cladding relaxation model

Various in-pile tests showed that the strain relaxation of the cladding occurred during a high power hold. The cladding decreases axially under a constant high power. It is suggested that cladding relaxation is caused by the dimensional changes of the pellet. The pellet thermally expands like an hourglass and the peripheral cusp of the pellet pushes out the cladding, causing the cladding to elongate and ridge. Change in the pellet volume reduces the size of the pellet cusp and its force pushing out the cladding. Then cladding relaxation occurs.

Irradiation creep strain has also been used as a model for the pellet deformation causing to reduce the size of the pellet cusp. The irradiation creep strain rate [11] is written by:

$$\dot{\epsilon}_{irr} = A\dot{F}\bar{\sigma} \quad (8)$$

where $\dot{\epsilon}_{irr}$ is the effective strain rate for the irradiation creep (s^{-1}), A is a constant describing the creep resistance of the pellet ($s\text{-fissions}/m^3/s\text{-MPa}$)⁻¹, \dot{F} is the fission rate ($\text{fissions}/m^3/s$), and $\bar{\sigma}$ is the effective stress at the deformed region of pellet (MPa).

Validation of the finite element modelling module

Results from the FEM module were compared with those from the commercial structural analysis software ABAQUS [12] in order to validate the developed FEM module. The geometric, material and loading data are shown in Table 2. Figure 5 shows the temperature distribution in the pellet and the cladding at various powers. The temperature distribution was calculated in INFRA. Displacement, strain, stress and contact pressure were calculated at various powers between 13 and 60 kW/m and at various friction coefficients between 0 and 1 using the FEM module and ABAQUS. It is assumed that the pellet and the cladding have thermal, elastic and plastic characteristics.

Table 2. Geometric, material and loading data for the test calculation

Data	Value
Pellet material	Uranium dioxide
Pellet outside diameter (mm)	10.86
Pellet length (mm)	12.70
Dish depth (mm)	0.0343
Spherical radius of dish (mm)	25.3
Dish shoulder (mm)	1.28
Fractional density of UO ₂	0.99
Gap thickness (mm)	0.02
Cladding material	Zircaloy
Cladding outside diameter (mm)	12.79
Cladding inside diameter (mm)	10.91
Gas pressure (MPa)	0.230 ~ 0.233
Coolant pressure (MPa)	3.447
Axial pressure on cladding (MPa)	12.034 ~ 12.044

Figure 5. Temperature distribution in a fuel rod for the test

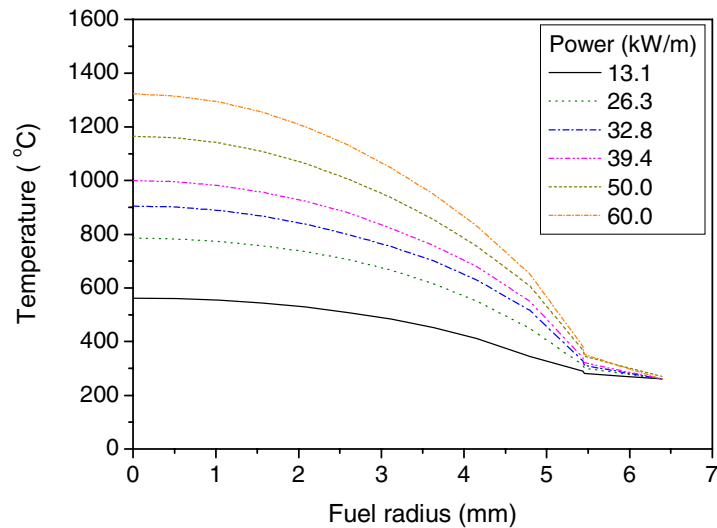


Figure 6 shows the circumferential strain at the Gauss points near the top of the pellet and the cladding at 13 and 60 kW/m. Figure 7 displays the circumferential stress at the Gauss points near the top and the axial centre of the pellet and the cladding at 13 and 60 kW/m. Circumferential strain and stress from both programs are in good agreement. Figure 8 represents the radial and axial contact pressure for the inner surface of the cladding at various powers. Both radial and axial contact pressure increase with the power. The results from ABAQUS and the FEM module are in good agreement.

Figure 9 indicates the effects of the frictional coefficients on the axial stress and strain at a power of 50 kW/m. Axial strain and stress increase with the frictional coefficients near the radial centre, and vice versa near the pellet surface. Frictional resistance for the pellet's expansion at the pellet surface increases with the frictional coefficients. And that accelerates the pellet material expansion near the radial centre more easily because the top part of the pellet is not constrained. Figure 10 shows the hourglass-like deformation of the pellet and the cladding. The pellet is more axially displaced than the cladding because all the contact nodal pairs are in the slip state.

Figure 6. Circumferential strain at the top points of a half-pellet and cladding ($\mu = 0.3$)

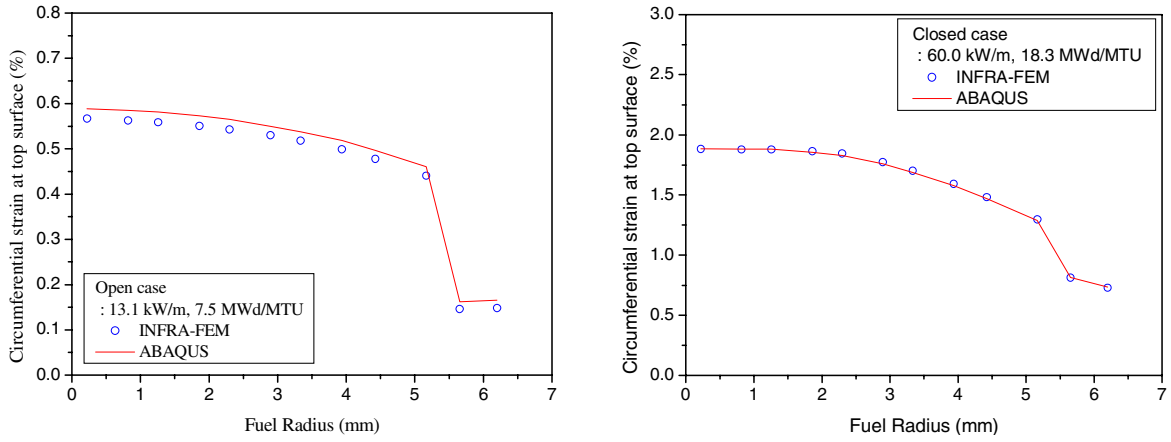


Figure 7. Circumferential stress at the top points of a half-pellet and cladding ($\mu = 0.3$)

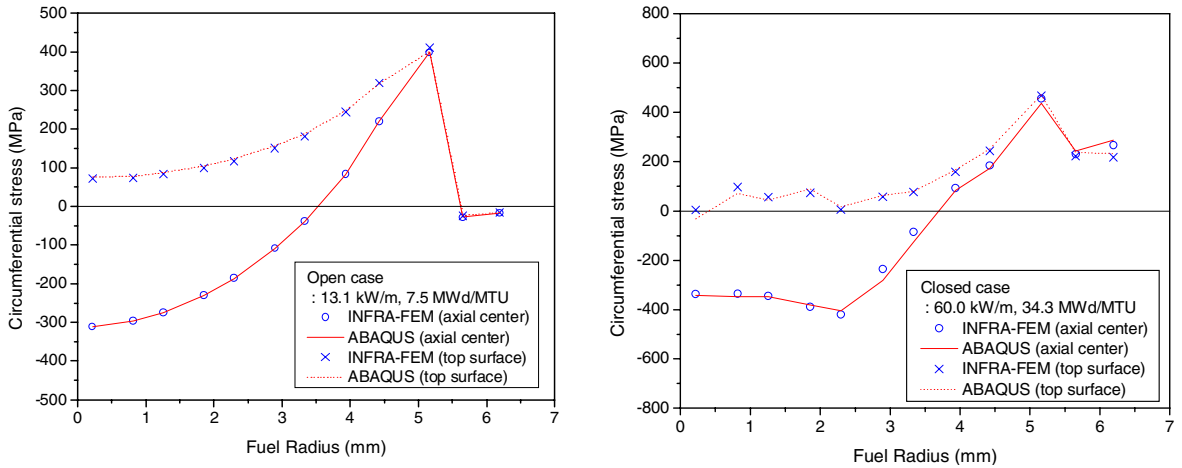


Figure 8. Contact pressure at various powers

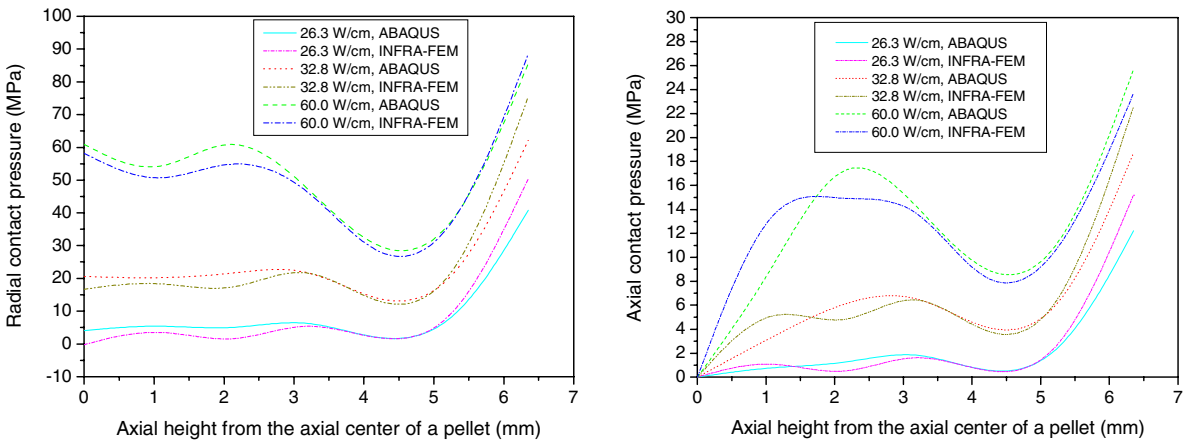


Figure 9. Effect of the frictional coefficients on the axial stress and strain

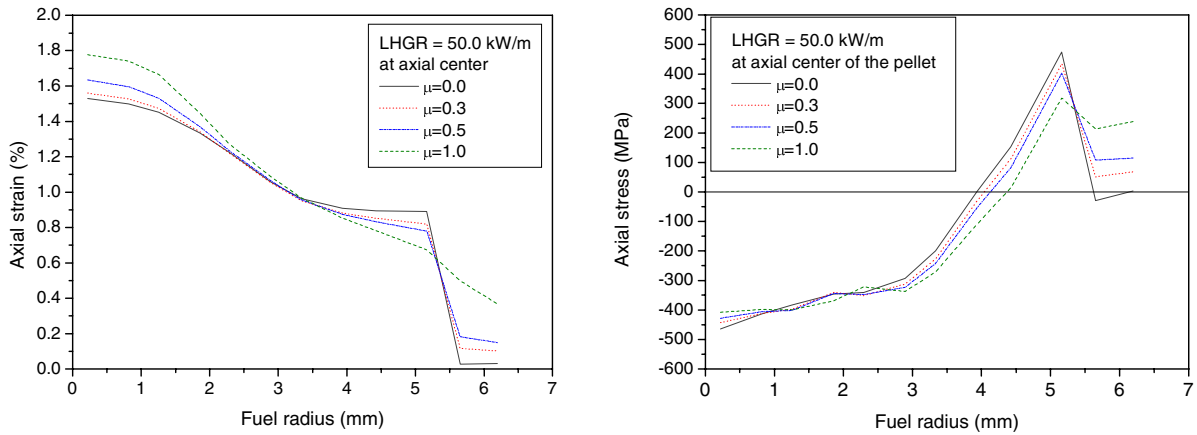
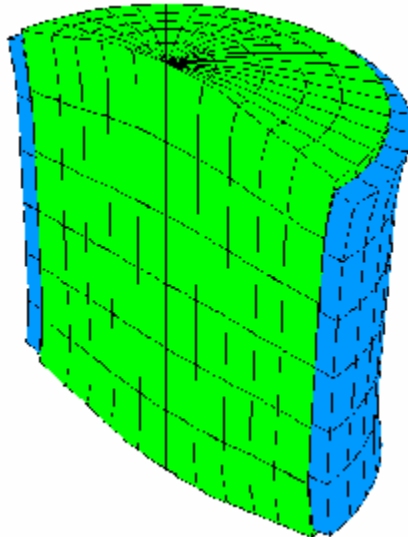


Figure 10. Deformed shape of the pellet and cladding



Calculation of the cladding relaxation

Cladding elongation calculated by the FEM module in INFRA was compared with the re-irradiation results of a UO_2 PWR rod fuel rod, which is operated up to 60 MWd/kg UO_2 . The history of the power and the temperature at the fuel centre of the rod is shown in Figure 11. The temperature at the fuel centre in Figure 11 was calculated by INFRA. Figure 12 shows the burn-up history. Burn-up was 67 to 70 MWd/kgU during the in-pile test. The cladding elongation of the second and the last ramp was calculated when the irradiation creep is applied to the pellet.

Figure 13 represents the cladding elongation of the second ramp. The value of constant A in Eq. (8) is $5 \times 10^{-30} (\text{s} \cdot \text{fissions}/\text{m}^3/\text{s} \cdot \text{MPa})^{-1}$. The value of the frictional coefficient is 0.8. The result from the calculation depicts the relaxation behaviour of the cladding in the experimental data well. However, the results of calculation were underestimated at the increasing power and overestimated at the decreasing power.

Figure 11. Power and temperature history

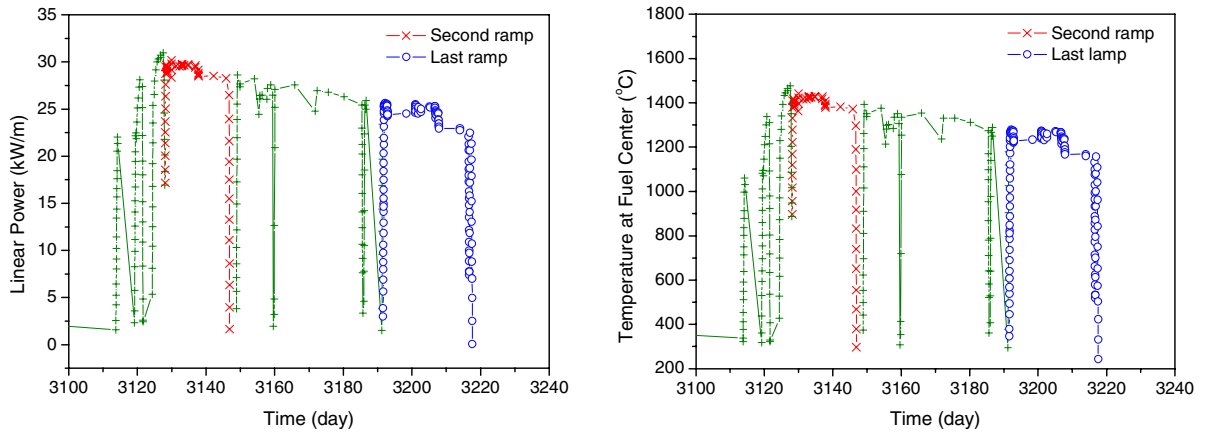


Figure 12. Burn-up history

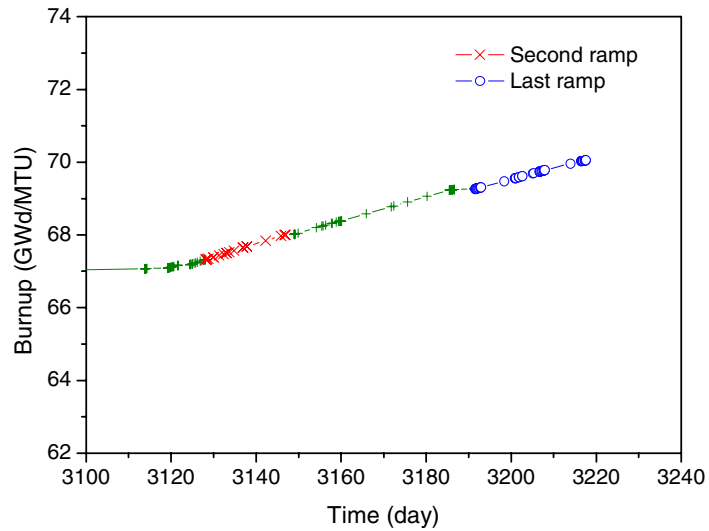


Figure 13. Cladding elongation of the second ramp according to power level and time

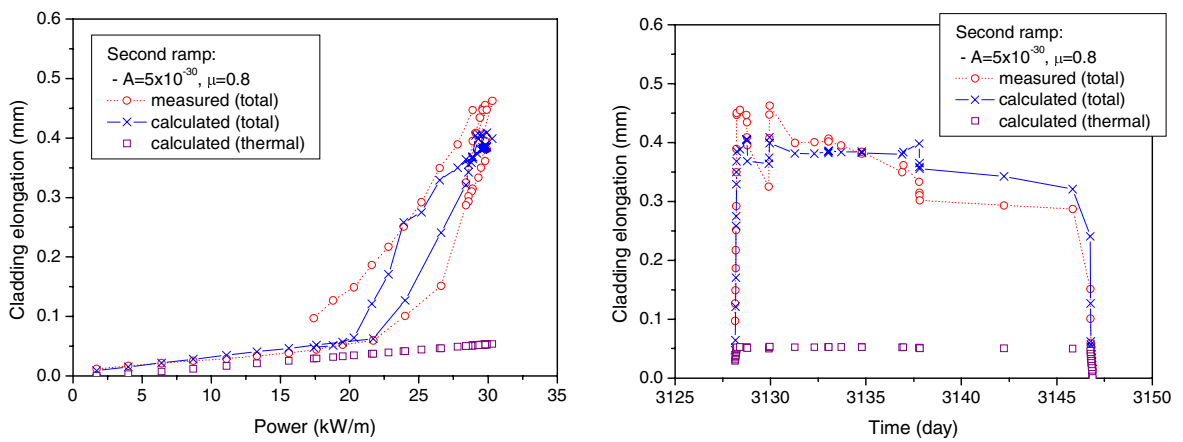


Figure 14 shows the cladding elongation of the last ramp. The value of the frictional coefficient is 0.35. It is lower than the value of the second ramp, meaning that the hardness of the pellet becomes weak in the last ramp. The value of constant A in Eq. (8) is also 5×10^{-30} (s-fissions/m³/s-MPa)⁻¹. The calculated cladding elongation is larger than the measured one when the power is increasing from 15 to 22 kW/m. The pellet usually becomes quite fractured after it experiences many transient periods. Thus a strong pellet cusp is not formed as with the unimpaired pellet. The present PCMI model does not yet consider this kind of phenomenon. The calculated elongation was decreased after about 20 kW/m, the reason being that the pellet slips on the surface of the cladding at that power. Figure 15 represents the cladding elongation of the last ramp according to the power level after adding experimental permanent deformation of cladding, which is about 0.04 mm. The permanent deformation was not calculated in the FEM module. In the FEM result, the cladding had not been plasticised over the entire time interval.

Figure 14. Cladding elongation of the last ramp according to power level and time

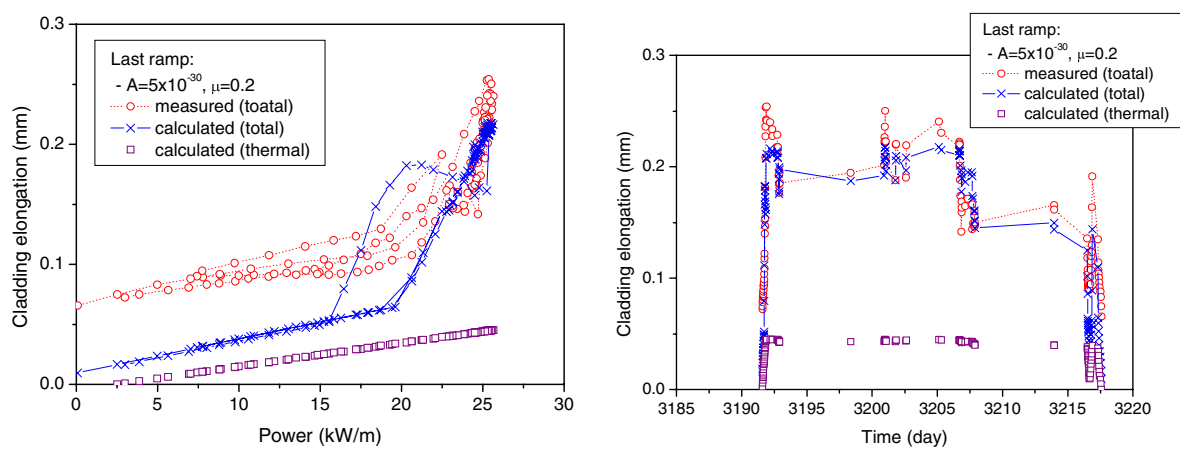
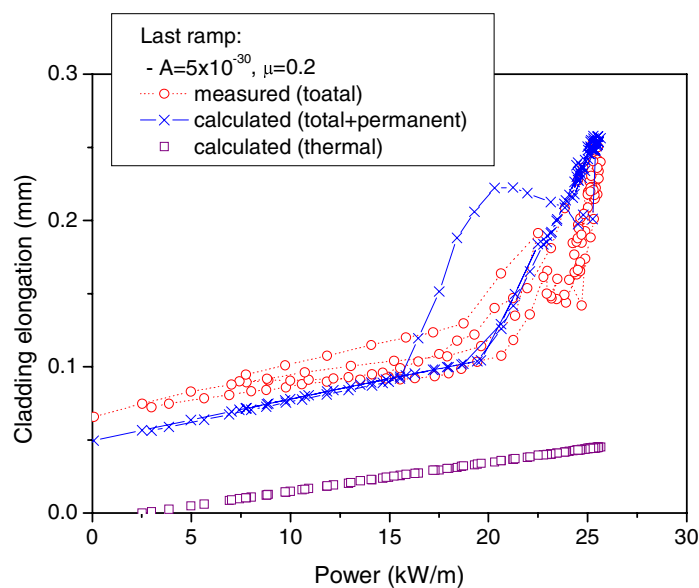


Figure 15. Cladding elongation of the last ramp according to power level after adding experimental permanent deformation



Conclusion

A model to analyse the pellet and cladding contact was developed by the Lagrange multiplier method and was successfully applied to PCMI estimation. A FEM module for the mechanical behaviour analysis of a fuel rod was developed and validated by comparison with the commercial FEM code predictions. Stress, strain and PCMI results for the fuel rod were calculated at powers between 13 and 60 kW/m and at frictional coefficients between 0 and 1 using the FEM module and ABAQUS. Both results showed a very good agreement.

The cladding relaxation at the ramps for the 60 MWd/kgU fuel was well described by the irradiation creep. The results are not exactly in agreement. The irradiation creep of the pellet is one of the causes of cladding relaxation. The frictional coefficients are 0.8 at the ramp during the early stage and 0.2 at the ramp during the later stage of the in-pile test. The constant describing creep resistance of the pellet was 5×10^{-30} . The weakening of the pellet cusp in the fractured pellet should be included in the present PCMI model.

Acknowledgement

This work has been carried out under the nuclear R&D programme supported by the Ministry of Science and Technology in Korea.

REFERENCES

- [1] Cunningham, M.E., C.E. Beyer, P.G. Medvedev and G.A. Berna, *FRAPTRAN: A Computer Code for the Transient Analysis of Oxide Fuel Rods*, NUREG/CR-6739, Vol. 1 (2001).
- [2] Massih, A.R., T. Rajala and L.O. Jernkvist, "Analyses of Pellet-clad Mechanical Interaction Behaviour of Different ABB Atom Fuel Rod Designs", *Proc. SMiRT-12* (1993).
- [3] Levy, S., J.P.D. Wilkinson, "A Three-dimensional Study of Nuclear Fuel Rod Behavior During Startup", *Nucl. Eng. Des.*, 29, pp. 157-166 (1974).
- [4] Suzuki, M., *Light Water Reactor Fuel Analysis Code FEMAXI-V (VER.1)*, JAERI-Data/Code 2000-030 (2000).
- [5] Massih, A.R., T. Rajala, L.O. Jernkvist, "Analyses of Pellet-clad Mechanical Interaction Behaviour of Different ABB Atom Fuel Rod Designs", *Nucl. Eng. Des.*, 156, pp. 383-391 (1995).
- [6] Lee, C-B., J-G. Bang, D-H. Kim, Y-M. Kim, Y-S. Yang, Y-H. Jung, "Development of UO₂ Fuel Rod Performance Code, INFRA", *KNS Topical Meeting* (Autumn 2001).
- [7] Bathe, K.J., P.A. Bouzinov, "On the Constraint Function Method for Contact Problems", *Computers & Structures*, 64(5/6), pp. 1069-1085 (1997).

- [8] Zienkiewicz, O.C., "The Finite Element Method", 4th ed., McGraw-Hill (1989).
- [9] Underhill, W.R.C., M.A. Dokainish, G.E. Oravas, "A Method for Contact Problems Using Virtual Elements", *Comput. Methods Appl. Mech. Engrg.*, 143, pp. 229-247 (1997).
- [10] Landenberger, A., A. El-Zafrany, "Boundary Element Analysis of Elastic Contact Problems using Gap Finite Elements", *Computers & Structures*, 71, pp. 651-661 (1999).
- [11] Olander, D.R., *Fundamental Aspects of Nuclear Reactor Fuel Elements*, TID-26711-P1, US-DOE (1976).
- [12] *ABAQUS/Standard, User's Manual, Ver. 5.8*, Hibbitt, Karlsson & Sorensen, Inc., USA (1998).

SESSION V

Modelling of the Mechanical Interaction Between Pellet and Cladding (Part 2)

Chairs: J.A. Turnbull, N. Waeckel

**TWO-DIMENSIONAL (2-D) PELLETT-CLADDING
MODELLING USING FEM AT NRI REZ PLC**

Mojmír Valach, Jiří Zymák
Nuclear Research Institute Rez plc, Czech Republic

Abstract

The method and calculation results of 2-D (r-z) and 2-D (r-φ) contact elasto-thermal solutions of pellet-cladding configuration are presented. Calculations were performed with coupled thermal and mechanical methods with inner sources and appropriate material properties dependent on temperature. Preliminary results of those simulations will be appropriate for advanced Russian TVEL fuel geometry recently delivered to the Dukovany NPP. Validation on experiment will be the subject of further work.

Introduction

The necessary assumption concerning wider nuclear energy development is the maintenance and improvement of the safety of nuclear fuel. On the other hand there is an imperative to operate NPPs economically. The importance of nuclear fuel as a basic part of each NPP is ever more apparent, so the effort of our work is to more accurately describe the behaviour of the cylindrical fuel rods under more stringent operational conditions, obviously achieving high burn up. This implies that modern fuel rod computer models are required to predict a “margin” of cladding tube integrity loss under normal operation and operational transients more reliably. One of the critical moments, which occurs during the fuel duty, is pellet-cladding contact (and also modified pellet-pellet contact after a thermo-mechanical interaction). The difficulty of contact event modelling can be documented by a very simple example: one core in one loading of one reactor contains $\sim 10^4$ fuel rods, each fuel rod contains $\sim 10^2$ fuel pellets; where, when, how and in what detail must it be predicted and modelled?

Unilateral contact

Mathematical modelling of unilateral contact problems is a quite new area in applied mathematics; practical realisation indicates the application of the finite element method (FEM). The principle of the method is based on the fact that a zone of unilateral contact of two solid bodies need not be defined *a priori*; its correct definition is one of the results of the solved problem.

The classical analysis of this problem, begun by Herz in 1896, was limited to simple geometries. The age of high-speed computers brought a qualitative change to the analysis of the contact problems. On the basis of suitable discretisation – by means of finite differences or FEM – the problems can be solved approximately even for complex geometrical situations and boundary conditions. As a technical problem, this was originally formulated by A. Signorini in 1993 for the case of unilateral contact of an elastic body with the ideal rigid and smooth basis (the so-called “Signorini’s problem”). From a mathematical point of view the unilateral contact problem performs the application of variational inequalities, which today forms the basis for convex analysis and is the link between mathematical physics problems and optimisation ones. As opposed to classical variational equations, the solution of variational inequalities is not found on the whole function space but on some closed part of it. The problem tends to seek the conditional extreme of the functional of deformation energy. These problems are non-linear, due not only to existing material non-linearities, but also by the set on which the solution is being found, which can change during the solution process.

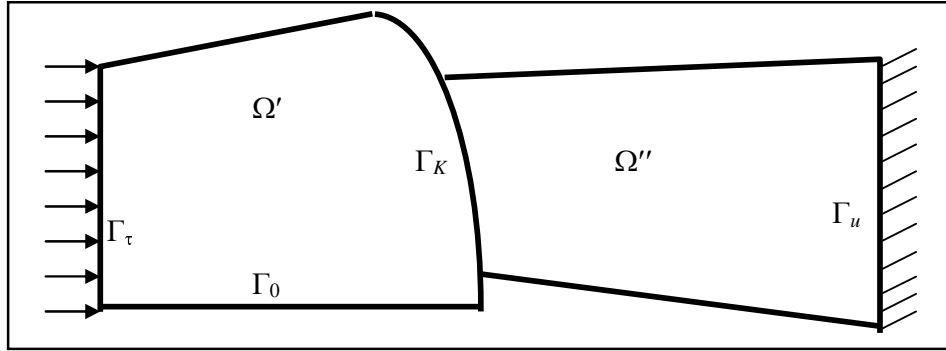
Let two bodies occupy the bounded regions Ω', Ω'' with Lipschitz boundaries. In the following, one or two primes denote that the quantity is referred to the body Ω' or Ω'' , respectively. Let $\mathbf{x} = (x_1, x_2)$ be Cartesian co-ordinates. We seek the displacement vector field $\mathbf{u} = (u_1, u_2)$ over $\Omega' \cup \Omega''$, i.e. $\mathbf{u}' = (u'_1, u'_2)$ on Ω' and $\mathbf{u}'' = (u''_1, u''_2)$ on Ω'' and the associated strain tensor field e_{ij} . The stress tensor τ_{ij} is related to the strain tensor by means of the generalised Hooke’s law. The stress tensor satisfies the equation of equilibrium in $\Omega' \cup \Omega''$ and some (classical) conditions on boundaries $\partial\Omega' \cup \partial\Omega''$ of the domains $\Omega' \cup \Omega'' = \Omega$.

Now we shall focus on the parts of the domains $\Omega' \cup \Omega''$, where a possible contact may occur. We distinguish two classes of contact problems, as follows: 1) bounded contact zone, 2) enlarging contact zone, which differ significantly with regard to the character of the contact. For the sake of simplicity let us consider now the case of zero friction.

Bounded contact zone

First let us consider the case, when the contact zone cannot enlarge during the deformation process. Such an assertion is determined by the geometrical shape of the two bodies in a neighbourhood of the possible contact zone (Figure 1).

Figure 1. Illustration of unilateral contact with bounded contact zone



Let the body Ω' be fixed on a part Γ_u of its boundary, let the surface traction be prescribed on a part Γ_τ of the body Ω' , let the condition of the axis symmetry is defined on a part Γ_0 of the body Ω' . Hence we may define the contact zone $\Gamma_K = \partial\Omega' \cap \partial\Omega''$. We purport that a unilateral bounded contact occurs on Γ_K if:

$$u'_n + u''_n \leq 0 \tag{1}$$

holds on Γ_K , where $u'_n = u'_i \cdot n'_i$, $u''_n = u''_i \cdot n''_i$ are projections of displacement components into the outward unit normal $\mathbf{n}' = (n'_1, n'_2)$, $\mathbf{n}'' = -\mathbf{n}'$ corresponding to the sets Ω', Ω'' (summation convention is used over the repeating index). Eq. (1) signifies the non-penetrating of both bodies.

Next let us consider the contact forces. By virtue of the law of action and reaction we have:

$$T'_t = T''_t, \quad T'_n = T''_n \text{ on } \Gamma_K$$

On the other hand, the tangential components vanish because of zero friction and the normal contact force cannot be tensile, i.e.

$$T'_t = T''_t = 0, \quad T'_n = T''_n \leq 0$$

Altogether, we define the boundary conditions on Γ_K as follows:

$$u'_n = u''_n \leq 0, \quad T'_n = T''_n \leq 0 \tag{2}$$

$$(u'_n + u''_n) \cdot T'_n = 0 \tag{3}$$

$$T'_t = T''_t = 0 \tag{4}$$

Eq. (3) signifies that at points without contact no contact force may occur.

Enlarging contact zone

In some important cases the contact zone can enlarge during the deformation process. Such a situation occurs if two bodies Ω' and Ω'' have smooth boundaries in the neighbourhood of $\Gamma_K = \partial\Omega' \cap \partial\Omega''$. Then the definition of the contact condition must be changed. Let us consider the case of Figure 2. A co-ordinate system (ξ, η) is placed in such a way that the ξ -axis coincides with the direction of \mathbf{n}'' and η -axis with the common tangent of $\partial\Omega'$ and $\partial\Omega''$ at a "central" point $P \in \partial\Omega' \cap \partial\Omega''$.

Figure 2. Illustration of unilateral contact with enlarging contact zone

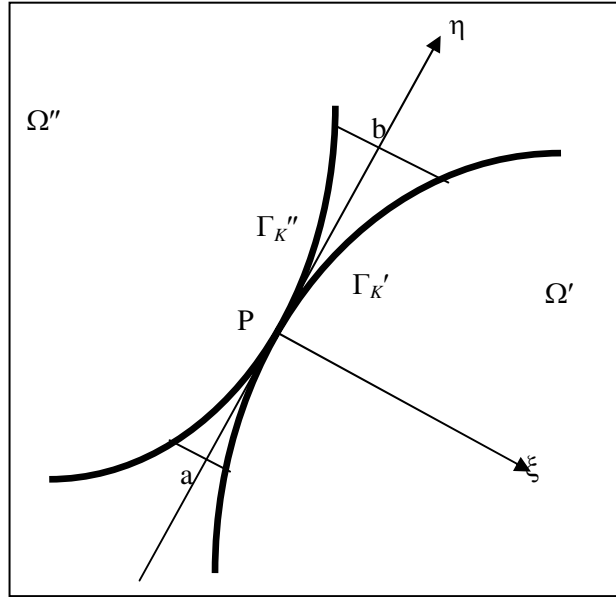


Figure 2 corresponds with the situation before the deformation. The parts of $\partial\Omega'$ and $\partial\Omega''$, which come into a contact during the deformation process, can be estimated as follows:

$$\Gamma_K^M = \{(\xi, \eta); a \leq \eta \leq b, \xi = f^M(\eta)\}, \quad M = ', ''$$

where f', f'' are continuous on $\langle a, b \rangle$. (The interval has to be chosen *a priori*.) Arguing similarly as in the previous section, we are led to the following condition:

$$u_\xi'' - u_\xi' \leq \varepsilon(\eta) \quad \forall \eta \in \langle a, b \rangle \quad (5)$$

where $\varepsilon(\eta) = f''(\eta) - f'(\eta)$ is the distance of the two boundaries before deformation; u_ξ' and u_ξ'' are projections of the displacement vectors into the direction of (positive) ξ -axis.

Also using the law of action and reaction, we arrive at the conditions:

$$-T_\xi'(\cos\alpha')^{-1} = T_\xi''(\cos\alpha'')^{-1} \leq 0 \quad (6)$$

$$T_\eta' = T_\eta'' = 0 \quad (7)$$

$$(u_\xi'' - u_\xi' - \varepsilon) \cdot T_\xi'' = 0 \quad (8)$$

which hold at all points of $\Gamma'_K \cup \Gamma''_K$ with the same co-ordinates $\eta \in \langle a, b \rangle$. Here:

$$(\cos \alpha^M)^{-1} = \left(1 + \left(\frac{df^M}{d\eta} \right)^2 \right)^{1/2}, \quad M = ', ''$$

α^M being the angle between η -axis and the tangent to Γ_K^M , respectively. The condition in Eq. (8) follows from this consideration: at points without contact, i.e. if $u''_{\xi} - u'_{\xi} - \varepsilon < 0$, no contact force may occur, i.e. $T'_{\xi} = T''_{\xi} = 0$. Eq. (7) approximates the zero friction – after neglecting the projection $T^M_{\xi} \cdot \sin \alpha^M$.

Variational formulation

To the above-mentioned unilateral contact problems a variational formulation – principle of minimum potential energy – can be associated. Instead of the standard variational formulations, the unilateral contact problems minimise the functional:

$$\mathbf{L}(\mathbf{v}) = 1/2 \mathbf{A}(\mathbf{v}, \mathbf{v}) - \mathbf{L}(\mathbf{v}) \quad (9)$$

on the set of admissible displacements \mathbf{K} , which fulfils Eq. (1) in the case of bounded contact zone and Eq. (5) in the case of enlarging contact zone. The quadratic part of the functional \mathbf{L} :

$$\mathbf{A}(\mathbf{v}, \mathbf{v}) = \int_{\Omega} c_{ijkl} \tau_{ij}(\mathbf{v}) \cdot \varepsilon_{kl}(\mathbf{v}) dx$$

is the strength energy of the bodies ($\Omega' \cup \Omega'' = \Omega$), the linear part $\mathbf{L}(\mathbf{v}) = \int_{\Omega} F_i \cdot v_i dx + \int_{\Gamma_{\tau}} P_i \cdot v_i dS$ is the work of the body forces and of the surface tractions.

A function $\mathbf{u} \in \mathbf{K}$ is called a weak (variational) solution of the unilateral contact problem, if:

$$\mathbf{L}(\mathbf{u}) \leq \mathbf{L}(\mathbf{v}) \quad \forall \mathbf{v} \in \mathbf{K} \quad (10)$$

Due to the fact that the set \mathbf{K} does not form the whole space, but only this closed subset, the variational inequality in Eq. (10) does not tend to a system of linear equations, it has to be solved as a bonded extreme problem – to seek the minimum of the functional \mathbf{L} on the set \mathbf{K} .

Each numerical realisation of the particular unilateral contact problem leads to a system of linear equations, which has to be solved. This system is not directly connected with the derivation of the functional but results from the applied numerical method for solving non-linear optimisation problems (Lagrangian multipliers, conditional conjugate gradients method, Newton-Raphson method, etc.).

Available tools used for modelling

The problem has been solved by means of the COSMOS/M software system. It is a complete, modular finite element system, which includes for instance modules to solve linear and non-linear static problems in addition to problems of heat transfer. Developing a reliable model capable of predicting the behaviour of structural systems represents one of the most difficult problems facing the analyst.

The FEM provides an effective vehicle for performing these problems due to its versatility and the great advancement in its adaptation to computer use. The success of a finite element analysis depends largely on how accurately the geometry, the material behaviour and the boundary conditions of the actual problem are idealised. One has to take into consideration that all real structures are non-linear in some way. In addition, the unilateral contact problems are non-linear due to their optimisation substance as was mentioned above. The unilateral contact forms the basis for adequate pellet-cladding modelling and it was used in all calculated problems.

After opening with the thermo-elastic linear cases, all further problems of pellet-cladding interaction were solved as non-linear ones in some ways: a geometrical non-linearity and the thermal, mostly non-linear dependencies of all used material properties. Heat transfer with inner sources included was always solved as the initial one for the next mechanical problem. The bulk heat generation density was considered as $6.9247 \cdot 10^8 \text{ W/m}^3$, which corresponds to the linear heat generation density $\sim 301 \text{ W/cm}$.

Results of pellet-cladding modelling

Fuel models without clad oxidation

Several results of 2-D (r-z) and (r- ϕ) pellet-cladding modelling are introduced in this chapter. All presented cases were solved as steady-state problems with zero friction. You can see the basic dimensions of the WWER fuel rod components considered in Table 1.

Table 1. Basic dimensions of WWER fuel rod components considered

Fuel rod inner radius [m]	$0.7 \cdot 10^{-3}$
Fuel rod outer radius [m]	$3.785 \cdot 10^{-3}$
Cladding inner radius [m]	$3.86 \cdot 10^{-3}$
Cladding outer radius [m]	$4.55 \cdot 10^{-3}$
Fuel pellet height [m]	$10 \cdot 10^{-3}$

The initial pellet-cladding P-C radial gap was set at $75 \mu\text{m}$ for the data from Table 1. To simulate a P-C contact, the fuel rod outer radius was only varied to the value of $3.84 \cdot 10^{-3} \text{ m}$, so the P-C radial gap was changed to $20 \mu\text{m}$. The temperature distributions of both (r-z) cases are shown in Figure 3 and Figure 4; maximum calculated temperatures are $1\ 619 \text{ K}$ and $1\ 313 \text{ K}$, respectively.

Figure 3. The radial temperature profile in the case of the radial gap $75 \mu\text{m}$, without the P-C contact

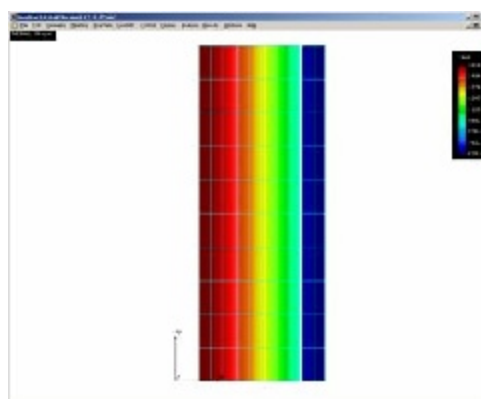
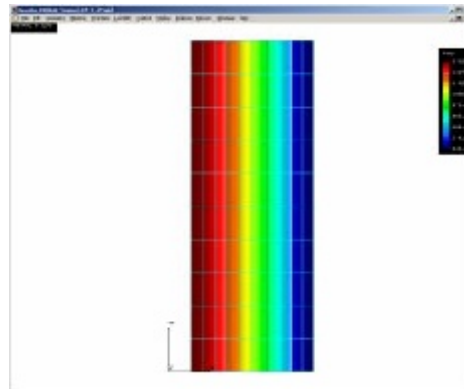


Figure 4. The radial temperature profile in the case of the radial gap 20 μm , with the P-C contact



The von Mises effective stress distributions of the two cases are shown in Figure 5 and Figure 6, respectively.

Figure 5. Effective stress in deformed state without the P-C contact

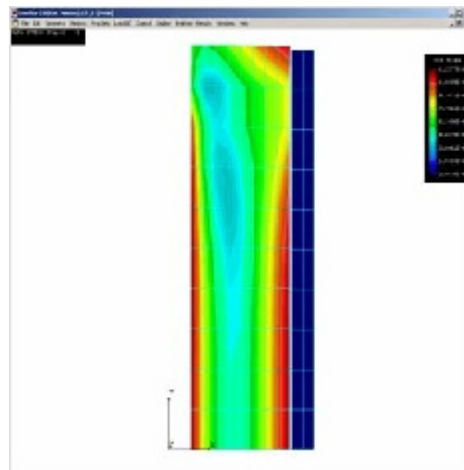
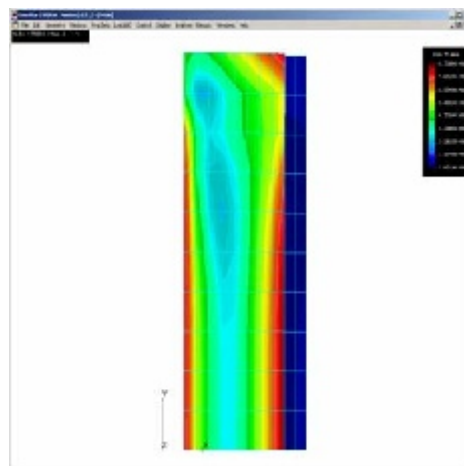


Figure 6. Effective stress in deformed state with the P-C contact



In Figures 7 and 8, the comparison of calculated radial temperature profiles in (r- ϕ) and (r-z) models of the case without P-C contact can be seen.

Figure 7. Radial temperature profile in (r- ϕ) model without P-C contact

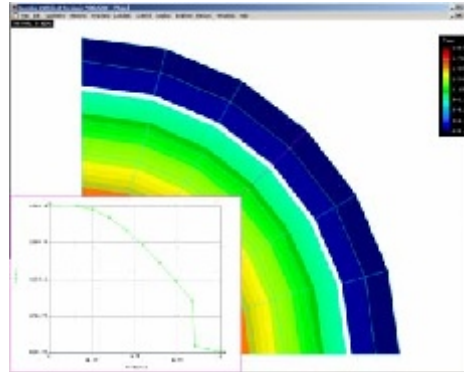
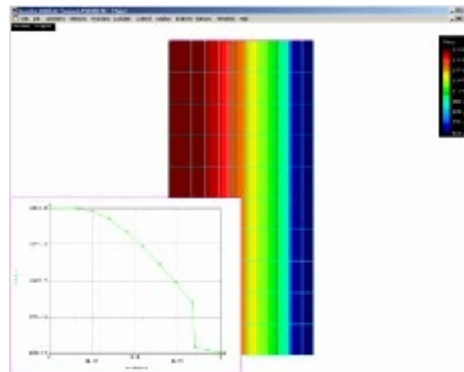


Figure 8. Radial temperature profile in (r-z) model without P-C contact



The maximum calculated temperatures in (r- ϕ) and in (r-z) are 1 598 K and 1 619 K, respectively (we believe due to meshing).

Creating of cladding oxide model

The ZrO₂ material with its temperature dependent material properties was created in COSMOS/M library by use of the MATPRO-SCDAP material library. The ZrO₂ scale is used to simulate partially burned nuclear fuel. The first calculations with the two-sided cladding oxide layers were performed. Each oxide thickness of 25 μm was used; the remaining thickness of the metal clad was set at 50 μm smaller. The radial temperature profiles of the fuel rod with bilateral clad oxidation in both models (r-z) and (r- ϕ) are shown in Figure 9 and Figure 10. Maximum calculated temperatures are 1334.9 K and 1335.4 K, respectively.

Let us introduce the example with non-uniform cladding oxidation. Now, let us assume that the oxide layer occurred on the clad inner side at the point where the local P-C contact first appeared. The oxide layer at clad outer side is assumed uniform. Meshing of the (r- ϕ) segment is displayed in Figure 11. The oxide layers are dark; the clad metal layer is light. Due to the symmetry, the example solves the problem with two opposite inner oxide layers (Figure 12).

Figure 9. Radial temperature profile of (r-z) fuel rod model with bilateral oxidation and with P-C contact

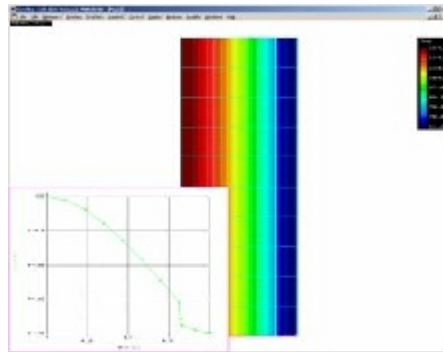


Figure 10. Radial temperature profile of (r-φ) fuel rod model with bilateral oxidation and with P-C contact

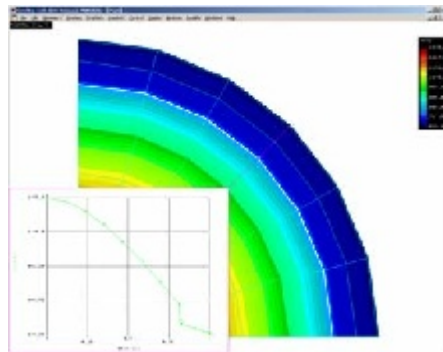


Figure 11. Non-uniform cladding oxidation example

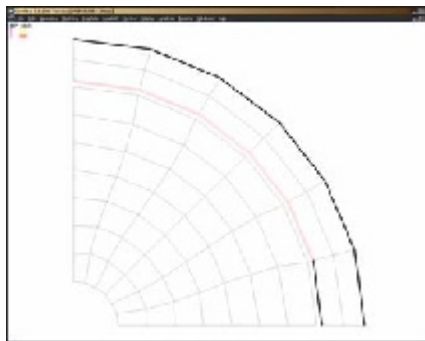
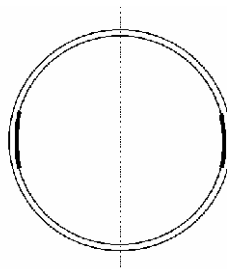


Figure 12. The complete example with non-uniform inner clad oxidation



In Figure 13, the non-uniform tangential temperature profile in the nodal points of inner cladding surface (from the left to the right) is shown. In Figure 14, you can see the von Mises effective stress, especially the higher values in the inner cladding side close to the inner oxide layer. The initial (P-C) radial gap was 20 μm , to establish the P-C contact.

Figure 13. Tangential temperature profile in the clad inner surface nodal points (from left to right)

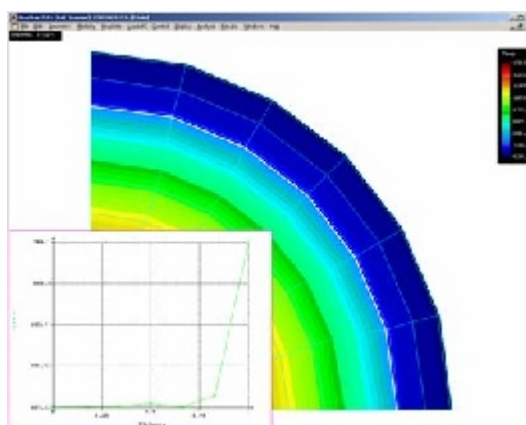
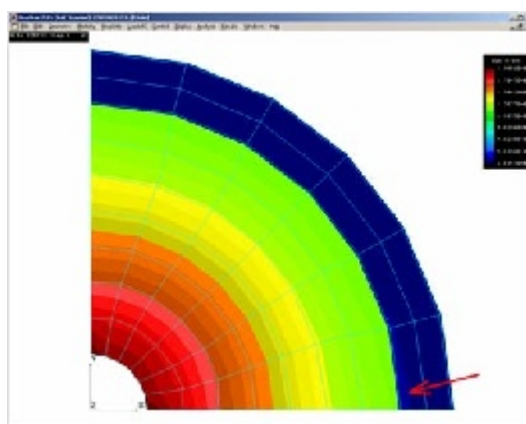


Figure 14. Effective stress profile with signed stress non-uniformity



To compare the combined effects of an inner cladding oxidation range and of possible P-C unilateral contact, two sets of calculations were performed. The first one was undertaken without P-C contact (radial gap: 75 μm), the second one with P-C contact (radial gap: 20 μm). All of them were performed with four types of the inner clad oxide range, no oxide; one “oxide” finite element (which simulates 1/6 of the inner oxide circumference, see Figure 11 and the arrow in Figure 14); three adjoining “oxide” finite elements (which simulates two quarters of the inner oxide circumference – see Figure 12); full inner surface oxidation. All cases were computed with a fully oxidised outer clad surface.

Von Mises effective stress values of the selected inner “oxide” finite element (see Figure 11 and the arrow in Figure 14) are shown in Table 2. It can be said that the “cladding stress” increases with the increasing inner clad oxide azimuthal surface, in both contact cases. The stress level is a little higher in the case with P-C contact.

Table 2. Dependence of effective stress values [MPa] of selected finite element on the inner oxidation surface and on the P-C contact

Circumferential oxide range	Without P-C contact	With P-C contact
No oxide	181	369
2/12 of the circumference	419	486
2/4 of the circumference	439	492
The whole circumference	449	503

Conclusion

The method and calculation results of 2-D (r-z) and 2-D (r- ϕ) contact elasto-thermal solutions of pellet-cladding configuration were presented. All calculations were performed using the COSMOS/M software system. The formerly developed non-linear, thermal-dependent material properties were applied.

In the near future, anelastic fuel and cladding material behaviour will be addressed, the most important of these being fuel and clad creep models. These steps will also be related to cladding crack (crack growth and crack stability) modelling.

All considered contact problems were solved with zero friction between the contact regions. Moreover, the COSMOS/M system allows using various types of friction models – including structure sliding.

REFERENCES

- [1] Timošenko, Š., *Strength of Materials I, II*. Technicko-vědecké vydavatelství, Praha 1951 (in Czech).
- [2] Hlaváček, I., J. Haslinger, J. Nečas, J. Lovíšek, “Solution of Variational Inequalities in Mechanics”, Alfa, Bratislava (1982) (in Slovak).
- [3] Hinton, E., D.R.J. Owen, *Finite Element Programming*, AP, London (1977).
- [4] *COSMOS/M 2.5 for Windows*, On-line manuals, SRAC (1999).
- [5] *COSMOS/M 2.8 for Windows*, On-line manuals, SRAC (2003).
- [6] Hagrman, D.L., *et al.*, *SCDAP/RELAP/MOD3.1 – MATPRO*, NUREG/CR-6150, EGG-2720, Idaho (1993).
- [7] Valach, M., J. Zymák, A. Miasnikov, “Open Questions on the “Interface” Between Classical Fuel Behaviour Modelling and Detailed 3-D Mechanistic Simulation Using Finite Element Method”, *TRANSURANUS Users Club Meeting*, 22-23 September 2003, NRI Rez plc, UJV 11943-T, M.

MODELLING 3-D MECHANICAL PHENOMENA IN A 1-D INDUSTRIAL FINITE ELEMENT CODE: RESULTS AND PERSPECTIVES

V. Guicheret-Retel,¹ F. Trivaudey,¹ M.L. Boubakar,¹ R. Masson,² Ph. Thevenin²

¹LMARC, 24 rue de l'Épitaphe, F-25000 Besançon

²EDF/DER, CEA Cadarache, DEC/SESC, F-13108 St-Paul-lez-Durance Cedex

Abstract

Assessing fuel rod integrity in PWR reactors must enjoin two opposite goals: a one-dimensional finite element code (axial revolution symmetry) is needed to provide industrial results at the scale of the reactor core, while the main risk of cladding failure [e.g. pellet-cladding interaction (PCI)] is based on fully three-dimensional phenomena. First, parametric three-dimensional elastic calculations were performed to identify the relevant parameters (fragment number, contact pellet-cladding conditions, etc.) as regards PCI. Axial fragment number as well as friction coefficient are shown to play a major role in PCI as opposed to other parameters. Next, the main limitations of the one-dimensional hypothesis of the finite element code CYRANO3 are identified. To overcome these limitations, both two- and three-dimensional emulations of CYRANO3 were developed. These developments are shown to significantly improve the results provided by CYRANO3.

Introduction

Thermal stresses combined with the fragile tensile behaviour of uranium dioxide lead the fuel pellet to crack during the first rise to power [1]. This fragmentation induces both tangential and axial dependencies of the displacement field throughout fuel rod. As a result, one-dimensional finite element analysis (axial revolution symmetry) underestimates the rod radial extension while the pellet's radial distribution of stresses is overestimated. Furthermore, friction between cladding and pellet induces a hoop stress concentration in inter-pellet areas in front of fuel radial cracks (denoted hereafter “triple point” areas) [2].

This paper aims toward deriving one-dimensional thermo-mechanical models taking into account previous phenomena. It starts with a parametric study based on three-dimensional elastic calculations. These calculations were performed to identify the relevant parameters (fragment number, contact pellet-cladding conditions, etc.) as regards PCI. Moreover, these calculations provide reference results illustrating the main limitations of the one-dimensional hypothesis of the finite element fuel rod EDF code CYRANO3 [3]. The next section is devoted to a new model, which takes into account the friction between pellet and cladding and the opening up of pellet radial cracks. The last section is devoted to a fragmentation model. This model stands on assumptions consistent with previous ones [4,5] but its implementation in CYRANO3 is still different.

Three-dimensional parametric study of PCI

The aim of this study (see Ref. [6] for additional details) was to assess and classify the influence of certain parameters on hoop stress concentrations in the cladding during a power transient. Fuel rod thermo-mechanical calculations to a power transient have been improving continuously for many years [7]. Nevertheless, improvements in the physical knowledge concerning constitutive behaviour (the effect of irradiation on pellet behaviour, for instance) as well as simulation codes (up-to-date constitutive law, coupling phenomena, etc.) are still necessary. This is why the calculations that follow are based on a crude (but conservative) thermo-elastic description of pellet and cladding behaviours. Conversely, this thermo-elastic description allows performing quite a few three-dimensional calculations, including friction effects. Here, the focus is on hoop stress variations with respect to geometrical parameters.

Parametric study

The parameters are the number of axial and radial pellet cracks, the relative size of pellet fragments, the initial location of the fragments, the pellet-pellet and the pellet-cladding friction coefficients. For this study, we consider a half-height cladding portion, in front of two half-height and half-width pellet fragments. The finite element method is used; calculations are performed with the EDF general-interest thermo-mechanical code Code_Aster (www.code-aster.org). The set of fragments and cladding is meshed with hexahedral and prismatic linear elements. To avoid rigid body motions, in the modelling an element designated the “discrete element” is added. This permits to link the pellet fragments with the fuel column. The next step is the parametrical study, which is undertaken by varying the parameters from a standard configuration. The variation fields of the parameters are given in Table 1. Parameter notations are given in Figure 1, where $hau = 6.7468$ mm, $rextgai = 4.701$ mm, $epgai = 0.577$ mm and e_i is defined by $e_i = (rextgai - epgai) - (jeu_i + rext)$. Pellet geometrical data are given in Figure 2. For numerical reasons, a fictitious internal radius ($rint = 0.1$) is used to define the size of the mesh near the centre of the pellet. For the standard case, corresponding to the most likely case, the parameters values

Table 1. Parameter variation fields

Parameter	Values
Pellet-cladding Coulomb's friction coefficient (mug)	0/0.2/0.4/0.6/0.8
Pellet-pellet Coulomb's friction coefficient (mup)	0/0.2/0.4/0.6/0.8 / 1
Radial pellet crack number ($nbfr$)	4/6/8/10/12/14 (with $teta1 = teta2$)
Axial pellet crack number ($nbfax$)	1/2/3/4
Fragment size ($teta1$, with $teta1 + teta2 = 45^\circ$)	6.5/10.5/14.5/18.5/22.5°
Relative fragment displacement ($jeu2$ with $jeu1 = 0$)	7/14/21/27.9 μm

Figure 1. Geometrical data definition: (X,Z) (left) and (X,Y) (right)

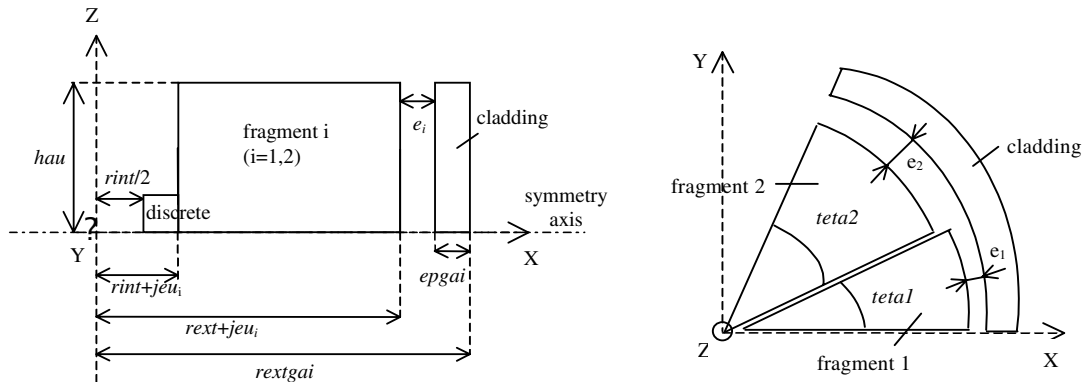
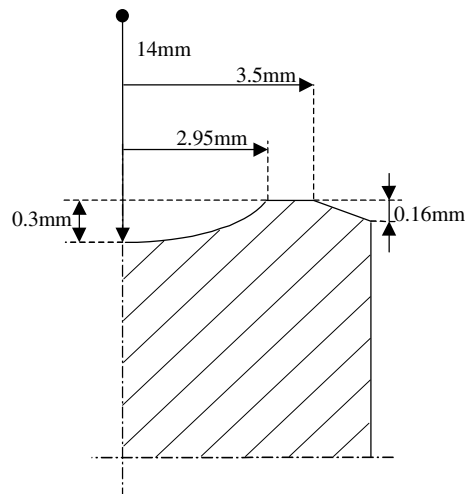


Figure 2. Definition of the geometry of the ends of the pellet



are: $teta1 = teta2 = 22.5^\circ$, $jeu1 = jeu2 = 0.009$ mm (minimum value numerically accepting to have maximal gap between each pellet fragment and the cladding), one axial and eight radial pellet cracks, a zero pellet-pellet friction coefficient and a 0.2 pellet-cladding friction coefficient.

To determine the thermomechanical loading applied to the structure, a CYRANO3 calculation of a fuel rod is done. It consists of two PWR cycles (with a power equal to about 200 W/cm) followed by a power transient (with a maximum power equal to 412 W/cm). The result for the thermal loading (in $^\circ\text{C}$) for the pellet and the cladding are respectively $T_p(r) = -59.4555 r^2 - 56.2636 r + 1765.54$ and

$T_c(r) = -128.906 r + 972.262$, and for the mechanical loading: a 12.2 MPa internal pressure, a 15.5 MPa external pressure, a 420 MPa axial pressure on pellet and a -325 MPa axial pressure on cladding. The material properties are given in Table 2.

Table 2. Material properties

	Pellet	Cladding	Discrete element
Young's modulus (MPa)	186 847	75 910	2 700
Poisson's ratio	0.31	0.252	0.31
Thermal expansion coefficient ($10^{-6} \text{ }^\circ\text{C}^{-1}$)	7.868	6.326	0

Main results

In order to classify the six parameters according to their respective effect on the hoop stress level on the internal face of the cladding, the difference between the maximum and the minimum hoop stresses ($\Delta\sigma$) obtained at the inter-pellet/inter-fragment point on the whole parameter variation range was introduced. The results are given in Table 3. Two amongst the six parameters have a significant influence on the PCI for the base case suggested by EDF: the pellet-cladding friction coefficient and the axial pellet crack number.

Table 3. $\Delta\sigma$ for each parameter

Parameter	$\Delta\sigma$ (MPa)
Pellet-cladding friction coefficient (<i>mug</i>)	407
Pellet-pellet friction coefficient (<i>mup</i>)	91
Radial pellet crack number (<i>nbfr</i>)	57
Axial pellet crack number (<i>nbfax</i>)	394.3
Fragment size (<i>teta1</i> , with <i>teta1</i> + <i>teta2</i> = 45°)	8
Relative fragment displacement (<i>jeu2</i> with <i>jeu1</i> = 0)	58

A model of cladding stress concentration consistent with one-dimensional code

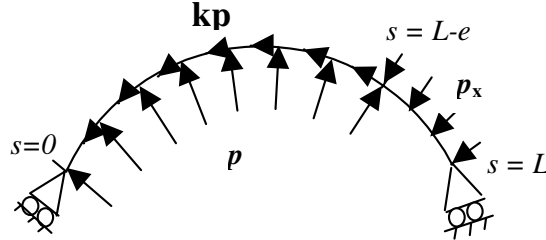
Previous results underline that the hoop stress concentration at the triple point is mainly due to the crack lips being caught on the cladding (because of the friction between cladding and pellet) and to the opening of the crack during power transients. A 1-D model has been developed in CYRANO3 in order to take the phenomenon of hoop stress concentration in the cladding into account.

The model

According to previous results, friction between pellet and cladding and crack opening effect must be taken into account for an accurate prediction of stress level. These phenomena are multi-dimensional, while the code is based on a 1-D axisymmetrical description of the rod. A methodology has been used to integrate multi-dimensional effects into a 1-D model. First, an analytical 2-D model (reference model) was developed, accounting for the multi-dimensional effects. This model permits to determine hoop stress at triple point. Then the 1-D modelling of the code was described with an analytical model, where the pressure on the cladding is considered as a parameter. The hoop stresses of both models are equalled in order to determine the value of the pressure. Then, by changing the pressure on the cladding, the code can ascertain the hoop stress level due to crack opening.

Hoop stress concentration phenomenon appears in case of PCI. The mechanical loading on the cladding is then composed of external pressure (coolant pressure), internal pressure in the rod and pellet fragments thrust. We modelled the part of cladding opposite a half fragment of pellet and a half crack width using a curvilinear thin beam model (see Figure 3).

Figure 3. 2-D modelling of cladding



The p , kp and p_x data are efforts per unit length. p comes from external pressure and contact pressure. p_x comes from external and internal pressures. The half crack width is designated e . The length, section and curve radius of the beam are respectively noted L , S and R . We represent the friction effect between cladding and pellet due to the crack opening by the circumferential effort kp , where k is the pellet-cladding friction coefficient. The boundary conditions are symmetry conditions: only radial displacement of the ends of the beam is allowed. The material is considered elastic with a Young's modulus E .

The aim of this 2-D model is to assess hoop stress at the triple point (the point where curvilinear abscissa is $s = L$). The principle of virtual works is applied on the curvilinear thin beam model where the strain component along the co-ordinate line s with reference to a Frenet frame is:

$$\varepsilon_{ss} = \frac{d\bar{u}}{ds} - r \frac{d}{ds} \left(\frac{\bar{u}}{R} + \frac{d\bar{v}}{ds} \right) - \frac{\bar{v}}{R} \quad (1)$$

r being the co-ordinate following the thickness line and \bar{u}, \bar{v} , respectively, tangential and normal displacements. So:

$$\left\{ \begin{array}{l} \delta V(\bar{u}, \bar{v}) = \int_0^L \left(\frac{d\delta\bar{u}}{ds} - \frac{\delta\bar{v}}{R} \right) ES \left(\frac{d\bar{u}}{ds} - \frac{\bar{v}}{R} \right) ds + \int_0^L \frac{d}{ds} \left(\frac{\delta\bar{u}}{R} + \frac{d\delta\bar{v}}{ds} \right) EI \frac{d}{ds} \left(\frac{\bar{u}}{R} + \frac{d\bar{v}}{ds} \right) ds \\ \quad - \int_0^{L-e} p \delta\bar{v} ds - \int_0^{L-e} k p \delta\bar{u} ds - \int_{L-e}^L p_x \delta\bar{v} ds = 0 \\ \bar{u}(0) = 0, \bar{u}(L) = 0, \frac{d\bar{v}}{ds}(0) = 0, \frac{d\bar{v}}{ds}(L) = 0 \\ \delta\bar{u}(0) = 0, \delta\bar{u}(L) = 0, \frac{d\delta\bar{v}}{ds}(0) = 0, \frac{d\delta\bar{v}}{ds}(L) = 0 \end{array} \right. \quad (2)$$

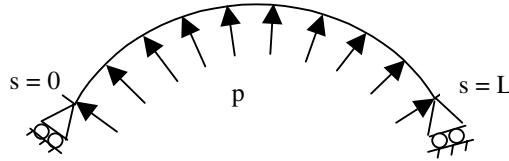
where $\delta\bar{u}, \delta\bar{v}$ are, respectively, the tangential and normal virtual displacements and I the quadratic moment of the beam.

The hoop stress ($\sigma_{\theta\theta}$) is then obtained by solving the problem given in Eq. (2). At the triple point ($s = L$ and $r = 0$) the hoop stress is equal to:

$$\sigma_{\theta\theta}(L) = -\frac{Rp}{S\sin\left(\frac{L}{R}\right)} \left[k \left(1 - \cos\left(\frac{L-e}{R}\right) \right) + \sin\left(\frac{L-e}{R}\right) \right] - \frac{Rp_x}{S} \left(1 - \frac{\sin\left(\frac{L-e}{R}\right)}{\sin\left(\frac{L}{R}\right)} \right) \quad (3)$$

In CYRANO3, the pellets and the cladding are modelled by 1-D axisymmetrical elements. Then, the loading is axisymmetrical too. We developed an analytical 1-D axisymmetrical model (denoted the “equivalent model”) to represent the code modelling. As for the reference model, the curvilinear thin beam model is used (cf. Figure 4). It is based on the same geometry and the loading is replaced by an axisymmetrical loading p_e : effort per unit length resulting from external pressure and equivalent contact pressure.

Figure 4. 1-D axisymmetrical modelling of cladding



Hoop stress at the triple point ($S = L$) is then equal to $\sigma_{\theta\theta} = -\frac{Rp_e}{S}$. The equivalent pressure (p_e) is determined by equalling hoop stresses between the reference model and the 1-D equivalent model:

$$p_e = \frac{p}{\sin\left(\frac{L}{R}\right)} \left[k \left(1 - \cos\left(\frac{L-e}{R}\right) \right) + \sin\left(\frac{L-e}{R}\right) \right] + p_x \left(1 - \frac{\sin\left(\frac{L-e}{R}\right)}{\sin\left(\frac{L}{R}\right)} \right) \quad (4)$$

The thus-obtained equivalent pressure does not depend on the height or on the material parameters.

Implementation

In the CYRANO3 code, each rod is divided into axial slices (named standard slices) in order to take into account the evolution of variables along the rod. For the finite element calculation, a 1-D axisymmetrical element is used, which is a radial element (two-node segment). Pellets and cladding of each slice are modelled with several elements and the gap between pellet and cladding is represented by one element. Thus the strains and stresses calculated in standard slices are average values. The option, named “fictive slice” provides an assessment of the local stresses in the cladding due to the hourglass shape of the pellet. In this case, a local increase in the apparent diameter of the pellet is assessed after the calculation of the standard slice. Then, a second mechanical calculation is performed with an increased pellet diameter, maintaining the same thermal gradient as in a standard slice. The fictive slice in CYRANO3 represents in fact the inter-pellet area. The “triple point” functionality developed in CYRANO3 is based on the same principles as the “fictive slice” functionality. As the triple point is a specific point of the inter-pellet area, the geometry and the mechanical loading are retrieved after the calculation of the fictive slice. Then the new loading is determined with the previous model and a mechanical calculation is performed with the modified loading on the cladding. This calculation gives then the hoop stress level on the cladding at the triple point, which is due to the stress concentration effect.

Validation

The developed model has been validated by comparing the results obtained with CYRANO3 to previous 3-D finite element simulations. As for 3-D calculations, the materials were considered elastic. The aim is to compare the hoop stresses at triple point for different pellet-cladding friction coefficient values. Because of axial interaction phenomena, the height of the pellet in the 3-D calculation is adjusted for a friction coefficient of 0.1, so that the meaning of hoop stresses on the internal face of cladding in front of the inter-pellet area is equal to the hoop stress on the internal face of the cladding of the fictive slice calculated in CYRANO3. This adjustment is necessary for the validation of the model, considering the hypothesis and the processing of the 1-D code compared with a 3-D calculation. This one is more representative but is based on a certain number of hypotheses as well, especially concerning the fragmented state of fuel material. Hoop stresses at triple point obtained in both codes are almost the same (see Table 4).

Table 4. Comparison of CYRANO3 and Code_Aster results

Friction coefficient (μ_{g})	Hoop stress at triple point Code_Aster (MPa)	Hoop stress at triple point CYRANO3 (MPa)
0	606	575
0.1	590	587
0.2	600	599
0.3	611	611
0.4	622	623
0.5	633	634
0.6	644	646
0.7	654	658

While further finite element calculations should confirm these encouraging preliminary results, the next section focuses on a related problem: the effect of fragmentation on pellet displacement and stress fields. This effect would improve on estimation of pellet-cladding gap. As a result, previous PCI calculations would also be improved.

A one-dimensional model of pellet fragmentation

As concerns the cladding stress concentration model, the method consisting in describing the phenomenon with a reference model and then modelling it with a 1-D code consistent model is used. In the following, both models are presented.

Reference model

After pellet cracking, pellet fragments are bulged because of thermal expansion. In the case of PCI, the cladding tends to collect pellet fragments, which are then in contact along a short length represented by the ring on Figure 5.

For the modelling, the pellet is considered divided into eight equal fragments, which corresponds to the most likely situation. Therefore, the studied fragment (see Figure 6) has an angle of 45° . Its geometry is defined by the three radii R_1 , R_2 and R_{ext} , where R_1 and R_2 define the area where fragments are in contact and R_{ext} is the external radius of the pellet.

Figure 5. Contact between adjacent fragments

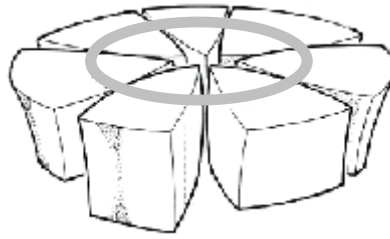
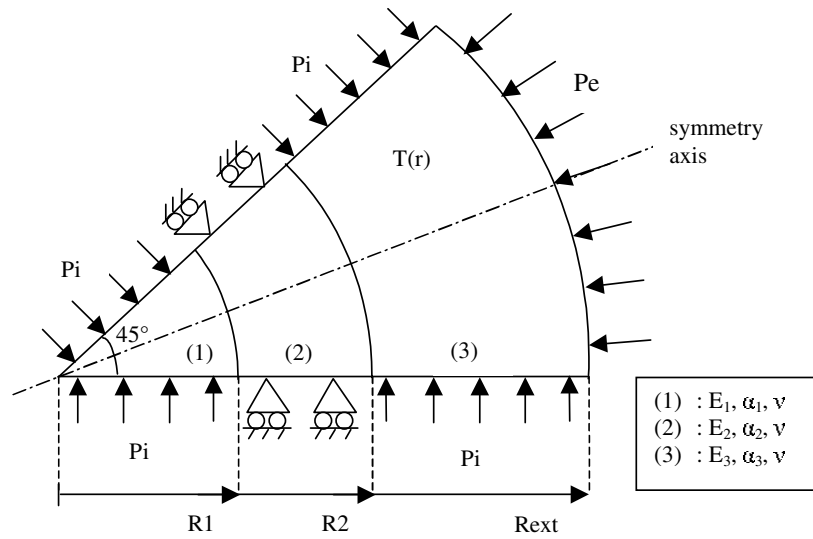


Figure 6. 2-D modelling of a fragment for pellet-cladding contact case



The loading on the fragment consists of the internal rod pressure on the sides of the fragments where there is no contact, the pressure P_e on the external side of the fragment, which represents the pellet-cladding contact pressure, and a radial and parabolic temperature gradient, whose form is $T = ar^2 + br + c$.

To account for the temperature dependency of the material properties, three materials are considered: for each area (i) ($i = 1, 2, 3$, see Figure 3) of the fragment are defined a Young's modulus E_i and a thermal expansion coefficient α_i , which are respectively the mean values of Young's modulus E and thermal expansion coefficient α on each area (i). The Poisson's ratio ν is constant on the fragment. The height of the fragment is considered large enough compared to fragment dimensions in the plane perpendicular to the axial direction, to make the hypothesis of plane strain valid. Besides, the hoop displacement u_θ is assumed to be null such as only radial displacement is considered (denoted u hereafter). As the material is assumed elastic and isotropic, the thermo-mechanical behaviour law (Hooke-Duhamel law) can be written:

$$\begin{pmatrix} \sigma_{rr} \\ \sigma_{\theta\theta} \\ \sigma_{zz} \end{pmatrix} = \frac{E}{(1+\nu)(1-2\nu)} \begin{bmatrix} 1-\nu & \nu & \nu \\ \nu & 1-\nu & \nu \\ \nu & \nu & 1-\nu \end{bmatrix} \begin{pmatrix} \varepsilon_{rr} \\ \varepsilon_{\theta\theta} \\ 0 \end{pmatrix} - \frac{E\alpha\Delta T}{(1-2\nu)} \begin{pmatrix} 1 \\ 1 \\ 1 \end{pmatrix} \quad (5)$$

where:

$$\varepsilon_{rr} = \frac{du}{dr} \text{ and } \varepsilon_{\theta\theta} = \frac{u}{r} \quad (6)$$

These equations describe the material behaviour in the “cast rigid” area (area 2). In cracked areas (areas 1 and 3), on the fragment side, the hoop stress is equal to $-P_i$:

$$\sigma_{\theta\theta}(r,\theta) = \sigma_{\theta\theta}(r) = \sigma_{\theta\theta} = -P_i \quad (7)$$

The previous equations then become:

$$\sigma_{rr} = \frac{E}{(1+\nu)(1-\nu)} \varepsilon_{rr} - \frac{\nu}{1-\nu} P_i - \frac{E\alpha}{(1-\nu)} \Delta T \quad (8)$$

with:

$$\varepsilon_{rr} = \frac{du}{dr} \text{ and } \varepsilon_{\theta\theta} = \frac{(1+\nu)}{(1-\nu)} \alpha \Delta T - \frac{(1+\nu)(1-2\nu)}{(1-\nu)E} P_i - \frac{\nu}{(1-\nu)} \varepsilon_{rr} \quad (9)$$

The radial equilibrium equation yields $\frac{d}{dr} \left(\frac{1}{r} \frac{d(ru)}{dr} \right) = \frac{(1+\nu)}{(1-\nu)} \alpha \frac{dT}{dr}$ for a “cast rigid” material, and

$\frac{d}{dr} \left(r \frac{du}{dr} \right) = (1+\nu) \alpha \left(r \frac{dT}{dr} + \Delta T \right) - \frac{(1-2\nu)(1+\nu)}{E} P_i$ for a “cracked” material.

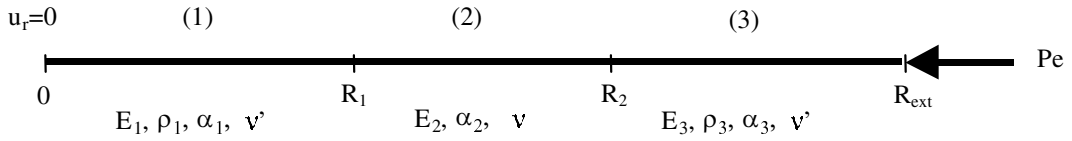
The solution is found by solving these equations analytically and applying boundary conditions and continuity conditions. To validate the hypothesis and especially to determine the limits of the reference model, we proceeded to a comparison with 2-D numerical results (see Ref. [8] for more details).

One-dimensional equivalent model

The aim of this equivalent model is to simulate stress and strain relaxation due to the fragmentation phenomenon, in the 1-D axisymmetrical code, considering a cast rigid pellet. To describe fragmentation effects, that is to say, decreasing of stress level in the pellet centre and increasing of the radial displacement at pellet periphery, the best solution is to damage the material [8]. An anisotropic material is thus considered for the “cracked” parts, with a hoop Young’s modulus E' different from the radial E (we note $\rho = \frac{E}{E'}$) and with a Poisson’s ratio ν' different from the initial ν :

$$\begin{pmatrix} \varepsilon_{rr} \\ \varepsilon_{\theta\theta} \\ 0 \end{pmatrix} = \begin{pmatrix} \frac{1}{E} & -\frac{\nu'}{E'} & -\frac{\nu'}{E} \\ -\frac{\nu'}{E'} & \frac{1}{E'} & -\frac{\nu'}{E'} \\ -\frac{\nu'}{E} & -\frac{\nu'}{E'} & \frac{1}{E} \end{pmatrix} \begin{pmatrix} \sigma_{rr} \\ \sigma_{\theta\theta} \\ \sigma_{zz} \end{pmatrix} + \begin{pmatrix} \alpha \Delta T \\ \alpha \Delta T \\ \alpha \Delta T \end{pmatrix} \quad (10)$$

Figure 7. Equivalent model for a cracked pellet in case of pellet-cladding contact



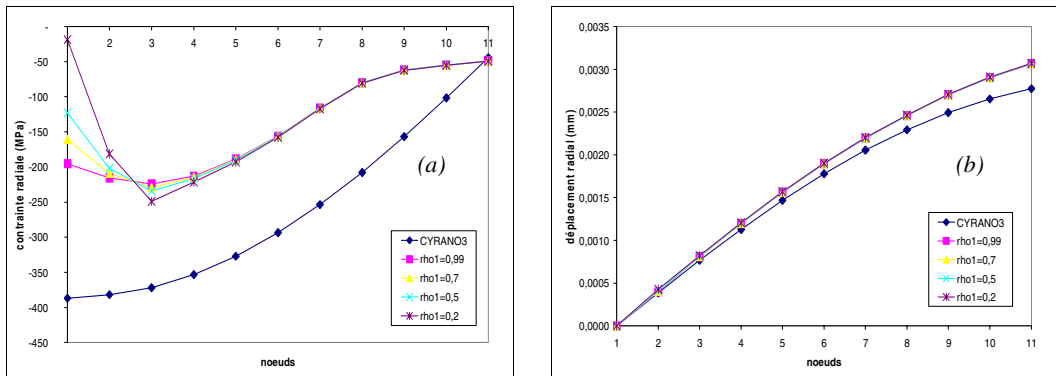
The geometry and loading data are the same as for the reference model. In area 2 (contact between fragments), the material is cast rigid and defined as in the reference model [Eqs. (5) and (6)]. In areas 1 and 3, the material is considered “cracked” and is defined by the damage material [Eqs. (10) and (6)]. Poisson’s ratios are ν for the cast rigid material, and ν' for the cracked materials. Hence, if pellet cracks close up, areas 1 and 3 tend to disappear and the pellet is then defined by the material of area 2 with the initial Poisson’s ratio and Young’s modulus. Thus the model is able to account for crack closure.

To solve the problem, an equilibrium equation is solved for each area of the fragment and constants are determined by applying boundary and continuity conditions. The three model parameters (ρ_1 , ρ_3 and ν') are adjusted equalling specific results for the reference model and equivalent model (radial and hoop stresses of pellet centre and the radial displacement of pellet periphery). Both models were developed for the general case, describes in Figure 6, with an elastic material behaviour. The models have been extended for the hydrostatic case (when there is no contact between adjacent fragments) and for a viscoplastic behaviour law [8].

Results

Once introduced in CYRANO3, several power transients were simulated to validate this model. As depicted in Figure 8 for one of these transients, radial displacement at pellet periphery is increased while radial and hoop stresses at its centre are relaxed [8]. These results are qualitatively satisfactory but additional comparisons with two-dimensional finite element calculations are still needed.

Figure 8. Radial stress (a) and radial displacement (b)



Conclusions, future works

On the whole, both the triple point localisation and fragmentation models presented here provide good results without significantly modifying computing times. Further comparisons are still needed. Particular attention should be paid to radial displacement as well as radial distribution of equivalent and hydrostatic stresses which are related to the onset of viscoplastic flow and swelling, respectively.

The next stage should include comparisons with FE calculations, including viscoplastic pellet and cladding behaviours. The extension of quantitative triple point model validation to viscoplastic behaviour should also be considered. Once validated, coupling these two models would lead to improved uni-dimensional predictions. Finally, it is worth mentioning that triple point stress localisation as a function of the crack pellet opening reads:

$$\sigma_{\theta\theta}(L) \approx -\frac{R}{S} \xi p - \frac{e}{R} \left[(p_x - p) \cotg\left(\frac{L}{R}\right) + kp \right]$$

where ξ is constant with respect to $\frac{e}{R}$ ($\xi = 1$ if friction collapses). This last expression proves that the proposed localisation coefficient depends on pellet tangential displacement. This linear dependency should be confirmed through more sophisticated calculations. In any case, crack pellet opening being a decreasing function of the number of pellet fragments, this model could predict the beneficial effects of chromium oxide-doped fuel's fragmentation behaviour.

REFERENCES

- [1] Mezzi, G.-P., F. Caligara and BLANK, H. Thermoelastic stresses in pellet fragments and conditions for fragments formation. *Nuclear Engineering and Design*, vol. 73, pp.83-93, 1982.
- [2] Gittus, J.H., D.A. Howl, H. Hughes, "Theoretical Analysis of Cladding Stresses and Strains Produced by Expansion of Cracked Fuel Pellets", *Nucl. Appl. Technol.*, 9, 40-46 (1970).
- [3] Baron, D., *et al.*, "Cyrano3 : un logiciel de nouvelles générations pour simuler le comportement des crayons combustibles en réacteur", *Epure* 55, 29-40 (1997).
- [4] Ritzhaupt-Kleissl, H.J. and M. Heck, *SATURN-FSI. A Computer Code for Thermal-mechanical Fuel Rod Analysis*, Kernforschungszentrum Karlsruhe, report KFK 5203 (1993).
- [5] Garcia, Ph., C. Struzik, M. Agard and V. Louche, "Mono-dimensional Mechanical Modelling of Fuel Rods Under Normal and Off-normal Operating Conditions", *Nuclear Engineering and Design*, 216, pp. 183-201 (2002).
- [6] Retel, V., F. Trivaudey, L.M. Boubakar, D. Perreux, P. Thevenin, "Comparative Effects of Structural and Material Parameters Variability on Pellet-cladding Interaction in a PWR Fuel Rod, *Nuclear Engineering and Design*, 228, pp. 35-46 (2004).
- [7] Bentejac, F., N. Hourdequin, "Toutatis, an Application of the Cast3M Finite Element Code for PCI Three-dimensional Modelling", *International Seminar on Pellet-clad Interaction in Water Reactor Fuels* (2004).
- [8] Retel, V., "Contribution à la modélisation mécanique et numérique de l'interaction pastille-gaine dans les crayons combustibles de réacteurs nucléaires", PhD Thesis, Université de Franche-Comté (2002).

THE COPERNIC MECHANICAL MODEL AND ITS APPLICATION TO DOPED FUEL

C. Garnier, P. Mailhe, P. Vesco, L.C. Bernard, C. Delafoy, P. Garcia*

FRAMATOME ANP Nuclear Fuel, Lyon, France

*Commissariat à l'Énergie Atomique, Centre d'Études de Cadarache, St. Paul-lez-Durance, France

Abstract

COPERNIC is an advanced fuel rod performance code developed by FRAMATOME ANP. The main objectives of COPERNIC are to accurately predict steady-state and transient operations at high burn-ups and for advanced materials such as FRAMATOME ANP Cr₂O₃-doped fuel pellets. With demanding PWR conditions like load-follow operation, PCMI and its associated risk of cladding failure remains of utmost concern. Thus, mechanisms that lead to PCMI must be thoroughly modelled. Experimental evidence has shown that Cr₂O₃-doped pellets reduce the PCMI risk as compared to standard UO₂ pellets. First, cladding model predictions are presented on the basis of key experimental data that prevail in PCMI tests: hardening/relaxation, thermal creep, burst tests and power ramps. Then, the modelling of doped pellets will be assessed. Improved behaviour of doped fuel is currently understood to be a favourable combination of fuel creep and cracking properties. The MEFISTO model handles both mechanisms and has been implemented into COPERNIC. A model for pellet dish evolution, which also plays a role, has been added. Results on doped fuel creep and hardening data are presented.

Introduction

COPERNIC is an advanced fuel rod performance code developed by FRAMATOME ANP to provide accurate steady-state and transient fuel performance predictions. The COPERNIC code has been qualified from an extensive database that includes UO_2 , $\text{UO}_2\text{-Gd}_2\text{O}_3$ and MOX fuel pellets [1,2]. It is based on the TRANSURANUS code [8], which contains fast, accurate and numerically stable solutions. It also offers flexibility regarding the incorporation of new fuel rod models.

This paper highlights the main features of the mechanical models of COPERNIC. These models have been qualified through many analytical tests as well as by data from power and test reactors. Good mechanical modelling is particularly important in order to thoroughly assess the risk of clad failure as a result of pellet-cladding mechanical interaction (PCMI). Therefore, we focus on high-stress situations that prevail under PCMI conditions.

The description is in cylindrical co-ordinates and is basically mono-dimensional in the radial direction. Stresses and strains are obtained as solutions of the equilibrium balance and compatibility equations with the proper boundary conditions assuming an axial plane strain. Some multi-dimensional effects are included as specific models that are explained. Several conditions of pellet-cladding contact are possible. However, the option of perfect contact, i.e. no slip between pellet and cladding, proved to be adequate in mono-dimensional modelling and is used throughout.

In the first part, the results are presented for standard (non-doped) fuel pellets. The pellet is chosen as a solid and pellet cracking is taken into account as an extra strain calculated by a so-called “pellet fragment relocation” model. No pellet creep is used; as for a solid pellet, calculated stresses are high and the computed creep strain would be unduly high. Analytical high-stress mechanical tests on cladding are also presented here.

In the second part of the paper, pellet creep is presented. Then, a pellet cracking model is needed as well to maintain realistic stress levels inside the pellet. The MEFISTO model [7] handles both pellet cracking and creep. This model is implemented in COPERNIC with a further improvement: the pellet dish is chosen as an initial crack and its evolution is calculated. An overview of the model is presented. The pellets doped with chromium oxide developed by FRAMATOME ANP behave better than standard pellets with respect to PCMI. It is believed that a combination of cracking and creep is favourable for doped pellets. Out-of-pile experiments at the Commissariat à l'Énergie Atomique (CEA) provide a large set of data to thoroughly model pellet creep both for standard and doped fuels. In particular, primary creep is well addressed. This is important as primary creep is likely to prevail during a condition of highest cladding stress during a power ramp.

COPERNIC mechanical analysis

High-stress zircaloy-4 tests

Cladding strains during strong mechanical interaction with the pellet are a combination of creep and elastic-plastic strains, including stress relaxation. The share of each strain depends on the loading encountered. During a ramp, the pellet expansion under the influence of the rising of power induces a stable and high cladding strain rate in the 10^{-5} - 10^{-4} s^{-1} range. Then stress relaxation is controlled by the cladding short-term properties during the power plateau. It is therefore important to correctly predict hardening tests at constant strain rate imposed in this range, assumed to be representative ramp conditions, as well as relaxation tests. The cladding creep is primarily controlled by thermal creep for high stress levels. The plastic and creep properties of non-irradiated and irradiated zircaloy-4 were

evaluated on many tests conducted at CEA that include thermal creep tests and internal pressure burst tests. A classical Von Mises stress and an isotropic Prandtl-Reuss relation are used to redistribute the equivalent plastic and creep strains in the three spatial directions.

Plastic strain

An isotropic work hardening model (see for instance Ref. [9]) is applied to the cladding material. The yield stress σ_{ys} bounds the load surface which the equivalent stress σ cannot exceed. The model correlates the yield stress and the equivalent plastic strain ϵ_p as follows:

$$\sigma_{ys} = g(T, \Phi) \left(1 + a \times \epsilon_p^n \right)$$

where g is a function of temperature T and of fast neutron fluence Φ , and a and n are coefficients. The model is validated from internal pressure burst tests, run on specimens before and after irradiation within the ranges: 350-400°C, 0-10²¹ neutrons/cm². Strain rates are in the range 2.10⁻⁶ to 8.10⁻³ s⁻¹. Figures 1 and 2 illustrate the good agreement between predictions and measurements.

Figure 1. Internal pressure burst test on non-irradiated zircaloy-4

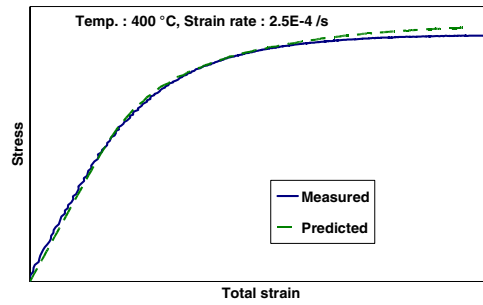
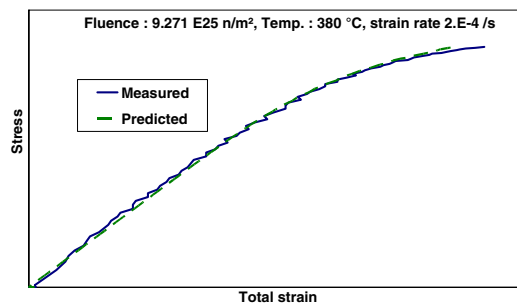


Figure 2. Internal pressure burst test on irradiated zircaloy-4



Thermal creep

The thermal creep model correlates the equivalent thermal creep strain ϵ_T and the equivalent stress as follows:

$$\epsilon_T = f(\sigma, \Phi) \exp\left(-\frac{T_0}{T}\right) \sinh(c\sigma) t^d$$

where f is a decreasing function of Φ , expressing irradiation hardening, t is time, and T_0 , c and d are coefficients. The model was benchmarked within the following ranges: 200-550 MPa, 350-400°C and $0-10^{21}$ neutrons/cm² and is incorporated into COPERNIC with a strain-hardening algorithm. Figure 3 compares predictions and measurements. Creep relaxation tests are also performed in approximately the same ranges as thermal creep tests and are illustrated in Figures 4 and 5.

Figure 3. Thermal creep tests on zircaloy-4

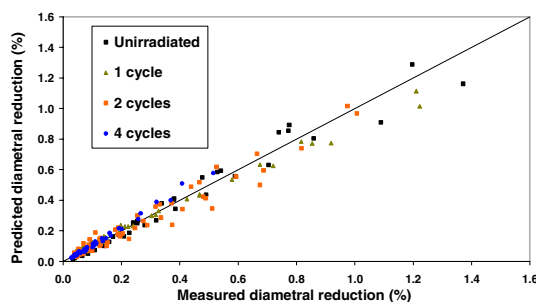


Figure 4. Relaxation test on non-irradiated zircaloy-4

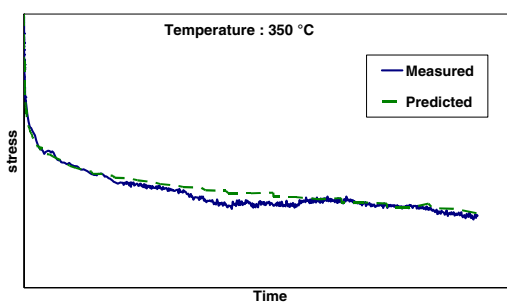
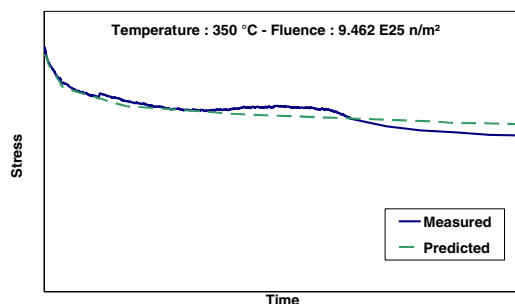


Figure 5. Relaxation test on irradiated zircaloy-4



Pellet fragment relocation model

During PCMI, all pellet strains contribute of course to cladding loading. We illustrate hereafter the two most important pellet contributions, namely, pellet fragment relocation and gaseous swelling.

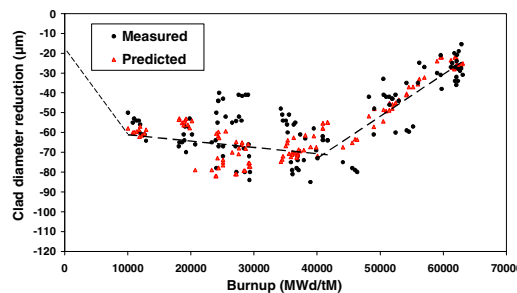
Pellet fragmentation is modelled with an empirical relocation model that represents the outward shift of the pellet fragments at BOL when the gap is open and the inward “rearrangement” of the pellet fragments when the gap closes. The model for the relocation strain, ϵ_R , is expressed as follows:

$$\dot{\epsilon}_R = -aP_C \epsilon_R, \epsilon_{R(t=0)} = b \frac{G}{D}$$

where P_C is the contact pressure between the pellet and the cladding, G is the initial cold diametral gap, D is the initial pellet diameter, and a and b are constants.

The shift and rearrangement of the fuel fragments were derived from PWR cladding diameter measurements as shown in Figure 6. There are clearly three distinct regions reflecting the state of the contact between pellet and cladding. At low burn-up, there is a “no contact” region resulting in the inward creep of the cladding. The pellet shift is calibrated in this region. At intermediate burn-up, there is a “soft contact” region where fragment rearrangement takes place and overtakes the outward creep due to solid swelling. The net effect is a slight diameter reduction with burn-up. The pellet rearrangement is calibrated in this region. At high burn-up, there is a “hard contact” region where rearrangement is fully established resulting in the outward creep of the cladding driven by solid swelling.

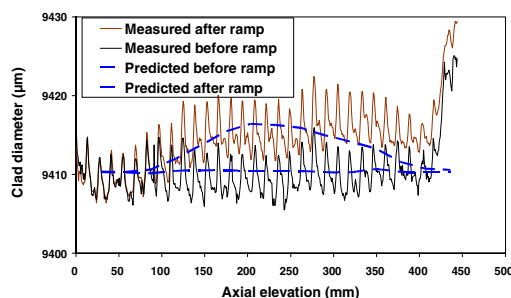
Figure 6. Measured and predicted clad diameter evolution



The thermal expansion of a fragment is also modelled. Simple considerations [12] show that the bulge of a fragment due to thermal expansion is proportional to the pellet temperature gradient. We have used such a term with corrective terms up to the third order in temperature gradient with a limit at high temperature because of viscoplastic effects. The model parameters were derived from power transient data with short hold times that minimised gaseous swelling effects. An example is shown in Figure 7.

Figure 7. OSIRIS ramp test: measured and predicted clad deformation

413 W/cm, 27 GWd/tM, ramp in 118 s, no hold time



Gaseous swelling model

The gaseous swelling phenomenon is complex and includes, among other factors, the generation, growth, coalescence and interconnection of gas bubbles and their impact on UO_2 creep and deformation. For simplicity, a semi-empirical formulation for the model was chosen.

Gaseous swelling and fission gas release are closely linked. The model uses information from the COPERNIC fission gas release model that is explained in detail elsewhere [3]. In particular, the onset of gaseous swelling is supposed to be at the temperature threshold for thermal fission gas release. Above this threshold, gaseous swelling increases with temperature and burn-up. This effect is mitigated by fuel re-densification at high temperatures. During transients, gaseous swelling increases with a kinetics that is proportional to the transient fission gas release.

Steady-state gaseous swelling was calibrated with NFIR porosity data [5], and indirectly qualified with the full FRAMATOME ANP database. Transient gaseous swelling was qualified with cladding deformations that were measured before, during and after transients that ranged from seconds to several hours. Figures 8 and 9 show the comparison between predicted and measured cladding deformations on rodlets ramped in the STUDESVIK test reactor. Clad deformations are measured at mid-pellet location as deformations at inter-pellet location are affected by the inward creep of the fuel. This inward creep induces the filling of the pellet dishes and is a multi-dimensional effect that is not modelled here but will be addressed in the second part of the paper.

Figure 8. STUDESVIK ramp test: measured and predicted clad deformations at different cycles

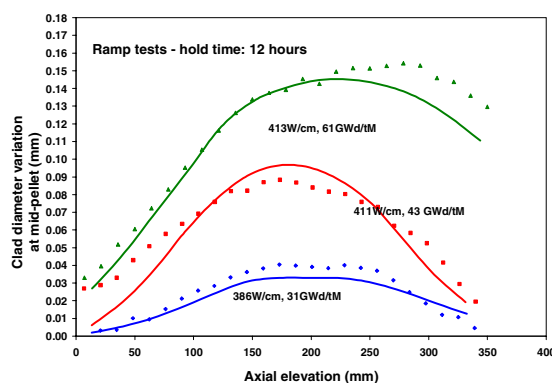
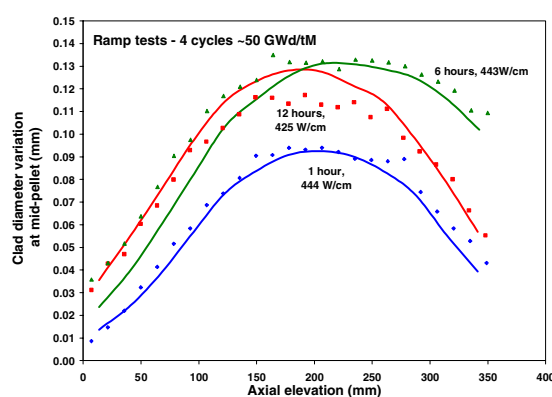


Figure 9. STUDESVIK ramp test: measured and predicted clad deformations at different hold times



Power ramp tests

Many power ramp tests are performed at CEA test reactors and at STUDESVIK in order to assess the limit of clad failure. Rodlets re-fabricated from rods irradiated from 1 to 5 cycles are used. Ramp hold times are in 0-12 hour range. Ramp rates are close to $100 \text{ W.cm}^{-1}.\text{mn}^{-1}$ to be representative of

Class II incidents. Ramp peak power is in the range 400-600 W.cm⁻¹. These power ramps are most important to test the global validity of all the models. Typically, if the prediction at peak power is good, the prediction at any rod elevation is also good.

Modelling of doped fuel pellets

Depending on market needs, operational flexibility and manoeuvrability are required to adapt reactor load to the grid demand at any time. Such requirements warrant the development of fuel products that reduce the risk of cladding failure during PCMI in order to maintain appropriate safety margins. The addition of chromium oxide as a doping compound changes the microstructure of UO₂, notably by enlarging the grain size. The experimental results obtained show that this advanced doped fuel can reach high linear power levels without failing in relation to an enhancement in the fuel creep rates and an increase in cracking at the pellet periphery [6]. The future FRAMATOME ANP fuel rod code will be able to take into account these specific properties in order to enhance the advanced fuel. The solution chosen to implement a new mechanical model taking into account pellet cracking and creep is presented hereafter. This ongoing work is developed by the three regional divisions (French, German, US) of the FRAMATOME ANP Fuel Business Group, and is drawn in part from their experiences and other codes (CARO, RODEX, SIERRA [4]).

Pellet creep

The post-ramp examinations on Cr₂O₃-doped fuel showed an enhancement of the fuel creep leading to the filling of pellet ends at low power levels (40 kW.cm⁻¹) [10] and an associated loading on the cladding at inter-pellet planes. This points to the need to have a suitable pellet creep model to calculate the fuel behaviour under transient conditions and to enhance Cr₂O₃-doped fuel.

FRAMATOME ANP established a creep law which allows predicting both creep tests and tests with constant strain rate. To maintain consistent modelling, a single formulation was chosen for standard UO₂ and for doped fuel. The model of the pellet creep equivalent strain rate, $\dot{\epsilon}_c$, follows:

$$\dot{\epsilon}_c = (v_p - v_s) \exp\left(-\frac{\epsilon_c}{a}\right) + v_s$$

where one can see that v_p and v_s represent the primary and secondary creep rates and the variable a is a measure of the transition between the two rates when ϵ_c increases. This classical form is particularly useful for integrating the strain with respect to time in order to fit the law with experimental data:

$$\epsilon_c = a \ln \left\{ 1 + \frac{v_p}{v_s} \left[\exp\left(\frac{v_s t}{a}\right) - 1 \right] \right\}$$

The quantities a , v_p , and v_s are of the form $a = a_0 \sigma^n \exp(-T_0/T)$ where a_0 , n and T_0 are either constants or depend on initial chromium oxide concentration only. The model is validated from uniaxial creep tests and from tests at constant strain rate within the following ranges: 1 358-1 575°C, 20-90 MPa for Cr₂O₃-doped fuel and 30-60 MPa for UO₂ fuel. Two tests with their predictions are illustrated in Figures 10 and 11.

Figure 10. Uniaxial test at constant strain rate with doped fuel. Measured and predicted stress vs. strain.

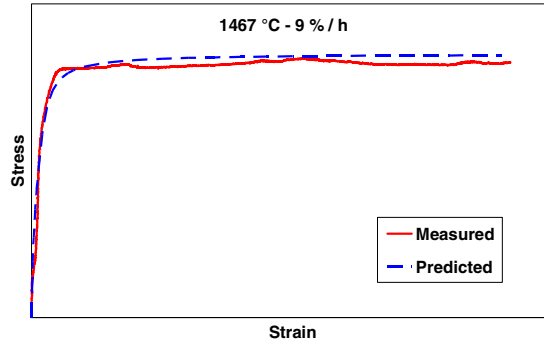
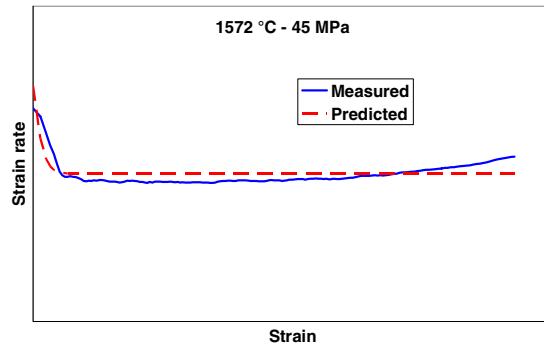


Figure 11. Uniaxial creep test with doped fuel. Measured and predicted strain rate vs. strain.



To take into account the effects of irradiation, a factor of amplification due to irradiation is introduced as well as a term of creep induced by irradiation, where K_1 , K_2 and T_{irr} are constants. Typically, irradiation-induced creep is weak and dominant at steady-state low power irradiation, and $\dot{\epsilon}_c$ becomes dominant during a power ramp.

$$\dot{\epsilon}_{irr} = \dot{\epsilon}_c \times \left(1 + K_1 \phi\right) + K_2 \sigma \phi \exp\left(-\frac{T_{irr}}{T}\right), \text{ with the fission density } \phi \text{ (m}^{-3}\cdot\text{s}^{-1}\text{)}$$

As for the cladding, a Von Mises stress and an isotropic Prandtl-Reuss relation are used to redistribute creep strains in the three spatial directions.

The MEFISTO model

A mechanical model called MEFISTO has been implemented in a COPERNIC development version. This model comes from the thermal-mechanical fuel rod code METEOR developed at the CEA [11], based also on the TRANSURANUS code. This common origin has been an advantage in making the implementation a success. The MEFISTO model is explained in detail elsewhere [7]. The basic formalism is recapitulated only to understand the dish filling model presented hereunder.

Without considering the cracking, the model uses a classical finite element method to resolve the mechanical problem. From the inelastic strains ϵ^{nel} computed out of the mechanics, the displacements u are solutions of a linear system $K \cdot u = B \cdot \epsilon^{nel}$ with an invertible stiffness matrix K and a matrix

force B obtained from the equations of the mechanics. The compatibility relations allow the total strains ε^{tot} to be obtained from the displacements. Finally, the stresses are calculated using Hooke's law $\sigma = D \cdot (\varepsilon^{tot} - \varepsilon^{nel})$ for each material.

Cracking model

As soon as the fuel viscoplasticity behaviour is introduced, it is necessary to take into account relaxation of stress by cracking, in order that the stress levels be realistic. Then the cracking model of MEFISTO is described. A pellet element can be either intact, or present cracks normal to the radius r (radial cracks), normal to the axis z of the pellet (axial cracks), or in both directions. Cracks following the hoop direction θ are not authorised in order to keep the pellet in a single block. Otherwise, relative movement between pellet fragments could occur without applied stress. We always assume a continuous material which possesses behaviour laws identical to that of an un-cracked material.

Let us take the example of a radial crack. Cracking is introduced whilst retaining the assumption of axial symmetry. One could argue that when a radial crack appears, the symmetry of the problem is lost. It is a multi-dimensional effect which cannot be taken into account here. The MEFISTO model approaches the effect of a large number of radial cracks distributed throughout the periphery of the pellet. That is why it is called a "diffuse" crack model. In an element of material, a radial crack is understood as a volume of void extending in the radial direction and surrounded with material, and by a relaxation of the hoop stress around the crack. The idealised view of a radial crack in a model of continuous material is an additional volume corresponding to a hoop strain, associated with a threshold value of the hoop stress in the part considered cracked. This introduces the notion of the crack hoop strain $\varepsilon_{\theta}^{crack}$, associated with the hoop stress σ_{θ}^{crack} of the cracked material. The latter is an input model parameter assumed to be equal to the rod internal pressure. It is directly introduced in the model through a modified form of Hooke's law:

$$\sigma = \tilde{D} \cdot (\varepsilon^{tot} - \varepsilon^{nel} - \varepsilon^{crack}) + \sigma_{\theta}^{crack} \times F$$

where \tilde{D} and F are derived from D which depends on compression and shear moduli of the fuel only. The hoop stress is not an unknown any more but a new one appears with the crack hoop strain. The hoop component of $\tilde{D} \cdot \varepsilon$ is zero. Therefore the crack hoop strain need not be known during the mechanical resolution. It is obtained once the mechanical problem is solved by:

$$\varepsilon_{\theta}^{crack} = \varepsilon_{\theta}^{tot} - \varepsilon_{\theta}^{nel} - \varepsilon_{\theta}^{el}$$

The same method is used for the axial cracking, differently recombining Hooke's law according to the state of cracking of each fuel element. Two criteria govern the opening and the closure of a crack. The pellet is initially intact. A crack opens when the stress reaches the tensile fracture stress which is an input parameter for the model. It closes when the crack strain becomes zero at the end of the mechanical calculation. The treatment of creep and plasticity requires additional schemes, which will not be detailed here.

Pellet dish model

The potential gain for PCMI brought by the creep and the cracking of the doped fuel cannot be fully reflected in a one-dimensional generalised plane strain model, which describes rather what takes place in the mid-pellet plane. Indeed in this case the material tends to flow by creep towards the

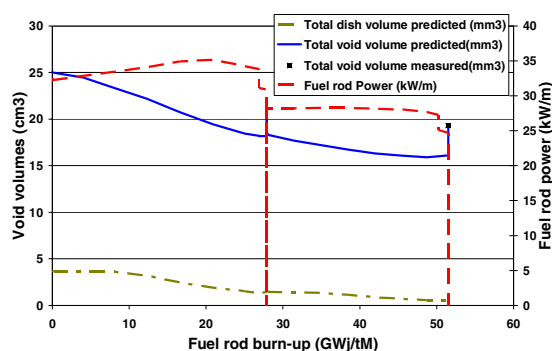
outside, loading more the cladding than without creep. Now in the inter-pellet plane where PCMI failures are observed in power ramps, a significant part of the material fills dished pellet ends during a ramp or at high enough power ratings. Roughly speaking, the dished ends can be considered as a large initial axial crack where mechanical conditions are close to plane axial stress conditions. It is exactly the kind of problem that the MEFISTO model is able to solve, without questioning the mathematical formulation of impossibility between plane stress and plane strain. The treatment of cracking as described above is just a particular case of this problem. By imposing a given value of stress (the internal pressure) where there is a crack in one direction, it introduces an additional strain in this direction which is interpreted as a crack (a void volume in the pellet). Considering this additional strain as a part of the total strain, compatibility equations and equilibrium balance are still valid in the whole pellet. In a similar way, if the dish is considered as an initial free volume, its behaviour can be compared to an axial crack, and physical strains can fill it if an additional strain balances the total strain. But in this case, the lower limit of this additional strain is no longer zero as in the crack problem, but less than zero in such a way that its value is compatible with the following equation:

$$\epsilon_z^{tot} = \epsilon_z^{el} + \epsilon_z^{nel} + \epsilon_z^{dish}$$

The dish can be filled when ϵ_z^{dish} varies from zero to the negative lower limit. This lower limit is equal in absolute value to the volume part of the dish in the element normalised to the volume of the element. In the pellet shoulder, the plane strain approximation is still applied as before, with the possibility of modelling cracks, as is also the case when the pellet end becomes closed in each element.

To illustrate both pellet creep and dish filling models, Figure 12 shows the change with burn-up of the contribution of pellet ends to the rod free volume, for a FRAMATOME ANP fuel rod irradiated in a heavy duty reactor. The total void volume is correctly predicted thanks to the dish volume decrease. It should be noted that dish filling is rapidly much less important at lower power levels.

Figure 12. Heavy duty reactor: measured and predicted void volumes, predicted dish filling vs. burn-up



Conclusion and prospects

The mechanical model of COPERNIC has been presented, highlighting phenomena occurring during strong PCMI. The main cladding models playing a significant role are the viscoplastic high-stress effects, along with the plastic model and the thermal creep model of the zircaloy-4 cladding. The pellet relocation model includes the fragmentation and rearrangement phenomenon and thermal expansion of a fragment. The latter is derived from power ramps with short hold times, whereas gaseous swelling becomes dominant for long hold times. The models have been successfully assessed against experimental data from tests run on FRAMATOME ANP rods and materials.

The present mechanical model must be expanded to be able to include the physical phenomena involved in PCMI remedies such as Cr₂O₃-doped fuel. Developments are in progress concerning the introduction of the pellet creep associated with the cracking consideration. Creep laws for standard and doped FRAMATOME ANP fuels were established from out-of-pile tests and implemented in the code. The MEFISTO model [7] has been used for that purpose and extended with the dish filling treatment.

REFERENCES

- [1] Bernard, L.C., *et al.*, “The FRAMATOME COPERNIC Fuel Rod Performance Code, Recent High Burn-up and Advanced Cladding Developments”, *Proceedings of the Int. Topical Meeting in Light Water Reactor Fuel Performance*, Park City, USA (2000).
- [2] Bernard, L.C., *et al.*, “COPERNIC FRAMATOME ANP Fuel Rod Performance Code. Status and Development to Assess High Demanding Operations and Advanced Materials”, *13th Pacific Basin Nuclear Conference*, Shenzhen, China (2002).
- [3] Bernard, L.C., *et al.*, “An Efficient Fission Gas Release Model”, *J. Nuclear Mater.*, Vol. 302, 125-134 (2002).
- [4] Billaux, M.R., *et al.*, “SIERRA: A Fuel Performance Code to Predict the Mechanical Behaviour of Fuel Rods Up to High Burn-up”, *ANS Meeting*, Portland, USA (1997)
- [5] Blanpain, P., *et al.*, *Properties of UO₂ Irradiated to High Burn-ups*, Final report EPRI NP-5191-LD, Project X 101-5 (1987).
- [6] Delafoy, Ch., *et al.*, “Advanced PWR Fuels for High Burn-up Extension and PCI Constraint Elimination”, *TCM on Improved Fuel Pellet Materials and Designs*, Brussels, Belgium, 20-24 October 2003.
- [7] Garcia, P., *et al.*, “Mono-dimensional Mechanical Modelling of Fuel Rods Under Normal and Off-normal Operating Conditions”, *Nuclear Engineering and Design*, 216, 183-2001 (2002).
- [8] Lassmann, K. and H. Blank, “Modelling of Fuel Rod Behaviour and Recent Advances of the TRANSURANUS Code”, *Nuclear Engineering and Design*, 106, 291-313 (1988).
- [9] Lemaitre, J. and J.L. Chaboche, “*Mécanique des matériaux solides*”, Dunod (1988).
- [10] Nonon, C., *et al.*, “PCI Behaviour of Chromium Oxide Doped Fuel”, *International Seminar on Pellet-clad Interaction in Water Reactor Fuels*, Aix-en-Provence, France, 9-11 March 2004.
- [11] Struzik, C., *et al.*, “High Burn-up Modeling of UO₂ and MOX Fuel with METEOR/TRANSURANUS Version 1.5”, *Proc. ANS Conference*, Portland, Oregon, 126-132 (1997).
- [12] Walton, L.A. and J.E. Matheson, “FUMAC – A New Model for Light Water Reactor Fuel Relocation and Pellet-cladding Interaction”, *Nucl. Technol.*, Vol. 64, 127-138 (1984).

**MODELLING OF THERMAL MECHANICAL BEHAVIOUR OF HIGH BURN-UP
VVER FUEL AT POWER TRANSIENTS WITH SPECIAL EMPHASIS ON THE
IMPACT OF FISSION GAS INDUCED SWELLING OF FUEL PELLETS**

V. Novikov, A. Medvedev, G. Khvostov, S. Bogatyr, V. Kuznetsov, L. Korystin
Federal State Unitary Enterprise VNIINM, Moscow, Russian Federation

Abstract

This paper is devoted to the modelling of unsteady state mechanical and thermo-physical behaviour of high burn-up VVER fuel at a power ramp. The contribution of the processes related to the kinetics of fission gas to the consequences of pellet-clad mechanical interaction is analysed by the example of integral VVER-440 rod 9 from the R7 experimental series, with a pellet burn-up in the active part at around 60 MWd/kgU. This fuel rod incurred ramp testing with a ramp value $\Delta W_l \approx 250$ W/cm in the MIR research reactor. The experimentally revealed residual deformation of the clad by 30-40 microns in the "hottest" portion of the rod, reaching a maximum linear power of up to 430 W/cm, is numerically justified on the basis of accounting for the unsteady state swelling and additional degradation of fuel thermal conductivity due to temperature-induced formation and development of gaseous porosity within the grains and on the grain boundaries. The good prediction capability of the START-3 code, coupled with the advanced model of fission gas related processes, with regard to the important mechanical (residual deformation of clad, pellet-clad gap size, central hole filling), thermal physical (fission gas release) and micro-structural (profiles of intra-granular concentration of the retained fission gas and fuel porosity across a pellet) consequences of the R7 test is shown.

Introduction

Of the many results obtained from post-irradiation examination (PIE) of high burn-up fuel rods subsequent to intensive power transients in research reactors [1,2], those based on Quantitative Image Analysis (QA), Electron Probe Micro Analysis (EPMA) and X-ray Fluorescence (XRF), testify to the significant changes in the macro- and micro-structural state of the fuel pellets. These changes appear to be:

- A partial or complete filling of the internal voids in fuel pellets (central hole, dishes etc.).
- Depression in the intra-granular area and total concentration of the retained fission gas in the high-temperature areas of the fuel pellets.
- Formation and enhanced development of fuel porosity in roughly the same areas of the fuel.

It is commonly agreed that the main inducement for these developments is constituted by the intensified diffusive mobility of the fission gases accumulated in the pellet bulk during the base irradiation previous to power ramps. From the point of view of rod reliability, the most unfavourable outcomes of the appropriate kinetic processes are the unsteady state swelling of the fuel and additional degradation of its thermal conductivity due to the formation and development of gas-inflated pores and bubbles. This evidently enlarges the pellet growth and, thereby, strengthens pellet-clad mechanical interaction (PCMI), which eventually can lead to clad damage and rod failure. The secondary effect of the fission gas kinetics implies its release into the free volume of the fuel rod, which worsens the conditions of pellet-to-clad heat conductance and increases gas pressure on the clad.

This is, in particular, why the development of the advanced model, which embraces the wide set of the kinetic processes related to fission gas and fuel micro-structure in the widest possible range of irradiation conditions, has been assumed to be a foreground task of the activity during improvement and verification of the START-3 code for some years. One of the advantages arising from the model application is the possibility to numerically analyse the contribution of the above-mentioned effects as concerns the thermal-mechanical behaviour of fuel rods at power transients under PCMI conditions.

The basic elements and scope of the advanced model describing overall behaviour of stable fission gas and evolution of fuel structure

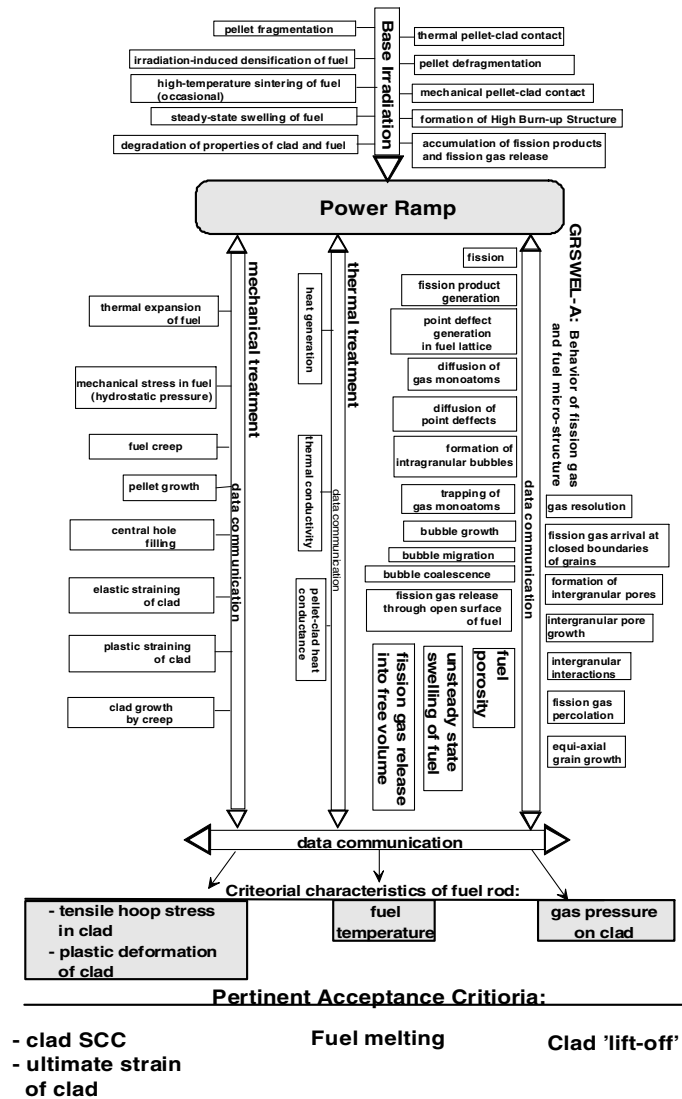
The dynamic model GRSWEL-A [3,4] addresses the overall behaviour of stable fission gas and the pertinent evolution of fuel microstructure. This is the advanced version of the model formerly referred to as GRSWEL, which was developed for the START-3 code [4,5]. This new model is being developed with a view toward analysis of fuel behaviour under in-pile and out-of-pile conditions; at extended rod- and pellet-average burn-ups (up to about 80 MWd/kgM), as well as at an ultra-high local burn-up in a pellet rim (up to about 200 MWd/kgM); in the exhaustive range of temperature, from the magnitudes, which are typical for the coolant, to the melting point of the fuel; in the long-term modes with slow or absent variation of the parameters of fuel thermal state, as well as at fast power transients including accidents with reactivity insertion.

The numerical analysis of fuel behaviour is reduced to integration with respect to time, of the set of rate equations for the array of dependent variables, which describes the current state of the fuel as comprehensively as possible. The model variables are logically divided into groups, which take into consideration the intra- and inter-granular processes, high burn-up structure features, high-temperature assisted re-crystallisation, as well as the dynamics of as-fabricated intra-granular porosity leading to early-in-life fuel densification or thermal sintering.

The calculation is carried out as applied to the set of zones in a fuel pellet, characterised by approximately uniform distribution of the external variables supplied by the mechanical and thermal physical modules of the code. The external variables of the model are the local magnitudes of temperature; temperature gradient; fission rate; hydrostatic pressure, which takes into account gas pressure in the plenum; and PCMI intensity.

Figure 1 represents the flowchart for the integral analysis of fuel performance at power ramps as realised in the START-3 code coupled with the advanced model GRSWEL-A. The flowchart shows schematically the analysed processes affecting transient behaviour of fuel and cladding, as well as the effects of base irradiation, which are essentially imposed on this behaviour. As seen from Figure 1 the GRSWEL-A model provides the integral calculation with the current local and pellet average magnitudes of different components of gas retention and porosity to calculate fuel thermal conductivity, mechanical properties and pellet strain; absolute and relative fission gas release to calculate gas pressure in the plenum and fuel-cladding heat conductance; average grain size, which affects mechanical properties of the fuel (an equi-axial character of grains is assumed).

Figure 1. Flowchart for integral analysis of fuel performance at power ramp as realised in the START-3 code coupled with the advanced model GRSWEL-A



Despite the complex set of feedbacks and feed-forwards between the thermo-mechanical behaviour of the fuel rod and micro-processes in the pellet analysed by the GRSWEL-A model, it is noteworthy that the resulting output of this model is transparent enough from the point of view of rod reliability due to the possible contribution to:

- Clad damage either by the mechanism of Stress Corrosion Cracking (SCC) or due to reaching the ultimate strain via the strengthened PCMI.
- Clad “lift-off” via the increase of gas pressure in the plenum.
- Fuel melting via the increase of temperature.

The theoretical approaches to modelling of intra- and inter-granular processes as well as their link to the effects of high burn-up structure (HBS) and high-temperature re-crystallisation, incorporated in the GRSWEL-A model, are comprehensively described in [3,4]. Here, it is worthwhile representing the final view of the relationships used for calculation of local fuel porosity in relation to fuel thermal conductivity:

$$\lambda(P_{tot}) = f(P_{tot}) \lambda(P_{tot} = 0)$$

and volumetric swelling due to the fission products by assuming its isotropy $\Delta V/V = 3\Delta L/L$.

The total value of fuel porosity is calculated as the sum of intra- and inter-granular components:

$$P_{tot} = P_G + P_F$$

The intra-granular component is calculated as [4]:

$$P_G = \frac{4\pi}{3} \sum_{s=1}^{N_b} r_i^3 B_i + P_{G.as-fabricated}$$

Here, the first term summarises the results of modelling for the size distribution of intra-granular bubbles with the radii r_i and concentrations B_i ; the second term takes responsibility for the dynamics of as-fabricated intra-granular porosity during early-life densification (or high-temperature sintering).

The equation for the sum of inter-granular porosity is as follows [3]:

$$P_F = B_{nv} \frac{4}{3} \pi r_f^3 [k_{v0} (1 - \varepsilon) + \varepsilon] + B_{vn} \frac{4}{3} \pi r_{f(vn)}^3 k_{v0} + P_{F.as-fabricated}$$

On the right-hand side of this equation, the first term corresponds to the porosity due to closed pores with the current radius of surface curvature r_f and volumetric concentration B_{nv} ; the second represents the contribution of the vented pores; the third is the time-constant as-fabricated inter-granular porosity. The time-dependent variable ε and coefficient k_{v0} account for the current relationship between the numbers of lenticular and spherical pores confined to grain boundaries [4], thereby defining their mean-effective shape in the re-crystallised fuel. The overall measure of re-crystallisation is calculated as suggested in Ref. [6]:

$$1 - \varepsilon = \prod_i (1 - \varepsilon_i)$$

where i identifies the type of fuel re-structuring, so that $i = 1$ when this is HBS; $i = 2$ for equi-axial grain growth.

The geometric factor relating the volume of a lenticular pore to a sphere is expressed as:

$$k_{v,0} = 1 - 3\cos(\theta)/2 + \cos^3(\theta)/2 = 0.186, \text{ assuming } \theta = 50^\circ$$

The final equation for irradiation-induced swelling of the fuel is as follows:

$$\frac{\Delta V}{V_0} = E_{fuel} \approx (P_F - P_{F,as-fabricated}) + B_0 n_0 v_g + E_{intra}$$

Here, the first term corresponds to swelling due to grain boundary pores; the second represents gas clusters on the boundaries of grains; the third is the intra-granular swelling.

The component of fuel swelling relating to the intra-granular processes is calculated from the expression:

$$E_{intra} = \alpha_{solid} b + v_g \left(\bar{C}_1 + \sum_1^s N_i B_i \right) + \frac{4\pi}{3} \sum_{s+1}^{N_b} r_i^3 B_i$$

Here, the first term is responsible for strains due to solid fission products ($\alpha_{solid} = 0.32$ vol.% per 1% h.a. of burn-up b); the second term accounts for the volumetric strain due to mono-atoms of fission gas in fuel matrix as well as small nucleuses of gaseous bubbles, which are assumed as solid spheres (N_i is the number of gas atoms in the bubble, $v_g = 85 \text{ \AA}^3$ is the volume occupied by one generalised atom of fission gas); the last term accounts for the size distribution of intra-granular bubbles.

Finally, the relative fission gas release is calculated via the rate of the specific absolute gas loss L_2 (atoms/cm³/s), as a ratio of release to cumulative generation:

$$f_{fr}(t) = \frac{\int_{V_{fuel}} \int_0^t L_2(r, \tau) d\tau dV}{\int_{V_{fuel}} \int_0^t G_{fg}(r, \tau) d\tau dV}$$

where $G_{fg}(r, \tau)$ is the gas generation density, and integration is carried out with respect to the total volume of the fuel stack V_{fuel} and irradiation time t .

Design parameters and results of PIE after base irradiation for integral rod 9 in R7 experiment

Of the six fuel rods re-irradiated at RIAR over the course of the R7 test [1], carried out in 1995, integral rod 9 was characterised by the highest level of fuel burn-up in the active part of the total fuel stack (60 MWd/kgU) subjected to power transient in the MIR research reactor. This is probably the prime cause of the especially pronounced gas-induced swelling effects in this particular case. That (as well as available results of PIE) is why this rod has been chosen here as a referent example for the detailed numerical investigations.

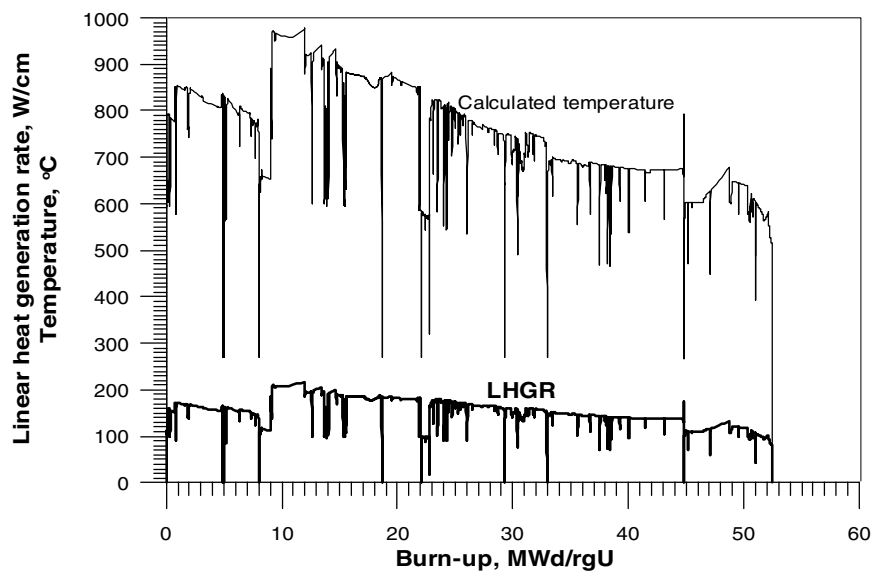
Fuel rod design and base irradiation conditions

Rod 9 was extracted from fuel assembly (FA) No. 222 after a five-year irradiation in Unit 3 of Kola NPP VVER-440 to a rod average burn-up of 52 MWd/kgU. The main characteristics of rod design and base irradiation, assumed as the input data for the numerical analysis by the START-3 code, are given in Table 1 and shown in Figure 2 [7].

Table 1. Parameters of rod design and base irradiation conditions

Parameter	Value
<i>Fuel rod</i>	
FA type	VVER-440
FA no.	222
Fuel stack length, mm	2 420
Length of plenum, mm	85
Fuel loading mass, g	1 087
Initial filling gas	0.6 MPa He
Mean gap size (diametral), μm	200
<i>Pellet</i>	
Outer diameter, mm	7.56
Inner diameter, mm	1.6
Enrichment by ^{235}U , wt. %	4.4
Fuel density, %TD	95
Grain size (mean linear intercept), μm	6.5
Open porosity (relative contribution to total porosity), %	10 (assumed)
Densification, vol. %	1.2 (assumed)
Stoichiometry (O/U)	2.005 (assumed)
<i>Cladding</i>	
Clad material	Zr+1%Nb
Outer diameter, mm	9.1
Inner diameter, mm	7.76
<i>Characteristics of base irradiation</i>	
Place of operation	Kola NPP Unit-3
Rod average burn-up, MWd/kgU	52
Maximum pellet burn-up, MWd/kgU	60
Fission gas release (in sibling rod), %	2.08

Figure 2. Maximum linear power and calculated fuel temperature in the leading rod of FA 222



As seen from Figure 2 the base irradiation was carried out under rather moderate conditions, such that the calculated fuel temperature is much less than the empiric threshold for thermal fission gas release throughout operation. Thus, according to the calculation, the most of generated fission gas was accumulated in the fuel matrix at the end of base irradiation, except for the HBS zone at the pellet rim (see Figures 12, 13 with regard to the pellet rim). As analysis shows, the HBS effects are primarily responsible for the fission gas release of 2.08%, as measured by puncture method in the sibling rod 14 of FA 222.

Regarding the mechanical state of the fuel rod after base irradiation, the important evidence arising from the PIE is the absence of any considerable gap (mechanical) between pellets and clad. This testifies to the onset of PCMI in the fuel rod before the end of operation in the power reactor.

With the exception of pellet fragmentation, no change in pellet macro-structure in comparison to that of fresh fuel was found by optical ceramography (see the pellet state before the test on Figure 8).

Fuel rod re-irradiation in the MIR research reactor

Table 2 represents the main test conditions for rod 9.

Table 2. Parameters of rod 9 re-irradiation during the R7 test in the MIR research reactor

Parameter	Value
Length of fuel active part (estimated), mm	≈750
Fuel burn-up in active part, MWd/kgU	60
Axial form factor for linear power in active part (estimate for time-average value), 1/1	≈1.25
Maximum linear heat generation rate during low-power holding, W/cm	178
Linear heat generation rate at the ramp terminal level, W/cm	430
Coolant pressure, MPa	16
Temp. of cladding outer surface in the hottest section for the low-power holding, °C	240
Temp. of cladding outer surface in the hottest section at the ramp terminal level, °C	320

Figures 3 and 4 illustrate the conditions of the test with respect to linear heat generation rate (LHGR) and fuel temperature. As seen from Figure 3, the test irradiation submits the sequence of power modes, which are as follows:

- Low power holding with a maximum local LHGR of 178 W/cm, which implies a certain rise of the local linear power in comparison to that at the end of base irradiation (about 120 W/cm according to our estimate).
- Power ramp by $\Delta W_l \approx 250$ W/cm during a relatively short period of time (less than about 20 min).
- High power “holding” with a tendency for the LHGR to gradually increase.

Figure 3. Maximum linear power (LHGR) history for rod 9 of the R7 test

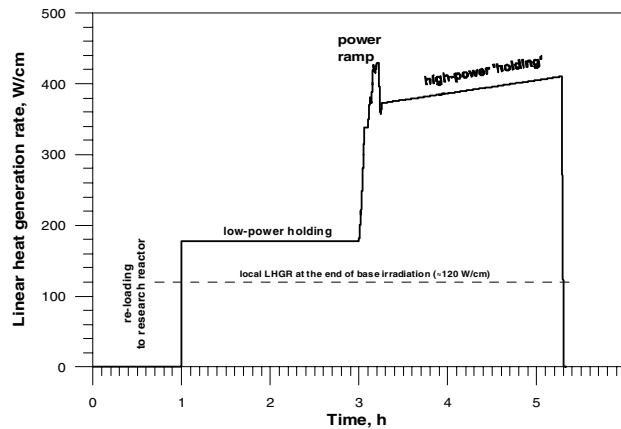
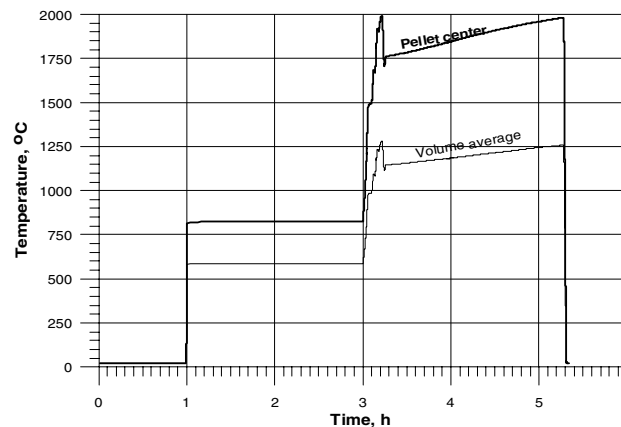


Figure 4. Calculated fuel temperature in the “hottest” section of rod 9 during the R7 test



Fuel rod behaviour at power transient: Results of modelling against experimental data

Thermo-mechanical behaviour

The main mechanical consequences of the R7 test with fuel rod 9, as calculated by the START-3 code coupled with the GRSWEL-A model, and according to the PIE, are quantified in Table 3 (see Model A in the table). As the comparison shows, the results of advanced modelling (Model A) agree reasonably with the experimental data for:

- Residual deformation of the clad as a result of the strong PCMI during the ramp mode (Figures 5-7).
- Central hole filling by the fuel (Figure 8,9) as a result of fuel creep towards the pellet centre under the conditions of elevated temperature (Figure 4) and compressive stress in the pellets.
- Rise of the pellet-clad gap size resulting from the combination of the two above-mentioned conditions.

TOUTATIS: AN APPLICATION OF THE CAST3M FINITE ELEMENT CODE FOR PCI THREE-DIMENSIONAL MODELLING

Fabrice Bentejac, Nicolas Hourdequin
DM2S/SEMT/LM2S, CEA Saclay, France

Abstract

TOUTATIS is a thermo-mechanical simulation tool based on the finite element code Cast3M. It has been developed in order to locally and accurately model the three-dimensional effects induced by PCI. Three new developments are presented. The first is related to the renovation of the computing scheme, which takes into account thermal and mechanical coupling induced by the heat exchange evolution in the pellet-cladding gap at every time step. The second is the improvement of the pellet fragmentation modelling, which cladding deformations are extremely dependent upon. The third is the implementation of a Coulomb friction model at pellet-cladding interface. Associated with the initial pellet cracking, it shows stress and inelastic strain concentration at the inter-pellet level in front of the fuel radial cracks. A sensitivity study on both the friction coefficient and the boundary conditions influences has been carried out to determine the most representative computation hypothesis and the most relevant mechanical parameters as concerns PCI/SCC cladding failure.

Introduction

During normal and incidental PWR operating conditions, reactor manoeuvrability is limited by the prevention against fuel rod cladding failure by Pellet-cladding Interaction/Stress Corrosion Cracking (PCI/SCC) for severe power transients. To reduce this penalty, PCI modelling is under development in the framework of the CEA PCI research project, in order to contribute to a better understanding of PCI mechanisms and to help in the selection of remedies.

To obtain an accurate evaluation of the cladding mechanical state, refined finite element (FE) modelling is being developed at the pellet scale of the fuel rod. Thus the simulation of the fuel rod mechanical behaviour, under nominal operating and transient conditions, has been programmed in the TOUTATIS code [1], which is based on the FE code Cast3M [2], to solve the mechanical equilibrium of the pellet-cladding system taking into account geometrical and material non-linearities.

Several developments are in progress to improve the mechanical state forecasts. Among them, three points will be hereby discussed. The first point is related to the renovation of the computing scheme. The second is the improvement of the pellet fragmentation modelling, upon which cladding deformations are extremely dependent [3,4]. The third point is the implementation of a Coulomb friction model at pellet-cladding interface [4]. The objective of this last development is to evaluate the stress and strain concentration in the cladding in front of a pellet crack, where cladding failure by a PCI/SCC mechanism is experimentally observed [5,6]. The application of these developments in the simulation of experimental power transients on pre-irradiated fuel rods is done to estimate the improvements. Comparisons between numerical and experimental results focus on the cladding residual diametral deformations.

PCI mechanical phenomena

During the first power increase to nominal conditions, the fuel pellets are fractured by the internal stresses due to the restrained thermal expansion (thermal gradient: 450°C for 4 mm in radius). A typical fragmentation pattern is shown in Figure 1. Schematically a pellet is radially fragmented into four to eight sectors and axially fragmented into three to five sections. This fragmentation leads to a pellet expansion, combined with a reduction of the internal stresses. Due to the temperature gradient, the expansion is higher in the central part than in the external part, thus the pellet gets a specific shape called “hourglassing” (Figure 2).

Figure 1. Transversal and axial macrographies of a fuel rod irradiated for two annual PWR operating cycles

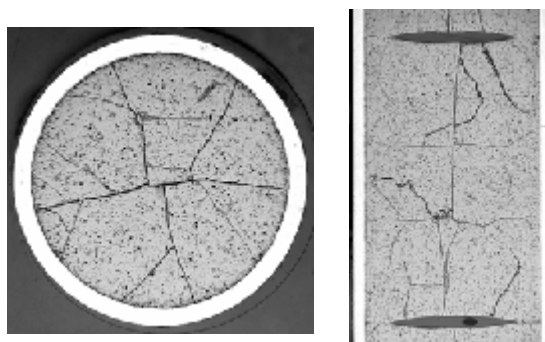
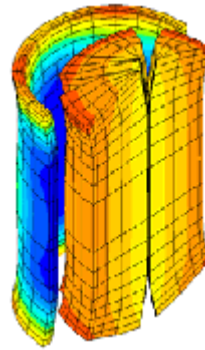
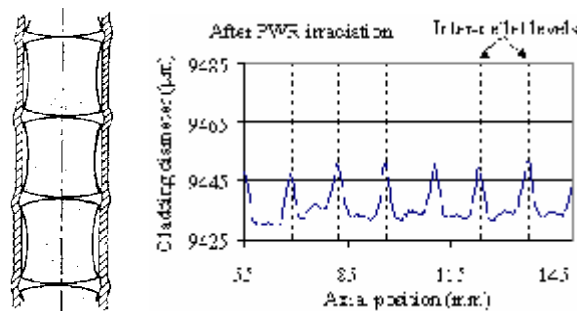


Figure 2. “Hourglassing” shape of a fragmented pellet computed with TOUTATIS 3-D



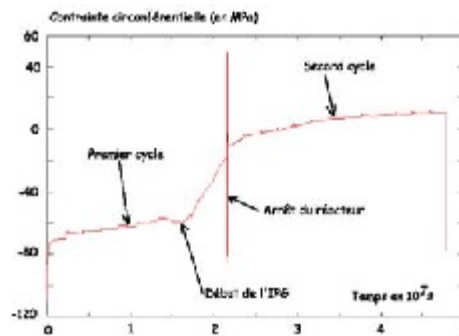
At the beginning of the irradiation, the cladding creeps in compression due to the differential pressure of the system. This, combined with the pellet swelling induced by fission products, leads to a progressive pellet-cladding gap closure. Due to the hourglass pellet shape, the first contact occurs at the inter-pellet level where the gap is the lowest. This mechanism has been correlated with the remanent “primary” ridges identified on the cladding diametral measurements after irradiation (Figure 3).

Figure 3. Primary ridges on diametral measurements for a fuel rod irradiated for two annual PWR operating cycles



While the gap closes, the cladding, initially loaded in compression, progressively gets in contact with the pellets and becomes loaded in tension. The tensile stress increases slowly up to about 20 to 30 MPa, which corresponds to an equilibrium value, according to the cladding creep rate and the pellet swelling rate. So, under nominal conditions, the cladding easily accommodates the pellet swelling kinetic by a neutron flux activated creep deformation: the cladding is loaded by low PCI (Figure 4).

Figure 4. Cladding hoop stress $\sigma_{\theta\theta}$ as a function of time computed under nominal conditions for two annual PWR operating cycles



During transients (power ramps), the thermal gradient largely and quickly increases to reach within a few minutes a value almost three times higher than the nominal value (1 200°C for 4 mm in radius). High tensile stresses, resulting in the cladding from contact with the strongly and swiftly dilated pellet, cannot be easily accommodated by visco-plasticity (Figure 5). Meanwhile, due to the high temperatures, the fuel visco-plasticity is also activated in the pellet centre and leads to a progressive filling of the dishings. The fuel creep has been identified on macrographies (Figure 6) and is correlated with the formation of “secondary” ridges at the mid-pellet plane level (Figure 7). The high tensile stresses combined with a chemically aggressive environment (corrosive fission products) may lead to a cladding failure by a PCI/SCC mechanism [5,6] (Figure 8). Consequently, PCI is taken into account in fuel rod design to avoid such a risk for power transient of Class 2 incident.

Figure 5. Cladding hoop stress $\sigma_{\theta\theta}$ as a function of time computed during a power ramp after two annual PWR operating cycles

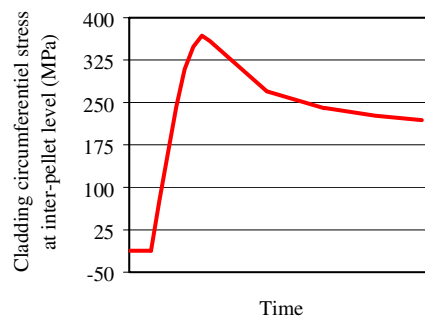


Figure 6. Axial macrography of a fuel rod irradiated for two PWR cycles and subjected to a power ramp until 45.7 kW/m maintained 7 min. at ramp terminal level (RTL)

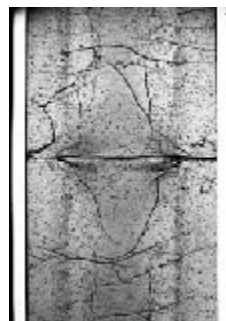


Figure 7. Diametral measurements of a fuel rod irradiated for two annual PWR operating cycles, before and after a power ramp (45.7 kW/m, 7 min. at RTL)

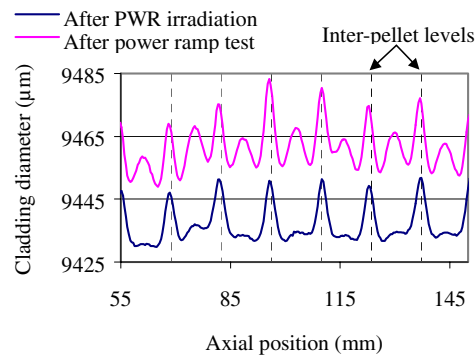
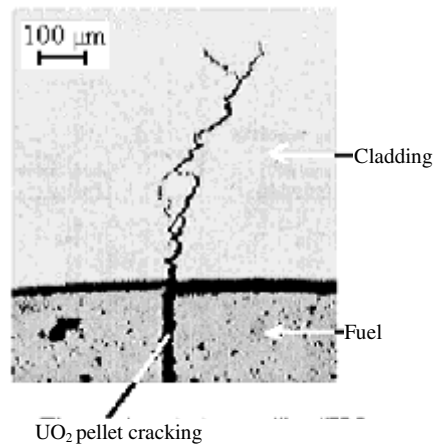


Figure 8. PCI/SCC cladding failure [5]



The TOUTATIS code

The main objective of the TOUTATIS code is to propose the modelling and computing scheme suitable for an accurate simulation of the cladding mechanical behaviour under PCI conditions, taking into account material and geometrical non-linearities such as:

- Fuel creep activated by fissions or by high temperatures in the pellet centre.
- Cladding viscoplasticity activated by the fast neutron flux or by high stresses.
- Contacts between surfaces warped by the thermal gradient (lateral surfaces or bases of a pellet fragment).

To model all these non-linearities, FE discretisation and non-linear resolution algorithms are required to solve the mechanical equilibrium of the pellets-cladding system. Thus, in TOUTATIS, the general FE code Cast3M developments are used to elaborate a computing scheme applicable for a complete simulation of the mechanical behaviour of pellet-cladding system under nominal and transient conditions (i.e. soft and strong PCI conditions), using 2-D or 3-D discretisations of a fuel rod at the pellet scale.

Since the pellet-cladding system accumulates inelastic deformations, especially with the formation of the “primary” ridges on the cladding, its initial state before a power ramp has to be taken into account for an accurate prediction of the mechanical state during the transient. In consequence, the computing scheme [3] developed in the TOUTATIS code is based on a complete simulation of the fuel rod irradiation under nominal and transient conditions.

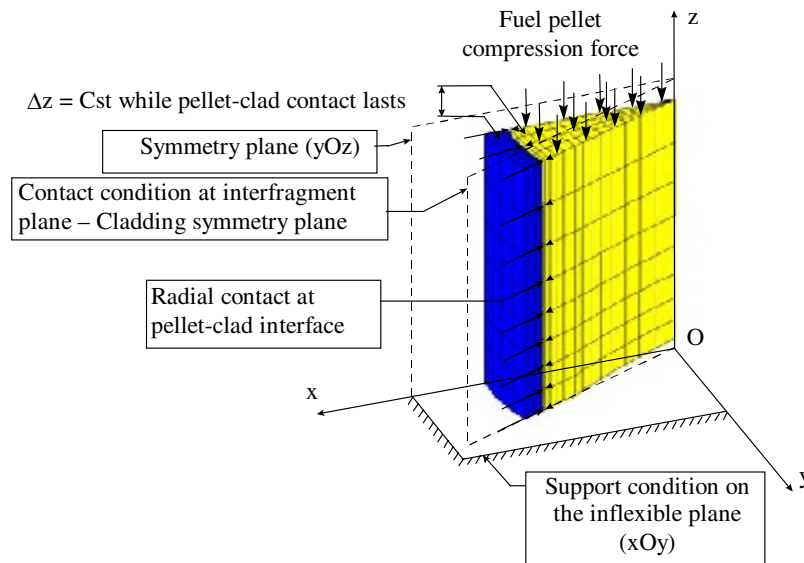
The main phenomena taken into account within the TOUTATIS code are:

- *Nominal conditions*: thermal dilatation, in-pile fuel densification and fuel swelling, cladding creep under the coolant/rod differential pressure, evolution of the fuel-cladding gap thermal conductance, PCI which involves the formation of ridges on the cladding at pellet interfaces.
- *Transient conditions*: Intensification of PCI due to the fuel temperature increase, internal fuel creep and cladding visco-plasticity under high stresses.

Since the development of the first 2-D(r,z) discretisation [7], more accurate modelling has been developed. In the usually-used version [8], the 3-D modelling presents the following characteristics:

- To take into account the fragmentation due to nominal conditions, fuel pellets are assumed to be pre-fractured into equal fragments (classically four or eight) by radial cracks extending to the fuel centre line, this hypothesis being acceptable since fuel fracture occurs at the early stage of irradiation. This idealised fracture pattern has been suggested by transversal macrographies (Figure 1).
- Using suitable boundary conditions, the discretisation is limited to one quarter of a pellet fragment and the associated cladding portion (Figure 9). Using symmetries, this volume can be considered as representative of the total rod.
- Concerning the mechanical conditions at pellet-cladding interface, the imposed relations are:
 - Radial contact without friction.
 - No axial relative movement between pellets and cladding at mid-pellet level when contact is established.

Figure 9. 3-D discretisation of $\frac{1}{4}$ fragment for a pellet supposed radially fragmented in eight equal sectors and corresponding boundary conditions



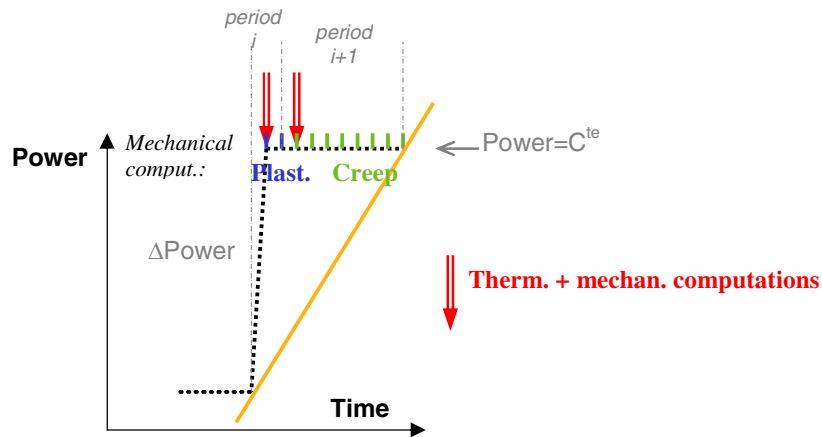
Computing scheme

The computing scheme takes into account thermal and mechanical coupling induced by the heat exchange evolution in the pellet-cladding gap.

In preceding versions, the software computed slow transients depicted as a succession of permanent states, or “periods”. The notion of “period” corresponded to a time lapse during which temperature variation can be neglected, so it may be considered as constant. As a result, temperature was computed once for the whole period (Figure 10).

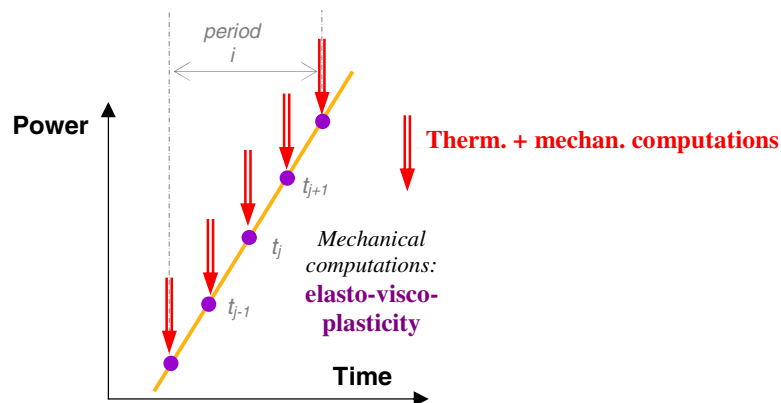
It is to be noted that, at that time, instantaneous plastic deformations and creep deformations could not be computed simultaneously. As a result, each permanent state was divided into two successive periods at the same power level (consequently, their thermal states were very close): a short plasticity period, and a period corresponding to creep (Figure 10).

Figure 10. Old scheme



In the latest version 3 of the TOUTATIS code, thermal and mechanical coupling is computed at every time step (Figure 11). With the help of the MISTRAL modulus [9], elastic and inelastic strains (elasto-visco-plasticity) accumulated in the cladding are computed simultaneously at every time step too. Furthermore, this scheme allows the computation of severe thermal transients.

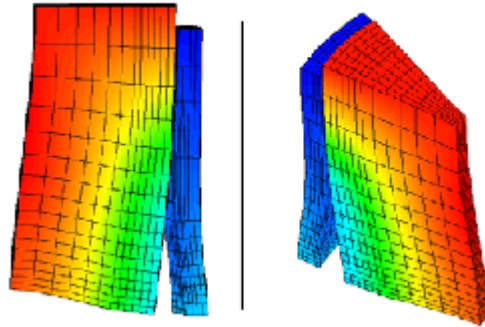
Figure 11. New scheme



Fragmentation model development

Using a radially fragmented 3-D model seems to be more accurate than a 2-D(r,z) model. However, this 3-D model is hard to compare to experimental results, mainly cladding shape after unloading, as it presents an artefact at the secondary ridges level. Those ridges are proven to be overestimated in comparison with measured values [8]. In fact, due to the inelastic strain accumulation in the pellet during the irradiation, the pellet gets a barrel shape after unloading and, consequently, the pellet remains in contact with the cladding at the mid-pellet level. This remanent PCI leads to the formation of secondary ridges in the elastic range (Figure 12).

Figure 12. Pellet global deformation mechanism



In order to verify if this artefact is correlated or not to the account of the transversal pellet fracture, new calculations have been performed with the 3-D model, considering both radial and transversal fragmentations [3]. The pellet is assumed to be fractured by eight radial cracks and three transversal cracks extending to the fuel centre line.

As for the pellet radial fracture, the axial fragmentation leads to a pellet expansion combined with a reduction of the axial internal stresses (Figure 13). Moreover the reduced length of each single fragment compared to the whole pellet induces a slight reduction of the barrel effect and the secondary ridge amplitude after unloading (Figures 14 and 15).

Figure 13. Axial stress σ_{zz} in the pellet for nominal conditions

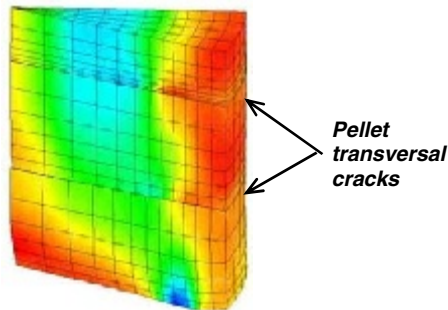


Figure 14. Cladding deformation after two annual PWR operating cycles as a function of axial position along the pellet

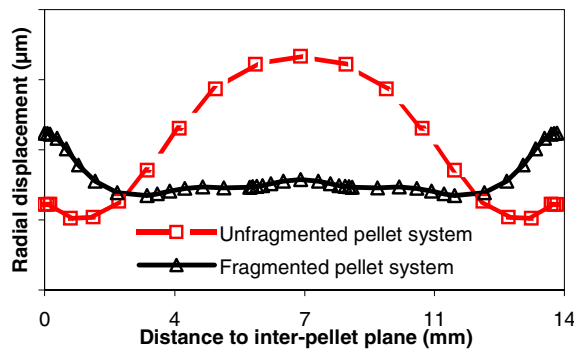
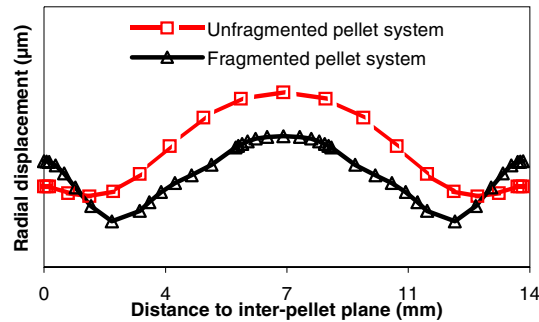


Figure 15. Cladding deformation for fuel irradiated during two annual PWR operating cycles after a power ramp as a function of axial position along the pellet



Another interesting point is the evolution of the hourglassing effect. During the base irradiation, when the pellet-cladding gap is opened, both mid-pellet level and inter-pellet level fragments present an hourglass shape since the global axial pellet deformation is not restrained. During the power ramp, however, the strong pellet-cladding contact limits the radial deformation but also the axial pellet deformation. As a result, the hourglassing effect is driven back to the pellet basis where the dishes allow an axial deformation. Finally, the deformation of the system, including axially fragmented pellets, clearly shows a significant reduction of the mid-pellet over-deformation although there is still a slight PCMI effect at this location. Thus, the computed deformations present a better agreement with experimental values.

Contact with friction at pellet-cladding interface

A Coulomb friction model at pellet-cladding interface has been implemented in the latest version of TOUTATIS 3-D. The first results confirm those obtained in 2-D(r,θ) plane geometry [4]. They show that friction, associated with the initial pellet cracking, induces stress and inelastic strain concentration on the cladding inner surface, at the inter-pellet level in front of the fuel radial cracks, so-called the “PCI critical area” (Figure 16). These results are consistent with experimental observation of PCI/SCC cladding failures initiating in this area during power ramp.

A sensitivity study on the friction coefficient influence has been carried out to determine the most relevant mechanical parameters in the PCI/SCC cladding failure.

For some of the studied mechanical parameters, their value in the PCI critical area increases with the friction coefficient. Such is the case for deviatoric hoop stress $s_{\theta\theta}$ and also inelastic equivalent deformation ε_{eq}^{vp} , those concentrations remain in this area during the ramp and the hold period at ramp terminal level (RTL). Thus, these parameters are good indicators of the loading magnification at the inner cladding surface in the PCI critical area. It is worthy of note that this is not the case for the hoop stress $\sigma_{\theta\theta}$, which relaxes during the hold period at RTL because of the materials’ visco-plasticity (Figure 17).

Two sets of boundary conditions imposed on the modelled fuel rod segment allow to close up the unknown load resulting from the friction in the remaining un-modelled part. Axial locking (or not) between pellet and cladding at mid-pellet plane after the first pellet-cladding contact, provides respectively an upper (lower) bound of that load.

Nevertheless, comparison between computation and experimental results, concerning the cladding residual diametral deformations, reveals a significant difference according to the boundary condition.

Figure 16. Cladding hoop stress computed in the middle of the ramp (300 W/cm) and cladding inelastic equivalent strain computed at the top of the ramp (424 W/cm), with friction (right) or not (left)

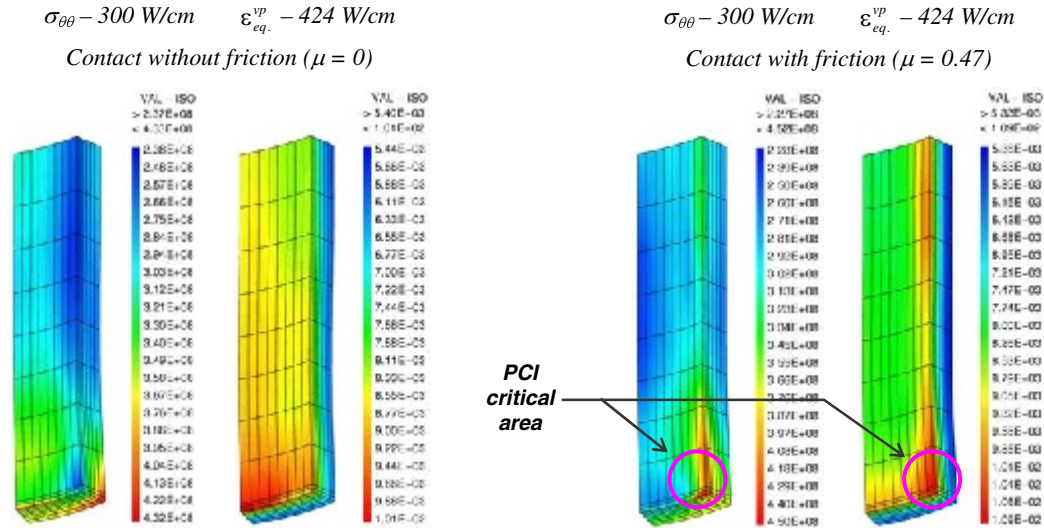
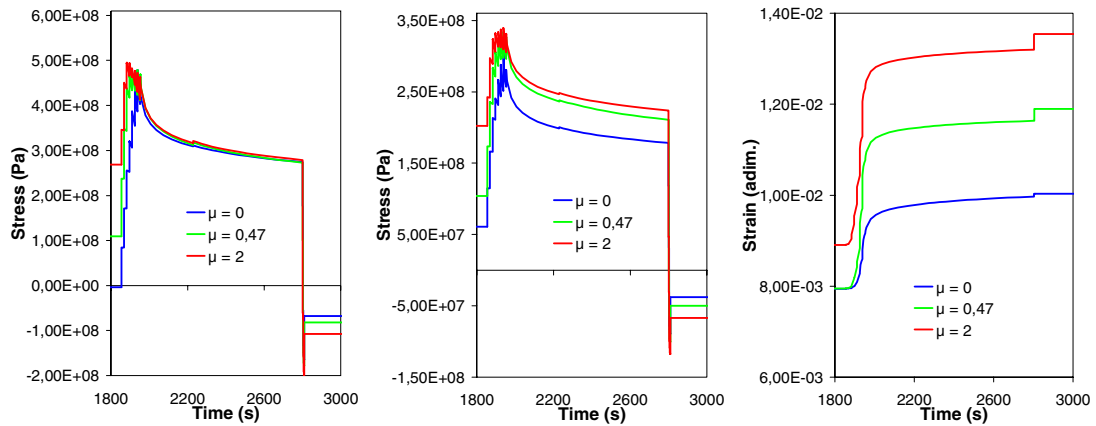


Figure 17. Hoop stress $\sigma_{\theta\theta}$ (left), deviatoric hoop stress $s_{\theta\theta}$ (middle) and inelastic equivalent strain ε_{eq}^{vp} (right) as a function of time, computed in the cladding PCI critical area during the ramp and the hold period at RTL, for different friction coefficient values

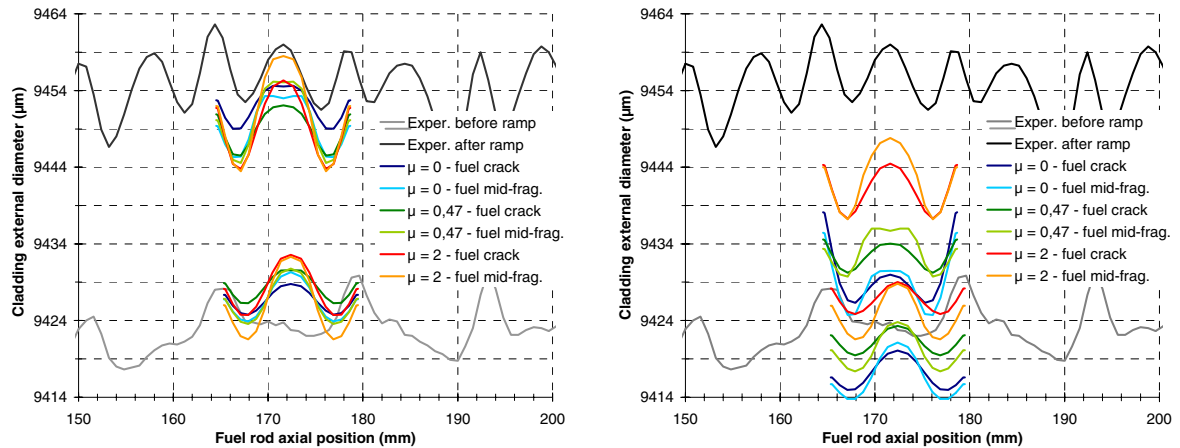


Computations with axial locking between pellets and cladding at mid-pellet plane after the first pellet-cladding contact (Figure 18, left) provide a mean position of the cladding external profile in good agreement with experimental results, especially before the ramp and slightly under-evaluated after the ramp. The evaluation of the cladding mean diameter increasing during the ramp is satisfying.

On the other hand, computations without axial locking (Figure 18, right) provide results that are far from consistent with experimental ones. The computed mean position of the cladding external profile is slightly under-evaluated before the ramp, but strongly after the ramp. Thus, the evaluation of the cladding mean diameter increase during the ramp is significantly under-evaluated.

The boundary condition of axial locking between pellets and cladding at mid-pellet plane after the first pellet-cladding contact appears to be the most representative computation hypothesis.

Figure 18. Comparison between computed and experimental cladding residual diametral deformations, before and after the ramp. Computations with axial locking (left) or not (right) between pellet and cladding at mid-pellet plane after the first pellet-cladding contact.



These computations have been performed with the classical radially fragmented pellet 3-D model. It should be noted that, in this case, there is an artefact at secondary ridges which is overestimated, as has been detailed before.

Assuming that axial locking is the most representative computation hypothesis, the precedent comparative study between computation and experimental results shows the negligible influence of friction coefficient on the mean position of the cladding external profile. Even if a slight influence of friction coefficient is perceptible on the primary ridge height, which increases with the friction coefficient value, the ridge height variation obtained is included in the interval of experimental dispersion. Consequently it is impossible to deduce from this study a plausible value for the friction coefficient.

Conclusion and prospects

The refined 3-D FE modelling developed within the TOUTATIS code allows a good description of the thermo-mechanical aspects of the PCI problem in a fuel rod irradiated for two annual PWR operating cycles and subjected to a power ramp. Computations show that taking into account the pellet fragmentation is important for an accurate forecast of the pellet-cladding mechanical response at both global and local levels. In addition, taking into account contact with friction at the pellet-cladding interface is necessary for an accurate evaluation of the local mechanical state in the cladding in front of a pellet crack at the precise location where stress corrosion cracking may appear. However, the most realistic value of the friction coefficient is not yet determined. In order to improve the computation representativeness, the work is in progress in the following directions:

- Programming of fuel constitutive laws developed at CEA/DEC to take into account micro-cracks.
- Use of quadratic FE to improve stress and strain variations computed in the cladding PCI critical area.
- Programming of cladding SCC model developed at CEA/DMN.

REFERENCES

- [1] Brochard, J, F. Bentejac, N. Hourdequin, “Non-linear Finite Element Studies of the Pellet Cladding Mechanical Interface in PWR Fuel”, *Transactions of the 14th SMIRT*, Lyon, France (1997).
- [2] Verpeaux, P., T. Charras, A. Millard, “CASTEM 2000: Une Approche Moderne du Calcul des Structures”, in *Calcul des Structures et Intelligence Artificielle*, Éditions Pluralis (1988).
- [3] Bentejac, F., S. Bourreau, J. Brochard, G. Delette, N. Hourdequin, S. Lansart, “Fuel Rod Modelling During Transients: The TOUTATIS Code”, *TCM AIEA*, Windermere, UK (2000).
- [4] Brochard, J, F. Bentejac, N. Hourdequin, S. Seror, C. Verdeau, O. Fandeur, S. Lansart, P. Verpeaux, “Modelling of the Pellet Cladding Interaction in PWR Fuel”, *Transactions of the 16th SMIRT*, Washington, DC, USA (2001).
- [5] Davies, J.H., H.S. Rosenbaum, J.S. Armijo, R.A. Proebstle, T.C. Rowland, J.R. Thompson, E.L. Esch, G. Romeo, D.R. Rutkin, “Irradiation Tests to Characterize the PCI Failure Mechanism”, *Proceedings of the ANS Topical Meeting on Water Reactor Fuel Performance*, pp. 230-242 (1977).
- [6] Fandeur, O., “Étude Expérimentale et Modélisation Mécanique de la Corrosion sous Contrainte des Gaines en Zircaloy-4”, Ph.D., École Centrale Paris, France (2001).
- [7] Bourreau, S., S. Lansart, P. Couffin, C. Verdeau, G.M. Decroix, M.C. Grandjean, H. Hugot, F. Mermaz, E. Vanschel, “Influence of Hold Time on the Fuel Rod Behaviour During a Power Ramp”, *Fuel Chemistry and Pellet-clad Interaction Related to High Burn-up Fuel*, IAEA TECDOC-1179, pp. 63-73, Niköping, Sweden (1998).
- [8] Bourreau, S., J. Brochard, F. Bentejac, P. Couffin, C. Verdeau, S. Lansart, N. Cayet, M.C. Grandjean, F. Mermaz, P. Blanpain, “Ramp Testing of PWR Fuel and Multi-dimensional Finite Element Modelling of PCMI”, *Proceedings of the 2000 International Topic Meeting on Light Water Reactor Fuel Performance*, Park City, Utah (2000).
- [9] Limon, R., *Module MISTRAL (Version 2.0): Description du Modèle Général de Déformation de Matériau de Gainage Anisotrope*, Rapport interne CEA (2002).

METHODOLOGY FOR MULTI-DIMENSIONAL SIMULATION OF POWER RAMP TESTS

Christine Struzik, David Plancq, Bruno Michel, Philippe Garcia, Chrystelle Nonon
Commissariat à l'Énergie Atomique, Direction de l'Énergie Nucléaire
Département d'Étude du Combustible, Services d'Étude et de Simulation du Combustible
F-13108 Saint Paul-lez-Durance, France

Abstract

Within the framework of pellet-cladding interaction studies, CEA has developed 1.5-D modelling (METEOR) and 3-D modelling (TOUTATIS). Both are used to understand PWR fuel rod behaviour in case of power ramp conditions.

The 1.5-D description allows for modelling of the whole phenomena involved in case of ramp test (thermo-mechanical behaviour or fission gas swelling particularly) and the 3-D description enables a local description of the stress and strain fields on the scale of the pellet and the corresponding cladding piece. The main hypotheses and some elements of experimental validation of them are evoked here. The methodology employed to simulate a power transient experiment with the available tools, is also presented.

TOUTATIS calculations can be chained to METEOR ones. This method allows a good description of the medium pellet plan during power ramp tests in every case and a good evaluation of the geometrical changes experimentally observed.

Finally, the new software presently developed (PLEIADES) for various applications concerning fuel element modelling will be presented. The PLEIADES PWR application integrates advances in French R&D programmes dedicated to pellet-cladding mechanical interaction, high-performance fuels and advanced materials and provides a multi-dimensional unified tool for research and industrial fuel rod performance modelling.

Introduction

Within the framework of studies concerning fuel rod behaviour under Class 2 transients, it is well known that failure, if it occurs, is induced by stress corrosion cracking. Thus, in order to predict the cladding failure and better the time to failure under transient conditions, modelling must first calculate as accurately as possible the mechanical loading of the cladding.

To that end, two types of modelling are developed at CEA, supported by its industrial partners EDF and FRAMATOME ANP. One-dimensional modelling with the METEOR code [1], with which it is possible to profit from the low computation time to develop high-level physical chemical modelling. Three-dimensional modelling with TOUTATIS [2], in which there is no fission gas behaviour model, but which can describe the local geometrical effect on the mechanical loading of the cladding.

Under PWR conditions two types of cladding mechanical interaction can be distinguished: soft, which occurs during normal conditions and slightly affects the axial expansion and the external diameter of the rod and, strong, which occurs during Class 2 transients and possibly leads to cladding failure.

Experimental support

To illustrate the purpose of this paper, some experiments will be discussed in the text that follows. They all have been performed on UO_2 fuel enriched at 4.5% ^{235}U with stress-relieved Zy-4 cladding. The pellets all have double dishes. The rods were initially irradiated in an EDF-PWR reactor and then re-fabricated as shorter rods for testing in the CEA experimental reactors OSIRIS (Saclay) or SILOE (Grenoble). More specifically, the following cases will be considered:

- *Case 1:* Base irradiation in PWR during five cycles up to 60 GWd/tM, average power is about 17.5 kW/m, 21.5 kW/m, 18.5 kW/m, 15 kW/m, 14.5 kW/m during cycles 1, 2, 3, 4 and 5, respectively.
- *Case 2:* Re-fabricated rod initially irradiated in PWR during two cycles up to 28 GWd/tM, whole rod average power is about 19 kW/m and 20 kW/m during cycles 1 and 2, respectively. Ramp test was performed in OSIRIS up to 42 kW/m with 10 kW/m/min ramp rate, holding time at high level was around 15 min.
- *Case 3:* Re-fabricated rod initially irradiated in PWR during four cycles up to 50 GWd/tM, the average power is about 22 kW/m, 20 kW/m, 17.5 kW/m, 14.5 kW/m during cycles 1, 2, 3 and 4 respectively. Ramp test was performed in SILOE in the GRIFFON loop equipped with the DECOR device. DECOR [3] allows the cladding diameter change measurement in power. Power was increased from 25 kW/m to 40 kW/m with 5 kW/m/min ramp rate, the holding time at high level was around six days.
- *Case 4:* Re-fabricated rod initially irradiated in PWR during two cycles up to 28 GWd/tM, whole rod average power is about 18 kW/m and 23.5 kW/m during cycles 1 and 2, respectively. Ramp test was performed in OSIRIS up to 46 kW/m with 10 kW/m/min ramp rate, holding time at high level was around 7 min.

One-dimensional modelling

The mechanical modelling is described in detail in Ref. [4]. Only the main points are recalled here.

Hypotheses

In this case, the whole rod is described. It is discretised in axial slices and radial meshes, and each axial slice can represent more than one pellet.

For each axial slice, it is considered that the problem is axisymmetric, with generalised plane deformation hypothesis without shear or bending.

The external conditions considered are the spring force, the coolant pressure and the internal gas pressure.

It is also considered that in case of contact, no axial motion is authorised between fuel and cladding. It is the same if the gap is closed on a slice higher than those considered.

The total strain is considered to be the sum of the elementary strains.

Strains considered in 1-D analysis

For the fuel pellet, depending on local quantities such as temperature (T), fission density (F), burn-up (τ) and hydrostatic stress (σ), the following strains are considered:

- The strains which are calculated before the mechanical loop:
 - Thermal expansion (T), densification (T,F, τ), solid swelling (τ) due to solid fission products, fuel relocation which simulates the 3-D effects relative to the hourglassing of the pellet due to the thermal temperature distribution, fuel repositioning (σ).
- The strains which are calculated inside the mechanical loop:
 - Cracking strains: Fuel is considered as cracked in one direction if the corresponding calculated stress is greater than 150 MPa. Stress in that direction is then considered to be equal to the opposite of internal pressure. Four states are considered for each mesh, which could be not cracked, cracked in tangential direction, cracked in axial direction, or cracked in axial and tangential direction.
 - Creep strains: Creep law considers irradiation creep, which intervenes at low temperature (below 1 000°C), and thermal creep, which is dominant during power ramp test.
- The strains which are calculated between mechanical and thermal analysis (the convergence of the calculation is then obtained by iteration):
 - Gas swelling: this deformation is strongly correlated to the thermal regime of fuel. Before transient, this regime determines the gaseous population distribution (inter- or intra-granular) and during the power transient itself temperature strongly affects the gas evolution. The hydrostatic stress distribution in the pellet and the evolution [5] of stresses is also of major importance.

For the cladding, the following strains are considered:

- The strains which are calculated before the mechanical loop:
 - Thermal expansion, axial growth due to the impact of irradiation damage on the hexagonal structure of the zirconium.
- The strains which are calculated inside the mechanical loop:
 - Creep and instantaneous plasticity. These two strains can be calculated with the Von Mises criterion or with the Hill criterion, in order to take into account the possible anisotropic behaviour of zircaloy all the more if the alloy is re-crystallised.

Main phenomena described

Normal conditions

Under standard conditions, during the first cycle, fuel and cladding are not in contact and the mechanical evolution of each material is independent from the other.

When the gap between fuel and cladding is closed, fuel is repositioned due to the external pressure influence and the cladding radius continues to be reduced. After fuel repositioning, solid fuel swelling induces an increase in the cladding radius. The axial strains of the two materials increase at the same rate.

For experimental case 1, Figure 1 represents the evolution of fuel and cladding radii versus irradiation time, associated with the contact pressure evolution between fuel and cladding. Figure 2 presents the evolution of the axial expansion.

Figure 1. Radius evolution under steady-state conditions

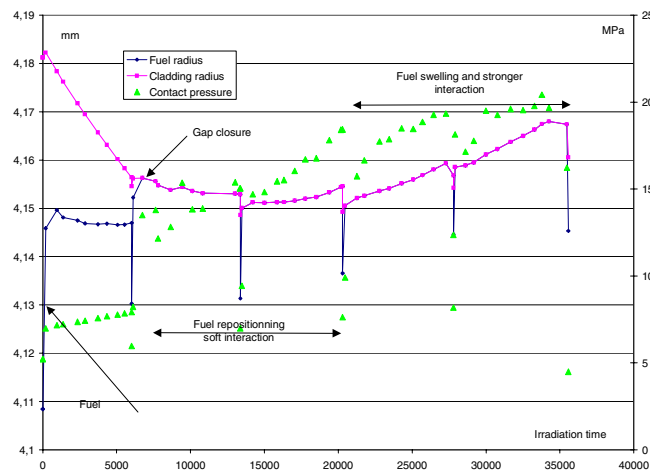
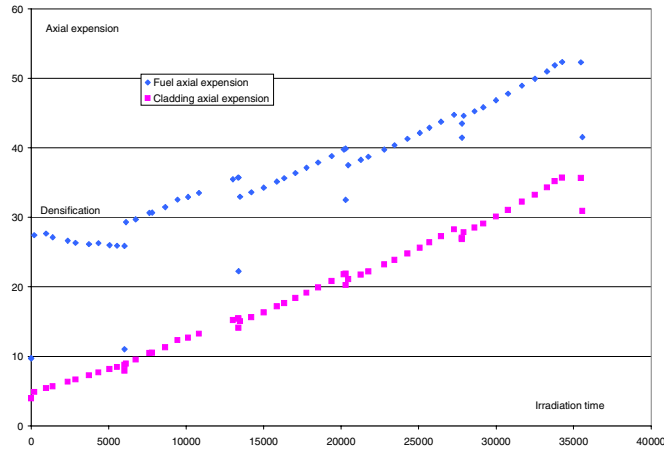


Figure 2. Axial expansion under steady-state conditions



Transient conditions

Under transient conditions, the thermal loading associated with gaseous swelling leads to strong PCI conditions and important stresses are developing in the cladding.

At the top of the power ramp, the central part of the fuel is in a highly compression state. The compressive stresses will decrease during the high power level due to fuel and cladding visco-plastic properties on the one hand and, for high burn-up particularly, to the onset of gas release, which induces a decrease in the gaseous swelling, on the other hand. For experimental case 2, the following figures present the temperature and stresses radial distribution on the pellet at the top of the power ramp (Figure 3) and few minutes later (Figure 4). On the cladding, stresses reach their maximum value during the first moments of the high-level power.

Figure 3. Stresses distribution at the top of the ramp

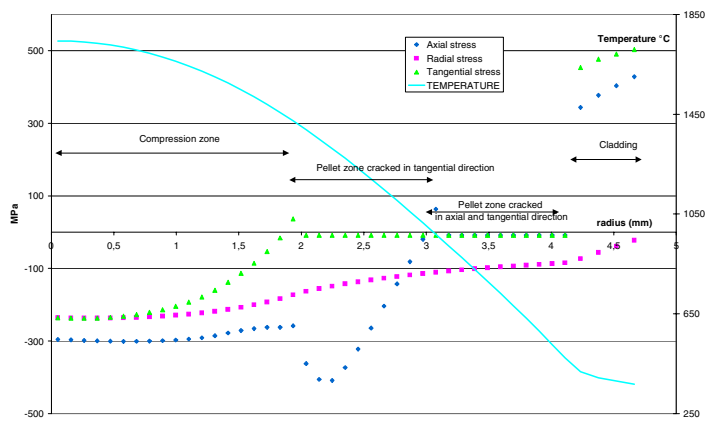
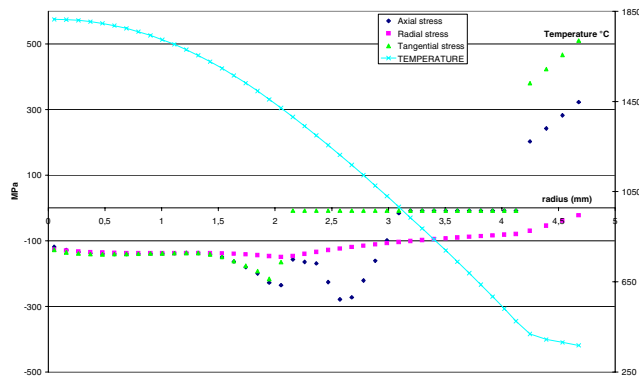


Figure 4. Stresses distribution 15 minutes later

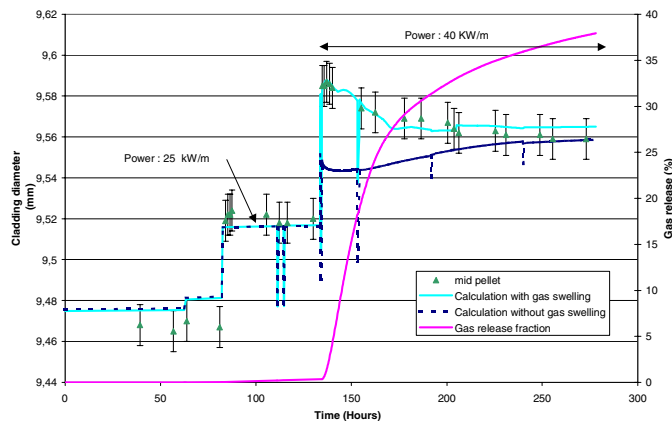


Gaseous swelling

The fuel gaseous swelling strains take an important part in the total loading of the cladding. It is possible to quantify them with the help of experimental measurements, such as cladding external diameter changes, before and after ramp, which are measured in hot cells, or in pile measurements of cladding diameter evolution with a special device like DÉCOR [6].

The following figures present the results relative to the two methods for experimental cases 3 and 4. In Figure 5, the cladding radius evolution, measured during experimental irradiation case 3, is plotted with the estimated error bars versus calculations with fission gas swelling and without.

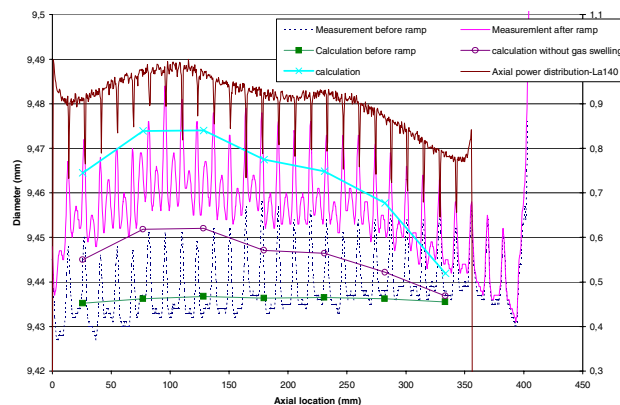
Figure 5. Cladding diameter measurement



In Figure 6 (case 5), the gamma scanning measurement of the axial distribution of the short-lived fission product lanthanum 140 takes the form of the axial power distribution to which diametral strains are strongly correlated.

The calculations performed without fission gas swelling underestimate the diameter measurement in the two cases, especially at the beginning of the ramp in Figure 5. It is clear that fuel gaseous swelling has a great influence on cladding strains and thus on cladding loading even for short holding time.

Figure 6. Cladding diameter measurement before and after ramp test (case 4)



Discussion

Let us return to what happens in the pellet during a strong power increase. Pellet hourglassing is enhanced due to the increase of thermal loading. Fuel is swelling and creeping and the geometry is modified as follows:

- Filling of the dish volume.
- Simultaneously, second ridges appear or are enhanced if they already existed before ramp.

In power ramp test, the 1-D description is then quite representative of the behaviour of the mid-pellet, due in particular to the fact that the dishes may be considered as sufficiently far from the mid-pellet plane such that their filling does not influence fuel motion at that location. It is then possible with a mono-dimensional tool to analyse the ramp database with phenomenological criteria, which are able to determine whether or not cladding failure is likely to occur, under certain conditions. These criteria are generally based on the calculated stress at the inner surface of the cladding or on the evaluation of the visco-plastic power or energy dissipated in the cladding during the ramp.

But the mono-dimensional tool is structurally unable to describe the local geometrical changes and their influence on the cladding loading. Since it has been observed that cladding failures are generally located at the inter-pellet level, the 1-D description is not sufficient to mechanistically predict the cladding loading and of course the occurrence of a failure and the moment of failure, without having previously ramp-tested many rods of the same design.

Then CEA has developed a three-dimensional calculation tool in order to be able to calculate these local effects and thus to improve the predictive capability of numerical simulation.

3-D modelling

TOUTATIS is a 3-D application based on the Cast3M finite element code. The aim of the modelling is to represent as accurately as possible the thermo-mechanical behaviour of a pre-fractured pellet. The simulation results presented here have been obtained with the validated version.

Hypotheses

The following hypotheses are considered:

- Pellet is considered to be fractured in the tangential direction into eight equal parts.
- One-fourth ($\frac{1}{4}$) of the pellet fragment is modelled: one tangential plane is a symmetry plane, the other is a face of the fragment and unilateral contact is assumed at fragment/fragment interface.
- Pellet mid-plane is considered as a symmetry plane; the axial displacements are the same for all points separately in fuel and cladding at this plane and are coupled when the gap between cladding and fuel is closed wherever on the pellet.
- In case of contact between fuel and cladding, sliding is perfect.
- No additional fuel cracking is modelled during the irradiation and the stiffness of the external part of the pellet is limited by the modelling of fuel plasticity in tension.

All the fuel strains described in the previous paragraphs are taken into account in the 3-D description, except gas swelling. The visco-plastic cladding behaviour is considered.

Validation of the hypotheses

The first element for validation consists in the reproduction of the observed strains after base irradiation as well as after power ramp test. That is to say:

- The cladding diametral global strain.
- The height of the primary and the secondary ridges.
- The filling of the dishes.

In order to take into account the fission gas swelling, the 1-D METEOR calculation and the 3-D TOUTATIS calculation are chained:

- The fuel swelling is calculated by the METEOR 1-D code.
- The strain at each time step is injected as a fixed strain in the TOUTATIS calculation.

Figures 7 and 8 present, for experimental cases 2 and 4, the filling of the dishing calculated versus metallographies performed after test. The agreement between observation and calculation is fairly good. At the higher power, it appears that gaseous swelling is needed to properly reproduce the observed dish filling.

Figure 9 presents the calculated diameter profile versus measurement for experimental case 2. The overall diameter change and also primary and secondary ridges evolution are also quite fairly estimated.

Figure 7. Ramp test 424 W/cm 14 min, experimental case 2

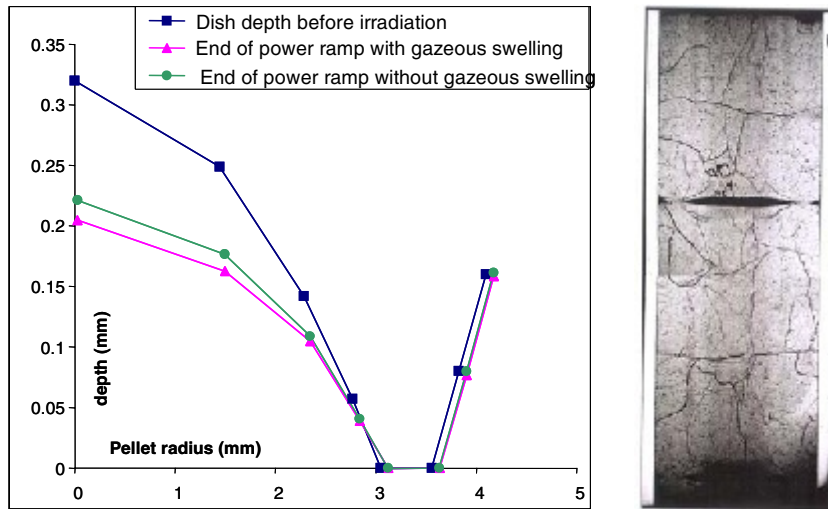


Figure 8. Ramp test 460 W/cm 7 min, experimental Case 3

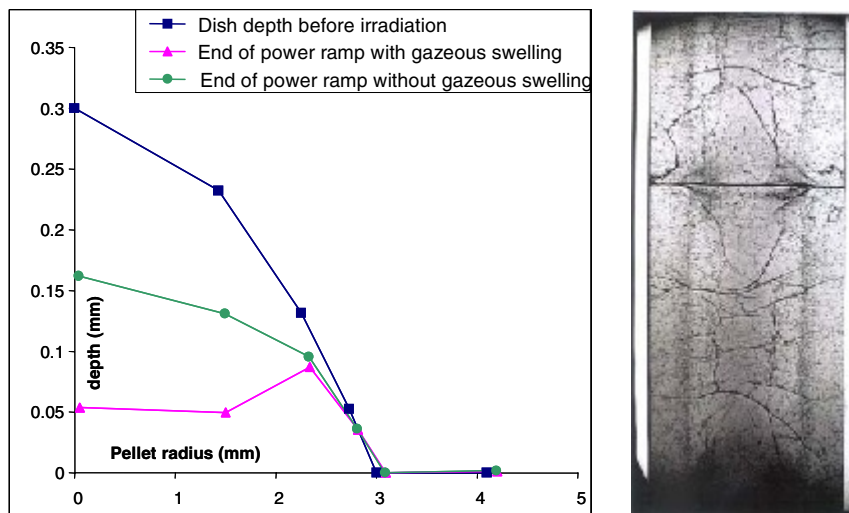
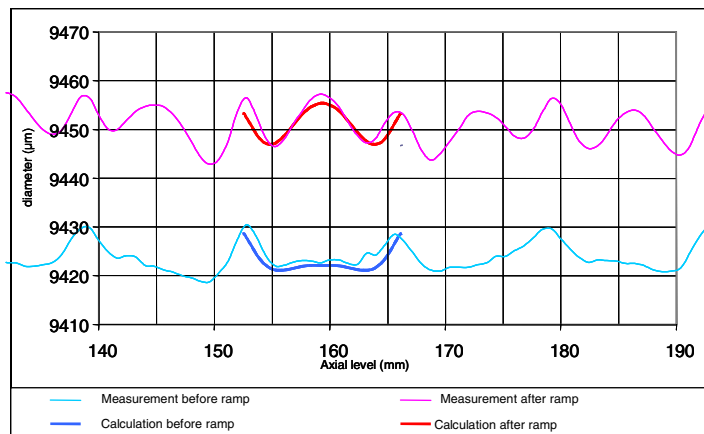


Figure 9. Diameter measurement before and after a ramp test, experimental case 2



Conclusion and prospects

Modelling

The mono-dimensional code allows to determine all the quantities relative to the whole rod (fission gas release, internal pressure, general axial and diametral changes, micro-structural evolution such as high burn-up structure). Its very short computation time allows the introduction of sophisticated physical models such as MARGARET for fission gas behaviour [7] or MOGADOR for densification [8]. However, it is unable to correctly describe the local effects such as strains and stresses concentration. It is then used to give the cladding temperature and the gaseous swelling rate at each time step as input data to the three-dimensional procedure.

Examples have been given of the good agreement between the measured dimensional changes of fuel and cladding and the ones calculated with the 3-D TOUTATIS code, chained to METEOR.

However, some hypotheses of the three-dimensional analysis remain questionable. Work is still in progress to improve the evaluation of the local mechanical loading of the cladding during transient, especially at the end of power increase and at the very beginning of the holding time at high power level:

- A friction model between pellet and clad has been developed in order to improve the analysis [9] and replace the hypothesis of sliding in case of contact between cladding and fuel. It is presently being validated for different experimental cases.
- Modelling of the cracking evolution during power increase and subsequent high power level also seems a promising means of improving stress estimation; new models, of the so-called “cohesive zones” type, are being studied in order to improve the prediction [10].
- On the other hand, gaseous swelling is strongly dependent on stress and it could be necessary to use precise values near the dishing singularity for a good representation of rod evolution at very high power or high burn-up.

Perspective: A unified multi-dimensional software called PLEIADES

METEOR and TOUTATIS have been developed separately using two different software structures, which led to some difficulties in the coherence of the modelling. It is indeed difficult to take benefit in one code of a development performed in the other one.

Moreover, special attention must be paid to the possible little differences in laws and models available in the two codes, which can affect the whole methodology validation.

It has therefore been decided to develop the PLEIADES software, based on innovative oriented object architecture, providing an easy integration and coupling of any numerical component.

The PLEIADES software will integrate within the same environment the 1-D METEOR and 3-D TOUTATIS modelling, capitalising in a modern structure the knowledge concerning PCMI standard fuel modelling as well as high-performance or advanced concept fuel modelling. The exchange between the two analyses will be much simpler.

Further, EDF decided to join the PLEIADES project in integrating its industrial code CYRANO3, enabling in a near future the direct use in its industrial tool of any interesting R&D progress.

The PLEIADES software is also being developed in order to be a part of a large nuclear reactor calculation chain, inducing neutron physic (DESCARTES platform), thermo-hydraulic (NEPTUNE platform) and fuel behaviour (PLEIADES platform).

REFERENCES

- [1] Struzik C., M. Moyne, J-P. Piron, "High Burn-up Modelling of UO₂ and MOX Fuel with METEOR/TRANSURANUS Version 1.5", *Proceedings ANS Conference*, Portland, Oregon, 126-132.
- [2] Brochard, Bentejac, Hourdequin, "Non-linear Finite Element Studies of the Pellet-cladding Mechanical Interaction in a PWR Fuel", *SMIRT 14*, France, 17-22 August 1997.
- [3] L. Caillot, C. Lemaignan, C. Joseph, "In Situ Measurements of Cladding Strains During Power Transient Using DECOR Device", *Proceedings ANS International Topical Meeting on LWR Fuel Performance*, West Palm Beach, Florida, 188-195.
- [4] Garcia, Ph., C. Struzik, M. Agard, V. Louche, "Mono-dimensional Mechanical Modelling of Fuel Rods Under Normal and Off-normal Operating Conditions", *Nuclear Engineering and Design*, 216, 183-201 (2002).
- [5] Garcia, Ph., C. Struzik, M. Agard-Moyne, "The Effect of Fission Gas Swelling on Cladding Strains During Power Ramp Tests", *Proceedings IAEA Conf. on Fuel Chemistry and Pellet Cladding Interaction Related to High Burn-up Fuel*, Nyköping, Sweden, IAEA TECDOC 1179 (1998).
- [6] Caillot, L., C. Lemaignan, C. Joseph, "In Situ Measurements of Cladding Strains During Power Transient Using DECOR Device", *Proceedings ANS International Topical Meeting on LWR Fuel Performance*, West Palm Beach, Florida, 188-195.
- [7] Noirot, L., Ph. Garcia, C. Struzik, "A Mechanistic Fission Gas Behaviour Model for UO₂ and MOX Fuels", *AEN NEA International Seminar on Fission Gas Behaviour in Water Reactor Fuel*, Cadarache, France, September 2000.
- [8] Boulore, A., "Étude et Modélisation de la Densification en Pile des Oxydes Nucléaires UO₂ et MOX", PhD, TD 249, École Nationale Supérieure des Mines de Sainte-Etienne, Institut National Polytechnique de Grenoble.
- [9] F. Bentejac, N. Hourdequin, "TOUTATIS: An Application of the Cast3M Finite Element Code for PCI Three-dimensional Modelling", these proceedings.
- [10] Helfer, T., Ph. Garcia, J-M. Ricaud, D. Plancq, C. Struzik, F. Sideoroff, L. Bernard, "Modelling the Effect of Oxide Fuel Fracturing on the Mechanical Behaviour of Fuel Rods", these proceedings.

MODELLING OF PELLETT-CLAD INTERACTION DURING POWER RAMPS

G. Zhou,¹ J.E. Lindbäck,¹ H.C. Schutte,² L.O. Jernkvist,³ A.R. Massih^{3,4}

¹Westinghouse Electric Sweden AB, SE-72163 Västerås, Sweden

²Westinghouse Electric Company, 5801 Bluff Road, Columbia, SC 29209, USA

³Quantum Technologies AB, Uppsala Science Park, SE-75183 Uppsala, Sweden

⁴Malmö University, SE-20506 Malmö, Sweden

Abstract

A computational method to describe the pellet-clad interaction phenomenon is presented. The method accounts for the mechanical contact between fragmented pellets and the zircaloy clad, as well as for chemical reaction of fission products with zircaloy during power ramps. Possible pellet-clad contact states, soft, hard and friction, are taken into account in the computational algorithm. The clad is treated as an elastic-plastic-viscoplastic material with irradiation hardening. Iodine-induced stress corrosion cracking is described by using a fracture mechanics-based model for crack propagation. This integrated approach is used to evaluate two power ramp experiments made on boiling water reactor fuel rods in test reactors. The influence of the pellet-clad coefficient of friction on clad deformation is evaluated and discussed. Also, clad deformations, pellet-clad gap size and fission product gas release for one of the ramped rods are calculated and compared with measured data.

Introduction

Pellet-clad interaction (PCI) is one of the major issues in fuel rod design and reactor core operation in light water reactors (LWRs). PCI-induced clad tube failure is caused by a combination of stresses in the zircaloy clad due to the pellet-clad contact pressure and chemical reaction of corrosive fission products, such as iodine released during operation, with zircaloy under a power ramp. If the induced stresses in the clad are sufficiently large and the concentration of the fission product is amply high, clad failure may occur. PCI has been a topic of numerous experimental and computational studies with a great amount of accumulated field experience. This has led to PCI-resistant designs and operation guidelines, which have dramatically reduced the propensity for such failures in recent years. Overviews, from industrial perspective, on PCI testing and computations relating to LWR fuels can be found in [1,2]. Cox has reviewed the PCI failure mechanism in [3]. Some recent analyses on both structural and fracture aspects of PCI are given in [4,5].

In this paper, we present a computational method to describe PCI. The pellet-clad contact model used accounts for friction and soft/hard contact due to fragmented (relocated) fuel pellets. The effect of the iodine-induced stress corrosion cracking is described by using a fracture mechanics-based model for crack propagation in line with ref. [6]. We evaluate two power ramp experiments made on boiling water reactor (BWR) fuel rods in test reactors; a power ramp test made on a fresh fuel pin in the Halden reactor some years ago; and a recent test made on a modern Westinghouse fuel pin, irradiated in a Swedish BWR and then ramped in the Studsvik R2 reactor.

The plan of this paper is as follows: First, we outline the principal PCI models used in our analysis. Next, the ramp tests under consideration are briefly described, followed by the results of our computations on these tests. Finally, we discuss the results of our computations in light of the experimental data.

The models

Mechanics

The pellet cladding mechanical interaction (PCMI) model used includes the effect of friction and axial mechanical interaction and associated rod elongation. The UO_2 fuel pellet is considered as rigid, but can deform by thermal expansion, densification and fission product swelling. The pellet radial (normal) displacement u_n^p is expressed as: $u_n^p = u_T + u_D + u_S$ where u_T , u_D , u_S , are the radial pellet displacement due to thermal expansion, fuel densification and fuel swelling, respectively. Pellet fragments can also relocate during power rise. Pellet radial displacement due to relocation u_R is assumed to be a function of the radial contact pressure P_n defined as:

$$u_R(P_n) = \begin{cases} G_n^m (1 - P_n/P_n^m) & \text{if } 0 \leq P_n \leq P_n^m \\ 0 & \text{if } P_n^m < P_n \end{cases} \quad (1)$$

where G_n^m is the maximum pellet relocation, i.e. under zero contact pressure condition, and P_n^m is the minimum contact pressure to fully remove the relocation, $u_R = 0$ [7]. Pellet relocation in the axial direction is not considered.

A finite element (FE) method is used to calculate stresses and strains in the clad. The FE model assumes that the clad tube is an axisymmetric shell. The clad material is a zirconium alloy and it deforms by thermal expansion, elastic-plastic deformation and creep (viscoplastic deformation). The following assumptions are made in the mechanical model for the clad: (i) The clad tube is divided

axially into a number of segments. (ii) Within each segment, stresses and strains are spatially constant. (iii) Within each segment, the axial displacement $v(r,z)$ is independent of radius r . (iv) Within each segment, the radial displacement $u(r,z)$ is independent of z .

The constitutive relation for Zircaloy clad that include thermoelasticity, plasticity, and creep is written as: $\sigma = D (\varepsilon_m - d\varepsilon_p)$, where $\varepsilon_m = \varepsilon - \varepsilon_p + d\varepsilon_p - \varepsilon_c - \varepsilon_T = \varepsilon_e + d\varepsilon_p$ is the modified elastic strain tensor and σ is the stress tensor. Here, ε is the total strain tensor, ε_p the total accumulated plastic strain, $d\varepsilon_p$ the increment of plastic strain, ε_c include other strains (thermal, accumulated creep, irradiation growth), ε_T , the thermoelastic strain, ε_e the elastic strain and D is the elasticity matrix. The yield stress σ_y of zircaloy cladding is a function of strain, temperature and fast neutron fluence (≥ 1 MeV). If yielding occurs, the plastic strain increment $d\varepsilon_p$ is calculated through the Levy-Mises flow rule of associated plasticity. Isotropic hardening is assumed. For material properties of UO₂ and zircaloy, we have employed the correlations given in [8], for zircaloy creep [9] and pellet relocation [7].

The pellet-clad gap, defined as: $G = G_0 + u^c + u^p$, where, for each pellet-clad node-pair in the FE model, $G = (G_n, G_t)$ is the current gap size, $G^0 = (G_n^0, G_t^0)$ the initial gap, $u^p = (u_n^p, u_t^p)$ the pellet outer surface displacement, $u^c = (u_n^c, u_t^c)$ the clad inner surface displacement; and the subscripts n and t denote the radial (normal) and the axial (tangential) gap components, respectively. G_n is the “relocated” gap, defined as $G_n = g_n + u_R$, where g_n is the non-relocated gap. Once G_n is known, g_n and P_n are computed according to the radial gap conditions tabulated below. Note that pellet relocation leads the to the states of soft and hard pellet-clad contact.

Radial gap conditions and states

G_n condition	g_n condition	P_n condition	Gap state
$G_n = g_n + G_n^m \geq G_n^m$	$g_n = G_n - G_n^m \geq 0$	$P_n = 0$	Open
$0 \leq G_n \leq G_n^m$ $G_n = G_n^m (1 - P_n / P_n^m)$	$g_n = 0$	$0 \leq P_n \leq P_n^m$ $P_n = P_n^m (1 - G_n / G_n^m)$	Soft
$G_n = 0$	$g_n = 0$	$P_n^m \leq P_n$	Hard

Upon pellet-clad contact, the radial mechanical gap becomes zero and friction forces between the pellet and clad are generated. These friction forces (or stresses) are assumed to follow the Coulomb friction law, which describes the limiting friction needed to overcome prior to any sliding between the pellet and clad. Let P_t be the axial (tangential) friction contact stress and μ the friction coefficient, the friction contact conditions for $g_n = 0$ and $P_n > 0$ are:

$$|P_t| \leq \mu P_n ; P_t = \text{sgn}(\Delta G_t) \mu P_n \quad (2)$$

where the first relation on the left designates the stick condition, and the second one the slip condition. Here, ΔG_t indicates the change in axial (tangential) gap G_t .

Fission product gas release

The fission product gas release process is modelled by assuming that UO₂ consists of spherical grains of equal size [10]. The fission product gases are produced at a rate $\beta(t)$ in a grain of radius $R(t)$. The gases migrate to grain boundaries by diffusion with a diffusion coefficient $D(t)$. The gas atoms reaching the boundary precipitate into inter-granular bubbles with a local density of $N(t)$ (per unit area)

and a grain boundary re-resolution rate of $B(t) = b\lambda/2$, where b is the grain boundary re-resolution frequency, and $\lambda/2$ the re-resolution depth from the grain face. All these variables are assumed to be time-dependent. Gas atom concentration at position r at time t in the grain, $C(r,t)$, is described by:

$$\frac{\partial C(r,t)}{\partial t} = D(t)\nabla^2 C(r,t) + \beta(t) \text{ for } 0 < r < R(t) \quad (3)$$

The imposed boundary conditions are $\partial C(0,t)/\partial r = 0$ and $C(R,t) = B(t)N(t)/D(t)$, with the initial condition $C(r,0) = 0$. Gas diffusion and grain growth may occur simultaneously. Analytical solutions to the problem of gas diffusion in expanding medium have been used [11]. The inter-granular gas density $N(t)$ is found to be:

$$N(t) = \frac{2}{3} R \int_0^t \beta(s) ds - \frac{2 \int_0^R r^2 C(r,t) dr}{R^2} \quad (4)$$

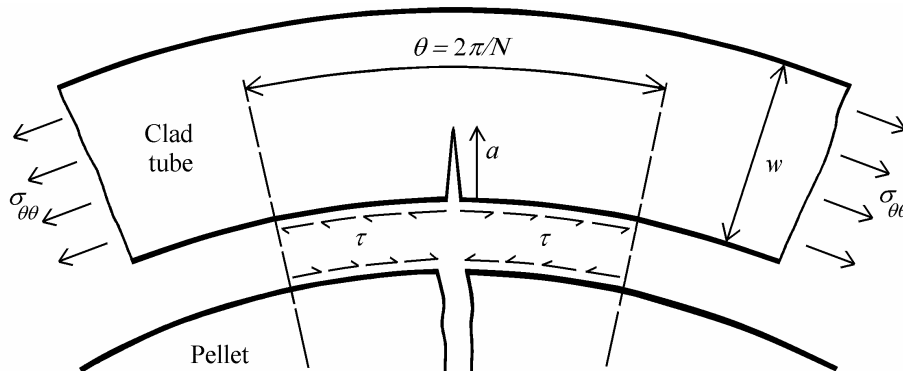
When the gas concentration at the grain boundary reaches a certain threshold level, given by $C_{\max}(t) = B(t)N_s(t)/D(t)$, gas release will occur. The gas atom density per unit area of grain boundary at saturation N_s is calculated through the ideal gas equation of state.

As can be noted from Eq. (3), only the release of stable fission product gases (Xe and Kr) are calculated. Moreover, only the release of stable (long-lived) iodine isotopes is considered, and is assumed to be proportional to the release of Xe [12].

Stress corrosion cracking

The combined effects of mechanical and chemical interaction with the fuel pellets may cause failure of the clad tube through stress corrosion cracking (SCC). This kind of failure is predicted with a model, in which the propagation of stress corrosion cracks is treated by use of linear elastic fracture mechanics (LEFM). The cracks are supposed to nucleate at pre-existing flaws at the clad inner surface, which are subjected to local stress concentrations induced by the opening of radial pellet cracks; see Figure 1. The initial clad flaws are assumed to start growing transgranularly, provided that the stress intensity exceeds a critical threshold and that the clad material is chemically sensitised and thus

Figure 1. N symmetrically spaced radial pellets cracks are assumed. When the cracked fuel pellet expands, the cladding experiences local shear stresses from pellet-clad sliding, $\tau = \mu P_n$, where μ is the coefficient of pellet-clad friction, and P_n is the pellet-clad normal contact pressure.



susceptible to SCC; the latter condition is cast in the form of a threshold iodine concentration in the pellet-clad gap. The transgranular crack growth rate is in our model correlated to clad temperature T , stress intensity K_I , and iodine concentration C_I at the clad inner surface through [6]:

$$\frac{da}{dt} = F(C_I) \left(\frac{K_I}{K_{Isc}} \right)^n e^{-Q/RT} \quad (5)$$

Here, a is the crack length, F is a function of the iodine concentration, Q and n are constants and K_{Isc} is a material- and temperature-dependent threshold stress intensity for transgranular SCC. The incremental crack growth in each time step of an analysis is evaluated through Eq. (5) for each axial segment of the fuel rod. The stress intensity factor is estimated from the current crack length, pellet-clad contact pressure and clad average hoop stress through superposition of analytical solutions [12].

$$K_I = \frac{\tau R_i \theta}{\sqrt{\pi a}} f_1 \left(\frac{R_i \theta}{2a} \right) f_2 \left(\frac{a}{w} \right) + \sigma_{\theta\theta} \sqrt{\pi a} f_3 \left(\frac{a}{w}, \frac{R_i}{w} \right) \quad (6)$$

Here, f_1 , f_2 and f_3 are dimension-free functions and R_i is the clad inner radius; other parameters are defined in Figure 1. The first term on the right-hand-side of Eq. (6) accounts for the local effect of frictional shear forces ($\tau \equiv P_t = \mu P_n$) from the pellet, whereas the second term is related to the uniform loading in the hoop direction ($\sigma_{\theta\theta}$).

Ramp tests

The aforementioned integrated models have been used to evaluate some power ramp experiments made on BWR fuel rods in test reactors. In particular are analysed a “classical” power ramp test that was made on fresh fuel pins, with a narrow pellet-clad gap, in the Halden reactor some years ago; and a recent test made on modern Westinghouse fuel, irradiated in a Swedish BWR, and then ramped in the Studsvik R2 reactor.

Halden IFA404 test

The first power ramp experiment evaluated in our paper is a PCMI test performed in the Halden reactor in Norway within the Instrumented Fuel Assembly, IFA-404 test series [13]. In particular, we consider pin number 403 in the test IFA-404-1. The pin was an un-irradiated BWR fuel rod with a rather small pellet-clad gap size. The technical data for this rod are presented in Table 1. One objective of this test was to measure the diameter increase and the length changes of the pin as a function of linear heat generation rate (LHGR) during power cycling. The power ramp was performed by increasing the LHGR of the pin from nearly zero to a peak value of around 50 kW/m. The power was kept at this level for nearly 24 h, and then slowly reduced. Figure 2 displays the power history for this test. Both the elongation and the diameter profile of the rod were measured during the power cycling. The results in terms of the clad circumferential and axial strains versus LHGR, extracted pointwise from continuous measurements, are presented in Table 2.

Studsvik SVEA-96S test

The considered test was conducted on a Westinghouse 10×10 SVEA96-S fuel assembly rod, base irradiated in the Barsebäck 2 BWR in Sweden, 1999-2002, to a rod burn-up of about 32 MWd/kgU, Figure 3. A test pin of length 570 mm with UO₂ fuel pellets was disassembled from the original

Table 1. Data on fuel pins subjected to ramp tests

Case	Halden	IFA404-1	Studsvik	SVEA96-S
Fuel pellet			As-fabricated	After BI
Material		UO ₂	UO ₂	–
Diameter	mm	12.64	8.25	8.34*
Length	mm	15	10	NM
Density	kg/m ³	10 400	10 600	NM
²³⁵ U content	Wt. %	7	4.2	–
Cladding			With ZrSn liner	–
Material*		RXA zircaloy-2	RXA zircaloy-2	–
Outer diameter	mm	14.3	9.63	9.61
Wall thickness	mm	0.8	0.635	NM
Pin				
Fill gas		Helium	Helium	
Fill pressure	MPa	0.1	0.4	NM
Active length	mm	500	472	475.5
Plenum volume	mm ³	8 700	1 560	NM

RXA: Re-crystallised-annealed; *Calculated mean; BI: Base irradiation; NM: Not measured.

Figure 2. Power history and axial power profile along the fuel column for the Halden pin

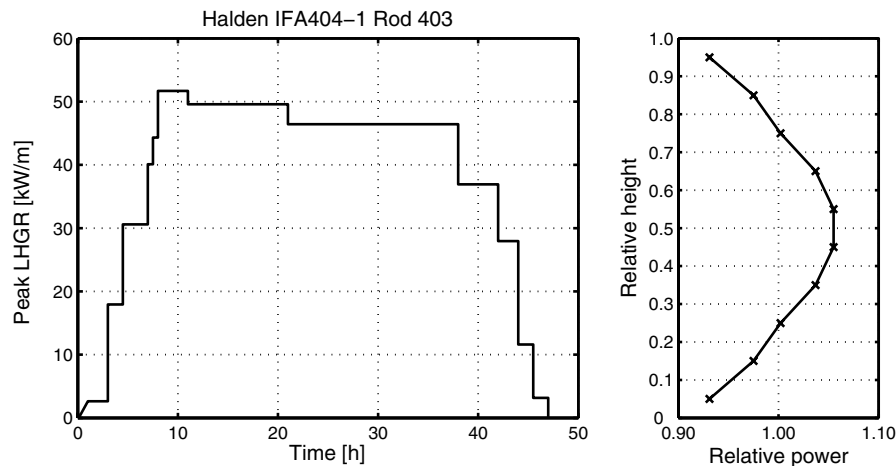
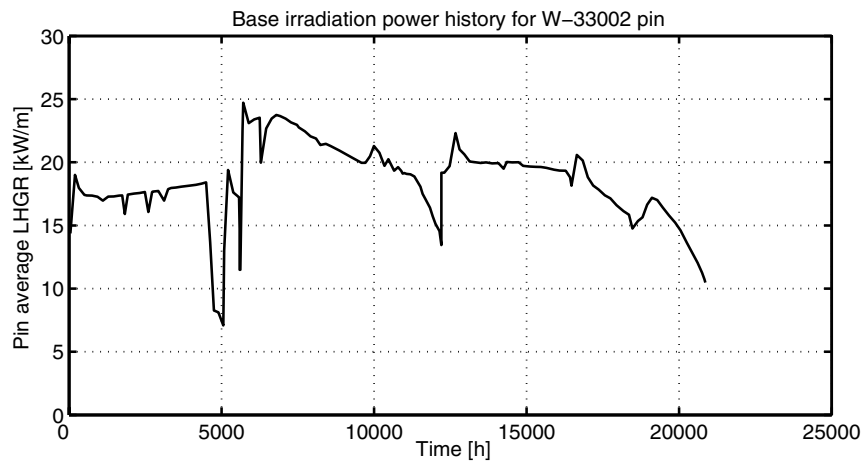


Table 2. Halden IFA404-1 cladding hoop and axial strains vs. peak linear heat generation rate (PLHGR)

PLHR kW/m	Hoop %	Axial %	PLHR kW/m	Hoop %	Axial %
0	0	0	46.4	–	–
1.1	0	0	43.3	–	0.095
9.5	–	0.007	39.6	0.295	–
19.0	–	0.035	36.9	0.3	0.083
24.3	0.1	–	31.7	–	0.072
29.5	–	0.068	28	–	–
38.6	–	0.115	19.5	–	–
48.5	–	0.15	11.6	–	0.063
51.7	0.435	0.158	1.1	0.2	–

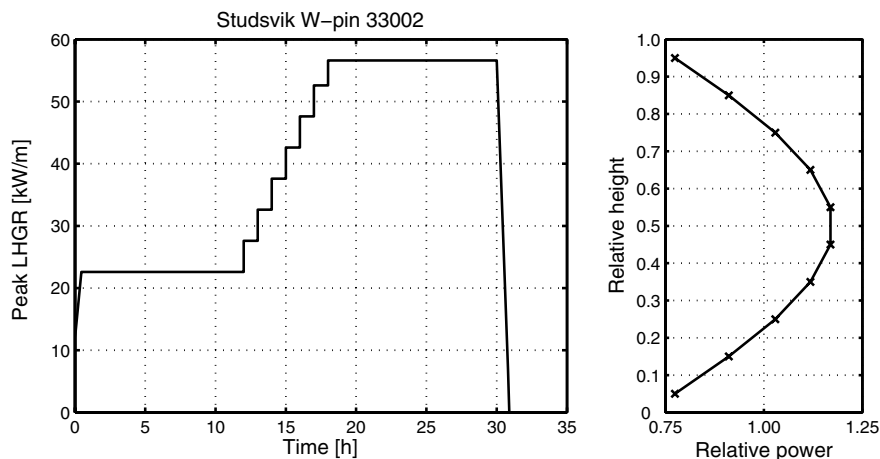
Figure 3. Base power history for the Studsvik pin, irradiated in the Barsebäck-2 BWR



(segmented) rod for power ramp testing in the Studsvik R2 reactor. Basic technical data on the fuel pin are given in Table 1. The pin was non-destructively examined in a hot cell at Studsvik. Examination covered pin diameter measurements and γ spectrometry. The R2 test facility and experimental technique for fuel ramp test is described in [14]. For the considered test, a pressurised water loop was used to simulate BWR coolant conditions (9 MPa, 285°C). The rod surface temperature was limited by sub-cooled surface boiling, implying that the rod surface temperature may not exceed the saturation temperature (303°C) by more than a few degrees.

The pin was subjected to irradiation in R2 by first raising the power from zero to 12 kW/m very rapidly. This initial power step was followed by a slow power increase over a period of 25 minutes until the conditioning LHGR of 22.5 kW/m was reached. “Conditioning” indicates that a fuel pin reaches a state of thermo-mechanical equilibrium at a constant LHGR after a sufficient period of time, in this case about 12 h. After conditioning, the pin was subjected to a power ramp, where a ramp step height of around 5 kW/m and a step duration of 1 h were utilised. The step ramp rate is about 6.4 kW/m/min. The ramp terminal level (RTL) was about 56.5 kW/m. Power was held at RTL for about 15 h, then LHGR was finally reduced to 7 kW/m after 50 minutes, upon which the irradiation was terminated. The pin survived the ramp. Figure 4 shows the power history during the ramp test.

Figure 4. Ramp power history and axial power profile along the fuel column for the Studsvik pin



After the ramp test, the pin underwent post-irradiation examination (PIE) in a hot cell at Studsvik. The PIE included γ spectrometry, pin diameter, pellet-clad gap size, fuel density and fission product gas release measurements. The γ spectrometry was performed along the pin for determination of specific nuclides comprising $^{137,134}\text{Cs}$. The rod diameter measurements were made at four circumferential positions along the pin. The pellet-clad gap size of the pin was determined by compressing the rod transversally between two parallel flat edges and measuring the pin deformation as a function of applied force during the load cycle. The measurements were corrected for the elastic deformation of the apparatus. Fission product gas release was determined by first puncturing the pin in the plenum region, then measuring the internal gas pressure and determining the free volume. The amounts of released Xe and Kr gases were determined by mass spectroscopy analysis from retrieved samples. The fraction of fission gas release was determined by dividing the measured amount with the calculated amount of the generated inventory of these gases. Optical inspection of the clad inner surface revealed a large number of $\approx 10\ \mu\text{m}$ deep flaws, but no through-wall cracks.

Table 3 lists pellet-clad gap size measurements, including the data on clad outer diameter. Figure 6 shows the profilometry data on clad diameter before and after ramp, and Figure 7 displays the relocated gap size along the fuel. The fraction of fission gas (Xe, Kr) release measured after ramp amounted to 32%, with a corresponding rod internal pressure of 2.14 MPa at STP.

Table 3. Pin dimensions measured at Studsvik after ramp

Axial position from bottom mm	Relocated diametral gap μm	Compressed diametral gap μm	Clad OD mm
82	24	48	9.658
92	26	56	9.664
102	38	65	9.676
274.5	12	62	9.728
284.5	18	58	9.731
294.5	12	75	9.727
386	13	70	9.693
396	18	65	9.684
406	23	73	9.675

OD: Outer diameter.

Computations

The models described in the foregoing sections are included in the fuel rod thermal-mechanical code STAV. This code was used to evaluate the Halden and the Studsvik ramp tests. The Halden IFA-404 test was performed on a fresh fuel pin with virtually no fission gas release. Thus, it was purely a PCMI test. The results of the computations on hoop and axial strains are presented in Figures 5(a) and 5(b), respectively, along with some measured data (see also Table 2). Calculations were performed for $\mu = 0.0$ and $\mu = 0.014$. From Figure 5, it is seen that the results are satisfactory for $\mu = 0.014$. The peak clad hoop stress is calculated to be $\sigma_{\theta\theta} = 320\ \text{MPa}$, while the corresponding pellet-clad contact pressure is $P_n = 65\ \text{MPa}$. Our calculations show that SCC of the clad tube does not occur, since the amount of iodine in the pellet-clad gap is negligible. The calculated maximum stress intensity at an assumed, $10\ \mu\text{m}$ deep, clad inner surface flaw was $2.3\ \text{MPam}^{1/2}$.

Figure 5. Comparison between measured and calculated clad strains as a function of linear heat generation rate for the IFA404-1 pin, (a) hoop strain, (b) axial strain

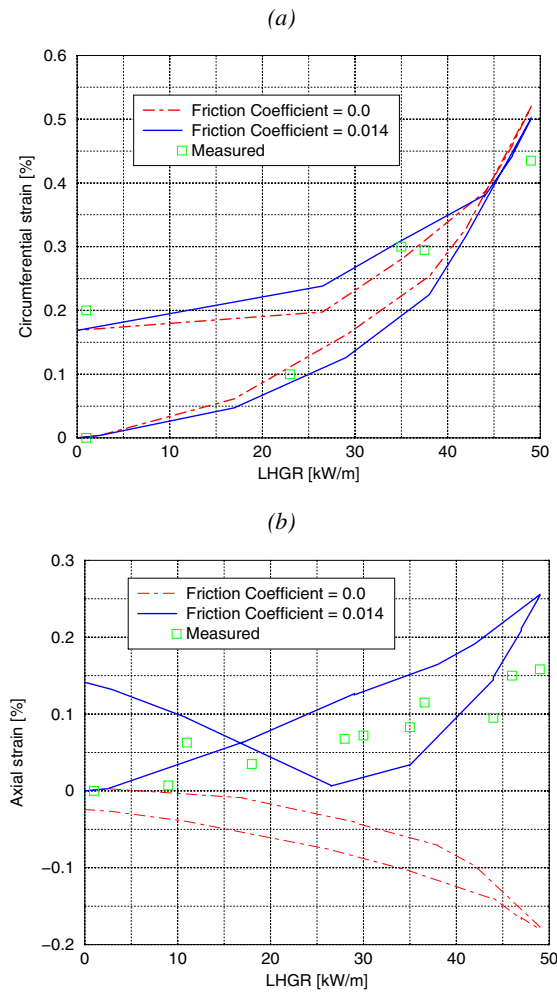


Figure 6. Comparison between measured and calculated clad outer diameter along the pin before and after ramp for the Studsvik pin

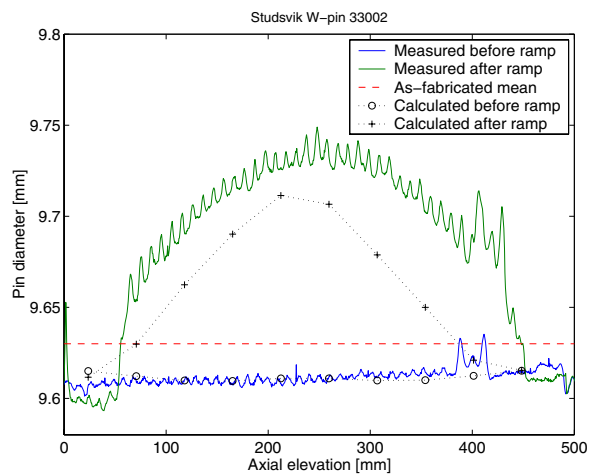
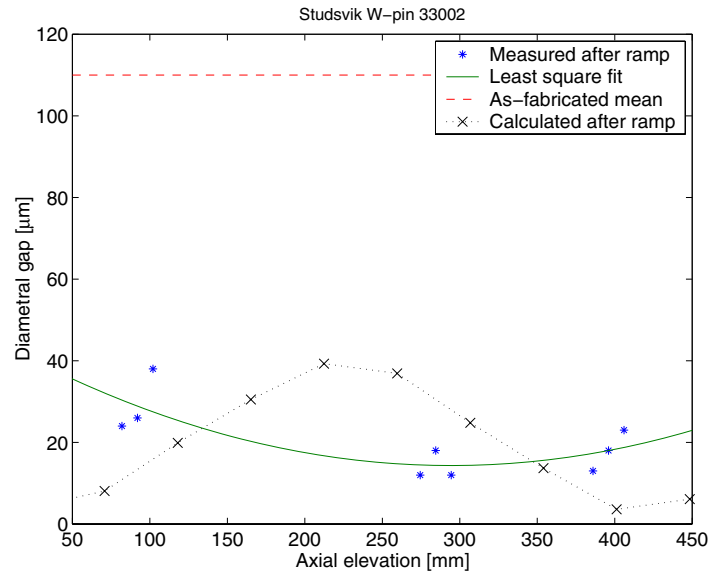


Figure 7. Comparison between measured and calculated pellet-clad gap along the fuel after the ramp for the Studsvik pin. The least squares fit line is to the measured data.



Computations for the Studsvik test were performed with $\mu = 0.014$. Results are presented in terms of calculated clad outer diameter before and after ramp, together with measured data in Figure 6. Figure 7 depicts the calculated relocated pellet-clad gap vs. measured values along the fuel. The peak hoop stress is calculated to be $\sigma_{\theta\theta} = 790$ MPa with the corresponding contact pressure $P_n = 123$ MPa. The yield strength in that location of the clad is calculated to be 679 MPa. Hence, some pure plastic deformation occurs, even for highly irradiation-hardened zircaloy, under such a severe ramp. Our calculations show that the maximum stress intensity at the observed 10 μm deep flaws at the clad inner surface is $4.9 \text{ MPam}^{1/2}$. The base irradiation fission gas release fraction is calculated to be around 0.3%, while the value after the ramp is calculated as 26.3%, which is below the measured value of 32%.

Discussion

The results of the calculations on the Halden pin show the strong effect of friction forces on the behaviour of axial clad deformations during PCMI (Figure 5). Thus a proper modelling of the contact problem is essential for prediction of fuel deformation during strong PCMI. The friction coefficient used in our calculations ($\mu = 0.014$) is considered to be an effective (empirical) value that includes the influence of pellet relocation and cracking. It differs from the measured value of the dynamic friction coefficient, between UO_2 and zircaloy, which is reported to be in the range 0.5-0.7 [15].

In the case of the Studsvik pin, it can be observed from Figure 6 that the clad outer diameter is somewhat underestimated after the ramp. This is mainly attributed to the gaseous fuel swelling during power ramp, which is not taken into account in the present model. Neither have we modelled the thermal creep deformations of UO_2 , which is expected to occur for $T > 0.5T_m$, with T_m being the melting temperature. The precise calculation of pellet-clad gap is more involved, since the pellets undergo complex cracking and distortion under the influence of temperature gradients during a ramp (Figure 7). The calculated fission gas release fraction is underestimated by the gas atom diffusion model utilised here. At RTL of 56.6 kW/m (Figure 4) the peak calculated fuel central temperature is 2 530 K, with a corresponding pellet surface temperature 767 K. Consequently, the fuel is subjected to a considerable temperature gradient at the ramp terminal power. This kind of temperature gradient can trigger other

modes of fission gas migration in the fuel than the atomic diffusion considered in our calculations, e.g. gas bubble motion and bubble coalescence. Furthermore, the PCMI method utilised here is essentially a one-dimensional model, although the effect of axial forces on the clad is accounted for through a finite element method. Therefore, the occurrence of the pronounced clad ridging observed cannot be captured (Figure 6). This requires a more detailed two- and three-dimensional modelling, which is beyond the intention of the fast 1-D fuel rod thermal-mechanical analysis code used here.

In the presented SCC failure model, transgranular crack growth is assumed to initiate at pre-existing internal flaws. This approach is based on the observation that surface defects, up to a depth of about 20 μm , do exist in commercial clad tubes. An alternative approach would be to model the process of crack initiation from an initially smooth surface, which for iodine-induced SCC in zirconium alloys entails chemical preconditioning and slow inter-granular crack growth. Another simplification made in our failure model is that the pellet-clad contact pressure and the clad hoop stress are calculated without consideration of the increase in clad tube compliance as the crack grows through the tube wall. Moreover, according to the ASTM standard E399, LEFM is not applicable to cracks shorter than $2.5(K_{Isc}/\sigma_y)^2$. For irradiated zircaloy-2 at 630 K, σ_y is approximately 700 MPa and K_{Isc} 2.3 MPam^{1/2}. Hence, the shortest cracks for which LEFM is valid are in this case 25-30 μm . These limitations can be overcome by use of non-linear fracture mechanics in a finite element framework, as described in Ref. [6]. However, this approach is computationally arduous, and is not suitable for standard design analyses.

Our correlation for stress corrosion crack growth in Eq. (5) is based on results from tests performed on mono-tubes of zircaloy, and therefore must be extended to treat fuel rods with liner cladding. However, it is interesting to note that the calculated maximum stress intensity at the observed 10 μm long clad flaws in the liner rod was 4.9 MPam^{1/2}. In a non-liner rod, this stress intensity would most likely have led to propagation of the flaws and to penetration of the clad tube.

Acknowledgements

We wish to extend our thanks to K. Kitano and U. Engman at Studsvik Nuclear, Sweden, for their valuable communications.

REFERENCES

- [1] Gärtner, M., G. Fischer, *J. Nucl. Mater.*, 149, 29-40 (1987).
- [2] Massih, A.R., L.O. Jernkvist, T. Rajala, *Nucl. Eng. Des.*, 156, 383-391 (1995).
- [3] Cox, B., *J. Nucl. Mater.*, 172, 249-292 (1990).
- [4] Brochard, J., *et al.*, *Trans. SMiRT 16*, paper # 1314, Washington, D.C., August 2001.

- [5] Rousselier, G., S. Leclercq, O. Diard, *Trans. SMiRT 17*, paper # C03-3, Prague, August 2003.
- [6] Jernkvist, L.O., *Nucl. Eng. Des.*, 156, 393-399 (1995).
- [7] Forsberg, K., A.R. Massih, *IAEA Proceedings, IWGFPT/32*, 293-301, IAEA, Vienna (1989).
- [8] Hagrman, D.L., G.A. Reyman, *MATPRO 11 Handbook*, USNRC, NUREG/CR-0497 (1979).
- [9] Limbäck, M., T. Andersson, ASTM STP 1295, 448-468, ASTM, W. Conshohocken, PA (1996).
- [10] Speight, M.V., *Nucl. Sci. Eng.*, 37, 180-185 (1979).
- [11] Forsberg, K., A.R. Massih, *Trans. SMiRT 16*, paper # 1931, Washington, D.C., August 2001.
- [12] Jernkvist, L.O., Quantum Technologies report, TR04-004 (2004).
- [13] Kolstad, E., *EHPG Meeting*, Report HRP 190, Geilo, Norway, (1975).
- [14] Carlsson, M., U. Engman, Studsvik technical note, N(R)-99/063 (1999).
- [15] Shchavelin, V.M., *et al.*, *Atomnaya Energiya*, 61(3), 175-178 (1986).

LIST OF PARTICIPANTS

ARGENTINA

MARINO, Armando Carlos
División DAEE
Centro Atómico Bariloche
Comisión Nacional de Energía Atómica
8400 Bariloche

Tel: +54 2944 445 256
Fax: +54 2944 445 178
Eml: marino@cab.cnea.gov.ar

BELGIUM

BAIRIOT, Hubert
Consultant
Nuclear Fuel Experts sa (FEX)
Lijsterdreef, 20
B-2400 Mol

Tel: +32 (14) 31 25 33
Fax: +32 (14) 32 09 52
Eml: bairiot.fex@pophost.eunet.be

DALLEUR, Jean-Paul
Tractebel Energy Engineering
Avenue Ariane, 7
B-1200 Brussels

Tel: +32 2 773 7742
Fax: +32 2 773 7560
Eml: jean-paul.dalleur@tractebel.com

FERNANDEZ, Javier
Belgonucléaire
Avenue Ariane, 4
B-1200 Brussels

Tel: +32 2 774 06 20
Fax:
Eml: j.fernandez@belgonucleaire.be

HOLLASKY, Nadine
Association Vinçotte Nuclear (AVN)
Nuclear Safety Institute
Rue Walcourt, 148
B-1070 Brussels

Tel: +32(0)2 528 02 44
Fax: +32(0)2 528 01 02
Eml: nh@avn.be

LIPPENS, Marc
Belgonucléaire
Avenue Ariane, 4
B-1200, Brussels

Tel: +32 2 774 0625
Fax: +32 2 774 0614
Eml: m.lippens@belgonucleaire.be

SOBOLEV, Vitali
SCK•CEN
Reactor Physics and MYRRHA
Centre d'Étude de l'Énergie Nucléaire
Boeretang, 200
B-2400 Mol

Tel: +32 (0)14 33 2267
Fax: +32 (0)14 32 1529
Eml: vsobolev@sckcen.be

VAN DEN BERGHE, Sven
SCK•CEN
Boeretang, 200
B-2400 Mol

Tel: +32 14 33 30 64
Fax: +32 14 32 12 36
Eml: svdbergh@sckcen.be

BULGARIA

MANDEV, Ivatz
Institute for Nuclear Research
and Nuclear Energy
Bulgarian Academy of Sciences
72, Tzarigradsko Chaussee

Tel: +359 2 7144 203
Fax: +359 2 975 36 19
Eml: Ivatz@inrne.bas.bg

CANADA

TAYAL, Mukesh
Atomic Energy of Canada Limited, SP2F4
Sheridan Park Research Community
2251 Speakman Drive
Mississauga, Ontario L5K 1B2

Tel: +1 905 823 9060
Fax: +1 905 822 0567
Eml: tayalm@aecl.ca

CZECH REPUBLIC

BELOVSKY, Ladislav
ALIAS CZ s.r.o.
Bachova 1586/16
CZ-149 00 Praha-415

Tel: +420 272 921 678
Fax: +420 257 212 866
Eml: belovsky@telecom.cz

NOVOTNY, Michal
Nuclear Research Institute
Dept. of Reactor Technology
Nuclear Safety Power Division
CZ-250 68 Rez u Prahy

Tel: +420 266 172 464
Fax: +420 266 172 100
Eml: nom@ujv.cz

STECH, Svatobor
Dukovany Nuclear Power Plant
Dep. 4200
CZ-67 550 Dukovany

Tel: +420 618 813 690
Fax: +420 618 866 495
Eml: stechs1.edu@mail.cez.cz

VALACH, Mojmir
Nuclear Research Institute Rez, plc.
Dept. of Reactor Technology
CZ-250 68 Rez u Prahy

Tel: +420 266 172 101 or 464
Fax: +420 266 172 100
Eml: val@ujv.cz

ZYMAK, Jiri
Department of Reactor Technology
Nuclear Research Institute Rez plc.
CZ-250 68 Rez u Prahy

Tel: +420 266 172 464
Fax: +420 266 172 100
Eml: zym@ujv.cz

FINLAND

KELPPE, Seppo
VTT Processes
Nuclear Energy
P.O. Box 1604
Tekniikantie 4C Espoo
FIN-02044 VTT

Tel: +358 9 456 5026
Fax: +358 9 456 5000
Eml: seppo.kelpp@vtt.fi

FRANCE

ANSELMET-VITIELLO, Marie-Christine
CEA
DEC/SESC/LIPA
Cadarache, Bât. 151
F-13108 St. Paul-lez-Durance Cedex

Tel:
Fax:
Eml: Marie-Christine.Anselmet@cea.fr

AUBRUN, Isabelle
CEA
DEC/SA3C/L2EC
Cadarache, Bât. 316
F-13108 St. Paul-lez-Durance Cedex

Tel: +33 (0)4 42 25 20 05
Fax: +33 (0)4 42 25 36 11
Eml: isabelle.aubrun@cea.fr

BARON, Daniel
CEA
DEN/DEC
Cadarache, Bât. 315
F-13108 St. Paul-lez-Durance Cedex

Tel: +33 (0)1 60 73 61 05
Fax: +33 (0)1 60 73 61 49
Eml: daniel.baron@edf.fr

BASINI, Virginie
CEA
DEC/SPUA
Cadarache, Bât. 717
F-13108 St. Paul-lez-Durance Cedex

Tel: +33 (0)4 42 25 32 71
Fax: +33 (0)4 42 25 47 17
Eml: virginie.basini@cea.fr

BAUER, Mireille
CEA
DEC/SESC/LIPA
Cadarache, Bât. 151
F-13108 St. Paul-lez-Durance Cedex

Tel: +33 (0)4 42 25 34 56
Fax: +33 (0)4 42 25 37 13
Eml: mireille.bauer@drncad.cea.fr

BEGUIN, Stéphane
Electricité de France
EDF-SEPTEN
12-14, avenue Dutriévoz
F-69628 Villeurbanne Cedex

Tel: +33 (0)4 72 82 76 21
Fax: +33 (0)4 72 82 77 11
Eml: stephane.begu@edf.fr

BENTEJAC, Fabrice
CEA
DEN/SAC/DM2S/SEMT/LM2S
Saclay, Bât. 607
F-91191 Gif-sur-Yvette Cedex

Tel: +33 (0)1 69 08 52 17
Fax: +33 (0)1 69 08 86 84
Eml: Fabrice.Bentejac@cea.fr

BERNARD, Louis-Christian FRAMATOME ANP 10, rue Juliette Récamier F-69456 Lyon Cedex 06	Tel: +33 (0)4 72 74 72 94 Fax: +33 (0)4 72 74 88 33 Eml: louis.bernard@framatome-anp.com
BIZ, Sophie Dept. Mécanique et Technologie des Composants Les Renardières Route de Sens, Ecuelles F-77250 Moret-sur-Loing	Tel: Fax: Eml: sophie.biz@edf.fr
BLANPAIN, Patrick FRAMATOME ANP 10, rue Juliette Récamier F-69456 Lyon Cedex 06	Tel: +33 (0)4 72 74 89 27 Fax: +33 (0)4 72 74 81 45 Eml: patrick.blanpain@framatome-anp.com
BOULORE, Antoine CEA DEC/SESC/LSC Cadarache, Bât. 151 F-13108 St. Paul-lez-Durance Cedex	Tel: +33 (0)4 42 25 44 15 Fax: +33 (0)4 42 25 29 49 Eml: boulore@michigan.cad.cea.fr
BRUNEL, Laurence CEA DEC/SESC Cadarache, Bât. 151 F-13108 St. Paul-lez-Durance Cedex	Tel: +33 (0)4 42 25 65 28 Fax: +33 (0)4 42 25 47 47 Eml: laurence.brunel@cea.fr
CAILLOT, Laurent CEA DEC/SA3C/L2EC Cadarache, Bât. 316 F-13108 St. Paul-lez-Durance Cedex	Tel: Fax: Eml: Laurent.Caillot@cea.fr
CASTELIER, Etienne CEA DEC/SESC/LLCC Cadarache, Bât. 151 F-13108 St. Paul-lez-Durance Cedex	Tel: +33 (0)4 42 25 62 44 Fax: +33 (0)4 42 25 37 13 Eml: etienne.castelier@cea.fr
CAZALIS, Bernard IRSN DPAM/SEMCA/LEP BP 3 F-13115 St. Paul-lez-Durance Cedex	Tel: +33 (0)4 42 25 77 36 Fax: +33 (0)4 42 25 61 43 Eml: bernard.cazalis@irsn.fr
CHANTOIN, Pierre M. 232, Impasse du Haut Colombier F-04100 Manosque	Tel: +33 (0)4 92 72 01 03 Fax: +33 (0)4 92 72 01 03 Eml: pierre.chantoin@wanadoo.fr

CHARPENEL, Jean
IRSN
DPAM/SEMCA.LEC
BP 3
F-13115 St. Paul-lez-Durance Cedex

Tel: +33 (0)4 42 25 77 36
Fax: +33 (0)4 42 25 61 43
Eml: jean.charpenel@irsn.fr

CHIARELLI, Gérard
COGEMA
BU Recyclage
BP
F-94176 Bagnols-sur-Cèze Cedex

Tel:
Fax:
Eml: gchiarelli@melox.fr

COULON-PICARD, Emmanuelle
CEA
DEC/SESC/LIPA
Cadarache, Bât. 151
F-13108 St. Paul-lez-Durance Cedex

Tel: +33 (0)4 42 25 49 97
Fax: +33 (0)4 42 25 37 13
Eml: emmanuelle.coulon-picard@cea.fr

COUTY, Jean-Christophe
Électricité de France
EDF-SEPTEN
12-14, avenue Dutrievoz
F-69628 Villeurbanne Cedex

Tel:
Fax:
Eml: jean-christophe.couty@edf.fr

DEHAUDT, Philippe
CEA
DEN/DSNI
Saclay, Bât. 121
F-91191 Gif-sur-Yvette Cedex

Tel: +33 (0)1 69 08 76 57; 06 76 72 84
Fax: +33 (0)1 69 08 98 17
Eml: dehautd@cea.fr

DELAFOY, Christine
FRAMATOME ANP
10, rue Juliette Récamier
F-69456 Lyon Cedex 06

Tel: +33 (0)4 42 25 81 29
Fax: +33 (0)4 42 25 81 45
Eml: christine.delafoy@framatome-anp.com

DELHAYE, Benoît
Électricité de France
EDF-SEPTEN
12-14, avenue Dutrievoz
F-69628 Villeurbanne Cedex

Tel: +33 (0)4 72 82 72 12
Fax: +33 (0)4 72 82 77 11
Eml: benoit.delhaye@edf.fr

DESGRANGES, Lionel
CEA
DEC/SESC/LIPA
Cadarache, Bât. 316
F-13108 St. Paul-lez Durance Cedex

Tel: +33 (0)4 42 25 31 59
Fax: +33 (0)4 42 25 48 78
Eml: desrang@come.cad.cea.fr

DESQUINES, Jean
IRSN
CEA Cadarache
F-13108 St. Paul-lez-Durance Cedex

Tel: +33 (0)4 42 25 75 75
Fax: +33 (0)4 42 25 61 43
Eml: jean.desquines@irsn.fr

DUBOIS, Sylvie
CEA
DEC/SESC/LIPA
Cadarache, Bât. 151
F-13108 St. Paul-lez-Durance Cedex

Tel: +33 (0)4 42 25 43 52
Fax: +33 (0)4 42 25 37 13
Eml: dubois@drncad.cea.fr

DUCROS, Gérard
CEA
DEC/SA3C
Cadarache, Bât. 315
F-13108 St. Paul-lez-Durance Cedex

Tel: +33 (0)4 76 88 31 74
Fax: +33 (0)4 76 88 51 51
Eml: Gerard.Ducros@cea.fr

FAURE-GEORGS, Hélène
CEA
DEC/SESC/LIPA
Cadarache, Bât. 315
F-13108 St. Paul-lez-Durance Cedex

Tel: +33 (0)4 42 25 61 50
Fax: +33 (0)4 42 25 37 31
Eml: faure-geors@drncad.cea.fr

FEDERICI, Eric
DEN/CEN Cadarache
F-13108 St. Paul-lez-Durance Cedex

Tel: +33 (0)4 42 25 24 44
Fax: +33 (0)4 42 25 70 42
Eml: eric.federici@ipsn.fr

FORGERON, Thierry
CEA
DEN/DSNI
Saclay, Bât. 121
F-91191 Gif-sur-Yvette Cedex

Tel:
Fax:
Eml: Thierry.Forgeron@cea.fr

FOURNIER, Lionel
CEA
DEN/SAC/DMN/SEMI/LCMI
Saclay, Bât. 625
F-91191 Gif-Sur-Yvette Cedex

Tel: +33 (0)1 69 08 94 20
Fax: +33 (0)1 69 08 93 24
Eml: lionel.fournier@cea.fr

FRIZONNET, Jean-Michel
IRSN
DPAM/SEMCA.LEC
B.P. 3
F-13115 St. Paul-lez-Durance Cedex

Tel: +33 (0)4 42 25 77 36
Fax: +33 (0)4 42 25 61 43
Eml: jean-michel.frizonnet@irsn.fr

GARCIA, Philippe
CEA
DEN/SESC/LLCC
Cadarache, Bât. 151
F-13108 St Paul-lez-Durance Cedex

Tel: +33 (0)4 42 25 41 88
Fax: +33 (0)4 42 25 37 13
Eml: Philippe.Garcia@cea.fr

GARNIER, Christophe
FRAMATOME ANP
10, rue Juliette Récamier
F-69456 Lyon Cedex 06

Tel: +33 (0)4 72 74 80 18
Fax: +33 (0)4 72 74 88 33
Eml: christophe.garnier@framatome-anp.com

GATT, Jean-Marie
CEA
DEC/SESC/LLCC
Cadarache, Bât. 151
F-13108 St Paul-lez Durance Cedex

Tel: +33 (0)4 42 25 46 67
Fax: +33 (0)4 42 25 37 13
Eml: gatt@drncad.cea.fr

GUÉRIN, Yannick
CEA
DEC/SESC
Cadarache, Bât. 151
F-13108 St. Paul-lez-Durance Cedex

Tel: +33 (0)4 42 25 79 14
Fax: +33 (0)4 42 25 47 47
Eml: yannick.guerin@cea.fr

GUICHERET-RETEL, Violaine
Laboratoire de Mécanique
Appliquée R. Chaléat
Institut FEMTO-ST
UMR 6174
24, rue de l'Épitaphe
F-25000 Besançon

Tel: +33 (0)3 81 66 60 41
Fax: +33 (0)3 81 66 67 00
Eml: violaine.retél@univ-fcomte.fr

GUILLET, Jean-Luc
CEA
DEN/DSNI
Saclay, Bât. 121
F-91191 Gif-sur-Yvette Cedex

Tel: +33 (0)1 69 08 62 98
Fax: +33 (0)1 69 08 98 17
Eml: jean-luc.guillet@cea.fr

HELPER, Thomas
CEA
DEC/SESC/LLCC
Cadarache, Bât. 151
F-13108 St. Paul-lez-Durance Cedex

Tel:
Fax:
Eml: helper@drncad.cea.fr

HOURDEQUIN, Nicolas
CEA
DEN/SAC/DM2S/SEMT/LM2S
Saclay
F-91191 Gif-sur-Yvette Cedex

Tel: +33 (0)1 69 08 93 80
Fax: +33 (0)1 69 08 86 84
Eml: Nicolas.Hourdequin@cea.fr

HUET, François
CEA
DEC/SESC/LIPA
Cadarache, Bât. 151
F-13108 St. Paul-lez-Durance Cedex

Tel: +33 (0)4 4225 7547
Fax: +33 (0)4 4225 3713
Eml: francois.huet@cea.fr

HUMBERT, Jean-Marc
CEA
DEN/SAC/DM2S/SEMT
Saclay
F-91191 Gif-sur-Yvette Cedex

Tel:
Fax:
Eml: Jean-Marc.Humbert@cea.fr

KALLENB, Marie-Claire CEA DEN/DIR/AFF-INT Cadarache, Bât. 101 F-13108 St. Paul-lez-Durance Cedex	Tel: +33 (0)4 42 25 46 50 Fax: +33 (0)4 42 25 41 42 Eml: kallend@drncad.cea.fr
LAMBERT, Thierry CEA DEC/SESC/LIPA Cadarache, Bât. 151 F-13108 St. Paul-lez-Durance Cedex	Tel: +33 (0)4 42 25 38 56 Fax: +33 (0)4 42 25 37 13 Eml: t.lambert@drncad.cea.fr
LANSIART, Sylvie CEA DEC/SESC Cadarache, Bât. 151 F-13108 St. Paul-lez-Durance Cedex	Tel: +33 (0)1 69 08 23 80 Fax: +33 (0)1 69 08 26 81 Eml: sylvie.lansiart@cea.fr
LE BOULCH, David CEA DEN/SAC/DMN/SEMI/LCMI Saclay, Bât. 625 F-91191 Gif-sur-Yvette Cedex	Tel: +33 (0)1 69 08 83 86 Fax: +33 (0)1 69 08 93 24 Eml: david.leboulch@cea.fr
LEFUR, Brigitte CEA DEN/DIR/AFF-INT Cadarache, Bât. 101 F-13108 St. Paul-lez-Durance Cedex	Tel: +33 (0)4 42 25 22 57 Fax: +33 (0)4 42 25 41 42 Eml: Brigitte.Lefur@cea.fr
LEMAIGNAN, Clément CEA DEN/DEC/DIR 17, rue des Martyrs F-38054 Grenoble Cedex 9	Tel: +33 (0)4 38 78 44 71 Fax: +33 (0)4 38 78 51 51 Eml: Clement.Lemaignan@cea.fr
LEMOINE, Francette IPSN DRS/SEMAR CEN Cadarache, Bât. 702 F-13108 St. Paul-lez-Durance Cedex	Tel: +33 (0)4 42 25 43 14 Fax: +33 (0)4 42 25 61 43 Eml: lemoine@drscad.ipsn.fr
MAILHE, Pierre FRAMATOME ANP 10, rue Juliette Récamier F-69456 Lyon Cedex	Tel: +33 (0)4 72 74 80 18 Fax: +33 (0)4 72 74 88 38 Eml: pierre.mailhe@framatome-anp.com
MAILLARD, Serge CEA DEC/SESC/LSC Cadarache, Bât. 151 F-13108 St. Paul-lez-Durance Cedex	Tel: +33 (0)4 42 25 20 36 Fax: +33 (0)4 42 25 29 49 Eml: serge.maillard@cea.fr

MARTIN, Philippe
CEA
DEN/DIR
Cadarache, Bât. 151
F-13108 St. Paul-lez-Durance Cedex

Tel: +33 (0)4 42 25 76 34
Fax: +33 (0)4 42 25 73 01
Eml: MARTIN@drncad.cea.fr

MASSON, Renaud
CEA
DEC/S3C
Cadarache, Bât. 224
F-13108 St. Paul-lez-Durance Cedex

Tel: +33 (0)4 42 25 47 75
Fax: +33 (0)4 42 25 37 13
Eml: Renaud.Masson@edf.fr

MENUT, Patrick
CEA
DEC/SESC/LIPA
Cadarache, Bât. 151
F-13108 St. Paul-lez-Durance Cedex

Tel: +33 (0)4 42 25 59 71
Fax:
Eml: dec100839@drncad.cea.fr

MICHEL, Bruno
CEA
DEC/SESC/LSC
Cadarache, Bât. 151
F-13108 St. Paul-lez-Durance Cedex

Tel: +33 (0)4 42 25 34 73
Fax: +33 (0)4 42 25 29 49
Eml: bruno.michel@cea.fr

MONERIE, Yann
IRSN
DPAM/SEMCA/LEC
B.P. 3
F-13115 St. Paul-lez-Durance Cedex

Tel: +33 (0)4 42 25 77 36
Fax: +33 (0)4 42 25 61 43
Eml: yann.monerie@irsn.fr

MOREL, Étienne
FRAMATOME ANP Nuclear Fuel
Fuel Technologies
Design and Sales Division
10, rue Juliette Récamier
F-69456 Lyon Cedex 06

Tel: +33 (0)4 72 74 81 46
Fax: +33 (0)4 72 74 88 33
Eml: tienne.morel@framatome-anp.com

MOUGEL, Caroline
CEA
DEN/SAC/DMN/SEMI/LM2E
Saclay, Bât. 604
F-91191 Gif-sur-Yvette Cedex

Tel: +33 (0)1 69 08 82 72
Fax: +33 (0)1 69 08 90 73
Eml: caroline.mougel@cea.fr

NABOT, Jean-Philippe
CEA
DEC/DIR
Cadarache, Bât. 151
F-13108 St. Paul-lez-Durance Cedex

Tel: +33 (0)4 42 25 71 47
Fax: +33 (0)4 42 25 73 01
Eml: jean-philippe.nabot@cea.fr

NOIROT, Jean
CEA
DEC/SA3C/LECMI
Cadarache, Bât. 151
F-13108 St. Paul-lez-Durance Cedex

Tel: +33 (0)4 42 25 44 97
Fax: +33 (0)4 42 25 36 11
Eml: jnoirot@cea.fr

NONON, Chrystelle
CEA
DEN/DEC
Cadarache, Bât. 315
F-13108 St. Paul-lez-Durance Cedex

Tel: +33 (0)4 42 25 62 43
Fax: +33 (0)4 42 25 37 13
Eml: chrystelle.nonon@cea.fr

OBRY, Patrick
CEA
DEC/SESC/LSC
Cadarache, Bât. 151
F-13108 St. Paul-lez-Durance Cedex

Tel: +33 (0)4 42 25 73 34
Fax: +33 (0)4 42 25 29 49
Eml: Patrick.Obry@cea.fr

PAPIN, Joëlle
IRSN
CE Cadarache
BP 3, Bât. 702
F-13108 St. Paul-lez-Durance Cedex

Tel: +33 (0)4 42 25 34 63
Fax: +33 (0)4 42 25 6143
Eml: joelle.papin@irsn.fr

PELLETIER, Michel
CEA
DEC/SESC/LSC
Cadarache, Bât. 151
F-13108 St. Paul-lez-Durance Cedex

Tel: +33 (0)4 42 25 79 68
Fax: +33 (0)4 42 25 29 49
Eml: michel.pelletier@drncad.cea.fr

PETIT, Marc
IRSN
SEMAR/LEC
Cadarache, BP 3
F-13115 St. Paul-lez-Durance Cedex

Tel: +33 (0)4 42 25 6131
Fax: +33 (0)4 42 25 6143
Eml: marc.petit@irsn.fr

PETITPREZ, Benoît
Électricité de France
EDF/SEPTEN
12-14, Avenue Dutrievoz
F-69628 Villeurbanne Cedex

Tel: +33 (0)4 72 82 72 82
Fax: +33 (0)4 72 82 77 11
Eml: benoit.petitprez@edf.fr

PLANCQ, David
CEA
DEC/SESC/LSC
Cadarache, Bât. 151
F-13108 St. Paul-lez-Durance Cedex

Tel: +33 (0)4 42 25 32 68
Fax: +33 (0)4 42 25 29 49
Eml: david.plancq@cea.fr

PONTILLON, Yves CEA DEC/SA3C Cadarache, Bât. 316 F-13108 St. Paul-lez-Durance Cedex	Tel: +33 (0)4 42 25 72 26 Fax: +33 (0)4 42 25 44 79 Eml: yves.pontillon@cea.fr
RICAUD, Jean-Marc CEA DEC/SESC/LSC Cadarache, Bât. 151 F-13108 St. Paul-lez-Durance Cedex	Tel: +33 (0)4 42 25 75 29 Fax: +33 (0)4 42 25 29 49 Eml: ricaud@michigan.cad.cea.fr
ROUSSETTE, Sophie CEA DEC/SESC/LLCC Cadarache, Bât. 151 F-13108 St. Paul-lez-Durance Cedex	Tel: +33 (0)4 24 45 46 74 Fax: +33 (0)4 42 25 37 13 Eml: sophie.roussette@cea.fr
SAINTE-CATHERINE, Claude CEA DEN/SAC/DMN/SEMI/LCMI Saclay, Bât. 625P F-91191 Gif-sur-Yvette Cedex	Tel: +33 (0)1 69 08 88 56 Fax: +33 (0)1 69 08 93 24 Eml: Claude.Sainte-Catherine@cea.fr
STRUB, Claude CEA Saclay DEN/DMN F-91191 Gif-sur-Yvette Cedex	Tel: +33 (0)1 69 08 52 93 Fax: Eml: Claude.Strub@cea.fr
STRUZIK, Christine CEA DEC/SESC/LSC Cadarache, Bât. 151 F-13108 St. Paul-lez-Durance Cedex	Tel: +33 (0)4 42 25 23 35 Fax: +33 (0)4 42 25 29 49 Eml: christine.struzik@cea.fr
THOUVENIN, Gilles CEA DEC/SESC/LSC Cadarache, Bât. 151 F-13108 St. Paul-lez-Durance Cedex	Tel: +33 (0)4 42 25 44 91 Fax: +33 (0)4 42 25 29 49 Eml: gilles.thouvenin@cea.fr
TOURASSE, Martine CEA DEC/SA3C Cadarache, Bât. 315 F-13108 St. Paul-lez-Durance Cedex	Tel: +33 (0)4 42 25 45 29 Fax: +33 (0)4 42 25 47 75 Eml: martine.tourasse@cea.fr
VALOT, Carole CEA DEC/SESC/LLCC Cadarache, Bât. 151 F-13108 St. Paul-lez-Durance Cedex	Tel: +33 (0)4 42 25 21 37 Fax: +33 (0)4 42 25 37 13 Eml: valot@drncad.cea.fr

VESCO, Philippe
FRAMATOME ANP Nuclear Fuel
Fuel Technologies
Design and Sales Division
10, rue Juliette Récamier
F-69456 Lyon Cedex 06

Tel: +33 (0)4 72 74 87 32
Fax: +33 (0)4 72 74 87 32
Eml: philippe.vesco@framatome-anp.com

WAECKEL, Nicolas
Électricité de France
12-14 Avenue Dutriévoz
F-69628 Villeurbanne Cedex

Tel: +33 (0)4 72 82 72 44
Fax: +33 (0)4 72 82 77 11
Eml: nicolas.waeckel@edf.fr

WEISS, Thomas
EDF/SEPTEN
12-14 Avenue Dutrievoz
F-69628 Villeurbanne Cedex

Tel: +49 (0)4 72 82 76 17
Fax: +49 (0)4 72 82 77 11
Eml: thomas.weiss@edf.fr

GERMANY

DEWES, Peter
FRAMATOME ANP GmbH
Freyeslebenstr. 1
D-91058 Erlangen

Tel: +49 9131 189 3778
Fax: +49 9131 189 5751
Eml: peter.dewes@framatome-anp.com

KOCK, Paul
TÜV Hannover/Sachsen-Anhalt e.V.
Am TÜV 1
D-30519 Hannover

Tel: +49 511 986 1131
Fax: +49 511 986 2899 3131
Eml: pkock@tuev-nord.de

LANDSKRON, Horst
Framatome-Anp GmbH
KWU NBTM
P.O. Box 3220
D-91050 Erlangen

Tel: +49 9131 18 92014
Fax: +49 9131 18 94799
Eml: Horst.Landskron@framatome-anp.de

SONTHEIMER, Fritz
FRAMATOME ANP GmbH, Abt. FGTM
Postfach 3220
Bunsenstrasse 43
D-91058 Erlangen

Tel: +49 9131 18 92856
Fax: +49 9131 18 94799
Eml: fritz.sontheimer@framatome-anp.com

HUNGARY

GRIGER, Agnes
KFKI Atomic Energy Research
Institute Budapest XII
Konkoly Thege ut 29-33
P.O. Box 49
H-1525 Budapest 114

Tel: +36 (1) 395 90 41
Fax: +36 (1) 395 91 62
Eml: griger@sunserv.kfki.hu

JAPAN

KAMIMURA, Katsuichiro
Reactor Core and Fuel Reliability Group
Safety Standard Division
Japan Nuclear Energy Safety Organization
Fujitakanko Toranomom Bldg. 7F
3-17-1 Toranomom, Minato-ku, Tokyo, 105-0

Tel: +81 3-4511-1770
Fax: +81-3-4511-1897
Eml: kamimura-katsuichiro@jnes.go.jp

KOREA (REPUBLIC OF)

CHEON, Jin-Sik
Korea Atomic Energy Research Institute
Yusong
PO Box 105
Taejon 305-600

Tel: +82 42-868-2648
Fax: +82 42-864-1089
Eml: jscheon@kaeri.re.kr

KIM, Jun-Hwan
Zirconium Fuel Cladding Team
Korea Atomic Energy Research Institute
PO Box 105
Yuseong, Daejeon, 305-600

Tel: +82 42-868-8623
Fax: +82 42-862-0432
Eml: junhkim@kaeri.re.kr

KIM, Young-Min
LWR Fuel Development Division
Korea Atomic Energy Research Institute
PO Box 105
Yuseong, Daejeon, 305-600

Tel: +82 42-868-8798
Fax: +82 42-863-0565
Eml: nymkim@kaeri.re.kr

RYU, Ho-Jin
Senior Researcher
Korea Atomic Energy Research Institute
150 Deokjin-dong, Yuseong-gu
Daejeon, 305-353

Tel: +82 42-868-8845
Fax: +82 42-868-8824
Eml: hjryu@kaeri.re.kr

NETHERLANDS

VAN BLOOIS, J.T.
NPP Borssele
Zeedijk 32
NL-4454 PM Borssele

Tel: +31 1 13 35 64 07
Fax: +31 1 13 35 24 34
Eml: j.van.bloois@epz.nl

ROMANIA

PARASCHIV, Adrieana
Institute for Nuclear Research
PO Box 78
0300 Pitesti

Tel: +40 248 213 400, Ext. 389
Fax: +40 248 262 449
Eml: mariusparaschiv@easynet.ro

RUSSIAN FEDERATION

BOUROUKINE, Andrey V.
Senior Researcher
FSUE "SSC RF RIAR"
Dimitrovgrad-10,
Ulyanovsk Region, 433510

Tel: +7 842 353 2021
Fax: +7 842 353 5648
Eml: adm@niiar.ru

KHVOSTOV, Grigori
A.A. Bochvar All Russian
Research Institute of Inorganic Materials
VNIINM
Str. Rogova 5, PO Box 369
123060 Moscow

Tel: +7 095 190 8192
Fax: +7 095 196 6591
Eml: grig@bochvar.ru

KORYSTINE, Leonid
A.A. Bochvar All Russia Institute
of Inorganic Material
Str. Rogov 5, PO Box 369
123060 Moscow

Tel: +7 095 190 8781
Fax: +7 095 742 5720
Eml: lion@bochvar.ru

KRYUKOV, Fedor N.
FSUE SSC of Russia
RIAR, Material Science Division
Dimitrovgrad 10
4333510 Ulyanovsk Region

Tel: +7 095 190 8192
Fax: +7 095 742 5720
Eml:

LIKHANSKII, Vladimir
SRC RF "TRINITI" Troitsk
Institute for Innovation and Fusion Research
142190 Troitsk, Moscow Region

Tel: +7 095 334 6182
Fax: +7 095 334 5158
Eml: likhansk@trinit.ru

POLENOK, Vladimir
SSC Institute of Atomic Reactors (RIAR)
Dimitrovgrad 10
4333510 Ulyanovsk Region

Tel: +7 842 353 2021
Fax: +7 842 353 5648
Eml:

SMIRNOV, Aleksei V.
Head of Laboratory, Deputy Head of Dept.
Research Institute of Atomic Reactors
NIIAR
433510, Dimitrovgrad, Ulyanovsk Region

Tel: +7 842 353 2021
Fax: +7 842 353 5648
Eml: jvv@niiar.ru

SPAIN

BARRIO, Felix
CIEMAT
Departamento de Fision Nuclear
Avenida Complutense 22
E-28040 Madrid

Tel: +34 913 46 62 36
Fax: +34 913 46 62 33
Eml: felix.barrio@ciemat.es

SERNA, Juan J.
Santiago Rusinol 12
ENUSA Industrias Avanzadas SA
E-28003 Madrid

Tel: +34 913 47 42 77
Fax: +34 913 47 42 15
Eml: jjs@enusa.es

SWEDEN

ALVAREZ, Anna-Maria
Studsvik Nuclear AB
SE-611 82 Nyköping

Tel: +46 (0)155 22 14 85
Fax: +46 (0)155 26 31 50
Eml: anna-maria.alvarez@studsvik.se

COSIN, Carolina
Studsvik Nuclear AB
SE-611 82 Nyköping

Tel: +46 (0)155 22 14 78
Fax: +46 (0)155 26 31 50
Eml: caroline.losin@studsvik.se

LINDBACK, Jan-Erik
SKI – Swedish Nuclear Power Inspectorate
SE-106 58 Stockholm

Tel: +46 (0)8 698 84 98
Fax: +46 (0)8 661 90 86
Eml: janerik.lindback@ski.se

LYSELL, Gunnar
Studsvik Nuclear AB
SE 611 82 Nyköping

Tel: +46 (0)155 22 16 62
Fax: +46 (0)155 26 31 56
Eml: Gunnar.Lysell@studsvik.se

NORDSTROEM, Eric
Nuclear Design and Analysis
PWR
Vatten Braensle AB
SE-16787 Stockholm

Tel: +46 (0)8 739 73 76
Fax: +46 (0)8 717 86 40
Eml: erik.c.nordstrom@vattenfall.com

RUDLING, Peter
ANT International
Ekbacken 33
SE-735 35 Surahammar

Tel: +46 (0)220 334 00
Fax: +46 (0)220 334 00
Eml: peter.rudling@antinternational.com

ZHOU, Gang
Fuel Performance Modeling
Westinghouse Electric Sweden AB
SE-72163 Västerås

Tel: +46 (0)21 34 72 36
Fax: +46 (0)21 34 75 80
Eml: Gang.zhou@se.westinghouse.com

SWITZERLAND

NORDSTROEM, Lars
Paul Scherrer Institute
CH-5232 Villigen PSI

Tel: +41 56 310 2737
Fax: +41 56 310 4726
Eml: ake.nordstroem@psi.ch

NORDSTROM, Lars Ake
Paul Scherrer Institute
CH-5232 Villigen PSI

Tel: +41 56 310 2737
Fax: +41 56 310 2205
Eml: ake.nordstroem@psi.ch

UNITED KINGDOM

BARKER, Matthew
BNFL
B582/2S
Sellafield, Seascale, Cumbria CA20 1PG

Tel: +44 (0)1 946 785978
Fax: +44 (0)1 946 775350
Eml: matthew.a.barker@bnfl.com

COOK, Paul M.A.
BNFL
Sellafield, Seascale, Cumbria, CA20 1PG

Tel: +44 (0)1 946 775937
Fax: +44 (0)1 946 785389
Eml: Paul.ma.cook@bnfl.com

HARBOTTLE, John
Severnvale Nuclear Services (SNS) Ltd.
The Beeches, Old Farm Court
Redhill Lane, Elberton, Bristol BS35 4AE

Tel: +44 (0)1 454 281240
Fax: +44 (0)1 454 281238
Eml: john.h@pfi.co.uk

SHEA, John
British Energy Nuclear Technology Branch
Engineering Division
Barnett Way, Barnwood
Gloucester GL4 3RS, Gloucestershire

Tel: +44 (0)1 452 653702
Fax: +44 (0)1 452 652206
Eml: john.shea@british-energy.com

TURNBULL, James Anthony
Cherry-Lyn
The Green
Tockington, Bristol BS32 4NJ

Tel: +44 (0)1 454 620887
Fax: +44 (0)1 454 620887
Eml: tonyt@cherry-lyn.demon.co.uk

WHITE, Rodney J.
18 Green Close
Uley, Dursley, Gloucestershire GL11 5TH

Tel: +44 (0)1 453 860046
Fax:
Eml: rodinuley@btinternet.com

UNITED STATES OF AMERICA

ARIMESCU, Viorel-Ioan
Pr. Engineer
FRAMATOME ANP
2101 Horn Rapids Road
Richland, WA 99352

Tel: +1 (509) 375-8411
Fax: +1 (509) 375-8965
Eml: ioan.arimescu@framatome-anp.com

BILLAUX, Michel R.
FRAMATOME ANP
2101 Horn Rapids Road
Richland, WA 99352

Tel: +1 (509) 375-8130
Fax: +1 (509) 375-88965
Eml: Michel.Billaux@framatome-anp.com

MITCHELL, David
Westinghouse Electric Company
5801 Bluff Road
Columbia, SC 29250

Tel: +1 (803) 647-3611
Fax: +1 (803) 695-4151
Eml: mitched@westinghouse.com

MONTGOMERY, Robert O.
Anatech Research Corporation
5435 Oberlin Drive
San Diego, CA 92121

Tel: +1 (858) 455-6350, Ext. 133
Fax: +1 (858) 455-1094
Eml: rob@anatech.com

RASHID, Joseph
Chairman
Anatech Research Corporation
5435 Oberlin Drive
San Diego, California 92121

Tel: +1 (858) 455-6350
Fax: +1 (858) 455-1094
Eml: joe@anatech.com

YAGNIK, Suresh K.
NFIR Program Manager
EPRI
Nuclear Power Sector
3412 Hillview Avenue
Palo Alto, CA 94304

Tel: +1 (650) 855-2971
Fax: +1 (650) 855-1076
Eml: syagnik@epri.com

INTERNATIONAL ORGANISATIONS

KILLEEN, John C.
Nuclear Fuel Cycle and Materials Section
IAEA
Wagramerstrasse 5
P.O.Box 100
A-1400 Vienna

Tel: +43 1 2600 22763
Fax: +43 1 2600 7 22763
Eml: j.killeen@iaea.org

SARTORI, Enrico
OECD/NEA Data Bank
Le Seine Saint-Germain
12 boulevard des Iles
F-92130 Issy-les-Moulineaux

Tel: +33 (0)1 45 24 10 72/78
Fax: +33 (0)1 45 24 11 10/28
Eml: sartori@nea.fr

VITANZA, Carlo
Nuclear Safety Division
OECD/NEA
Le Seine Saint-Germain
12, boulevard des Iles
F-92130 Issy-les-Moulineaux

Tel: +33 (0)1 45 24 10 62
Fax: +33 (0)1 45 24 11 29
Eml: carlo.vitanza@oecd.org

VAN UFFELEN, Paul
European Commission
Directorate General JRC
Institute for Transuranium Elements
Materials Research
Postfach 2340
D-76125 Karlsruhe

Tel: +49 7247 951 384
Fax: +49 7247 951 99 384
Eml: Paul.VanUffelen@itu.fzk.de

WALKER, Clive
European Commission
Joint Research Centre
Institute for Transuranium Elements
Postfach 2340
D-76125 Karlsruhe

Tel:
Fax: +49 (7247) 951 590
Eml: clive.walker@itu.fzk.de

TVERBERG, Terje
Institutt for Energiteknikk
OECD Halden Reactor Project
PO Box 173
N-1751 Halden

Tel: +47 69 21 23 43
Fax: +47 69 21 22 01
Eml: terjet@hrp.no

WIESENACK, Wolfgang
Project Manager
OECD Halden Reactor Project
Institutt for Energiteknikk
Os Alle 13, PO Box 173
N-1751 Halden

Tel: +47 69 21 2347
Fax: +47 69 21 2201
Eml: wowi@hrp.no

OECD PUBLICATIONS, 2, rue André-Pascal, 75775 PARIS CEDEX 16

PRINTED IN FRANCE

(66 2005 10 1 P) ISBN 92-64-01157-9 - No. 54167 2005